



**RMUTK**  
ราชภัฏนครปฐม

**BATTANAKOSIN**  
**RMUTR**

**BS**  
**RS**

**BANSOMDEJ**  
**CHAOPRAYA**  
RAJABHAT UNIVERSITY



**MAKE**



**nt**  
โทรคมนาคม  
แห่งชาติ



**KMITL** วิทยาเขตชุมพร  
**FIGHT TOGETHER**



# The 4<sup>th</sup> International Conference

**Vol.3** Informatics, Agriculture,  
Engineering, Sciences and Technology

**May 24 - 26, 2023**

King Mongkut's Institute of Technology Ladkrabang  
Prince of Chumphon Campus, Chumphon, Thailand

## Conference Proceedings The 4<sup>th</sup>

### International Conference on Informatics, Agriculture, Engineering, Sciences and Technology: IAMBEST 2023

#### **Organized by:**

King Mongkut's Institute of Technology Ladkrabang, Prince of Chumphon Campus and  
University Network

© Copyright 2022 King Mongkut's Institute of Technology Ladkrabang, Prince of Chumphon  
Campus All rights reserved. No part of this publication may be reproduced, stored in  
a retrieval system or transmitted in any form or by any means, electronic, mechanical,  
photocopying, recording or otherwise, without written permission from King Mongkut's  
Institute of Technology Ladkrabang, Prince of Chumphon Campus. All full papers in the  
proceedings are reviewed and accepted for publication. Responsibility for the contents of  
the papers rests with the authors.

**1<sup>st</sup> Published:** May 24<sup>th</sup>, 2023

**Cover Page Design:** Mr. Sarawut Sawasdee

#### **Published by:**

King Mongkut's Institute of Technology Ladkrabang Prince of Chumphon Campus,

Chumphon 17/1 Moo 6 Chumko Pathio Chumphon 86160 Thailand 86160

**Tel:** (+66) 77 506-410

## MESSAGE FROM THE EXECUTIVE VICE PRESIDENT KMITL, PRINCE OF CHUMPHON CAMPUS



The 4<sup>th</sup> International Conference on Informatics, Agriculture, Management, Business Administration, Engineering, Science and Technology (IAMBEST 2023) along with the 8<sup>th</sup> National Conference on Informatics, Agriculture, Management, Business Administration, Engineering, Science and Technology are the conference for academics, experts, and researchers in the six fields. The conferences are hosted by the King Mongkut's Institute of Technology Ladkrabang (KMITL), Prince of Chumphon Campus during the 24<sup>th</sup> – 26<sup>th</sup> of May 2023. The aim of this conference is the exchange stage of idea, knowledge, and research between the researchers from various fields. The continue development of the research provides the exchange the knowledge, connection, collaboration, and integration each other's. All above make the development the community, society, and country.

As the chairman of the IAMBEST 2023, I sincerely thank all committee members for your time and determination of organizing this wonderful conference. I thank all attendees and guests for sharing your research and innovation. The success of this conference is from all of you. I wish exchanging of idea and sharing of knowledge from this conference will give you another step to advance your knowledge and technology and to benefit your communities and countries.

Best wish to all of you.



(Assoc. Prof. Dr. Kamronwit Thipmanee)  
Executive Vice President,  
KMITL, Prince of Chumphon Campus  
Chairman of the Organizing Committee

## KEYNOTE SPEAKERS

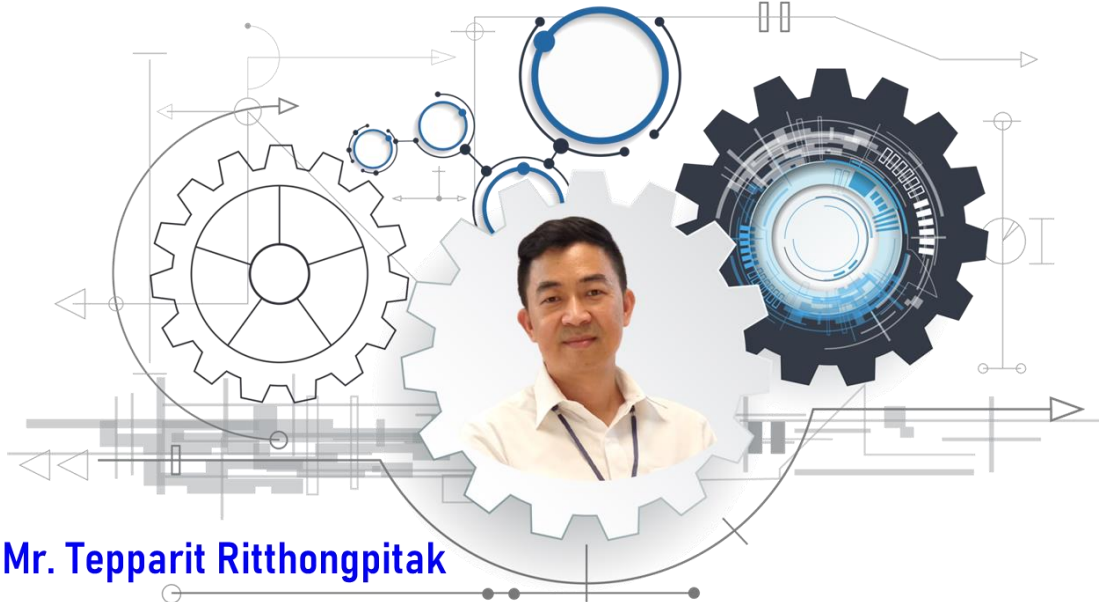
### Visual Sensors in Digital Transformation Era



**Prof. Dr. Kosin Chamnongthai**

**King Mongkut's University of Technology Thonburi  
Vice president (conference) of APSIPA Association**

### Smart Pier



**Mr. Tepparit Ritthongpitak**

**National Telecom Public Company Limited**

## Contents

<b>Message from the Executive Vice President</b>	I
<b>Keynote Speakers</b>	II
<b>Contents</b>	III
<b>Conference Program</b>	VIII
<b>List of reviewers</b>	XVII
<b>Oral Presentation</b>	1
<b>Group I: Informatics</b>	
OI-21 Decentralized identity application: how to use a verifiable credentials as an electronic signature to sign a contract online. <i>Yosnai Chanatrutipan and Nuttapong Chentanez</i>	2
<b>Group A: Agriculture</b>	
OA-13 Molecular characterization and tissue expression of <i>dnd</i> in striped catfish ( <i>Pangasianodon hypophthalmus</i> ) <i>Kunlanan Booncherd and Surintorn Boonanuntanasarn</i>	8
OA-30 Sulfur application rates affected grain yield and 2-acetyl-1- pyrroline content in fragrant rice <i>Sirilak Chaiboontha, Chananath Chanauksorn,         Paradee Thammapichai, Choochad Santasup and Fapailin Chaiwan</i>	14
OA-47 Short-term feeding of dietary Oestradiol-17 $\beta$ supplementation during fry stage did not increase female ratio in Snakeskin Gourami ( <i>Trichopodus pectoralis</i> ) <i>Apinat Kabpha, Suksan Kumkhong and Surintorn Boonanuntanasarn</i>	18
OA-79 Comparison of Hemp Producing Practices of Farmers in Chiang Mai and Tak Province <i>Ritdeach Suta and Juthathip Chalermphol</i>	23
<b>Group E: Engineering</b>	
OE-4 Model for prediction of tube diameter, and tube length of titanium dioxide nanotubes prepared by anodization. <i>Hathaiporn Sudchai and Ampai Chanachai</i>	28
OE-22 Performance study of Bifacial solar panel with and without Solar Tracking system <i>Jirayu Baengthit and Sarawut Polvongsri</i>	34

OE-25	Decarbonization Innovation Affecting Sustainability in Port Operations in Thailand <i>Kanokporn Nakchatree and Jaruwit Prabnasak</i>	40
OE-32	Effects of Potential Determining Ions on Dissolution of Dolomite during Low Salinity Waterflooding <i>Nuttapol Junput and Falan Srisuriyachai</i>	51
OE-43	SIZE SUITABLE OF SOLAR COMPRESSED AIR STORAGE SYSTEM FOR NILE TILAPIA PRODUCTION UNDER BIOFLOC SYSTEM <i>Theerapan Sangsuwan and Sarawut Polvongsri</i>	57
OE-60	Data-Driven Approach to Bogie Overhaul Planning <i>Panin Srisombat, Alexander Brezing, Nuksit Noomwongs and Sompoap Tala</i>	62
OE-74	Fish Food Pellet Characteristics After Coating Using Fluidized Bed Technique <i>Jatupat Maikaew, Chairat Phetkeri, Chayaphon Polnakarn, Nopadol Katpimol, Naruebodee Srisang and Siriwan Srisang</i>	67
OE-75	The Development of a Rain Storage System for Highland Agriculture Using Lightweight Composite Sandwich Panels <i>Alexander Nikolaus Brezing, Sirichai Torsakul, Chawalit Inpunyo, Julapot Chiravachradej, Anucha Watanapa, Eakanat Krajangthimaphorn and Wisitsree Wiyaratn</i>	72
OE-76	Preparation of polyvinyl alcohol and carboxymethyl cellulose hydrogel crosslinked with polyethylene glycol diacrylate for wound dressing <i>Paweena Meedecha, Patipat Srisongkram and Siriwan Srisang</i>	79
OE-81	Application of Monte Carlo Simulation Techniques for Appropriate Minibus Service Management During Rush Hours <i>Sanguan Vongchavalitkul, Marut Khodphan and Supagrid Prewthaisong</i>	84
OE-88	The effects of solution height and titanium dioxide photocatalyst concentration on atrazine photodegradation efficiency <i>Chatiya Ardchon, Chanintorn Patipatranon, Nootprawee Singkwang, Patthranit Wongpromrat and Hsisheng Teng</i>	89
OE-90	$\alpha$ -Tocopherol-Loaded Urushibara nickel as an Oxygen Scavenger <i>Khunpat Aksornnam, Penjit Srinophakun, Anusith Thanapimmetha, Nutchapon Chiarasumran and Maythee Saisriyoot</i>	94
OE-91	Crop Evapotranspiration Estimation Using Vegetation Index Method in the Northern Region of Thailand <i>Teerawat Suwanlertcharoen, Thanaporn Supriyasilp and Kobkiat Pongput</i>	98

OE-93	Physically-distributed hydrological model for the poorly gauged basin of Nong Han Lake <i>Thodsapol Chaturabul, Kobkiat Pongput, Thanaporn Supriyasilp and Jongkon Chongwilaikasem</i>	105
OE-95	Crash-Simulation-based Validation of a Safety-Frame Concept with Crash-Boxes for Maximized Protection of Motorcycle Taxi Passengers <i>Phairat Yuenyong and Alexander N. Brezing</i>	111
OE-99	Nanoporous carbon materials synthesized by carbonization of hemp waste as bio-based adsorbents <i>Korn Sukphunphoncharoen, Napat Kaewtrakulchai, Sutee Chutipaijit, Tawat Suriwong, Pramote Puengjinda, Gasidit Panomsuwan, Masayoshi Fuji and Apiluck Eiad-ua</i>	118
OE-106	An innovative solar reactor for thermochemical conversion process: concept design, fabrication, and temperature test <i>Atthawit Saengpradab, Jirayut Tathong, Hattakit Kongsrichay and Srirat Chuayboon</i>	122
OE-118	The Improvement of Loss Time Recording System for Grout Packing Process <i>Phummarin Thavitchasri and Jakrapan Nanthaphunkul</i>	126
OE-120	An investigation of micro-scale flow boiling in serpentine tube <i>Suphattharachai Khauntakob, Sira Saisorn, Adirek Suriyawong and Sakkarin Chingulpitak</i>	132
 <b>Group S: Sciences</b>		
OS-11	Effect of Irradiation and <i>Wolbachia</i> Endosymbiont on Flight Ability of <i>Aedes aegypti</i> Mosquito Vector <i>Jiraporn Yongyai, Parinda Thayanikul and Pattamaporn Kittayapong</i>	136
OS-29	Production of activated carbon from <i>Typha angustifolia</i> Linn. using ZnCl <sub>2</sub> and KOH as activating reagent <i>Lapprasertmesuk S. and Pornpakakul S.</i>	141
OS-35	The Optimal Portfolio in Semi-Static Investment with Multiple Maturity Assets by Conditional Value-at-Risk <i>Sirinya Nawamawat, Walailuck Chavanasporn, Phiraphat Sutthimat and Udomsak Rakwongwan</i>	145
OS-39	Isolation of gamma oryzanol through chromatographic and precipitation techniques <i>Muhammad Waqar Nasir and Surachai Pornpakakul</i>	152

OS-49	qNMR Application for the Quantification of eugenol and methyl eugenol in essential oil <i>Sirinat Chalkual and Surachai Pornpakakul</i>	155
OS-61	Forecasting PTT and BCP Stock Prices in the Stock Exchange of Thailand: An Application of ARIMA and ARIMAX Models <i>Patchanok Srisuradetchai</i>	160
OS-63	Thermal characteristic and morphology of biodegradable blends containing grafted nanocomposites <i>Phanitchanun Thanawattana and Siriwan Phattananarudee</i>	166
OS-100	Decomposing cortical alpha suppression during dexterity performance in healthy aging participants <i>Rodiya Manor, Dania Cheaha, Nifareeda Samerphob and Ekkasit Kumarnsit</i>	171
OS-102	Antiproliferative activity of Kratinphiman mushroom ( <i>Phellinus</i> sp.) extract against lung cancer and neuroblastoma cell lines <i>Kulrut Pichayaphinyo and Surachai Pornpakakul</i>	176
OS-122	Investigation of the GloA-homologous Gene Function under Stressful Conditions in <i>Pseudomonas aeruginosa</i> <i>Chalita Homjan, Jintana Duang-nkern and Adisak Romsang</i>	181
OS-123	Functional Characterization of <i>Pseudomonas aeruginosa</i> ppk encoding Polyphosphates Biosynthesis Enzyme in an Oxidative Protection from Host Immunity <i>Kritaun Thammakitkosol, Chanikarn Jantharakarnkun, Chularat Luangjindarat, Pongsak Utaisincharoen and Adisak Romsang</i>	187
<b>Group T: Technology</b>		
OT-50	Digital data analytics platform for Community Innovation 4.0 model community on the banks of the Mekong River, Nakhon Phanom Province. <i>Decha Wongpatsa, Montri Sangsuriyun and Saravut Rachamanee</i>	192
<b>Poster presentation</b>		
<b>Group E: Engineering</b>		
PE-68	Study on the efficiency of Nickel Manganese Cobalt Oxides cylindrical Li-ion battery under ambient temperature adjustment condition <i>Wiwat Keyoonwong, Nataphol Boonsai, Natthaphol Wongwiriyanukit, Nutthaphon Siripitakchai and Thanomphon Fungpaisanpong</i>	199



PE-70	Estimating efficiency and life cycle of different types of Li batteries for EVs <i>Wiwat Keyoonwong, Korn Ratsamipenyathip, Kamolpach Inkleang, Kulthida Klomkleang and Kunakorn Kakandee</i>	204
<b>Group S: Sciences</b>		
PS-24	A Novel Diazotizing Agent for Determination of Nitrite in Sausage <i>Aekgphoonnada Yenuthok, Tharinee Saleepochn, Saijai Charnsethikul and Pongsak Lowmunkhong</i>	210
PS-82	Fabrication and Characterization of Eco-friendly Ethyl Cellulose Nanofibers for Use as Air Filtration <i>Sarat Nudchapong, Jate Panichpakdee, Busarin Noikaew and Siriporn Larпкиattaworn</i>	215
PS-116	A Case Study on Ex Situ Conservation of Keaw Savoey and Nam Dok Mai Mango ( <i>Mangifera indica</i> L.) Trees from Ban Noin Thong, Ban Kho, Mueang District, Khon Kaen Province through Local Plantation <i>Preeya Puangsomlee Wangsomnuk</i>	219
PS-125	Isolation of rhizospheric and endophytic actinomycetes from five medicinal plants and their antimicrobial activities <i>Khanungkan Klanbut, Praewpilai Jaidee, Supanida Saykaew and Supawich Natanod</i>	225
PS-126	Isolation of acidophilic fungi for probable using in copper bioleaching process <i>Nilnate Assavasirijinda</i>	230

**The 8<sup>th</sup> National Conference and the 4<sup>th</sup> International Conference on Informatics, Agriculture,  
Management, Business administration, Engineering, Sciences and Technology**

24 - 26 May 2023

Hybrid Conference

Time	Activity	Room
May 24, 2023		
08.30-08.50 am	Registration: Invention & innovation competition/ Academic seminar	Building C
08.50-09.30 am	Opening ceremony for Invention & innovation competition Opening remarks by Assoc. Prof. Dr. Kamronwit Thipmanee Executive Vice President, KMTIL, Prince of Chumphon Campus	D406
09.30-10.30 am	Academic seminar (Thai language): Digital Transformation in Agriculture by LoRaWAN for Smart and Precision Farming By Assoc. Prof. Dr. Sarawut Chaimoon Khon Kaen University	
10.30-12.00 am	Invention & Innovation Competition: High school education/ Vocational education/ Undergraduate	Building D & E
12.00-01.00 pm	Lunchtime	
01.00-02.30 pm	Invention & Innovation Competition: Undergraduate	Building D & E
02.30-04.00 pm	Award declarations: Invention & innovation competition	D406
06.00-08.00 pm	Welcome dinner	E301
May 25, 2023		
08.30-08.50 am	Registration	Building C
08.50-09.00 am	Opening Ceremony for IAMBEST 2023 Opening remarks by Assoc. Prof. Dr. Kamronwit Thipmanee Executive Vice President, KMTIL, Prince of Chumphon Campus	D406
09.00-09.40 am	Keynote address: Visual Sensors in Digital Transformation Era By Professor Dr. Kosin Chamnongthai King Mongkut's University of Technology Thonburi/ Vice president (conference) of APSIPA Association	
09.40-10.20 am	Keynote address: Smart Pier By Mr. Tepparit Ritthongpitak National Telecom Public Company Limited	
10.20-10.30 am	Coffee break	
10.30-10.55 am	Memorandum of Understanding: Smart Digital/ Telecommunication	D406
10.30-12.00 am	Posters and Oral Presentations International conference (Oral presentation) Session 1 Engineering Session 3 Social Science & Humanities Session 4 Agriculture	BA208 E109 BA207

	International conference (Poster presentation)	
	Session 2 Engineering and Sciences	E108/ E301
	National conference (Oral presentation)	
	Session 1 Informatics and Engineering	E306
	Session 2 Sciences	E302
	Session 3 Management and Business administration	E305
	Session 4 Management and Business administration	E103
	Session 5 Agriculture	E303
	Session 6 Technology	E104
	National conference (Poster presentation)	
	Session 2 Sciences and Engineering	E302/ E301
12.00-01.00 pm	Lunchtime	
01.00-03.30 pm	Posters and Oral Presentations (Continuation)	
	International conference (Oral presentation)	
	Session 1 Engineering	BA208
	Session 2 Sciences	E108
	Session 3 Informatics, Technology and Engineering	E109
	Session 4 Management	BA207
	National conference (Oral presentation)	
	Session 1 Informatics and Engineering	E306
	Session 4 Management and Business administration	E103
	Session 5 Agriculture	E303
	Session 6 Social Sciences & Humanities	E104
	National conference (Poster presentation)	
	Session 5 Agriculture	E301
04.30 pm	Award declarations: IAMBEST2023	D406
06.00-08.00 pm	Dinner	
May 26, 2023		
09.00 am –	Knowledge sharing	
04.00 pm		

IAMBEST 2023 PROGRAM

May 25, 2023

Oral International Section 1 I: Informatics E: Engineering

Chairperson	Assoc. Prof. Dr. Sira Saisorn	KMITL Prince of Chumphon
	Assoc. Prof. Dr. Weerapun Duangthongsuk	Southeast Asia University
Time	Code	Topic
10.30 - 10.45	OE-25	Decarbonization Innovation Affecting Sustainability in Port Operations in Thailand <i>Kanokporn Nakchatree and Jaruwit Prabnasak</i>
10.45 - 11.00	OE-43	Size Suitable of Solar Compressed Air Storage System for Nile Tilapia Production Under Biofloc System <i>Theerapan Sangsuwan and Sarawut Polvongsri</i>
11.00 - 11.15	OE-74	Fish Food Pellet Characteristics After Coating Using Fluidized Bed Technique <i>Jatupat Maikaew Chairat Phetkeri Chayaphon Polnakarn Nopadol Katpimol Naruebodee Srisang and Siriwan Srisang</i>
11.15 - 11.30	OE-76	Preparation of polyvinyl alcohol and carboxymethyl cellulose hydrogel crosslinked with polyethylene glycol diacrylate for wound dressing <i>Paweena Meedecha Patipat Srisongkram and Siriwan Srisang</i>
11.30 - 11.45	OE-106	An innovative solar reactor for thermochemical conversion process: concept design, fabrication, and temperature test <i>Atthawit Saengpradab Jirayut Tathong Hattakit Kongsrichay and Srirat Chuayboon</i>

IAMBEST 2023 PROGRAM

May 25, 2023

Oral International Section 1 E: Engineering

Chairperson	Asst. Prof. Dr. Siriwan Srisang	KMITL Prince of Chumphon
	Assoc. Prof. Dr. Punyawit Jamjareegulgarn	KMITL Prince of Chumphon
Time	Code	Topic
13.00 - 13.15	OE-90	<b>α</b> -Tocopherol-Loaded Urushibara nickel as an Oxygen Scavenger <i>Khunpat Aksornnam Penjit Srinophakun Anusith Thanapimmetha Nutchapon Chiarasumran and Maythee Saisriyoot</i>
13.15 - 13.30	OE-91	Crop Evapotranspiration Estimation Using Vegetation Index Method in the Northern Region of Thailand <i>Teerawat Suwanlertcharoen Thanaporn Supriyasilp and Kobkiat Pongput</i>
13.30 - 13.45	OE-93	Physically-distributed hydrological model for the poorly gauged basin of Nong Han Lake <i>Thodsapol Chaturabul Kobkiat Pongput Thanaporn Supriyasilp and Jongkon Chongwilaikasem</i>
13.45 - 14.00	OE-95	Crash-Simulation-based Validation of a Safety-Frame Concept with Crash-Boxes for Maximized Protection of Motorcycle Taxi Passengers <i>Phairat Yuenyong and Alexander N. Brezing</i>
14.00 - 14.15	OE-99	Nanoporous carbon materials synthesized by carbonization of hemp waste as bio-based adsorbents <i>Korn Sukphunphoncharoen Napat Kaewtrakulchai Sutee Chutipajjit Tawat Suriwong Pramote Puengjinda Gasidit Panomsuwan Masayoshi Fuji and Apiluck Eiad-ua</i>
14.15 - 14.30	OE-118	The Improvement of Loss Time Recording System for Grout Packing Process <i>Phummarin Thavitchasri and Jakrapan Nanthaphunkul</i>
14.30 - 14.45	OE-120	An investigation of micro-scale flow boiling in serpentine tube <i>Suphattharachai Khauntakob Sira Saisorn Adirek Suriyawong and Sakkarin Chingulpitak</i>
14.45 - 15.00	OE-22	Performance study of Bifacial solar panel with and without Solar Tracking system <i>Jirayu Baengthit and Sarawut Polvongsri</i>

IAMBEST 2023 PROGRAM

May 25, 2023

Oral International Section 2 S: Sciences

<b>Chairperson</b>	Asst. Prof. Dr. Jongjit Jantra	KMITL Prince of Chumphon
<b>Co-chairperson</b>	Asst. Prof. Dr. Sujittra Poorahong	Walailak University
<b>Committee</b>	Dr. Usa Sukkha	KMITL Prince of Chumphon
	Asst. Prof. Dr. Sirichatnach Pakdeepromma	KMITL Prince of Chumphon
	Dr. Monsicha Tipawanna	KMITL Prince of Chumphon
Time	Code	Topic
13.00 - 13.15	OS-63	Thermal characteristic and morphology of biodegradable blends containing grafted nanocomposites <i>Phanitchanun Thanawattana and Siriwan Phattanarudee</i>
13.15 - 13.30	OS-29	Production of activated carbon from <i>Typha angustifolia</i> Linn. using ZnCl <sub>2</sub> and KOH as activating reagent <i>Suchanya Lapprasertmesuk and Surachai Pornpakakul</i>
13.30 - 13.45	OS-39	Isolation of gamma oryzanol through chromatographic and precipitation techniques <i>Muhammad Waqar Nasir and Surachai Pornpakakul</i>
13.45 - 14.00	OS-49	qNMR Application for the Quantification of eugenol and methyl eugenol in essential oil <i>Sirinat Chalkual and Surachai Pornpakakul</i>
14.00 - 14.15	OS-11	Effect of Irradiation and <i>Wolbachia</i> Endosymbiont on Flight Ability of <i>Aedes aegypti</i> Mosquito Vector <i>Jiraporn Yongyai Parinda Thayanikul and Pattamaporn Kittayapong</i>
14.15 - 14.30	OS-100	Decomposing cortical alpha suppression during dexterity performance in healthy aging participants <i>Rodiya Manor Dania Cheaha Nifareeda Samerphob and Ekkasit Kumansit</i>

IAMBEST 2023 PROGRAM

May 25, 2023

Oral International Section 2 S: Sciences

<b>Chairperson</b>	Asst. Prof. Dr. Jongjit Jantra	KMITL Prince of Chumphon
<b>Co-chairperson</b>	Asst. Prof. Dr. Sujittra Poorahong	Walailak University
<b>Committee</b>	Dr. Usa Sukkha	KMITL Prince of Chumphon
	Asst. Prof. Dr. Sirichatnach Pakdeepromma	KMITL Prince of Chumphon
	Dr. Monsicha Tipawanna	KMITL Prince of Chumphon
Time	Code	Topic
14.30 - 14.45	OS-102	Antiproliferative activity of Kratinphiman mushroom ( <i>Phellinus</i> sp.) extract against lung cancer and neuroblastoma cell lines <i>Kulrut Pichayaphinyo and Surachai Pornpakakul</i>
14.45 - 15.00	OS-122	Investigation of the GloA-homologous Gene Function under Stressful Conditions in <i>Pseudomonas aeruginosa</i> <i>Chalita Homjan Jintana Duang-nkern and Adisak Romsang</i>
15.00 - 15.15	OS-123	Functional Characterization of <i>Pseudomonas aeruginosa</i> ppk encoding Polyphosphates Biosynthesis Enzyme in an Oxidative Protection from Host Immunity <i>Kritaun Thammakitkosol Chanikam Jantharakamkun Chularat Luangjindarat Pongsak Utaisincharoen and Adisak Romsang</i>
15.15 - 15.30	OS-35	The Optimal Portfolio in Semi-Static Investment with Multiple Maturity Assets by Conditional Value-at-Risk <i>Sirinya Nawamawat Walailuck Chavanasporn Phiraphat Sutthimat and Udomsak Rakwongwan</i>
15.30 - 15.45	OS-61	Forecasting PTT and BCP Stock Prices in the Stock Exchange of Thailand: An Application of ARIMA and ARIMAX Models <i>Patchanok Srisuradetchai</i>

IAMBEST 2023 PROGRAM

May 25, 2023

Oral International Section 3 T: Technology E: Engineering		
Chairperson		Assoc. Prof. Dr. Chaiwat Rattanamechaikul Asst. Prof. Dr. Kittisak Phetpan
		KMITL Prince of Chumphon KMITL Prince of Chumphon
Time	Code	Topic
13.00 - 13.15	OT-50	Digital data analytics platform for Community Innovation 4.0 model community on the banks of the Mekong River, Nakhon Phanom Province. <i>Decha Wongpatsa Montri Sangsuriyun and Saravut Rachamanee</i>
13.15 - 13.30	OE-4	Model for prediction of tube diameter, and tube length of titanium dioxide nanotubes prepared by anodization <i>Hathaiporn Sudchai and Ampai Chanachai</i>
13.30 - 13.45	OE-32	Effects of Potential Determining Ions on Dissolution of Dolomite during Low Salinity Water flooding <i>Nuttapol Junput and Falan Srisuriyachai</i>
13.45 - 14.00	OE-60	Data-Driven Approach to Bogie Overhaul Planning <i>Panin Srisombat Alexander Brezing Nuksit Noomwongs and Sompoap Talabgaew</i>
14.00 - 14.15	OE-81	Application of Monte Carlo Simulation Techniques for Appropriate Minibus Service Management During Rush Hours <i>Sanguan Vongchavalitkul Marut Khodphan and Supagrid Prewthaisong</i>
14.15 - 14.30	OE-88	The effects of solution height and titanium dioxide photocatalyst concentration on atrazine photodegradation efficiency <i>Chatiya Ardchon Chanintorn Patipattranon Nootprawee Singkwang Patthranit Wongpromrat and Hsisheng Teng</i>
14.30 - 14.45	OE-75	The Development of a Rain Storage System for Highland Agriculture Using Lightweight Composite Sandwich Panels <i>Alexander Nikolaus Brezing Sirichai Torsakul Chawalit Inpunyo Julapot Chiravachradej Anucha Watanapa Eakanat Krajangthimaporn and Wisitsree Wiyaratn</i>
14.45 - 15.00	OI-21	Decentralized identity application: how to use a verifiable credentials as an electronic signature to sign a contract online. <i>Yosnai Chanatrutipan and Nuttapong Chentanez</i>



IAMBEST 2023 PROGRAM

May 25, 2023

Oral International Section 4 A: Agriculture

<b>Chairperson</b>	Assist. prof. Dr. Hathairat Chokthaweepanich	School of Integrated Science, Kasetsart University
	Assoc. Prof. Dr. Pornprapa Kongtragoul	KMITL Prince of Chumphon
Time	Code	Topic
10.30 - 10.45	OA-13	Molecular characterization and tissue expression of <i>dnd</i> in striped catfish ( <i>Pangasianodon hypophthalmus</i> ) <i>Kunlanan Booncherd and Surintorn Boonanuntanasarn</i>
10.45 - 11.00	OA-30	Sulfur application rates affected grain yield and 2-acetyl-1-pyrroline content in fragrant rice <i>Sirilak Chaiboontha Chananath Chanauksorn Paradee Thammapichai Choochad Santasup and Fapailin Chaiwan</i>
11.00 - 11.15	OA-47	Short-term feeding of dietary Oestradiol-17 $\beta$ supplementation during fry stage did not increase female ratio in Snakeskin Gourami ( <i>Trichopodus pectoralis</i> ) <i>Apinat Kabpha Suksan Kumkhong and Surintorn Boonanuntanasarn</i>
11.15 - 11.30	OA-79	Comparison of Hemp Producing Practices of Farmers in Chiang Mai and Tak Province <i>Ritdeach Suta and Juthathip Chalermphol</i>

IAMBEST 2023 PROGRAM

May 25, 2023

Poster International Section 2 E: Engineering S: Sciences

<b>Chairperson</b>	Assoc. Prof. Dr. Apiluck Eiad-Ua	KMITL
	Asst. Prof. Dr. Jongjit Jantra	KMITL Prince of Chumphon
	Dr. Usa Sukkha	KMITL Prince of Chumphon
<b>Time</b>	<b>Code</b>	<b>Topic</b>
10.30 - 10.40	PE-68	Study on the efficiency of Nickel Manganese Cobalt Oxides cylindrical Li-ion battery under ambient temperature adjustment condition <i>Wiwat Keyoonwong Nataphol Boonsai Natthaphol Wongwiriyanukit Nutthaphon Siripitakchai and Thanomphon Fungpaisonpong</i>
10.40 - 10.50	PE-70	Estimating efficiency and life cycle of different types of Li batteries for EVs <i>Wiwat Keyoonwong Korn Ratsamipenyathip Kamolpach Inkleang Kulthida Klomkleang and Kunakorn Kakandee</i>
10.50 - 11.00	PS-116	A Case Study on Ex Situ Conservation of Keaw Savoey and Nam Dok Mai Mango ( <i>Mangifera indica</i> L.) Trees from Ban Noin Thong, Ban Kho, Mueang District, Khon Kaen Province through Local Plantation <i>Preeya Puangsomlee Wangsomnuk</i>
11.00 - 11.10	PS-125	Isolation of rhizospheric and endophytic actinomycetes from five medicinal plants and their antimicrobial activities <i>Khanungkan Klanbut Praewpilai Jaidee Supanida Saykaew and Supawich Natanod</i>
11.10 - 11.20	PS-82	Fabrication and Characterization of Eco-friendly Ethyl Cellulose Nanofibers for Use as Air Filtration <i>Sarat Nudchamong Jate Panichpakdee Busarin Noikaew and Siriporn Larpiattaworn</i>
11.20 - 11.30	PS-24	A Novel Diazotizing Agent for Determination of Nitrite in Sausage <i>Aekgphoonnada Yenuthok Tharinee Saleepochn Saijai Charnsethikul and Pongsak Lowmunkhong</i>
11.30 - 11.45	PS-126	Isolation of acidophilic fungi for probable using in copper bioleaching process <i>Nilnate Assavasirijinda</i>

## List of reviewers

Asst. Prof. Dr. Anirut Kantasa-Ard	Burapha University, Thailand
Asst. Prof. Dr. Mintra Seel-audom	Chiang Mai University, Thailand
Assoc. Prof. Dr. Wasana Prachayasakul	Chiang Mai University, Thailand
Dr. Jassada Saingamsook	Chiang Mai University, Thailand
Dr. Kittipat Aupalee	Chiang Mai University, Thailand
Asst. Prof. Dr. Chanchai Boonla	Chulalongkorn University, Thailand
Asst. Prof. Dr. Chodsana Sriket	Dusit Thani College, Thailand
Dr. Kutubuddin Ansari	Integrated Geoinformation (IntGeo) Solution Private Limited, India
Asst. Prof. Dr. Satid Chatchaiphan	Kasetsart University, Thailand
Assoc. Prof. Dr. Panchit Seeniang	Kasetsart University, Kamphaeng Saen Campus, Thailand
Asst. Prof. Dr. Duangkamol Panrosthip Thunmathiwat	King Mongkut's Institute of Technology Ladkrabang, Thailand
Asst. Prof. Dr. Lin Min Min Myint	King Mongkut's Institute of Technology Ladkrabang, Thailand
Asst. Prof. Dr. Nattawut Chaomuang	King Mongkut's Institute of Technology Ladkrabang, Thailand
Asst. Prof. Dr. Patthranit Wongpromrat	King Mongkut's Institute of Technology Ladkrabang, Thailand
Dr. Jiraphat Yokrattanasak	King Mongkut's Institute of Technology Ladkrabang, Thailand
Assoc. Prof. Dr. Raumjit Nokkoul	King Mongkut's Institute of Technology Ladkrabang, Prince of Chumphon, Thailand
Assoc. Prof. Dr. Pornprapa Kongtragoul	King Mongkut's Institute of Technology Ladkrabang, Prince of Chumphon, Thailand
Asst. Prof. Acting Sub Lt. Dr. Kittisak Phetpan	King Mongkut's Institute of Technology Ladkrabang, Prince of Chumphon, Thailand
Asst. Prof. Dr. Duangjai Pisuttharachai	King Mongkut's Institute of Technology Ladkrabang, Prince of Chumphon, Thailand
Asst. Prof. Dr. Sarun Duangsuwan	King Mongkut's Institute of Technology Ladkrabang, Prince of Chumphon, Thailand
Asst. Prof. Dr. Thiamphop Kanloun	King Mongkut's Institute of Technology Ladkrabang, Prince of Chumphon, Thailand
Asst. Prof. Dr. Rattapong Suwalak	King Mongkut's Institute of Technology Ladkrabang, Prince of Chumphon, Thailand
Asst. Prof. Dr. Chanadda Phawachalotorn	King Mongkut's Institute of Technology Ladkrabang, Prince of Chumphon, Thailand
Asst. Prof. Dr. Jongjit Jantra	King Mongkut's Institute of Technology Ladkrabang, Prince of Chumphon, Thailand
Asst. Prof. Dr. Piyada Tavitchasri	King Mongkut's Institute of Technology Ladkrabang, Prince of Chumphon, Thailand
Asst. Prof. Dr. Sirichatnach Pakdeepromma	King Mongkut's Institute of Technology Ladkrabang, Prince of Chumphon, Thailand
Dr. Albert Abad Braga	King Mongkut's Institute of Technology Ladkrabang, Prince of Chumphon, Thailand
Dr. Naruethai Chanthap	King Mongkut's Institute of Technology Ladkrabang, Prince of Chumphon, Thailand
Dr. Punjapha Pitigraisorn	King Mongkut's Institute of Technology Ladkrabang, Prince of Chumphon, Thailand

Dr. Usa Sukkha	King Mongkut's Institute of Technology Ladkrabang, Prince of Chumphon, Thailand
Ms. Kanchalar Keeratirawee	King Mongkut's Institute of Technology Ladkrabang, Prince of Chumphon, Thailand
Ms. Yenying Chongchit	King Mongkut's Institute of Technology Ladkrabang, Prince of Chumphon, Thailand
Asst. Prof. Dr.Santi Chuetor	King Monkut's University of Technology North Bangkok, Thailand
Prof. Dr. Maurice Yolles	Liverpool John Moores University, The United Kingdom
Assoc. Prof. Dr. Sakda Yainoy	Mahidol University, Thailand
Assoc. Prof. Dr. Nittaya Junka	Nakhon Pathom Rajabhat University, Thailand
Dr. Wanwitoo Wanmolee	National Nanotechnology Center, NSTDA, Thailand
Dr. Sunpet Assavapanumat	Nuovo plus Co., Ltd., Thailand
Asst. Prof. Dr. Chairat Burana	Panyapiwat Institute of Management, Thailand
Assoc. Prof. Dr. Chongdee Buranachai	Prince of Songkla University, Thailand
Assoc. Prof. Dr. Kwanruthai Tadpetch	Prince of Songkla University, Thailand
Assoc. Prof. Dr. Sirinya Chantarak	Prince of Songkla University, Thailand
Asst. Prof. Dr. Natta Tansila	Prince of Songkla University, Thailand
Dr. Kunlapat Thongkaew	Prince of Songkla University, Thailand
Dr. Aekkaraj Nualla-ong	Prince of Songkla University, Thailand
Assoc. Prof. Dr. Aniruth Phon-on	Prince of Songkla University, Pattani Campus, Thailand
Asst. Prof. Dr. Nifatamah Makaje	Prince of Songkla University, Pattani Campus, Thailand
Asst.Prof.Dr. Kittisak Tinpun	Prince of Songkla University, Pattani Campus, Thailand
Asst.Prof.Dr.Yaowaphan Sontikun	Prince of Songkla University, Suratthani Campus, Thailand
Mr. Putipong Lakachaiworakun	Rajamangala University of Technology Phra Nakhon, Thailand
Dr. Pathomporn Narato	Rajamangala University of Technology Srivijaya, Thailand
Assoc. Prof. Dr. Siriwan Teepoo	Rajamangala University of Technology Thanyaburi, Thailand
Assoc. Prof. Dr. Sompong Sansenya	Rajamangala University of Technology Thanyaburi, Thailand
Asst. Prof. Dr. Kanokorn Wechakorn	Rajamangala University of Technology Thanyaburi, Thailand
Dr. Chehasan Cheubong	Rajamangala University of Technology Thanyaburi, Thailand
Dr. Pornpong Sakdapat	Securities and Exchange Commission, Thailand
Dr. Orawan Aumporn	Silpakorn University, Thailand
Dr. Petcharat Lovichakorntikul	Stamford International University, Thailand
Dr. Chutinan Noobutra	Suratthani Rajabhat University, Thailand
Asst. Prof. Dr. Chutima Kaewpi boon	Thaksin University, Thailand
Dr. Tanawat Srirugsa	Thaksin University, Thailand
Dr. Kanjana Ongkasin	Ubon Ratchathani University, Thailand
Asst. Prof. Dr. Napapan Kangwan	University of Phayao, Thailand
Asst. Prof. Dr. Wittaya Chaiwangyen	University of Phayao, Thailand
Asst. Prof. Dr. Sujittra Poorahong	Walailak University, Thailand

# **Oral Presentation**

# Decentralized identity application: how to use a verifiable credentials as an electronic signature to sign a contract online.

**Yosnai Chanatrutipan, Nuttapong Chentanez**

Department of Computer Engineering, Faculty of Engineering, Chulalongkorn University

**Abstract:** In this paper, I proposed a new method to digitally sign a contract using the verifiable credential, a new open standard for digital credential base on decentralized identity framework created by W3C organization, in which the user credential can be verified by a secure cryptographic algorithm directly from the blockchain. The contracts signed with this method are secured, tampered-proof, time-stamped, and completely anonymous. Its integrity can be verified and authenticated by anyone without having to go through the authoritative source or identity provider.

**Index Terms—** blockchain, contract signing, digital signature, decentralized identity, ION blockchain, BITCOIN, Ethereum, verifiable credentials, verifiable presentation

## I. INTRODUCTION

A good requirement for signing a contract online depends on the level of security and authenticity required for the contract in question. A contract between schools and parents about the small deposit fee would not need the same level of integrity as the contract between two companies dealing with millions of dollars. In this paper, we will focus on the contracts that are highly staked, meaning that the contract should be signed in a secure manner.

A contract can be signed digitally with an electronic signature. The electronic signature can be anything that can be used to verify the owner, such as a digital hand-drawing, a name in a plaintext format typed in Microsoft word, a signature created from the secure cryptographic method, or a signature issued by a trusted authority. In legal setting, all signatures are equally valid and legally equivalence to the handwritten signature done on paper. However, using a too-simple signature can lead to a problem later. For example, it would be hard to prove that the digital hand drawing signature belongs to a certain person. This type of signature can also be forged. However, if one uses an electronic signature created from a cryptographic algorithm or one that was issued by a trusted authority, then their signature can be verified and traced back to the real identity of signer. This type of signature is recommended when dealing with a contract that is high staked. The standard way to obtain such a signature is through a trusted third party such as certificate authority or private identity provider company.

However, the certificate authority or private company is centralized by nature, which has a single point of failure and a privacy problem. We will discuss these issues in Section II and propose a solution in the Section III.

There are two important requirements that all digital contracts should have, the quality of the signature, and the fairness of the signing process.

First, the quality of the signature and the identity of the signer. Both parties should be able to verify each other identity before the signing process begin and the signature itself must be verifiable and timestamped with a secure cryptographic method. The signature should also be non-repudiable, which means that the signers cannot refuse that they sign the contract later. The de facto standard is to use a digital certificate issued by the certificate authority as a proof of identity that links cryptographic signature to the real-world identity.

Second, the signing process must be fair. In the past, both parties came face to face and signed a contract at the same place and at the same time. They also receive the same copy of the signed document. However, it is hard to achieve this level of fairness in an online setting since simultaneous exchange is hard to achieve. Generally, both parties have to take turns sending each other information over an email and sign the contract alternately. This can be disadvantageous to one party and disadvantageous to another. The solution to this is to use a trusted third party to act as an intermediary. However, this solution comes with a privacy and security concern. The trusted third party can be malicious, and even if they are not malicious, they can still see and record the

user's activity. For example, company A wants to sign an agreement with company B. To make an online signing as fair and as professional as possible, they use a trusted third-party contract signing service provided by company C. Company C may leak the confidential detail that company A and company B are in contacted, which might cause financial trouble or bad publicity.

In this paper, we will use the verifiable credentials as the means to sign the contract, to authenticate the signature, and to verify the integrity of the signed contract. As for the fair signing process, we will discuss on how to build an application that can handle the signing operation that does not jeopardize the user privacy.

## II. BACKGROUND KNOWLEDGE

The verifiable credentials are digital credentials that can be self-verified using a cryptographic algorithm. It utilized the power of the blockchain, basically making it virtually impossible to be tampered with. We will use verifiable credentials to link our identity to the signature that we use to sign a contract. You can think of verifiable credentials as a digital ID that are integrated with the blockchain. Let's review the fundamental concept of the decentralized framework.

### A. Digital signature and public key infrastructure (PKI)

Using a secure cryptographic method, each person generates key pairs, the public key, and the private key. The public key can be shared with anyone, while the private key is the secret only known to the owner. The document can be signed with the private key, producing a piece of code called digital signature. This digital signature can be used as a non-repudiation proof that the signer with the corresponding public key did indeed sign the message. Anyone can use the author's public key, along with the digital signature to verify the integrity and authenticity of the signed document. However, these keys and digital signatures alone cannot be used to identify the real-world identity of the signer. The use of a third-party services such as certificate authority is needed to link the cryptographic key (online identity), to the real-world identity.

### B. Certificate authority (CA)

A certificate authority is a trusted third party that issues digital certificates, which are used to establish the identity of individuals, organizations, and devices in a secure manner. Digital certificates contain information about the identity of the certificate owner, as well as an owner's public key.

A certificate authority is responsible for verifying the identity of individuals and organizations before issuing digital certificates to them. They use a variety of methods to verify identity, including checking government-issued identification documents, verifying business licenses, and performing background checks. Once an individual or

organization's identity has been verified, the certificate authority issues a digital certificate that can be used to establish their identity and sign the document.

A Certificate authority plays a crucial role in the operation of many online systems, including ecommerce, online banking, and other applications that require secure communication and authentication. They are typically highly trusted entities, and their digital certificates are widely accepted as evidence of identity in online contexts.

The simplest way to think about digital certificate in the context of our paper, is to see them as an electronic file that can be used to authenticates the identity of the individual from their cryptographic key. For example, Bob can use his private key to sign a contract. Anyone can use Bob's public key to verify that Bob is the one who signed the contract. The digital certificate is then used to verify whether this public key belongs to the real Bob or not.

### C. Blockchain

Blockchain is a special type of a distributed ledger. The simplest way to understand blockchain is to think of it as a digital ledger. Back in the old day, a ledger is a book where all transaction is recorded. Now, instead of one book, there are many identical copies of that book held by different person. All of them keep checking each other book to make sure that all their book are identical. Whenever a new record is to be added, there must be a consensus among all the book holders. This is called a consensus mechanism.

The blockchain works in the same way. Instead of multiple books, we store the same data on different computers, or in other word, a network. Transactions are stored in block. Each block represents a group of transactions, a new block is appended to the previous block forming a chain of blocks, hence the name Blockchain. Note that there exist hundreds of blockchain networks. The most popular ones being Bitcoin and Ethereum. The difference between each blockchain is irrelevant to our work

One benefit of the blockchain is that it is decentralized. No single entity has control over it. It is also protected by cryptographic algorithms making it less vulnerable to hacking. Blockchain can be used more than just for financial transactions. For example, it can be used to store information or create a new digital currency.

In this paper, we use blockchain to store the proof of identity. Have you ever had to perform KYC for different services? e.g., scanning your face, uploading the picture of your ID for the mobile banking application. Instead of doing this each time for different service, we do it once, and store that proof on the blockchain. Now, we can reuse our proof of identity to apply for a new service as many times as we want without having to perform a KYC again and again. Note that, this proof of identity is stored on the

public blockchain, which anyone can look at. Therefore, we generally don't store all our information on it. When we obtain the proof of identity, we store part of it on blockchain and the rest privately on our own device. Everyone can view it, but only the owner who has the other part can make use of it. Anyone can also verify our credentials through the blockchain directly without a middleman or any authority. This concept is called Decentralized identity.

#### D. Decentralized identity

Decentralized identity is a system of identity management that uses blockchain technology to enable individuals and organizations to have more control over their own digital identities and personal data. In this system, identity information is stored in a decentralized manner, rather than being controlled by a single centralized authority. This means that individuals and organizations can use their own digital identities to access online services and resources, without having to rely on a central authority to verify their identity. Decentralized identity is currently being developed by multiple organizations. The leading organization are World Wide Web Consortium (W3C) and Decentralized Identities Foundation (DIF), whose goal are both to create an open ecosystem of decentralized identity that is accessible to anyone and interoperable across different organization.

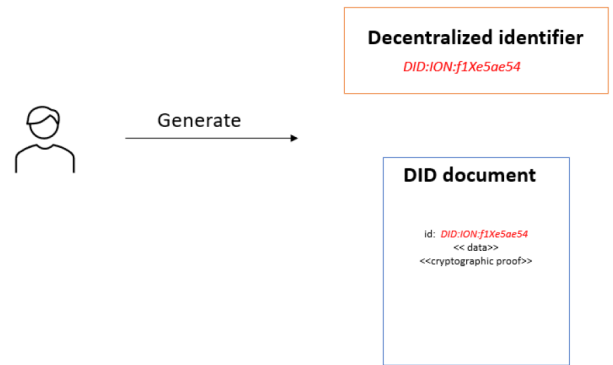
In the decentralized identity framework, each person is uniquely identified by a string, called Decentralized Identity Identifier (DID). It can be used to refer to any person or an organization. DID document is the document that contains a person decentralized information. This document is stored on the blockchain.

A credential is a claim about someone about something. For example, a diploma is a credential that proves a person graduate from a university. Credentials can be shared. The main problem with online credential is that it can be hard to verify online. Sometimes we want to verify to other parties that we are the legit owner of the credential, like presenting a diploma when applying for a job. It can be hard to trust someone online since the evidence can be forged, and a person can be impersonated. The verifiable credential is introduced to solve this problem.

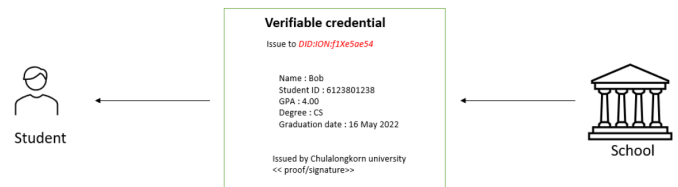
A verifiable credential is a digital credential combined with a digital signature. Its ownership and integrity can be verified through a cryptographic algorithm hence the name "verifiable". It can be verified by anyone, but only an owner can claim it. The verification and the proof of ownership does not require any trusted third party to perform unlike their digital certificate counterpart. Once issued, it stays on the owner device and does not exist anywhere else. The owner is the sole controller of their data, hence, the name decentralized identity. Later in this paper, we will propose a new way to sign a contract using this verifiable credential as a signature instead of a digital certificate issue by the certificate authority.

To share a verifiable credential to each other, the user can select the information inside the verifiable credential they want to share and wrap them up in a "verifiable presentation". A verifiable presentation is a wrapper around one or more verifiable credential. Think of a wallet with a credit card and national ID inside it. In this case, the wallet is a presentation that contains the credentials (credit card, national ID).

The picture below shows an example of how to use verifiable credentials. For the full specification of verifiable credentials and decentralized identity standards, the reader is advised to read the official documentation.



**Fig. 1.** A person creates a DID and an associate DID document and publish it on the blockchain. f1xe5ae54 is the unique identifier of the user (the actual id is longer than this), and ION refer to the method used to create this DID. In this picture, the student created DID and deploy it on ION, a layer 2 distribute ledger operate on top bitcoin. If the DID was created on Ethereum, the ID would then be DID:ETH:f1Xe5ae54. The middle part of the identifier always refers to the method used to create DID.



**Fig. 2.** A student can request a proof of graduation in a form of the verifiable credentials from the school. Note that this verifiable credential is linked to his decentralized identity (DID), it can not be tampered once issued. The student may use this verifiable credential as many time as he want without the school knowing, anyone can verified this credentials through blockchain directly without needing to contact the school. Note that, the school can also set an expiration dates or other conditions when issue a verifiable credentials. The potentials of verifiable credentials

### III. METHODOLOGY

In this section we proposed a new method to digitally sign a contract using a verifiable credential as a replacement for digital certificate.



### A. Obtaining the digital Identity

Users who wish to sign a contract must create their decentralized identity by obtaining a DID and publish a DID document on to the blockchain of their choice. Then perform a KYC with an identity provider to obtain a verifiable credential. The verifiable credentials should contain the information necessary to sign a contract, such as name and birthdate, or national ID. Extra information can be added depending on the nature of the contract. For example, one can request a university to issue a verifiable credential that contains the diploma as proof of graduation. Note that, if the user has already had a DID or a verifiable credential for other used before, he can reuse them without requesting a new one. For example, the signer may reuse his identity issue by the school rather than making a new one. It all depends on the other party whether they trust the organization that issued you the verifiable credential or not. This is the perk of decentralized identity. Once issued, DID and verifiable credential can be reused as many times as they can if users hold a corresponding private key.

At this point, the user has the following credentials.

- DID – a unique digital ID representing a person.
- DID private key – secret key used to operate DID.
- DID public key – public key associated with DID.
- DID document – DID info store on the public blockchain.
- Verifiable credentials – a credential associated with DID.

### B. User authentication

Prior to the signing, both parties select their credential that they want to reveal from the verifiable credential and turn it into a verifiable presentation. Both parties see each other's credentials by exchanging the verifiable presentation. There are two verification steps that the user must perform here. First, the user must prove that they are the legit owner of the verifiable credential. This can be done using DIDs private key. Second, they must check that the verifiable credential of the other party is issued by a trusted identity provider. This can be performed by using the identity provider public key. Note that the identity provider in this case also belongs to the decentralized identity system, they have a DID like the user. After this step, both parties are aware of each other's real world identity and personal information.

### C. Draft and Sign

When drafting a contract, the user must fill in the document with their information. This information can be extract from the verifiable presentation and embed it into the document itself.

Once the document is filled and finalized. Both parties sign the contract with their electronic signature. As I mention

before, the current standard is to sign with a private key issued by a certificate authority, which can be authenticated with the digital certificate. However, doing this is redundant in our case. The user already has DID and verifiable credential, which basically is the better version of digital certificate built on top of the blockchain technology. We can use them as an electronic signature.

Dealing with DID and Verifiable credential directly on their own are too complicated for a general user. Therefore, those steps that I mentioned earlier should be done via a software, or a web application made by an experience developer.

Currently, there is no known document signing service provider or a company that are compatible with verifiable credential and decentralized identity. The main goal of this paper is to give an example of how to build such an application.

The web application will act as a relying party providing an easy-to-use signing platform for the user. The web application should create their own decentralized identity and authenticate themselves with the identity provider so that the user can trust them. The application must provide the user with an option to read, trade, and verify verifiable presentation of the other party. To make the signing fair, the web application must ensure that both users agree on the state of the contract, whether to keep on editing the document or both are ready to sign. This can be done by opening a secure communication channel between both parties. The communication between two parties must also be encrypted in such a way that the web application themselves cannot read them to ensure the privacy of the users. There are many ways to achieve this, for example, a decentralized messenger is a messaging methodology that does not rely on the central server for a communication between users, but the encrypted message is broadcast through the blockchain node, ensuring the integrity while maintaining full privacy.

We proposed 2 signing methods. The first method uses user's DIDs private key to sign the contract. The second method, use the web application's DIDs private key.

#### 1) Use user DIDs private key as a signature.

The user can sign the contract with DID private key. The web application sends a request to the user asking for a signature, then place that signature on to the correct position of the document. Note that this requires the user to have a digital wallet that can sign a transaction.

#### 2) User web application DIDs private key

In this method, users do not sign the contract themselves, rather, they give a permission to the web application, to sign the contract for them. This can be done by the following step,

1. Users reveal their verifiable credentials to the web application.
2. The web application verifies user identity and merges the verifiable credential with the contract document.
3. The web application then signed the contract with their DID private key.

In this method, the verifiable credentials are embedded inside the document.

#### D. Store

The web application sends a copy of a signed contract to both users. The user can then store the hash of the contract on the blockchain of their choice. If privacy is not a concern, users can choose to store an actual document on the blockchain directly. The blockchain is timestamped and tampered proof. The integrity and the safety of the signed contract is now secured.

#### E. Verify (in case of disputed)

If one party fails to fulfill the terms of the contract, the lawyer may have to look at the signed document. This can be done with the following step.

1. The lawyer compares the document with the one store on the blockchain to make sure that this is the original document with no tampering.
2. The lawyer examines the content of the document. Remember that the document is signed with a DID private key; therefore, it can be authenticated and verified with the corresponding public key. The public key of all involved parties, the signers, the web application, and identity provider can be obtained manually from the blockchain. All can be done without needing to contact any authority.
3. The verifiable credential can only be used by its owner, It is undeniable proof that the owner of this verifiable credentials signed the contract. The authenticity of the contract and the information inside it cannot be denied.

#### F. Lease agreement example

Let's say that Bob wants to sign an apartment leasing contract. Bob is a tenant and Alice is a landlord. Bob creates his decentralized identity on the blockchain of his choice. Bob contacts a decentralized identity provider of his choice, tells them his DID and perform an identity check. The DID and Verifiable credentials from different blockchain are interoperable, it does not matter which one Bob pick if he chooses from the well know and secured blockchain one such as BITCOIN, Ethereum, ION, and etc.

Once his identity is verified, the identity provider issues him the verifiable credential that is tie to his DID. Bob's

credential such as his name, national ID, and birthday are contained within the verifiable credential. Bob stores this verifiable credential privately on his own device. Verifiable credential can be reused, which mean that Bob can use this verifiable credential for some other application too, for example, he can use this verifiable credential to register as a merchant for online shopping application that required identity proofing.

Bob can now get into contact with the Alice, the landlord. Alice verifies Bob's identity by checking his verifiable credential. She also checks that it was issued from the identity provider that she trusted. At this point, Bob identity and necessary credential is proven to Alice and is ready to sign a contract. In the high staked contract, Alice can perform extra identification as she need. Note that Alice identity and organization can be proven to Bob by the same mean.

Let's say that some organization made a web application that I guideline above. Alice and Bob can use this web application to communicate and sign the lease agreement contract. The web application injects Bob and Alice information obtain from the verifiable credential into the contract as their signature. The web application then signs the contract with its private key and publishes the document to the blockchain. Bob and Alice information from the verifiable credential is embedded into the contract document by the web application, which mean that, Bob and Alice cannot refuse that they sign the contract, since they are the only one who can give the web application a permission to use their verifiable credential. Note that even if the web application become compromised days or months after the signing, the contract is still valid because it is stored on the blockchain which contain times-tamped of the transaction that can be used to indicate that the signing happens before the day the application become compromised.

In conclusion, the web application gives the user an ability to sign the contract with their verifiable credential as a signature (to be more precise, the users give web application permission to use their credential, and we use that credential to sign the contract).

## IV. RESULTS AND DISCUSSION

We created a demo web application as a proof of concept. Decentralized identity and verifiable credentials are free to use through an opensource code. However, it is more convenient to use a service from a company who offers a decentralized identity management as a service. In this example, we use Microsoft Entra to issue and verify the verifiable credentials.

In this demo, we simulate 3 entities.

1. an identity provider to issue a verifiable credentials
2. A web application, a service to sign the contract.
3. The users who want to digitally sign the contract.

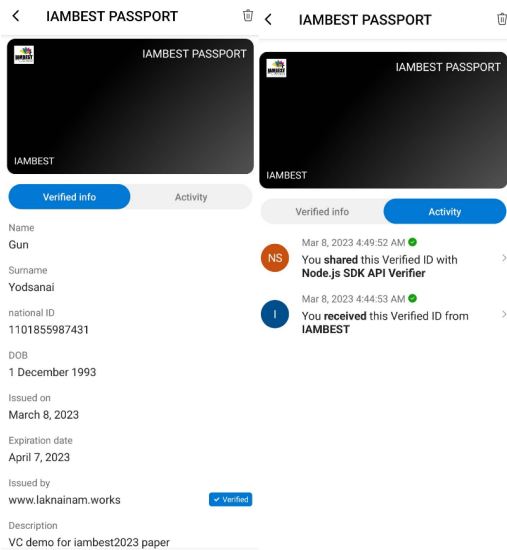
In Figure 3, the user obtains their decentralized identity using open-source ION-tools. To tie this identity to the real-world identity, the user performs an identity check with the identity provider. We created a dummy identity provider called “IAMBEST” that can issue a verifiable credentials through a QR code. Note that in an actual setup, the user must perform KYC to get this QR code. There are many digital wallets that can store the verifiable credential, in this example, we use Microsoft authenticator mobile app to receive and store verifiable credentials.

```
did:ion:EiChsCtGVwKyKLu7U3CrVCA-f1NpoI2IKMx4UstVX0dLUg
```

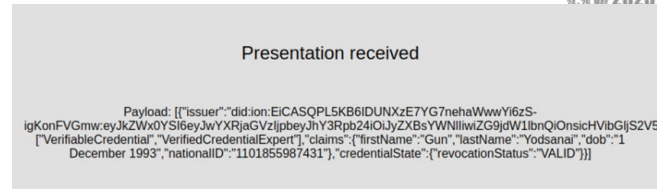
**Fig. 3.** A user creates a decentralized identity on ION blockchain using an open-source SDK. The first line is DID. The second line is the public key. The private key are not showed.



**Fig. 4.** Microsoft Entra allow website to register as an identity provider that can issue a verifiable credentials to its customer. In this paper, we create an “IAMBEST” identity provider that can issue a verifiable credential through a QR code.



**Fig. 5.** A verifiable credential stored on the user wallet.



**Fig. 6.** The verifiable presentation of the user can be shared in JSON format. The figure above shows what it’s look like when the web application receive the presentation from the user.

5. **Term and Termination:** This Contract ends on write the contract end date here, unless the Client or the Business ends the contract before that time. If one of the parties chooses to end the Contract prior to project completion, the Client is responsible for paying for all work and costs incurred up until that date.

The Parties hereto agree to the foregoing as evidenced by their signatures below.

Did:ion:EiChsCtGVwKyKLu7U3 1 December 1993  
Gun Yodsana1

Client Name, Client Date of Birth

Signed by webapplication  
09/march/23

DIGITAL SIGNATURE :

05c9fa30ae2d6b3  
1fc275c049ef4c3  
7a25f7bedabe074  
c0c77fa5138a0c8  
6d4607bbd997eb9  
e47979686e73c1d  
f64f8b365b32d80  
c0d542cd4aa004a  
bd450d7f

**Fig. 7.** The web application extract the user information from the verifiable presentation receive in fig 5 and insert it into the contract as an electronic signature. The web application also signs the document with its private key (see red mark)

## V. CONCLUSION

Decentralized identity is an identity management system built on top of the blockchain that allows user to manage their own credential in the form of a verifiable credential. These credentials can be used as a proof of identity. We insert part of these credentials inside the contract document, since it can be verified and authenticated, it counts as an electronic signature. The contract signed with an electronic signature can then be used legally. We also review the basic concept necessary to understand the verifiable credential and how to build a web application that can be used to sign a contract with it. The concept of verifiable credential is new. There are not many applications that utilize it yet. There is no known service provider that uses it as a signature to sign a legal agreement. This paper serves as an example of one possible use case of the verifiable credential.

## REFERENCES

- [1] Berkowsky, J.A. and T. Hayajneh. Security issues with certificate authorities. In 2017 IEEE 8th Annual Ubiquitous Computing, Electronics and Mobile Communication Conference (UEMCON), 2017.
- [2] Ben-Or, M., et al., A fair protocol for signing contracts. IEEE Transactions on Information Theory, 1990, 36(1): p. 40-46.
- [3] Ermoshina, K., Musiani, F., Halpin, H. (2016). End-to-End Encrypted Messaging Protocols: An Overview. In et al. Internet Science. INSCI 2016.
- [4] Sedlmeir, J., Smethurst, R., Rieger, A. et al. Digital Identities and Verifiable Credentials. Bus Inf Syst Eng 63, 603–613 (2021).
- [5] Decentralized identifiers (dids) v1.0. W3C. (n.d.). Retrieved March 9, 2023, from https://www.w3.org/TR/2022/REC-did-core-20220719/
- [6] Verifiable credentials data model V1.1. W3C. (n.d.). Retrieved March 9, 2023, from https://www.w3.org/TR/2022/REC-vc-data-model-20220303/

# Molecular characterization and tissue expression of *dnd* in striped catfish (*Pangasianodon hypophthalmus*)

Kunlanan Booncherd and Surintorn Boonanuntasarn\*

School of Animal Technology and Innovation, Institute of Agricultural Technology, Suranaree University of  
Technology, 111 University Avenue, Muang, Nakhon Ratchasima 30000, Thailand

\*Corresponding author: surinton@sut.ac.th

**Abstract:** Molecular markers that are specific to germ cells are necessary to study the molecular mechanisms associated with the reproductive biology of fish. In this study, we cloned and characterized *dnd* in striped catfish (*Pangasianodon hypophthalmus*) and designated it as *Phy-dnd*. The partial cDNA of *Phy-dnd* contained 1,513 bp, including an ORF encodes 399 amino acid residues and 372 bp of partial 3'-UTR. *Phy-dnd* contains all the predicted consensus motifs that are shared among *dnd* in other fish species, including the RNA recognition motif (RRM), N-terminal regions (NR), and four C-terminal regions (CR1-4). Phylogenetic analysis demonstrated that *Phy-Dnd* clustered within the teleost *Dnd*. Reverse transcription polymerase chain reaction (RT-PCR) indicated that *Phy-dnd* mRNA occurred only in the testes and ovaries. Quantitative RT-PCR showed that *dnd* was highly expressed in the ovaries and testes. Overall, our findings provide valuable molecular information on *dnd* in striped catfish that can be applied in further reproductive biological studies.

**Index Terms**— *dnd*, striped catfish, gene marker, reproductive biology

## I. INTRODUCTION

Advances in reproductive biotechnology can enable seed production of fish species that are otherwise limited to reproduction in captivity. Germ cell markers are required to develop reproductive biotechnology-based research. Several germ cell markers such as DEAD (Asp-Glu-Ala-Asp) box polypeptide 4 (*vasa*) [1], microRNA-mediated repression inhibitor1 (*dnd*) [2], nanos protein (*nanos*) [3], and deletion in azoospermia-like (*dazl*) [4] have been utilized as DNA markers for germline and gonadal development. Additionally, these germ cell markers have been used in research related to sex determination and sex differentiation in fish [5,6]. Among the germ cell markers, *dnd* is a germ plasm-specific maternal RNA that encodes an RNA-binding protein in fish and vertebrates. It plays an essential role in the migration, survival, and proliferation of primordial germ cell (PGC) [6,7] and prevents germ cell-specific RNA degradation by inhibiting miRNA function through binding to the 3'-untranslated regions (3'UTRs) of germ cell-specific RNAs [8]. Moreover, *dnd* has been used as a germ cell marker to investigate gonadal development in several fish, such as olive flounder (*Paralichthys olivaceus*) [2], gibel carp (*Carassius gibelio*) [5], medaka (*Oryzias latipes*) [9], turbot (*Scophthalmus maximus*) [10], starry flounder (*Platichthys stellatus*) [11], and snakeskin gourami (*Trichopodus pectoralis*) [12].

Striped catfish (*Pangasinodon hypophthalmus*) is an economically important white fleshed fish product in the global market. It belongs to the Pangasiidae family, some

members of which are considered as endangered species, such as the Mekong giant catfish (*P. gigas*) and the Chao phraya giant catfish (*P. sanitwongsei*). Recently, germ cell transplantation technology has been developed for fish which has proved to be a useful tool for development of surrogate broodstock technology. This technology can be applied to reproduce fish which are difficult to reproduce in captivity. Since a full-cycle culture of striped catfish has been developed, it can be used as a recipient fish for germ cell transplantation of donor species in the Pangasiidae family. Therefore, germ cell markers in striped catfish are required for reproductive biology-based studies. A previous study on the characterization of *vasa* in striped catfish has reported it to be specifically expressed in testes and ovaries. In addition, the expression of *vasa* was demonstrated in PGC during larval development which was used to study the migration and proliferation of PGC. Indeed, more gene markers that are specifically expressed in the germline needed to be studied to facilitate molecular reproductive research. Accordingly, this study aimed to clone and characterize *dnd* from striped catfish. Furthermore, we demonstrated its specific expression in the gonads along with its expression levels in the testes and ovaries of adult fish.

## II. METHODOLOGY

### Experimental fish, sampling and total RNA extraction

All experiments were approved by the Ethics Committee of the Suranaree University of Technology Animal Care and Use Committee (approval no. SUT-IACUC-003/2023). Juvenile and adult striped catfish (*P. hypophthalmus*) were cultured in earthen ponds (800 m<sup>2</sup>) at the University Farm,

Suranaree University of Technology, Nakhon Ratchasima, Thailand. The fish were fed to satiety with a commercial diet (25% crude protein, 3% fat) at 2% body weight, twice daily at 10:00 and 16:00. For *dnd* cloning, juvenile fish (~300 g body weight; 1.74 g gonad weight; GSI, 0.58%) were sampled for total RNA extraction. For reverse transcription PCR (RT-PCR) and real-time PCR, adult males (n = 3, ~2.5 kg body weight; 29 g gonad weight; GSI, 1.16%) and females (n = 3, ~3.2 kg body weight; 54 g gonad weight; GSI, 1.65%) were sampled for total RNA extraction. Fish were euthanized with 1 % clove oil. Subsequently, the fish were sacrificed and the brain, gill, muscle, liver, spleen, intestine, testes, and ovaries were collected for total RNA extraction. Total RNA was extracted from the sampled tissues (approximately 100 mg) using TRIzol reagent (Invitrogen, Carlsbad, CA, USA) and digested with RNase-free DNase I (Promega, Madison, WI, USA), according to the manufacturer's instructions.

#### Cloning of the partial *dnd* cDNAs

The *dnd* cDNA (*Phy-dnd*) was cloned using total RNA (1 µg) extracted from the gonads of striped catfish. First-strand cDNA was synthesized from total RNA using SuperScript III RNaseH-Reverse transcriptase kit (Invitrogen) with random primers (Promega, Madison, WI, USA), according to the manufacturer's protocol. A partial cDNA of *Phy-dnd* was cloned using primers (GSP-dnd-F1 and GSP-dnd-R1) (Table 1) which were designed based on the DNA sequence from NCBI (accession number: XM\_026918857.2). For PCR, 2.5 µL of cDNA, 1 µL of dNTP mix (2.5 mM each), 10 pmol of each primer, 2.5 mM MgCl<sub>2</sub>, 1.0X LA TaqTM buffer, and 1.25 U LA Taq (Takara Shuzo, Shiga, Japan) were used in a final reaction mix of 25 µL. PCR was performed at 95 °C for 3 min, followed by 35 reaction cycles of 45 s at 95 °C, 45 s at 60 °C, and 90 s at 72 °C. The final elongation step was carried out at 72 °C for 5 min. PCR products of the expected size were isolated and purified using the QIAquick Gel Extraction Kit (Qiagen, Crawley, UK). The PCR-amplified DNA fragment was cloned into a pGEM-T Easy plasmid (Promega). At least four sequenced clones from both cDNA directions were submitted for sequencing (Macrogen Inc., Korea). The plasmid containing partial *Phy-dnd* cDNA was used for further analysis. Multiple sequence alignment was conducted using CLUSTAL W (<https://www.genome.jp/tp/tools-bin/clustalw>, accessed on 25 February 2023) [13]. A phylogenetic tree of *Dnd* was constructed with 1000 bootstrap replications using the Mega 11 program and the UPGMA method [14,15].

#### Analysis of tissue expression of *dnd*

First-strand cDNA was synthesized using 1 µg of the total RNA extracted from the brain, gill, muscle, liver, spleen, intestines, and ovaries were analyzed using the SuperScript III RNaseH-Reverse transcriptase kit (Invitrogen) with random primers (Promega, Madison, WI, USA). A pair of primers (GSP-dnd-F2 and GSP-dnd-R2) was designed based on *Phy-dnd* and used to analyze the

TABLE I THE OLIGONUCLEOTIDE PRIMERS USED IN THIS STUDY

Primer name	5' to 3' Nucleotide Sequence	Purpose
GSP-dnd-F1	TTGCAGATGTTGAATCCGCAGA	Cloning
GSP-dnd-R1	GACAGACCACCTCTGGCAGTTTCTA	Cloning
GSP-dnd-F2	GAAGTCTCTGGAGAAGTGGCTTGAG	RT-PCR
GSP-dnd-R2	TGGTTTTCTCGCCTGCCACATG	RT-PCR
β-actinF	ACTACC TCA AGATCCTG	RT-PCR
β-actinR	TTGCTGATCCACATCTGCTG	RT-PCR
Dnd-RT-F	TCCTCGGGACGTGTACGAA	qPCR
Dnd-RT-R	CTCCTCCTGACGGTGAGCCT	qPCR
Actin-RT-F	TGGCAATGAGAGGTTCCG	qPCR
Actin-RT-R	TGCTGTTGTAGGTGGTTTCG	qPCR

expression of *Phy-dnd*. The β-actin gene (*actb*) served as an internal control, and accordingly, a pair of primers (β-actinF and β-actinR) [1] was used (Table 1). RT-PCR analysis was performed in a total volume of 10 µL consisting of 1 µL of cDNA template, 1 µL of dNTP mix (2.5 mM each), 10 pmol of each primer, 2.5 mM MgCl<sub>2</sub>, 5X GoTaq Flexi buffer, and 0.25 U GoTaq DNA polymerase (Promega). RT-PCR analysis was performed with an initial denaturation step at 95 °C for 3 min, followed by 35 reaction cycles of 45 s at 95 °C, 30 s at 60 °C, and 90 s at 72 °C. The final elongation step was carried out at 72 °C for 5 min. A plasmid containing *Phy-dnd* was used as the positive control. The PCR products of *Phy-dnd* and *actb* were verified using agarose gel electrophoresis and RedSafe Nucleic Acid Staining (JH Science, iNtRON Biotechnology, WA, USA).

#### Quantitative analysis of *Phy-dnd* mRNA expression

A pair of primers (Dnd-RT-F and Dnd-RT-R) was designed based on *Phy-dnd* to determine its expression level (Table 1). Real-time quantitative PCR (qPCR) amplification (in triplicates) was performed using a Light Cycler® 480 SYBR Green I Master Mix (Roche Applied Science, Indianapolis, IN, USA). For normalization, *actb* was used as an internal reference. The primers and annealing temperatures used for *Phy-dnd* and *actb* are listed in Table 1, which generated amplicons of 208 bp and 95 bp, respectively. Each PCR was performed using a final reaction mix of 10 µL consisting of 1 µL of cDNA template (synthesized from 1 µg of total RNA) or distilled water (negative control), 5 µL of Light Cycler® 480 SYBR Green I Master Mix, 1 µL of 5 µM of each primer, and 2 µL of distilled water. The PCR products were preincubated for 10 min at 95 °C, followed by 40 amplification cycles at 95 °C for 15 s, 60 °C for 10 s, and 72 °C for 15 s. The comparative cycle threshold (Ct) method was used to analyze the data. Upon completion of the amplification, PCR was performed to analyze the melting curve. An external standard curve for *Phy-dnd* was generated using a plasmid containing *Phy-dnd* with known copy numbers. For *actb*, an external standard curve was generated using pooled cDNA from all samples with serial dilution. Subsequently, the mRNA expression of *Phy-dnd* was normalized to that of *actb* using the following equation: log (copy number of *dnd*1)/dilution (%) of *actb*. Statistical analysis was

performed using SPSS for Windows version 25 (SPSS Inc., Chicago, IL, USA). The normalized *Phy-dnd* expression was subjected to one-way analysis of variance (ANOVA), followed by Tukey's procedure to rank the groups when significant differences ( $p < 0.05$  considered as significant) were observed among the groups.

```

ATGTTGCAGATGTTGAATCCGCAGAGACTGAAGTCTCGGAGAAGTGGCTTGAGGAAACC 60
M L Q M L N P Q R L K S L E K W L E E T 20
AACACACCCCTTGAACGAGGTTAAACGGCCAGCGCAGATATGGTGCCTCCCTCCGGGATGG 120
N T T L T Q V N G Q R R Y G A E P P P G W 40
AGAGTCCGCACACAGGTCAGGCTCGAGGTCCTTTAAGTCAGATCCCTCGGAGCAGTC 180
R G P T P G P G C E V F I S Q I P R D V 80
TACGAAGACCACTGATCCCGCTGTCCAGAGCGTGGCCCGCTCTACGAGTTCGCGCTC 240
Y E D Q L I P L F Q S V A P L Y E F R L 100
ATGATGAACCTTCAAGCGGCGAGAACCAGGCTTCGCGCTACGCGCAATACGGAGACACGGCT 300
M M N F S G Q N R G F A Y A K Y G D T A 120
AGCGCAGCCCGCCGATCCAGGCTCTAAACCTGTATCCAACTCCAGAGTGGCGTCAGGCTC 360
S A A A A I Q A L N L Y P I Q S G V R L 140
ACCGTCAGGAGGAGCAGCGGAGAGGAGCGCTGTCTCAGCGATCTGCGCTCCACCCATG 420
T V R R S T E K R Q L C L S D L F P T M 160
GAGCGCAACGAGCTGTGACAGTGTGCGCAAAATCGCTGACGGAGTGGAGGCGCTCACT 480
E R N E L L T V L Q Q I A D G V E G V T 180
ATGAGGACACCGGCTAAGGAGAGGAGCTCACTCGCTCGTGCACACTCTCCCTCCAC 540
M R T T G P K E K D V T A L V H Y S S H 200
TATGCTCCCTCCATGGCCAGAGGCTGTGGTGCAGCCCTCAGGAAAGCTGTACGGCGTG 600
Y A A S M A K K V L V Q A F R K L Y G V 220
TCCATCTCCGTCGGATGGATGTGTGAAACGCCAAATCCAGACACGAGGAGCATGACGAA 660
S I S V R W M S G N A K S R H E E H D E 240
GAGAGTGTCTCGCCCTCCTGGGCTGAATCCATGGCCGCGAATCTTTAAGCCCTCCA 720
E S A L A P P G L K S M A A N S L T P P 260
CGCTCCAGCTCAGCCGAGACCCGAGCATCTCCACCTCTTCCACTCCACCCCTCTCC 780
R F Q L S R D P E H P P L P T P P S P 280
CTTCAACCCGAGTCTTCTCGCGGGCAGTAGGGGTCACACCCCGCAGGTGACGAGTGTG 840
L H P Q F F S R A V G G P T P Q V T S V 300
ATGTTACCCCTGAAGCCCAAGGAGCGCGGAGGCCACCGCAGACTCGGTGCACACGCTC 900
M L P L K P R S A E E P P H D S V H Q L 320
CGTTGGCTGTGTGAGCTGCACGGGCTCGGCGATGCCGCTCTACAACGTGCGCTACGACC 960
R W L C E L H G L G M P L Y N V R Y D H 340
ACAGGCCCTGACGGCTTCTGATTTTGCCTACAGGGTGGTGGTGCAGGGCTGGCCATG 1020
T G P D S F L Y F A Y R V V V P G L A M 360
CCGTTCTCGGCGTAGTCCCGCTCCGCGCCAGCAGCTGCGCCACCAACATGGAGGCTGAG 1080
P F C G V V P V L P S T C A N N M E A E 380
GTTCATCGGCGCTGCCAAGCAGCTCTCAACGCCATGTGGCAGCGGAGAAAAACATGA 1140
V H R A A A K Q L N A M W Q A R K P * 399
gcttgacctcagatgcatcatctgttttgggtgagaaatgtgattttctgtagtagaag 1200
tggtcctggatgagcttctctatgtttaaactgttgaaaatacaaatctcagagatgtoa 1260
cagtcacagatggagctcgttagatgtattagagcagctagcatctcctccaagctgttt 1320
ctgtagctgttctctagctatattagaggagaaatagataaacaggaacatggattggcaat 1380
gtctaaactaagaaaaaaatgaagtaagctccaaatataataaagtaactaataatga 1140
aataaataaaatctcctcattgcaaacgctctgtaacttactgtctagaaactgcca 1500
gaggtggtctgtc 1513
    
```

Fig 1. Nucleotide sequence of *Phy-dnd* cDNA and translated amino acid sequence of the encoded protein. White box indicates motifs, including NR, RRM, CR1, CR2, CR3 and CR4.

### III. RESULTS

#### Molecular cloning and characterization of *Dnd* in striped catfish

The partial cDNA of *dnd* contained 1,513 bp, which included an ORF encoding 399 amino acid residues and

372 bp of partial 3'-UTR (Fig 1). The deduced amino acid sequence of the *Dnd* protein contained a typical RNA recognition motif (RRM) and five conserved regions, including an N-terminal region (NR) and four C-terminal regions (CR1-4). Multiple alignments of *Dnd* with other known *Dnd* protein homologues were highly conserved for typical RRM, NR, and CR1-4 (Fig 2). The calculated molecular weight and isoelectric point of the deduced amino acid sequence of *Dnd* were 42.15 kDa and 9.20, respectively. Indeed, *Dnd* shared the greatest identity (75.47% - 98.68%) with *Dnd* protein homologues of other fish species (Fig 2).

Phylogenetic tree analysis of the *Dnd* protein with other known vertebrate *Dnd* protein homologues revealed that the tree was divided into two branches, including the fish branch and that of other vertebrate species, with *Dnd* being located in the fish branch (Fig 3).

#### Tissue distribution of *Phy-dnd*

We analyzed the expression of *dnd* in various tissues, including the brain, gill, muscle, liver, spleen, intestine, testis, and ovary using RT-PCR, and the expression of *actb* was used as an internal standard. The expression of *dnd* was detected only in the testis and ovary, whereas that of *actb* was detected in all the examined tissues (Fig 4).

#### Expression levels of *Phy-dnd* in various tissues

Real time quantitative PCR was performed to evaluate the relative expression levels of *dnd* in the adult stage. Figure 5 shows that *dnd* was highly expressed in the ovaries and testes while very low expression levels were detected in the brain, gills, muscle, liver, spleen, and intestine. Note that brain, gill muscle, liver, spleen, and intestine were obtained from 1 female and 2 males (Fig 5).

### IV. DISCUSSION

Germ cell markers can serve as useful tools for the investigation of gonadal development and molecular reproductive research in fish. Among the germ cell markers, *dnd* which encodes an RNA-binding protein, plays an important role in the migration, survival, and proliferation of PGC [6,7]. In the present study, we cloned and characterized *Phy-dnd* and demonstrated its specific differential expression levels in the ovary and testes. Our information on *Phy-dnd* can be useful for further studies on its function during gonad development and its application in reproductive biotechnology.

Previous characterization of *dnd* in olive flounder [2], gibel carp [5], medaka [9] and turbot [10] demonstrated that *dnd* contains six conserved motifs, including the NR, RRM, and CR1-4. In addition, characterization of *Dnd* proteins has revealed conserved RRM1-2 motifs and DSRM (double-stranded RNA recognition motifs) in starry flounder [11], rare minnow (*Gobiocypris rarus*) [16] and tambaqui (*Colossoma macropomum*) [17]. In this study, the deduced amino acid sequence of *Phy-Dnd* contained a typical RRM and five conserved regions (NR and CR1-4). The RRM is reported to be the RNA-binding domain that is necessary for the regulation of protein localization in germ cells [18] and has been reported to play an important role in PGC development and survival [9,18]. Overall, *Phy-Dnd*

Identity Value to Dnd

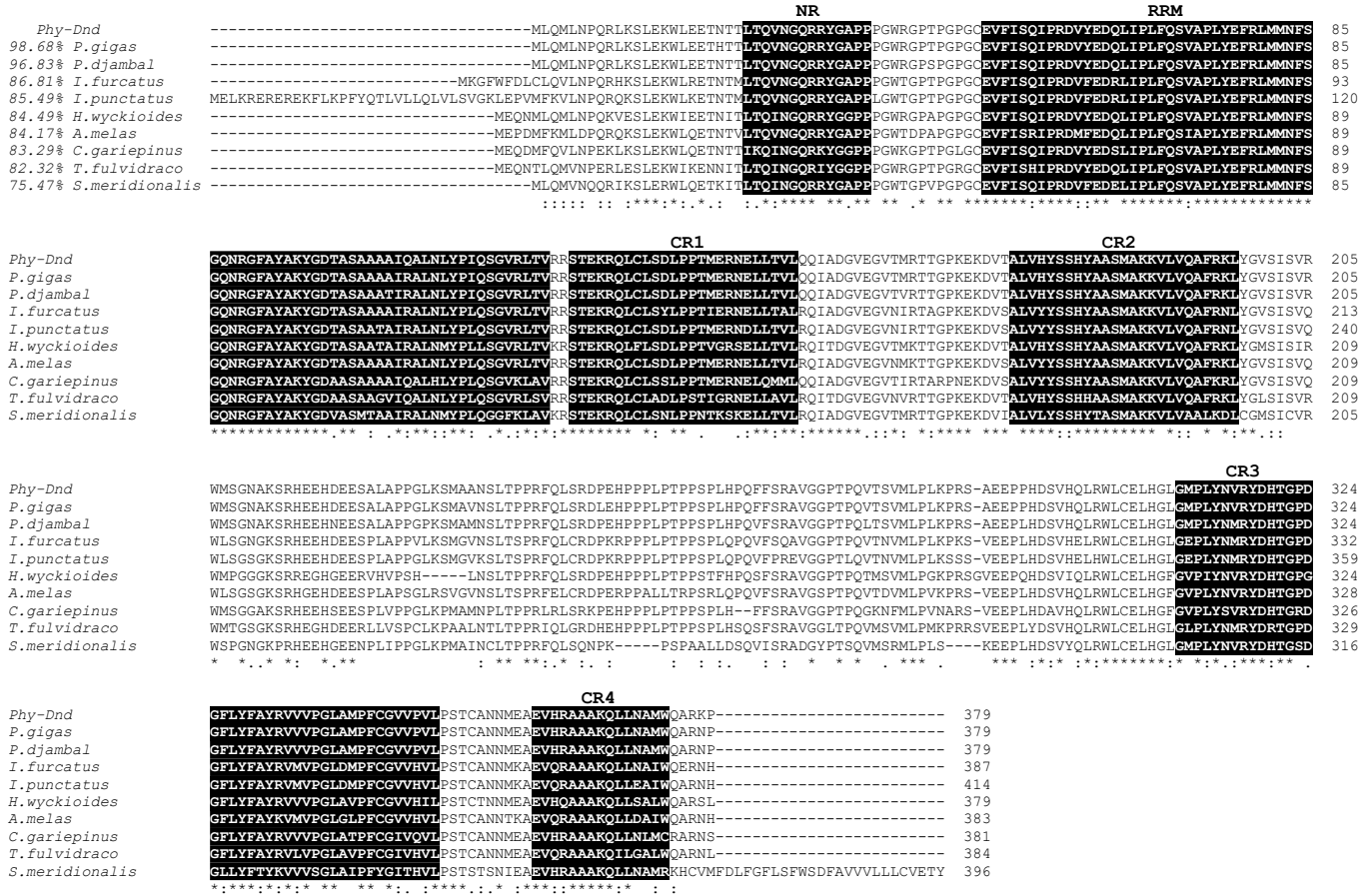


Fig 2. Multiple alignments of the Phy-Dnd amino acid sequence with known vertebrate protein homologues. The amino acid sequences were aligned using CLUSTAL W, and the percentage identities of Phy-Dnd with the other Dnd sequences that had the greatest sequence identity are shown in front of the sequence. Gaps that were introduced to maximize sequence homology are indicated by dashes. The conserved motifs, including NR, RRM, CR1, CR2, CR3, and CR4, are indicated by black boxes. Fully, highly, and less conserved amino acid residues are indicated by (\*), (:), and (.), respectively. The GenBank accession numbers of the Dnd protein homologues are as follows: *Pangasianodon gigas*, MCI4381563.1; *Pangasius djambal*, MCJ8735689.1; *Ictalurus furcatus*, XP\_053498456.1; *Ictalurus punctatus*, XP\_017340221.1; *Hemibagrus wyckioides*, KAG7324468.1; *Ameiurus melas*, KAF4081039.1; *Clarias gariepinus*, XP\_053342036.1; *Tachysurus fulvidraco*, XP\_027020922.2; *Silurus meridionalis*, XP\_046715472.1.

contained the essential motifs of a typical Dnd homologue. Phylogenetic analysis showed that Phy-Dnd clustered with the Dnd families of teleosts and showed the highest identity with *Pangasianodon gigas* and *Pangasius djambal* in the family Pangasiidae. Taken together, Phy-Dnd showed a consensus sequence of the typical domain structures of Dnd. It showed high sequence homology with other teleosts and clustered with teleost Dnd proteins.

Using RT-PCR, our results showed that *Phy-dnd* specifically expressed in the ovaries and testes of striped catfish. It has been demonstrated that *Phy-dnd* specifically expressed in the testes and ovaries of gibel carp [5], medaka [9], turbot [10], rere minnow [16], and tampaqui [17], Atlantic salmon (*Salmo salar*) [19], and pacific bluefin tuna (*Thunnus orientalis*) [20]. In addition, we determined the expression levels of *Phy-dnd* in the testes, ovaries, and other tissues. Notably, very low expression of *Phy-dnd* was found in the brain, gill, muscle, liver, spleen, and intestine, suggesting that *Phy-dnd* might not play an essential role in these tissues. Using qPCR analysis, our findings showed that in adult striped catfish, the expression of *Phy-dnd* in the ovary was higher than that in the testes.

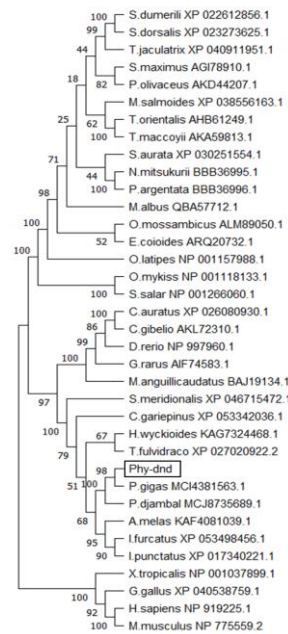


Fig 3. Phylogenetic tree of Dnd from different fish species and higher vertebrates. The tree was constructed using 1000 bootstrap replications with MEGA 11 using the UMPGA method [Sneath et al., 1973; Tamura et al., 2013]. The percentages of replicate trees in which the associated taxa clustered together in the bootstrap test (1000 replicates) are shown above the branches. The GenBank accession numbers of the Dnd proteins are provided in brackets.

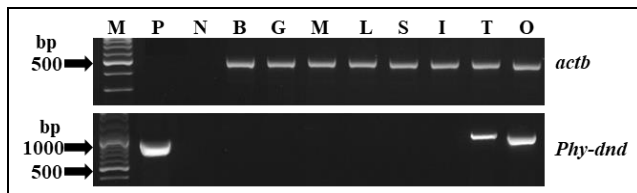


Fig 4. Reverse-transcription polymerase chain reaction (RT-PCR) of *actb*, and *Phy-dnd* mRNAs in various tissues of striped catfish. cDNA was synthesised using total RNA isolated from the brain (B), gill (G), muscle (M), liver (L), spleen (S), intestine (I), testis (T) and ovary (O). Distilled water was used as a negative control (N) and *Phy-dnd* plasmid (P) was used as a positive control. M represents the DNA marker.

This high expression of *Phy-dnd* in the ovary suggests its accumulation as a maternal RNA in eggs corroborating with other studies [7]. Similarly, higher expression in ovary, comparing to that in testis, was demonstrated in olive flounder [2] and starry flounder [11]. However, variable dimorphic expression of *dnd* between male and females has been observed in turbot, depending on age [10]. Therefore, differential expression of *dnd* between the testis and ovary in fish might depend on the fish species and developmental age.

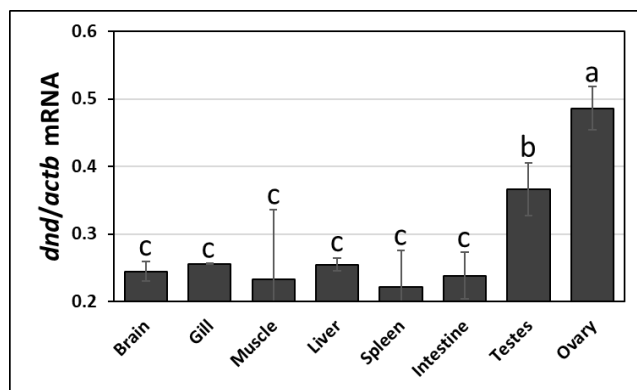


Fig 5. Expression levels of *Phy-dnd* in various tissues of striped catfish at mature stages. The expression level of *Phy-dnd* was normalized with the expression of *actb*. The values are expressed as mean + SD from 3 samples after triplicate qPCR analysis. One-way ANOVA followed by Tukey's range test was performed to rank the expression level in different tissues. Different letters in the bar graph indicate significant differences ( $p < 0.05$ ).

## V. CONCLUSION

In conclusion, *Phy-dnd* in striped catfish was cloned and characterized, and it showed a consensus sequence of typical domain structures of teleost *dnd*. The specific expression of *Phy-dnd* was found in the ovary and testis, with comparatively higher expression observed in the ovary than in the testis.

## ACKNOWLEDGMENT

This work was supported by the Suranaree University of Technology (SUT), Thailand Science Research and Innovation (TSRI), and the National Science, Research, and Innovation Fund (NSRF) [FF3-303-65-24-52(12), FF3-304-65-24-12]. Financial support was also received from the project 'Utilization of Thailand Local Genetic Resources to Develop Novel Farmed Fish for Global Market' under the Japan Science and Technology Agency (JST) and the Japan

International Cooperation Agency (JICA) joint program of the Science and Technology Research Partnership for Sustainable Development (SATREPS). We would like to thank Mr. Sunai Plymee (Suranaree University Technology Farm) for maintaining broodstock.

## REFERENCES

- [1] Duangkaew, R., Jangprai, A., Ichida, K., Yoshizaki, G., & Boonanuntanasarn, S. (2019). Characterization and expression of a vasa homolog in the gonads and primordial germ cells of the striped catfish (*Pangasianodon hypophthalmus*). *Theriogenology*, 131, 61-71.
- [2] Wang, X., Liu, Q., Xiao, Y., Yang, Y., Wang, Y., Song, Z., . . . Xu, S. (2015). The *dnd* RNA identifies germ cell origin and migration in olive flounder (*Paralichthys olivaceus*). *BioMed Research International*, 2015.
- [3] Gribouval, L., Sourdain, P., Lareyre, J.-J., Bellaiche, J., Le Gac, F., Mazan, S., . . . Gautier, A. (2018). The *nanos1* gene was duplicated in early Vertebrates and the two paralogs show different gonadal expression profiles in a shark. *Scientific Reports*, 8(1), 6942.
- [4] Qu, L., Wu, X., Liu, M., Zhong, C., Xu, H., Li, S., . . . Liu, X. (2020). Identification and characterization of germ cell genes *vasa* and *dazl* in a protogynous hermaphrodite fish, orange-spotted grouper (*Epinephelus coioides*). *Gene expression patterns*, 35, 119095.
- [5] Li, S.-Z., Liu, W., Li, Z., Wang, Y., Zhou, L., Yi, M.-S., & Gui, J.-F. (2016). Molecular characterization and expression pattern of a germ cell marker gene *dnd* in gibel carp (*Carassius gibelio*). *Gene*, 591(1), 183-190.
- [6] Weidinger, G., Stebler, J., Slanchev, K., Dumstrei, K., Wise, C., Lovell-Badge, R., . . . Raz, E. (2003). Dead end, a novel vertebrate germ plasm component, is required for zebrafish primordial germ cell migration and survival. *Current Biology*, 13(16), 1429-1434.
- [7] Baloch, A. R., Franěk, R., Saito, T., & Pšenička, M. (2021). Dead-end (*dnd*) protein in fish—a review. *Fish physiology and biochemistry*, 47, 777-784.
- [8] Kedde, M., Strasser, M. J., Boldajipour, B., Vrieling, J. A. O., Slanchev, K., le Sage, C., . . . Ørom, U. A. (2007). RNA-binding protein *Dnd1* inhibits microRNA access to target mRNA. *Cell*, 131(7), 1273-1286.
- [9] Liu, L., Hong, N., Xu, H., Li, M., Yan, Y., Purwanti, Y., . . . Hong, Y. (2009). Medaka dead end encodes a cytoplasmic protein and identifies embryonic and adult germ cells. *Gene expression patterns*, 9(7), 541-548.
- [10] Lin, F., Zhao, C., Xu, S., Ma, D., Xiao, Z., Xiao, Y., . . . Li, J. (2013). Germline-specific and sexually dimorphic expression of a dead end gene homologue in turbot (*Scophthalmus maximus*). *Theriogenology*, 80(6), 665-672.
- [11] Yoon, J.-H., Cho, Y.-S., Lee, H.-B., Park, J.-Y., & Lim, H.-K. (2021). Dead-End (*dnd*) Gene Cloning and Gonad-Specific Expression Pattern in Starry Flounder (*Platichthys stellatus*). *Animals*, 11(8), 2256.
- [12] Nakhathai, C., Sreebun, S., Kabpha, A., Phueng, T. V., & Boonanuntanasarn, S. (2022). Characterization of *ddx4* and *dnd* Homologs in Snakeskin Gourami (*Trichopodus pectoralis*) and Their Expression Levels during Larval Development and in Gonads of Males and Females. *Animals*, 12(23), 3415.
- [13] Thompson, J. D., Higgins, D. G., & Gibson, T. J. (1994). CLUSTAL W: improving the sensitivity of progressive multiple sequence alignment through sequence weighting, position-specific gap penalties and weight matrix choice. *Nucleic acids research*, 22(22), 4673-4680.
- [14] Sneath, P. H., & Sokal, R. R. (1973). Numerical taxonomy. The principles and practice of numerical classification.
- [15] Tamura, K., Stecher, G., Peterson, D., Filipiński, A., & Kumar, S. (2013). MEGA6: molecular evolutionary genetics analysis version 6.0. *Molecular biology and evolution*, 30(12), 2725-2729.
- [16] Duan, J., Feng, G., Chang, P., Zhang, X., Zhou, Q., Zhong, X., . . . Zhao, H. (2015). Germ cell-specific expression of dead end (*dnd*) in rare minnow (*Gobiocypris rarus*). *Fish physiology and biochemistry*, 41, 561-571.
- [17] Vasconcelos, A. C. N., Streit Jr, D. P., Octavera, A., Miwa, M., Kabeya, N., & Yoshizaki, G. (2019). The germ cell marker dead end reveals alternatively spliced transcripts with dissimilar expression. *Scientific Reports*, 9(1), 2407.
- [18] Slanchev, K., Stebler, J., Goudarzi, M., Cojocar, V., Weidinger, G., & Raz, E. (2009). Control of Dead end localization and activity—implications for the function of the protein in antagonizing miRNA function. *Mechanisms of development*, 126(3-4), 270-277.



[19] Nagasawa, K., Fernandes, J. M., Yoshizaki, G., Miwa, M., & Babiak, I. (2013). Identification and migration of primordial germ cells in Atlantic salmon, *Salmo salar*: characterization of vasa, dead end, and lymphocyte antigen 75 genes. *Molecular Reproduction and Development*, 80(2), 118-131.

[20] Yazawa, R., Takeuchi, Y., Morita, T., Ishida, M., & Yoshizaki, G. (2013). The Pacific bluefin tuna (*Thunnus orientalis*) dead end gene is suitable as a specific molecular marker of type A spermatogonia. *Molecular Reproduction and Development*, 80(10), 871-880.

# Sulfur application rates affected grain yield and 2-acetyl-1-pyrroline content in fragrant rice

Sirilak Chaiboontha<sup>1</sup>, Chananath Chanauksorn<sup>2</sup>, Paradee Thammapichai<sup>3</sup>,  
Choochad Santasup<sup>1</sup>, Fapailin Chaiwan<sup>1\*</sup>

<sup>1\*</sup>Department of Plant and Soil Sciences, Faculty of Agriculture, Chiang Mai University, Chiang Mai 50200, Thailand

<sup>2</sup>Surin Rice Research Center, Rice Department, Surin 32000, Thailand

<sup>3</sup>Department of Agronomy, Faculty of Agriculture, Kasetsart University, Bangkok 10900, Thailand

**Abstract:** Sulfur can increase in grain yield and 2-Acetyl-1-Pyrroline (2AP) content, which is the major fragrant compound in fragrant rice grains. This experiment aimed to find out the appropriate rates of S fertilizer on grain yield with high 2AP content. Fragrant rice cultivar KDML 105 was grown in field conditions during the 2021 and 2022 early seasons in Chiang Rai and Surin provinces, the main areas for fragrant rice production in northern and northeast Thailand, respectively. Sulfur fertilizer was applied at a rate of 0 (control), 30, 60, 90, and 120 kg S ha<sup>-1</sup>. Grains were harvested at maturity and evaluated for yield and 2AP content. The results showed that both grain yield and 2AP content were affected by S rates across the years. The highest grain yield with high 2AP content was recorded in treatments with 60 and 90 kg S ha<sup>-1</sup> for Chiang Rai and Surin locations, respectively. The study indicated that producing fragrant rice along with an appropriate rate of S fertilizer not only increased agronomic yield but also enhancement of 2AP.

**Index Terms** - fragrant rice, sulfur, 2AP content, fragrant aroma.

## I. INTRODUCTION

Fragrant rice is highly valued and popular by rice consumers globally. The consumers prefer the taste due to its distinctive properties: the cooked rice is soft and contains a natural fragrant aroma. [1], 2-Acetyl-1-Pyrroline (2AP) is the first aroma compound found in three rice types: Jasmine, Basmati and Jasmati) [2].

Yield, grain quality and aroma of fragrant rice are influenced by soil texture, pH, OM, etc. Plant nutrient management also plays an important role in controlling rice yield and aroma. According to Osotsapar, grain yield and quality of rice were determined by genetics, environment factors and field management practices [3]. Previous studies on the effects of fertilizer application on grain yield, grain quality and 2AP of fragrant rice focused on the role of individual nutrients especially Nitrogen (N), Phosphorus (P) and Potassium (K). For example, Potcho et al. found that NH<sub>4</sub>HCO<sub>3</sub> fertilizer application affected the biosynthesis of 2AP, cooked rice elongation and amylose content in rice [4]. Kongpun and Prom-u-Thai found that grain yield and content of N and 2AP of different varieties were affected by N rates differently [5]. Phosphorus was found to affect also the quality and grain yield according to Shahane et al. They studied nutrient interactions of two aromatic rice varieties and found that application of N, P, and Zn increased dry matter and grain yield of rice [6]. In addition, potassium was showed to increase tillering, grain size and weight, and disease

resistance. It was demonstrated that about 75% of plant K remains in leaves and stems, and the rest was translocated to grains. Atapattu et al. also studied increasing rate of potassium fertilizer at the time of heading and found that applying K fertilizer at 18.75 kg K ha<sup>-1</sup> rate increased the yield and grain quality [7]. Not only N P and K are macronutrient affected grain yield and 2AP, sulfur is also one of macronutrient can enhance yield and 2AP.

Sulfur (S) not only plays an important role as a constituent of essential amino acids (cysteine, methionine) involved in chlorophyll production, increasing tillering and spikelets per panicles, enhancement of rice plants resistance to abiotic stress conditions [8], but also in regulating the biosynthesis of 2AP, the precursors ornithine and glutamate that can produce a common metabolite  $\Delta$ 1-pyrroline-5-carboxylic acid (P5C) through enzymes ornithine aminotransferase (OAT), and  $\Delta$ 1-pyrroline-5-carboxylic acid synthetase (P5CS). Apart from this, ornithine is also metabolized to the polyamine putrescine through ornithine diamine oxidase (DAO) that further gets converted to  $\Delta$ 1-pyrroline [9]. Under stress conditions, putrescine is changed to spermidine and spermine through S-adenosylmethionine decarboxylase (SAMDC). This pathway SAMDC is derived from methionine metabolized by the enzyme SAM synthase, which facilitate spermidine and spermine converted to  $\Delta$ 1-pyrroline and 2AP [10].

Additionally, S element relates to 2-Acetyl-2-Thiazoline (2AT), the second aroma compound found only in

fragrant rice. Methionine and cysteine are the precursor of 2AT biosynthesis pathway [2]. Sulfur was shown to affect the quality and aroma of fragrant rice. Prasertsak et al. studied on nutrient management on grain quality and yield of KDML105 and RD15 rice, and applied sulfur as basal fertilizer for all treatments except the control (without N P and K fertilizers). They found that S fertilizer can increase yield and the content of 2AP compared to the control [11].

The above information clearly indicates that S is an important element for fragrant rice yield and quality, and it is critical to determine the appropriate rate of S fertilizer for the production of fragrant rice.

## II. METHODOLOGY

### Soil Sample Collection and Analysis

Soil composite samples were taken from 5 sub-samples collecting from randomly selected locations and were analyzed for physical and chemical properties (Table 1).

**Table 1.** Soil physical and chemical properties in the field experiment before planting in Chiang Rai and Surin provinces in 2021 and 2022.

Location	pH	OM (%)	NH <sub>4</sub> <sup>+</sup> -N (ppm)	Available		exchangeable K (ppm)	soil texture
				P (ppm)	S (ppm)		
<b>2021</b>							
Chiang Rai	4.5	2.1	46.6	70.8	21.7	80.7	Sandy loam
Surin	4.9	1.3	6.6	10.1	2.7	57.6	Sandy loam
<b>2022</b>							
Chiang Rai	4.8	1.7	64.0	111.5	46.6	43.4	Sandy loam
Surin	4.4	0.9	22.3	2.9	9.0	13.5	Sandy loam

### Field Experiment

The field experiment was conducted in Chiang Rai province (19°36'55.6"N 99°47'19.1"E) and Surin province (14°56'47.7"N 103°30'40.0"E), representing the main areas for fragrant rice production in the northern and northeast Thailand, respectively. The experiment was repeated during July-November 2021 and 2022 early season. The agrometeorological data during the rice-growing season in Chiang Rai and Surin provinces by Agromet Station is showed in Table 2. and Table 3.

**Table 2.** Temperature (°C), Humidity (%) and Rain (mm.) during July-November 2021 and 2022 in Chiang Rai province.

Month	Chiang Rai province									
	Temperature (°C)				Humidity (%)				Rainfall (mm.)	
	2021		2022		2021		2022		2021	2022
	Max.	Min.	Max.	Min.	Max.	Min.	Max.	Min.		
July	36.6	23.2	32.4	23.1	96.0	71.0	96.0	65.0	257.5	530.3
August	31.6	23.0	32.1	22.3	96.0	70.0	96.0	64.0	314.0	510.3
September	32.0	22.2	31.7	21.8	96.0	67.0	96.0	65.0	308.7	346.5
October	30.4	21.4	30.9	20.0	96.0	66.0	96.0	59.0	210.0	157.1
November	30.0	19.6	31.4	18.2	96.0	63.0	95.0	52.0	77.0	2.6

**Table 3.** Temperature (°C), Humidity (%) and Rain (mm.) during July-November 2021 and 2022 in Surin province.

Month	Surin province									
	Temperature (°C)				Humidity (%)				Rainfall (mm.)	
	2021		2022		2021		2022		2021	2022
	Max.	Min.	Max.	Min.	Max.	Min.	Max.	Min.		
July	33.5	24.1	33.7	24.8	90.0	61.0	95.0	64.0	162.5	244.2
August	32.4	24.1	33.1	24.6	93.0	59.0	95.0	64.0	166.8	305.4
September	31.7	23.5	31.6	24.2	97.0	72.0	96.0	70.0	268.7	643.4
October	31.2	22.6	31.7	21.9	95.0	68.0	93.0	60.0	262.3	47.3
November	31.3	20.5	32.9	22.1	90.0	57.0	94.0	54.0	16.8	44.5

Seedlings were transplanted into the fields with 3 seedlings/hill. The experiment was conducted in randomized complete block design (RCBD) with 4 replications. Five rates of sulfur fertilizer at rate of 0 (control), 30, 60, 90 and 120 kg S ha<sup>-1</sup> along with P and K were applied as basal fertilizer, and N in the form of urea was split-applied at the basal (50%) and at the panicle initiation stage (50%) at a rate recommended by the Rice Department of Thailand.

### Data Collection

The plant growth, yield and yield component were evaluated at two stages of tillering and maturity. The effect of sulfur application on plant growth and productivity was determined based on the collected data. The 2AP compound was analyzed in the grain among different treatments of sulfur application.

### Data analysis

Statistical analysis of the data was carried out by R software version 4.2.0. Means were compared using a one-way ANOVA. The differences between treatments were compared using the Duncan's Multiple Range Test (DMRT) at a significance level of 0.05.

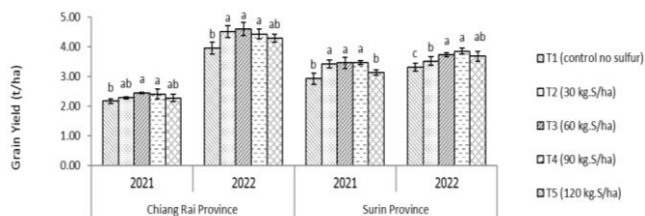
## III. RESULTS AND DISCUSSION

### Effects of different S rates on grain yield

Different grain yields were observed among treatments in 2021 and 2022. In Chiang Rai 2021, grain yields of all S-applied treatments were significantly higher than control with high grain yield being recorded in 60 and 90 kg S ha<sup>-1</sup> followed by 30 and 120 kg S ha<sup>-1</sup>. All four S treatments did not differ significantly while control had low grain yield. In 2022, high grain yield was recorded in 30, 60 and 90 kg S ha<sup>-1</sup> followed by 120 kg S ha<sup>-1</sup>, and all four S treatments did not differ significantly while control had low grain yield. In Surin 2021, S rates at 30, 60 and 90 kg S ha<sup>-1</sup> showed high, followed by 120 kg S ha<sup>-1</sup> in 2022, high grain yield was recorded in 60, 90 and 120 kg S ha<sup>-1</sup> and there was no significant difference among three S treatments while control had the lowest grain yield (Fig 1).

In Chiang Rai 2021, rice grain yields were lower than those in 2022 because more rainfall during the heading stage (mid October)-before harvesting (mid November) and the difference between min-max level in temperature and humidity, which were conducive conditions for rice blast and dirty panicle disease leading to the decreased yields. According to Jiehui et al. higher relative humidity and more moderate temperatures increase the severity of rice disease,

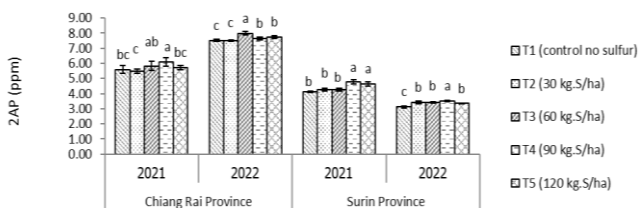
temperature and rainfall during the heading stage affected the occurrence of rice false smut [12].



**Fig 1.** Effect of sulfur application rates on grain yield in Chiang Rai and Surin provinces in 2021 and 2022. Values sharing a common letter for the same S treatment did not differ significantly at  $p < 0.05$  according to DMRT test.

### Effects of different S rates on 2AP content

Different 2AP content were observed among treatments in 2021 and 2022. In Chiang Rai 2021, high 2AP was recorded in 60 and 90 kg S ha<sup>-1</sup> with no significant difference between each other. In 2022, the highest 2AP was recorded in 60 kg S ha<sup>-1</sup> while the control and 30 kg S ha<sup>-1</sup> had the lowest 2AP. In Surin, in 2021, S rates at 90 and 120 kg S ha<sup>-1</sup> did not differ significantly though both showed high 2AP while the control, 30 and 60 kg S ha<sup>-1</sup> treatments had low 2AP. In 2022 the highest 2AP was recorded in 90 kg S ha<sup>-1</sup> while the control had the lowest 2AP (Fig 2).



**Fig 2.** Effect of sulfur application rates on 2AP in Chiang Rai and Surin provinces in 2021 and 2022. Values sharing a common letter for the same S treatment did not differ significantly at  $p < 0.05$  according to DMRT test.

Correlation between S fertilizer rates and grain yields showed significant positive correlations in both 2021 ( $r=0.57^{**}$ ) and 2022 ( $r=0.64^{**}$ ). Correlation between S fertilizer rates and 2AP was only significant in 2022 ( $r=0.53^*$ ). Likewise, grain yield and 2AP showed significant positive correlation only in 2022 ( $r=0.44^*$ ) (Table 4).

**Table 4.** Correlation between S fertilizer rates, grain yield and 2AP in Chiang Rai province, in 2021 and 2022.

	Grain yield		2AP	
	2021	2022	2021	2022
S- rate	0.39**	0.74**	0.78**	0.66**
Grain yield			0.22	0.70***

**Note:** \*\*, \*\*\* significant at  $p < 0.01$  and  $p < 0.001$ , respectively

Correlation between S fertilizer rates and grain yields showed significant positive correlations in both 2021 ( $r=0.39^{**}$ ) and 2022 ( $r=0.74^{***}$ ). The correlation analysis between S fertilizer rates and 2AP also showed significant positive correlations in both 2021 ( $r=0.78^{***}$ ) and 2022 ( $r=0.66^{**}$ ). For grain yield and 2AP, there was no correlation in 2021 while in 2022 the correlation analyses showed significant positive correlations ( $r=0.70^{***}$ ) (Table 5).

**Table 5.** Correlation between S fertilizer rates, grain yield and 2AP in Surin province, in 2021 and 2022.

	Grain yield		2AP	
	2021	2022	2021	2022
S- rate	0.57**	0.64**	0.37	0.53*
Grain yield			0.24	0.44*

**Note:** \*, \*\* significant at  $p < 0.05$  and  $p < 0.01$ , respectively

The results indicated that S is an essential nutrient element that can increase rice grain yield and enhanced 2AP. In Chiang Rai, the highest grain yields were recorded in all four S treatments (30, 60, 90 and 120 kg S ha<sup>-1</sup>) compared the control. In contrast, in Surin all treatments showed differences in both grain yields and 2AP contents. Especially, in 2021 2AP content was higher than those in 2022 because of the low rainfall/water resulting in 2AP. According to Chutipajit and Sompornpailin under drought stress, polyamine (putrescine) is changed to spermidine and spermine through S- adenosylmethionine decarboxylase (SAMDC), which facilitate spermidine and spermine converted to  $\Delta 1$ -pyrroline and 2AP [10]. Chen et al. also reported that foliar application of polyamine (putrescine) at an appropriate level can trigger physiological processes and induce the biosynthesis of osmotic adjustment substances, proline, lead to produce 2AP [13]. Nevertheless, 2AP contents were different among treatments because S in soil was at low levels. Therefore, consideration of S level in soil is needed prior to application of S fertilizer.

## IV. CONCLUSION

Sulfur rates affect grain yield and 2AP content. This study determines that the appropriate rates of S fertilizer for fragrant rice production with high grain yield, and 2AP base on soil analysis. In this study we used N, P and K in sufficient amounts for rice production at a rate recommended by the Rice Department of Thailand. However, on average application of S fertilizer enhanced grain yield by 8%, 13% and 15%, 11% compared to the control in both 2021 and 2022 in Chiang Rai and Surin provinces, respectively. Sulfur also enhanced 2AP content by 3.3%, 2.8%. and 9.3%, 9.5% compared to the control in both 2021 and 2022 in Chiang Rai and Surin province, respectively. The result suggested that farmers should apply 60 kg S ha<sup>-1</sup> for Chiang Rai and 90 kg S ha<sup>-1</sup> for Surin province to obtain higher grain yield and 2AP of fragrant rice.

### ACKNOWLEDGMENT

The author would like to acknowledge Dr. Duangjai Suriyaarunroj for advice and guidance throughout this research. Prof. Jim Wang of Louisiana State University Agricultural Center for the critical review of the manuscript. This research is financially supported by the Agricultural Research Development agency (ARDA).

### REFERENCES

- [1] Rice Department. "Khao Dawk Mali 105". Bureau of Rice Research and Development, Rice Department. Thailand. 59 p., 2010.
- [2] K. Mahattanatawee, and R. L. Rouseff. "Comparison of aroma active and sulfur volatiles in three fragrant rice cultivars using GC–Olfactometry and GC–PFPD". *Journal of Food Chemistry*. 154 (2014): 1–6, 2014.
- [3] Y. Osotsapar, "Soil Nutrition and fertilizer of rice". Soil and Fertilizer Society of Thailand. 454 p. (in Thai). 2015.
- [4] P. M. Potcho, N. E. Okpala, T. Korohou, M. Imran, N. Kamara, J. Zhang, K. D. Aloryi and X. Tang. "Nitrogen sources affected the biosynthesis of 2-acetyl-1-pyrroline, cooked rice elongation and amylose content in rice" *journal.pone.0254182*, 2021.
- [5] Kongpun, A. and C. T. Prom-u-Thai. "Effects of nitrogen fertilizer on grain yield and fragrant contents in two Thai rice varieties." *Journal of Biological Sciences*. 21 (3): 206-212, 2021.
- [6] A. Shahane, Y. S. Shivay, D. Kumar, R. Prasanna. "Interaction effect of nitrogen, phosphorus, and zinc fertilization on growth, yield, and nutrient contents of aromatic rice varieties." *Journal of Plant Nutrition* 41(5): 1-12, 2018.
- [7] A. J. Atapattu, B. D. R. Prasantha, K. S. P. Amaratunga and B. Marambe. "Increased rate of potassium fertilizer at the time of heading enhance the quality of direct-seeded rice." *Chemical and Biological Technologies in Agriculture*. 5(22): 1-9, 2018
- [8] A. Dobermann, and T.H. Fairhurst. "Handbook Series. Rice: Nutrient Disorders & Nutrient Management". International Rice Research Institute (IRR) and Potash & Phosphate institute/Potash (PPI) & Phosphate institute of Canada (PPIC): Oxford Graphic Printer Pte Ltd. 191p., 2000.
- [9] Renuka1, N., Vitthal T. Barvkar, Zahid Ansari, Chunfang Zhao, Cailin Wang, Yadong Zhang<sup>3</sup> & Altafhusain B. Nadaf. "Co-functioning of 2AP precursor amino acids enhances 2-acetyl-1-pyrroline under salt stress in aromatic rice (*Oryza sativa* L.) cultivars". *Scientific Reports* 12(1):3911. doi.org/10.1038/s41598-022-07844-7, 2022.
- [10] S. Chutipajit and K. Sompornpailin. "Polyamines in Plant Response to Various Abiotic Stresses". *SWU Sci. J. Vol. 27 No. 1* (2011) (in Thai), 2011.
- [11] A. Prasertsak, D. Suriyaarunroj, G. Suttasan, S. wongpiyachon, V. Chamareg, T. Chuenban, W. Wongboon, S. Chaiboontha, K. Sansean, Y. Tobdan, S. Pakkethathi, C. Worravechmongkol, V. Sukviwat, P. Maneenil, R. Mettakit, N. Sanguankampon, S. Kamkaew, C. Harat, V. Chayaprasert and K. Poniyom. "Management for quality and aromatic preservation along production chain of Hom Mali Rice". Ministry of Agriculture and Cooperatives. Rice Department. 407p, 2018.
- [12] S. Jiehui, W. Yan, C. Linrong, Z. Sijie, N. Chuan, Z. Di, L. You, L. Junfei, D. Zhi, G. Hui, D. Qigen, X. Ke, H. Zhongyang. "Higher relative humidity and more moderate temperatures increase the severity of rice false smut disease in the rice–crayfish coculture system". *Food and Energy security*. Volume11, Issue1. doi.org/10.1002/fes3.323, 2021.
- [13] D. Chen, Q. Shao, L. Yin, A. Younis and B. Zheng. "Polyamine Function in Plants: Metabolism, Regulation on Development, and Roles in Abiotic Stress Responses". *Front. Plant Sci.* 9:1945. doi: 10.3389/fpls.2018.01945, 2019.

# Short-term feeding of dietary Oestradiol-17 $\beta$ supplementation during fry stage did not increase female ratio in Snakeskin Gourami (*Trichopodus pectoralis*)

Apinat Kabpha, Suksan Kumkhong, Surintorn Boonanuntanasarn\*

School of Animal Technology and Innovation, Institute of Agricultural Technology, Suranaree University of Technology, 111 University Avenue, Muang, Nakhon Ratchasima, 30000, Thailand

\*Corresponding author: e-mail: surinton@sut.ac.th

**Abstract:** This study aimed to investigate the effects of oestradiol-17 $\beta$  (E2)-treated sex reversal by oral administration during fry stage. The experimental groups received dietary E2 supplementation at 0 (control), 100, 200, or 300 mg kg<sup>-1</sup>. Fry (7 days after hatching; dah) were fed the experimental diets for 45 days (7–52 dah). Intersex gonads were observed, indicating that E2 might be used for feminization induction. However, E2 sex reversal did not significantly increase the female population, suggesting that dietary E2 supplementation from 7–52 dah was not sufficient for the production of an all-female population. There were no significant differences in the growth performance. The hepatopancreas was not significantly different between experimental groups. The gonadosomatic indices of female and E2-treated fish were higher than those of male fish ( $P < 0.05$ ). These results show that dietary E2 supplementation in fry from 7–52 dah might not efficiently produce all female populations of snakeskin gourami. Further investigations are required to extend the period of E2-treated during the fry stage to obtain E2-feminized females.

**Index Terms**-Oestradiol, snakeskin gourami, *Trichopodus pectoralis*, sex reversal

## I. INTRODUCTION<sup>1</sup>

Fish are susceptible to sex reversal manipulation; therefore, the administration of exogenous steroid hormones during early development influences phenotypic sex differentiation [1-3]. In aquaculture, sex reversals are used to produce monosex populations as monosex cultures of the faster-growing sex could increase productivity and can improve the body color of ornamental fish [4-8].

The snakeskin gourami (*Trichopodus pectoralis*) is an economically important fish species found in Thailand and other Southeast Asian countries. Snakeskin gourami exhibit sexual dimorphism in their growth characteristics, in which female fish are generally larger than male fish. Therefore, the production of female monosex populations is preferable to increase production yield. To date, a number of oestrogenic hormones have been shown to effectively increase female population in fish. Among them, 17 $\beta$ -oestradiol (E2), a natural estrogen, has been generally used to produce all female fish populations [9-10]. The concentration of exogenous hormones and the method of administration influence sex reversal efficiency and vary among fish species. Generally, the start time and duration of hormone treatment initiates undifferentiated gonad development and continues through gonad differentiation [1,4,5,9,8,11].

Therefore, this study investigated the effects of dietary E2 administration during the fry stage of snakeskin gourami. Evaluation of different levels of E2 on sex ratio. In addition, we evaluated the effects of exogenous dietary E2 during the early fry stage on the growth performance during the juvenile stage.

## II. MATERIALS AND METHODS

### A. Fish and fry production

All experimental protocols were approved by the Ethics Committee of Suranaree University of Technology Animal Care and Use Committee (Approval No. 1731039). Broodstock of snakeskin gourami (*T. pectoralis*) was collected from commercial farms and cultured at the University Farm, Suranaree University of Technology, Nakhon Ratchasima, Thailand. The fish were maintained in an earthen pond (800 M<sup>2</sup>) under a natural light-dark cycle. Fish were fed a commercial diet (32% crude protein, 4% fat) ad libitum, twice a day at 10:00 and 16:00.

Five concrete ponds (2 × 2 × 1 m<sup>3</sup>) with aeration were used as mating ponds. The cleaned floating aquatic plants were

placed in ponds to build bubble nests. Four male and two female patients (2:1 male-to-female sex ratio) were injected with a mixture of a luteinizing hormone-releasing hormone (LHRH) analog (Suprefact, Hoechst, Germany) and domperidone (Motilium-M, OLIC, Bangkok, Thailand). For the first injection, females were injected with the LHRH analog and domperidone at 10 µg/kg and 5 mg/kg body weight (BW), respectively. The second injection (12 h after the first injection) for females was an LHRH analog (20 µg/kg BW) and domperidone (10 mg/kg BW). Male rats were injected once with an LHRH analog (10 µg/kg BW) and domperidone (5 mg/kg BW). After 14 h, fertilized eggs were obtained and the fish larvae were cultured in a cement pond for six days after hatching (dah).

### B. Experimental design, sex reversal and fish culture

The experimental design was completely randomized, with four different dietary E2-supplemented levels, each replicated five times. Experimental diets were prepared to incorporate the E2 (Sigma-Aldrich Chemical Co., St. Louis, MO, USA) into a commercial diet (protein 50%, lipids 15%). The four different dietary E2-supplemented diets included a basal diet (control), 100 mg/kg E2-supplemented diet (E2-100), 200 mg/kg E2-supplemented diet (E2-200), and 300 mg/kg E2-supplemented diet (E2-300). Hormonal supplemented diets (E-100, E-200, and E-300) were prepared by dissolving E2 at 100, 200, and 300 mg, respectively, in 95% ethanol (240 ml) and sprayed over the diet (1 kg). The ethanol in the hormone-supplemented diet was allowed to evaporate for 6 h in the dark at room temperature. Subsequently, all experimental diets were kept at 4 °C in the dark until use.

Twenty hapas were placed in a cement pond (10 × 5 × 0.8 m<sup>3</sup>) with aeration and a 12:12 light-dark cycle. At 6 dah, 12,000 swim-up fry were transferred and randomly distributed to each hapa (600 fry/hapa). The basal or E2-supplemented diets were fed to the fry at 52 dah. The fry were fed four times daily (9:00, 11:30, 14:00, 16:30) with experimental diets at 30% BW/day (month one), 20% BW/day (month two), and 15% BW/day (month three). Subsequently, 100 fish were transferred to new hapas and were fed a commercial diet. The sex ratio was determined at age of 8 months. Air and water temperature were determined daily during the experimental period and were 28.0 ± 5.2 °C and 28.5 ± 1.2 °C 28.0–29.0 °C, respectively. Throughout experimental period, dissolved oxygen (DO) and pH were determined weekly using a DO and pH meter, respectively, and were within acceptable ranges of 5.66 ± 1.12 mg L<sup>-1</sup> and 7.93 ± 0.17, respectively. Dead fish were then recorded and removed. The growth performance of the experimental fish was evaluated. All fish were sampled and euthanized with 0.2% of 2-phenoxyethanol. Liver samples were collected and weighed to determine the hepatosomatic index (HSI). Gonads were collected and weighed to determine the gonadosomatic index (GSI). A portion of the gonads of all

fish was collected for histological analysis to determine sex.

### C. Histological examination of gonads

The sex ratio was determined in fish at age of 8 months. All gonad samples (n = 457) were collected and fixed at 4 °C for 16 h in Bouin's solution and subsequently preserved in 70 % ethanol until analysis. The fixed samples were dehydrated by increasing ethanol concentration from 70% to 100%. Samples were then embedded in paraffin wax and cut into 5 µm thick slices and mounted on glass slides. Paraffin sections were dewaxed and dehydrated by immersion in a xylene-ethanol series. Sections were stained with hematoxylin and eosin, and morphologically observed under a microscope.

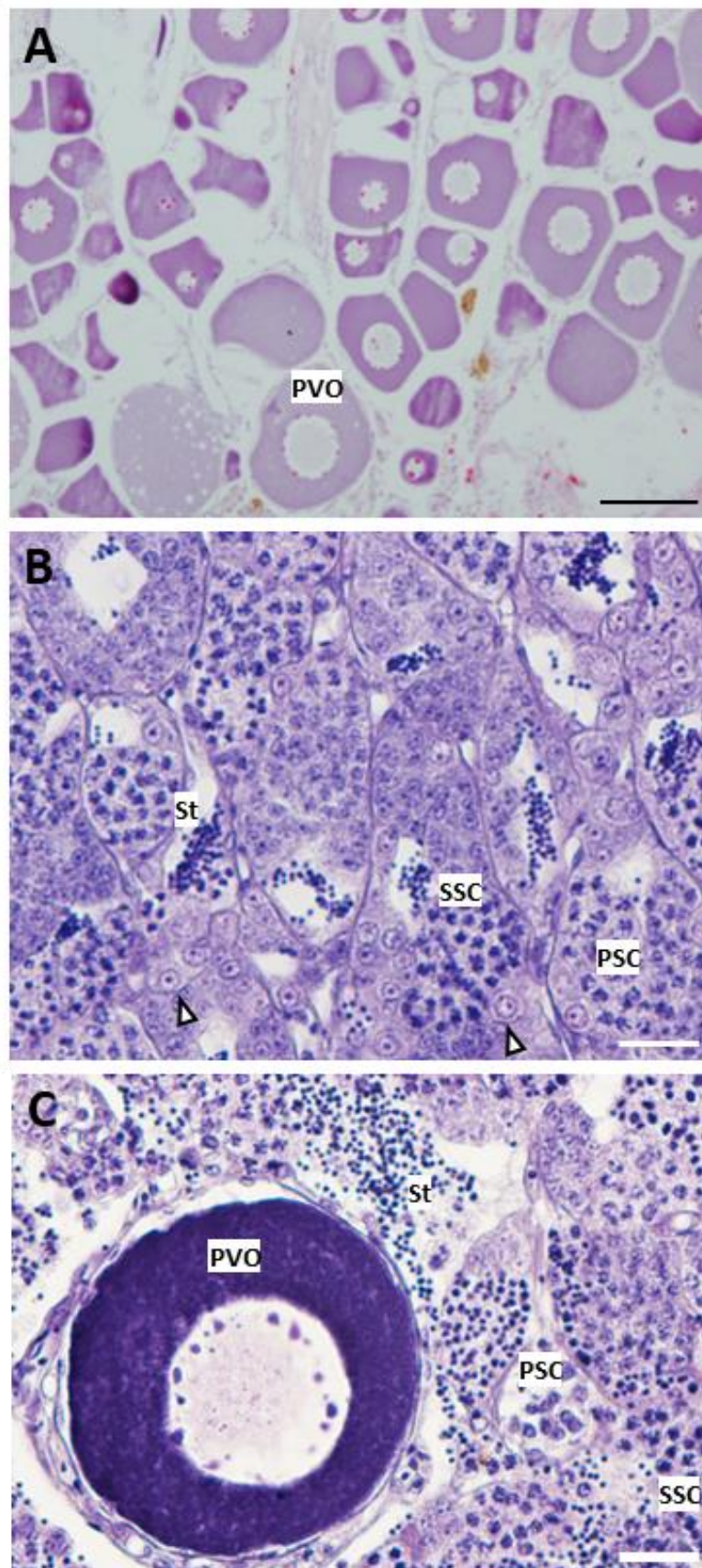
### D. Data analysis

Statistical analyses were performed using SPSS for Windows version 22 (SPSS Inc., Chicago, IL, USA). Subsequently, one-way analysis of variance (ANOVA) was performed for growth performance parameters. When significant differences were found among the groups, they were ranked using Tukey's procedure. Throughout the experiment, a P-value <0.05 was considered to indicate significant differences.

## III. RESULTS

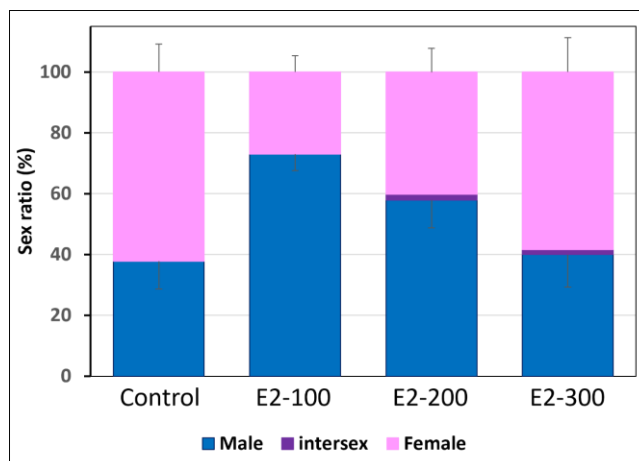
Differences in the external morphology of the body shape were observed at age of eight-months-old. Males appeared slimmer and darker than females. The females had a rounded belly and a short, rounded dorsal fin. At eight months, histological analysis revealed that the morphology of the testes contained primary spermatocyte (PSC), secondary spermatocyte (SSC), and spermatid (ST) (Figure 1). The ovaries contained both previtellogenic oocytes (PVO) and vitellogenic oocytes (VO) (Figure 1). Intersex gonads were observed after early feeding for 45 days. Nevertheless, none of the levels of E2 fed for 45 d increased the percentage of females. Our results showed that although increase dietary supplementation of E2 level did not produce more female fish, high level of E2 produced intersex fish. Therefore, there were no significant differences in the sex ratio compared to the control group (Figure 2). Note that no detrimental effects were observed in experimental fish fed with dietary E2 supplementation in all groups.

Throughout the culture period, the survival rates of fish in control and E2-treated groups appeared to be similar (P>0.05). This study determined the growth performances at age of eight months. There were no significant differences in growth performance, including final body weight, weight gain, average daily gain, specific growth rate, or feed conversion ratio (P>0.05) (Table 1). The GSI of the control and E2-treated fish were similar (P>0.05).



**Fig. 1.** Histological study of ovary (A), testes (B) and intersex gonad (C) snakeskin gourami at age of 8 months. Intersex gonad was sampling from E2-300 snakeskin gourami at age 8 months which were treated with E2-300 during 7 – 52 dph. Scale bars represent 100 μm (A) and 20 μm (B and C). PSC, primary spermatocyte; PVO, previtellogenic oocytes; SSC, Secondary spermatocyte; ST, spermatid.





**Figure 2.** Sex ratios of snakeskin gourami at age of 6 months which were treated with E2 during 7 – 52 dph. Four different dietary E2-supplemented levels including basal diet (control), 100 mg/kg E2-supplemented diet (E2-100), 200 mg/kg E2-supplemented diet (E2-200) and 300 mg/kg E2-supplemented diet (E2-300).

**TABLE 1 GROWTH PERFORMANCES OF E2-FEMINISED SNAKESKIN GOURAMI AT AGE OF 6 MONTHS WHICH WERE FED WITH E2-SUPPLEMENTED DIET FOR 45 DAYS (MEAN ± SD, N = 5)<sup>1</sup>**

Parameter	Control Male	Control Female	E2-100	E2-200	E2-300	P-values
Final body weight (g)	42.26 ± 9.32	42.84 ± 9.21	36.05 ± 9.91	39.28 ± 10.87	33.25 ± 14.54	0.515
Weight gain (g)	39.92 ± 9.34	40.49 ± 9.19	33.70 ± 9.90	36.93 ± 10.87	30.93 ± 14.54	0.516
ADG (g/day) <sup>2</sup>	0.51 ± 0.12	0.51 ± 0.12	0.43 ± 0.13	0.47 ± 0.14	0.39 ± 0.18	0.504
SGR (%/day) <sup>3</sup>	2.59 ± 0.23	2.60 ± 0.21	2.40 ± 0.28	2.50 ± 0.26	2.26 ± 0.52	0.345
FCR <sup>4</sup>	1.57 ± 0.12	1.56 ± 0.12	1.70 ± 0.20	1.62 ± 0.15	1.88 ± 0.51	0.238
GSI (%) <sup>5</sup>	0.18 ± 0.04 <sup>b</sup>	3.88 ± 2.76 <sup>ab</sup>	5.79 ± 4.83 <sup>a</sup>	4.73 ± 1.68 <sup>ab</sup>	5.41 ± 3.95 <sup>ab</sup>	0.03
HSI (%) <sup>6</sup>	2.70 ± 0.64	1.93 ± 1.01	2.77 ± 0.98	2.28 ± 0.35	2.38 ± 0.78	0.37
Survival rate (%)	29.44 ± 10.84		31.11 ± 2.72	31.67 ± 2.79	29.44 ± 6.80	0.53

<sup>1</sup>Means with different superscript in each row differ significantly from each other (P<0.05).

<sup>2</sup>Average daily gain (ADG) = (final body weight – initial body weight)/experimental days.

<sup>3</sup>Specific growth rate (SGR) = 100 × [(ln final body weight – ln initial body weight)/experimental days].

<sup>4</sup>Feed conversion ratio (FCR) = dry feed fed/wet weight gain.

<sup>5</sup>Gonadosomatic index (GSI) = 100 x (gonad weight/body weight)

<sup>6</sup>Hepatosomatic index (HSI) = 100 x (liver weight/body weight)

#### IV. DISCUSSION

Several factors affect sex manipulation, including the type and level of hormones, method of hormonal treatment, stage of fish (time of onset of sex reversal induction), and duration of treatment. For inducing feminization, it was reported that dietary hormonal supplementation during the fry stage was effective compared with other method such as water immersion in sunshine bass [11] and black crappie [4]. For production of all-female population, E2 is the most used [9-10]. Dietary supplementation with E2 increased the female population, and the dosage of E2 and the percentage of females varied depending on the fish species. For example, in electric blue hap (*Sciaenochromis ahli*) fry, dietary supplementation of E2 at 20, 40 and 60 mg/kg for four months produced 88.89– 93.33% females [7]. Supplementation with E2 at 120 mg/kg diet for a feeding period of 30 days was effective for the feminization of

sexually undifferentiated Nile tilapia (*Oreochromis*

*niloticus*) fry of Nile tilapia [12]. Dietary supplementation E2 with 120 mg/kg diet for six weeks increased the female population [13]. Similarly, E2 supplementation (2–20 mg/kg diet) for the duration of feeding (100–150 d) increased the percentage of females in the European eel (*Anguilla anguilla*) [5]. Moreover, E2 feeding treatment for duration of two or four months induced feminization of genotypic males in stable fish (*Anoplopoma fimbria*) [8]. In this study, intersex gonads indicated that E2-supplementation could perform sex reversal in snakeskin gourami. However, dietary supplementation with E2 during the fry stage for 45 days did not significantly increase the female population in snakeskin gourami, suggesting that the period of 45 days was not sufficient for complete feminization in snakeskin gourami. This might be because sex differentiation was not complete

in fry at 52 days post-hatching. Note that growth rate of fry culture in cement pond in this study might be lower comparing with previous studies in snakeskin gourami. For instance, it was revealed that dietary supplementation of 200 ppm E2 in snakeskin gourami fry from 2 weeks post-hatching for 60 days produced all females [14]. Nevertheless, oral administration of E2 at 200 mg/kg diet for 3 weeks in snakeskin gourami fry (from 2 weeks post-hatching) could produce all female snakeskin gourami [15]. Thus, differences in period of dietary E2 supplementation in snakeskin gourami fry might be because of culture systems. Therefore, to produce an all-female population, dietary E2 during the fry stage varies with the level of hormones, stage of fish, and duration of treatment, and is dependent on the species. Further investigation with longer feeding of E2-supplementation diet is required to achieve an all-female population in snakeskin gourami.

Previous studies have demonstrated that dietary treatment with E2 supplementation does not have negative effects on the survival rate of other fish species [8,6,10,12-13,16]. Survival rates among the experimental groups in this study were similar, suggesting that dietary supplementation with E2 had no detrimental effects on E2-induced feminization in snakeskin gourami. E2-induced sex reversal has been shown to improve the growth of sablefish [8] and European eel [5]. However, in past studies, the effects of E2-treated sex reversal on growth were detected in young fish, including in studies on tambaqui [13], stellate sturgeon (*Acipenser stellatus*) [6], and European catfish (*Silurus glanis*) [10]. In contrast, treatment with E2 has negative effects on the growth of Atlantic halibut (*Hippoglossus hippoglossus*) [17], largemouth bass (*Micropterus salmoides*) [18], shortnose sturgeon (*Acipenser brevirostrum*) [14], and sunshine bass (*Morone chrysops* × *Morone saxatilis*) [11]. Our results for snakeskin gourami showed no significant differences in the growth performance among the experimental groups. This may be because the female ratio did not increase. Whether a longer treatment with E2, which increases the female population in snakeskin gourami, has positive effects on growth performance remains to be investigated.

## V. CONCLUSION

In conclusion, although E2 supplementation during the fry stage could be used for sex reversal, dietary E2 supplementation during the fry stage for 45 days was not effective in increasing the female population. These E2 treatments had no effect on the growth performance of the snakeskin gourami.

## ACKNOWLEDGMENT

This study was supported by a grant from the Suranaree University of Technology.

## REFERENCES

[1] Budd, A.M., Banh, Q.Q., Domingos, J.A. and Jerry, D.R., 2015. Sex control in fish: approaches, challenges and opportunities for aquaculture. *Journal of Marine Science and Engineering* 3 (2), 329-355.

- [2] Lazaro-Velasco, A., Isidro-Cristobal, H.M., Alcántar-Vázquez, J.P., Antonio-Estrada, C., Calzada-Ruiz, D. and Torre, R.M.D.L., 2019. Effect of the combination of a cold-water temperature and exogenous estrogens on feminization, growth, gonadosomatic index and fat muscle content of Nile tilapia *Oreochromis niloticus* (Linnaeus, 1758). *Lat. Am. J. Aquat. Res.* 47, 52-64.
- [3] Dussenne, M., Gennotte, V., Rougeot, C., Mélard, C. and Cornil, C.A., 2020. Consequences of temperature-induced sex reversal on hormones and brain in Nile tilapia (*Oreochromis niloticus*). *Horm. Behav.* 121, 104728.
- [4] Arslan, T. and Phelps, R.P., 2004. Production of monosex male black crappie, *Pomoxis nigromaculatus*, populations by multiple androgen immersion. *Aquaculture* 234, 561-573.
- [5] Tzchori, I., Degani, G., Elisha, R., Eliyahu, R., Hurvitz, A., Vaya, J. and Moav, B., 2004. The influence of phytoestrogens and oestradiol-17 $\beta$  on growth and sex determination in the European eel (*Anguilla anguilla*). *Aquac. Res.* 35 (13), 1213-1219.
- [6] Falahatkar, B., Poursaeid, S., Meknatkha, B., Khara, H. and Efatpanah, I., 2014. Long-term effects of intraperitoneal injection of estradiol-17 $\beta$  on the growth and physiology of juvenile stellate sturgeon *Acipenser stellatus*. *Fish Physiol. Biochem.* 40, 365-373.
- [7] Karsli, Z., Aral, O. and Yeşilayer, N., 2016. The effects of different proportions of the 17 $\beta$ -estradiol and 17 $\alpha$ -methyltestosterone on growth, sex reversal and skin colouration of the electric blue hap (*Sciaenochromis ahli* Trewavas, 1935). *Aquac. Res.* 47, 640-648.
- [8] Luckenbach, J.A., Fairgrieve, W.T. and Hayman, E.S., 2017. Establishment of monosex female production of sablefish (*Anoplopoma fimbria*) through direct and indirect sex control. *Aquaculture* 479, 285-296.
- [9] Piferer, F., 2001. Endocrine sex control strategies for the feminization of teleost fish. *Aquaculture* 197, 229-281.
- [10] Król, J., Poblocki, W., Bockenheimer, T. and Hliwa, P., 2014. Effect of diethylstilbestrol (DES) and 17 $\beta$ -estradiol (E2) on growth, survival and histological structure of the internal organs in juvenile European catfish *Silurus glanis* (L.). *Aquac. Int.* 22, 53-62.
- [11] Davis, K.B. and Ludwig, G.M., 2004. Hormonal effects on sex differentiation and growth in sunshine bass *Morone chrysops* × *Morone saxatilis*. *Aquaculture* 231, 587-596.
- [12] Alcántar-Vázquez, J.P., Rueda-Curiel, P., Calzada-Ruiz, D., Antonio-Estrada, C. and Moreno-de la Torre, R., 2015. Feminization of the Nile tilapia *Oreochromis niloticus* by estradiol-17 $\beta$  Effects on growth, gonadal development and body composition. *Hidrobiológica* 25, 275-283.
- [13] Reis, V.R. and Almeida, F.L., 2019. Effect of 17 $\beta$ -oestradiol on the sex ratio of tambaqui, *Colossoma macropomum*. *Aquac. Res.* 50, 154-161.
- [14] Thongmee, B. 1995. Effect of 17 beta-estradiol on sex reversal of Sepat Siam, *Trichogaster pectoralis* (Regan). Kasetsart University, Bangkok (Thailand). Graduate School.
- [15] Pongthana, N., Baoprasertkul, B. and Thongmi, B. (1995). Hormonal feminization of snakeskin gourami (*Trichogaster pectoralis*). *Thai Fish. Gaz.* 48(4): 303-318.
- [16] Flynn, S.R. and Benfey, T.J., 2007. Effects of dietary estradiol-17 $\beta$  in juvenile shortnose sturgeon, (*Acipenser brevirostrum*), Lesueur. *Aquaculture* 270, 405-412.
- [17] Hendry, C.I., Martin-Robichaud, D.J. and Benfey, T.J., 2003. Hormonal sex reversal of Atlantic halibut (*Hippoglossus hippoglossus* L.). *Aquaculture* 219, 769-781.
- [18] Arslan, T., Phelps, R.P. and Osborne, J.A., 2009. Effects of oestradiol-17 $\beta$  or 17 $\alpha$ -methyltestosterone administration on gonadal differentiation of largemouth bass *Micropterus salmoides* (Lacepède). *Aquaculture Research* 40 (16), 1813-1822.

# Comparison of Hemp Producing Practices of Farmers in Chiang Mai and Tak Province

Ritdeach Suta<sup>1</sup>, Juthathip Chalermphol <sup>2\*</sup>

<sup>1</sup> Agricultural Extension and Rural Development, Department of Agricultural Economic and Development, Faculty of Agriculture, Chiang Mai University, s.ritdeach@gmail.com

<sup>2\*</sup> Assistant Professor, Department of Agricultural Economic and Development, Faculty of Agriculture, Chiang Mai University, juthathip.c@cmu.ac.th

**Abstract:** The research objectives were to study the producing practices of hemp crop by farmers in Chiang Mai and Tak province and to analyze the differences in hemp production practices in Chiang Mai and Tak province. The study was conducted on 159 peoples divided into Chiang Mai province 95 peoples and Tak province 64 peoples. The studied area is Chiang Mai and Tak province which are many hemp farmers in northern Thailand. This study was conducted on a group of hemp farmers in the area. Chiang Mai and Tak Province. Population and sample used in the study 95 hemp farmers in Chiang Mai and 64 hemp farmers in Tak Province were selected by population selection method of Taro Yamane, 1973. the research content was analyzed as follows. 1) Analyze the data according to the first objective to study the hemp planting practices of farmers in Chiang Mai and Tak province with descriptive statistical data analysis methods. The farmers' practices are analyzed by frequency distribution, percentage, mean and standard deviation. 2) Analyze the data according to the second objective to analyze differences in hemp production practices in Chiang Mai and Tak province. Statistical analysis is used to compare differences between two or more variables one-way ANOVA or T-Test. From studying the practices in hemp cultivation methods and comparing the practices of two provinces, it was found that for Chiang Mai province, the process that farmers follow the most is practices of registration and planting readiness (percent = 96.93). followed is practices of harvesting procedures and post-harvest care (percent = 94.74). followed is Practices of practical steps in planting (percent = 85.26) respectively. While in Tak province, the process that farmers follow the most is practices of registration and planting readiness (percent = 97.27). Followed are practices of practical steps in planting (percent = 80.00). Followed are practices of procedures for maintenance (percent = 74.65) respectively. When analyzing the practical comparison of Chiang Mai and Tak provinces by one-way ANOVA analysis found that in terms of differences in the practices of farmers in both provinces, was found that the practices of harvesting procedures and post-harvest care of farmers in Chiang Mai and Tak province. There were statistically significant (level of 0.01) differences in cultivation and practices. For practices of practical steps in the planting of Chiang Mai and Tak farmers, there were statistically significant (level of 0.05) differences in cultivation. The practices of hemp farmers in Chiang Mai and Tak provinces are similar. However, there are some processes that farmers in both provinces practice differently, Namely the process of planting and the process of preserving produce after harvest. If considered in different cultivations, It may be caused by the characteristics of the area and the environment that is conducive to the growth of hemp in each provinces. As for the treatment of different yields, it may be because Farmers utilize hemp in various parts are different.

## ***Index Terms*—Comparison, Hemp, Practices, Producing**

### I. INTRODUCTION<sup>1</sup>

Hemp is a plant belonging to the Cannabis sativa group that contains Cannabidiol (CBD) which has a relaxed effected and substance. Tetrahydrocannabinols (THC), which affects the nervous system and is a common cause of motion sickness, as well as Cannabis THC content in hemp plants and cannabis ranges typically from 3 to 15%. Grown hemp for industrial use in the Netherlands (and the European Union) are required to used of varieties that contain less than 0.2% THC, which cannot be used as a

drug. [1]

In Europe has been used hemp to produce paper, fabric, fiber and rope since ancient times. But begun to be planted hemp in use for industry and commerce in the 1970s because of the community. The European economy provides supported under the Common Agricultural Policy (CAP). In 2011, the country. Europe, with the largest hemp plantation area is France. There are approximately 10,000 hectares of cultivated land, followed by is the Netherlands has approximately 1,200 hectares of cultivated land. Made hemp cultivation. It is of interest in the European Union

because hemp is a plant that can with resisted the weather and temperature during the season. Europe's cold winter, while cotton needs a warm climate. In addition, hemp is a plant that does not needed a lot of water and does not needed fertilizer, able to grown consecutively without used other plants to rotate. Therefore, it is a plant that is considered to have sustainability. Therefore, hemp is an attractive industrial and commercial crop. [2]

In Thailand, hemp is regarded as an interested plant. Because hemp can be processed in a variety of ways. Both in food, medicine and cosmetics. Therefore, hemp is a crop that farmers wanted to grown. In Northern Thailand, A way of life has long been associated with the hemp culture is found in every highland area. In Chiang Mai and Tak provinces, reflecting beliefs, faith, customs and traditions, as well as processes and methods of utilization of fibers unique to each community or village, become 'Local wisdom' consists of knowledge, abilities combined with values. and beliefs about people and nature as well as people and supernatural things. Through the processed of customs, way of life, livelihood and rituals in the past to the present, the way of life of the Hmong and Hemp ethnic groups have been linked to local wisdom and culture. Nature and the environment for generations to become crystallized. [3]

In the present, Hemp can be cultivated in Thailand and has a high value. But it is also new knowledge for farmers. It is causing to the cultivation of hemp has not have high yields and less quality. The practices cultivation is essential to the quantity and quality of produce. However, Thailand still has less utilization of hemp. Due to legal limitations and difficulties in obtained permission to plant, although "Hemp" is a plant that has been promoted for economic and industrial used. Moreover, it also showed a cleared difference between hemp and marijuana, Both physically and drug addiction. But the concern about its used in the form of drugs is so great that hemp extraction benefits. For used in the food industry and cosmetics, so there is a hassle and to demonstrate other benefits that can helped reduce anxiety about drug used. This research therefore focuses on the study of planting practices, which will inform the cultivation methods used by most farmers in production and the practices of farmers in each hemp plant production process. to lead to the development of new farmers in the future. [4]

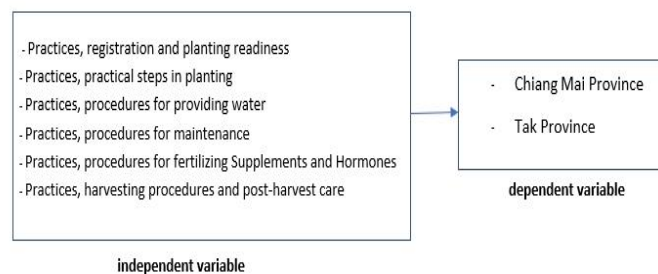


Fig. 1. Province are not dependent variable.

## II. LITERATURE REVIEW

### A. Hemp

Hemp is a same plant of cannabis or marijuana. Hemp has a scientific name is *Cannabis sativa* L. *Subsp*, which this plant contains important substances in the cannabinoid group as addictive substances. Previously. in Thailand, hemp was classified as an illegal plant. But now, Hemp is unlocked from illegal crops. People can grown hemp but it has to be controlled by the Ministry of Public Health. [5] Currently, The law allows the used of hemp in many areas by notification of the Ministry of Public Health on specifying the name and type of narcotic drugs, except dry bark, dry stem core, dry fiber and products made from dry bark, dried stem core, dry fiber on July 31, 2013. Including the announcement of the Ministry of Public Health on specifying the name of narcotics in category, specifying the name of hemp, whose scientific name is *Cannabis sativa* L. *subsp*. *Sativa*, which is a subspecies of the cannabis plant (*Cannabis sativa* L.), which includes all parts of the hemp plant such as leaves, flowers, shoots, seeds, stems that contain Tetrahydrocannabinol. (THC) and characteristics as prescribed by the committee excepted for Cannabidiol (CBD) that is 99% pure and contains no more than 0.01% THC, and products based on extracts that contain no more than 0.2 % THC can be used as pharmaceuticals. In addition, seeds and oil from the seeds can be used as food and cosmetics as of August 30, 2019. The legal cultivation of hemp always requires permission from the Ministry of Public Health before planting no exception. There is no free planted, currently it is still in the period that is limited to only government agencies as applicants for permission. The Ministry of Public Health has announced that it will announce that the general public can apply for permission around the beginning of the year 2020 onwards. [6]

However, hemp is a plant belonging to the genus and species same as marijuana. But different subspecies which

hemp it's scientific name is *Cannabis Sativa L. ssp. Sativa*. Hemp and marijuana are very similar in appearance. [Fig.2] Therefore, hemp and marijuana it difficult to separate from each other. However, There are some differences such as the appearance of hemp leaves is large. Female leaves and inflorescences are less fragrant than marijuana. As for the stems of hemp, there will be long joints, tall stems, few branches. In most cases, hemp planted farmers will plant in rows with a frequent planted distance of about 15 - 20 centimeters per plant. So that the tree is tall and has fewer branches resulting in good quality fibers. In Thailand, hemp is a crop that the government is paid to attention. Because hemp is a plant that can be processed in a variety of industries and medicine In Thailand, fibers from the bark are commonly used. And the trunk core is used as a construction ingredient such as hemp block, hemp concrete, pillar, roof, particle board. And heat insulation in hemp inflorescences, THC (Tetrahydrocannabinol), CBD (Cannabidiol) and terpene were found. Can be used to produce medical drugs. [7]

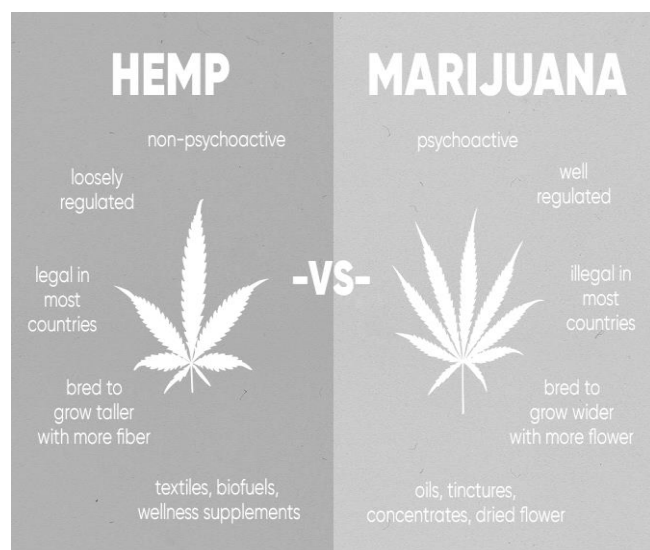


Fig. 2. The difference between Hemp and Marijuana.

### B. Practice and hemp Practice

The best practices refers to practices or procedures that made the organization successful or lead to excellence in accordance with its goals. Is accepted in that academic or professional circle and there is cleared evidence of succeeded with a summarized of the practiced or procedures as well as knowledge and experienced recorded as a document and disseminated to internal or external agencies to be able to use.

Best practice arises from obstacles any work has various obstacles. That prevents the worked from achieving its intended goals pressure from executives or competition from competitors These things will motivate us to seek guidance, problem solving process and overcome obstacles to achieve best practice.

Best practice caused by inspiration that wants to developed or found new ways for the satisfaction of the agency or their own in ordered to create better efficiency.

Managing knowledge to achieve that goal must made Best Practice that is knowledge of the person. Become the knowledge that can be revealed to be beneficial to the agency if the personnel are relocated, retired or resigned from worked. Then there won't be any problems later, for example, reports, manuals, and various operations. so that others in the department can access and knowledge to solve problems or can be extended so that new people who come in will not have to started from zero changed to start from knowledge management. Provided by the organization So this is important to senior management. In various organizations has given importance to best practice in terms of taught management or ways to worked better and more becoming a cycle for developed the organization to progress endlessly. [8]

Hemp production practices in Thailand The production system should be managed. Because hemp is a controlled plant. Hemp famers must follow the guidelines. Which the practiced is as follows registration process and planted readiness, practical steps in cultivation, procedures for providing water, maintenance procedures, procedures for fertilizing supplements and hormones and harvesting process and post-harvest care. which all practices farmers will be able to attend training or receive information from agencies promoted hemp cultivation. [9]

## III. METHODOLOGY

### 1. Population and Sample

This study was conducted on a group of hemp farmers in the area. Chiang Mai and Tak Province.

1.1. Chiang Mai 20 districts: San Sai, Mae Rim, Doi Lo, Fang, Samoeng, Hang Dong, Mae Wang, Mae Rim, Chiang Dao, Chom Thong, Mae Taeng, Muang, Doi Saket, Phrao, San Kamphaeng, Mae Ai, San Pa Tong, Chai Prakan, Mae and Saraphi.

1.2. Tak Province, 3 districts: Phop Phra, Mae Sot and Sam Ngao

The populations are 98 farmers in Chiang Mai province and 66 farmers in Tak province. Sample used in the studied 95 hemp farmers in Chiang Mai and 64 hemp farmers in Tak were selected by population selection method of Taro Yamane (1973). [10]

### 2. Data Analysis

The researcher used a research tool by Interview form. Chiang Mai and Tak hemp farmers. Then, the research content was analyzed as follows. 1) Analyze the data

according to the first objective to studied the hemp planted practices of farmers in Chiang Mai and Tak provinces which consists of registration process and planted readiness, practical steps in cultivation, procedures for providing water, maintenance procedures, procedures for fertilizing supplements and hormones and harvesting process and post-harvest care. with descriptive statistical data analysis methods. The farmers' practices are analyzed by frequency distribution, percentage, mean and standard deviation.

2) Analyzed the data according to the second objective to analyze differences in hemp production practices in Chiang Mai and Tak provinces. Statistical Analyzed is used to compare differences between two or more variables with one-way ANOVA or T-Test to compare the methods of farmers' practices in each step.

#### IV. RESULTS AND DISCUSSION

Studied the practices of hemp farmers in this studied are the hemp production process, methods of registration and planting readiness, techniques of practical steps in planting, practices procedures for providing water, practices procedures for maintenance, methods procedures for fertilizing supplements and hormones, and practices of harvesting procedures and post-harvest care. The analysis results of demographic from 159 respondents from 95 farmers in Chiang Mai province and 64 farmers from Tak province found that, in Chiang Mai province, the process that farmers follow the most is practices of registration and planting readiness (Percentage = 96.93) (Mean = 11.63), (Std. Deviation = 0.58). Followed are practices of harvesting procedures and post-harvest care (Percentage = 94.74), (Mean = 3.79), (Std. Deviation = 0.43). Followed are practices of practical steps in planting (Percentage = 85.26), (Mean = 4.26), (Std. Deviation = 0.76) respectively. While in Tak province, the process that farmers follow the most is Practices of registration and planting readiness (Percentage = 97.27), (Mean = 11.67), (Std. Deviation = 0.59). Followed is the practice of practical steps in planting (Percentage = 80.00), (Mean = 4.00), (Std. Deviation = 0.77). Followed are practices of procedures for maintenance (Percentage = 74.65), (Mean = 6.72), (Std. Deviation = 0.91) respectively. [TABLE I] From the analysis, Farmers will focus on most of the registration of planting and cultivation because there is a legal cause. In the process of fertilizing and adding hormones, most of the farmers in both provinces did not practice. The reason is that hemp plants are low-maintenance, similar to Muzyczek's studied (2012). [11]

TABLE I

Shows the percentage, mean and standard deviation of the practices of hemp farmers in Chiang Mai and Tak provinces.

process	Chiang Mai				Tak			
	N	Percent	X	Std. Deviation	N	Percent	X	Std. Deviation
1. Practices, registration and planting readiness	95	96.93	11.63	0.58	64	97.27	11.67	0.59
2. Practices, practical steps in planting	95	85.26	4.26	0.757	64	80.00	4.00	0.77
3. Practices, procedures for providing water	95	66.74	3.34	0.80	64	65.00	3.25	0.73
4. Practices, procedures for maintenance	95	71.81	6.46	0.97	64	74.65	6.72	0.91
5. Practices, procedures for fertilizing Supplements and Hormones	95	56.69	3.97	0.92	64	55.80	3.91	2.07
6. Practices, harvesting procedures and post-harvest care	95	94.74	3.79	0.43	64	71.48	2.86	1.04
<b>Total</b>	<b>95</b>	<b>78.70</b>	<b>5.58</b>	<b>0.74</b>	<b>64</b>	<b>74.03</b>	<b>5.40</b>	<b>1.02</b>

In terms of differences in the practices of farmers in both provinces, it was found that the methods of harvesting procedures and post-harvest care of farmers in Chiang Mai and Tak provinces were statistically significant (level of 0.01) differences in cultivation and practices. Ways of practical steps in planting farmers in Chiang Mai and Tak provinces there were statistically significant (level of 0.05) differences in cultivation. At the same time, other processes were not statistically different. [TABLE II] Most hemp farmers in Tak province are ethnic groups whose culture and production techniques have been inherited from their ancestors, difference from farmers in Chiang Mai provinces, who are primarily plain people. Thus, there is a difference in cultivation practices and methods of pre-harvest storage. [12]

TABLE II

Shows the comparison of practices of hemp farmers in Chiang Mai and Tak province.

process	province	N	Mean	Std. Deviation	t	sig
1. Practices, registration and planting readiness	Chiang Mai	95	11.6316	.58442	-4.23	.673
	Tak	64	11.6719	.59240		
2. Practices, practical steps in planting	Chiang Mai	95	4.2632	.76089	2.112*	.037
	Tak	64	4.0000	.77664		
3. Practices, procedures for providing water	Chiang Mai	95	3.3368	.80702	.702	.484
	Tak	64	3.2500	.73463		
4. Practices, procedures for maintenance	Chiang Mai	95	6.4632	.97643	-1.679	.095
	Tak	64	6.7188	.91667		
5. Practices, procedures for fertilizing Supplements and Hormones	Chiang Mai	95	3.9684	.92774	.256	.798
	Tak	64	3.9063	2.08333		
6. Practices, harvesting procedures and post-harvest care	Chiang Mai	95	3.7895	.43503	7.703***	.000
	Tak	64	2.8594	1.05209		
<b>Total</b>	<b>Chiang Mai</b>	<b>95</b>	<b>33.4526</b>	<b>1.94482</b>	<b>-560</b>	<b>.577</b>
	<b>Tak</b>	<b>64</b>	<b>33.6875</b>	<b>3.33750</b>		

\*p<.05 \*\*\*p<.01

## V. CONCLUSION

The practices of hemp farmers in Chiang Mai and Tak provinces are different. However, there are some processes that farmers in both provinces practice differently, namely the process of planting and the process of preserving produce after harvest. If considered in different cultivations, it may be caused by the characteristics of the area and the environment that is conducive to the growth of hemp in each province. As for the treatment of different yields, it may be because farmers utilize hemp in various parts such as seeds, fibers, leaves and roots are different.

## ACKNOWLEDGMENT

The authors would like to acknowledge the hemp farmers in Chiang Mai and Tak province for provided cultivation information including Highland Research and Development Institute (Public Organization) for hemp farmers information. and thanks to the Faculty of Agriculture, Chiang Mai University for supported in doing this research.

## REFERENCES

- [1] Rungthip Luilao. "Hemp Innovation for Sufficient and Sustainable Community and Environment Development". *Environmental Journal*, Vol. 23 (No. 3). 2019.
- [2] Office of International Trade Promotion in The Hague Department of International Trade Promotion Ministry of Commerce. The exploitation of hemp and commercial cannabis in the Netherlands. 2022.
- [3] Dhakal U.; Berardi U.; Gorgolewski M.; and Richman R., The use of hemp fibres as reinforcements in composites. In *Biofiber reinforcements in composite materials*: Elsevier. Dhakal, U., Berardi. 2015
- [4] Narcotics Control Division. Guidelines for officials on the supervision of narcotic drugs, type 5, only hemp (Hemp). Bangkok: Printing Office of the National Buddhism. 2018
- [5] Pronchanok Janesirisak "Cannabis and hemp in cosmetic productst". *Journal of health consumer protection*. Vol.1 No.2 July – December. 2021
- [6] Ratya Yanaphan. "Hemp cultivation under a controlled system". Research article. research institutes and Highland Development (Public Organization). 2019.
- [7] Sarita Pinmanee, "Industrial Hemp Processing". Research article. research institutes and Highland Development (Public Organization). 2020.
- [8] Chanathip leenin, "Get to know good practices:Best Practice". Blog Best Practice RMUT+2 KM Knowledge Management Network. 2018.
- [9] Narcotics Control Division. Handbook of competent officials in the supervision of narcotic drugs category 5, only hemp (Hemp). Bangkok: National Buddhism Printing Office. 2018.
- [10] Yamane, T..*Statistics: An Introductory Analysis*. 3rded. Harper andRow, New York. 1973
- [11] Muzyczek, M. 10 - The use of flax and hemp for textile applications. In R. M. Kozłowski (Ed.), *Handbook of Natural Fibres* (Vol. 2): Woodhead Publishing. 2012.
- [12] Tang, K., Struik, P. C., Yin, X., Thouminot, C., Bjelková, M., Stramkale, V., and Amaducci, S. Comparing hemp (*Cannabis sativa* L.) cultivars for dual-purpose production under contrasting environments. *Industrial Crops and Products*. 2016.

# Model for prediction of tube diameter, and tube length of titanium dioxide nanotubes prepared by anodization.

Hathaiporn Sudchai<sup>1</sup>, and Ampai Chanachai<sup>2\*</sup>

<sup>1</sup> Department of Chemical Engineering, Faculty of Engineering, King Mongkut's University of Technology Thonburi, 126 Pracha Uthit Rd., Bangmod, Thung Khru, 10140, Thailand  
Email: <sup>1</sup> bowwiebeeboo@gmail.com, <sup>2\*</sup> Ampai.cha@kmutt.ac.th

**Abstract:** Organic pollutants can be effectively removed using a photocatalytic reaction. In addition, the anodizing titanium dioxide nanotube arrays (TNAs), can be efficiency used as a catalyst of the photocatalytic reaction. The tube diameter and tube length are important characteristic of TNAs affecting photocatalytic reaction. Nevertheless, no model has yet been able to predict the tube diameter and length obtained under various anodization condition. Regression model of TNAs tube diameter and length with anodization condition from literature were conduct using Minitab program. The result model showed that the linear equation for tube diameter modeling and the exponential equation for tube length modeling have the lowest average errors of -0.53% and 9.44%, respectively. As a result, the linear and exponential equations were chosen to be adjusted for predicting tube diameter and length, respectively. Based on the adjusted model, the average of both errors decreased to 0% by comparing the tube diameter or length obtained from the adjusted model with the research.

**Keywords:** Anodization, Minitab, Photocatalytic, Titanium dioxide nanotubes

## I. INTRODUCTION

The photocatalytic process [1] removes organic materials that produce a radical with strong oxidizing properties and converts it to a stable molecule. Carbon dioxide and water react in light, with the semiconductor acting as a catalyst. This method has the advantage of being both low-cost and environmentally friendly. It is highly efficient at removing pollution. As a result, it has become the most widely used technology.[2] Catalysts include zinc oxide and titanium dioxide. Many studies on the use of titanium dioxide are currently being conducted. This is because there are various types of radial energy band gaps. Titanium dioxide is chemically more stable than other types of catalysts, corrosion-resistant, and cost-effective. As a result, it is a viable option for consideration. In the photocatalysis process, it acts as a catalyst.[3]

The synthesis of titanium dioxide improves the photocatalytic process efficiency because nanotubes are more efficient in photocatalytic degradation due to their larger reaction area. Titanium dioxide nanotubes (TNAs) have been extensively researched and tested for pollution control. There are several methods for fabricating titanium dioxide. The anodization process is used to synthesize titanium dioxide into nanotubes. Anodization is accomplished using an electrolysis cell to form a film layer on the sheet representing a nanotube. This increases the surface area of the reaction more than the titanium dioxide film used in other methods.

In addition, there are several ways to discover titanium dioxide manufacturing, such as dip coating. The film can be

created at room temperature and atmospheric pressure; however, the workpiece must be pulled at a constant speed. To ensure the surface of the workpiece is uniform [4]. The film is readily and cheaply made using the sol-gel technique, but the pH of the catalyst is controlled, and keeping a constant temperature is difficult [5]. The chemical vapor deposition (CVD) procedure produces an almost consistent layer thickness, but it requires significant time and energy and is difficult to control the reaction [6]. Titanium dioxide cannot be produced using nanotubes. The anodizing technique (Anodization) is a method for synthesizing titanium dioxide into nanotubes by employing an electrolysis cell to build a film layer in the form of nanotubes on the workpiece, which improves the reaction surface area compared to the titanium dioxide film produced by other methods.

The photocatalytic reaction was affected by tube diameter, length, and TNA crystal structure. [7,8,9] Currently, three methods for producing crystalline titanium dioxide are anatase, brookite, and rutile. The anatase titanium dioxide crystal structure appears to have energy band gaps that allow all radial bodies and are larger than the crystalline structure. Hydroxyl radicals and superoxide radicals are produced by rutile and other catalysts. As a result, anatase crystalline titanium dioxide is commonly used. Along with not having too much activation energy, as seen in titanium dioxide. [10] Additionally, the factors affecting the anodization process were studied. The conditions for producing TNAs for removing organic matter were determined using acid electrolytes NH<sub>4</sub>F, organic electrolyte composed of EG, electric water potential, temperature, time for anodizing, electrolyte stirring, the distance between nodes and pH.



Furthermore, acknowledge the significance of producing TNAs for the most efficient removal of organic matter. However, a model to predict the required tube diameter and length of TNAs has yet to be developed, and several factors affect tube diameter and length. Using the regression method in Minitab, this study includes data from multiple research studies to create a model to predict tube diameter and length to the factors that include the acid electrolytes NH<sub>4</sub>F, organic electrolyte composed of EG, electric water potential, temperature, time for anodizing, electrolyte stirring, the distance between nodes, and pH.

prepared with a pH range discovered to be 5 - 7. However, there are various acid electrolytes NH<sub>4</sub>F, organic electrolytes composed of ethylene glycol, electric water potential, temperature, time for anodizing, electrolyte stirring, the distance between nodes, and pH potential the use.

The data shown in Table I are obtained from the data collection of factors affecting tube diameter, and tube length of TNAs, which are EG electrolyte, water, NH<sub>4</sub>F electrolyte electric potential, temperature, time for anodizing, electrolyte stirring, and distance between nodes.

## II. DATA USED

From the literature, the TNAs samples were primarily

TABLE I

THE VALUE OF EG ELECTROLYTE, WATER, NH<sub>4</sub>F ELECTROLYTE, ELECTRIC POTENTIAL, TEMPERATURE, TIME FOR ANODIZING, ELECTROLYTE STIRRING, DISTANCE BETWEEN NODES TUBE DIAMETER AND TUBE LENGTH.

No.	EG electrolyte (%wt)	Water (%wt)	NH <sub>4</sub> F electrolyte (%wt)	Electric potential (V)	Temp. (°C)	Time for anodizing (hr)	Stirring (rpm)	Distance between nodes (cm)	Diameter (nm)	Length (µm)	Ref.
1	98	2	0.3	30	25	6	150	3	81	9	
2	98	2	0.3	45	25	6	150	3	125	12	
3	98	2	0.3	60	25	6	150	3	131	46	
4	98	2	0.1	60	25	6	150	3	112	30	
5	98	2	0.3	60	25	6	150	3	131	46	
6	98	2	0.5	60	25	6	150	3	171	20	
7	98	2	0.3	60	25	3	150	3	127	24	[11]
8	98	2	0.3	60	25	6	150	3	131	46	
9	98	2	0.3	60	25	12	150	3	128	71	
10	98	2	0.3	60	5	6	150	3	103	16	
11	98	2	0.3	60	15	6	150	3	119	24	
12	98	2	0.3	60	25	6	150	3	131	46	
13	98	2	0.3	60	45	6	150	3	140	57	
14	94.5	5	0.5	20	25	3	0	5	50	2.2	
15	94.5	5	0.5	30	25	3	0	5	70	4.4	
16	94.5	5	0.5	40	25	3	0	5	85	5	[12]
17	94.5	5	0.5	50	25	3	0	5	100	6.6	
18	94.5	5	0.5	60	25	3	0	5	120	10.4	
19	98	1.79	0.38	30	20	3	0	3	58	15	
20	98	1.79	0.38	40	20	3	0	3	63	21	
21	98	1.79	0.38	50	20	3	0	3	66	32	[13]
22	98	1.79	0.38	60	20	3	0	3	70	40	
23	98	1.79	0.38	70	20	3	0	3	72	51	

TABLE I (CONTINUE.)

THE VALUE OF EG ELECTROLYTE, WATER, NH<sub>4</sub>F ELECTROLYTE, ELECTRIC POTENTIAL, TEMPERATURE, TIME FOR ANODIZING,  
ELECTROLYTE STIRRING, DISTANCE BETWEEN NODES TUBE DIAMETER AND TUBE LENGTH.

No.	EG electrolyte (%wt)	Water (%wt)	NH <sub>4</sub> F electrolyte (%wt)	Electric potential (V)	Temp. (°C)	Time for anodizing (hr)	Stirring (rpm)	Distance between nodes (cm)	Diameter (nm)	Length (µm)	Ref.
24	98	2	0.5	40	25	5	0	5	54	6.84	
25	98	2	0.5	50	25	5	0	5	71	8.248	[14]
26	98	2	0.5	60	25	5	0	5	101	10.6	
27	99	1	0.3	58	28	17	0	5	90	60	
28	98	2	0.3	58	28	17	0	5	102	154	
29	97	3	0.3	58	28	17	0	5	130	135	
30	96	4	0.3	58	28	17	0	5	135	98	
31	94	6	0.3	58	28	17	0	5	150	81	[15]
32	92	8	0.3	58	28	17	0	5	163	69	
33	90	10	0.3	58	28	17	0	5	170	50	
34	88	12	0.3	58	28	17	0	5	181	32	
35	97	3	0.5	40	20	1.5	0	5	100	4.4	
36	97	3	0.5	60	20	1.5	0	5	102	8.6	[16]
37	97	3	0.5	80	20	1.5	0	5	104	8.8	
38	97.5	2.5	0.5	20	25	2	0	1.5	58	2.6	
39	97.5	2.5	0.5	30	25	2	0	1.5	72	2.73	
40	97.5	2.5	0.5	40	25	2	0	1.5	90	6.92	[17]
41	97.5	2.5	0.5	50	25	2	0	1.5	105	8.39	

### III. METHODOLOGY

This research is the modeling procedure, which includes the following steps: (1) The factors affecting tube diameter, and tube length of titanium dioxide nanotubes (TNAs) were imported into Minitab 18 program. (2) Go to the correlation function in Minitab. Enter the factors affecting tube diameter, tube length and number of tubes of titanium dioxide nanotubes (TNAs) in the variables field. To see the correlation coefficient between the factors and tube diameter, the correlation coefficient between the factors, and the correlation coefficient between the factors and tube length of titanium dioxide nanotubes (TNAs), how much each factor affects the tube diameter, and tube length of titanium dioxide nanotubes (TNAs). (3) Create the equation in the following function formats: exponential, linear, and square root. (4) To determine the error, the model was validated by comparing the tube diameter, and tube length of titanium dioxide nanotubes (TNAs) obtained from the model with the research. (5) Choose the function that has

the lowest error to know what function the model should be in. (6) Adjust the equation.

### IV. RESULTS AND DISCUSSION

In this section, the factors affecting tube diameter and length of TNAs were imported into Minitab 18 program. The equation of tube diameter and tube length of TNAs in the following function formats: exponential, linear, and square root, are shown in Table II.

TABLE II  
THE EQUATION OF TUBE DIAMETER AND TUBE LENGTH OF

TNAS IN THE EXPONENTIAL, LINEAR, AND LOGARITHM

Function form	The modeling predicts the tube diameter
Linear	$D = a + bE + cW + dA + eV + fT + gt + hR + iS$ (1)
Exponential	$D = \exp(a + bE + cW + dA + eV + fT + gt + hR + iS)$ (2)
Square root	$D = (a + bE + cW + dA + eV + fT + gt + hR + iS)^{0.5}$ (3)

Here, a, b, c, d, e, f, g, h, and i were the constant of tube diameter, and tube length of titanium dioxide nanotubes (TNAs) that shown in Table III. D is tube diameter (nm). L is tube length (µm). E is organic electrolyte (%wt). W is water (%wt). A is acid electrolyte (%wt). V is voltage (V). T is temperature ( °C). t is time for anodize (hr). R is ellectrolyte stirring (rpm). S is distance between nodes(cm).

TABLE III

CONSTANTS IN TUBE DIAMETER AND TUBE LENGTH MODELS

The model was validated by comparing the tube diameter

Eq.	a	b	c	d	e	f	g	h	i
(4.1)	-2508	24.5	33.1	110.2	1.134	0.0875	2.401	0.2827	-3.82
(4.2)	-19.5	0.224	0.296	1.02	0.01275	0.00826	0.0216	0.002739	-0.031
(4.3)	-113.7	1.159	1.545	5.24	0.05953	0.0423	0.1129	0.01382	-0.169
(4.4)	4460	-44.6	-51.5	-53.9	0.631	0.89	5.739	-0.1118	-3.88
(4.5)	137.5	-1.353	-1.485	-3.86	0.04040	0.02	0.1259	-0.00236	-0.1926
(4.6)	368	-3.65	-4.09	-7.11	0.0741	0.0676	0.3986	-0.00759	-0.436
		E	W	A	V	T	t	R	S

or length of TNAs obtained from the model with the research. The error of tube diameter and tube length of TNAs in the following function formats: linear, exponential, and square root, are shown in Table IV and Table V, respectively.

TABLE IV

THE AVERAGE ERROR OF TUBE DIAMETER OF IN THE LINEAR, EXPONENTIAL, AND SQUARE ROOT

Function form	Average error (%)
Linear	-0.53%
Exponential	-8.23%
Square root	2.00%

TABLE V

THE AVERAGE ERROR OF TUBE DIAMETER OF IN THE LINEAR, EXPONENTIAL, AND SQUARE ROOT

Function form	Average error (%)
Linear	-5.40%
Exponential	9.44%
Square root	20.42%

In the section of tube diameter modeling test, Table IV shows the average tube diameter in the linear, exponential, and square root is -0.53%, -8.23%, and 2.00%, respectively. Table IV shows that the linear equation has the lowest average error, equal to -0.53%. And Fig.1, Fig. 2, and Fig. 3 which comparing all the tube diameter points obtained from the model in the following function formats: linear, exponential, and square root research. It was discovered that the linear equation inclined closest towards the line at 45 degrees.

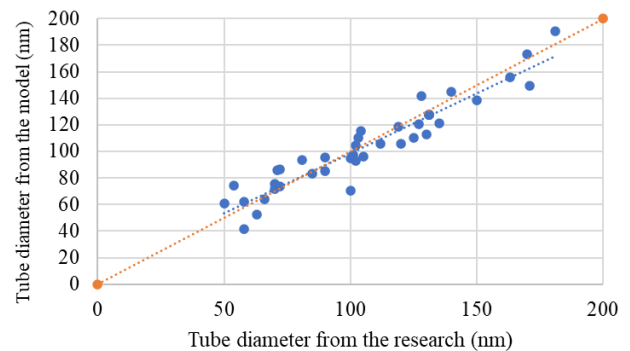


Figure 1. Comparing all data of the tube diameter obtained from the model in form of linear equation with the literature.

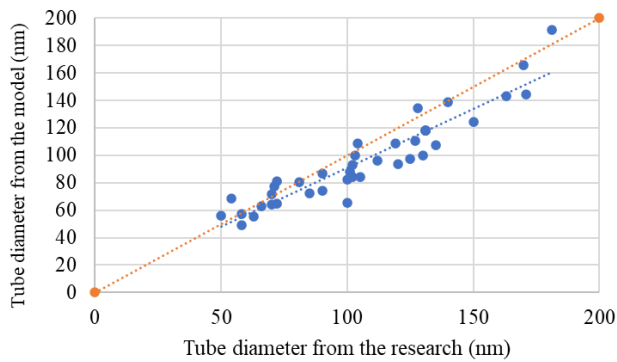


Figure 2. Comparing all data of the tube diameter obtained from the model in form of linear equation with the research.

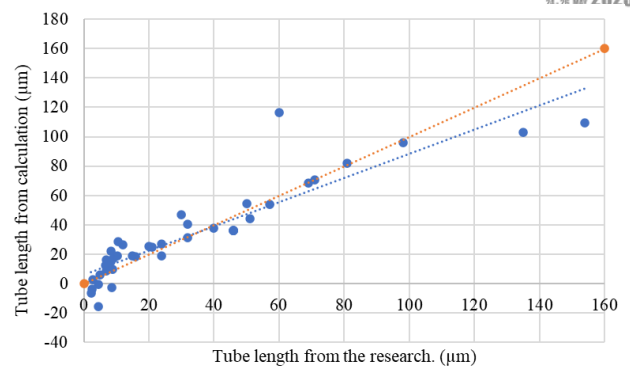


Figure 4. Comparing all data of the tube length obtained from the model in form of linear equation with the research.

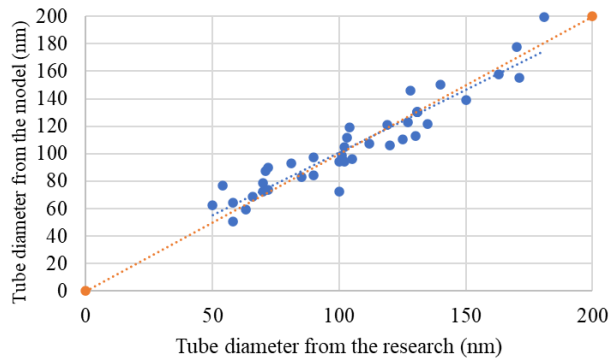


Figure 3. Comparing all data of the tube diameter obtained from the model in form of linear equation with the research.

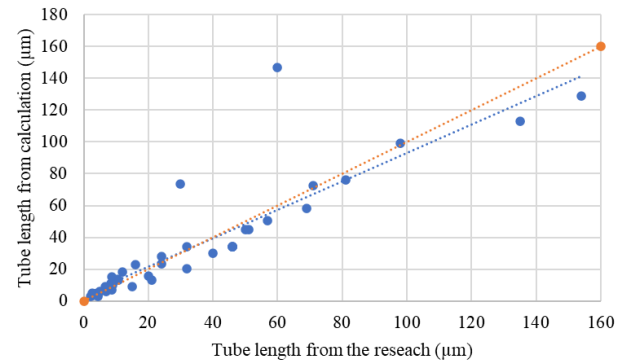


Figure 5. Comparing all data of the tube length obtained from the model in form of linear equation with the research.

As a result, the linear equation was chosen to be adjusted to create a method for predicting tube diameter. Following the development of the linear equation, a linear fitting equation can be given in Eq (1).

$$D = a + bE + cW + dA + eV + fT + gt + hR + iS + 0.078R/t \quad (1)$$

The constants in equation (1) are shown in Table III.

The model was validated to determine the error by comparing the tube diameter obtained from the adjusted model as a linear equation with the research. As a result, the average error was reduced to 0%.

And the section of tube length modeling test, Table V, shows the average tube diameter in the linear, exponential, and square root is -5.40%, 9.44%, and 20.42%, respectively. Table V shows that the exponential equation has the lowest average error, 9.44%. And from Fig. 4, Fig. 4, and Fig. 6 compare all the tube diameter points obtained from the model in the following function formats: linear, exponential, and square root with the research. It was discovered that the exponential equation inclined closest towards the line at 45 degrees.

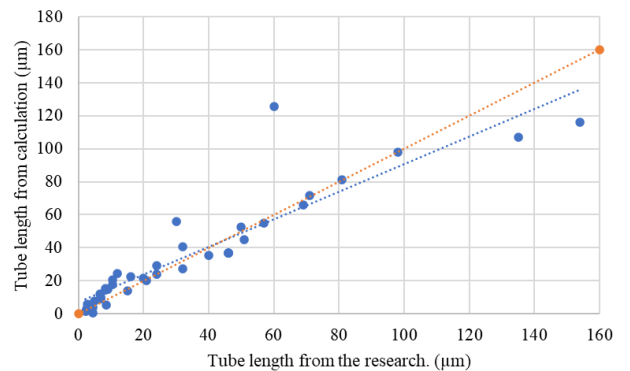


Figure 6. Comparing all data of the tube length obtained from the model in form of linear equation with the research.

As a result, the exponential equation was chosen to be adjusted to create a method for predicting tube length. Following the development of the exponential equation, the form of an exponential fitting equation can be given in Eq. (5).

$$L = \exp(a + bE + cW + dA + eV + fT + gt + hR + iS) - 0.2685R/t \quad (5)$$

The constants in Eq. (5) are shown in Table III.

The model was validated to determine the error by comparing the length diameter obtained from the adjusted model as an exponential equation with the literature. As a result, the average error was reduced to 0%.

## V. CONCLUSION

Based on this study, the TNAs samples were primarily generated with a pH range of 5 - 7. Electrolyte components created by EG, ammonium fluoride concentration, voltage, water-based electrolytes, electrolyte stirring, time for anodizing, the distance between nodes, temperature, and pH determine tube diameter and length of TNAs.

According to the results, the factors affecting tube diameter and length of TNAs were imported into Minitab 18 program. The equation of tube diameter and length of TNAs in the following function formats: exponential, linear, and square root. The model was validated by comparing the tube diameter or length of TNAs obtained from the model with the literature. The error of tube diameter or length of TNAs in the following function formats: linear, exponential, and square root, are calculated. The linear equation in tube diameter modeling and the exponential equation in tube length modeling have the lowest average errors of -0.53% and 9.44%, respectively. As a result, the linear equation and the exponential equation were chosen to be adjusted to create a method for predicting tube diameter and tube length, respectively. Based on the adjusted model, the average of both errors was decreased to 0% by comparing the tube diameter or length obtained from the adjusted model with the literature. This research should be developed, and additional literature data will be required for higher accuracy.

## REFERENCES

[1] Rachanon Klondon, 2013, Photocatalytic Air Pollution Removal by Coating Titanium Dioxide and Silicon Dioxide Compounds on Dan Kwian Pottery Surfaces, Master of Engineering Thesis. Department of Chemical Engineering Faculty of Engineering, Suranaree University of Technology, page 1-2.

[2] Montira Sathitsathien, Wichitra Pakasit and Karaket Thessri, 2019, "Optimization of Acceleration with Light for Photovoltaics". "Properties for Benzene Degradation in Lead Media by Nano Titanium Dioxide Catalyst Modified by Silver Nanoparticles", Burapha Science, Vol. 24, No. 3, pp. 1266-1282.

[3] Kukkong Pornsathitpong, 2012, Photocatalytic Oxidation of Ethanol Solution for Hydrogen Production on CuO/TiO<sub>2</sub> Catalyst., Master of Science thesis in Technical Chemistry Faculty of Science Chulalongkorn University, page 3-4.

[4] Ekarat Wongkaew, 2014, Synthesis of mixed metal oxide films for photoactivation properties for stain free glass applications. Doctor of Engineering Thesis, Department of Chemical Engineering Faculty of Engineering Burapha University, page 16-17

[5] Chanjira Siwaprathankul, 2015, Application of activated carbon coated with titanium dioxide and fluorine on surfaces for wastewater treatment. Master of Science Thesis Department of Physics, Faculty of Science and Technology Thammasat University, pages 18-19.

[6] Thongchai Sae-lim and Hatayarat Panichnawa, 2012, Influence of electrode position and stirring load cycle on the co-deposition of titanium particles on a nickel substrate. Thesis, Bachelor of Engineering, Department of Materials Engineering, Faculty of Engineering Kasetsart University, page 2.

[7] Atipol Sawangarom, 2015, Efficiency study of gold-coated titanium dioxide nanotubes on methylene blue degradation by photocatalytic process, master's thesis. Faculty of Science Department of Materials Science, Srinakharinwirot University, page 2 - 5.

[8] Lin, C. J., Yu, Y. H., Chen, S. Y. and Liou, Y. H., 2010, "Anodic growth of highly ordered titanium dioxide nanotube arrays: Effects of critical anodization factors on their photocatalytic activity", Engineering and Technology International Journal of Chemical and Molecular Engineering, Vol. 4, No. 5, pp. 333 - 378.

[9] Wang, D., Liu, Y., Yu, B., Zhou, F., and Liu, W., 2009, "TiO<sub>2</sub> nanotubes with tunable morphology, diameter, and length: Synthesis and photo - electrical/catalytic performance", Chemistry of Materials, Vol. 21, No. 7, pp. 1198 - 1206.

[10] Singh R. and Dutta S., 2018, "A review on H<sub>2</sub> production through photocatalytic reactions using TiO<sub>2</sub> /TiO<sub>2</sub> -assisted catalysts", Fuel, Vol. 220, pp. 607-620.

[11] Tahmasebpoor, R., Babaluo, A.A., Shahrouzi, J.R., Tahmasebpoor, M., and Shahrezaei, M., 2017, "Theoretical and experimental studies on the anodic oxidation process for synthesis of self-ordering TiO<sub>2</sub> nanotubes Effect of TiO<sub>2</sub> nanotube lengths on photocatalytic activity", Journal of Environmental Chemical Engineering, Vol. 5, No. 1, pp. 1227-1237.

[12] Sun, K.-C., Chen, Y.-C., Kou, M.-Y., Wang, H.-W., Lu, Y.-F. Chung, J.-C., Liu, Y.-C., and Zeng, Y.-Z., 2011, "Synthesis and characterization of highly ordered TiO<sub>2</sub> nanotube arrays for hydrogen generation via water splitting". Material Chemistry and Physics, Vol. 129, No. 1-2, pp. 35-39.

[13] Kar, A., Smith, Y. R., and Subramanian, V. (Ravi), 2009, "Improved photocatalytic degradation of textile dye using titanium dioxide nanotubes formed over titanium wires", Environmental Science & Technology, Vol. 43, No. 9, pp. 3260 - 3265

[14] Pasikhani, J.V., Gilani, N., Pirbazari, A.E., 2016, "The effect of the anodization voltage on the geometrical characteristics and photocatalytic activity of nanotube arrays", NanoStructures & Nano-Objects, Vol. 8, pp. 7-14.

[15] Zhu, W., Liu, X., Liu, H., Tong, D., Tang, J., and Peng, J., 2011, "An efficient approach to control the morphology and the adhesion properties of anodized TiO<sub>2</sub> nanotube arrays for improved photoconversion efficiency", Electrochimica Acta, Vol. 56, No. 6, pp. 2618-2626.

[16] Lin, C.J., Yu, Y.-H., Chen, S.-Y., and Liou, Y.H., 2011, "Anodic growth of highly ordered titanium oxide nanotube arrays: Effects of critical anodization factors on their photocatalytic activity", International Journal of Chemical and Molecular Engineering, Vol. 4, No. 5, pp. 373-378.

[17] Raja, K.S., Gandhi, T., and Misra, M., 2007, "Effect of water content of ethylene glycol as electrolyte for synthesis of ordered titania nanotubes", Electrochemistry Communications, Vol. 9, No. 5, pp. 1069-1076.

# Performance study of Bifacial solar panel with and without Solar Tracking system

Jirayu Baengthit<sup>1</sup>, Sarawut Polvongsri<sup>1\*</sup>

<sup>1</sup> School of Renewable Energy, Maejo University, Chiang Mai, 50290, Thailand

<sup>1\*</sup> Corresponding author: sarawut-energy@hotmail.com

**Abstract:** In the study, to study performance of bifacial panel with and without tracking system was used to verify the stability of a solar tracking system. In addition, it evaluates efficiency, power and generates electricity. And the accuracy of the solar tracking system for the bifacial panel comparing the panels to the solar tracking system and without it. Under the same condition (Albedo 0.5: white concrete, height from surface level 1 m and inclination angle 18° south). Result research found the output power of the solar tracker was increased by 22.22%, the electric power increased by 19.09%, and the efficiency increased by 11.89%. The temperature of the bifacial panel tracker was about 1.1 °C higher than that of the non-tracker under irradiation. low sun and about 1.4 °C lower under high solar radiation values.

**Keywords:** *Solar tracking system, Bifacial panel, Performance.*

## I. INTRODUCTION

At present, the technology of producing solar panels (Photovoltaic, PV) has undergone great developments and advances. Consequently, the cost of producing solar panels has been reduced continuously. In the past and present, it was still popular to produce electricity from mono-facial panels. (Mono-facial, mPV), which has an efficiency of 10-20%, uses the principle of direct sunlight on one side, but currently has developed a technology to produce solar panels to be very efficient. Climb Passivated Emitter Rear Contact (PERC) technology is applied to produce bifacial (bPV) photovoltaic modules with an efficiency of 18 – 21% using the principle of direct sunlight and reflection. Sang (Wanlapa Thiraporn, 2017). But some factors affect the efficiency of bifacial panels. The bifacial panel has been studied in foreign countries. The study albedo, surface height, and inclination angle. The study found that an albedo of 0.9, a height of 1.5 m and an inclination angle of 35° were most effective using a PVsyst program (Ufuk et al., 2014). Subsequently, data from NASA for an average of 22 years were analyzed and found that an albedo of 0.5, an altitude of 1 m and an inclination angle of 15° were the most effective (Xingshu et al., 2018). After that, reference data from Taizhou city, China were analyzed using the MATLAB program. It was found that albedo 0.4 and height 0.5 m – 0.7 m (more or less will create a shadow under the panel) (Yunkun et al., 2021). Therefore, installing a solar tracking system is recommended for maximum efficiency. Because the panel is always perpendicular to the sun. Then, a study of the efficiency of bifacial panels equipped with solar tracking systems showed a 21.2% and 1.35-fold increase in efficiency compared to a fixed angle (Rao et al.,

2015) (Shahriar et al., 2014). One-axis solar tracking systems also offer cost-effectiveness, maintenance, and panel power efficiency that are more cost-effective than both fixed and two-axis solar trackers. The bifacial panel with a solar tracking system is also being studied and not-solar tracking system is also being studied. The study was conducted to study the efficiency of electricity generation from bifacial solar panels compared to mono-facial solar panels. Between with and without solar tracking system from the experimental results, it was found that bifacial solar panels compared with mono-facial solar panels in fixed tilt angles. The power generation efficiency of bifacial solar panels has been increased by approximately 10% (Patel et al., 2021) because the bifacial solar panels can absorb solar radiation from both the front and back. The back of the panel uses the principle of surface reflection. And found that when comparing the use of solar tracking systems, The power generation efficiency of bifacial solar panels has increased by approximately 15% (Oya & Murat, 2020) as the installation of a solar tracking system keeps the solar panels perpendicular to the sun at all times. This makes the power generation efficiency of bifacial solar panels higher than that of mono-facial solar panels. But in Thailand, there are few studies of bifacial solar panels and also in the study of solar tracking systems, the results will depend on the location of each area.

However, there are few studies on bifacial solar tracking systems in Thailand, and the solar tracking performance depends on the location of each area. Therefore, this research focuses on the study performance of bifacial panel with and without tracking system. The experimental results of bifacial solar panels with and without a solar tracking system are compared.

## II. DATA USED

The solar tracking system has a working principle (Hmong, 2020) is to track the movement of the sun in the sky each day. Thus, the solar panel's surface is at an angle that receives full sunlight, according to the latitude of each installation area. To allow perpendicular contact with the solar panel using a solar tracking system can improve the efficiency of solar panels. While the rotation of the earth relative to the fixed position of the solar panel power generation system which the system rotates according to the sun will look like a mechanical arm that acts to rotate the solar panel. It uses a programmable command system. The solar tracking system is a system that adjusts the angle of the solar panel to be perpendicular to the sun. This ensures maximum sunlight power and higher power generation than conventional angle adjustments.

### A. Types of Solar Tracking Platforms

There are various types of solar tracking systems, but the types differ in the techniques and command set designs used. The main types of solar tracking systems are divided into two categories, including one-axis solar tracking systems and two-axis solar tracking systems. as shown in Fig. 1.

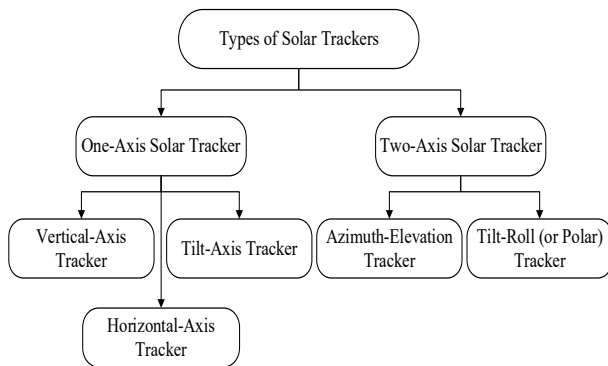


Fig. 1. Type of existing solar tracking platforms.

There are typically three types of one-axis sun tracking designs available. This includes a horizontal-axis tracker (the tracking axis is to remain parallel to the surface of the earth, and it is always oriented along east-west or north-south direction); a tilted-axis tracker (the tracking axis is tilted from the horizon by an angle oriented along the north-south direction e.g., latitude-tilted-axis sun tracker); and vertical-axis tracker (the tracking axis is collinear with the zenith axis) also known as an azimuth solar tracker (Chong et al., 2014).

Two-axis or dual-axis solar trackers, such as the azimuth-elevation and the tilt-roll solar tracking systems, follow the sun in the horizontal and vertical plane. In the azimuth, elevation solar tracking system, the solar collector must be free to rotate about the azimuth and the elevation axes. In these systems, the tracking angle about the azimuth axis is the solar azimuth angle and the tracking angle about the elevation axis is the solar elevation angle. Such two-axis tracker systems track the sun on two axes, such that the sun

vector is normal to the aperture to attain near 100% energy collection efficiency.

The solar tracking system under study is a one-tilted-south solar tracking system with an inclination angle of 18°. The height of the structure (measured from the midpoint of the frame) is 1 m and it is coated with white paint as the study uses white concrete or albedo. It is shown in Figure 2. The structure used for comparison is a fixed-tilt structure as shown in Figure 2(A) compared to the structure with solar tracking system using a linear motor as the driving mechanism and the control set using ESP32 board as shown in Figure 2(B).

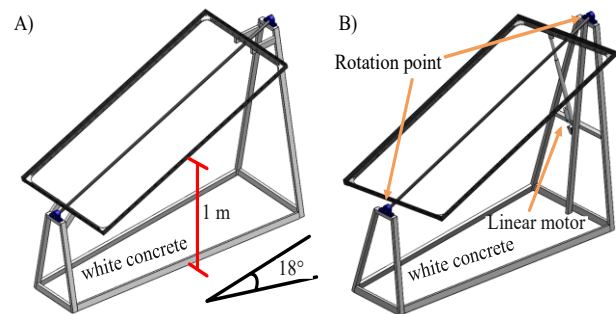


Fig. 2. The structure of the solar tracking system.

### B. Bifacial panel module

The main component in a bifacial panel system (Wembo et al., 2021) is a bifacial panel module, which includes five layers, namely one layer of bifacial panel cells, and two layers of glass and encapsulation material as presented in Fig. 3 (A). The bifacial panel modules can collect sunlight (direct, diffused and reflected light) from the front and rear sides simultaneously to generate more power output than the mono-facial panel if the rear side also receives solar radiation. However, the research on the bifacial panel technology is limited due to the complicated processes, namely optical, electrical and thermal processes, and the tightly coupled relationship with each other as illustrated in Fig. 3 (B). The majority of sunlight is transmitted through the glass and absorbed by the bifacial panel cells, although a small part is absorbed by the glass. The photon passes its energy to the carrier so that the radiant energy is absorbed to generate electricity due to the photoelectric effect. The extra and unabsorbable energy is transformed into heat (transmission loss and thermalization loss), which is then conducted to the front and rear glasses by conduction, and finally dissipated by convection and radiation.

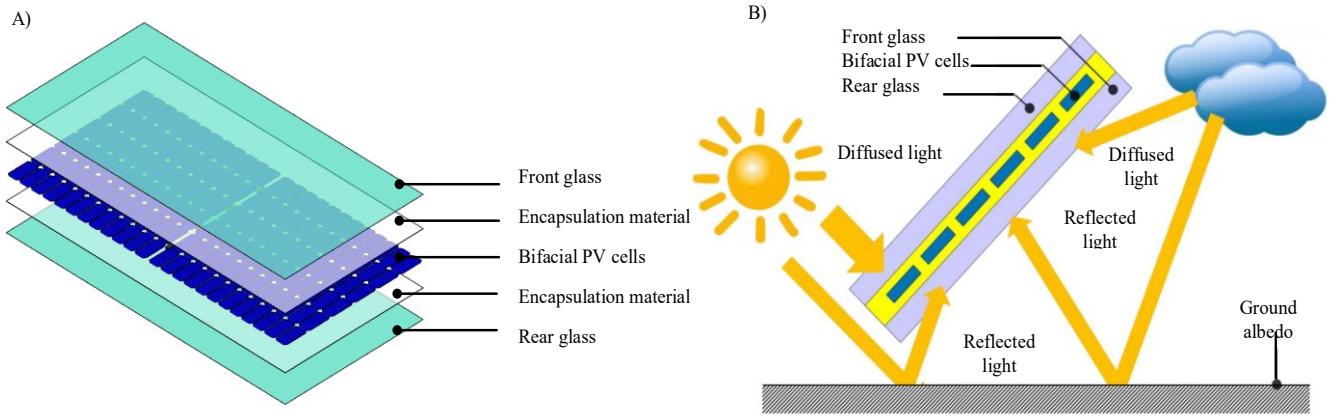


Fig. 3. Structure and energy flows of a bifacial module A) structure and B) energy flows.

### III. METHODOLOGY

Key module parameters of the bifacial panel (model: LR-72HBD-425M) under standard test conditions (STC) in the experiment are listed in Table 1.

TABLE I  
KEY PARAMETERS OF THE PV MODULES IN THE EXPERIMENT

Specification	Bifacial panel module
Maximum Power ( $P_{mpp}$ )	430 W
Open Circuit Voltage ( $V_{oc}$ )	48.9 V
Short Circuit Current ( $I_{sc}$ )	11.30 A

Specification	Bifacial panel module
Voltage at Maximum Power ( $V_{mpp}$ )	40.60 V
Current at Maximum Power ( $I_{mpp}$ )	10.60 A
Module Efficiency (%)	19.80 %

#### A. Other equipment

In the field experiment, the panel performance parameters of the bifacial panel are greatly affected by various weather parameters. Therefore, various measuring instruments are necessary to obtain related weather and output parameters, by specifying various measurement points as shown in Fig. 4. The solar power meter, infrared thermometer, and solar module analyzer and their specifications and function are summarized in Table 2.

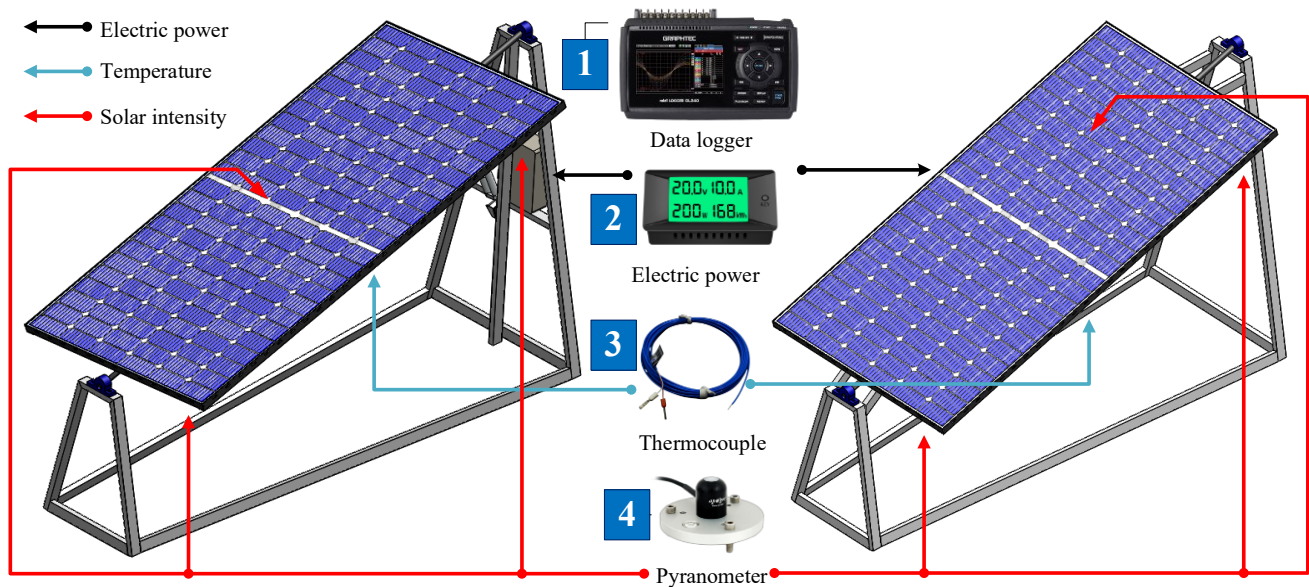


Fig. 4. Configuration of the bPV experimental system.



TABLE II  
MEASURING EQUIPMENT IN THE BPV EXPERIMENTAL SYSTEM

No.	Measuring instrument (model)	Specifications	Function
1	GRAPHTEC midi LOGGER (GL240)	Range: voltage 20mV-100V, Thermocouple: K, J, E, T, R, S, B, N, W(WRe5-26)	Data logger solar power and temperature.
2	Peacefair (PZEM-025)	Range: DC 0-300V ( $\pm 1\%$ ), 50A ( $\pm 1\%$ ), Power 0-90kW ( $\pm 1\%$ )	Measure DC voltage, current, power
3	Thermocouple (Type K)	Range: 0 to 200°C	Measure temperature
4	Pyranometer (SP-110-SS)	Range: 0-400mV, Calibration Factor 5 W/m <sup>2</sup> /mV, Non-stability (Long-term Drift) less than 2%/year	Measure solar intensity.

## B. Evaluation methods

### a. Sun position angle

Finding the sun's angle in a solar tracking system, that is, the sun hour angle ( $\omega$ ) (Serm Janjai., 2017). Can be calculated as equation (1) – (4).

$$\omega = 15(12 - ST) \quad (1)$$

$$ST = LST + 4(L_{STM} - L_{local}) + EOT \quad (2)$$

$$EOT = 9.87\sin(2B) - 7.53\cos(B) - 1.5\sin(B) \quad (3)$$

$$B = (360 / 365) (n - 81) \quad (4)$$

where the ST refers to called the time correction factor (hour, h), LST is the local solar time (h: min),  $L_{STM}$  is the longitude used for the local standard time reference (degree,°),  $L_{local}$  is the longitude of the interested place (degree,°), EOT is called the equation of time, B is day angle (degree,°) and n is a day of the year.

### b. Electrical performance

Solar cell characteristic curve when I-V curve at zero voltage (Ramos-Hernanz et al., 2013) zero short circuit current ( $I_{sc}$ ), open circuit voltage ( $V_{oc}$ ). Voltage there is an important point that causes maximum power point ( $P_{mpp}$ ). This point makes you know the current at maximum power point ( $I_{mpp}$ ) and voltage at maximum power point ( $V_{mpp}$ ). The P-V curve lets you know the solar panel's maximum power as shown in Fig. 5.

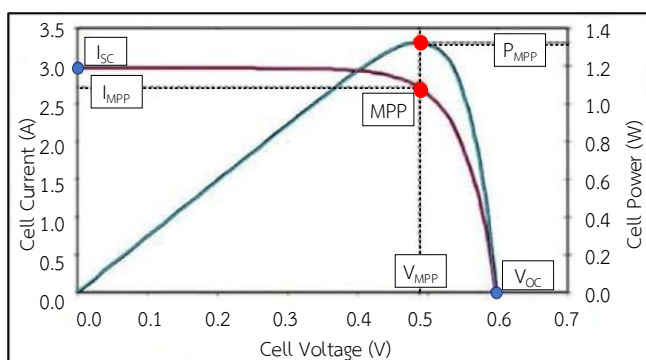


Fig. 5. Structure of experimental results and discussion.

This is caused by the electric current and voltage when multiplied together to determine the maximum power of the solar panel, which can be calculated using equation (5).

$$P_{MPP} = I_{MPP} \times V_{MPP} \quad (5)$$

where  $I_{MPP}$  and  $V_{MPP}$  are the current (A) and voltage (V) at MPP on the characteristic curve of the bifacial module, respectively.

The panel power generation at MPP in the experiment can be obtained directly by the solar power meter. Combined with measured solar irradiance, the bifacial panel electrical efficiency can be calculated as equation (6).

$$\eta_{bPV} = (P_{MPP} \times \Delta T) / (A \times I_0 \times \Delta T) \quad (6)$$

where the A is Solar panel light receiving area (m<sup>2</sup>),  $I_0$  is the solar radiation (W/m<sup>2</sup>) and  $\Delta T$  is the time (min).

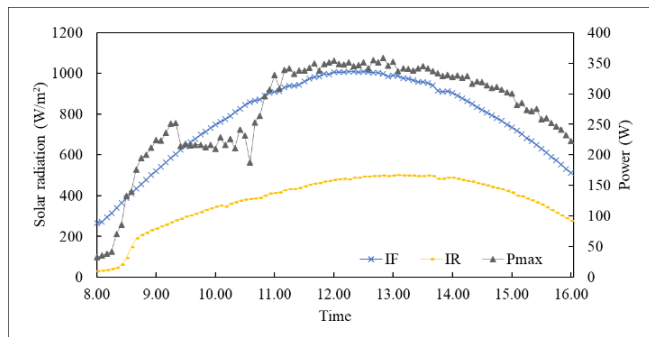
## IV. RESULTS AND DISCUSSION

From the experimental setting, some experimental results were obtained. divided into three cases The first case is the evaluation of the solar tracking system. And the next case is a comparison between with and without solar tracking systems. Evaluate efficiency, power, and electrical energy produced.

### A. Solar radiation and the power output

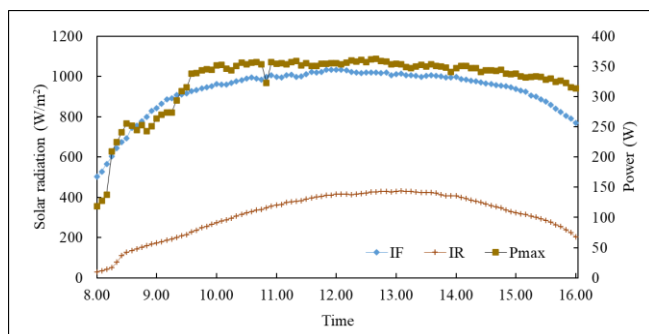
Fig. 6 shows the relationship between solar radiation (Front, IF and Rear, IR) and the power output ( $P_{max}$ ) of a non-solar tracking system. It was found that the electric power increased continuously according to the solar radiation value from 8:00 a.m. until reaching its peak at 12:50 p.m. at a power output of 358.72  $W_p$ , solar radiation front value of 998.71 W/m<sup>2</sup>, solar radiation rear value of 499.66 W/m<sup>2</sup> and the lowest power at 8.00 a.m. power output of 33.15  $W_p$ , solar radiation value of 226.56 W/m<sup>2</sup>, solar radiation rear value of 29.8 W/m<sup>2</sup> and electrical power produced 2.19 kWh/day. The generated power curve has an increasing value up to the period. 9.25 a.m. – 10.55 a.m. will decrease because, at the experimental site, a wind

turbine pillar casts a shadow on the solar panel. On average throughout the day, the electricity power value is at 272.95 W, the front solar irradiance value is at 774.22 W/m<sup>2</sup> and the back is at 376.41 W/m<sup>2</sup>.



**Fig. 6.** The relationship between solar radiation and the power output of a non-solar tracking system.

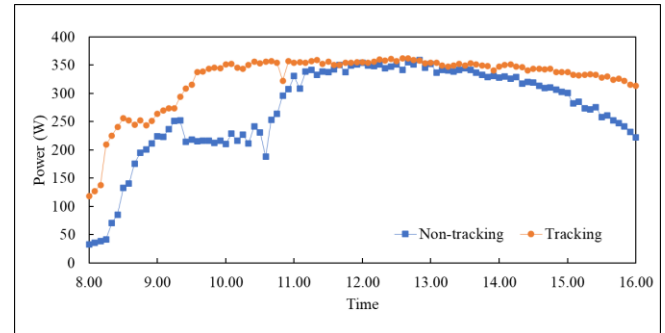
Fig. 7 shows the relationship between solar radiation and the power output of a solar tracking system. It was found that the electric power increased continuously according to the solar radiation value from 8:00 a.m. until reaching its peak at 12:40 p.m. at a power output of 362.41 W<sub>p</sub>, solar radiation value of 1,019.38 W/m<sup>2</sup>, solar radiation rear value of 427.28 W/m<sup>2</sup> and the lowest power at 8.00 a.m. power output of 118.16 W<sub>p</sub>, solar radiation value of 502.15 W/m<sup>2</sup>, solar radiation rear value of 30.29 W/m<sup>2</sup> and electrical power produced 2.61 kWh/day. The generated power curve has an increasing value up to the period. 8.35 a.m. – 9.30 a.m. will decrease because, at the experimental site, a wind turbine pillar casts a shadow on the solar panel. From 10:00 a.m., power and solar radiation start to stabilize. Since it is equipped with a solar tracking system, the solar panels are perpendicular to the sun. On average throughout the day, the electricity power value is at 325.81 W, the front solar irradiance value is at 929.10 W/m<sup>2</sup> and the back is at 313.58 W/m<sup>2</sup>.



**Fig. 7.** The relationship between solar radiation and the power output of solar tracking system.

Fig. 8 shows the power output of with and without solar tracking. The maximum electricity capacity is at 358.72 W<sub>p</sub>, the minimum electricity capacity is at 33.15 W<sub>p</sub>, and the average electricity capacity is at 0.27 kWh/day.

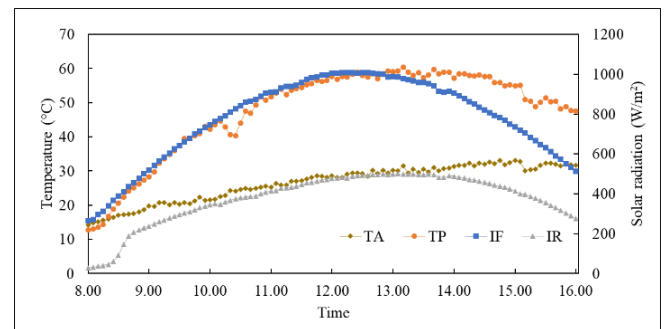
Meanwhile, the maximum electricity capacity of the solar tracking system is at 362.41 W<sub>p</sub>, the minimum electricity capacity is at 118.16 W<sub>p</sub>, and the average electricity capacity is at 0.33 kWh/day. The difference in electricity capacity between the with and without solar tracking system is at 22.22%. The electricity capacity decreases in the morning due to the wind turbine shadowing the solar panel in the test area.



**Fig. 8.** Power output of with and without solar tracking system.

### B. Temperature and solar radiation

Fig. 9 shows the relationship between temperature (Ambient, TA and Panel TP) and the irradiation (Front, IF and Rear, IR) of a non-solar tracking system. It was found that the panel temperature continued to increase according to the solar radiation value. The ambient temperature continued to increase. The maximum panel temperature was 60.4 °C, the ambient temperature was 31.5 °C, the solar radiation was 976.53 W/m<sup>2</sup> and the lowest panel temperature was 12.7 °C, the ambient temperature was 14.2 °C, and the solar radiation was 266.56 W/m<sup>2</sup>, with the average panel temperature being 47.54 °C/day. The average ambient temperature was 26.52 °C/day.



**Fig. 9.** The relationship between the temperature and the solar radiation of non-tracking system.

Fig. 10 shows the relationship between temperature (Ambient, TA and Panel TP) and the irradiation (Front, IF and Rear, IR) of a non-solar tracking system. It was found that the panel temperature continued to increase according to the solar radiation value. The ambient temperature continued to increase. The maximum panel temperature was

61.7 °C, the ambient temperature was 31.5 °C, the solar radiation was 1,006.39 W/m<sup>2</sup> and the lowest panel temperature was 13.8 °C, the ambient temperature was 14.2 °C, and the solar radiation was 502.15 W/m<sup>2</sup>, with the average panel temperature being 50.92 °C/day The average ambient temperature was 26.52 °C /day.

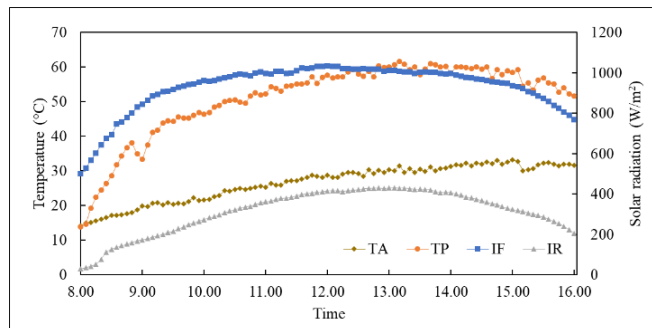


Fig. 10. The relationship between the temperature and the irradiation of solar tracking system.

### C. The characteristic parameter comparisons

Comparison of characteristic parameters between with and without solar tracking system. The value of solar radiation in front has changed significantly. with an increase of 20%, while the value of solar radiation behind is the opposite value, with a decrease of 16.70% due to the solar tracking system that the panel is perpendicular to the sun This creates a shadow behind the panel caused by the reflected angle of the light. The back therefore receives a small amount of solar radiation. as shown in Table 3.

TABLE III  
THE CHARACTERISTIC PARAMETER COMPARISONS  
BETWEEN WITH AND WITHOUT SOLAR TRACKING  
SYSTEM

Data list	Non-tracking	Tracking
Average solar intensity (Front) (W/m <sup>2</sup> )	774.22	929.10
Average solar intensity (Rear) (W/m <sup>2</sup> )	376.41	313.58
Total solar energy (kWh/m <sup>2</sup> )	4.63	4.99
Reference yield (YR, kWh/kW)	4.63	4.99
Average power DC (kW)	0.27	0.33
Total DC energy (kWh)	2.20	2.62
Array yield (YA, kWh/kW <sub>p</sub> )	5.11	6.08
Average panel efficiency (%)	12.03	13.46

### V. CONCLUSIONS

This research tested the output power, electric power and efficiency from 9:00 a.m. – 4:00 p.m. of with and without solar tracking system. The tilt-axis tracking system tilted to the south 18° at the height of the structure 1 m albedo 0.5

(white concrete). Result research found the output power of the solar tracker was increased by 22.22%, the electric power increased by 19.09%, and the efficiency increased by 11.89%. The temperature of the bifacial panel tracker was about 1.1 °C higher than that of the non-tracker under irradiation. low sun and about 1.4 °C lower under high solar radiation values.

It can be concluded that the bifacial solar tracker equipped has better performance than those without solar trackers. It is advisable to install bifacial panel on a high albedo with an appropriate inclination angle according to the appropriate latitude of each location.

### ACKNOWLEDGMENT

The authors would like to thank the School of Renewable Energy, Maejo University for supporting the study with a grant funded under the program Strategic Scholarships from “Project and Development of the Renewable Energy Potential Graduates ASEAN”. We would to thank the Energy Conservation and Promotion Fund Office, Ministry of Energy. We would like to thank the staff of Smart Energy and Environmental Research Unit (SEEU) for supporting many suggestions, knowledge, and instruments.

### REFERENCES

- [1]Wanlapa Thiraporn. 2017. Bifacial Sokar. Retrieved from <http://goc.eगत.co.th/images/qcc-event/2560/articles/15-article.pdf>.
- [2]Ufuk, A. Y., Tae, H. L., Tobias, M. P., Andreas, H., Lejo, J. K., Corrado, C., Heinrich, K. (2014). Simulation of Energy Production by Bifacial Modules with Revision of Ground Reflection. Energy Procedia, 55, 5242-5247.
- [3]Xingshu, S., Mohammad, R. K., Chris, D., & Muhammad, A. A. (2018). Optimization and performance of bifacial solar modules: A global perspective. Applied Energy, 212, 1601-1610.
- [4]Yunkun, T., Jianbo, B., Pachauri, R. K., Yue, W., Jian, L., & Attaher, H. K. (2021). Parameterizing mismatch loss in bifacial photovoltaic modules with global deployment A comprehensive study. Applied Energy, 127, 117636.
- [5]Rao, R. R., Swetha, H. R., Jayaraman, S., & Sheela, R. (2015). Comparison of performance of solar photovoltaics on dual axis tracker with fixed axis at 13° N latitude. Current Science, 11, 2087-2094.
- [6]Shahriar, B., Reza, K., Shahrokh, F., & Amir, G. (2014). A Study on the Effects of Solar Tracking Systems on the Performance of Photovoltaic Power Plants. Power and Energy Engineering, 2, 718-728.
- [7]Patel, M. T., Ahmed, M. S., Imran, H., Butt, N. Z., Khan, M. R., & Alam, M. A. 2021. Global analysis of next-generation utility-scale PV: Tracking bifacial solar farms. Applied Energy, 290(116478).
- [8]Oya, K., & Murat, K. 2020. Bifacial and monofacial module with tracker system analysis. Journal of Amasya University the Institute of Sciences and Technology, 1(2), 101-115.
- [9]Hmong. 2020. Solar Tracking. Retrieved from [https://hmong.in.th/wiki/Solar\\_tracker](https://hmong.in.th/wiki/Solar_tracker).
- [10] Chong, K.-k., Wong, C.-w., Tunku, U. and Rahman, A. 2014. General Formula for On-Axis SunTracking System. Universiti Tunku Abdul Rahman Malaysia, no. Chapter 3, pp. 263–291.
- [11] Wenbo, G., Senji, L., Xing, L., Zhenwu, C., Xiaochun, Z., & Tao, M. 2021. Experimental investigation of the bifacial photovoltaic module under real conditions. Renewable Energy, 173, 1111-1122.
- [12] Serm Janjai. 2017. Solar Radiation. Department of Physics, Faculty of Science, Silpakorn University.
- [13] Ramos-Hernanz, J., Campayo, J., Zulueta, E., Barambones, O., Eguía, P., & Zamora, I. (2013). Obtaining the characteristics curves of a photocell by different methods. Renewable Energies and Power Quality, 2172-2038.
- [14] Thanawat Choowan. 2020. A study of the economic value of the paperless system in the company P.C. Takashima (Thailand) Co., Ltd. Master of Science (Environmental Management).

# Decarbonization Innovation Affecting Sustainability in Port Operations in Thailand

Kanokporn Nakchatree<sup>1</sup>, Jaruwit Prabnasak<sup>2</sup>

<sup>1</sup>Department of Civil Engineering,

School of Engineering, King Mongkut's Institute of Technology Ladkrabang, Bangkok, Thailand.

Puinoon\_334@hotmail.com

<sup>2</sup>Department of Civil Engineering,

School of Engineering, King Mongkut's Institute of Technology Ladkrabang, Bangkok, Thailand.

jaruwit.pr@kmitl.ac.th

**Abstract:** This study suggests a conceptual model that analyses both the direct and indirect effects of sustainability in port operations in Thailand. The concept of Low-Carbon Operation, Port Strategies to Reduce Emissions, Green Logistics, Green Port Management, and Sustainable Development, drawing from NRBV theory through the conceptual framework. The data collection of 400 structured questionnaires were distributed to our targeted respondents. The results also found that high-quality maritime education and training directly and significantly contribute to the adoption of green maritime practices including LCO, GL, PSRE, and GPM by maritime stakeholders. It is also implied that the adoption of green marine practices by maritime authorities, such as LCO, GL, PSRE, and GPM, directly and favorably impacts SD in the maritime sector. Additionally, the results demonstrate a strong and direct correlation between SD and high-quality maritime education and training. The results also suggest that LCO, GL, PSRE, and GPM have a substantial mediating effect on the connection between high-quality maritime education and training and SD.

**Index Terms:** Low-Carbon Operation, Sustainable development, Port Operations, Green Logistics, Green Port Management

## I. Introduction

Recently, progress of climate change consequences caused by global increase in carbon dioxide (CO<sub>2</sub>) emissions has clearly demonstrated. In order to mitigate those consequences, world needs to intensify its serious efforts to reduce carbon dioxide generated from the sectors that are the main sources of the emission, such as, energy, agriculture, heavy industrial, construction, and transportation sectors (Ruangchoengchum, 2015). Decarbonization is the process of reducing or eliminating carbon dioxide emission from its sources by the use of technology, process improvement, and mandated and voluntary measures (Hwang & Kim, 2020). In 2015, United Nation issues new mission to confront with the climate change, called the 'Goal 13: Climate Action. The mission intends to implement substantial actions to mitigate climate change globally and decarbonization initiatives play important role to achieve the goals (Zhou et al., 2023). In the Asia-Pacific region, a number of international organizations, including ASEAN, the Asian Development Bank (ADB), APEC, and UNESCAP, have already launched campaigns to increase public awareness of the "green" or "low carbon" agenda and to encourage participation from key players, such as businesses and

governments (APEC Energy Working Group, 2012; ASEAN Secretariat (a), 2019; Asian Development Bank, 2019; United Nations, 2010).

To reduce carbon footprint of the major seaports, technology and innovation are required. In general, majority of carbon emissions generated in ports as well as other large transportation hubs comes from use of fossil fuel, particular diesel fuel, to power vehicles, machines, equipment, facilities and heat. These activities sometime can cause substantial amount of smoke affecting public livings in adjacent cities. (Elhattab et al., 2016) In order to circumvent this issue, several transportation hubs have to switch to use of biofuels or electricity instead. To counteract this issue, certain transportation hubs gather data on individual ship emissions using mobile devices to assure safe travel. These 'limiting devices' enable transportation managers to immediately discover issues with vehicle maintenance and take corrective action, all while reducing fuel expenditures. Additionally, reducing automobile usage reduces carbon emissions since fewer people must go to work daily. Providing employees with extra bus routes minimizes the quantity of fossil fuel required for their

trip. Everyone may make their workplace more pleasant and energy-efficient by inquiring about these practices at their place of employment. Implementing new approaches for minimizing carbon footprints at seaports saves carbon emissions and shipping costs without jeopardizing employee or customer safety or comfort. This study contributes to the extension of the natural resource-based view (NRBV) paradigm by evaluating a conceptual model that investigates the direct and indirect effects of green marine practices on sustainable development. In addition, the conceptual model in connection to the NRBV theory implies that the adoption of green maritime practices indirectly encourages maritime stakeholders toward green maritime operations and services. This study offers maritime authorities and stakeholders with a very informative tool and information on green maritime practices for both onshore and offshore maritime operations that improve environmental performance and assure the maritime industry's sustainability. (Manno, 2014).

In Thailand, Bangkok Port (BKP) is one of the two major seaports of the country. Also the BKP is located in inner Bangkok area where is noticeably adjacent to the city center and the business area of Bangkok Metropolitan Area. However, until now it is remaining unclear about the preparations and contributions of the Thailand port authority to the sustainable developments for the BKP. For this reason, this study aims at investigating the causal factors influencing sustainability development (SD) and how to contribute to the improvement of sustainability in the BKP.

## II. Literature Reviews on Port Sustainability Policies and Measures

In this study, seven policies and measures related and widely used in port sustainability developments are reviewed and used as background of the further analysis in this study.

### Carbon Reduction Policy

The rise in temperature of the entire world as a result of increasing carbon dioxide and other greenhouse gases in the atmosphere is known as global warming. It is mostly driven by human influences, such as increased temperatures and less visibility due to rising greenhouse gas levels. People are concerned about this topic since it has so many bad consequences. Before it's too late, it is vital to find realistic measures to cut carbon emissions. There have been many proposed ways to mitigate global warming, but not all of them are realistic. In contemporary times, carbon-reduction strategies have grown in significance. It is now more vital than ever for seaports to adopt these new procedures due to the global surge in environmental consciousness. Changing from standard diesel fuel to alternative fuel sources, such as

biodiesel or LNG, is one of the most common strategies for seaport management today. In addition to reducing emissions, these alternative fuels have the potential to drastically lower prices. Additionally, the use of alternative energy sources such as solar and wind is gaining popularity. This not only reduces carbon emissions, but also makes the port considerably more sustainable over time. Utilizing energy-efficient containers and equipment to decrease carbon emissions is also gaining popularity. Numerous institutions and commercial businesses generate innovative carbon reduction strategies. These concepts are discussed at conferences where sustainability professionals convene. Each expert returns to their business with new knowledge and results to share with teammates. After analyzing these facts, experts propose particular plans to governments. These strategies promote government policies that are based on them. This information helps the public understand how almost any community group may minimize their carbon footprints. Everyone concerned works together to communicate this message.

### Decarbonization Policies

Ports assist several commercial operations. Their diversity of businesses helps future decarbonization initiatives in Europe, such as the transition to sustainable energy (Sattich, 2015). Numerous ports assist the shipping industry and its associated operations in addition to cargo. In addition, they assist energy-intensive businesses, such as manufacturing (Primova, n.d.), cement production, and electrical networks. Larger ports are known as "mini-cities" and play an essential role in supporting other economic activities. They assist power generation, import and export, and grids, which all need significant energy (Hübner, 2018). Transitioning to sustainable energy involves coordination between port authorities and interested parties. This is due to the complicated multilayer structure of ports, which needs the use of different tactics and methodologies (Sovacool et al., 2022). Adoption of alternative energy sources must occur via several industrial clusters or channels. In order to considerably cut their emissions, ports must adopt a variety of initiatives across all industry sectors. Through technological advancement, port emissions may be drastically reduced. Utilizing this innovation can provide ports with an advantage over more conservative ports (Arrigo et al., 2022; Fay et al., 2015; Ferrari et al., 2022; Ren et al., 2022; Singh et al., 2023)

### Sustainability seaport

The administration of seaports must be carried out in an efficient and sustainable way, as they are a vital element of the global economy. Consequently, seaport administration must consider its environmental impact, particularly in terms of lowering carbon emissions. In order for seaports to achieve their objectives, various

novel carbon-reduction strategies have been devised and deployed (European Investment Bank, 2022). The introduction of hybrid and electric-powered cargo handling equipment is one of the most successful strategies for lowering carbon emissions in harbor management. By deploying such vehicles, seaports may dramatically cut their consumption of diesel fuel and, consequently, their production of carbon emissions. In addition, by removing the need for exhaust gases, the use of electric-powered equipment can aid in the reduction of air pollution in the surrounding region (Lenox & Duff, 2021; Verb et al., 2022). Utilizing renewable energy sources is an additional ingenious method for seaports to lessen their carbon impact. The administrators of seaports are attempting to devise more ingenious ways to cut carbon emissions. Installing solar panels at seaports and utilizing renewable energy sources such as wind and wave power are among the cutting-edge technologies now being investigated (Mulvaney, 2020; Sivaram, 2018). The administration of seaports is also investigating the usage of hybrid boats, which combine traditional fossil fuel engines with cleaner renewable energy sources. In addition, the utilization of innovative maritime logistics and data analytics can assist in optimizing vessel itineraries, therefore lowering both travel time and carbon emissions (Ren et al., 2022).

### **Low-Carbon Operation**

Ports play a crucial role in the transformation of ships to greener energy. They develop stations that give bioenergy, green hydrogen, and recharging capabilities for the new propelled vessels. This will contribute to a 24% reduction in transportation-related CO<sub>2</sub> emissions (Dupont & Oberthür, n.d.). In addition, shipping accounts for 10% of total ship-related transport CO<sub>2</sub> emissions. By integrating an electric motor with a regular diesel engine, ships can be hybridized. When the engine is running, diesel fuel is not burnt, avoiding greenhouse gas emissions (Ferrari et al., 2022; Singh et al., 2023). Monitoring port fuel consumption to reduce the carbon impact of supply networks Ports generate a range of carbon emissions due to logistics operations such as diesel-powered quayside structures and equipment (Dupont & Oberthür, n.d.). This includes the usage of power for buildings, lights, and machinery, diesel engines used to transport containers and other equipment, and emissions from vehicles used to deliver and load goods (Fay et al., 2015; Sivaram, 2019). The related warehouses that host delivery and loading activities produce additional pollutants. Ports may be able to decarbonize these activities by substituting nonrenewable energy sources with renewable energy sources, increasing energy efficiency, implementing intelligent transportation and logistics technologies, providing shoreside electricity for docked ships, and employing lighter materials (Arrigo et al., 2022; Fay et

al., 2015; Sivaram, 2019; Yang et al., 2022).

### **Port Strategies to Reduce Emissions**

There are a variety of industries inside various ports. These industries can include automotive, construction materials, electrical power, fish processing, food, petroleum, shipbuilding, and steel. Infrastructure and port size determine which ports include many types of industries. The carbon tax is an incentive for some companies to minimize their carbon impact. This stimulates the development of alternate production methods for energy-intensive items such as chemicals and steel. These sectors may lower their carbon footprint by the use of renewable heat in their operations or by improving the efficiency of their present production techniques. In addition to circular production models, green hydrogen as a feedstock, and waste heat, they may also utilize additional technologies.

### **Green Logistics**

Ports are an ideal site for offshore wind farms since they already have robust power networks connecting a large number of users (Mallouppas & Yfantis, 2021). Due to the enormous number of people that dock at ports, these areas are excellent for large-scale offshore wind projects. Consequently, they are crucial to the development of renewable energy sources (DeCotis et al., 2022; Sadriev & Kuzmin, 2023). Ports also have the potential to serve as sites for the development of large-scale energy storage. This will be important to maintain equilibrium between variable supply and demand and to allow the transfer of green hydrogen (Groves et al., 2022).

### **Green Port Management**

Continuous maintenance and building opportunities for decarbonization are available at ports. With ports, dredging businesses are able to replace the engines on their boats and hybridize their equipment and vehicles (Dupont, n.d.; Shah, 2021). Additional prospects include powering tools with on-grid renewable energy storage and replacing diesel-powered equipment with electrified alternatives (Kingston, 2022). Using non-polluting energy to power the company's facilities. The buildings of port companies are intended to include greener energy sources and digital heat control and heat management software (Sadriev & Kuzmin, 2023). This will facilitate their shift to renewable energy sources, hence reducing emissions in these areas. Both environmental impacts and emissions should be monitored and reported. Sustainability requires the reporting of efforts to manage and discuss activities done. Currently, significant corporations in the EU are required to report on the nonfinancial components of their activities (such as emissions) using particular technology and procedures. This is also how smaller enterprises disclose their emissions voluntarily. Measurement of sustainability

impacts necessitates an avalanche of data, which has spurred the development of novel data management tools (Bao et al., 2023; Ren et al., 2022).

### III. Research Methodology

This study involves the use of a quantitative research approach to examine the significant correlation between the latent variables. The targeted population for the purpose of this study encompasses very key and vibrant maritime stakeholders operating at the BKP. From a population of about 750 maritime stakeholders, Krejcie and Morgan's sampling technique was adopted to skew the population to a sample size of 524 stakeholders. A total of 400 structured questionnaires were distributed to our targeted respondents via the e-mail system. Before the respondents were made to address the questionnaires, all ethical protocols for the various firms were duly acknowledged by firstly sending them an invitation notice detailing the objective of this survey via the e-mail system. All the institutions acknowledged their invitation to participate in this study. The respondents were given 25 working days to address the questionnaire. Within this period, reminder emails were sent every Friday to alert respondents. Respondents who could not finish answering their questionnaire within the allotted time frame were given five extra working days to complete it. The rationale for extending the allotted time frame was to enhance the sample size and response rate. A total of 645 responses were received as feedback but only 635 valid ones could be used for the purpose of this study due to missing data, hence, representing a 96.8% response rate. According to Agyabeng-Mensah *et al.* (2021), the above response rate is deemed satisfactory to undertake a supply chain-related survey.

In this study, six study hypothesis are set as follows while the study framework is presented in **Fig. 1**:

- H1*: Decarbonization Policies positively and significantly influence Green Port Management.
- H2*: Low-Carbon Operation positively and significantly influence Green Port Management.
- H3*: Port Strategies to Reduce Emissions positively and significantly influence Green Port Management.
- H4*: Green Port Management positively and significantly influence Sustainability Development of BKP.
- H5*: Green Logistics positively and significantly influence Sustainability Development of BKP.
- H6*: Green Logistics plays a significant mediation role between Green Port Management and Sustainability Development of Seaport

### IV. Results and Findings

From the results of the study of the general information of the sample, it was found that a total of 24 measuring items, each with a five-point Likert-type scale ranging from 1 to 5, were created to assess the individual latent variables. Most of the respondents were female, aged 30-40 years old, and had 1-5 years of work experience. Analysis of mean, standard deviation, skewness and kurtosis to descriptive data presented in TABLE 2., the mean and standard deviation (SD) values were, respectively, between 3.80 and 4.165 and 0.902 and 1.014. The mean and SD scores reveal no discernible difference between the latent variables analyzed. Additionally, it was determined that the skewness and kurtosis were within the range of 1, indicating that the dataset for this investigation was normally distributed. TABLES 2 and 3 display specifics about the measurement items and descriptive statistics. The demographic details of the respondents as shown in TABLE 1.

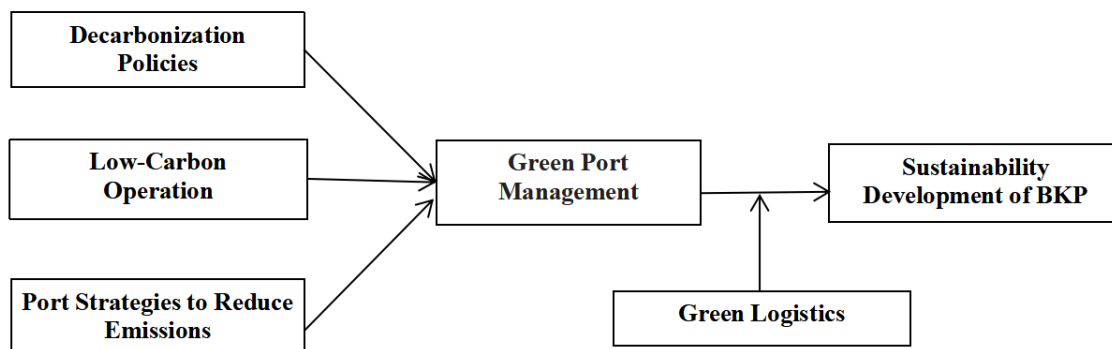
Various methods were used to analyze the study's common method bias (CMB). First and foremost, the sample size and respondents were chosen based on the ideologies of specialists and maritime institutions that were actively engaged in marine operations and activities. Additionally, statistical analysis utilizing the exploratory factor analysis (EFA) recommended by Podsakoff et al. was done to look at the cumulative variance (2012). EFA evaluates CMB by taking into account all of the model's latent variables. When assessed, the cumulative variance value should be less than 50%, according to Podsakoff et al. (2012). The test's results showed a score of 42.71%, which is below the highest level recommended by Podsakoff et al. (2012) and suggests that this study has no issues with CMB.

Analysis of the dataset and study's hypotheses was done using partial least square structural equation modeling (PLS-SEM). Due to its superior characteristics to other statistical techniques, PLS-SEM has been quite popular in recent statistical surveys and studies (Peng and Lai, 2012). PLS can handle a very limited number of datasets and is appropriate for the early phases of theory construction, according to Hair et al. (2020). It can handle both reflective and formative variables and is robust with strong predictive relevance. By evaluating the measurement model and structural model of the investigation, the dataset of the model was examined. The validity and reliability of the measurement model are examined during assessment. It assesses the relationship between the latent variables and the components of their measurements. On the other hand, evaluation of the structural model looks at how the latent variables are related. Additionally, the model's goodness of fit (GoF), which assesses the average variable's geometric mean for

the outer model and the average R-square for the inner model, was measured between 0 and 1. With values of 5,000 and 300, respectively, bootstrapping and the PLS algorithm were used to calculate the t-statistics and the correlation between the latent variables. The algorithm's default value for blindfolding, which gauges the data omission point, was predicted to be D 7. (Hair et al., 2020). The inner VIF was measured to resolve any multicollinearity-related issues that emerged during the investigation. Kock (2015) asserts that VIF readings should be less than 3.3 when measured. TABLE 4's VIF scores demonstrate that this study is free of multicollinearity problems because they fell within the range of 1.201 to 2.378 when tested. While control factors with p-values over 1 have no direct beneficial influence on SD, those with p-values below 1 have a direct and significant impact on SD. The measurement model is evaluated. As was previously said, the evaluation of the measurement model quantifies the model's validity and dependability. It assesses the relationship between the latent variables and the components of their measurements. By evaluating the model's internal consistency reliability (Cronbach's alpha and composite reliability), convergent validity (average variance extracted [AVE]), and discriminant validity, the reflectiveness of the model was investigated (Fornell-Larcker criterion and Heterotrait-Monotrait Ratio [HTMT]). Cronbach's alpha and composite reliability construct reliability measurements taken from the model. Inferring from TABLE 3, By evaluating the model's internal consistency reliability (Cronbach's alpha (CA), and composite reliability (CR)) were all between 0.789 and 0.832 and 0.831 to 0.914, respectively, which satisfies the criteria suggested by Hair et al. (thus, >0.70). (2020). The AVE scores, which indicate the convergent validity of the model, fell between 0.589 and 0.745. These results are in line with Hair et al suggested threshold (>0.50). (2020). As stated by Hair et al., the

values for the factor loadings in TABLE 3 were all over 0.707. (2020). The Fornell-Larcker criterion and the HTMT ratio were then used to test discriminant validity, which measures the uniqueness of the model. The recorded Fornell-Larcker and HTMT ratio scores from TABLEs 5 and 6 were all between 0.572 and 0.845 and 0.673 to 0.842, respectively. The model of this study is said to have attained discriminant validity when compared to the suggested criterion (0.85) by Henseler (2017).

The structure model is evaluated. The structural model's evaluation looks at the correlation between the study's latent variables. Predictive relevance (Q2), variance explained (R2), and the model's effect size (f2) are all measured in order to assess the measurement model. The endogenous constructs with the highest R2 scores from TABLE 7 are GPM (54.4%), and SD (33.9%). R2 values of 0.544 and 0.339 are regarded as strong, moderate, and weak, respectively, as stated by Chin (1998). It may be stated that the model has attained moderate to strong R2 values based on the values that were reported for this investigation. By calculating Q2, the predictive usefulness of the model was also calculated. Henseler (2017) asserts that Q2 values must above the 0.000 cutoff. All of the values for Q2 in TABLE 7: GPM (0.338), and SDS (0.253) supported the research model. According to Hair et al. (2019), f2 values of 0.003, 0.074, 0.121, 0.178, 0.062, and 0.013 are referred to as small and medium respectively. As can be seen from TABLE 7, the model's recorded f2 values ranged from 0.003 to 0.178, indicating that the model had attained medium to large effect sizes. Additionally, an approximate value of 0.641 was assigned to the GoF of the model, which assesses the geometric mean of the average variable and the average R-square of the outer and inner models, respectively (TABLE 7 and Fig. 2).



**Figure 1** Conceptual framework



**TABLE 1** Demographic data of respondents

Demographic information	Frequency	Percent
<b>Gender</b>		
Male	191	47.75
Female	209	52.25
<b>Age</b>		
Below 30 years	86	21.50
30-40 years	208	52.00
41-50 years	78	19.50
51 plus	28	7.00
<b>Worked in maritime industry</b>		
1-5 years	196	49.00
6-10 years	82	20.50
11-15 years	51	12.75
16-20 years	33	8.25
20 years plus	38	9.50

**TABLE 2** Mean, standard deviation, skewness and kurtosis

Item	Mean	Standard Deviation	Skewness	Kurtosis
DP1	4.065	0.902	-0.685	-0.074
DP2	3.848	0.955	-0.559	-0.119
DP3	3.975	0.878	-0.554	-0.286
DP4	3.960	0.869	-0.544	-0.131
LCO1	4.013	0.839	-0.612	0.364
LCO2	3.918	0.844	-0.421	-0.305
LCO3	3.958	0.859	-0.443	-0.287
LCO4	3.995	0.850	-0.483	-0.339
GL1	4.090	0.899	-0.656	-0.105
GL2	3.968	0.979	-0.707	-0.072
GL3	3.845	0.956	-0.655	0.237
GL4	3.970	0.936	-0.622	-0.240
PSRE1	4.010	0.852	-0.556	0.019
PSRE2	3.893	0.926	-0.488	-0.269
PSRE3	3.940	0.913	-0.437	-0.535
PSRE4	3.915	0.959	-0.634	-0.130
GPM1	4.098	0.812	-0.603	0.076
GPM2	3.875	0.934	-0.473	-0.313
GPM3	3.935	0.932	-0.618	-0.025
GPM4	3.943	0.949	-0.715	0.277
SDS1	3.903	0.985	-0.673	0.007
SDS2	3.805	0.940	-0.584	0.156
SDS3	3.800	1.014	-0.577	-0.093
SDS4	3.825	0.976	-0.604	0.039

**TABLE 3** Measurement item, CA, CR and AVE

Constructs	Measurement item	Factor loadings	CA	CR	AVE
<b>Decarbonization Policies</b>	<b>DP1:</b> BKP has systems for enhancing safety of navigation/operations in the maritime industry	0.825	0.880	0.918	0.736
	<b>DP2:</b> BKP has systems for enhancing safety awareness industry	0.845			
	<b>DP3:</b> BKP has systems for enhancing safety culture in the maritime industry	0.887			
	<b>DP4:</b> BKP has systems for enhancing occupational safety and hazard in the maritime industry.	0.874			
<b>Low-Carbon Operation</b>	<b>LCO1:</b> BKP has the capacity for promoting and influencing the automation of certain terminal operations in the seaport settings.	0.856	0.858	0.903	0.701
	<b>LCO2:</b> BKP has the capacity for promoting and influencing energy management systems in the seaport settings.	0.845			
	<b>LCO3:</b> BKP has the capacity for promoting and influencing dry port development, operations, and integration in seaport operations.	0.814			
	<b>LCO4:</b> BKP has the capacity for promoting and influencing green logistics system in port supply chain.	0.832			
<b>Green Logistics</b>	<b>GL1:</b> BKP has the capacity for promoting and influencing the automation of certain terminal operations in the seaport settings	0.788	0.826	0.884	0.655
	<b>GL2:</b> BKP has the capacity for promoting and influencing energy management systems in the seaport settings.	0.802			
	<b>GL3:</b> BKP has the capacity for promoting and influencing dry port development, operations, and integration in seaport operations.	0.823			
	<b>GL4:</b> BKP has the capacity for promoting and influencing green logistics system in port supply chain	0.823			
<b>Port Strategies to Reduce Emissions</b>	<b>PSRE1:</b> BKP has the capacity for promoting ballast water management.	0.831	0.851	0.900	0.692
	<b>PSRE2:</b> BKP has the capacity for promoting clean ocean fishing.	0.809			
	<b>PSRE3:</b> BKP has the capacity for promoting the use of double bottom tanks by oil tankers.	0.869			
	<b>PSRE4:</b> BKP has the capacity for promoting the installation of waste treatment plants in the maritime industry.	0.818			
<b>Green Port Management</b>	<b>GPM1:</b> BKP has the capacity for supplying or using energy efficient fuel in its operations	0.782	0.831	0.888	0.664
	<b>GPM2:</b> BKP has the capacity for supplying or using eco-generators in supporting its operations	0.821			
	<b>GPM3:</b> BKP has the capacity for promoting and influencing shippers the use of container transport in shipping.	0.808			
	<b>GPM4:</b> BKP has the capacity for green seaport management.	0.848			
<b>Sustainability Development of Seaport</b>	<b>SDS1:</b> BKP has significantly improved emission control measures.	0.882			
	<b>SDS2:</b> BKP has significantly improved pollution control measures.	0.902			
	<b>SDS3:</b> BKP has significantly improved resource utilization measures.	0.904			
	<b>SDS4:</b> BKP has significantly improved the social benefits on the maritime industry.	0.895			

**TABLE 4** Path Coefficient (Direct effects)

Hypothesis	Path	Beta values	<i>t</i> -statistics	<i>p</i> -values	VIF	Supported
H1	DP -> GPM	0.121	1.999	0.046	2.378	Yes
H2	LCO -> GPM	0.282	4.116	0.000	2.833	Yes
H3	PSRE -> GPM	0.413	7.317	0.000	2.102	Yes
H4	GPM -> SDS	0.376	7.184	0.000	1.760	Yes
H5	GL -> SDS	0.287	5.315	0.000	1.696	Yes
H6	Moderating Effect 1 -> SDS	0.032	1.281	0.201	1.201	No

**TABLE 5** The Fornell-Larcker criterion

Constructs	DP	GL	GPM	LCO	Moderating Effect 1	PSRE	SDS
DP	0.858						
GL	0.665	0.809					
GPM	0.593	0.631	0.815				
LCO	0.746	0.705	0.664	0.837			
Moderating Effect 1	-0.301	-0.344	-0.389	-0.332	1.000		
PSRE	0.634	0.631	0.689	0.706	-0.287	0.832	
SDS	0.532	0.508	0.538	0.577	-0.197	0.553	0.896

**TABLE 6** Heterotrait-Monotrait Ratio (HTMT)

Constructs	DP	GL	GPM	LCO	Moderating Effect 1	PSRE	SDS
DP	0.858						
GL	0.665	0.809					
GPM	0.593	0.631	0.815				
LCO	0.746	0.705	0.664	0.837			
Moderating Effect 1	-0.301	-0.344	-0.389	-0.332	1.000		
PSRE	0.634	0.631	0.689	0.706	-0.287	0.832	
SDS	0.532	0.508	0.538	0.577	-0.197	0.553	0.896

**TABLE 7** Structural model showing  $R^2$ ,  $Q^2$ , and  $f^2$

Constructs	$R^2$	$Q^2$	$f^2$
DP			0.013
LCO			0.062
PSRE			0.178
GPM	0.544	0.338	0.121
GL			0.074
Moderating Effect 1			0.003
SDS	0.339	0.253	

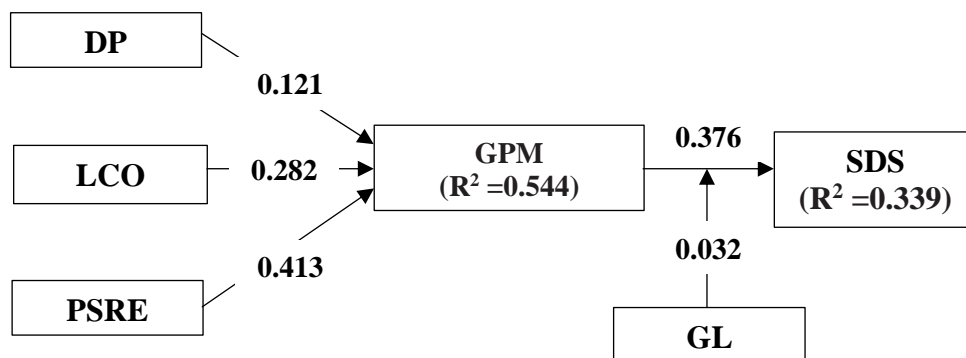


Fig. 2. Assessment of the structural model showing the Beta values and  $R^2$

TABLE 8 Path coefficient (indirect effect)

Hypothesis	Path	Beta values	<i>t</i> -statistics	<i>p</i> -values	Supported
H7	DP -> GPM -> SDS	0.045	1.808	0.071	No
H8	LCO -> GPM -> SDS	0.106	3.708	0.000	Yes
H9	PSRE -> GPM -> SDS	0.155	5.320	0.000	Yes

### Conclusions and Implications

The demand for SD on a global scale has forced the maritime industry to embrace green maritime practices in order to attain its SD. Even though the International Maritime Organization (IMO) ultimate purpose has always been to promote economic growth and SD, there is virtually little literature on maritime sustainability. This study suggests a conceptual model that analyses both the direct and indirect effects of high-quality maritime education and training, LCO, GL, PSRE, GPM, and SD, drawing conclusions from NRBV theory introduced by Hart (1995). Findings of the study have shown that the high-quality maritime education and training directly and significantly contribute to the adoption of green maritime practices including LCO, GL, PSRE, and GPM by maritime stakeholders. It is also implied that the adoption of green marine practices by maritime authorities, such as LCO, GL, PSRE, and GPM, directly and favorably impacts SD in the maritime sector. Additionally, the results demonstrate a strong and direct correlation between SD and high-quality maritime education and training. The results also suggest that LCO, GL, PSRE, and GPM have a substantial mediating effect on the connection between high-quality maritime education and training and SD. The findings on theoretical and practical ramifications are described below. According to the results of the study, the Port Authority should plan to upgrade it to be a leading port that meets international standards.

### Theoretical Implications

The work significantly advances the field of sustainable maritime practices and SD in several ways. First and foremost, this study contributes to proving and deepening the claim that seaports in emerging economies operate with less consideration for environmental concern (Dzidzornu, 1994; Onwuegbuchunam et al., 2017a, b; Lu and Wang, 2020) and to establish a balance relationship between studies conducted in developed maritime states such as Korea (Roh et al., 2021), Norway (Koilo, 2021), and China (Lam Second – the study aims to enhance our understanding of the possibility that government policies or support for GL may be insufficient for SD in order to broaden the theoretical lens of Ehlers (2016)).

This study instead stresses how government funding for maritime training institutions improves the standard of maritime education and training for maritime professionals, which strengthens GL practices for SD. Once more, this study expands and improves our knowledge of sustainable maritime techniques that can be used in the maritime sector. This study shows the maritime industry stakeholders that green maritime practices are a crucial instrument for boosting operational effectiveness, productivity, and competitiveness as well as for better energy management, environmental protection, and social performance. Additionally, by illustrating and endorsing both onshore and offshore green maritime practices that collectively contribute to the attainment of SD in the maritime industry, this study offers a very thorough insight into the literature. To the best of our knowledge, there has not been any empirical research looking into green marine methods for SD both on land and at sea.

Thus, the operational scope for SD has not received much attention. Previous research only focused on one of these two operating areas (Ehlers, 2016; Roh et al., 2021; Koilo, 2021; Onwuegbuchunam et al., 2017a, b). Finally, by analyzing the mediation role of LCO, GL, PSRE, and GPM on high-quality maritime education and training and SD, this study considerably adds to the body of literature. To the best of our knowledge, this is the first study in the maritime sector that has looked at the mediation role, therefore bridging the mediation gap between LCO, GL, PSRE, and GPM on high-quality maritime education and training and SD.

### Practical Implications

By applying the concepts from this study, namely Decarbonization Policies, Low-Carbon Operation Green Logistic, Port Strategies to Reduce Emissions, and Green Port Management is used to develop a strategy to drive the development of services and infrastructure to world-class standards. Evolving into a main trading gateway and transportation transformation center, developing business assets for added value. Service development and upgrading of work towards a high-performance organization This is to support the logistics network at the international level. This study presents a lot of practical consequences for managers and policymakers (industrial consortium and central government) in the maritime industry in addition to its impressive theoretical ramifications for existing theory and literature. First and foremost, this study educates and raises the awareness of maritime authorities and managers of maritime firms about the fact that, despite the adoption of green maritime practices significantly improving the competitiveness, operational, environmental, economic, and social performances of maritime firms, it may not be enough if maritime personnel are not given high-quality maritime education and training. In general, a holistic SD can be attained by providing all marine professionals with thorough maritime education and training. Additionally, this study offers stakeholders and maritime authorities greater decision-making options on green marine practices that may be used to support environmentally friendly operations and services for maritime sustainability. The adoption of green marine practices effectively gives maritime authorities and stakeholders the chance to implement green operations and services that enhance the organization's environmental performance and show compliance with environmental standards and criteria.

### Reference

A pathway towards more sustainable shipping in 2050: A possible future for automation and remote operations. (2014). In *Maritime-Port Technology and Development* (pp. 51–64).  
<https://doi.org/10.1201/b17517-7>

- Arrigo, R., Blume, R., Large, A. I., Velasco-Vélez, J. J., Hävecker, M., Knop-Gericke, A., & Held, G. (2022). Dynamics over a Cu-graphite electrode during the gas-phase CO reduction investigated by APXPS. *Faraday Discussions*, 236(0), 126–140.  
<https://doi.org/10.1039/d1fd00121c>
- Bao, Z., Xie, B., Li, W., Zhong, S., Fan, L., Tongsh, C., Gao, F., Du, Q., Benbouzid, M., & Jiao, K. (2023). High-consistency proton exchange membrane fuel cells enabled by oxygen-electron mixed-pathway electrodes via digitalization design. *Science Bulletin*.  
<https://doi.org/10.1016/j.scib.2023.01.034>
- DeCotis, P. A., Swartout, B., & Bablitch, E. (2022). Decarbonization and Electrification: The Case for Innovation. In *Climate and Energy* (Vol. 38, Issue 9, pp. 1–12). <https://doi.org/10.1002/gas.22280>
- Dupont, C. (n.d.). Decarbonization and EU Relations with the Caspian Sea Region. In *Decarbonization in the European Union*.  
<https://doi.org/10.1057/9781137406835.0015>
- Dupont, C., & Oberthür, S. (n.d.). Decarbonization in the EU. In *Decarbonization in the European Union*.  
<https://doi.org/10.1057/9781137406835.0007>
- Elhatab, A., Faculty of Engineering-Port Said University, & Egypt. (2016). Recent Positioning Techniques for Efficient Port Operations and Development of Suez Canal Corridor. In *Renewable Energy and Sustainable Development* (Vol. 2, Issue 2, pp. 126–136). <https://doi.org/10.21622/resd.2016.02.2.126>
- European Investment Bank. (2022). *EIB Impact Report 2020: Climate action, environmental sustainability and innovation for decarbonisation*. European Investment Bank.  
[https://books.google.com/books/about/EIB\\_Impact\\_Report\\_2020.html?hl=&id=FvNXEAAAQBAJ](https://books.google.com/books/about/EIB_Impact_Report_2020.html?hl=&id=FvNXEAAAQBAJ)
- Fakour, H., Imani, M., Lo, S.-L., Yuan, M.-H., Chen, C.-K., Mobasser, S., & Muangthai, I. (2023). Evaluation of solar photovoltaic carport canopy with electric vehicle charging potential. *Scientific Reports*, 13(1), 2136.  
<https://doi.org/10.1038/s41598-023-29223-6>
- Fay, M., Hallegatte, S., Vogt-Schilb, A., Rozenberg, J., Narloch, U., & Kerr, T. (2015). *Decarbonizing Development: Three Steps to a Zero-Carbon Future*. World Bank Publications.  
<https://play.google.com/store/books/details?id=VQ77CgAAQBAJ>
- Ferrari, G., Holl, E., Steinbrenner, J., Pezzuolo, A., & Lemmer, A. (2022). Environmental assessment of a two-stage high pressure anaerobic digestion process and biological upgrading as alternative processes for biomethane production. *Bioresource Technology*, 360, 127612.  
<https://doi.org/10.1016/j.biortech.2022.127612>
- Groves, C., Henwood, K., Pidgeon, N., Cherry, C., Roberts, E., Shirani, F., & Thomas, G. (2022).

- Putting visions in their place: responsible research and innovation for energy system decarbonization. In *Journal of Responsible Innovation* (pp. 1–28). <https://doi.org/10.1080/23299460.2022.2149954>
- Hübner, K. (2018). Decarbonization and unlocking. In *National Pathways to Low Carbon Emission Economies* (pp. 1–44). <https://doi.org/10.4324/9780429458118-1>
- Hwang, J., & Kim, S. (2020). Fine Dust and Sustainable Supply Chain Management in Port Operations: Focus on the Major Cargo Handled at the Dry Bulk Port. In *Journal of Marine Science and Engineering* (Vol. 8, Issue 7, p. 530). <https://doi.org/10.3390/jmse8070530>
- Kingston, E. (2022). Innovation, Deep Decarbonization and Ethics. In *Ethics, Policy & Environment* (Vol. 25, Issue 3, pp. 375–384). <https://doi.org/10.1080/21550085.2022.2132797>
- Lenox, M., & Duff, R. (2021). *The Decarbonization Imperative: Transforming the Global Economy by 2050*. Stanford University Press. [https://books.google.com/books/about/The\\_Decarbonization\\_Imperative.html?hl=&id=zfZNEAAQBAJ](https://books.google.com/books/about/The_Decarbonization_Imperative.html?hl=&id=zfZNEAAQBAJ)
- Mallouppas, G., & Yfantis, E. A. (2021). Decarbonization in Shipping Industry: A Review of Research, Technology Development, and Innovation Proposals. In *Journal of Marine Science and Engineering* (Vol. 9, Issue 4, p. 415). <https://doi.org/10.3390/jmse9040415>
- Mulvaney, D. (2020). *Sustainable Energy Transitions: Socio-Ecological Dimensions of Decarbonization*. Springer Nature. <https://play.google.com/store/books/details?id=Nc4MEAAQBAJ>
- Primova, R. (n.d.). The EU Internal Energy Market and Decarbonization. In *Decarbonization in the European Union*. <https://doi.org/10.1057/9781137406835.0008>
- Ren, N., Zhang, X., & Fan, D. (2022). Influencing Factors and Realization Path of Power Decarbonization-Based on Panel Data Analysis of 30 Provinces in China from 2011 to 2019. *International Journal of Environmental Research and Public Health*, 19(23). <https://doi.org/10.3390/ijerph192315930>
- Ruangchoengchum, P. (2015). Performance Measurements Related to Lean Manufacturing that Affect Net Profit of SMEs in the Manufacturing Sector of Thailand. In *Toward Sustainable Operations of Supply Chain and Logistics Systems* (pp. 223–240). [https://doi.org/10.1007/978-3-319-19006-8\\_15](https://doi.org/10.1007/978-3-319-19006-8_15)
- Sadriev, A. R., & Kuzmin, M. S. (2023). Patent activity in the field of decarbonization technologies. In *MIR (Modernization. Innovation. Research)* (Vol. 13, Issue 4, pp. 556–574). <https://doi.org/10.18184/2079-4665.2022.13.4.556-574>
- Sam, A. G., & Song, D. (2022). ISO 14001 certification and industrial decarbonization: An empirical study. *Journal of Environmental Management*, 323, 116169. <https://doi.org/10.1016/j.jenvman.2022.116169>
- Sankla, W., & Muangpan, T. (2022). Smart and Sustainable Port Performance in Thailand: A Conceptual Model. In *Journal of Sustainable Development* (Vol. 15, Issue 4, p. 1). <https://doi.org/10.5539/jsd.v15n4p1>
- Sattich, T. (2015). Electricity Grids: No Decarbonization without Infrastructure. In *Decarbonization in the European Union* (pp. 70–91). [https://doi.org/10.1057/9781137406835\\_4](https://doi.org/10.1057/9781137406835_4)
- Shah, Y. T. (2021). Hybrid Energy Systems—Strategy for Decarbonization. In *Hybrid Energy Systems* (pp. 1–18). <https://doi.org/10.1201/9781003159421-1>
- Shirakashi, R., Kozlakidis, Z., Yadav, B. K., Ng, W., Fachiroh, J., Vu, H., Tsuruyama, T., & Furuta, K. (2022). Decarbonization in Biobanking: A Potential New Scientific Area. *Biopreservation and Biobanking*, 20(5), 446–450. <https://doi.org/10.1089/bio.2022.0146>
- Singh, D., Buddhi, D., & Karthick, A. (2023). Productivity enhancement of solar still through heat transfer enhancement techniques in latent heat storage system: a review. *Environmental Science and Pollution Research International*, 30(1), 44–77. <https://doi.org/10.1007/s11356-022-23964-z>
- Sivaram, V. (2018). *Digital Decarbonization: Promoting Digital Innovations to Advance Clean Energy Systems*. Council on Foreign Relations Press. [https://books.google.com/books/about/Digital\\_Decarbonization.html?hl=&id=9tKXuAEACAAJ](https://books.google.com/books/about/Digital_Decarbonization.html?hl=&id=9tKXuAEACAAJ)
- Sivaram, V. (2019). *Taming the Sun: Innovations to Harness Solar Energy and Power the Planet*. MIT Press. [https://books.google.com/books/about/Taming\\_the\\_Sun.html?hl=&id=SVX6DwAAQBAJ](https://books.google.com/books/about/Taming_the_Sun.html?hl=&id=SVX6DwAAQBAJ)
- Sovacool, B. K., Geels, F. W., & Iskandarova, M. (2022). Industrial clusters for deep decarbonization. *Science*, 378(6620), 601–604. <https://doi.org/10.1126/science.add0402>
- Srisil, A. D. J. (n.d.). King’s Philosophy for Sustainable Development Innovation Toward National Strategy Thailand 4.0. In *SSRN Electronic Journal*. <https://doi.org/10.2139/ssrn.3349990>
- The Role of CCUS in North America Energy System Decarbonization. (2020). In *Journal of Strategic Innovation and Sustainability* (Vol. 14, Issue 6). <https://doi.org/10.33423/jsis.v14i6.2610>

# Effects of Potential Determining Ions on Dissolution of Dolomite during Low Salinity Waterflooding

Nuttapol Junput<sup>1</sup> and Falan Srisuriyachai<sup>2</sup>

<sup>1</sup>Department of Mining and Petroleum Engineering, Chulalongkorn University, Phayathai, Wangmai, Pathumwan, Bangkok, [nju@chevron.com](mailto:nju@chevron.com)

<sup>2</sup>Department of Mining and Petroleum Engineering, Chulalongkorn University, Phayathai, Wangmai, Pathumwan, Bangkok, Thailand, [falan.s@chula.ac.th](mailto:falan.s@chula.ac.th)

**Abstract:** Low Salinity Waterflooding (LSWF) is a technique that is often mentioned nowadays since this technique is a simple Enhance Oil Recovery (EOR) technique with cost effective. Several studies revealed that salinity of injected brine and concentration of potential determining ions play an important role in initiating oil recovery mechanisms. But most of those studies focused on sandstone reservoirs. In this study, regarding the fact that more than 50% of hydrocarbon reserves are in carbonate reservoirs, dolomite reservoirs were focused to investigate the feasibility of applying this method. In this study, Potential Determining Ions (PDI) were selected to perform dissolution test on dolomite samples. Dolomite powder was treated with crude oil to simulate oil-wet condition and treated samples were tested with different water formulations to identify their capacities in Multi-component Ion Exchange (MIE). From all water formulations, the results can be characterized based on dominated ions into four different zones including: 1) Calcium domination zone; 2) Combined effect zone; 3) Sulfate domination zone; and 4) Magnesium domination zone. In case of Calcium and Magnesium domination zones, Magnesium and Calcium ions from dolomite were replaced by the opposite ions. Sulfate ion was able to increase the dissolution of Magnesium and Calcium ions when adequate amount sulfate ion was presented as negative charge of Sulfate ion quickly balanced positive charge of dolomite surface, resulting in an ease of positive charge from Calcium ion or Magnesium ion to reach the dolomite surface. In case of Sulfate domination, Magnesium ion tended to be consumed by dolomite surface based on dolomitization process rather than the Magnesium dissolution. From this study, knowing different behaviors of different combined ionic solutions would lead to ability to select the best water formulation for specific dolomite reservoirs. The combination effect between Calcium and Sulfate ions would yield benefit in low salinity waterflooding in dolomite formation. This would lead to dissolution of Magnesium ion while Calcium ion is not largely consumed due to neutralization of positive charges of dolomite surface.

**Index Terms**—Dolomite Reservoir, Potential Determining Ions, Multi-component Ion Exchange, Low Salinity Waterflooding.

## I. INTRODUCTION

Low Salinity Waterflooding (LSWF) is a technique that is often mentioned nowadays since this technique is a simple Enhance Oil Recovery (EOR) technique with cost effective. LSFW has several advantages over conventional EOR for example it can provide additional increase in oil recovery while maintaining the investment to minimal. Moreover, this technique is environmentally friendly, LSFW does not contain harmful chemical so if it leaks to the environment or water aquifer, it would not be hazard to the environment. The implementation of LSFW is quite simple: injected water must be lower in terms of total salinity compared to that of formation water. Several studies showed that this condition leads to oil recovery mechanisms. Recently, it is found that the oil recovery mechanisms of LSFW were also triggered by many other additional factors. Srisuriyachai et al. [1] performed a series of studies, and they discovered that not only total salinity of injected water plays important role in

initiating oil recovery mechanisms, types of presented ions in injected water also played an even more important role. Several experimental studies demonstrated that LSFW can improve oil recovery in sandstone reservoirs. Laboratory study by Lager et al. [2] showed that injection of water with low salinity increased oil recovery up to 25%. But most of those studies focused on sandstone reservoirs. In this study, regarding the fact that more than 50% of hydrocarbon reserves are in carbonate reservoirs, we focused on dolomite reservoirs to investigate the feasibility of applying this method. In this study, Potential Determining Ions (PDI) for carbonate rocks including  $\text{Ca}^{2+}$ ,  $\text{Mg}^{2+}$  and  $\text{SO}_4^{2-}$  were selected to perform dissolution test on dolomite samples. Dolomite samples were treated with crude oil to simulate oil-wet condition and thereafter, they were tested with different water formulations to identify their capacities in Multi-component Ion Exchange (MIE) through dissolution. The supernatants obtained from dissolution test were collected and analyzed for concentrations of  $\text{Ca}^{2+}$  and  $\text{Mg}^{2+}$  as they

represent ions linking between dolomite surface and oil drop. The results from this study can be used to accompany selecting of appropriate water formulation for LSWF in specific dolomite reservoir.

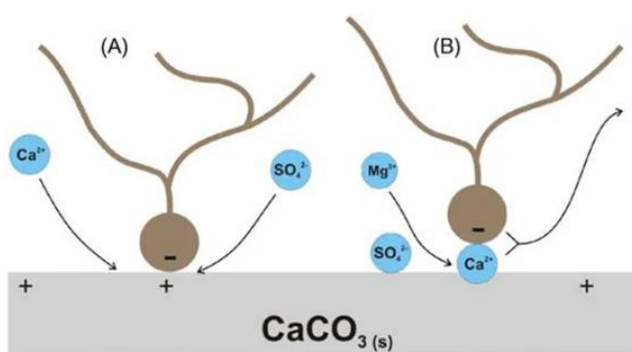
## II. DATA USED

Based on previous studies, various injected brine parameters have been suggested that affect to oil recovery improvement during LSWF in carbonate formations, the injected brine parameters are summarized in this section.

### (1) Ionic Composition

The effects of  $\text{Ca}^{2+}$ ,  $\text{Mg}^{2+}$  and  $\text{SO}_4^{2-}$ , 3 primary PDIs toward carbonate surfaces, have been extensively studied in the literature. According to Zhang and Austad [3], increasing the concentration of sulfate ions ( $\text{SO}_4^{2-}$ ) in seawater led the wettability to shift in favor of a more water-wet condition. Furthermore, after 30 days of imbibition, 32% more oil was recovered when the concentration of  $\text{Ca}^{2+}$  in seawater was increased. Additionally, they proposed that altering the wettability of chalk surfaces and enhancing oil recovery may be accomplished by changing the concentration of  $\text{Ca}^{2+}$  and  $\text{SO}_4^{2-}$  ions in seawater and the initial brine. It was discovered that the co-adsorption of  $\text{Ca}^{2+}$  and  $\text{SO}_4^{2-}$  ions onto chalk surfaces with increasing temperatures might lead to improve water-wetness conditions and improve oil recovery. This effect of  $\text{Ca}^{2+}$  and  $\text{SO}_4^{2-}$  ions on wettability modification of chalk surfaces was examined. Furthermore, it was proposed by Chandrasekhar and Mohanty [4] that  $\text{Mg}^{2+}$  and  $\text{SO}_4^{2-}$  ions were more effective than  $\text{Ca}^{2+}$  ions in altering the wettability and enhancing oil recovery of reservoir limestone.

The previous research has led to the conclusion that the injection brine for LSWF in carbonates should be depleted in NaCl, contain PDIs ( $\text{Ca}^{2+}$  and/or  $\text{Mg}^{2+}$ ,  $\text{SO}_4^{2-}$ ), and function at high temperatures (above 70 °C). However, there is a limit for increasing the concentration of  $\text{SO}_4^{2-}$  with increasing temperature, as high concentrations of  $\text{SO}_4^{2-}$  at high temperature results in precipitation of  $\text{CaSO}_4$  and reduces oil recovery. Figure 1 illustrates functions of PDIs during the LSWF in carbonates.



**Fig. 1.** Schematic for proposed effects of PDIs during LSWF in carbonates from Zhang et al. [5]. The presence of MIE between the injected brine and the rock surface causes a reduction in the ionic interaction between oil molecules and rock surface, which is the primary mechanism of increased oil recovery during LSWF.

### (2) Ionic Concentration

The effect of salinity on wettability alteration of carbonate rocks was studied using both diluted brine (formation water or seawater) and tuned brine. According to various experimental findings published in the literature, diluted seawater (up to 20 times) had a better potential to increase oil recovery from carbonate reservoirs than formation water and seawater. For instance, Yousef et al. [6] improved oil recovery from a carbonate reservoir (composite limestone cores) by employing synthetic saltwater (57,600 ppm) and up to 100 times diluted seawater. Both twice diluted seawater (28,800 ppm at 7-8.5% of OOIP) and ten times diluted seawater (5,760 ppm at 9-10% of OOIP) resulted in the highest levels of oil recovery. However, oil recovery improved just slightly (1–1.6% of OOIP) when seawater was 20 times diluted (2,880 ppm), and it did not increase at all when seawater was 100 times diluted. As a result, compared to conventional waterflooding, using diluted seawater resulted in an overall extra oil recovery of about 18%. Al-Harrasi et al. [7] made the case for the possibility of increased oil recovery in carbonate cores at significantly higher concentrations than those reported in the literature using formation water that was diluted 2, 5, 10, and 100 times at 70 °C. While the 100 times diluted formation brine (1,944 ppm) produced the highest oil output and the fastest oil production rate (up to 21% of OOIP), the high salinity twice diluted formation brine (9,225 ppm), showed enhanced oil recovery even at 10% of OOIP. Romanuka et al. [8] also found that lowering the salinity of seawater (up to 10-times diluted) in limestone and dolomite core plugs resulted in extra oil recovery from 4% to 20% of OOIP.

Despite the fact that low salinity brine has generally been found to improve oil recovery, it has been hypothesized that diluted brine with low concentrations of PDIs can enhance oil recovery from carbonates at high temperatures [9]. The concentration of PDIs is asserted to play a more significant function but reducing ionic concentration does not always improve oil recovery [10].

## III. METHODOLOGY

In this study, dolomite samples were tested with different water formulations to identify their capacities in Multi-component Ion Exchange (MIE). The supernatant obtained from stirring dolomite samples with water formulation were collected and analyzed for concentration of  $\text{Ca}^{2+}$  and  $\text{Mg}^{2+}$ . The details of the experiment are described below:

1. Dolomite powder was first checked for purity using XRD and XRF. After the quality was proved, the powder was soaked in crude oil, filtered, and dried to create oil-wet condition. For each experiment, 20 g of oil-covered powders were stirred with 100 ml of selected water formulation for 1 hr. Then, the supernatant was collected by filtrating the solution, using filter paper.



2. For water formulations, this study emphasized on three PDIs which are  $\text{Ca}^{2+}$ ,  $\text{Mg}^{2+}$  and  $\text{SO}_4^{2-}$ . Concentrations of water formulations were 1,000 ppm, 2,000 ppm, 5,000 ppm, and 10,000 ppm. In each concentration, 10 combined formulations were chosen as shown in Table I.

TABLE I  
CHEMICAL CONSTITUENT OF EACH WATER FORMULATION

Formulation no.	Calcium salt (%)	Sulphate salt (%)	Magnesium salt (%)	Composition Ratio
1	100	0	0	1:0:0
2	67	33	0	2:1:0
3	67	0	33	2:0:1
4	33	67	0	1:2:0
5	33.33	33.33	33.33	1:1:1
6	33	0	67	1:0:2
7	0	100	0	0:1:0
8	0	67	33	0:2:1
9	0	33	67	0:1:2
10	0	0	100	0:0:1

3. Dissolution of  $\text{Ca}^{2+}$  and  $\text{Mg}^{2+}$  from dolomite powder was detected from the supernatant, using color titration technique with EDTA. In titration test, sample was pipetted into volumetric flask and then titrated with Ethylene Diaminetetraacetic acid (EDTA) at specific concentration. At first step, total divalent ions ( $\text{Ca}^{2+}$  and  $\text{Mg}^{2+}$ ) were identified. Ammonium solution was added to sample and Eriochrome Black T (EBT) was used as color indicator. End point was detected when color was changed from red wine color to sky blue. Second test was performed to identify only the amount of  $\text{Ca}^{2+}$ . Sample of solution was added by a few drops of Sodium Hydroxide solution to precipitate  $\text{Mg}^{2+}$ . Hydroxy Naphthol Blue (HNB) was used as the color indicator in this case. Similar to the first step, the mixture was titrated with EDTA until end point. Concentrations of total divalent ions and  $\text{Ca}^{2+}$  were calculated and the amount of  $\text{Mg}^{2+}$  was obtained from the difference of these two values. In this study, only  $\text{Ca}^{2+}$  and  $\text{Mg}^{2+}$  were detected as they are ions in dolostone that are related to dissolution mechanism.

#### IV. RESULTS AND DISCUSSION

In this section, the results and discussion on each water formulation from laboratory experiment were discussed. Titration test was conducted to assess results from dissolution of dolomite surface including MIE mechanism with different water formulations. Concentrations of ion were results from contact between water formulation and rock power. Positive concentration value from the plot refers to dissolution of the ion whereas the negative value means the ion is consumed or adsorbed by clays during the ion exchange mechanism.

Figure 2 shows the ionic concentrations from the supernatants of water formulation No.1. Presence of  $\text{Ca}^{2+}$  without other ions in low salinity water led to the

replacement of  $\text{Mg}^{2+}$  by  $\text{Ca}^{2+}$ . However, it was observed that this replacement was not propositional replacement when the concentration of low salinity water was higher than 5,000 ppm. The similar result is observed from water formulation No.2 (Figure 3) which adding of  $\text{SO}_4^{2-}$  into  $\text{Ca}^{2+}$  solution but smaller dissolved ions.

Moreover, the ionic concentrations from the supernatants of water formulation No.3 (Figure 4) which presence of  $\text{Mg}^{2+}$  together with  $\text{Ca}^{2+}$  led to constant ratio of ion exchange as  $\text{Mg}^{2+}$  can replace also  $\text{Ca}^{2+}$  and hence, net amount of  $\text{Ca}^{2+}$  consumed was decreased. At concentration higher than 5,000 ppm, the dissolution of  $\text{Mg}^{2+}$  increased strikingly as same as in solution No.1.

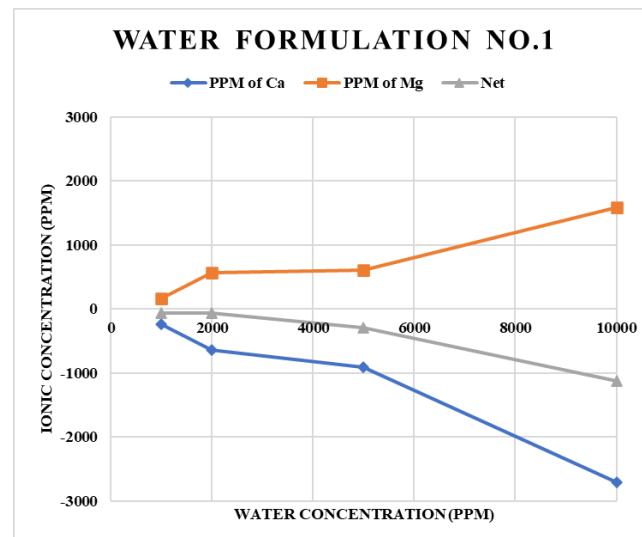


Fig. 2. Ionic concentration from the effluents with different water concentration of water formulation No.1.

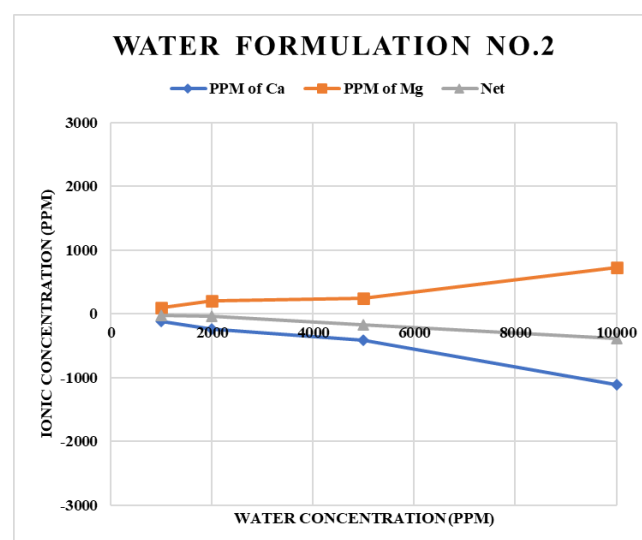


Fig. 3. Ionic concentration from the effluents with different water concentration of water formulation No.2.

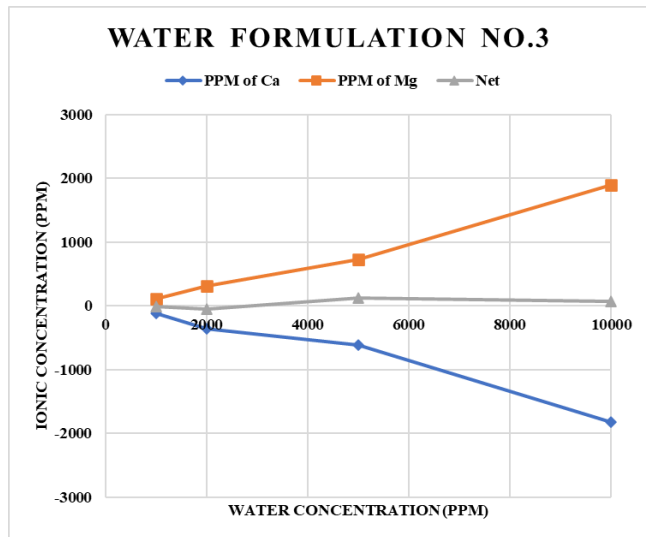


Fig. 4. Ionic concentration from the effluents with different water concentration of water formulation No.3.

Figure 5 illustrates the ionic concentrations from the supernatants of water formulation No.4. Increasing of  $SO_4^{2-}$  concentration led to the difficulty of  $Mg^{2+}$  dissolution but this effect was compensated when the low salinity water concentration was as high as 10,000 ppm with adequate amount of  $Ca^{2+}$ .

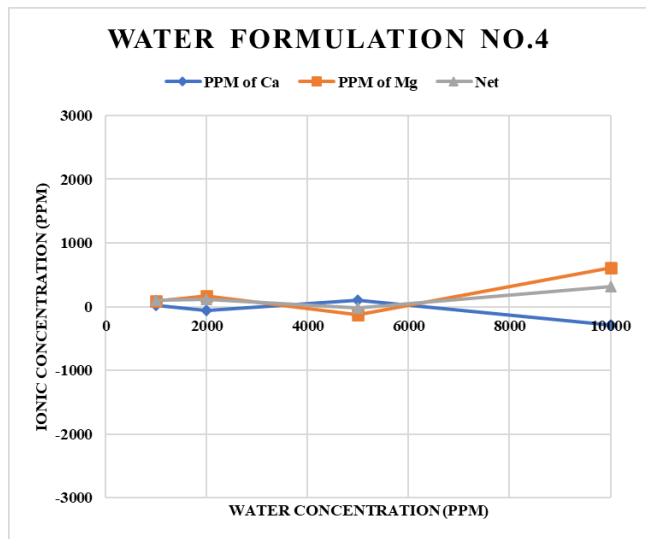


Fig. 5. Ionic concentration from the effluents with different water concentration of water formulation No.4.

Figure 6 presents the ionic concentrations from the supernatants of water formulation No.5. Combination of three ions ( $Ca^{2+}$ ,  $Mg^{2+}$  and  $SO_4^{2-}$ ) at the same portion provided good results in term of net ion dissolution.  $Ca^{2+}$  was consumed by dolomite to replace  $Mg^{2+}$  at 5,000 ppm and better result was observed at 10,000 ppm.

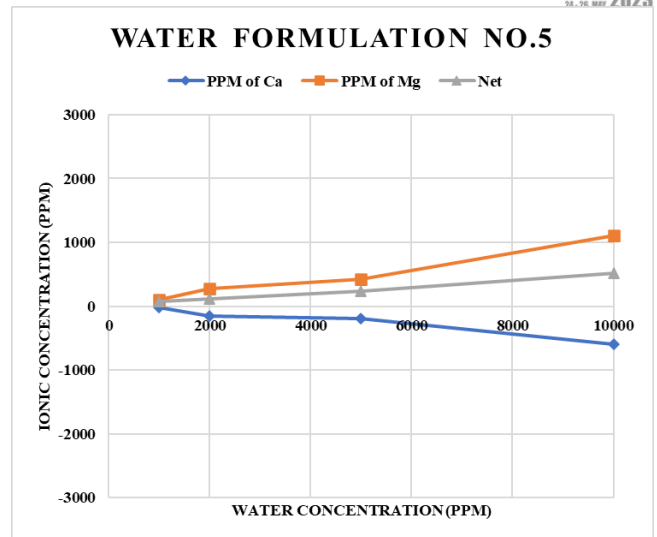


Fig. 6. Ionic concentration from the effluents with different water concentration of water formulation No.5.

Figure 7 shows the ionic concentrations from the supernatants of water formulation No.6. Presence of higher  $Mg^{2+}$  concentration together with lesser  $Ca^{2+}$  led to dissolution of both  $Mg^{2+}$  and  $Ca^{2+}$ . It can be observed that  $Ca^{2+}$  able to displace  $Mg^{2+}$  more than  $Mg^{2+}$  displaces  $Ca^{2+}$  and  $Ca^{2+}$  will be consumed more than  $Mg^{2+}$  ion at high concentration (10,000 ppm).

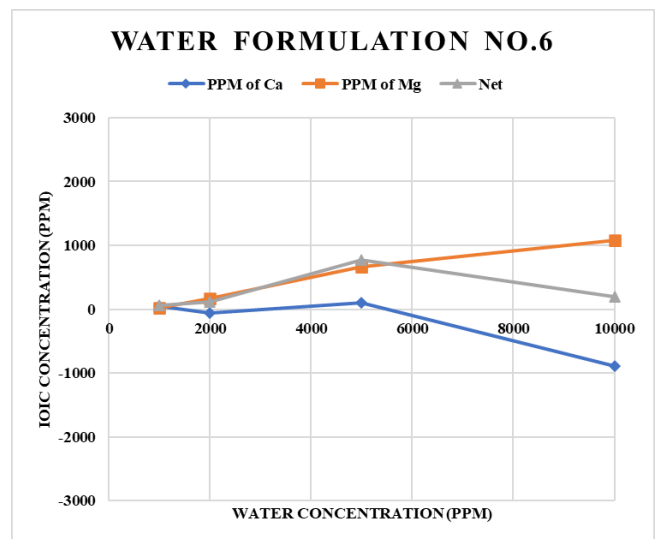


Fig. 7. Ionic concentration from the effluents with different water concentration of water formulation No.6.

Figure 8 illustrates the ionic concentrations from the supernatants of water formulation No.7. Presence of only  $SO_4^{2-}$  ion without other ions resulted in poor dissolution of both  $Mg^{2+}$  and  $Ca^{2+}$ . At 5,000 ppm, dissolutions of  $Mg^{2+}$  and  $Ca^{2+}$  were slightly increased. At higher concentration of  $SO_4^{2-}$ ,  $Mg^{2+}$  disappeared and this could be explained by dolomitization process where  $Mg^{2+}$  was stored back to dolomite by an aid of  $SO_4^{2-}$ .

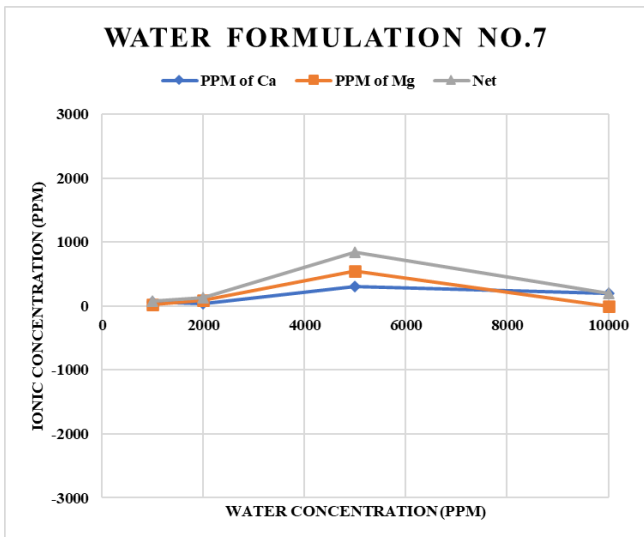


Fig. 8. Ionic concentration from the effluents with different water concentration of water formulation No.7.

Figure 9 reveals the ionic concentrations from the supernatants of water formulation No.8. The result was similar to that of water formulation No.7. Present of  $SO_4^{2-}$  together with  $Mg^{2+}$  might lead to an occurrence of the dolomitization process at high concentration of  $SO_4^{2-}$ .

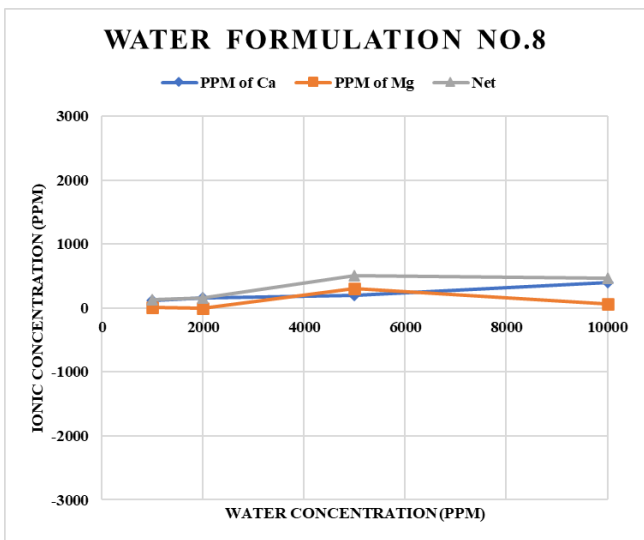


Fig. 9. Ionic concentration from the effluents with different water concentration of water formulation No.8.

Figure 10 depicts the ionic concentrations from the supernatants of water formulations No.9.  $Mg^{2+}$  worked together with  $SO_4^{2-}$  better at high concentration of  $Mg^{2+}$  ion especially at the highest concentration (10,000 ppm).

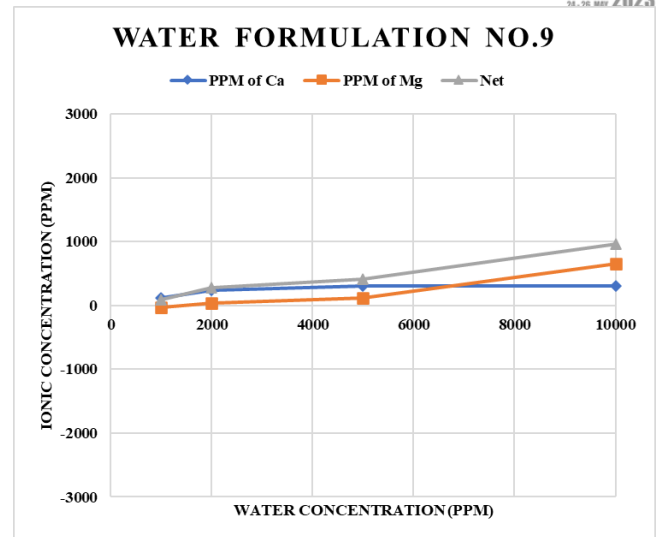


Fig. 10. Ionic concentration from the effluents with different water concentration of water formulation No.9.

Figure 11 illustrates the ionic concentrations from the supernatants of water formulation No.10. Presence of only  $Mg^{2+}$  without other ions in low salinity water provided better result compared to presence of only  $Ca^{2+}$  ion in terms of the ratio of replacement. However, the magnitude of replacement was not as good as in water formulation No.1. This could be explained by the complexity of hydrate form of Magnesium, resulting in smaller reactivity of  $Mg^{2+}$ . However, result was slightly improved at higher concentration (10,000 ppm).

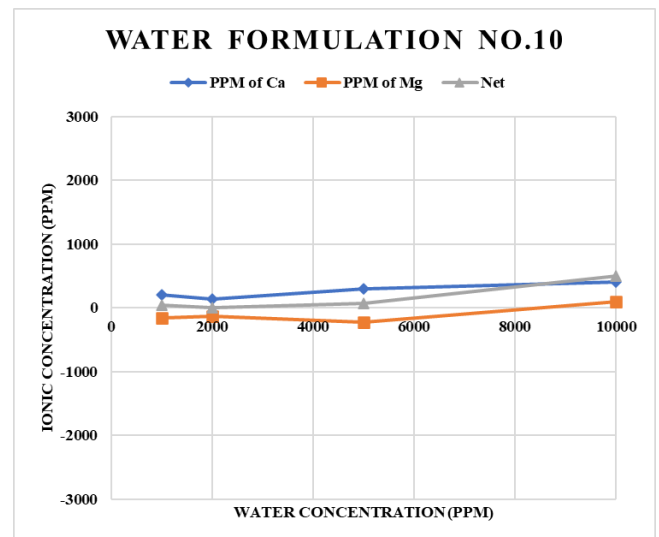


Fig. 11. Ionic concentration from the effluents with different water concentration of water formulation No.10.

From all the tests obtained from different water formulations, the results can be characterized based on ion domination into four different zones as follow:

1. Calcium domination:  $\text{Ca}^{2+}$  was mainly consumed to replace  $\text{Mg}^{2+}$ . Within this zone, presence of  $\text{SO}_4^{2-}$  reduced dissolution of  $\text{Mg}^{2+}$  whereas, the presence of  $\text{Mg}^{2+}$  increased the net divalent ion in the system. This zone included water formulation No.1, 2, and 3.

2. Combined effect:  $\text{Ca}^{2+}$  was consumed to replace  $\text{Mg}^{2+}$  but consumption was smaller than that of Calcium domination zone due to negative effects from  $\text{SO}_4^{2-}$ . However, the magnitude of dissolution was also smaller compared to the Calcium domination zone. This zone included water formulation No.4 and 5.

3. Sulfate domination:  $\text{Mg}^{2+}$  was consumed due to dolomitization effects. This happened at very high total concentration. This effect included water formulation No.7 and 8.

4. Magnesium domination:  $\text{Mg}^{2+}$  was consumed to replace  $\text{Ca}^{2+}$ . Nevertheless, due to hydrate structure of  $\text{Mg}^{2+}$ , the magnitude of dissolution of  $\text{Ca}^{2+}$  was not as high as  $\text{Ca}^{2+}$  replacing  $\text{Mg}^{2+}$ . This zone included water formulation No.6, 9, and 10.

Comparing these 4 different zones of water formulation, the combination effect between  $\text{Ca}^{2+}$  and  $\text{SO}_4^{2-}$  seems to be the best water formulation. Presence of  $\text{SO}_4^{2-}$  reduces positive charges of dolomite, resulting less consumption of  $\text{Ca}^{2+}$  during the dissolution mechanism.

## V. CONCLUSION

This paper presented the result of a capacity in Multi-component Ion Exchange (MIE) of Potential Determining Ions which were Calcium ion, Magnesium ion, and Sulfate ion on dolomite. The following summarizes the key outcomes of this study:

1. Calcium ion is powerful in replacing  $\text{Mg}^{2+}$ . Even though  $\text{Mg}^{2+}$  is smaller in ionic size, its hydrate structure is more complex, resulting reactivity in MIE.

2. Adequate amount of Sulfate ion may facilitate the overall dissolution of divalent ions. However, the magnitude may be reduced as positive charges of dolomite are neutralized by  $\text{SO}_4^{2-}$ .

3. In Sulfate domination,  $\text{Mg}^{2+}$  tends to be consumed by dolomite especially at very high concentration which can be explained by dolomitization process to capture  $\text{Mg}^{2+}$  back into matrix as  $\text{CaMg}(\text{CO}_3)_2$ .

4. From this study, the combination effect between  $\text{Ca}^{2+}$  and  $\text{SO}_4^{2-}$  would yield benefit in low salinity waterflooding in dolomite formation. This would lead to dissolution of  $\text{Mg}^{2+}$  while  $\text{Ca}^{2+}$  is not largely consumed due to neutralization of positive charges of dolomite surface.

## ACKNOWLEDGMENT

The authors would like to thank the Department of Mining and Petroleum Engineering, Chulalongkorn University for the laboratory equipment. Moreover, the authors would also like to thank the Chevron Thailand Exploration and Production Ltd. for providing the scholarship.

## REFERENCES

- [1] Srisuriyachai F.; Meekangwal, S.; Charoentanaworakun, C.; Vathanapanich, Y. "Effects of Potassium Ion on Low Salinity Waterflooding in Sandstone Formation". IOR 2017 - 19th European Symposium on Improved Oil Recovery, April 2017, vol. 2017, p.1-9. DOI: <https://doi.org/10.3997/2214-4609.201700297>.
- [2] Lager, A.; Webb, K.J.; Black, C.; Singleton, M.; Sorbie, K.S. "Low salinity oil recovery-an experimental investigation1". *Petrophysics* 2008, 49.
- [3] Zhang, P.; Austad, T. "Wettability and oil recovery from carbonates: Effects of temperature and potential determining ions". *Colloids Surf. A Physicochem. Eng. Asp.* 2006, 279, 179–187.
- [4] Chandrasekhar, S.; Sharma, H.; Mohanty, K.K. "Wettability alteration with brine composition in high temperature carbonate rocks". In *Proceedings of the Society of Petroleum Engineers Annual Technical Conference and Exhibition, Dubai, UAE, 26–28 September 2016*.
- [5] Zhang, P.; Tweheyo, M.T.; Austad, T. "Wettability alteration and improved oil recovery by spontaneous imbibition of seawater into chalk: Impact of the potential determining ions  $\text{Ca}^{2+}$ ,  $\text{Mg}^{2+}$ , and  $\text{SO}_4^{2-}$ ". *Colloids Surf. A Physicochem. Eng. Asp.* 2007, 301, 199–208.
- [6] Yousef, A.A.; Al-Saleh, S.H.; Al-Kaabi, A.; Al-Jawfi, M.S. "Laboratory investigation of the impact of injection-water salinity and ionic content on oil recovery from carbonate reservoirs". *Soc. Pet. Eng. Reserv. Eval. Eng.* 2011, 14, 578–593.
- [7] Al Harrasi, A.; Al-maamari, R.S.; Masalmeh, S.K. "Laboratory investigation of low salinity waterflooding for carbonate reservoirs". In *Proceedings of the Abu Dhabi International Petroleum Conference and Exhibition, Abu Dhabi, UAE, 11–14 November 2012*.
- [8] Romanuka, J.; Hofman, J.; Ligthelm, D.J.; Suijkerbuijk, B.; Marcellis, F.; Oedai, S.; Brussee, N.; van der Linde, H.; Aksulu, H.; Austad, T. "Low salinity EOR in carbonates". In *Proceedings of the Society of Petroleum Engineers Improved Oil Recovery Symposium, Tulsa, OK, USA, 14–18 April 2012*.
- [9] Mahani, H.; Menezes, R.; Berg, S.; Fadili, A.; Nasralla, R.; Voskov, D.; Joekar-Niasar, V. "Insights into the impact of temperature on the wettability alteration by low salinity in carbonate rocks". *Energy Fuels* 2017, 31, 7839–7853.
- [10] RezaeiDoust, A.; Puntervold, T.; Strand, S.; Austad, T. "Smart water as wettability modifier in carbonate and sandstone: A discussion of similarities/differences in the chemical mechanisms". *Energy Fuels* 2009, 23, 4479–4485.

# SIZE SUITABLE OF SOLAR COMPRESSED AIR STORAGE SYSTEM FOR NILE TILAPIA PRODUCTION UNDER BIOFLOC SYSTEM

Theerapan Sangsuwan<sup>1</sup> and Sarawut Polvongsri<sup>1\*</sup>

<sup>1</sup> School of Renewable Energy, Maejo University, Chiang Mai 50290, Thailand

<sup>1\*</sup> Corresponding author Email: sarawut-energy@hotmail.com

**Abstract:** This research was conducted to select the size of an air compressor suitable for a 3 m<sup>3</sup> air reserve tank system at a pressure of 7 bar to store compressed air for aeration of the Biofloc fishpond. The conditions in the experiment were to produce compressed air during the daytime without using daylight power consumption. The time used is between 9:00 a.m. and 4:00 p.m. to bring compressed air to use at night for 1-2 hrs. instead of normal aeration. The experiment was divided into 3 types: 1 set, 2 set, and 3 set in order to produce 7 bars of compressed air in the reserve tank suitable for the aforementioned time. By finding a suitable number of 1 hp air compressors, the compressed air backup system could be optimized. From the experimental results, air compressors of 1 set, 2 sets, and 3 sets have their initial compressed air production rates of 4.8 m<sup>3</sup>/hr, 9.4 m<sup>3</sup>/hr and 12.8 m<sup>3</sup>/hr respectively, at the final pressure. The compressed air production rates were 3 m<sup>3</sup>/hr, 5.3 m<sup>3</sup>/hr and 7.7 m<sup>3</sup>/hr respectively. The electric power used was 0.82 kW, 1.61 kW and 2.36 kW respectively. The electric energy was 5.35 kWh/day 6.01 kWh/day and 5.98 kWh/day and the air production time per set was 390 minutes, 224 minutes, and 152 minutes, respectively, with SPCs of 16.78 kW/m<sup>3</sup>/min, 17.66 kW/m<sup>3</sup>/min and 18.71 kW/m<sup>3</sup>/min respectively. According to the experimental conditions, a 3 set system was chosen to use as a compressed air backup, together with the on-grid solar power generation system with a total power generation capacity of 3.1 kWp. The payback period is 9.1 years.

**Keywords :** Air Compressor, Aeration, Solar Cell, Biofloc System

## I. INTRODUCTION

The cultivation of tilapia in the Biofloc system is a popular fish culture method nowadays. It has the advantage of saving space and requires very little water change throughout the rearing cycle. The system can raise fish at high density without producing a fishy odor because water brings microorganisms that help adjust the water condition to have a normal nitrogen value. These microbes also control the ammonia levels, which is toxic to aquatic animals, to a minimum. As a result, aquatic animals raised with this system have a higher survival rate than in normal culture. This system is called microbial sludge or Biofloc. Aeration is required all the time in the Biofloc system for fish farming to increase the dissolved oxygen in the water [1] and prevent sediment accumulation, which can become waste in the system [2] This constant aeration requires the aerator to be turned on 24 hours a day, resulting in relatively higher energy costs than conventional fish farming. To reduce these costs, it has become popular to adopt an on-grid solar power generation system for fish farming. However, this system can only reduce electricity

bills during the day, and if the main power system fails, the on-grid solar power systems will also be shut down. If there is a problem with the aeration power system, it may cause a decrease in the dissolved oxygen in the water. If the DO drops below 3 mg/L, it can cause the fish to suddenly lack oxygen, leading to damage and reduced productivity. Therefore, to reduce the risks that may affect productivity, the energy reserve system for fish farming in a Biofloc system needs to take many forms to ensure stability and minimize problems that may occur to the farmed crop.

Compressed air energy storage is an energy storage system that is of great interest in fish farming in biofloc systems, as it can be caused by the introduction of residual electrical energy.[3]To use this system, the electrical energy is converted into compressed air using an air compressor[4], which is then stored in a compressed air reserve tank. The stored compressed air can then be gradually used for further aeration purposes. However, there is no concrete study on the use of compressed air energy storage in fish farming. Although the investment of the compressed air storage system is quite high compared to other forms of energy storage, the advantage is that compressed air energy storage systems have a lifespan of 30 years[5], which is considerably longer than the lifespan of batteries[6]. According to the data from [7]the Provincial

Electricity Authority of Thailand, the Power System Reliability Index (SAIFI & SAIDI) in 2021 in rural areas had a SAIFI value of 2.19 times/person/year and a SAIDI value of 44.51 minutes/person/year. This information is used to design the air reserve system to be able to back up the air for 1-2 hours, which is enough to aerate a fishpond of less than 20 m<sup>3</sup> during an emergency. Compressed air energy storage systems are also of great interest to be applied in Biofloc tilapia farming.

Therefore, the researcher studied compressed air energy storage in conjunction with solar aeration for tilapia culture in the Biofloc system. The objectives of this research were to select the appropriate size of the compressed air energy storage system and on-grid solar power generation system suitable for the Biofloc tilapia farming application.

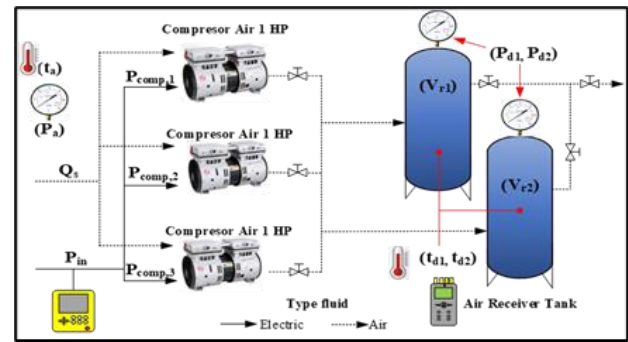
## II. METHODOLOGY

### A. Experimental design

An experimental system was tested in the area of the School of Renewable Energy at Maejo University in Chiang Mai to determine the size of the air reserve system that could be used for emergency aeration of Biofloc fishponds. The tested system consisted of two 1.5 m<sup>3</sup> air reserve tanks connected in parallel and capable of withstanding 8 bar air pressure. Compressed air was pumped into the tanks using an oil-free piston-type air compressor with a capacity of 1 hp single phase. The compressor had a compressed air production rate of 135 L/min and a maximum pressure of 8 bar when all three air compressors were used. The aim of this test was to determine the suitable number of air compressors to be used with the system.

The solar aerator will utilize solar energy to generate electricity during the day. The aerator will be designed to turn on and off according to a schedule of 30 minutes on and 20 minutes off. During each 20 minute off period, any excess electrical energy generated by the solar power system will be stored in the air reserve system. Between 9:00 a.m. and 4:00 p.m., there will be a total of 160 minutes available for the air compressor to produce enough air to be stored in the air reserve tank. This stored air can be used to aerate the fishpond for 1-2 hours during a power outage. The system will have three conditions, with a 1 hp size, 1 set, 2 sets and 3 sets. The air storage tanks will consist of two 1.5 m<sup>3</sup> tanks, totaling 3 m<sup>3</sup>, as shown in Figure 1. If air is stored at a pressure of 7 bar, it can provide approximately 21 m<sup>3</sup> of air, which can aerate a 20 m<sup>3</sup> fishpond for about 2 hours at a flow rate of 10 m<sup>3</sup>/h which is sufficient. The aim of this experiment is to determine the size of the air compressor required to produce 7 bar of spare air in the tank within the specified time of 160 minutes. The JIS B 8341:1983 standard [8] will be used in the experiment, following Equation 1 to calculate the compressed air production rate for each case and using Equation 2 to determine the specific energy consumption of each system. A meter will be installed and variables as shown in Figure 1 will be used for these calculations. In this research, two parts will be analyzed. Part 1 will focus on determining the

duration of use for each type of air compressor. Part 2 will evaluate the economics.



**Fig. 1.** Diagram of The Equipment in The System and The Measurement Instrument.

In the field of economics, Mono Crystalline solar panels with a maximum power of 445 Wp are used to generate electricity for an air compressor. The energy cost is charged based on the standard electricity rate of 4.3 baht/kWh.

### B. Measurement

A Type K thermocouple was connected to a 4-channel data logger (Lutron TM-1947SD model) to measure temperature (Accuracy  $\pm(0.4\%+1^\circ\text{C})$ ). Data were collected every 5 minutes for three variables:  $T_{d1}$ ,  $T_{d2}$ , and  $T_a$ , which represent measurements from the air compressor. To measure power and electrical energy, Electric Power (W) and Energy (kWh) were recorded every minute using Power analyzer (Metrel MI 2885 model Accuracy  $\pm 0.5\%$  Power(W)) A stopwatch was used to measure gauge pressure between 0 and 7 bar and the experiment was stopped after completion.

The apparatus used to determine the performance of the experimental compressed air system followed the JIS B 8341:1983 standard, with an ambient temperature of 20°C, relative humidity of 65%, and air density of 1.2 kg/m<sup>3</sup> at a pressure of 101.3 kPa (a). The equation used is as follows:

$$Q_s = \frac{V_r}{t_e} \times \frac{T_a}{P_a} \times \left( \frac{P_{d2}}{T_{d2}} - \frac{P_{d1}}{T_{d1}} \right) \quad (1)$$

The following variables were used in the equation:  $Q_s$ , which represents the average air volume converted to a value under standard suction conditions (m<sup>3</sup>/min);  $V_r$ , the volume of the reserve tank (m<sup>3</sup>);  $t_e$ , the operating time (min);  $T_a$ , the ambient air temperature (K);  $P_a$ , the atmospheric pressure (kPa);  $P_{d2}$ , the final pressure in the tank (kPa);  $P_{d1}$ , the initial pressure in the tank (kPa);  $T_{d2}$ , the temperature of the air at final pressure (K); and  $T_{d1}$ , the temperature of the air at initial pressure (K).

$$SPC_s = \frac{P_{in}}{Q_s} \quad (2)$$

Where  $SPC_s$  is the specific energy consumption of the air compressor under standard suction conditions. ( $kW/m^3/min$ ) and  $P_{in}$  is the power used by the air compressor ( $kW$ ).

The payback time can be calculated according to the following[9] equation:

$$PB = \frac{C_{inv}}{C_{Saving}} \quad (3)$$

The data for economic calculations are shown in Table 1.

TABLE I  
DATA OF COMPRESSED AIR SYSTEM AND SOLAR PV SYSTEM

List	Data
<b>CAES</b>	
<b>AIR COMPRESSOR</b>	
1. Power [HP]	1
2. Pressure Max (P) [bar]	8
3. Free Air Delivery (FAD) [L/min]	135
4. Cost [Baht]	3,500
<b>AIR STORAGE TANK</b>	
1. Volume ( $V_r$ ) [ $m^3$ ]	1.5
2. Pressure max ( $P_{vr}$ ) [bar]	10
3. service life [Year]	30
4. Cost [Baht]	49,000
<b>PV SYSTEMS</b>	
<b>PV MONO HALF BIFACIAL</b>	
1. Power max ( $P_{max}$ ) [ $W_p$ ]	445
2. Service Life [Year]	25
2. Cost [Baht]	6,900
<b>ON-GRID 3.3 KW</b>	
1. Power Electric Peek (P) [ $kW_p$ ]	3.1
2. Cost [Baht]	99,680

### III. RESULTS AND DISCUSSION

From the test results shown in Fig. 2, it was found that when using an air compressor with a 1 hp size, 1 set, 2 sets and 3 sets to compress air into an air compressor tank with a size of  $3 m^3$  and a pressure of 7 bar, it was found that increasing the pressure in the compressor tank would reduce the air compression rate. In the case of using 3 sets of air compressors, it can compress air into the tank at the maximum compression rate. When starting work, the compression rate is about  $12.8 m^3/h$  and gradually decreases until the pressure reaches 7 bar with a compression rate of  $7.7 m^3/h$ . In the case of using 2 sets of air compressors, when starting work, the compression rate is between  $9.4 m^3/h$  to  $5.3 m^3/h$ , while in the case of using 1

set of air compressor, it has the lowest compression rate with a starting compression rate of  $4.8 m^3/h$  and decreasing to  $3 m^3/h$  when the pressure reaches 7 bar.

From the results of the experiment in Figure 2, it can be seen that the compressors of all three sizes are able to compress air and store it in the tank up to 7 bars. However, the amount of compressed air produced depends on the number of compressors used. Additionally, when the compressed air reaches a higher pressure, the production rate of the compressor decreases because the compressor loses energy to the heat generated when compressing air at high pressures.

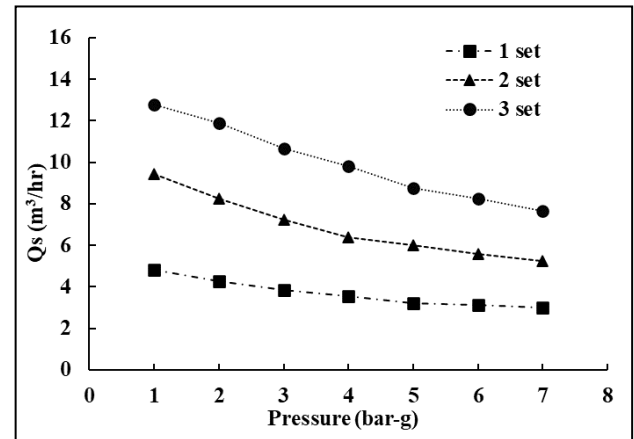
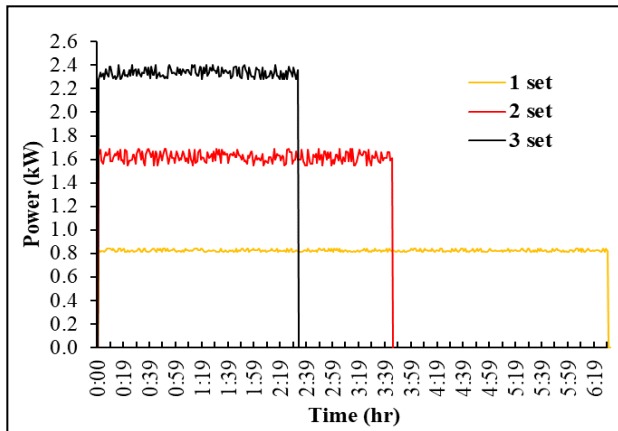


Fig. 2. The Average Air Volume of An Air Compressor of 1 Set, 2 Sets And 3 Sets

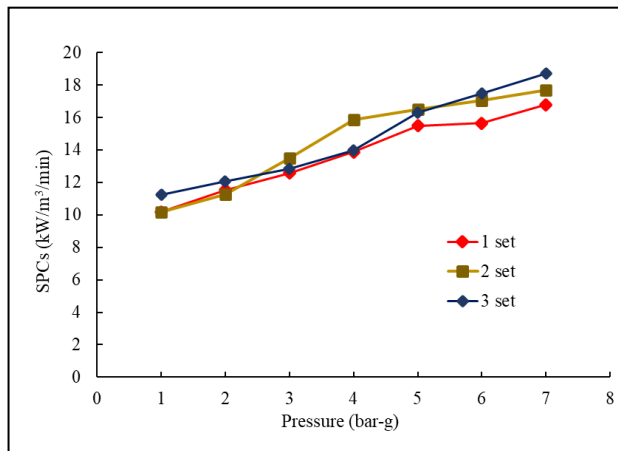
In each case of air compression, the amount of electrical power used by the air compressor varies depending on the number of air compressors used. A 1 hp air compressor measures an average electrical power of 0.82 kW and consumes a total of 5.35 kWh/day of electrical energy. On the other hand, 2 sets of air compressors measure an electrical power of 1.61 kW and consume a total of 6.01 kWh/day of electrical energy, while 3 sets of air compressors measure an electrical power of 2.36 kW and consume a total of 5.98 kWh/day of electrical energy, as shown in Figure 3. When considering the specific energy consumption ( $SPC_s$ ) of the air compressors under standard conditions, as shown in Figure 4, it is found that the  $SPC_s$  increases when the pressure in the air compression tank increases. This is because an increase in pressure reduces the rate of air compression while the electrical power consumption remains the same. The  $SPC_s$  of one set of air compressors is  $16.78 kW/m^3/min$ , while the  $SPC_s$  for 2 sets and 3 sets of air compressors are  $17.66 kW/m^3/min$  and  $18.71 kW/m^3/min$ , respectively.

The results of the experiment from Figure 3 show that the electrical power used increases according to the number of air compressors. The 3 set air compressor has the shortest working time. Among the 3 sizes, the 1 set compressor uses the least amount of energy at 5.35 kWh/day because it has a lower air flow rate and generates less heat compared to the other 2 sets, resulting in less energy loss of approximately 0.6 kWh/day Although the 1-set compressor uses the least amount

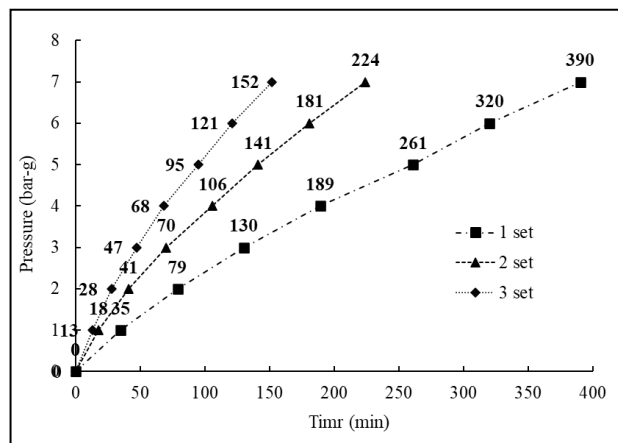
of energy, it is not suitable for use under the experimental conditions that require a 160 minute operation time.



**Fig. 3.** Electric power of air compressor 1 set, 2 sets and 3 sets



**Fig. 4.** Specific Power Consumption on Standard Suction Condition (SPCs)



**Fig. 5.** The Time Required to Compress Air for Three 1-Set, 2-Set, and 3-Set Air Compressors

TABLE II  
DATA OF PERFORMANCE OF THE EXPERIMENTAL COMPRESSED AIR SYSTEM FOLLOWED THE JIS B 8341:1983 STANDARD,

Results CAES Systems	1 HP	2 HP	3 HP
Absolute pressure $P_a$ (kPa)	1.00	1.00	1.00
Absolute temperature air $T_a$ (K)	293.15	293.15	293.15
Volume of air receiver tank $V_r$ (m <sup>3</sup> )	3.0	3.0	3.0
Time required for charging $t_c$ (min)	390	224	152
Initial absolute pressure $P_{d1}$ (kPa)	1.01	1.01	1.01
Final absolute pressure $P_{d2}$ (kPa)	8.01	8.01	8.01
Initial absolute temperature $T_{d1}$ (K)	305.13	303.05	308.05
Final absolute temperature $T_{d2}$ (K)	313.75	311.85	315.95
Power $P_m$ (kW)	0.82	1.61	2.36
Average air quantity $Q_s$ (m <sup>3</sup> /min)	0.05	0.09	0.13
Specific power consumption $SPC_s$ (kW/m <sup>3</sup> /min)	16.4	18.3	18.5

When considering the time taken to compress air from Figure 5, it was found that in the case of 3 air compressors, it takes the shortest time of 152 minutes to compress the air to 7 bar. The next fastest are the 2 and 1 air compressors, which take 224 and 390 minutes, respectively. Referring to the time interval during which the solar aerator stops working due to the air filling conditions, which has a total time of 160 minutes, it can be concluded that for the case of 1 set and 2 sets, the time required for air compression is more than 160 minutes, making them unable to operate under the given conditions. Only 3 sets of air compressors are able to operate within 160 minutes.

Based on the information provided, the research team has designed a solar power generation system using 7 monocrystalline solar panels with a capacity of 445 watts per panel, totaling 3.115 kWp. This is sufficient to power an air conditioning system with a 2 hp blower and reduce electricity costs in various areas.

The total investment budget is shown in Table 1, consisting of the cost of installing the compressed air storage system at 111,500 baht and the cost of installing a 3.1 kW solar power generation system at 99,680 baht, ( $C_{inv}$ ) totaling 211,180 baht.

The energy savings calculated from both systems include an average daily electricity generation of 14.77 kWh/day from the solar power generation system and a reduction of 2 hours/day in electricity usage from the fishpond aerator, which has an electric capacity of 1.7 kW, resulting in a total daily energy savings of 18.17 kWh/day. The fishpond aerator operates for 365 days per year, resulting in an annual energy savings of approximately 6,632.05 kWh/year. At an electricity rate of 4.3 baht/kWh, this results in a total annual cost savings ( $C_{saving}$ ) of 28,517.8 baht/year.

The payback period (PB) is estimated to be approximately 9.1 years.



#### IV. CONCLUSION

This research was conducted to select the size of an air compressor suitable for a 3 m<sup>3</sup> air reserve tank system at a pressure of 7 bar to store compressed air for aeration of the Biofloc fishpond. The conditions in the experiment were to produce compressed air during the daytime without using daylight power consumption. The time used is between 9:00 a.m. and 4:00 p.m. to bring compressed air to use at night for 1-2 hrs. instead of normal aeration. This is achieved by adjusting the air filling pattern that needs to be aerated all the time. It is aeration working for 30 minutes, alternating, stopping for 20 minutes, taking the time of the aerator that stops during that time to 160 minutes, taking the electric energy from the solar power generation system to supply to the compressed air storage system. The experiment was divided into 3 types: 1 set, 2 set, and 3 set in order to produce 7 bars of compressed air in the reserve tank suitable for the aforementioned time. By finding a suitable number of 1 hp air compressors, the compressed air backup system could be optimized.

From the experimental results, air compressors of 1 set, 2 sets, and 3 sets have their initial compressed air production rates of 4.8 m<sup>3</sup>/hr, 9.4 m<sup>3</sup>/hr and 12.8 m<sup>3</sup>/hr respectively, at the final pressure. The compressed air production rates were 3 m<sup>3</sup>/hr, 5.3 m<sup>3</sup>/hr and 7.7 m<sup>3</sup>/hr respectively. The electric power used was 0.82 kW, 1.61 kW and 2.36 kW respectively. The electric energy was 5.35 kWh/day 6.01 kWh/day and 5.98 kWh/day and the air production time per set was 390 minutes, 224 minutes, and 152 minutes, respectively, with SPC<sub>s</sub> of 16.78 kW/m<sup>3</sup>/min, 17.66 kW/m<sup>3</sup>/min and 18.71 kW/m<sup>3</sup>/min respectively.

According to the experimental conditions, a 3 set system was chosen to use as a compressed air backup, together with the on-grid solar power generation system with a total power generation capacity of 3.1 kWp. The payback period is 9.1 years. While the payback period is relatively long compared to other energy backup systems, the advantage of this system is that the energy storage equipment has a longer lifespan than battery-based energy storage systems, which require maintenance and battery replacements every 3-5 years. In this proposed system, the air storage tank has a minimum lifespan of 20 years.

#### ACKNOWLEDGMENT

The authors would like to thank School of Renewable Energy, Maejo University for supporting the study by a grant fund under the Generate and development of Graduate Student in Renewable Energy Research fund, in the ASEAN Countries in the graduate. The author thanks Supporting for graduate research in agriculture and agro-industry from Agricultural Research Development Agency (Public Organization) fiscal year 2022.

#### ABBREVIATIONS AND SYMBOLS

##### Symbol

C	Cost (Baht)
E	Electrical energy (kWh)
FAD	Compressed Air Delivery (L/min)
P	Power (kW)
P	Pressure (kPa)
PB	Payback Period (year)
Q	Compressed Air Production rate (m <sup>3</sup> /min)
SPC <sub>s</sub>	Specific Energy Consumption (kW/m <sup>3</sup> /min)
T	Temperature (K)
t	Time (min)
V	Volume (m <sup>3</sup> )
W	Motor Power (HP)

##### Subscript

a	Ambient
CAES	Compressed Air Energy Storage
d1	Initial absolute
d2	Final absolute
E	Electric
p	Power Peak
inv	Investment
r	Air Receiver Tank
Saving	Cost saving

#### REFERENCES

- [1] C. E. Boyd, "Pond water aeration systems," *Aquacultural Engineering*, vol. 18, no. 1, pp. 9-40, 1998/07/01, 1998.
- [2] B. Suárez-Puerto, M. Delgadillo-Díaz, M. J. Sánchez-Solís, and M. Gullian-Klanian, "Analysis of the cost-effectiveness and growth of Nile tilapia (*Oreochromis niloticus*) in biofloc and green water technologies during two seasons," *Aquaculture*, vol. 538, pp. 736534, 2021/05/30, 2021.
- [3] A. Berrada, K. Loudiyi, and I. Zorkani, "Toward an Improvement of Gravity Energy Storage Using Compressed Air," *Energy Procedia*, vol. 134, pp. 855-864, 2017/10/01, 2017.
- [4] S. B. Mousavi, P. Ahmadi, A. Pourahmadiyan, and P. Hanafizadeh, "A comprehensive techno-economic assessment of a novel compressed air energy storage (CAES) integrated with geothermal and solar energy," *Sustainable Energy Technologies and Assessments*, vol. 47, pp. 101418, 2021/10/01, 2021.
- [5] T. Bowen, I. Chemyakhovskiy, K. Xu, S. Gadzanku, and K. Coney, *USAID Grid-Scale Energy Storage Technologies Primer*, National Renewable Energy Lab.(NREL), Golden, CO (United States), 2021.
- [6] P. Breeze, *Power system energy storage technologies*: Academic Press, 2018.
- [7] PEA, *Annual Report 2021 Provincial Electricity Authority*, 2021.
- [8] EnergyAuditorThai. "Compressed Air System," 25 May 2021, 2021; <http://energyauditorthai.com/wp-content/uploads>.
- [9] A. Ahmadi, M. A. Ehyaei, D. H. Jamali, M. Despotovic, F. Esmaeilion, A. Abdaliosan, and E. B. Hani, "Energy, exergy, and economic analyses of integration of heliostat solar receiver to gas and air bottom cycles," *Journal of Cleaner Production*, vol. 280, pp. 124322, 2021/01/20, 2021.

# Data-Driven Approach to Bogie Overhaul Planning

Panin Srisombat<sup>1</sup>, Alexander Brezing<sup>2\*</sup>, Nuksit Noomwongs<sup>3\*</sup>, Sompoap Talabgaew<sup>4\*</sup>

<sup>1</sup>Railway Vehicle and Infrastructure Engineering, The Sirindhorn International Thai-German Graduate School of Engineering, Bangkok, Thailand, s6309096860019@email.kmutnb.ac.th

<sup>2\*</sup> Department of Mechanical and Automotive Engineering (MAE), The Sirindhorn International Thai-German Graduate School of Engineering, Bangkok, Thailand, alex.b@tggs.kmutnb.ac.th

<sup>3\*</sup> Department of Mechanical Engineering, Chulalongkorn University, Bangkok, Thailand, Nuksit.N@chula.ac.th

<sup>4\*</sup> Department of Teacher Training in Mechanical Engineering, Faculty of Technical Education, King Mongkut's University of Technology North Bangkok, Bangkok, Thailand, sompoap.t@fte.kmutnb.ac.th

**Abstract:** Rolling stock have to be maintained to ensure and sustain its reliability, availability, and safety. Bogie, one of the most important and critical system, has major maintenance called overhaul which comprises of extensive work and takes long maintenance interval, possibly affect the operation if the maintenance is not properly planned. Reliability-Centered Maintenance was selected and used as approach for optimization of bogie overhaul planning in this paper. First of all, the considered components were analyzed for their failure modes, effects, and causes. Then, Fuzzy FMEA was applied to prioritize the risk and actions. Finally, the integration of reliability analysis, RCM decision logic, and the estimation of maintenance interval cycle was performed to identify an outline of the optimum maintenance strategy.

**Index Terms**—Bogie overhaul, Fuzzy FMEA, Reliability Centered Maintenance (RCM), Rolling stock maintenance.

## I. INTRODUCTION

Railway transportation and the business of offering this public transportation service is characterized by very long lifecycles of the railway system, the intense utilization with operating hours of 18 or more hours every day and the required availability of the system of close to 100%. Rolling stock consists of many complex components. One of the most important is bogie since it plays a critical role in ensuring the safe, as a guidance system on the track, and reliable operation [1]. Additionally, the bogie always deals with many factors during its operation, i.e. loads, vibration, forces and etc. [2]. Therefore, maintenance is a key to ensure its availability, reliability, and safety. As a significant increase in railway business, many line and routes have been expanded and brought many new fleets into the operation. As a result, the maintainers have been facing the more complex and challenge of planning for the maintenance event, especially overhaul. Due to the extensive work and very long maintenance interval, the maintainers must meticulously schedule and plan in order to avoid the excessive maintenance cost and the breach of the requirements or

constraints from the customer, which could lead to the penalty that the maintainers will be fined for [3]. For defining the maintenance plans, Reliability Centered Maintenance (RCM) has been introduced and commonly applied as an approach for the maintenance optimization [4].

## II. DATA AND METHODS

### A. Data acquisition

This study is focusing on the bogie overhaul activities which have been planned for the metro system in Bangkok. To break down the bogie into component level, Bill of Material (BOM) of each subsystem is used as a material to identify the vital components to be considered. Subsequently, the list of the components from BOM should be filter and aligned with maintenance history, previous schedule activities, and faults record to clarify the criticality of those components. Furthermore, mentioned sources of data also provide the failure mode which can be found the effects, causes and maintenance tasks from the running maintenance manuals. **TABLE I** demonstrates the relative components of the bogie which have to be overhauled with the information for further analysis.

**TABLE I**  
FAILURE MODE, EFFECTS AND CAUSES OF EACH BOGIE COMPONENT

No.	Components	Failure mode	Failure effect	Failure Causes	Current Control	Maintenance actions
F1	Air spring	Pressure loss	Impaired suspension and cushion	Damaged or torn	Visual inspection	Renew/Replace
F2	Additional Spring	Crack	Poor riding quality	Wear and environmental influences	None	Renew/Replace
F3	Torsion bar /Guide bar	Broken or Crack	Damage surrounding components	Fatigue or Corrosion	Inspection	Renew/Replace
F4	Brake cylinder	Reduced or zero braking forces	Brake gets stuck or overheating	Physical damaged and leaking	None	Renew/Replace
F5	Brake caliper	Damage	Brake gets stuck or Low or zero braking force	Environmental impacts	None	Renew/Replace
F6	Current Collector	Broken	Jerking and vibration	Wrong positioning Obstacle on the track	None	Renew/Replace

F7	TBU	Damaged	Locked axle	Low or contaminated grease and mechanical damaged	Inspection	Renew/Replace
F8	Lateral Stop buffer	Crack or damaged	Low riding quality	Environmental influences and wear	Inspection	Renew/Replace
F9	Horizontal Damper	Leaking	Low riding quality	Damaged seals, aging	Visual inspection during maintenance	Renew/Replace
F10	Ball joint	Seized	Leveling valve stuck	Seized ball joint	Inspection	Renew/Replace
F11	Leveling Valve	Leaking	Leveling system malfunction	Aging and external influences	None	Renew/Replace
F12	Center Pin	Crack or broken	Disconnection between bogie and carbody	Excessive shock	Inspection	Renew/Replace
F13	Motor/Gear coupling	Crack or damaged	Vibration, noise, and overheat	Wear and external influences	Inspection	Renew/Replace
F14	Vertical Damper	Leaking	Low riding quality	Damaged seals, aging	Visual inspection during maintenance	Renew/Replace

### B. Failure Mode and Effects Analysis (FMEA)

FMEA is an analysis and evaluation method of an item or system in order to identify its potential failure mode, likelihood of occurrence, consequences and causes in the systematic way [5] [6]. The aim of FMEA is to prioritize, identify and implement the corrective action to mitigate the failure consequence [7]. The result from FMEA involves three main factors: Severity (S), Occurrence (O), and Detection (D) which are used to evaluate the priority of mitigation actions in the form of Risk Priority Number (RPN). Failure mode with a high RPN means the high priority for analysis and correction action [8]. The RPN can be calculated by using (1) and rated S, O, and D from the expert knowledge and experiences or analysis of the available data following the criteria as shown in the **TABLE II**.

$$RPN = S \times O \times D \quad (1)$$

### C. Fuzzy FMEA

The traditional FMEA has been criticized as its shortcoming of 1.) the relative importance of the main factors (S, O, and D) seems to be equal, 2.) various combination of main factors may cause the same RPN, making more difficult to interpret and determine the risk level of the failure [9]. Fuzzy logic or fuzzy set theory has been introduced in order to deal with the vagueness as the traditional FMEA was facing. The three main risk factors (S, O, and D) are fuzzified by the Membership function (MF) and evaluated through the Fuzzy Inference System (FIS) with the basis IF-THEN rules. The example of IF-THEN rules and the Fuzzy FMEA model are illustrated in **Fig. 1** and **Fig. 2**, respectively. In this study, the Fuzzy FMEA was carried out by using MATLAB software program. The model consists of 3 inputs and 1 output. Each input is fuzzified by gaussian membership functions due to its important characteristic of smooth, continuously model, making it simpler for analysis [10]. Subsequently, the fuzzified inputs will be evaluated with 125 designed IF-THEN rules [11]. Finally, the defuzzification will be conducted according to the output membership function and centroid method, results in F-RPN as shown in **TABLE III**.

**TABLE II**  
CRITERIA OF RISK INDEXED PARAMETER FOR RPN ESTIMATION [12] [13]

Severity Level (Effect)	Occurrence	Detection	Scale
Potential failure mode affects the operation and/or involves noncompliance with government regulation without warning. (Hazardous)	Very high: Failure is almost unavoidable. (> 1 in 2)	Control actions are not available for detection. (Not possible)	10
Potential failure mode affects the operation and/or involves noncompliance with government regulation with warning. (Very high)	Very high: Failure is almost unavoidable. (1 in 3)	Very remote likelihood that the current controls will detect the failure. (Very remote)	9
Inoperable with loss of primary function. (High)	High: Repeated failure (1 in 8)	Remote likelihood that the current controls will detect the failure. (Low)	8
Operable with loss of performance. Customer is dissatisfied. (Moderate High)	High: Repeated failure (1 in 20)	Low remote likelihood that the current controls will detect the failure. (Low)	7
Operable but loss to comfort/convenience. Customer experiences discomfort. (Moderate low)	Moderate: Occasional failure (1 in 80)	Low remote likelihood that the current controls will detect the failure. (Low)	6
Operable but loss to comfort/convenience. Customer has some discomfort. (Low)	Moderate: Occasional failure (1 in 400)	Moderate remote likelihood that the current controls will detect the failure. (Moderate)	5
Certain item characteristics do not conform to specification but noticed by most customers. (Very low)	Moderate: Occasional failure (1 in 2000)	Moderately high remote likelihood that the current controls will detect the failure. (Moderate high)	4
Certain item characteristics do not conform to specification but noticed by average customers. (Very Remote)	Low: Few failures (1 in 15000)	High remote likelihood that the current controls will detect the failure. (High)	3
Certain item characteristics do not conform to specification but noticed by some discriminating customers. (Remote)	Remote: Relatively few failures (1 in 150,000)	Very high remote likelihood that the current controls will detect the failure. (Very high)	2
No effect (None)	Remote: Failure is unlikely (1 in 1,500,000)	Current controls certainly detect the failure (Almost certain)	1

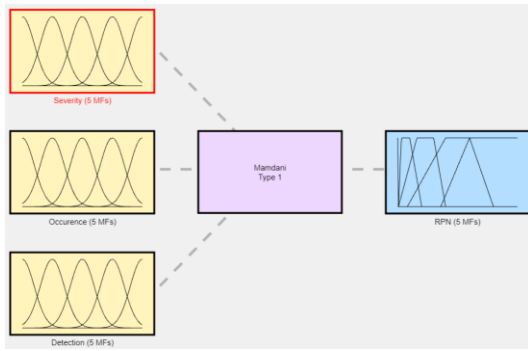


Fig. 1 FUZZY FMEA MODEL IN MATLAB SOFTWARE PROGRAM

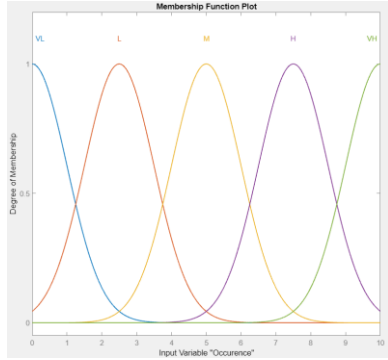


Fig. 2 MEMBERSHIP FUNCTION OF OCCURENCE

TABLE III  
COMPARISON OF TRADITIONAL FMEA AND FUZZY FMEA

No.	Severity	Occurrence	Detection	RPN	Rank	F-RPN	F-Rank
F1	6	6	3	108	4	293.04	3
F2	4	4	6	96	5	216.71	9
F3	6	4	3	72	8	259.62	6
F4	8	6	6	288	1	478.11	1
F5	8	6	6	288	1	478.11	1
F6	8	5	4	160	2	375.30	2
F7	6	5	3	90	6	260.90	5
F8	4	4	3	48	11	199.78	11
F9	5	4	2	40	12	185.77	12
F10	5	4	3	60	9	199.85	10
F11	5	4	6	120	3	286.81	4
F12	5	4	3	60	9	199.85	10
F13	5	5	3	75	7	217.39	8
F14	7	4	2	56	10	259.60	7

D. Reliability Analysis

Reliability means “the probability that an item can perform a required function under given conditions for a given time interval” [14]. Reliability demonstration in this study is assumed to follows the exponential distribution which can be expressed as shown in (2).

$$R(t) = e^{-\lambda t} \quad (2)$$

Where R(t) is the probability of the component at time t,  $0 < R \leq 1$ , and  $\lambda$  denotes the constant failure rate and can be described as a reciprocal of Mean Time to Failure (MTTF) [4].

$$\lambda = \frac{1}{MTTF} \quad (3)$$

MTTF represents the mean time that the non-repairable component or system work properly until it fails [15], can be described in the diagram and calculated the average as Fig. 3 and ), respectively.

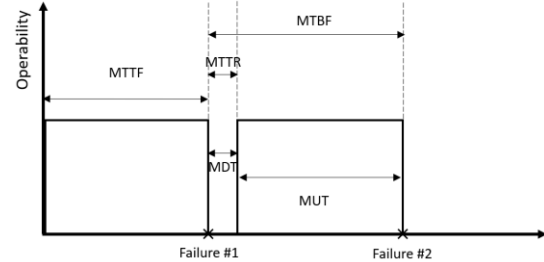


Fig. 3 MTTF, MTTR, MTBF, MUT, AND MDT ON TIME SCALE [16]

$$MTTF = \frac{\sum_{i=1}^n t_{o,i}}{n} \quad (4)$$

Where  $t_{o,i}$  is the total operational time interval until failure  $i$  occurs, and  $n$  denotes the total number of failures. MTTR is Mean Time to Repair, time interval that the system or component is under the maintenance. MUT is Mean Up time, time interval that the system or component is still in the continuous operation without any failure. MDT is Mean Down Time, time interval that the system or component is in down state which cannot perform its function [16]. The results of MTTF and Failure rate ( $\lambda$ ) from the calculation based on the data of operation, maintenance, and fault interval record obtained from the data acquisition phase are shown in the TABLE IV.

TABLE IV  
THE RESULTS OF RELIABILITY ANALYSIS

No.	Components	MTTF (h)	Failure rate (1/MTTF)
F1	Air spring	11,990.12	0.0000834
F2	Additional Spring	26,292.00	0.0000380
F3	Torsion bar /Guide bar	26,441.53	0.0000379
F4	Brake cylinder	22,214.05	0.0000450
F5	Brake caliper	40,096.89	0.0000249
F6	Current Collector	31,642.00	0.0000316
F7	TBU	36,036.00	0.0000278
F8	Lateral Stop buffer	42,660.00	0.0000234
F9	Horizontal Damper	33,950.66	0.0000295
F10	Ball joint	46,486.67	0.0000215
F11	Leveling Valve	26,257.65	0.0000381
F12	Center Pin	92,532.00	0.0000108
F13	Motor/Gear coupling	39,560.73	0.0000253
F14	Vertical Damper	15193.71	0.0000658

E. Maintenance decision and strategy

This study is interested in Reliability Centered Maintenance (RCM). Reliability Centered Maintenance (RCM) is a process or method based on functional failure mode and effect analysis (FMEA) to identify and opt for the strategy of failure management to achieve and sustain the required

availability, safety, and economy of the operation [17]. The aims of RCM are to reduce the need for the unnecessary maintenance activities and cost by focusing on the most important functions and improving the reliability. The seven basic questions have been stated prior the process of RCM as follows [18].

1. What are the functions and associated performance standards of the equipment in its present operating context?
2. In what ways can it fail to fulfill its functions?
3. What is the cause of each functional failure?
4. What happens when each failure occurs?
5. In what way does each failure matter?
6. What can be done to prevent each failure?
7. What should be done if a suitable preventive task cannot be found?

The core part of the RCM process is about the decision logic, the answers of the seven questions can be used and integrated with the decision logic tree, as shown in Fig. 4, to analysis of the maintenance approach for system or components [19]. Subsequently, the maintenance interval cycle has to be taken into account and also necessary to gain more precise and reasonable [20], From the reliability theory.

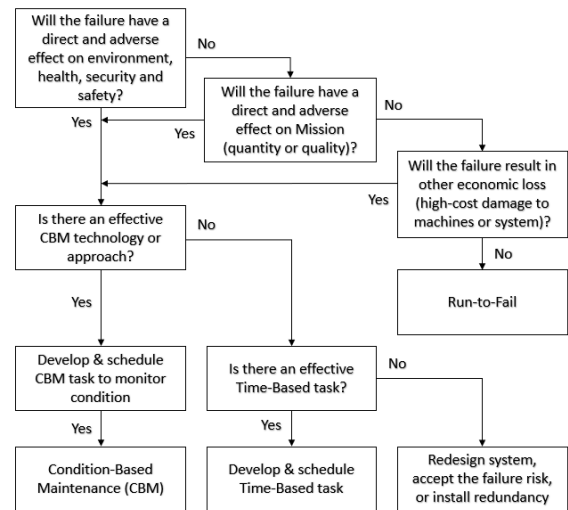


Fig. 4 RELIABILITY CENTERED MAINTENANCE (RCM) DECISION LOGIC TREE

Here,  $R(t)$  is a reliability of the component at time  $t$  and  $\lambda$  denotes the component failure rate. Therefore, reliable time or reliable life becomes as follow.  $T$  is reliable life or maintenance interval cycle for the required (targeted) reliability  $R(T)$  [21] [22].

Finally, substitute required (targeted) reliability  $R(T)$ , in this case 0.9 is chosen for  $R(T)$  as a targeted reliability, and failure rate  $\lambda$  of the components into (6) for the estimation of maintenance interval cycle  $T$ .

$$R(t) = e^{-\lambda t} = e^{-\frac{t}{MTTF}} \quad (5)$$

$$T = -\frac{\ln R(T)}{\lambda} \quad (6)$$

TABLE V  
RELIABILITY CENTERED MAINTENANCE OUTLINE FOR BOGIE COMPONENT

Components	Failure mode	Failure effect	Failure Causes	F-Rank	Maintenance strategy from RCM	MTTF (h)	Maintenance Interval (h)	Maintenance Interval (days)
Air spring	Pressure loss	Impaired suspension and cushion	Damaged or torn	3	Condition Based Maintenance	11,990.12	1,263.28	52.64
Additional Spring	Crack	Poor riding quality	Wear and environmental influences	9	Preventive maintenance	26,292.00	2,770.14	115.42
Torsion bar /Guide bar	Broken or Crack	Damage surrounding components	Fatigue or Corrosion	6	Preventive maintenance	26,441.53	2,782.73	115.95
Brake cylinder	Reduced or zero braking forces	Brake gets stuck or overheating	Physical damaged and leaking	1	Condition Based Maintenance	22,214.05	2,340.48	97.52
Brake caliper	Damage	Brake gets stuck or Low or zero braking force	Environmental impacts	1	Condition Based Maintenance	40,096.89	4,224.63	176.03
Current Collector	Broken	Jerking and vibration	Wrong positioning Obstacle on the track	2	Preventive maintenance	31,642.00	3,333.82	138.91
TBU	Damaged	Locked axle	Low or contaminated grease and mechanical damaged	5	Condition Based Maintenance	36,036.00	3,796.77	158.20
Lateral Stop buffer	Crack or damaged	Low riding quality	Environmental influences and wear	11	Preventive maintenance	42,660.00	4,494.68	187.28
Horizontal Damper	Leaking	Low riding quality	Damaged seals, aging	12	Condition Based Maintenance	33,950.66	3,577.06	149.04
Ball joint	Seized	Leveling valve stuck	Seized ball joint	10	Preventive maintenance	46,486.67	4,897.86	204.08
Leveling Valve	Leaking	Leveling system malfunction	Aging and external influences	4	Condition Based Maintenance	26,257.65	2,766.52	115.27
Center Pin	Crack or broken	Disconnection between bogie and carbody	Excessive shock	10	Preventive maintenance	92,532.00	9,749.22	406.22
Motor/Gear coupling	Crack or damaged	Vibration, noise, and overheat	Wear and external influences	8	Condition Based Maintenance	39,560.73	4,168.14	173.67
Vertical Damper	Leaking	Low riding quality	Damaged seals, aging	7	Condition Based Maintenance	15193.71	1,600.82	66.70

### III. RESULTS AND DISCUSSION

As a result of the Section I and II, the outline of reliability centered maintenance has been formulated as demonstrated in **TABLE V**, which consists of list of the components, failure modes, effects, causes Fuzzy-RPN, identified maintenance strategy from RCM Decision Logic tree, and estimated maintenance interval cycle. This outline is a guideline or an approach to optimize the overhaul planning by offering the alternative maintenance strategy from the reliability analysis. The methodology and consequences, i.e., condition monitoring, maintenance interval and cost, have to be taken into account and studied further before conducting.

### IV. CONCLUSION

In this study, the general statement of the importance, role and problem of the bogie has been described. Additionally, Reliability Centered Maintenance (RCM) methodology is selected and used for analysis. The analysis in this paper consists of three parts. Firstly, data acquisition phase which results in list of components and their information for FMEA analysis. Second, Fuzzy FMEA was adopted to eliminate the vagueness of the conventional FMEA and to prioritize the risk and corrective actions. Third, reliability analysis which involves the maintenance strategy decision from RCM logic decision tree and the estimation of the maintenance interval cycle of each bogie components. As a results, the reliability centered maintenance outline of the bogie components was created as a guideline or an approach for further study in other aspects.

### ACKNOWLEDGMENT

The completion of this study would not have been possible without kindness and supporting from the advisors and professor at The Sirindhorn international Thai-German Graduate School of Engineering (TGGS), and also the dedication of the researchers from all over the world, as mentioned in references. I would like to express all my appreciation and gratitude to these researchers for his/her valuable work.

### REFERENCES

- [1] H. Zhang, S. Qin, R. Li, Y. Zou and G. Ding, "Progressive modelling of feature-centred product family development," *International Journal of Production Research*, vol. 58, pp. 1-23, 07 2019.
- [2] H. Zhang, X. Wei, Q. Guan and W. Zhang, "Joint Maintenance Strategy Optimization for Railway," *Applied Sciences*, vol. 12, p. 6934, 07 2022.
- [3] R. Jiravanstitt and W. Thammaphornphilas, "Overhaul Resource Planning for Rolling Stock Using MIP Models," *Engineering Journal*, vol. 21(5), pp. 145-159, 9 2017.
- [4] Q. Mahboob and E. Zio, *Handbook of RAMS in Railway Systems*, 2018.
- [5] A. Ishak, K. Siregar, R. Ginting and A. Manik, "The Fuzzy Failure Mode and Effect Analysis (FMEA) Method to Improve Roofing Product's Quality (case study : XYZ Company)," *IOP Conference Series: Materials Science and Engineering*, vol. 1003, p. 012092, 12 2020.
- [6] B. Yssaad, M. Khiat and A. Chaker, "Reliability centered maintenance optimization for power distribution systems," *International Journal of Electrical Power & Energy Systems*, vol. 55, no. 0142-0615, pp. 108-115, 2014.
- [7] J. Ivančan and D. Lisjak, "New FMEA Risks Ranking Approach Utilizing Four Fuzzy Logic Systems," *Machines*, vol. 9, p. 292, 2021.
- [8] R. Fattahi, R. Tavakkoli-Moghaddam, M. Khalilzadeh, shahsavaripour and R. Soltani, "Risk Assessment by a New FMEA Model based on an Extended AHP Method under a Fuzzy Environment," *EEE*, 07 2021.
- [9] G. Jin, Q. Meng and W. Feng, "Optimization of Logistics System with Fuzzy FMEA-AHP Methodology," *Processes*, vol. 10, p. 1973, 9 2022.
- [10] A. Piegat, *Fuzzy modeling and control*, vol. 69, Physica, 2013.
- [11] N. Belu, N. Rachieru and D.-C. Anghel, "Fuzzy Failure Mode and Effect Analysis Application to Improve Laser Cutting Process," *Advanced Materials Research*, vol. 1036, pp. 280-285, 10 2014.
- [12] K.-S. Chin, A. Chan and J.-B. Yang, "Development of a fuzzy FMEA based product design system," *The International Journal of Advanced Manufacturing Technology*, vol. 36, pp. 633-649, 03 2008.
- [13] D. Kiran, "Chapter 26 - Failure Modes and Effects Analysis," in *Total Quality Management*, Butterworth-Heinemann, 2017, pp. 373-389.
- [14] *Railway applications - The specification and demonstration of Reliability, Availability, Maintainability and Safety (RAMS)*, BS EN 50126-1999.
- [15] G. Saritha, M. Tirumala Devi and T. Sumathi Uma Maheswari, "Reliability and Availability for Non-Repairable & Repairable Systems using Markov Modelling," *INTERNATIONAL JOURNAL OF ENGINEERING RESEARCH & TECHNOLOGY*, vol. 09, no. 03, 2020.
- [16] A. Hilt, G. Jaro and I. Bakos, "Availability Prediction of Telecommunication Application Servers Deployed on Cloud," *Periodica Polytechnica, Electrical Engineering*, vol. 60, pp. 72-81, 2016.
- [17] *Dependability management - Part 3-11: Application guide - Reliability centred maintenance*, IEC 60300-3-11:2009.
- [18] J. Moubray, *Reliability-Centered Maintenance*, Industrial Press Inc., 1997.
- [19] A. Pride, "https://www.wbdg.org/resources/reliability-centered-maintenance-rcm," 11 09 2016. [Online]. Available: <https://www.wbdg.org/resources/reliability-centered-maintenance-rcm>. [Accessed 2023].
- [20] F. Fang, Z.-J. Zhao, C. Huang, X.-Y. Zhang, H.-T. Wang and Y.-J. Yang, "Application of Reliability-Centered Maintenance in Metro Door System," *IEEE Access*, vol. PP, pp. 1-1, 12 2019.
- [21] H. F. Martz, "Reliability Theory," in *Encyclopedia of Physical Science and Technology (Third Edition)*, Third Edition ed., R. A. Meyers, Ed., New York, Academic Press, 2003, pp. 143-159.
- [22] J. Chen, F. Zhao, W. Zhu, L. Huang, Q. Zhou, Z. Shan and L. Liu, "Research and Analysis on the Reliability of Smart Energy Mete," *Journal of Physics: Conference Series*, vol. 1802, p. 042098, 03 2021.

# Fish Food Pellet Characteristics After Coating Using Fluidized Bed Technique

Jatupat Maikaew<sup>1</sup>, Chairat Phetkeri<sup>2</sup>, Chayaphon Polnakarn<sup>2</sup>, Nopadol Katpimol<sup>2</sup>,  
Naruebodee Srisang<sup>2\*</sup>, and Siriwan Srisang<sup>2</sup>

<sup>1</sup> Student in Master degree of Mechanical Engineering, King Mongkut's Institute of Technology Ladkrabang, Prince of Chumphon campus, Chumphon, 86160, Thailand, and Jatuphat.maikaew@gmail.com

<sup>2</sup> Department of Engineering, King Mongkut's Institute of Technology Ladkrabang, Prince of Chumphon Campus, Chumphon, 86160, Thailand, and naruebodee.sr@kmitl.ac.th

\*Corresponding author

**Abstract:** The quality improvement of fish food pellets (FFP) was necessary to elevate competitiveness. Therefore, this research investigated the FFP quality development using the top-spray fluidized bed technique combined with polyacrylic acid (PAA) and chitosan (CS) solution coating. The CS concentration was 0.25%(w/v), and the PAA amount in solution was used in three levels of 10, 15, and 20 mg. Their FFP properties were examined about the pellet durability index (PDI), pellet water solubility (PWS), sink ratio (SR), and microstructure using a field emission scanning electron microscope (FE-SEM). The results show that PDI values increased to 55% and PWS values reduced by around 40% because of increasing PAA concentrations. Meanwhile, the moisture of FFP between both groups showed no significant difference ( $p > .05$ ). On the other hand, increasing PAA concentrations causing have several porous. However, the SR in each group will not differ ( $p < .05$ ). Therefore, coating the PAA\_CS solution can improve the physical property of both PDI and PWS, which helps reduce toxicity in water sources and higher durability of the FFP.

**Keywords—** Polyacrylic Acid, Chitosan, Fish Food Pellets, Fluidized Bed Technique, Coating.

## I. INTRODUCTION

The PAA is applied for various purposes such as biomedical materials, medicine, food packing, and agriculture because it has a low price and suitable attributes, i.e., white powder, water solubility, and biological compatibility. The PAA is used as a supplement in food due to its low toxicity and high binding force [1]. Moreover, PAA is used in toxic absorption, as presented in the research of Gokmen, Yaman [2], who took the hydrogen mixed with PAA to remove the metal of  $M^{2+}$  and  $Fe^{3+}$  ions in the solution. Chitosan (CS) is a polymer in the Polysaccharide type, which has highlighted biological properties that can cause microbe inhibition, antioxidant, and anti-inflammatory [3]. Sahab, Waly [4] used chitosan combined with PAA to inhibit fungi in soybean seeds. The CS was coated in feed and human food to increase immunity [5], food preservation [6], and water treatment [7]. Iqbal, Riaz [8] produced the edible cheese surfer from chitosan combined with biopolymer coating. The CS of about 2 g/kg in food can remove the bacteria and increase white blood cells [9, 10].

The above research indicated the various advantages of PAA and CS, which conducted to the PAA and CS application in coating the FFP in this research. The spray coating is widely applied in the food industry for the prevention of nutrient leaching [11], immunity creation [7],

increasing antioxidant activity [12], and surface protection [13]. The top-spray fluidized bed coating technique (TFB) was used in this research to coat and dry the FFP. It provided the throughout mixing during the fluidization process and resulted in regular coating and drying. However, the effect of the top-spray fluidized bed coating technique on the physical characteristics of FFP has yet to be found.

Therefore, this research investigated the coating of PAA and CS on the FFP via the TFB. The effect of TFB on the microstructure and the physical attributes of FFP in terms of the pellet durability index, pellet water solubility, and sinking ratio were studied.

## II. METHODOLOGY

### A. Raw material

The main materials for FFP production are organic wastes in the seacoast communities, i.e., shrimp shells, crab shells, and seaweed, as shown in figure 1. The ingredients by weight in the FFP formulation consisted of shrimp shells 25.3%, crab shells 12.7%, seaweed 8%, rice bran 10%, fish oil 6%, dough 15%, multivitamin 2%, and water 16%. These raw materials were blended and formed into the pellet, as displayed in figure 2. The PAA and CS powder has a medium molecular weight which was obtained from Sigma-Aldrich (St. Louis, USA). The acetic acid (glacial)

was purchased from SupelcoTM.



**Figure 1** Main materials for FFP production A) shrimp shells, B) crab shells, and C) seaweed



**Figure 2** Fish food pellet

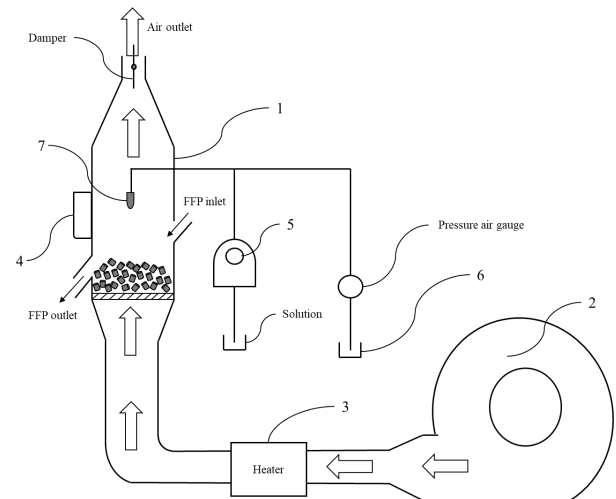
### B. Coating substance preparation

The chitosan solution (2.5 g) was dissolved by acetic acid (1% v/v) in water 1 L after finishing melting the chitosan. Next, bring the PAA solution concentration each for 10, 15, and 20 mg, respectively, and put it in the chitosan substance previously prepared. To continue, the substance was stirred by a magnetic stirrer at 300 rpm and room temperature for 24 hr. Due to the time, the substance was put in bottles and brought into the experiment.

### C. Coating and drying process

In experimental use, 2 kg/batch, which the coating and drying process was performed as shown in the diagram in figure 3. First, the heater (number 3) was opened when the temperature was stable at 110 C, filling the FFP in the drying room (number 1). Second, the blower (number 2) and halogen lamp (number 4) were opened together until fluidization happened at 10.7 m/s. Third, the solution pump (number 5) (model CNPB 0705; Prominent, Germany) and Air pump (number 6) (Tiger air compressors, model TGA33-150M, China) were set to 40 mL/min [14] and 4 bar, respectively, and opened, which solution was mixed with air inside the two-phase nozzle (model 1/4J series; Spraying Systems Co., Wheaton, IL, USA) (number 7) for atomization; The nozzle was equipped center of the drying

room[14]. Although, this experiment will use a processing time of 15 min because moisture content values must be lower than 13 %(w.b.)[15]. Finally, power off all machines and remove the coated FFP to cool off time for 10 min after keeping in a zip lock bag and freezing it at -4 °C for bring go analysis next.



**Figure 3** Diagram of coating and drying process

### D. Moisture content (MC)

The moisture content of FFP samples was measured and reported in the percentage of wet basis (w.b.). The FFP sample before the operation was weighed using an analytical balance with an instrumental resolution of 0.01 g. (GF-3002A multi-function balances, Japan). Then, the FFP sample was determined the dry weight via the hot air drying in oven (Mettler, model un55, Schwabach) at 105°C for 48 h until its moisture did not change. Both weights were used to calculate the moisture content of FFP as displayed in the equation (1).

$$MC (\% \text{ w.b.}) = \left( \frac{w - d}{d} \right) \times 100 \quad (1)$$

Where  $w$  is the FFP weight before operation (g)  
 $d$  is the FFP dry weight (g)

### E. Physical properties

#### 1) Pellet Durability Index (PDI)

The FFP samples were estimated the PDI using the pellet durability testing machine as according with the standard of ASAE S269.4 [16]. The FFP sample weight before PDI testing was recorded using an analytical balance with an instrumental resolution of 0.01 g. (GF-3002A multi-function balances, Japan). The FFP sample was centrifuged at 500 rpm within the sieve (hole size  $\approx$  3.4 mm) which installed inside the testing machine. The FFP sample weight after testing was recorded. Both FFP weights were used to estimate the PDI index using the equation (2) [11].



$$\text{Pellet durability index (\%)} = \frac{M_a}{M_b} \times 100 \quad (2)$$

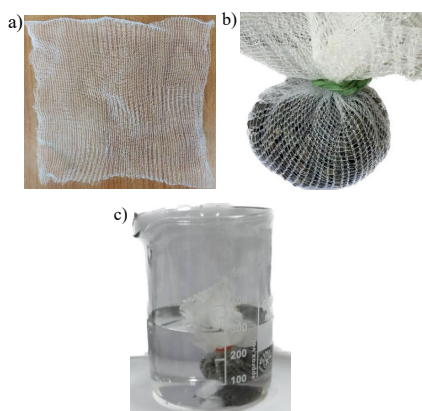
Where  $M_b$  is the FFP weight before centrifugation (g)  
 $M_a$  is the FFP weight after centrifugation (g)

### 2) Pellet water solubility (PWS)

The method for PWS evaluation adapted from the research of Wang et al. (2021) [17]. The FFP sample was weighed and put in the mesh bag size 18 x 18 cm (pore size 2.5 x 1.5 mm) as shown in figure 4a and 4b. The mesh bag was soaked in a beaker which contained the water about 300 mL for 20 min as shown in figure 4c. The FFP sample was removed from water and dried in the oven (Memmert, model un55, Schwabach) at the temperature of 135°C for 2 h. The FFP sample after drying was recorded the weight. The residual water amount within beaker after testing was measured by standard method AOAC, 2000. Both weights of FFP and the residual water percentage were taken to use the PWS calculation using the equation (3).

$$\text{Pellet water solubility (\%)} = \frac{m_1 \times (1-x) - m_2}{m_1 \times (1-x)} \times 100 \quad (3)$$

Where  $m_1$  is the FFP weight before soaking in water (g)  
 $m_2$  is the FFP weight after soaking in water and drying (g)  
 $x$  is a residual water amount within beaker after testing (decimal)



**Figure 4** Pellet water solubility experimental of FFP: a) Mesh bag, b) FFP in mesh bag, and c) The mesh bag was soaked in a beaker

### 3) Sinking ratio (SR)

The evaluation method of SR was adapted from the research of De Cruz, Kamarudin [18]. The number of pellets of FFP sample was counted before SR testing. The FFP sample was put in a beaker. The water 200 mL was added in beaker. The FFP sample was kept in the water for 10 min. The number of floated pellets of FFP sample was counted. The number of pellets were used to estimate the SR as represented in the equation (4).

$$\text{Sinking ratio (\%)} = \frac{P_i - P_f}{P_i} \times 100 \quad (4)$$

Where  $P_i$  is the number of pellets of the FFP sample before SR testing (piece)  
 $P_f$  is the number of floated pellets of the FFP sample (piece)

### F. Microstructure

The microstructure of FFP sample was examined by field emission scanning electron microscope (FE-SEM) (model SE, Apreo, FEI, Czech Republic). The FFP was photographed at 500X magnification and an accelerating voltage of 5 kV.

### G. Statistical analysis

The MC, PDI, PWS, and SR results were reported in average value from three duplications. All data were analyzed by IBM SPSS Statistics (v.29.0, SPSS Inc., Chicago, IL) via the analysis of variance (ANOVA) at the significance level of  $p \leq 0.05$ .

## III. RESULTS AND DISCUSSION

### A. Moisture content

Table I shows moisture content of FFP sample in each condition. The TFB could provide the FFP in every condition with less the moisture content than 13% which was desirable MC for FFP. Due to the process of this work, water amount is imported and out of the product's surface if the hot air temperature is enough to make the cooling process higher than the process imports the water [19]. This results in the amount of water entering the evaporation product first, which may result in the solution being coated disappearing. However, the CS coating layer is not significantly different from PAA\_CS because there is no different viscosity coating whereby the substance's viscosity will affect the moisture in the product coated on the surface.

TABLE I

Moisture content of FFP sample in each condition.

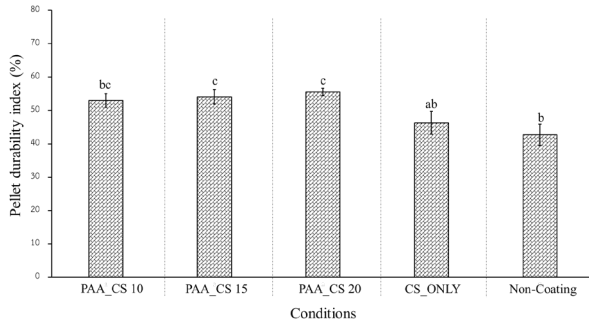
Sample	MC (% w.b.)
FFP non coating	3.00 ± 0.21 <sup>b</sup>
FFP coating CS	6.67 ± 0.14 <sup>ab</sup>
FFP coating PAA 10 mg and CS (PAA_CS 10)	6.00 ± 0.14 <sup>ab</sup>
FFP coating PAA 15 mg and CS (PAA_CS 15)	7.00 ± 0.07 <sup>a</sup>
FFP coating PAA 20 mg and CS (PAA_CS 20)	6.33 ± 0.07 <sup>ab</sup>

a, b Different superscripts are significantly different at  $p \leq 0.05$ . Turkey HSD's method

### B. Pellet durability index

The pellet durability index (PDI) indicates the durability of pellets, which transportation might cause the collision of pellets and affect broken pellets to become powder [20]. In Figure 5 presents that in the FFP coating with PAA\_CS, there is a highly increased PDI, which is different from FFP that is not significantly coated. The

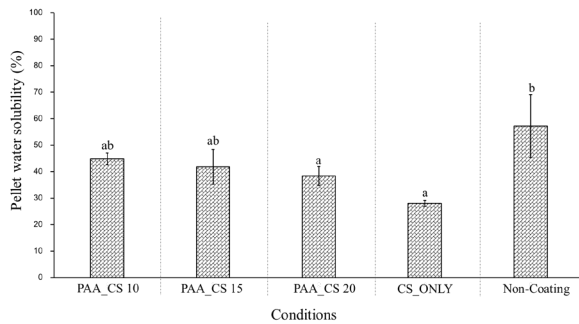
FFP coating with CS coating makes the PDI value show the increased trends. However, the PAA\_CS coating with a 10 mg concentration has a low PDI, which may be caused by low PAA coating. As a result, the addition of PAA affects the high PDI value, which can become the glue to biological [21].



a,b,c Different superscripts are significantly different at  $p \leq 0.05$ . Turkey HSD's method  
**Figure 5** Pellet durability index of fish feed pellets

### C. Pellet water solubility

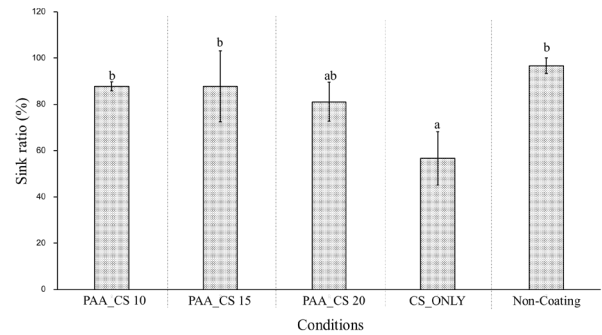
The PWS parameter indicates the standard index of stability pellets in water. If the low PWS parameter, it will reduce pollution aqua [22]. In figure 6 shows the CS coating, with FFP having lower values of PWS after CS coating compared to uncoated FFP significantly. While PAA and CS coating of FFP showed a higher trend, thus PWS values than CS coating, increasing the PAA content in the 10-20 mg range did not result in a significant difference in the PWS value of FFP.



a,b Different superscripts are significantly different at  $p \leq 0.05$ . Turkey HSD's method  
**Figure 6** Pellet water solubility of fish feed pellets

### D. Sink ratio

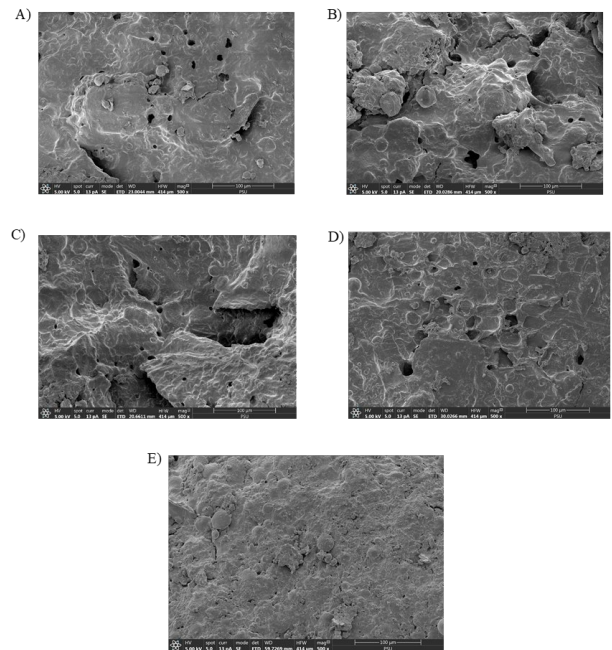
The sinking ratio (SR) was related to the bulk density by the high SR involved with the high bulk density which implied to the low porosity in pellets [22]. Figure 7 represents the SR of FFP after PAA and CS coating in every condition did not significantly difference with the non-coating of FFP. The SR after PAA and CS coating significantly increased as compared with the only CS coating, except, the FFP at PAA 20 mg and CS coating. As a result, PAA\_CS concentration at 20 mg and CS coating caused reduced SR and higher porosity, along with its effect on the down sinking slowly of the FFP. Although the character of the marine fish is a predator, like eating fall pellets slowly down to the ground because it looks like an animal was hunted [23]



a,b Different superscripts are significantly different at  $p \leq 0.05$ . Turkey HSD's method  
**Figure 7** Sink rate of fish feed pellets

### E. Field emission scanning electron microscope

Figure 8 presents the microstructure of FFP, observing that the PAA and CS-coated beads increase the porosity of the FFP, which differs from non-coated FFP, which observes no porosity. However, the characteristics of the PAA coating are rougher because PAA has higher acidity than CS coating. If the PAA concentration is high, the characteristics of the FFP will have more roughness. However, the absorbed substance coated on the surface causes eroded pellets which differ in the intensity of PAA during the drying process [17].



**Figure 8** Microstructure of FFP: A) PAA\_CS 10 mg, B) PAA\_CS 15 mg, C) PAA\_CS 20 mg, D) CS\_only, and E) Non\_coating

## IV. CONCLUSION

The coating PAA\_CS affected improved the physical property of the FFP, whereby the coating process caused a higher MC final compared with a non-coating. The concentration of 20 mg is optimal for improving physical property. The PDI increased higher to 55%. Although, it will have a low pellet water solubility related to very porous

pellets. By the way, it found that coating PAA\_CS has a sink rate of no difference significance that surface photography of the coated FFP PAA\_CS observed a high roughness and a clearly porous compared with the control group.

Nevertheless, this study spray-coated PAA\_CS in FFP with fluidized bed technical, whereby noticed coating characteristic microstructure FFP that has increased roughness and porous cause appropriate spray coating than another format coating. If it be, dip coating has the trend of decreased volume or density of FFP. Also, it found the increased performance of FFP physical side other viz pellet durability of FFP that help reduced loss of the product caused by bump between transportation its. Additionally, its lower pellet water solubility decreases the amount of feeding fish, affecting the entrepreneur's value.

#### ACKNOWLEDGMENT

This work is supported by King Mongkut's Institute of Technology Ladkrabang [KREF016510].

#### REFERENCES

[1] Arkaban H, Barani M, Akbarizadeh MR, Pal Singh Chauhan N, Jadoun S, Dehghani Soltani M, et al. Polyacrylic acid nanoplatfoms: Antimicrobial, tissue engineering, and cancer theranostic applications. *Polymers*. 2022;14:1259.

[2] Gokmen F, Yaman E, Temel S. Eco-friendly polyacrylic acid based porous hydrogel for heavy metal ions adsorption: characterization, adsorption behavior, thermodynamic and reusability studies. *Microchemical Journal*. 2021;168:106357.

[3] Aranaz I, Alcántara AR, Civera MC, Arias C, Elorza B, Heras Caballero A, et al. Chitosan: An overview of its properties and applications. *Polymers*. 2021;13:3256.

[4] Sahab A, Waly A, Sabbour M, Nawar LS. Synthesis, antifungal and insecticidal potential of Chitosan (CS)-g-poly (acrylic acid)(PAA) nanoparticles against some seed borne fungi and insects of soybean. *Int J Chem Tech Res*. 2015;8:589-98.

[5] Ranjan R, Prasad KP, Vani T, Kumar R. Effect of dietary chitosan on haematology, innate immunity and disease resistance of Asian seabass *Lates calcarifer* (Bloch). *Aquaculture research*. 2014;45:983-93.

[6] Hu Z, Gänzle MG. Challenges and opportunities related to the use of chitosan as a food preservative. *Journal of Applied Microbiology*. 2019;126:1318-31.

[7] Cha S-H, Lee J-S, Song C-B, Lee K-J, Jeon Y-J. Effects of chitosan-coated diet on improving water quality and innate immunity in the olive flounder, *Paralichthys olivaceus*. *Aquaculture*. 2008;278:110-8.

[8] Iqbal MW, Riaz T, Yasmin I, Leghari AA, Amin S, Bilal M, et al. Chitosan-based materials as edible coating of cheese: A review. *Starch-Stärke*. 2021;73:2100088.

[9] Kamali Najafabad M, Imanpoor MR, Taghizadeh V, Alishahi A. Effect of dietary chitosan on growth performance, hematological parameters, intestinal histology and stress resistance of Caspian kutum (*Rutilus frisii kutum* Kamenskii, 1901) fingerlings. *Fish physiology and biochemistry*. 2016;42:1063-71.

[10] Salem M. Utilization of Some Feed Additives in Improving the Nutritive Value of Marine Fish Diet (PhD Dissertation). Alexandria University, Egypt. 2015.

[11] Guo J, Davis R, Starkey C, Davis DA. Efficacy of various coated materials to prevent nutrient leaching for Pacific white shrimp *Litopenaeus vannamei* commercial diets. *Journal of the World Aquaculture Society*. 2021;52:195-203.

[12] Bhoopathy S, Inbakandan D, Rajendran T, Chandrasekaran K, Kasilingam R, Gopal D. Curcumin loaded chitosan nanoparticles fortify shrimp feed pellets with enhanced antioxidant activity. *Materials Science and Engineering: C*. 2021;120:111737.

[13] Fotovvati B, Namdari N, Dehghanghadikolaie A. On coating techniques for surface protection: A review. *Journal of Manufacturing and Materials processing*. 2019;3:28.

[14] Kongtragoul P, Junka N. Top-spray fluidization coating of paddy rice with zinc oxide nanoparticles to reduce infection from *Aspergillus* sp. *Journal of Food Processing and Preservation*. 2020;44:e14766.

[15] Marijani E, Kigadye E, Okoth S. Occurrence of fungi and mycotoxins in fish feeds and their impact on fish health. *International journal of microbiology*. 2019;2019.

[16] ASABE S. ASAE S269. 4-Cubes, Pellets, and Crumbles-Definitions and Methods for Determining Density, Durability, and Moisture Content. American Society of Agricultural and Biological Engineers Standards, St Joseph, MI, USA. 2007:624-6.

[17] Wang A, Lin J, Zhong Q. Spray-coating as a novel strategy to supplement broiler feed pellets with probiotic *Lactobacillus salivarius* NRRL B-30514. *Lwt*. 2021;137:110419.

[18] De Cruz C, Kamarudin M, Saad C, Ramezani-Fard E. Effects of extruder die temperature on the physical properties of extruded fish pellets containing taro and broken rice starch. *Animal Feed Science and Technology*. 2015;199:137-45.

[19] Palamanit A, Soponronnarit S, Prachayawarakorn S, Tungtrakul P. Effects of inlet air temperature and spray rate of coating solution on quality attributes of turmeric extract coated rice using top-spray fluidized bed coating technique. *Journal of food engineering*. 2013;114:132-8.

[20] Huang X, Christensen C, Yu P. Effects of conditioning temperature and time during the pelleting process on feed molecular structure, pellet durability index, and metabolic features of co-products from bio-oil processing in dairy cows. *Journal of dairy science*. 2015;98:4869-81.

[21] Khanlari S, Dubé MA. Bioadhesives: a review. *Macromolecular Reaction Engineering*. 2013;7:573-87.

[22] Wang H, Ma S, Yang J, Qin Y, Cheng H, Xue M, et al. Optimization of the process parameters for extruded commercial sinking fish feed with mixed plant protein sources. *Journal of Food Process Engineering*. 2021;44:e13599.

[23] Dunn RP, Hovel KA. Predator type influences the frequency of functional responses to prey in marine habitats. *Biology letters*. 2020;16:20190758.

# The Development of a Rain Storage System for Highland Agriculture Using Lightweight Composite Sandwich Panels

**Alexander Nikolaus Brezing<sup>1\*</sup>, Sirichai Torsakul<sup>2</sup>, Chawalit Inpunyo<sup>3</sup>, Julapot Chiravachradej<sup>4</sup>, Anucha Watanapa<sup>5</sup>, Eakanat Krajangthimaporn<sup>6</sup>, Wisitsree Wiyaratn<sup>7</sup>**

<sup>1</sup> The Sirindhorn International Thai-German Graduate School of Engineering, King Mongkut's University of Technology North Bangkok, Bangkok, Thailand, alex.b@tggs.kmutnb.ac.th

<sup>2</sup> Department of Industrial Engineering, Rajamangala University of Technology Thanyaburi, Pathum Thani, Thailand, Sirichai.to@en.rmutt.ac.th

<sup>3</sup> Department of Industrial Engineering, Rajamangala University of Technology Thanyaburi, Pathum Thani, Thailand, Chawalit.i@en.rmutt.ac.th

<sup>4</sup> Department of Civil Engineering, King Mongkut's University of Technology Thonburi, Bangkok, Thailand, julapot.chi@mail.kmutt.ac.th

<sup>5</sup> Department of Industrial Engineering, King Mongkut's University of Technology Thonburi, Bangkok, Thailand, anucha.wat@kmutt.ac.th

<sup>6</sup> Department of Sustainable Land Use and Resource Management, King Mongkut's University of Technology Thonburi, Bangkok, Thailand, eakanut.kar@kmutt.ac.th

<sup>7</sup> Department of Industrial Engineering, King Mongkut's University of Technology Thonburi, Bangkok, Thailand, wisitsree.wiy@kmutt.ac.th

**Abstract:** The Royal Agricultural Projects in the Mountains of the northern provinces of Thailand operate under challenging conditions while trying to set examples on sustainability, especially by minimizing the impact of the farming on the local ecosystem and the uniquely beautiful landscape. Managing water, which exists in over-abundance during the rainy season and is very scarce during the rest of the year, is a very demanding task, if using electric power for pumping and building multitudes of reservoirs into the landscape are no options. A flexible water storage system has been developed to satisfy a specific set of design constraints, including the option to install the containers on elevated levels inside green-houses or unprepared ground, and the possibility to install and de-install the storage-units multiple times without heavy machinery, as well as being in line with the overall motivation of maximized sustainability as well as minimized complexity and lifecycle costs. A concept is proposed which uses composite sandwich panels as structural elements, which are integrated into the overall structure without any connectors or sealing measures to satisfy all practical demands. This paper derives the design rationale from a functional discussion and covers the finite element simulations and the experimental testing of the mechanical properties of the employed sandwich material (stainless steel faces, PU-foam core) as well as the validation of the supporting steel structure. Two containers with a capacity of 27,000 liters each were built and tested on site.

**Index Terms— Composite Sandwich Panel, Rainwater Harvesting, Sustainable Agriculture.**

## I. INTRODUCTION

Traditionally, the so-called Hill Tribes in the mountains of northern Thailand practice subsistence farming, cultivating just enough plants for use as food to support the own household without intent to sell excess produce to generate an income. Some of these tribes practiced shifting cultivation (“slash-and-burn”), which is generally perceived

as harmful to the environment [1], while others introduced rotational cultivation. As there is no irrigation system for agriculture in this hardly accessible land with its complex topology, agriculture relies mainly on rain water and natural sources such as creeks, swamps, and marshes. Especially shifting cultivation cannot sustain the growing demand for produce resulting from a growing population, and highland agriculture has been becoming increasingly commercial and intensifying and therefore threatening to have a destructive impact on the natural environment. In the

Thai Highlands, the need for “Smart Farming” approaches which are capable of creating sufficient surpluses to support the population is clearly more urgent than in most other parts of the country.

The biggest challenge is to satisfy the large demand of water of good quality - both for agricultural use as well as for the population’s households - in places which are situated at higher altitude than natural sources. Pumping water is not sustainable, and it increases the cost of agricultural production.

Government agencies such as the Royal Irrigation Department have established dam lakes, with only gravity to realize the flow through the pipes, which are constructed into the complex terrain to supply water in the watershed areas. The reliability of this delivery system is constantly challenged by sinking ground in the karst topography, which can change the constructed slope of the pipes, as well as clogging from sediment or air bubbles. Other problems include the slag formation and crystallization fouling in the tubes, which causes the clogging of agricultural equipment such as sprinklers. Finally, the artificial lakes themselves can be considered a blemish to the environment.

The challenges are met with the great opportunity of over-abundant rainfall during the rainy season in the highlands, with rainwater being considered of good quality for agricultural use. The key concept to address water management in the Thai highlands, especially for greenhouse farming, therefore is to complement centralized supply systems with de-centralized rainwater harvesting systems (RHS), which do not suffer from the detriments inherent to long delivery tubes. As the greenhouses’ roofs already provide an effective catchment area, the missing element discussed in this paper is a reservoir to be erected directly next to the greenhouse.

The concept of catching and storing rainwater for agricultural use, also referred to as “runoff farming”, is as old as settled human lifestyle, and Bruins distinguishes multiple types of runoff farming which cover a wide range of application scales [2]. As a result of worldwide scarcity of water supplies for agricultural use the topic of rainwater harvesting (RH) for agricultural irrigation has received growing attention in global research during the past two decades, with multiple journals dedicated to this field [3]. As Velasco-Muñoz analysis shows, research focusses on climate analysis and climate models, food safety and potable water availability, groundwater depletion, irrigation systems and techniques, the monitoring of water and soil quality, economic and sustainability analyses, evaporation and infiltration, and agriculture adaptation and modernization processes [3]. Previous work with a focus on the design and specifically materials for rainwater storage systems could not be identified. Another easily overlooked aspect of the environmental and economic feasibility of RHS is the related energy demand for pumping the water, and it has been pointed out by Vieria et al. that the energy

demand is often underestimated, and in case of RHS for buildings, even well-designed systems have similar levels of energy intensity as conventional technologies such as municipal water supply systems [4].

## II. TECHNICAL BACKGROUND

In order to allow for a “smart” RHS with minimal or even zero energy demand, the water reservoir is placed on a level which is higher than the plants to be watered and lower than the catchment area. Consequently, the reservoir needs to be a structure of substantial strength, which can be installed and de-installed multiple times without heavy machinery and a lasting impact on the environment to satisfy the overall concept of sustainable highland farming. This unusual combination of design constraints requires lightweight materials, and composite sandwich panels provide the stiffness and strength at a fraction of the weight of comparable structures made from conventional steel or concrete materials.

### A. Composite Sandwich Panels and their Failure Modes

Composite Sandwich Panels use thin face layers of a high stiffness/high strength material bonded onto both sides of a thick layer of a material of low density, resulting in a high stiffness/weight ratio [5]. Including the bonding adhesive, there therefore are three components which determine the resulting loading capacity and the failure modes which can result from a multitude of load cases, Fig. 1. Such panels are ideally suited for pure bending loads, and ideally dimensioned if both failure modes (1) and (2) occur at the same load level, [5], [6].

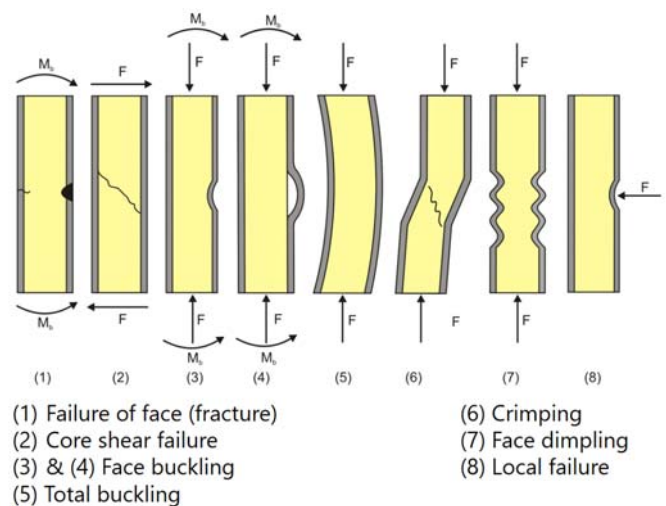


Fig. 1. Loads on sandwich panels and related failure modes [5]

### B. Experimental Testing of Mechanical Material Properties

While bending tests are suitable for characterizing the complete composite for bending load cases, shear testing focuses on determining the shear strength of the core material and the loading capacity of the adhesive bonds.

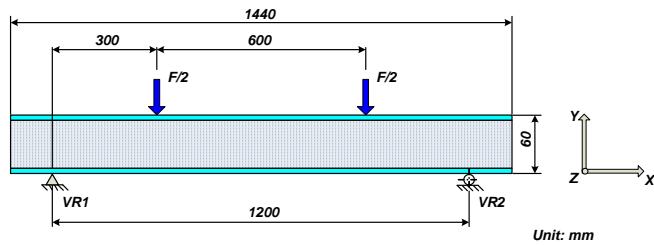


Fig. 2. Layout of a 4-point bending experiment for composite sandwich panels according to [8].

For this research, the selected materials were tested for shear properties of the core material and bonding strength according to ASTM C273 [7] and with 4-point bending experiments according to DIN 53293 [8] for overall bending strength.

### C. FEM-Simulation of Sandwich Panels

A challenge for FE-modelling load cases with sandwich panels is the small thickness of the face layers and the adhesive bonds in relation to the total dimensions of the panel or even the structure that the panel is part of. In order to minimize the duration of the calculation while maintaining a good accuracy of the simulation results, the face layers are modelled by plate-elements and the core by 3D-elements. The adhesive layer is not modelled at all, but the nodes of the elements representing the core material are directly bonded with the nodes of the plate elements. This simplification is justified by the assumption that the core material fails before the adhesive layer does, which needs to be proven by physical experiments. This modelling strategy is tested and described in [9].

## III. DESIGN RATIONALE

### A. Methodology, Requirements, Functional Discussion

Functional decomposition and a careful consideration of design constraints (requirements) are the key approaches of design methodology enabling the practitioner to identify ideal technical concepts. The term “architecture” in this context describes which technical elements (components, surfaces...) realize which functions as “function carriers” (FC), and architectures can be “functionally integrated” (few function carriers realize many functions) or characterized by a “division of tasks” (each function is realized by its own function carrier) [10].

The overall function of “storing water in its liquid state in a defined volume” is achieved by 4 sub-functions  $F_A...F_D$ :

- support the surface pressure resulting from mass of the water (to the bottom and sides of the volume),
- distribute the resulting total mass force of the volume of water so it can be sustained by a supporting ground or structure,
- create a barrier against the liquid to leak from the volume (to the bottom and sides of the volume), and
- prevent losses through vaporization.

A water balloon is an example for a fully functionally integrated architecture. A bottle integrates functions A-C into one function carrier as does an artificial pond lined with foil or concrete, and the different design is a result of differing magnitudes of the storage capacity and requirements on usability.

The requirements on the reservoir to be developed here have been defined as follows:

- multiple cycles of assembly and disassembly possible without special qualification and tools;
- transport and storage of components possible without heavy machinery;
- set-up on natural ground and elevated levels possible (to allow for draining without pumps when set up in greenhouses);
- good economic balance, while re-use of components after the end-of-life of the reservoir is to be considered;
- scalable solution with an initial capacity of 50 tons.

This capacity requirement e) was formulated by the farmer and results from the estimated water demand for the produce (tomatoes) for the time between two rainy seasons. Overall, the design task requires a robust solution with simple, reusable, storable and light-weight components and a simple assembly and disassembly. This task, especially in the light of the scale of the structural task, is best met with a “division of tasks” architecture, where each function is realized by a separate, highly specialized function carrier.

### B. Technical Concept

The selected concept for the water storage unit (“pool”, “reservoir”) follows the concept of the division of tasks:

Rectangular panels ( $FC(F_A)$ ) are placed in a frame ( $FC(F_B)$ ) without any fasteners or sealing measures, and a liner ( $FC(F_C)$ ) is placed on the inside of the resulting box to seal it, Fig. 3. An additional foil (not shown) is placed on the top to reduce losses through vaporization ( $FC(F_D)$ ). The frame features a “spiderweb” of strings to support the wall elements and adjustable feet.

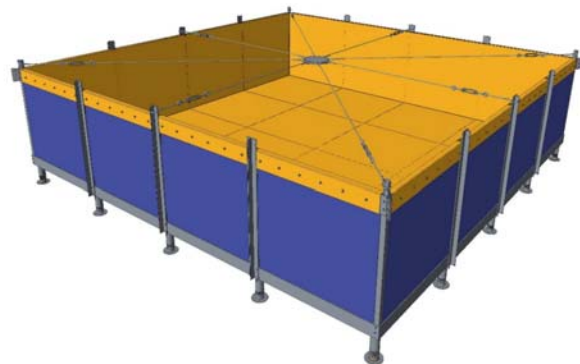


Fig. 3. Water storage unit.

### C. Choice of Materials, Dimensioning Strategy

Materials are chosen considering costs, availability, resistance against the elements, ease of handling and reusability/recyclability for the end-of-life of a storage unit or if a component needs to be replaced.

A composite sandwich of stainless steel face sheets with a PU-foam core is chosen for the panels, mainly because its high stiffness/weight ratio allows for a big panel size (small total number of panels) with a manageable weight. Construction steel is used for the frame, as it is easily available in a large variety of profiles, with good characteristics in all other categories.

The dimensioning of the panels and frame is an interesting optimization problem with various interdependencies to consider. Firstly, in order to avoid scrap losses of the costly sandwich material, the original dimensions of 1.2x2.4m<sup>2</sup> are to be used or divided into smaller panels without scrap losses. This also means that the depth of the reservoir is to be multiples of 1.2 meters. Secondly, the sandwich panels are available with multiple thicknesses of the face and core layers as well as multiple core densities, which in turn determine the core shear strength. For each considered panel dimension, which determines the support placement and therefore the bending moments resulting from the surface pressure, the layer thicknesses and core density have to be optimized to result in identical safety-factors and a target weight of the panel to ensure it can be handled. Generally, a maximum panel size is strived for to reduce the complexity of the supporting frame.

## IV. DIMENSIONING OF STRUCTURAL COMPONENTS

### A. Dimensioning by FEM-Simulation of Sandwich Panels

A series of FEM simulations of the panels was carried out early in the design process, as the results determine not only the panels' dimensions but also the configuration of the supporting frame. Only the floor panels are considered, as the loads on the side panels are only half as high, Fig. 4. The simulated load represents isostatic pressure resulting from a water depth of 1.2 meters only, as multiples of this depth soon proved to be unrealistic for this concept. Initial plans to use full-sized panels of 1.2x2.4m<sup>2</sup> were also dismissed because of the high weight of the panels (bad handling) and because this configuration requires additional supports by the frame which made the frame design inefficient. Fig. 5 shows the model and some results of one of the series of simulations as an example.

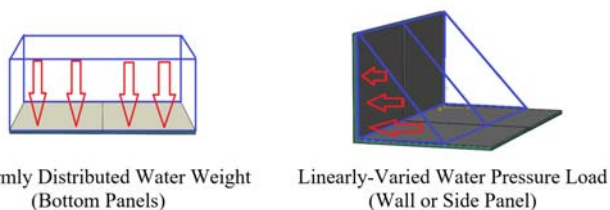


Fig. 4. Two types of loads acting on the sandwich panels.

The material characteristics of the PU foam are critical for the panel's performance and depend on the foam's density, which is available in a wide range of values. As the producer does not state the values for compressive modulus and strength and shear strength, we assumed values stated in [11] for our simulations (see TABLE I.) and validated these with experiments on the actual product, see below.

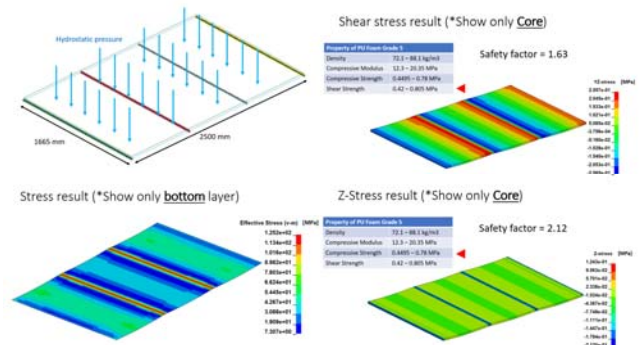


Fig. 5. FE-model and simulation results of a configuration with 4 parallel, crosswise, line-shaped supports, which was dismissed. The results for the steel face layers (left) are displayed separately from the results for the core (right), which is checked with regards to compressive strength and shear strength.

TABLE I

SIMULATION RESULTS OF SANDWICH PANELS 1200\*1200\*42MM<sup>3</sup>, SUPPORTED AT ALL 4 EDGES UNDER 1.2 METERS OF WATER, STAINLESS STEEL FACES OF 0.5 AND 1.0MM THICKNESS, WITH THE VARIANT HIGHLIGHTED THAT WAS CHOSEN AND APPLIED FOR THE DESIGN

Property of PU Foam					Property of SUS304		
Density [kg/m <sup>3</sup> ]	40	45	55	88	Density [kg/m <sup>3</sup> ]	7900	
Compressive Modulus [MPa]	2.76	4.21	7.34	12.3	Modulus [GPa]	193	
Compressive Strength [MPa]	0.09	0.14	0.26	0.45	Tensile Strength [MPa]	500	
Shear Strength [MPa]	0.155	0.2	0.31	0.42	Yield Strength [MPa]	200	

Density of PU [kg/m <sup>3</sup> ]	PU Thickness [mm]	Maximum Shear stress PU [MPa]	Safety Factor	SUS 304 Thickness [mm]	Von Mises stress SUS304 [MPa]	Safety Factor	Weight per panel [kg]
40	41	0.0989	1.57	0.5	92.94	2.15	14.96
	40	0.091	1.7	1	79.61	2.5	27.04

The chosen configuration is a 1.2x1.2m<sup>2</sup> square panel with a standard total thickness of 42mm. TABLE I. shows a comparison of the simulation results of such panel with a 40kg/m<sup>3</sup> core density and face sheets of 0.5 and 1mm thickness respectively. The shear strength of the core is critical for the panel's strength, but both variants show similar acceptable safety factors of more than 1.5. The variant with 0.5mm steel faces was finally chosen because it offers practically the identical overall safety against failure by shear failure of the core (S=1.57) with a substantially lower weight and cost for the panel.

The benefit of the sandwich concept can be illustrated impressively by a weight comparison of the chosen composite panel weighing 15kg with a solid steel plate with

identical bending stiffness, which would be 17.3mm thick and weigh 195kg.

The modular concept with a single panel size also determines the possible capacities of reservoir units, which are multiples of cubes with  $V=1.2^3m^3=1,728$  liters. To satisfy the requirement for a total capacity of 50 tons, a configuration of two square pools with 4x4 elements each was chosen, resulting in a total capacity of 55296 liters, or 27,648 liters per pool.

### B. Sandwich Material Property Testing

Both shear testing and 4-point bending experiments on samples of the panels used on the reservoirs verified the assumptions that the adhesive bonds are strong enough not to fail until the core suffers a shear failure, which reliably occurs both in shear testing as well as 4-point bending, Fig. 6. The face sheets are peeled off the core material immediately after the core fails. Furthermore, the tests confirm the values for core stiffness and strength well enough to expect that the safety factor against shear failure is clearly larger than 1 when used on the reservoir under full capacity. The relatively large variance with only three bending experiments (Fig. 7) does not allow for a more quantitative summary of the experimental results, but we conclude that with the given perfectly static load case, it is sufficient.



Fig. 6. Experimental testing on the used sandwich composite material. The left shows the specimen after a shear test with the characteristic separation in the core material under 45° as a result of shear failure. On the right: 4-point bending experiment.

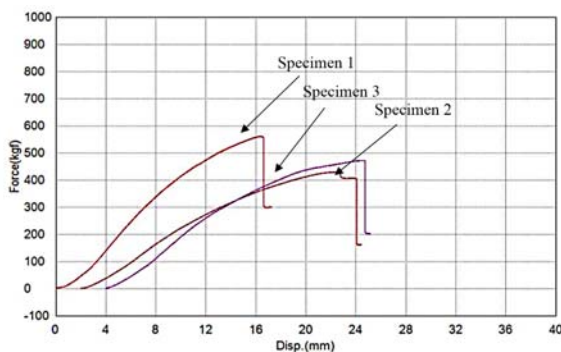


Fig. 7. Raw results of three 4-point bending experiments

### C. Steel Support Structure

The supporting frame consists of four types of elements, made from standard steel profiles: the T-beam, L-beam, column and belt. This configuration is result of the process of optimizing the design, more specifically realizing ideal support of the panels along all 4 edges each with standard steel profiles, uniform stress level, minimal amount of material to minimize material costs and most simple machining operations to minimize manufacturing costs. The positions of all of these components are depicted in Fig. 8, and the dimensioning criteria and calculated values are tabulated in TABLE II. The calculations follow the design code of the American Institute of Steel Construction [12]. Each component of the frame is dimensioned according to its critical member, i.e. the member that resists the highest loads.

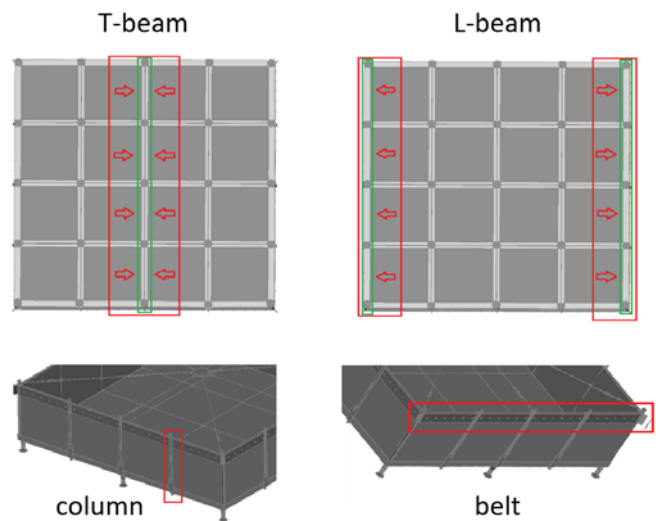


Fig. 8. The four types of elements of the steel support structure.

TABLE II  
SUMMARY OF THE PROOF OF STRENGTH FOR THE FRAME'S ELEMENTS

Criterion	T-Beam	L-Beam	Column	Belt
Steel	S5400	S5400	S5400	S5400
Cross-Section	T 100x50mm	120x120mm	45x45mm	150x4800x5 mm
$\lambda$	2.94	15	2.94	-
$\lambda_p$	124.06	15.03	124.06	-
$\lambda_r$	124.06	19	124.06	-
Type	Compact	Compact	Compact	Slender
Ma	112.17 kg*m	50.99 kg*m	346.7 kg*m	112.17 kg*m
Mn/ $\Omega$	314.97 kg*m	442.5 kg*m	-	421.5 kg*m
Pass/Not Pass	Pass	Pass	Ma = Mp	Pass
Flange, $\frac{b_f}{2t_f}$	2.94	7.5	2.94	-
Flange, $0.38 \sqrt{\frac{E}{F_y}}$	10.47	10.47	10.47	-
Pass/Not Pass	Pass	Pass	Pass	N/A
Web, $\frac{b_f}{t_f}$	7.5	7.5	7.5	-
Web, $1.46 \sqrt{\frac{E}{F_y}}$	103.66	103.66	103.66	-
Pass/Not Pass	Pass	Pass	Pass	N/A
Deflection Limit	0.5 cm	0.5 cm	0.5 cm	-
Max. Deflection	0.4935 cm	0.02 cm	N/A (1)	-
Pass/Not Pass	Pass	Pass	N/A (1)	N/A
Shear, $V_n/\Omega$	5389.22 kg	8622.75 kg	5389.22 kg	5838.32 kg
Shear, $V_a$	356.9 kg	183.55 kg	866.76 kg	142.76 kg
Pass/Not Pass	Pass	Pass	Pass	Pass

(1) The column deflection is controlled by the belt which can be tightened.



## V. FIELD TESTING, PROOF OF CONCEPT

Two identical reservoirs have been installed at the Royal Agricultural Station Pangda, Samoeng Tai Subdistrict, Samoeng District, Chiang Mai, in August 2019 and have been in use since then, Fig. 9.



Fig. 9. Two prototypes of the developed reservoir with a capacity of 27,000 liters each installed at greenhouses at the Royal Agricultural Station Pangda.

### A. Function, reliability, user satisfaction

A survey was conducted in 2023 to learn about the current state and use of the reservoirs as well as the satisfaction of the users. The feedback confirmed that the reservoirs were still in productive use for growing tomato seedlings in two greenhouses, and that they were still in perfect condition without having required any repairs or maintenance. The users stated that the system enhanced the agricultural productivity, mostly because the water buffer at the greenhouses stabilizes the production and reduces the risk of losses resulting from power cuts or other technical failures which regularly impede the water supply from sources further away. Regarding the dimensioning of the system's capacity (catchment by the greenhouses' roofs, storage capacity), the users stated that it is sufficient to solely rely on rain during the months of June to October, but additional water was required during the rest of the year. Furthermore, the users confirmed that the concept of flexible manual installation and de-installation was valuable and useful for applications in the Highlands of Thailand, even if the prototypes have not yet been removed but continuously used in the place of their initial installation.

### B. Economic feasibility

The total cost of engineering, manufacturing and setting up the two reservoir prototypes amounted to 537,900 THB in 2019, with the material costs of the composite panels and steel structure at about one third each. We estimate that this pair would be sold for 200,00 THB if commercially produced, with the economy of scale reducing material and manufacturing costs accordingly. The direct return of this invest are savings in electricity costs, which amounted to about 5,000 THB per year for the served greenhouses in 2019 and 7,500 THB per year in 2023 as a result of the

general rise in electricity costs. These returns would never commercially justify the investment under current conditions.

However, in a scenario without the current availability of free source water, with only electricity costs for pumping it from remote reservoirs, the investment would be related to the gross profit of the agricultural produce made possible by the RHS, which is about 100,000 THB/year for the tomato seedlings grown in the discussed greenhouse. Other benefits which might be expressed in monetary terms, are the increased safety against losing the crops in case of supply cuts due to the storage capacity, the flexibility with locating the reservoirs, the residual value of the materials and the minimal impact on the environment.

## VI. CONCLUSION

The concept for a Rainwater Harvesting System proposed in this paper is a proven solution for greenhouse agriculture, with the roofs of the greenhouses acting as collectors for large amounts of rain water during the rainy season. The water containers, the core component of the concept, use sandwich panels, which are so lightweight themselves that they can be handled without heavy machinery, to support the weight of the water while the build concept allows for taking down and setting up the containers multiple times with minimal impact on the natural environment. The steel structure of the containers, which is bolted together so it can also be taken apart completely, allows them to be installed on a level under the collecting roofs but higher than the produce which is to be watered, so that the system can be operated completely without electricity. The concept has been technically validated by productive use since its installation in 2019.

Composite sandwich panels and the supporting steel structure are costly, and it has been demonstrated that under commercial considerations, traditional reservoirs such as artificial lakes and the electricity costs for pumping the water are preferable under normal conditions.

However, the purpose of this research study and the proposed concept is not to compete with available techniques and technologies for commercial farming under conventional circumstances, but to test new technologies and make them available for future applications, while the growing scarcity of water for agricultural production and rising energy costs are already changing the economic balance. The concept of using advanced structural materials for the storage of water has been technically validated as robust and it is enthusiastically accepted by the users. The installed prototype of a complete small-scale Rainwater Harvesting System with a storage capacity of 54,000 liters allows for further detailed research on rainwater and energy balances and required capacities of water rainwater catchment area and water storage at the Royal Agricultural Station Pangda. The productive use of the reservoir has already revealed that the initial calculations led to an

underestimation of required catchment and storage capacities for the water-intense production of tomato seedlings, which underlines the value of such research and data for future designs of Rainwater Harvesting Systems to support smart and sustainable farming techniques.

#### ACKNOWLEDGMENT

The authors would like to thank the Agricultural Research Development Agency (Public Organization) for funding this project under the project-ID code PRP610502170, and the Royal Project Foundation for providing their expertise and information as well as access to the agricultural projects.

#### REFERENCES

- [1] Wikipedia: Hill tribe (Thailand). [https://en.wikipedia.org/wiki/Hill\\_tribe\\_\(Thailand\)](https://en.wikipedia.org/wiki/Hill_tribe_(Thailand))
- [2] Bruins, H.J.; Evenari, M.; Nessler, U. Rainwater-harvesting agriculture for food production in arid zones: the challenge of the African famine. *Applied Geography*, Volume 6, Issue 1, 1986, Pages 13-32, ISSN 0143-6228, [https://doi.org/10.1016/0143-6228\(86\)90026-3](https://doi.org/10.1016/0143-6228(86)90026-3).
- [3] Velasco-Muñoz, J.F.; Aznar-Sánchez, J.A.; Batlles-delaFuente, A.; Fidelibus, M.D. Rainwater Harvesting for Agricultural Irrigation: An Analysis of Global Research. *Water* 2019, 11, 1320. <https://doi.org/10.3390/w11071320>
- [4] Vieira, A.S.; Beal, C.D.; Ghisi, E.; Stewart, R.A. Energy intensity of rainwater harvesting systems: A review. *Renewable and Sustainable Energy Reviews*, Volume 34, 2014, Pages 225-242, ISSN 1364-0321, <https://doi.org/10.1016/j.rser.2014.03.012>.
- [5] Zenkert, D. *The Handbook of Sandwich Construction*. London: EMAS, 1997.
- [6] Allen, H.G. *Analysis and Design of Structural Sandwich Panels*. London: Pergamon Press, 1969.
- [7] ASTM C 273, Standard testing method for Shear Properties of Sandwich Core Materials Testing, ASTM International.
- [8] DIN 53293, Prüfung von Kernverbunden: Biegeversuch, Deutsche Institut für Normung e.V. 1982.
- [9] Feldhusen, J.; Torsakul, S.; Brezing, A.; Krishnamoorthy, S. Numerical modeling and experimental investigation of the failure modes of the cellular foam sandwich structures. MSAT-5: Proceedings of the 5th Thailand Materials Science and Technology Conference; Materials Technology for Climate Change. September 16 - 19, 2008, Mircale Grand Convention Hotel, Bangkok, Thailand. - Thailand : QES , 2008. - S./Art. 79-81
- [10] G. Pahl, G.; Beitz, W.; Feldhusen, J.; Grote, K-H. *Engineering Design: A Systematic Approach*. ISBN-13: 978-1846283185.
- [11] ASTM International Designation: F 1839 – 08: Standard Specification for Rigid Polyurethane Foam for Use as a Standard Material for Testing Orthopaedic Devices and Instruments
- [12] AMERICAN INSTITUTE OF STEEL CONSTRUCTION, AISC: ANSI/AISC 303-16 - Code of Standard Practice for Steel Buildings and Bridges. June 15, 2016.

# Preparation of polyvinyl alcohol and carboxymethyl cellulose hydrogel crosslinked with polyethylene glycol diacrylate for wound dressing

**Paweena Meedecha<sup>1</sup>, Patipat Srisongkram<sup>1</sup>, Siriwan Srisang<sup>2\*</sup>**

<sup>1</sup> Department of Energy Engineering, King Mongkut's Institute of Technology Ladkrabang, Prince of Chumphon Campus, Chumphon, paweenameedechea@gmail.com

<sup>1</sup> Department of Fundamental of Physics Laboratory, King Mongkut's Institute of Technology Ladkrabang, Prince of Chumphon Campus, Chumphon, patipat.sr@kmitl.ac.th

<sup>2\*</sup> Department of Energy Engineering, King Mongkut's Institute of Technology Ladkrabang, Prince of Chumphon Campus, Chumphon, siriwan.sr@kmitl.ac.th

**Abstract:** Wound dressings are essential in improving the quality of life for patients by protecting and promoting wound healing. Polyvinyl alcohol (PVA)-based hydrogel dressings have become increasingly important due to their versatile applications in various research fields. PVA can be combined with other synthetic polymers such as PEG, PU, PVP, AM, as well as natural polymers such as HA, chitosan, collagen, and carboxymethyl cellulose (CMC) to form composites with improved multifunctional properties, including mechanical and hydrophilic properties. This paper presents the determination of PVA/CMC for producing hydrogel wound dressings from a combination in ratios of 9:1, 7:3, and 1:1 composite synthesized using chemical cross-linking polyethylene glycol diacrylate (PEGDA) by freeze-thaw method. The aim was to determine the optimal PVA/CMC concentration ratio for potential application as a wound dressing material. Swelling water, tensile testing, and maximum load experiments were performed to assess the performance of the hydrogel. The results showed an increased 48h swell rate of 270%, 167%, and 256% respectively, and increase in maximum load and tensile strength by 0.14, 0.26, and 0.37 MPa, respectively, for different ratios of PVA/CMC. The optimum condition was the 9:1 PVA/CMC ratio due to suitable swelling and mechanical properties for wound dressing applications. This hydrogel composite has the potential to improve wound healing outcomes and has development application in wound healing.

**Keywords:** carboxymethyl cellulose, polyvinyl alcohol, hydrogel, wound dressing

## 1. <sup>1</sup>Introduction

Skin is a crucial part of the human body but is also fragile due to constant exposure to the environment. [1] While the body can heal wounds on its own, there are various factors that can hinder the healing process, such as inflammation, external pollution, and underlying medical conditions [2].

Wound dressings are necessary for promoting wound healing and protecting the wound from infections. An ideal wound dressing should have the ability to absorb excess fluid, provide moisture to prevent sticking to the wound [3], reduce the risk of repetitive injuries, and have sufficient mechanical strength to keep out external bacteria. Several types of wound dressings, such as foams, films, hydrocolloids, alginates, and hydrogels, have been developed to aid wound healing. [4] Hydrogels have become a major focus of research due to their hydrophilic nature, biocompatibility, and the growing demand for ideal

wound dressings. Hydrogel preparation can be achieved through various cycles, including the freeze-thaw process. This involves repeated freeze-thaw cycles that cause phase separation in the polymer solution, leading to the formation of hydrogels [5]. Polymer crystals also form at lower temperatures, creating a cross-sectional area that forms an insoluble polymer network. Freeze-thaw hydrogels are preferred over chemical methods due to their superior elastic properties [6].

CMC is a biocompatible polymer with good water solubility and biodegradability. It is widely used as a stabilizing and thickening agent in food and pharmaceutical emulsions [7]. PVA is another commonly used polymer in wound dressings and has been combined with various natural and synthetic polymers to form hydrogels. PVA is a partially crystalline polymer made by hydrolyzing PVA, and its good water solubility, biocompatibility, and biodegradability make it useful in a variety of applications, such as the food industry, pharmaceuticals, and textiles [8, 9]. PEGDA is also an important additive in hydrogel formation. In Browning's study [10], PEGDA at 10% as compared to PEGDAA at 10% as a hydrogel for enhanced biocompatibility and prevention of degradation failure over

long-term use. Both hydrogels showed similar cell adhesion and capacity for incorporating bioactivity, indicating that PEGDAA can be substituted for PEGDA. PEGDA is commonly used in the production of foams and sheets for technical and medical applications. It is a non-toxic chemical made from polyethylene, making it safe for human use [11]. Physical crosslinking methods, such as hydrogen bonding, Van der Waals bonding, or freeze-thaw, can be used to form a hydrogel. The freeze-thaw method is considered the safest for hydrogel formation [12].

Thus, this study has been conducted built upon previous research using PEGDA 10% to prepare composite hydrogels by investigating the potential benefits of adding CMC to PVA. The objective of this review is to explore various polymers that have been combined with PVA for wound dressings and to highlight the advancements in modern wound dressings. Biopolymers, synthetics, and composites have been used as PVA-based hydrogel additives to simplify the wound healing process and reduce sticking between the skin and the dressing during replacement. While hydrogel dressings are an attractive option that meets most requirements, their low mechanical stability remains a challenge. One possible solution is to blend multiple polymers and avoid using bonding agents to improve their mechanical properties.

## 2. Material and methods

### 2.1 Material

PVA, with a molecular weight of 89000-9800, was purchased through Sigma-Aldrich (St. Louis, USA). CMC was purchased through Krungthepchemi Co., Ltd. PEGDA Mn 700 was purchased through Aldrich Chemistry. Deionized water and all analytical grade solvents were purchased from Labvalley (Bangkok, Thailand) and used without further purification.

### 2.2 Methods

#### Preparation of PVA/CMC composite hydrogel

The hydrogel, PVA and CMC were dissolved in a solution containing PEGDA at 10% concentration [8]. The suitability of the concentration ratios of PVA 1 g in 100 ml and CMC 1 g in 100 ml at 1:1, 7:3, and 9:1 (PVA solution : CMC solution) was determined based on the relationship of hydrophilic changes in PVA and CMC ratio was adapted from a previously published of Pavandi et al. and Zhu et al. [5, 13] and known for their water solubility and non-toxicity. The slurries were properly selected, and their contents were controlled for each experimental purpose. The PVA and CMC were then dissolved in deionized water at room temperature ( $25 \pm 5$  °C) using a heated stirrer at 400 RPM for 3 hours to achieve even dispersion [12]. Next, the 10% PEGDA was added to the mixture and stirred for an additional 3 hours until well blended. The mixture was poured into a glass petri dish and subjected to 8 cycles of freeze-thaw, with each cycle consisting of 48 hours at -20°C followed by 24 hours at room temperature ( $25 \pm 5$  °C). The resulting hydrogel sheet will be further tested as a potential material for wound dressing.

### 2.3 Swelling ratio analysis

The swelling-level capability of hydrogels was evaluated to assess their inflation behavior. [14] Since the weight, size, and volume of hydrogels change with inflation, these parameters can be used to characterize their inflation capacity. This study was based on the literature of Djumaev et al. After freeze-drying, the samples were stored at room temperature. To measure the swelling rate, a 20 mm x 20 mm sample of the dressing was cut and weighed. The sample was then immersed in 4 mL of deionized water, and this process was repeated for 48 hours. [15] The inflation ratio of the balance weight and the equilibrium volumetric expansion rate [14, 16], also known as the swelling ratio, were used to measure the material's water uptake. The swelling ratio is defined as the ratio of the weight of water absorbed by the hydrogel upon inflation to its initial weight, as expressed by equation (1):

$$\text{Swelling ratio \%} = (W_t - W_o) / W_o \times 100\% \quad (1)$$

When  $W_t$  = weight of sample after immersion  $W_o$  = weight of dry sample. The swelling ratio was 0% when the sample was unable to absorb water and 1% when the sample was fully swollen, indicating a higher water absorption capacity of the material.

### 2.4 Mechanical properties

The mechanical properties of the wound dressing material were evaluated through tensile testing and maximum load using a Texture Analyzer according to the ASTM D288. Samples of the material were taken for analysis and were incubated at 50°C for 5 hours. The samples were then cut to a size of 2 cm x 10 cm using a Stable Micro Systems model TA-XT plus. The head movement speed was set at 10 mm/min and the samples were measured under a load of 100 N. [15]. Maximum load and tensile strength are two distinct material properties that have differences as follows maximum load is the weight that a material can withstand before cracking or other damage occurs. This property is typically determined through load tests, such as torsion or compression tests. Tensile strength is a measure of the maximum resistance of a material to fracture under tension. This property is typically determined through tensile tests. While maximum load and tensile strength are different material properties, they are related in that the maximum load of a material is dependent on its tensile strength. [17] The stress at maximum load in hydrogel refers to the amount of stress that the hydrogel material is experiencing at the point of maximum load during a mechanical testing process. Factors that can influence the stress at maximum load in hydrogels include their chemical composition, crosslinking density, and swelling behavior. Understanding the stress at maximum load in hydrogels is essential for developing and evaluating hydrogel-based materials for a wide range of applications, such as tissue engineering, drug delivery, and wound healing [18].

The study aimed to investigate the effects of different PVA/CMC/PEGDA10% ratios on the swelling ratio and tensile strength of the obtained PVA/CMC composite hydrogels. The best hydrogels with the highest swelling ratio and tensile strength were chosen as the standard, and hydrogels were prepared using various numbers of freeze-thaw cycles at different freezing times (Table 1) to achieve this goal.

### 3. Results and discussion

#### 3.1 General aspects

The PVA/CMC hydrogels were prepared through freeze-thaw cycles, in which during the freezing process, the frozen water in the PVA/CMC mixture led to phase separation into a water-rich phase and a polymer-rich phase. The polymer chains in the polymer-rich area created hydrogen bonds and crystallites. The thawing process promoted the interactions between the polymers and the crystalline regions. Thus, the hydrogel networks were created [6]. The swelling ratio and tensile strength of the achieved products varied from 279.95 to 405.38% and from 0.14 to 0.42 MPa.

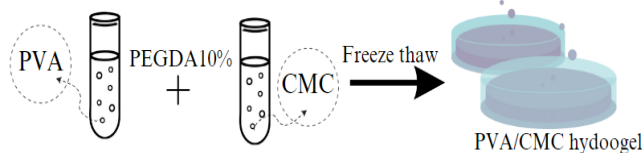


Fig. 1. Schematic illustration of the formation of freeze thaw, PVA/CMC hydrogels

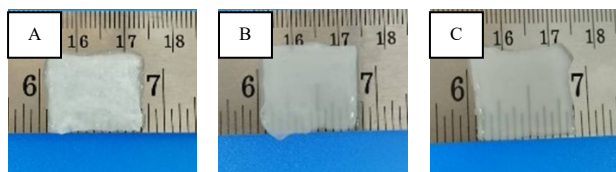


Fig. 2. Photographs of PVA/CMC membranes

#### 3.2 Swelling ratio

The swelling characteristics of PVA/CMC of the impact of inflation time on the inflation ratio of a reinforced polymer hydrogel in Deionized Water at neutral pH and room temperature. The weight of the PVA/CMC was measured at specific intervals. Figure 3 indicates that the swelling ratio of the PVA/CMC reaches its peak during the first 2 hours of swelling. The addition of CMC had a significant impact on the swelling ratio, as demonstrated by the higher swelling ratio at the 1:1 ratio. The swelling behavior of PVA/CMC at 9:1 and 7:3 both showed similar swelling ratios compared to the 1:1 ratio at both 2 until 48 hours. The swelling ratios were recorded for 48 hours, and the highest swelling rates at 2 hours were 311.47%, 405.38%, and 279.95%, respectively, after which they began to decline until the end of the test

period. The maximum swelling values at 48 hours were 270%, 167%, and 256%, respectively. This behavior is attributed to the permeable structure of the polymer hydrogel, which transforms into a fully saturated structure upon achieving maximum swelling due to the increased flexibility of the hydrogel polymer matrix. The osmotic inflation pressure explains the edema phenomenon, where water molecules and bonds form a fixed hydration shell around the hydrophilic group, resulting in an increased inflation ratio. [19, 20] Conversely, the water molecules trapped between the bonds are released after reaching the equilibrium rate of edema, which damages the PVA/CMC matrix and ultimately results in a reduced ratio. Un increase in swelling water was observed after 2 hours, and instead, a decrease was noted. Zhan et al. explained this result by demonstrating that the addition of crosslinking agents reduced the swelling property of the hydrogel and increased its mechanical strength, leading to a decrease in the inflation ratio. [14] PVA: CMC formed at a ratio of 1:1 exhibited the highest water absorption capacity, but it was not as stable as the hydrogel formed at a ratio of 9:1, which showed more consistent swelling water properties.

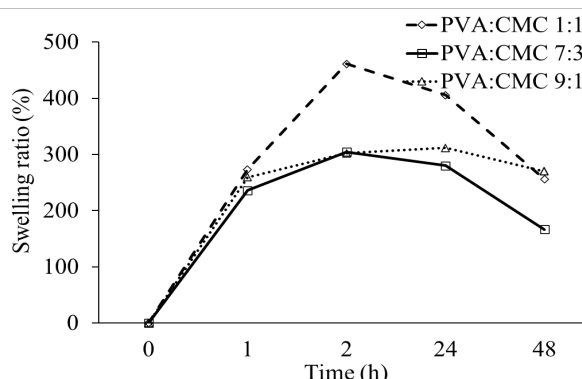


Fig. 3. Swelling ratio PVA/CMC hydrogel

#### 3.3 Mechanical properties

Mechanical properties are essential for the development of effective wound dressings that can maintain integrity and protect the damaged area from external forces. [17] Therefore, tensile tests were performed to evaluate the stretchability of wound dressings with different compositions. The maximum load for a wound dressing typically refers to the maximum amount of force or pressure that can be applied to the dressing before it becomes damaged or loses its ability to protect the wound. The results revealed that swelling is a relevant factor in hydrogel characteristics, representing the hydrogel's ability to absorb and bind water. However, the use of hydrogels in wound dressings requires consideration not only of swelling properties but also of the polymer's resistance to excessive deformation, which is associated with the maximum load value, the tensile properties of the hydrogel, and its ability to return to its original state when subjected to external interference and polymer network structure [21]. Tensile strength corresponds to maximum load and indicates the polymer's resistance to excessive deformation. In Figure 3a,

an increase in PVA makes the hydrogel maximum load at 1.5, 4.5, and 5 N respectively and tensile strength at 0.14, 0.26, and 0.37 MPa respectively in figure 3b, while a decrease in CMC makes it more flexible. Moreover, the increasing trend of swelling value results in decreased tensile strength. Hydrogels are soft, gel-like materials that can exhibit unique mechanical properties, such as high-water content, high deformability, and low mechanical strength. The stress at maximum load in hydrogels can provide insights into the material's ability to withstand mechanical stress before experiencing failure or damage. In figure 3c the stress at maximum load in hydrogels can influence the swelling behavior of the material in water. Hydrogels can absorb large amounts of water, which can cause them to swell and change in size and shape. The degree of swelling in hydrogels is influenced by various factors, such as crosslinking density, polymer composition, and external mechanical stimuli. When hydrogels are subjected to mechanical stress, such as tension or compression, it can affect their ability to absorb water and swell. High stress at maximum load can cause the hydrogel to deform and reduce its ability to absorb water, while low stress at maximum load may allow the hydrogel to absorb more water and swell to a greater degree. [22] Therefore, the stress at maximum load in hydrogels can influence the swelling behavior of the material, which is an important consideration for developing hydrogel-based materials for various applications, such as drug delivery and tissue engineering.

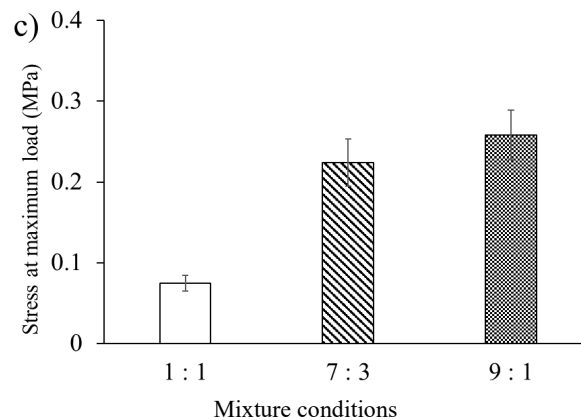
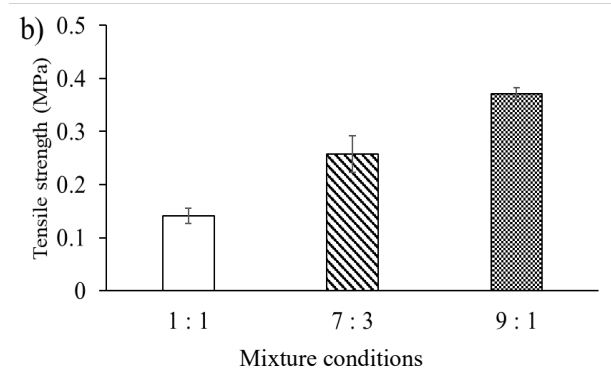
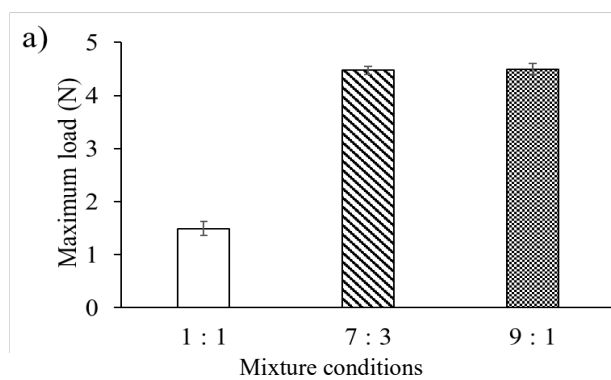


Fig. 4. Mechanical test of the PVA/CMC wound dressing: a) maximum load b) tensile strength c) Stress at maximum load

#### 4. CONCLUSION

In conclusion, the study demonstrated that the combination of PVA and CMC with PEGDA using the freeze-thaw technique has potential as a wound dressing material. By varying the PVA/CMC ratio, it was found that the 9:1 ratio composite exhibited optimal swelling and mechanical properties for wound dressing applications. The hydrogel showed an increase in maximum load and tensile strength, as well as a high swell rate. This finding has important clinical implications as the development of new and improved wound dressings can have a significant impact on patient care and outcomes.

#### Acknowledgment

This work was supported and financially funded by KREF016424

#### REFERENCES

- Kong, Y., et al., Degradable tough chitosan dressing for skin wound recovery. *Nanotechnology Reviews*, 2020. 9(1): p. 1576-1585.
- Qu, J., et al., Antibacterial adhesive injectable hydrogels with rapid self-healing, extensibility and compressibility as wound dressing for joints skin wound healing. *Biomaterials*, 2018. 183: p. 185-199.
- Farid, E., et al., PVA/CMC/attapulgitte clay composite hydrogel membranes for biomedical applications: factors affecting hydrogel membranes crosslinking and bio-evaluation tests. *Journal of Polymers and the Environment*, 2022. 30(11): p. 4675-4689.
- Kamoun, E.A., E.-R.S. Kenawy, and X. Chen, A review on polymeric hydrogel membranes for wound dressing applications: PVA-based hydrogel dressings. *Journal of advanced research*, 2017. 8(3): p. 217-233.
- Pavandi, N., E. Taghavi, and N. Anarjan, preparatoin of carboximethyl cellulose and polyvinyl alcohol (CMC/PVA) hydrogels using freeze-thaw processes for adsorption of Zn<sup>2+</sup> and Cu<sup>2+</sup>. *cellulose chemistry and tecnology*, 2021. 55(3-4): p. 375-383.
- Hong, K.H., Polyvinyl alcohol/tannic acid hydrogel prepared by a freeze-thawing process for wound dressing applications. *Polymer Bulletin*, 2017. 74(7): p. 2861-2872.
- Mali, K., et al., Citric acid crosslinked carboxymethyl cellulose-based composite hydrogel films for drug delivery.

- Indian Journal of Pharmaceutical Sciences, 2018. 80(4): p. 657-667.
8. Wang, L.-Y. and M.-J. Wang, Removal of heavy metal ions by poly (vinyl alcohol) and carboxymethyl cellulose composite hydrogels prepared by a freeze–thaw method. *ACS Sustainable Chemistry & Engineering*, 2016. 4(5): p. 2830-2837.
  9. Kenawy, E.-R., et al., Physically crosslinked poly (vinyl alcohol)-hydroxyethyl starch blend hydrogel membranes: Synthesis and characterization for biomedical applications. *Arabian Journal of Chemistry*, 2014. 7(3): p. 372-380.
  10. Browning, M.B. and E. Cosgriff-Hernandez, Development of a biostable replacement for PEGDA hydrogels. *Biomacromolecules*, 2012. 13(3): p. 779-786.
  11. Debroy, D., J. Oakey, and D. Li, Interfacially-mediated oxygen inhibition for precise and continuous poly (ethylene glycol) diacrylate (PEGDA) particle fabrication. *Journal of colloid and interface science*, 2018. 510: p. 334-344.
  12. de Paiva, P.H.E.N., et al., Film production with flaxseed mucilage and polyvinyl alcohol mixtures and evaluation of their properties. *Journal of Food Science and Technology*, 2021. 58: p. 3030-3038.
  13. Zhu, J., et al., Effect of Na<sub>2</sub>CO<sub>3</sub> on the microstructure and macroscopic properties and mechanism analysis of PVA/CMC composite film. *Polymers*, 2020. 12(2): p. 453.
  14. Zhan, Y., et al., Advances in versatile anti-swelling polymer hydrogels. *Materials Science and Engineering: C*, 2021. 127: p. 112208.
  15. Djumaev, A. and S. Tashmukhamedova, Physical and chemical properties of PVA-CMC based hydrogel carrier loaded with herbal hemostatic agent for application as wound dressings. *National Journal of Physiology, Pharmacy and Pharmacology*, 2020. 10(10): p. 905-905.
  16. Dimatteo, R., N.J. Darling, and T. Segura, In situ forming injectable hydrogels for drug delivery and wound repair. *Advanced drug delivery reviews*, 2018. 127: p. 167-184.
  17. Annabi, N., et al., Engineering a sprayable and elastic hydrogel adhesive with antimicrobial properties for wound healing. *Biomaterials*, 2017. 139: p. 229-243.
  18. Horkay, F. and P.J. Basser, Hydrogel composite mimics biological tissues. *Soft Matter*, 2022. 18(23): p. 4414-4426.
  19. Mittal, H., A. Maity, and S.S. Ray, Gum ghatti and poly (acrylamide-co-acrylic acid) based biodegradable hydrogel-evaluation of the flocculation and adsorption properties. *Polymer Degradation and Stability*, 2015. 120: p. 42-52.
  20. Kamaliya, B., P.N. Dave, and P.M. Macwan, Rheological investigations and swelling behaviour of hydrogels based on gum ghatti-cl-poly (N-isopropyl acrylamide-co-acrylic acid)/CoFe<sub>2</sub>O<sub>4</sub> nanoparticles. *Polymer Bulletin*, 2022: p. 1-22.
  21. Fu, R., et al., A tough and self-powered hydrogel for artificial skin. *Chemistry of Materials*, 2019. 31(23): p. 9850-9860.
  22. Chen, Y., et al., Biomimetic anisotropic poly (vinyl alcohol) hydrogels with significantly enhanced mechanical properties by freezing–thawing under drawing. *Journal of Materials Chemistry B*, 2019. 7(20): p. 3243-3249.

# Application of Monte Carlo Simulation Techniques for Appropriate Minibus Service Management During Rush Hours

**Sanguan Vongchavalitkul<sup>1</sup>, Marut Khodphan<sup>2</sup>, Supagrid Prewthaisong<sup>3\*</sup>**

<sup>1,2</sup>Department of Engineering Management, Faculty of Engineering, Vongchavalitkul University, Nakhon Ratchasima, [sanguan\\_vong@vu.ac.th](mailto:sanguan_vong@vu.ac.th) and [marut\\_kho@vu.ac.th](mailto:marut_kho@vu.ac.th)

<sup>3\*</sup> Student, Engineering Management, Faculty of Engineering, Vongchavalitkul University, Nakhon Ratchasima, [therobot44@hotmail.com](mailto:therobot44@hotmail.com)

**Abstract:** The purpose of this research is to study the appropriate management of minibus services in order to reduce wait times during rush hours. Because minibus services currently lack a system that meets the needs of service users, there may be congestion and overcrowding on minibuses, as well as unsafe trips. The researcher conducted surveys and data collection in four key locations: the bus stop in front of Payup Temple, New Klang Plaza Department Store, Suranaree Wittaya School, and Nakhon Ratchasima Rajabhat University. The data were then simulated using the Monte Carlo method under the queuing theory, and the average number of people waiting at the bus stop was dealt with using the Pareto Diagram, and the analysis results were used as a guideline for minibus operation management. The research results can be divided into two categories: Case 1: Minibus service during the morning rush hours for inbound trips by taking into consideration increasing the number of minibus lines 1, 4, 5, 6, 7, 8, 15, 4287, and 4424 by one service unit each; for outbound trips by taking into consideration increasing the number of minibus lines 2, 4, 5, 6, 7, 14 and 18 by one service unit each. Case 2: Minibus service during the evening rush hours for inbound trips by taking into consideration increasing the number of minibus lines 1, 4, 5, 6, 7, 8, 11, 14, and 4424 by one service unit each; for outbound trips by taking into consideration increasing the number of minibus lines 2, 4, 5, 6, 7, 10, and 14 by one service unit each.

**Keywords:** Monte Carlo, Minibus, Management of minibus, Pareto.

## I. INTRODUCTION

Nakhon Ratchasima Province has stepped into being a metropolis of the northeastern region and a center of economic investment according to the smart city development plan or smart city that is building a city for sustainable growth. At the same time, there is an increase in population. According to the Nakhon Ratchasima Provincial Statistical Office [1] the total population is approximately 2.6 million people, ranking second in the country. Mueang Nakhon Ratchasima District has a population of approximately 500,000 people, or 615.3 people per square kilometer. There is also a rapid increase in latent population as more rural workers migrate to cities to live and work. As a result, traffic volume has increased over the last few years. The traffic condition faces congestion problems. Traffic is delayed during rush hours and is likely to intensify. The government also recognizes the need for a more efficient mass transit system in the future to alleviate traffic congestion in Nakhon Ratchasima and to support the development of a sub-regional economic center city that contributes to the long-term benefits of

Nakhon Ratchasima Province, such as improving people's quality of life and promoting the province's tourism. However, public buses of the minibus remain important for passenger transportation in Nakhon Ratchasima and have been popular for a long time. At present, it is not possible to find other types of public transportation that are better to support the trips needs of the people in the city. But passenger transport services of minibuses still need to be improved due to the high demand of passengers during rush hours. As a result, minibuses in some areas are unable to serve as well as they should, particularly in urban areas near Thao Suranaree Monument, schools, and universities, where the number of passengers using bus services exceeds the capacity of the existing transportation system or carrying passengers exceeding the vehicle capacity standards specified by the Department of Land Transport.

For this reason, the researcher is interested in studying the appropriate way to manage the service of the minibus and create satisfaction for the customers during rush hours with the Monte Carlo simulation method under the queuing theory and deal with the problem of the average number of people waiting around the bus stop by applying the Pareto Diagram to consider increasing the number of minibuses to solve further problems. This research will also help to



improve minibus management in the municipality of Nakhon Ratchasima in the future.

## II. RELATED THEORY

### 1. Simulation

Simulation is the creation of a hypothetical situation based on facts. To attempt to solve the problem and analyze the results of the experiment before applying to real-world problems [2]. In terms of discrete event replication from queuing theory, the results obtained can be used to analyze the number of service units that are most appropriate. According to the model's queuing structure, M/M/1 is a single channel-multiple phase system, and M/M/S is a multiple channel-multiple phase system [3], where the number of service units can be added based on the service users.

Monte Carlo modeling generates simulated events by utilizing event probabilities [4]. By assuming how much each event will occur based on the probability of that event using random numbers is a tool that generates random events with RAND() from Microsoft Excel which The model is used to predict the probability of a variety of outcomes when the possibility of random variables exists, and it is appropriate for issues that are too complex to solve using mathematical approaches.

### 2. Statistical Analysis

This time, the statistical analysis of the arrival times of the service units and service users makes use of the normal probability distribution model [5], and the cumulative distribution function (CDF) is chosen for this research as shown below in (1)

$$F(x) = \Phi\left[\frac{(x-\mu)}{\sigma}\right] \quad (1)$$

Here,  $\Phi(\cdot)$ ,  $\mu$  and  $\sigma$  are the cumulative distribution function values, mean and standard deviation respectively.

Then transform  $F(x)$  of the normal distribution into a linear form, the random variable  $x$  [6] that appears in (1) can be obtained as shown below in (2)

$$x = \sigma\Phi^{-1}[F(x)] + \mu \quad (2)$$

For the number of times ( $n$ ) in the simulation is shown below in (3)

$$n = \left(\frac{\sigma Z_{\alpha/2}}{E}\right)^2 \quad (3)$$

Here,  $Z_{\alpha/2}$  and  $E$  are the upper bound at significance level  $\alpha$ , the value of error at level 0.05 respectively.

### 3. Pareto Diagram

A Pareto chart is used to examine organizational problems and determine which problems are the most important in order. Then, bring those problems or causes to be categorized or classified and sorted in descending order, to demonstrate how the ratio of each problem to all problems is represented by a bar graph, with the highest being the most common problem, and the organization must pay attention to solving it [7].

Pareto's law is as follows:

1) 80 percent problems result from a given situation or system determined by 20 percent of causes. The percentages are not always 80/20, they can be different but focus on what is important.

2) Applying Pareto's law in the organization is characterized by doing less but getting more results and allow us to prioritize what needs to be developed first or later, which will help executives and employees to work more efficiently.

## III. RESEARCH METHODS

### 1. Study area and data collection

The researcher chose an urban sub-district area as the study area to collect data on service units and service users of minibus services in Nakhon Ratchasima Province because most minibuses run into the city center. To cover all objectives of the target group, this research conducted a survey of information in places that are the travel centers of each target group, such as educational institutions, government offices, private companies, department stores, and others, as well as accommodation along the route of the mass transit system within a radius of not more than 1 kilometer, which can be divided into four main bus stops, as follows:

1) At the bus stop in front of Payap Temple, there are 11 minibuses consisting of 5, 7, 8, 11, 15, 20, 1307, 4140, 4234, 4287 and 4416.

2) At the bus stop in front of the New Klang Plaza Department Store, there are 19 minibuses consisting of 1, 2, 4, 5, 6, 7, 10, 11, 12, 13, 14, 15, 18, 20, 1307, 4140, 4234, 4287 and 4416.

3) At the bus stop in front of Suranaree Witthaya School, there are 6 minibuses consisting of 4, 5, 6, 11, 4234 and 4416.

4) At the bus stop in front of Nakhon Ratchasima Rajabhat University, there are 5 minibuses consisting of 1, 6, 14, 4139 and 4424 as shown in Fig. 1.

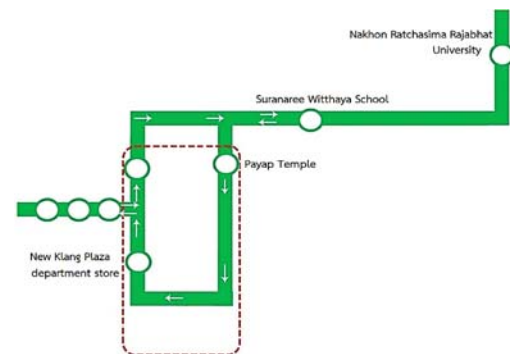


Fig. 1. Location for surveying and collecting data

Collecting data by observing the measurement of time and the number of people in the target area at the bus stop between 12-18 November 2020 from Monday to Sunday. By dividing the time into 2 periods, namely morning rush hours from 7:00 a.m. to 8:30 a.m. and evening rush hours from 4:00 p.m. to 6:00 p.m. and recording on the survey

form as follows: Minibus arrival time, Number of people on the minibus, Number of people getting off the minibus and Number of people boarding the minibus.

## 2. Simulation methods

1) Create a model by using MS-Excel as a tool for analyzing and evaluating the results of the system. By setting the number of service units from 1 unit to the maximum service unit studied is 4 units by using RAND() command in which the service system does not roll back and everyone who enters the system must be serviced.

2) Start time of the system at 7.00 a.m. and 4.00 p.m. by releasing the first minibus into the system and determining that there is no service unit in the system. At this time, random numbers will be used instead of events of possible events, to find the result of minibus arrival time, number of people on the minibus, number of people getting off the minibus and number of people boarding the minibus in each period.

3) The service users can get on the minibus if there are empty seats on the minibus but they must not go up to the minibus's capacity. (The standard capacity of the minibus can seat 10 people without standing) and if there are passengers in the minibus that are full or more than the minibus's capacity, service users cannot get on the minibus. But if there are people getting off at this bus stop and there are empty seats, service users can get on the minibus.

4) Service users must wait for the next minibus when the number of passengers in the minibus is full or more than the minibus's capacity. Although there are people getting off at this bus stop, but there are passengers on the minibus that are more than or equal to the capacity of the bus, so they cannot get on the minibus. An example of the simulation of the minibus line 5 at the bus stop in front of Payap Temple is shown in Fig. 2.

No. 5	bus arrival time	time h:mm:ss	Number of people on the minibus	Number of people boarding the minibus	Number of people getting off the minibus	Total people take a trip by minibus	Number of available seats	People waiting for this minibus	Cumulative number of people waiting
							Seats no more than 10 people		
1	07:12:40	00:11:43	7.88	0.30	1.61	6.57	3.43	0.00	0.00
2	07:24:23	00:10:50	8.83	2.15	3.66	7.32	2.68	0.00	0.00
3	07:35:13	00:06:19	9.01	0.00	0.00	9.01	0.99	0.00	0.00
4	07:41:32	00:10:04	6.63	2.45	0.00	9.08	0.92	0.00	0.00
5	07:51:35	00:08:34	11.45	2.50	1.48	10.00	0.00	2.47	2.47
6	08:00:09	00:09:41	12.43	4.03	0.00	12.43	0.00	4.03	6.50
7	08:09:50	00:10:19	5.27	2.24	0.99	6.52	3.48	0.00	3.02
8	08:20:09	00:10:44	7.55	2.27	1.86	7.96	2.04	0.00	0.98
9	08:30:53	00:07:34	5.48	2.43	0.00	7.91	2.09	0.00	0.00
10	08:38:27	00:12:19	9.08	0.00	1.71	7.37	2.63	0.00	0.00
11	08:50:46	00:08:58	10.19	0.00	1.63	8.56	1.44	0.00	0.00
12	08:59:43	00:12:17	13.00	0.00	0.73	12.27	0.00	0.00	0.00
13	09:12:01	00:10:22	10.73	0.00	2.61	8.12	1.88	0.00	0.00
14	09:22:23	00:06:56	9.07	0.00	2.89	6.18	3.82	0.00	0.00
15	09:29:19	00:07:59	6.60	3.37	3.20	6.77	3.23	0.00	0.00
Average			8.70	1.39	1.62	8.14	2.05	0.34	0.61
S.D.			2.13	1.23	1.16	1.80	1.42	0.98	1.48

Fig. 2. Monte Carlo simulation example

## IV. RESEARCH RESULTS

### 1. Analyze simulation results

#### 1) In front of Payap Temple

The average number of people waiting are calculated from 100 replications of the simulation based on Equation (3).

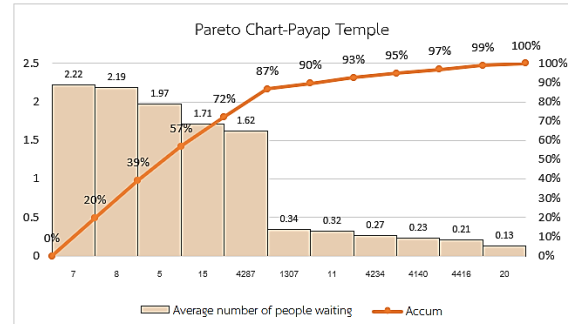


Fig. 3. Pareto sorts data from critical points descending in the morning rush hours

According to the simulation results, the minibus line 7 had the highest average number of people waiting at the bus stop during the morning rush hours in front of Payap Temple, with 2.22 people, followed by line 8 with an average of 2.19 people, and line 20 had the fewest passengers, with an average of 0.13 people. Consider the proportion of the problem at 80% according to Pareto's law; in this instance, the cutoff is 87%, as shown in Fig. 3, it was discovered that the cause of the highest average number of people waiting at this bus stop was lines 7, 8, 5, 15, and 4287, respectively. As a result, the cause of these minibuses should first be considered to be solved by increasing the number of these minibuses by one service unit each. So that the minibus can provide enough services to meet the needs of service users.

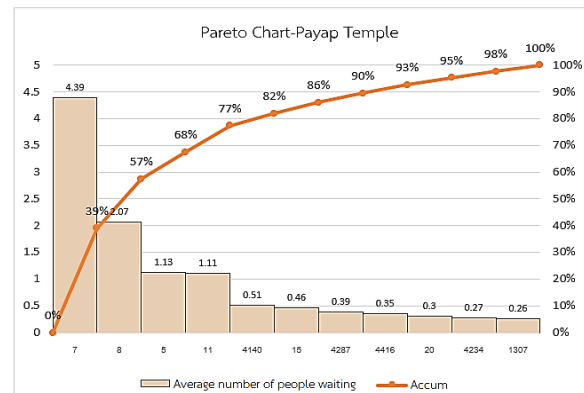


Fig. 4. Pareto sorts data from critical points descending in the evening rush hours

According to the simulation results, the minibus line 7 had the highest average number of people waiting at the bus stop during the evening rush hours in front of Payap Temple, with 4.39 people, followed by line 8 with an average of 2.07 people, and line 1307 had the fewest passengers, with an average of 0.26 people. Consider the proportion of the problem at 80% according to Pareto's law; in this instance, the cutoff is 82%, as shown in Fig. 4, it was discovered that the cause of the highest average number of people waiting at this bus stop was lines 7, 8, 5, 11 and

4140, respectively. As a result, the cause of these minibuses should first be considered to be solved by increasing the number of these minibuses by one service unit each. So that the minibus can provide enough services to meet the needs of service users.

In analyzing the simulation results to find the average number of people waiting at the bus stop in front of Klang Plaza Department Store, Suranaree Wittaya School, and Nakhon Ratchasima Rajabhat University can explain the result in the same way as in front of Wat Payap, which had the following simulation results:

#### 2) In front of Klang Plaza Department Store

According to the simulation results during the morning rush hour, minibus line 7 had the highest average number of people waiting at 2.98 people, followed by line 4 with an average of 2.36 people, and line 13 with the fewest passengers, with an average of 0.37 people. The analysis of the results in the Pareto Chart revealed that it was discovered that the cause of the highest average number of people waiting at this bus stop was lines 7, 4, 2, 6, 15, 18, 4287, 5, and 1. During the evening rush hours, the minibus line 7 had the highest average number of people waiting at 3.55 people, followed by line 6 with an average of 3.15 people, and line 4234 with the fewest passengers, with an average of 0.45 people. The analysis of the results in the Pareto Chart revealed that it was discovered that the cause of the highest average number of people waiting at this bus stop was lines 7, 6, 5, 2, 4, 14, 10, and 11. Therefore, the cause of these minibuses should be first considered to be solved by increasing the number of these minibuses by one service unit each. So that the minibus can provide enough services to meet the needs of service users.

#### 3) In front of Suranaree Wittaya School

##### 3.1) Minibus inbound

According to the simulation results during the morning rush hour, minibus line 6 had the highest average number of people waiting at 2.72 people, followed by line 5 with an average of 2.66 people, and line 4234 with the fewest passengers, with an average of 0.46 people. The analysis of the results in the Pareto Chart revealed that it was discovered that the cause of the highest average number of people waiting at this bus stop was lines 6, 5, and 4. During the evening rush hour, the minibus line 4 had the highest average number of people waiting at 3.18 people, followed by line 5 with an average of 3.08 people, and line 4234 with the fewest passengers, with an average of 0.53 people. The analysis of the results in the Pareto Chart revealed that it was discovered that the cause of the highest average number of people waiting at this bus stop was lines 4, 5, 6, and 11. Therefore, the cause of these minibuses should be first considered to be solved by increasing the number of these minibuses by one service unit each. So that the minibus can provide enough services to meet the needs of service users.

##### 3.2) Minibus outbound

According to the simulation results during the morning rush hour, minibus line 4 had the highest average number of people waiting at 2.08 people, followed by line 5 with an average of 1.97 people, and line 4234 with the fewest passengers, with an average of 0.54 people. The analysis of

the results in the Pareto Chart revealed that it was discovered that the cause of the highest average number of people waiting at this bus stop was lines 4, 5, and 6. During the evening rush hour, the minibus line 4 had the highest average number of people waiting at 2.41 people, followed by line 5 with an average of 2.25 people, and line 4234 with the fewest passengers, with an average of 0.54 people. The analysis of the results in the Pareto Chart revealed that it was discovered that the cause of the highest average number of people waiting at this bus stop was lines 4, 5, and 6. Therefore, the cause of these minibuses should be first considered to be solved by increasing the number of these minibuses by one service unit each. So that the minibus can provide enough services to meet the needs of service users.

#### 4) In front of Nakhon Ratchasima Rajabhat University

##### 4.1) Minibus inbound

According to the simulation results during the morning rush hour, minibus line 1 had the highest average number of people waiting at 2.09 people, followed by line 4424 with an average of 1.76 people, and line 4139 with the fewest passengers, with an average of 0.38 people. The analysis of the results in the Pareto Chart revealed that it was discovered that the cause of the highest average number of people waiting at this bus stop was lines 1, 4424, and 6. During the evening rush hour, the minibus line 1 had the highest average number of people waiting at 4.06 people, followed by line 14 with an average of 1.17 people, and line 4139 with the fewest passengers, with an average of 0.48 people. The analysis of the results in the Pareto Chart revealed that it was discovered that the cause of the highest average number of people waiting at this bus stop was lines 1, 14, and 4424. Therefore, the cause of these minibuses should be first considered to be solved by increasing the number of these minibuses by one service unit each. So that the minibus can provide enough services to meet the needs of service users.

##### 4.2) Minibus outbound

According to the simulation results during the morning rush hour, minibus line 6 had the highest average number of people waiting at 2.49 people, followed by line 14 with an average of 2.13 people, and line 4139 with the fewest passengers, with an average of 0.37 people. The analysis of the results in the Pareto Chart revealed that it was discovered that the cause of the highest average number of people waiting at this bus stop was lines 6 and 14. During the evening rush hour, the minibus line 6 had the highest average number of people waiting at 2.16 people, followed by line 14 with an average of 1.48 people, and line 1 with the fewest passengers, with an average of 0.36 people. The analysis of the results in the Pareto Chart revealed that it was discovered that the cause of the highest average number of people waiting at this bus stop was lines 6 and 14. Therefore, the cause of these minibuses should be first considered to be solved by increasing the number of these minibuses by one service unit each. So that the minibus can provide enough services to meet the needs of service users.

## V. CONCLUSION

In this study area, the minibus route runs from the bus stop in front of Payap Temple to the bus stop in front of Klang Plaza Department Store, then continues in front of Suranaree Witthaya School and ends in front of Nakhon Ratchasima Rajabhat University, a total distance of approximately 5 kilometers. and not all minibuses must pass through these four points because some pass through only two or one point at times. The distance from Payap Temple to Klang Plaza Department Store is a one-way route, and the distance from Suranaree Wittaya School to Nakhon Ratchasima Rajabhat University is a two-way route. Therefore, when considering increasing the number of minibus in each line, all four bus stops will be considered simultaneously by looking at the data showing the critical point with the average number of people waiting at the bus stop by the Pareto Chart that is used as a guideline for minibus service management, which can be divided into 2 cases as follows:

Case 1: Minibus service during the morning rush hours for inbound trips by taking into consideration increasing the number of minibus lines 1, 4, 5, 6, 7, 8, 15, 4287, and 4424 by one service unit each; for outbound trips by taking into consideration increasing the number of minibus lines 2, 4, 5, 6, 7, 14 and 18 by one service unit each.

Case 2: Minibus service during the evening rush hours for inbound trips by taking into consideration increasing the number of minibus lines 1, 4, 5, 6, 7, 8, 11, 14, and 4424 by one service unit each; for outbound trips by taking into consideration increasing the number of minibus lines 2, 4, 5, 6, 7, 10, and 14 by one service unit each.

However, in increasing the number of minibuses, the researcher took into account the necessity and value of each trip. Whether it's a variable expense like fuel, depreciation, wear and tear, or other costs that affect the number of additional minibuses, it's important for service users to be comfortable and safe during their trips.

## ACKNOWLEDGMENT

The author would like to acknowledge Vongchavalitkul University for supporting and students from faculty of engineering who helped collect data for this research.

## REFERENCES

- [1] Nakhon Ratchasima Provincial Statistical Office. "Nakhon Ratchasima Province Statistical Report," n.p., Nakhon Ratchasima, 2020.
- [2] J. Muensrichai, "Finding the quantity of raw material purchases under uncertainty with the Monte Carlo simulation method," Master's thesis, Dept. Industrial Engineering, Faculty of Engineering, King Mongkut's University of Technology North Bangkok, Bangkok, 2008.
- [3] C. Ruangsoon, "An approximation of estimated time of arrival for SUT internal bus services using intelligence transportation system." Master's thesis, Dept. Telecommunication and Computer Engineering, Faculty of Engineering, Suranaree University of Technology, Nakhon Ratchasima, 2020.
- [4] A. Tamwai, "Identifying the optimal safety stock level by using monte carlo simulation," Master's thesis, Dept. Industrial Engineering, Faculty of Engineering, Rajamangala University of Technology Thanyaburi, Pathum Thani, 2014.
- [5] E. E. Lewis, "Introduction to Reliability Engineering," 2nd ed. Evanston, Illinois: John Wiley & Sons Inc, 1994.

[6] N. Chumrit, "Engineering Statistics," Bangkok: SE-ED Publishing, 2013.

[7] R. Budpech and J. Aonsuwan, (2022, September 19), "7 Quality Control Tools," [Online], Retrieved from [http://sc2.kku.ac.th/stat/statweb/images/Eventpic/60/Seminar/02\\_13\\_-7-.pdf](http://sc2.kku.ac.th/stat/statweb/images/Eventpic/60/Seminar/02_13_-7-.pdf)

# The effects of solution height and titanium dioxide photocatalyst concentration on atrazine photodegradation efficiency

Chatiya Ardchon<sup>1</sup>, Chanintorn Patipatranon<sup>1</sup>, Nootprawee Singkwang<sup>1</sup>,  
Patthranit Wongpromrat<sup>1\*</sup>, Hsisheng Teng<sup>2</sup>

<sup>1</sup> Department of Chemical Engineering, King Mongkut's Institute of Technology Ladkrabang, Bangkok 10520, Thailand, staffcotch@gmail.com

<sup>1</sup> Department of Chemical Engineering, King Mongkut's Institute of Technology Ladkrabang, Bangkok 10520, Thailand, chanintorn.pn@gmail.com

<sup>1</sup> Department of Chemical Engineering, King Mongkut's Institute of Technology Ladkrabang, Bangkok 10520, Thailand, nootprawee.sin@gmail.com

<sup>1\*</sup> Department of Chemical Engineering, King Mongkut's Institute of Technology Ladkrabang, Bangkok 10520, Thailand, patthranit.wo@kmitl.ac.th

<sup>2</sup> Department of Chemical Engineering, National Cheng Kung University, Tainan 70101, Taiwan, hteng@mail.ncku.edu.tw

**Abstract:** Photodegradation reaction is reaction that use light to provide energy to the reactants, which are absorbed by chemical bonds in the molecules of the substance and cause the bond cleavage to form new substances of smaller size. Photodegradation reaction can be classified into 2 types: without and with the catalyst. This research studied the photodegradation of atrazine by using UVC light source with the wavelength of 253.7 nanometers. The effects of reaction parameters such as solution height and titanium dioxide photocatalyst concentration were demonstrated. The concentrations of atrazine were analyzed by High Performance Liquid Chromatography (HPLC). The experimental results showed that the atrazine can be degraded by such UVC lamp. For the without catalyst reaction case, the experimental results were satisfactorily obeyed by the first-order kinetic model and the increase in solution height leads to the decrease in degradation efficiency because increasing height of solution decreased the ability to transfer energy from the surface to the bottom of solution. In case that the catalyst was used, the catalyst concentrations either increased or decreased the degradation efficiency. The increase in efficiency occurred when the concentrations of the catalyst were 1, 2 and 4 g/L at 3 and 4 cm-heights of solution leading to acceleration of the reaction rate compared with the case that the catalyst was not used. This implied that the catalyst was able to provide a new reaction pathway with lower activation energy. On the other hand, the decrease in degradation efficiency was also observed when the concentration of the catalyst was more than 1 g/L at 2 cm-height of solution. This may be caused by the sedimentation of catalyst at high concentrations, resulting in the decrease in the active reaction sites which were the surface area of the catalyst.

**Index Terms**—Atrazine, Photodegradation, Photocatalysis, Photocatalyst Concentration

## I. INTRODUCTION

Atrazine is a triazine herbicide that is effective in controlling broadleaf, narrow leaf weeds, grass weeds and a variety of weeds to promote the growth of many plants [1]. The use of atrazine has been begun in 1958 and global production has been begun in 1987 at approximately 70,000 metric tons [2]. In 1993, United States Environmental Protection Agency (EPA) has stated that approximately 32,000 to 34,000 metric tons of atrazine are used in agricultural sector [3]. In Thailand, variety of herbicides such as atrazine, glyphosate, paraquat, ametrine have been used. From 2010 to 2019, more than 80,000 tons of

herbicides were imported per year in total. Among these atrazine is one of the top imported chemicals in Thailand. It is widely used in many agricultural areas such as cornfield, pineapple plantations, sugar cane plantations across the country [4,15].

Atrazine applications must be handled with cautions because winds may blow atrazine where it is not intended to be, causing damage to other plants, the contamination into water, atmosphere and land resulting in highly polluted areas. It is reported that atrazine was not only found in agricultural fields but was also found in the excessive amounts of contamination in water sources and other environments [8]. Due to the high severity of its effects, some people are now becoming aware of and have opposed to use atrazine. Some countries have begun legislation to

regulate the concentration and dosage of atrazine used. The European Union has banned its use in the relevant countries since 2004, although people are well aware of the negative effects of the atrazine. Although there are several advantages, its degradation is rather difficult. Therefore, the problem of atrazine is decisively irreparable [5].

From the studies and research, many methods have been used to degrade atrazine, i.e., physical methods such as adsorption and the use of membrane separation, but the material selection is the big issue that must be considered. For the destruction by heat or pyrolysis, even though the removal efficiency is high, but it produces toxic and/or corrosive gases. For the biodegradation, microbial remediation or phytoremediation, their disadvantages are slow degradation [4,5].

Therefore, in this work, the batch of photocatalytic degradation of atrazine was studied because it is the clean and low-cost process. It is also a fast and highly efficient method which is able to decompose the chemicals even though the catalyst is not used. Significantly, the photocatalytic degradation generates very little waste from the degradation process [6,7]. Titanium dioxide ( $\text{TiO}_2$ ) is the photocatalyst most widely used for technological applications because of its outstanding properties, such as high chemical stability, strong oxidizing power, non-toxicity and great acceleration of radicals generation [26,27]. Factors affecting the efficiency of atrazine degradation, particularly the depth of solution and the catalyst addition concentration were studied for the optimum degradation rate in the removal of large amounts of atrazine. The data from this study will be used for further designing the continuous systems being suitable for various conditions.

## II. EXPERIMENT SECTION

### A. Experimental procedures

The experiments in this study were divided into 2 parts which were the photodegradations of the atrazine with and without the use of titanium dioxide with the particle size of 15 nm as a catalyst. The experiments were started from preparing the 40 ppm atrazine solution from the solid atrazine (90 wt%) by dissolving in DI water:methanol (RCI Labscan<sup>TM</sup>, 99.9%) mixture with the ratio of 30:70. After that, the obtained solution was added into the dark (11.4 x 18.9 x 13.4 cm) rectangular container for preventing the deviation of experimental results from external light. as shown in Fig. 1. In order to find the appropriate level of atrazine in the container, the heights of the solution were varied to be 2, 3, 4, 8 and 12 cm. Then, the UVC lamp (PHILIPS Model TUV 8W T5) with the wavelength of 253.7 nm was turned on. During the without catalyst experiments, the solution samples were collected, 1 ml per time (at 10, 20, 30, 45, 60, 75, 90, 120 and 150 min), and analyzed by High Performance Liquid Chromatography (P2000 HPLC, 223 nm UV detector, C18 Quasar<sup>TM</sup> column with the length and inner diameter of 250 mm and 4.6 mm, respectively) for examining the remaining atrazine in the solution. The mobile phase was DI water:methanol mixture

with the ratio of 40:60. For studying the effects of the catalyst concentrations, the titanium dioxide was added into the atrazine solution and stirred until homogeneity before turning the UVC lamp. The concentrations of titanium dioxide were 1, 2 and 4 g/L. Similar to without catalyst case, 1 ml of the solution was sampled each time (at 10, 20, 30, 45, 60, 75, 90, 120, 150, 180, 210 and 240 min) and analyzed by HPLC.

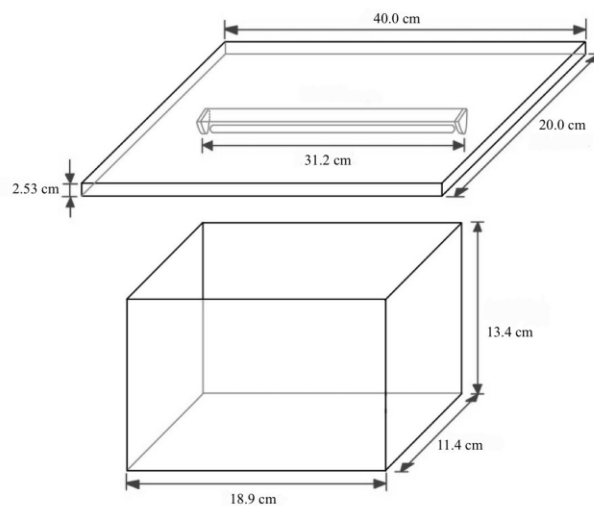


Fig. 1. Photodegradation of atrazine experimental design

## III. RESULTS AND DISCUSSION

### A. Photodegradation of atrazine without catalyst

The wavelength for the degradation experiment of a particular substance should be selected for the wavelength that the substance can absorb energy the most. The 254 nm wavelength can provide the best excitation state for atrazine degradation, making atrazine destabilized and reactive easily [25]. Therefore, all experiments in this study use the 253.7 nm wavelength UVC lamp, which is close to 254 nm.

The degradations of atrazine with the different solution heights are shown Fig. 2. It can be seen that the concentrations of atrazine decreased non-linearly. At the solution heights of 2, 3, 4, 8 and 12 cm, atrazine was approximately degraded for 47.77%, 42.66%, 39.73%, 30.77% and 18.63% respectively in 150 min. This implied that the height of the solution affects the atrazine degradation efficiency because atrazine molecules are degraded by light energy absorption. Increasing height of solution will decrease the ability to transfer light energy from the surface to the bottom of solution and at the height of solution 8 and 12 cm was not suitable for atrazine degradation due to very low atrazine degradation efficiency [12,13].

The analysis of reaction kinetics was achieved by assuming that the reaction rates depended only on the atrazine concentrations. The zero-, first- and second-order kinetic models were considered and their rate equations were expressed in TABLE I. After fitting the results in the models, the rate constants ( $k$ ) were attained and are reported, as well as the  $R^2$ , in TABLE II. Considering the

R<sup>2</sup> value, among these, the first-order kinetic seemed to be the most accurate model in this experiments implying that reaction depends solely on the concentration of one reactant (also called a unimolecular reaction) and often represents a degradation reaction. The rate constant (k) is a constant showing the change in concentration over time. At the solution height 2 cm, the largest k value indicates the highest rate of atrazine degradation or means that the least amount of atrazine at a specified time.

Only the first-order kinetic models have a linear relationship between the natural log and the concentration (ln[C]) and time (t) with a slope equal to -k. ln[C] and the rate constants are inversely proportional, which makes sense since the concentration of a reactant will decrease over time by a certain reaction rate [18,19].

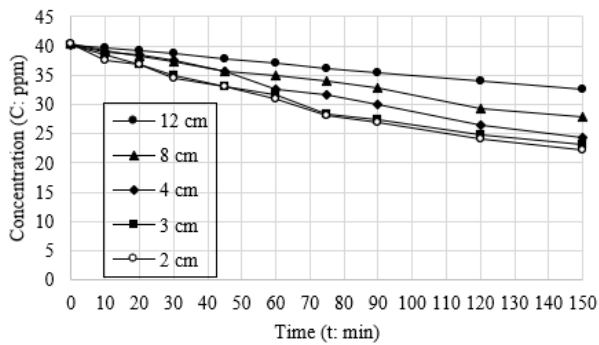


Fig. 2. The concentration of atrazine in the solution during photodegradation without catalyst at the different solution heights.

TABLE I  
RELATED KINETICS MODEL

Order	Rate equation	Linearized rate equation	Half-Life
0	$-r_A = k$	$[C]_A = -kt + [C]_{A0}$	$\frac{[C]_{A0}}{2k}$
1	$-r_A = k[C]_A$	$\ln[C]_A = -kt + \ln[C]_{A0}$	$\frac{\ln 2}{k}$
2	$-r_A = k[C]_A^2$	$\frac{1}{[C]_A} = kt + \frac{1}{[C]_{A0}}$	$\frac{1}{k[C]_{A0}}$

TABLE II  
KINETIC MODELS OF PHOTODEGRADATION OF ATRAZINE  
WITHOUT CATALYST EXPERIMENT

Height of solution (cm)	R <sup>2</sup>	(k) <sup>A</sup>	Equation number
<b>Zero-order kinetic model</b>			
12	0.9992	0.0509	(1)
8	0.9893	0.0835	(2)
4	0.9904	0.1114	(3)
3	0.9698	0.1170	(4)
2	0.9800	0.1263	(5)
<b>First-order kinetic model</b>			
12	0.9993	0.0014	(6)
8	0.9899	0.0025	(7)

4	0.9922	0.0035	(8)
3	0.9874	0.0038	(9)
2	0.9953	0.0042	(10)
<b>Second-order kinetic model</b>			
12	0.9975	0.000039	(11)
8	0.9846	0.000074	(12)
4	0.9848	0.000112	(13)
3	0.9944	0.000127	(14)
2	0.9931	0.000146	(15)

<sup>A</sup> Rate constant of zero, first, second-order kinetic model expressed in ppm/min, 1/min and 1/ppm.min, respectively.

Fig. 3. Is the prediction of degradation rate of atrazine by first-order kinetic model. The results showed that the concentration of atrazine decreased non-linearly with increasing time. In the first period of the experiments, the rates of change of atrazine concentrations were high and it would be decreased with time. It could be assumed that the optimum time for atrazine degradation was approximately up to 600 to 800 min. After that, the degradation rate of atrazine decreased insignificantly.

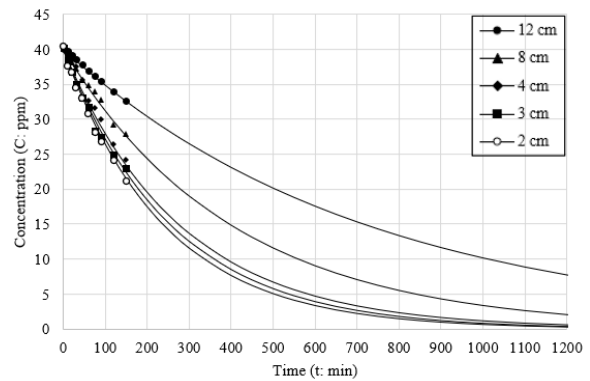
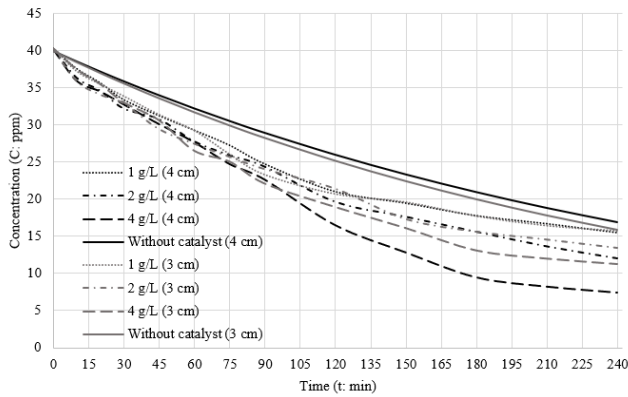


Fig. 3. First-order kinetic model results prediction (line) compared to the actual results (points).

### B. Photodegradation of atrazine with titanium dioxide catalyst

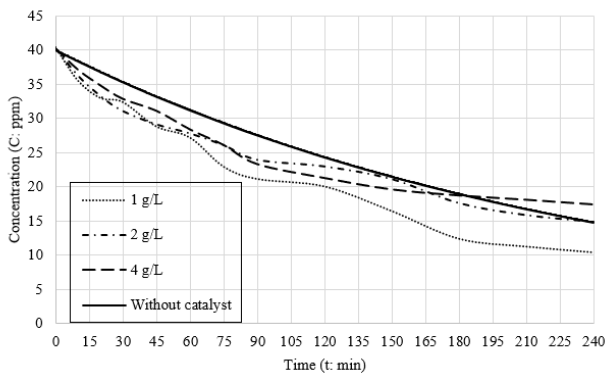
From Fig. 4., for 3 and 4 cm-heights of solution, the tendencies of both results were the same. They can be unsurprisingly seen that the degradation rates of atrazine when the titanium dioxide was used as a catalyst was higher than that of without catalyst. This indicated that titanium dioxide catalyst is a factor affecting the rate of atrazine degradation. In addition, the increase in catalyst concentration resulted in the increase in the rates of atrazine degradation and then the atrazine degradation efficiency.

The catalyst increase the reaction rate by providing a new reaction pathway with lower activation energy so that more reactant molecules collide with enough energy to enter the excited state and form electron-hole pairs at the conduction and valence bands of the catalyst resulting in the production of free radicals that degrade atrazine [23,24].



**Fig. 4.** Photodegradation of atrazine with the different amount of titanium dioxide catalyst. The height of the solution was controlled at 4 cm (line) and 3 cm (dash line).

Fig. 5. Shows the photodegradation of atrazine when the solution height was 2 cm. Inversely to that of 3 and 4 cm of solution heights, the increasing of the catalyst concentrations resulted in the decrease in atrazine degradation rate, causing the excess catalyst. The decrease in the degradation rate can be caused by the accumulation of catalyst in the bottom of the container because the lower solution height leads to faster sedimentation. This led to less active reaction sites in the system. In addition, the catalyst may scatter the light scattering at the water surface resulting in less light entering the solution (light penetration) and then less energy absorbed [20,21,22].

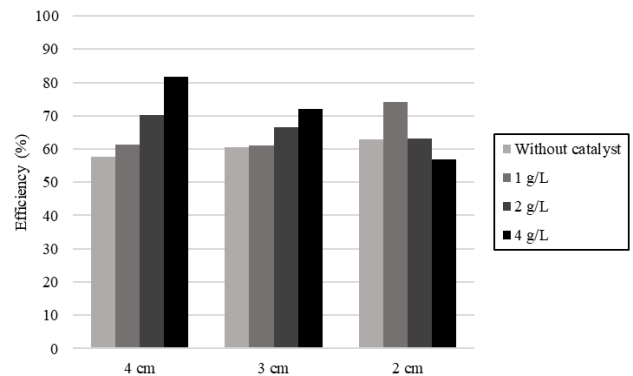


**Fig. 5.** Photodegradation of atrazine with the different amount of titanium dioxide catalyst. The height of the solution was controlled at 2 cm.

Considering the catalyst added from both Fig. 4. And 5., it can be observed that, in first 90 minutes of the experiments, the concentrations of catalyst do not affect the atrazine degradation. This revealed that the degradation rate was limited by rate of catalytic reaction. After 90 minutes, the concentrations of catalyst became more significant since the degradation rates were dependent on the catalyst concentrations. It means that the overall degradation was controlled by the diffusion of atrazine to the catalyst surfaces where the reaction takes place. This was probably due to the lowering concentration of atrazine in the system

leading to longer diffusion path to the catalyst surfaces. [16,17].

From all results, it can be summarized that the solution heights and catalyst concentrations were influenced the photodegradation of atrazine, especially for 2, 3 and 4 cm-height. The atrazine removal efficiencies of each batch of the experiments were calculated and compared as shown in Fig. 6. It can be seen that, for 3 and 4 cm-height, the concentration of catalyst significantly affected the efficiency and degradation rate of atrazine. The catalyst provided a positive effect on the degradation reaction by providing a new reaction pathway with lower activation energy which makes the reaction faster. An increase the surface area of contact between solution and surface of the catalyst is the mechanism of more free radicals formation [9,10,11]. On the other hand, the catalyst can adversely affect the reaction by reflecting, obstructing and scattering the light resulting in the decrease in light entering into the solution and reducing the light energy absorbed. Furthermore, the catalyst that is denser than the solution can settle at the bottom of the container, reducing the surface area, thereby slowing down the reaction [14].



**Fig. 6.** Efficiency of atrazine degradation at different solution height.

#### IV. CONCLUSION

1). The atrazine photodegradation by 253.7 nm of UVC lamp was both affected by the level of the solution in the container and the catalyst concentration. After varying the solution heights, without adding some catalyst, to be 2, 3, 4, 8 and 12 cm, 8 and 12 cm-heights of solution provided the worst efficiencies resulted from too deep levels of the solution, so the light energy was too low to penetrate the solution to the bottom of the container.

2). By fitting to the kinetic model, the first-order kinetic model seemed to be the best fitted for every level of the solution implying that reaction is a unimolecular reaction and represent a degradation reaction. The largest  $k$  value at 2 cm-height of solution indicates highest rate of atrazine degradation. From this model, it can be extrapolated to predict that the optimum time for atrazine degradation was around 600 – 800 min.

3). The additions of titanium dioxide catalyst can either accelerate by reducing the activation energy of the reaction



or obstruct the photodegradations of atrazine by scattering the light and settling to the bottom of the container.

4). During the first 90 min, the overall photodegradation was limited by the reaction. After that, it was controlled by diffusion due to the less concentration of atrazine in the system leading to longer diffusion path to the reactive sites.

#### ACKNOWLEDGEMENT

This project was carried out in the laboratories of Department of Chemical Engineering, School of Engineering, King Mongkut's Institute of Technology Ladkrabang.

#### REFERENCES

- [1] E. Pellizzetti et al., "Photocatalytic Degradation of Atrazine and Other s-Triazine Herbicides," *Environ. Sci. Technol.*, vol. 24, no. 10, pp. 1559–1565, 1990.
- [2] World Health Organisation, *Atrazine Health and Safety Guide*, 47<sup>th</sup> ed., no. 47. Geneva: World Health Organization for the International Programme on Chemical Safety, 1990.
- [3] N. Shapir and R. T. Mandelbaum, "Atrazine Degradation in Subsurface Soil by Indigenous and Introduced Microorganisms," *J. Agric. Food Chem.*, vol. 45, no. 11, pp. 4481–4486, 1997.
- [4] W. Laohaudomchok et al., "Pesticide use in Thailand: Current situation, health risks, and gaps in research and policy," *Hum. Ecol. Risk Assess.*, vol. 0, no. 0, pp. 1–23, 2020.
- [5] S. Singh et al., "Toxicity, degradation and analysis of the herbicide atrazine," *Environ. Chem. Lett.*, vol. 16, no. 1, pp. 211–237, 2018.
- [6] H. He, Y. Liu, S. You, J. Liu, H. Xiao, and Z. Tu, "A review on recent treatment technology for herbicide atrazine in contaminated environment," *Int. J. Environ. Res. Public Health*, vol. 16, no. 24, 2019.
- [7] R. K. Pathak, "Various Techniques for Atrazine Removal," *Int. Conf. Life Sci. Technol.*, vol. 3, pp. 19–22, 2011.
- [8] "Atrazine Fact Sheet." [Online]. Available: <http://npic.orst.edu/factsheets/atrazine.html>.
- [9] G. Drouin, B. Droz, F. Leresche, S. Payraudeau, J. Masbou, and G. Imfeld, "Direct and indirect photodegradation of atrazine and S - metolachlor in agriculturally impacted surface water and associated C and N isotope fractionation," *Environ. Sci. Process. Impacts*, 2021.
- [10] J. A. Khan et al., "Kinetic and mechanism investigation on the photochemical degradation of atrazine with activated H<sub>2</sub>O<sub>2</sub>, S<sub>2</sub>O<sub>8</sub><sup>2-</sup> and HSO<sub>5</sub><sup>-</sup>," *Chem. Eng. J.*, vol. 252, pp. 393–403, 2014.
- [11] R. C. Neuman, Chapter 11 Free Radical Substitution and Addition Reactions.
- [12] Z. Moeini, "Photo-Degradation of Atrazine in Water Using UV and investigating its by-Products," vol. 6, no. 1, 2018.
- [13] N. Shamsedini, "Photodegradation of Atrazine by Ultraviolet Radiation in Different Conditions," vol. 3, no. 3, 2015.
- [14] S. Parra, S. E. Stanca, I. Guasaquillo, and K. Ravindranathan Thampi, "Photocatalytic degradation of atrazine using suspended and supported TiO<sub>2</sub>," *Appl. Catal. B Environ.*, vol. 51, no. 2, pp. 107–116, 2004.
- [15] P. On-anong et al., "The Residues and Transportation of Atrazine Herbicide in Maize (*Zea mays* L.) Cultivated Upland Soil, Soil Sediment and Stream Water in Huay Kapo Watershed, Nam Nao District, Phetchabun Province," *Proceedings of 49<sup>th</sup> Kasetsart University Annual Conference: Natural Resources and Environment.*, pp. 1-11, 2011.
- [16] P. Tufvesson., J. Lima-Ramos, J.S. Jensen, N. Al-Haque, W. Neto, J.M. Woodley, "Process considerations for the asymmetric synthesis of chiral amines using transaminases," *Biotechnol. Bioeng.*, pp. 1479–1493, 2011.
- [17] Mosleh S, Ghaedi, "Photocatalytic reactors: technological status, opportunities, and challenges for development and industrial upscaling," In: *Interface science and technology*. Elsevier, Amsterdam, pp 90–761, 2021.
- [18] Petrucci, Ralph H, "General Chemistry: Principles and Modern Applications" 9<sup>th</sup> Ed. New Jersey: Pearson Education Inc, 2007.
- [19] "First Order Reaction." [Online]. Available: <https://www.studysmarter.co.uk/explanations/chemistry/kinetics/first-order-reaction/>.

- [20] Pio Forzatti and Luca Lietti, "Catalyst deactivation," *Catalysis Today.*, vol. 52, pp. 165–181, 1999.
- [21] Debye, P., Nauman, R.V., "A light scattering study of the aggregation of acidified sodium silicate solutions," *J. Phys. Chem.* 65, 10-12, 1961.
- [22] France, J. L.; Reay, H. J.; King, M. D.; Voisin, D.; Jacobi, H. W.; Domine, F.; Beine, H.; Anastasio, C.; Macarthur, A.; Lee-Taylor, J, "Hydroxyl Radical and NO<sub>x</sub> Production Rates, Black Carbon Concentrations and Light-Absorbing Impurities in Snow from Field Measurements of Light Penetration and Nadir Reflectivity of Onshore and Offshore Coastal Alaskan Snow," *J. Geophys. Res.* 2012, 117 (D14), D00R12.
- [23] Wamer WG, Yin J-J, Wei RR, "Oxidative damage to nucleic acids photosensitized by titanium dioxide," *Free Radic Biol Med*, pp 851–858, 1997.
- [24] "Rates of reaction – (CCEA)." [Online]. Available: <https://www.bbc.co.uk/bitesize/guides/zdkr6v4/revision/8>.
- [25] A. T. Shawaqfeh and F. A. Al Momani, "Photocatalytic treatment of water soluble pesticide by advanced oxidation technologies using UV light and solar energy," *Sol. Energy*, vol. 84, no. 7, pp. 1157–1165, 2010.
- [26] Yang Y, Cao H, Peng P, Bo H, "Degradation and transformation of atrazine under catalyzed ozonation process with TiO<sub>2</sub> as catalyst," *J Hazard Mater*, 279:444–451, 2014.
- [27] C. Belver, C. Han, J.J. Rodriguez, D.D. Dionysiou, "Innovative W-doped titanium dioxide anchored on clay for photocatalytic removal of atrazine," *Catal. Today* 280, pp 21–28, 2017.

## $\alpha$ -Tocopherol-Loaded Urushibara nickel as an Oxygen Scavenger

Khunpat Aksornnam<sup>1(a)</sup>, Penjit Srinophakun<sup>1(b)</sup>, Anusith Thanapimmetha<sup>1(c)</sup>,  
Nutchapon Chiarasumran<sup>1(d)</sup>, Maythee Saisriyoot<sup>1(e)\*</sup>

<sup>1</sup> Department of Chemical Engineering, Faculty of Engineering, Kasetsart University, Bangkok 10900, Thailand  
khunpat.a@ku.th<sup>(a)</sup>, fengpjs@ku.ac.th<sup>(b)</sup>, fengjrc@gmail.com<sup>(c)</sup>, fengnpc@ku.ac.th<sup>(d)</sup>, fengmts@ku.ac.th<sup>(e)\*</sup>

**Abstract:** The  $\alpha$ -tocopherol-loaded Urushibara nickel catalyst (U-Ni-A) is an oxygen scavenger that preserves the product and prolongs the product's lifespan. This catalyst digested the precipitate metals with an acid solution and mixed it with  $\alpha$ -tocopherol using ultra-sonication.  $\alpha$ -tocopherol loaded U-Ni-A to promote oxygen absorption capacity. O<sub>2</sub> pulse chemisorption was determined using Micromeritics Autochem II, and O<sub>2</sub> adsorption capacity was investigated using a Neofox oxygen sensor. The O<sub>2</sub> pulse chemisorption value was 0.25 ml/g catalyst, while the O<sub>2</sub> adsorption capacity was 0.27 ml/g catalyst. The study concluded that  $\alpha$ -tocopherol on the U-Ni-A reacts with the active site of the U-Ni-A, decreasing the scavenger's oxygen absorption capacity.

**Index Terms**— Urushibara nickel,  $\alpha$ -tocopherol, oxygen adsorption capacity, oxygen scavenger.

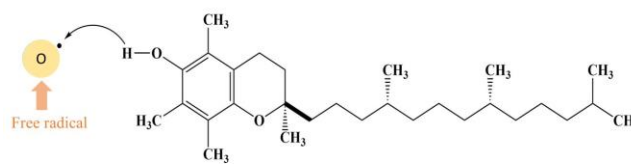
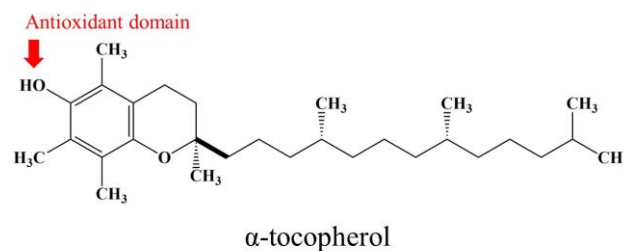
### I. INTRODUCTION

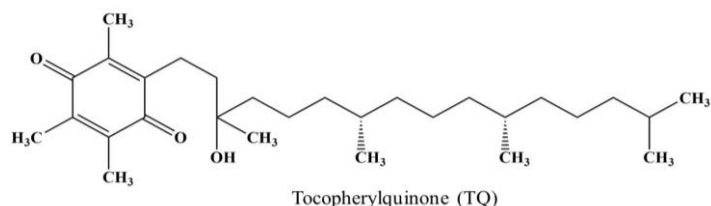
Residual oxygen in packaging can promote the growth of aerobic bacteria or mold growth. Furthermore, oxidation is frequently the cause of various food deterioration reactions, such as the development of off-flavors, colors, and nutritional losses[1-3]. To eliminate oxygen in the package prior to sealing, modified atmosphere packaging has been frequently employed[4]. However, this method cannot remove the oxygen that permeates from the outside environment into the package through the packaging material. Oxygen scavengers have been commercialized for use in the food packaging industry. These scavengers can remove oxygen that permeates through the packaging material into the package during storage and residual oxygen that may have been trapped inside the package prior to sealing. Oxygen-scavenging systems are used in various forms such as sachets, plastic films, labels, plastic trays, and bottle crowns. These oxygen scavenging systems employ various approaches, with the most widely used concepts being iron oxidation, ascorbic acid oxidation, photosensitive dye oxidation, and others[5, 6].

The most popular and effective oxygen scavengers are based on the iron oxidation principle. Sachets of iron-based oxygen scavengers are commonly utilized. However, iron-based oxygen-scavenging sachets have several drawbacks. These sachets may constitute a health concern if people inadvertently swallow them. As a result, the packaging sector should benefit from the development of innovative oxygen-scavenging methods that do not require a moisture activation phase[7]. Furthermore, oxygen scavenging systems that use natural compounds as the basis for the oxygen scavenger may be advantageous. In addition, oxygen scavenging systems that use natural compounds as

the basis for the oxygen scavenger may be advantageous.  $\alpha$ -tocopherol is one such possible chemical.  $\alpha$ -tocopherol is a naturally occurring free radical scavenger that has a favorable consumer perception (Fig.1) [8, 9]. To decrease oxidation in food goods, it has been added into polymer materials as a stabilizer and as an antioxidant in controlled-release packaging[10].

The aim of this research was to develop an oxygen scavenging system using  $\alpha$ -tocopherol, a natural free radical scavenger, and Urushibara nickel (U-Ni-A) which is a transition metal not need moisture activation. The study looked into the oxygen-scavenging capabilities of U-Ni-A and  $\alpha$ -tocopherol loaded.





**Fig. 1.** The Antioxidant Oxygen Scavenger.

## II. METHODOLOGY

### Materials

Nickel chloride ( $\text{NiCl}_2 \cdot 6\text{H}_2\text{O}$ ) was purchased from Univar, Zinc powder (Zn) 99.9% was purchased from KemAus, Acetic acid (99.99%), ethanol (99.95%), and  $\alpha$ -tocopherol (98%) were obtained from Merk. Deionized (DI) water  $18.3 \Omega$  and distilled water and used as received.

### Method

**Synthesis Precipitate metals:** To a suspension of Zn powder 10 g in hot distillation water 3 ml was added rapidly to a solution of  $\text{NiCl}_2 \cdot 6\text{H}_2\text{O}$  4 g in hot distillation water 10 ml with vigorous magnetic stirring. Stirring was continued until the evolution of hydrogen had abated. The resulting mixture was decanted and the precipitated metal was washed with hot water 200 ml. [11].

**Synthesis U-Ni-A:** To the precipitate metal was added 13% acetic acid 160 ml and the mixture was first stirred for 4 min at room temperature and heated at  $40^\circ\text{C}$  with magnetic stirring for 4 min. The solution was decanted and the U-Ni-A was washed with water until neutral and then stored under absolute alcohol 20 ml [12].

**Synthesis U-Ni-A and  $\alpha$ -tocopherol:** The U-Ni-A was freeze-dried for 48 hr. and kept its in the modified atmosphere bottle. Prepare  $\alpha$ -tocopherol 2 g diluted with ethanol 20 ml. Add U-Ni-A 5 g in  $\alpha$ -tocopherol solution 20 ml combined with ultrasonication at 50Hz. The ultrasonicate's time is 30 min; that is sonicated 5 min and wait 5 min in the iced bath and stored in ethanol at  $4^\circ\text{C}$  [13].

### Catalyst characterization

#### Pulse Oxygen Chemisorption

$\text{O}_2$  pulse chemisorption studies were all conducted using the Micromeritics Autochem II 2920. After ca. 0.5 g of sample was packed into a U-tube quartz microreactor with 6 mm internal diameter, the analysis was carried out with 99 vol-% Helium (He) at the flow rate of 30 mL/min by ramping from  $25^\circ\text{C}$  to  $105^\circ\text{C}$  at  $10^\circ\text{C}/\text{min}$  to removed moisture for 6 hr. Subsequently, the sample was purged in 10%  $\text{O}_2/\text{He}$  (30 mL/min) at  $45^\circ\text{C}$  for 10 min followed by cooling down to  $40^\circ\text{C}$  in  $\text{O}_2/\text{He}$ . Fifty-eight pulses of 10%  $\text{O}_2/\text{He}$  were admitted at intervals of 10 min, and the exit pulses were monitored by a TCD. Pulse calibration was run 3 times for each pulse chemisorption analysis [14].

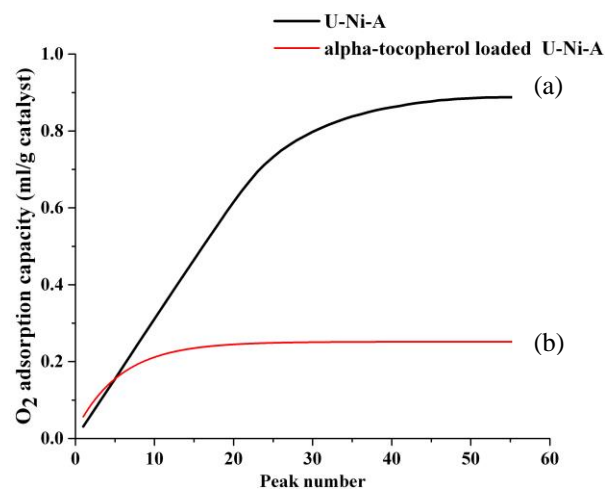
#### Oxygen scavenging capacity

A NEOFOX oxygen phase fluorometer from Ocean

Optics, Inc. (Dunedin, FL, USA) with fluorescent optical sensors was used to determine the dissolved oxygen concentration in a bottle. Oxygen concentrations were measured non-destructively by holding the NEOFOX oxygen phase fluorometer probe in the sample's bottle. Calibration was performed with gases containing  $<0.01\%$  oxygen obtained by continuously purging pure nitrogen, 99.9% purity at  $35^\circ\text{C}$  for at least 5 min and atmospheric air to standardize the fluorescent optical sensors against known oxygen concentrations and temperatures as instructed by Ocean Optic, Inc.. Samples 0.5 g from freeze dryer were monitored over time in an incubator stored at  $40^\circ\text{C}$  [9, 15].

## III. RESULTS AND DISCUSSION

The oxygen adsorption capacity of U-Ni-A and  $\alpha$ -tocopherol loaded U-Ni-A is displayed in Figure 2. The concentration of U-Ni-A was incrementally increased until peak number 50 was reached and stabilized. At peak number 20, the  $\alpha$ -tocopherol-loaded U-Ni-A was observed to be gradually increasing and eventually became stable. These results indicate that the presence of  $\alpha$ -tocopherol in the U-Ni-A reduces its oxygen adsorption capacity.



**Fig. 2.** Pulse oxygen chemisorption curve for U-Ni-A (a) and  $\alpha$ -tocopherol loaded U-Ni-A (b)

Table 1. shows the oxygen adsorption capacity of  $\alpha$ -tocopherol observed by fluorescent optical sensors to estimate the dissolved and headspace oxygen concentrations in the gas cell (containing 0.4 g  $\alpha$ -tocopherol) [8]. The oxygen adsorption capacity of  $\alpha$ -tocopherol and U-Ni-A was nearly identical, however, the oxygen adsorption capacity of  $\alpha$ -tocopherol loaded U-Ni-A was reduced.

Table 1  
The Oxygen Adsorption Capacity

Transition metals	O <sub>2</sub> adsorption (ml/g)	Reference
$\alpha$ -tocopherol	0.67	[8]
U-Ni-A	1.12	This work
$\alpha$ -tocopherol loaded U-Ni-A	0.27	

Figure 3(a) presents the model of U-Ni-A's oxygen adsorption, which shows that U-Ni-A adsorbs oxygen to NiO, leading to the production of oxygen-free radicals. This indicates that U-Ni-A is supported by chemisorption rather than physisorption, as shown in Figure 2(a). The oxygen adsorption capacity of  $\alpha$ -tocopherol loaded U-Ni-A decreased, suggesting that the hydroxyl functional group of  $\alpha$ -tocopherol reacted with the active site of U-Ni-A, as depicted in Figure 3(b). Figure 3(c) shows the hydrocarbon chains of  $\alpha$ -tocopherol covering the active site of U-Ni-A. However, the optimal ratios of  $\alpha$ -tocopherol and U-Ni-A were not used, which led to a decrease in the oxygen adsorption capacity[13]. These observations indicate that the  $\alpha$ -tocopherol-loaded U-Ni-A is only capable of physisorption adsorption.

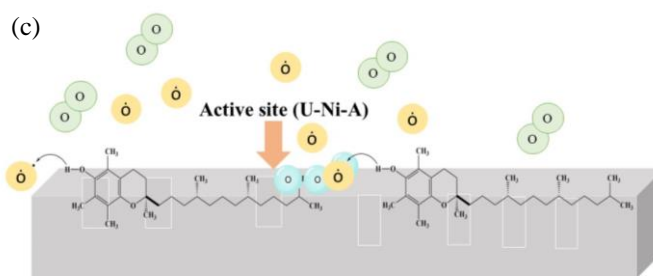
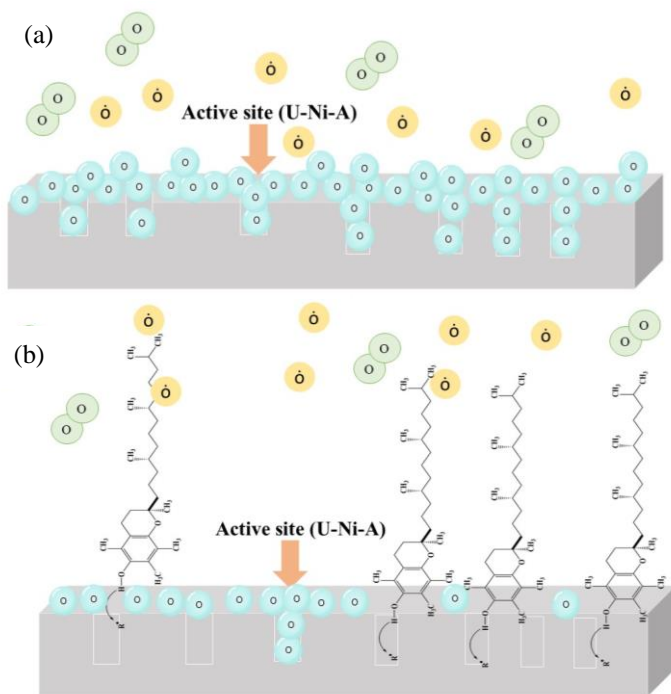


Fig. 3. Proposed model of U-Ni-A's oxygen adsorption (a), the hydroxyl functional group of  $\alpha$ -tocopherol reacted with the U-Ni-A's active site(b), and the  $\alpha$ -tocopherol's hydrocarbon chains cover the U-Ni-A's active site (c).

#### IV. CONCLUSION

The result of The oxygen adsorption capacity of  $\alpha$ -tocopherol loaded U-Ni-A decreased due to the hydroxyl functional group of  $\alpha$ -tocopherol reacting with the active site of U-Ni-A. Meanwhile, the hydrocarbon chains covered the active site of U-Ni-A, and the optimal ratios between  $\alpha$ -tocopherol and U-Ni-A were not achieved. The decrease in the active site of U-Ni-A and the hydroxyl functional group of  $\alpha$ -tocopherol directly affected the oxygen adsorption capacity. Therefore, adjusting the ratio of  $\alpha$ -tocopherol loaded on U-Ni-A could improve the oxygen adsorption capacity.

#### ACKNOWLEDGEMENT

The authors would like to thank the Department of Chemical Engineering from Kasetsart University, The graduate school of Kasetsart University

#### REFERENCES

1. Dey, A. and S. Neogi, *Oxygen scavengers for food packaging applications: A review*. Trends in Food Science & Technology, 2019. **90**: p. 26-34.
2. Cichello, S.A., *Oxygen absorbers in food preservation: a review*. J Food Sci Technol, 2015. **52**(4): p. 1889-95.
3. Gaikwad, K.K., S. Singh, and Y.S. Lee, *Oxygen scavenging films in food packaging*. Environmental Chemistry Letters, 2018. **16**(2): p. 523-538.
4. Gibis, D. and K. Rieblinger, *Oxygen scavenging films for food application*. Procedia Food Science, 2011. **1**: p. 229-234.
5. Gomes, C., et al., *Effect of oxygen-absorbing packaging on the shelf life of a liquid-based component of military operational rations*. J Food Sci, 2009. **74**(4): p. E167-76.
6. Gaikwad, K.K., et al., *Novel polyisoprene based UV-activated oxygen scavenging films and their applications in packaging of beef jerky*. Lwt, 2020. **117**.
7. Kombaya-Touckia-Linin, E.-M., et al., *Hybrid iron montmorillonite nano-particles as an oxygen scavenger*. Chemical Engineering Journal, 2019. **357**: p. 750-760.
8. Scarfato, P., et al., *Preparation, characterization, and oxygen scavenging capacity of biodegradable  $\alpha$ -tocopherol/PLA microparticles for active food packaging applications*. Polymer Composites, 2017. **38**(5): p. 981-986.
9. Johnson, D.R., R. Inchingolo, and E.A. Decker, *The ability of oxygen scavenging packaging to inhibit vitamin degradation and lipid oxidation in fish oil-in-water emulsions*. Innovative Food Science & Emerging Technologies, 2018. **47**: p. 467-475.

10. Ren, J., et al., *TiO<sub>2</sub>-containing PVA/xylan composite films with enhanced mechanical properties, high hydrophobicity and UV shielding performance*. Cellulose, 2014. **22**(1): p. 593-602.
11. Urushibara, Y., *The Urushibara Catalysts*. 1952.
12. Isaac Jacob, M.F., Zeev Hadari, Mordechay Herskowitz, Jaime Wisniak, Noah Shamir, And Moshe Mintz, *The Leaching-Activation Process of Urushibara Catalysts*. Journal of Catalysis, 1986. **101**.
13. Byun, Y., et al., *Development of oxygen scavenging system containing a natural free radical scavenger and a transition metal*. Food Chemistry, 2011. **124**(2): p. 615-619.
14. Kumar, P., et al., *Kinetics of hydrodeoxygenation of stearic acid using supported nickel catalysts: Effects of supports*. Applied Catalysis A: General, 2014. **471**: p. 28-38.
15. Vickers, J.W., et al., *Collecting meaningful early-time kinetic data in homogeneous catalytic water oxidation with a sacrificial oxidant*. Phys Chem Chem Phys, 2014. **16**(24): p. 11942-9.

# Crop Evapotranspiration Estimation Using Vegetation Index Method in the Northern Region of Thailand

Teerawat Suwanlertcharoen<sup>1\*</sup>, Thanaporn Supriyasilp<sup>2</sup>, Kobkiat Pongput<sup>1</sup>

<sup>1</sup> Department of Water Resources Engineering, Faculty of Engineering, Kasetsart University, Bangkok Campus, Bangkok, Thailand

<sup>2</sup> Department of Civil Engineering, Faculty of Engineering, Chiang Mai University, Chiang Mai, Thailand

\* Corresponding author: [teerawat.suwan@ku.th](mailto:teerawat.suwan@ku.th)

**Abstract:** Evapotranspiration (ET) is a vital water balance component. ET data can be obtained with various measurement methods. One of the methods for estimating crop evapotranspiration ( $ET_c$ ) is derived from remote sensing using the vegetation index method. This method is widely used due to the ability to measure over large areas for water resource management and crop water requirements. Longan and rice are the primary agricultural products in northern Thailand. The objectives of this study were 1) to determine the relation between the normalized difference vegetation index (NDVI) derived from Landsat imagery and the crop coefficient ( $K_c$ ) derived from FAO-56 single crop coefficient method using a linear regression and 2) to estimate the  $ET_c$  during crop growth period by using  $K_c$  from above relationship multiplied by reference evapotranspiration. Note that the relation between NDVI and  $K_c$  was assessed only for rice, while the relation between NDVI and  $K_c$  for longan was obtained from previous literatures. The results showed that the correlation between the  $K_c$  values obtained from NDVI and FAO-56 single crop coefficient method for rice at the satellite acquisition date were in good agreement with the coefficient of determination ( $R^2$ ) of 0.74. Comparing the  $ET_c$  obtained from the relation between NDVI and  $K_c$  with that calculated with the FAO-56 single crop coefficient method of all sample plots in dry season year 2018-2020, the difference between the cumulative  $ET_c$  values of each plot ranges from 0.91%–7.53% for rice and 8.03%–12.02% for longan. Furthermore, the average daily  $ET_c$  in agricultural areas showed that the  $ET_c$  of paddy fields were higher than the  $ET_c$  of longan. Moreover, after compared the spatiotemporal distribution of seasonal  $ET_c$  during the dry season for three years, it was clearly seen that the distributions were consistent with variations in climate, crop phenology, and human activities.

**Keywords:** Evapotranspiration, NDVI, Crop coefficient, Crop phenology, Landsat, Northern Region of Thailand.

## I. INTRODUCTION

Evapotranspiration (ET) is a vital water balance component. ET data can be obtained with various measurement methods such as lysimeters, the Bowen ratio, the eddy covariance, sap flow, soil water balance, and satellite-based remote sensing (including surface energy balance and vegetation indices methods) [1]. One of the methods for estimating crop evapotranspiration ( $ET_c$ ) is derived from remote sensing using the vegetation index (VI) method. This method is widely used due to the ability to measure over large areas for water resource management and crop water requirements. Northern Thailand is the foremost longan-producing [2], with drained rice fields and gently sloping fields in the upper Ping River Basin foothills as the main production areas [3].

According to Allen et al. [1] the VI is the simple method is utilized to estimate crop coefficients ( $K_c$ ). Generally, vegetation density and transpiration are closely related to  $ET_c$ . As a vegetation cover, leaf area, and transpiration increase, thereby increasing ET. In this method, satellite imagery data can be used to evaluate  $K_c$  using normalized

difference vegetation index (NDVI). NDVI is calculated by measuring surface reflectance between the infrared and visible red bands, which can be derived from Landsat imagery. As a result, a high NDVI value is related to healthy vegetation. To our knowledge, some researchers have studied in Thailand using VI to estimate  $K_c$  for rice, such as Nam-in et al. [4] and [5], which applied of NDVI-based  $K_c$  method derived from MODIS satellite imagery. Also, Yensakunsuk and Chayakula [6] studied the relationship between NDVI derived from Sentinel-2 satellite imagery and  $K_c$ . However, they focus on the irrigated area of central Thailand, especially in the Chao Phraya River Basin.

Moreover, the correlation between  $K_c$  and NDVI value can help identify the period of crop growth that can be used to evaluate  $ET_c$ . In addition, the temporal VI has been widely used for vegetation phenology and extracting vegetation growing periods [7] and [8].

The objectives of this study are as follows: (1) to determine the relation between the NDVI derived from Landsat-8 imagery and the  $K_c$  derived from FAO-56 single crop coefficient method for rice using a linear regression; and (2) to estimate the  $ET_c$  during crop growth period by using  $K_c$  multiplied by reference evapotranspiration.

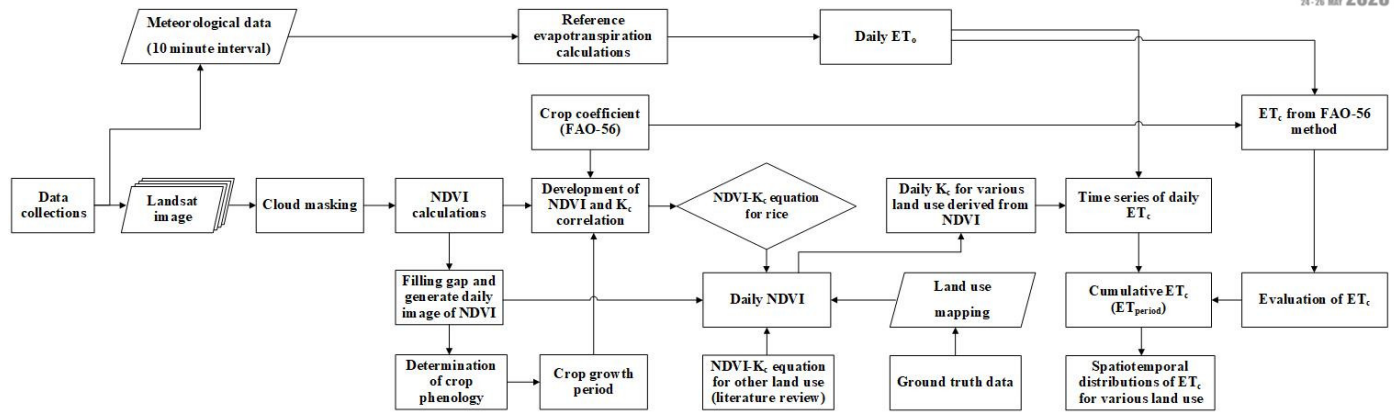


Fig. 1. Flowchart diagram of the study

## II. MATERIALS AND METHODS

An outline of the methods, procedures, and workflow used in this study are presented in Fig. 1.

### A. Study Area

The study area is the part of the Muang Luang Irrigation Project located in the Chom Thong District, Chiang Mai Province (Fig. 2). This area is located downstream of the Muang Luang Weir. The study area includes land utilization areas, especially agricultural areas in irrigated areas as community irrigation systems. Fig. 2 shows that paddy fields and longan orchards cover approximately 68% and 26% of the total area, respectively. The boundary of this area is in the north at the Tae Sam Nga diversion weir, which splits into three irrigation canals. The study area is located between the Na Sai and Na Ngu ditches, covering an area of 2.12 km<sup>2</sup> [9]. The general climate of this area is affected by southwest and northeast monsoons, which is the rainy season covering from mid-May to October. The dry season is a period of the year during which there is a lack of rainfall and low humidity, covering from the end of October to mid-May.

### B. Data Collection

#### 1) Satellite Imagery

Landsat-8 Operational Land Imager (OLI) and Thermal Infrared Sensor (TIRS) images with a spatial resolution of 30 m were collected with level-1 products with terrain precision correction (L1TP) from the U.S. Geological Survey (USGS) Earth Explorer via <https://earthexplorer.usgs.gov/>. In this study, A total of 41 Landsat-8 OLI/TIRS images (Path 131/Row 47) were used with cloud-free conditions. It covers the study area and crop growth period in the dry season from October 2017 to May 2020 (12, 14, and 15 images for 2018, 2019, and 2020 respectively).

#### 2) Meteorological Data

Meteorological data were obtained from the nearest weather station to compute the daily reference crop evapotranspiration for the grass reference ( $ET_0$ ). The weather data, including air temperature, relative humidity, wind speed, and air pressure, were collected from Lamphun station with the automatic weather system (AWS) of the Thailand

Meteorological Department, which records meteorological data every 10 minutes. Rainfall data were collected from stations at the Chom Thong station closest to the study area.

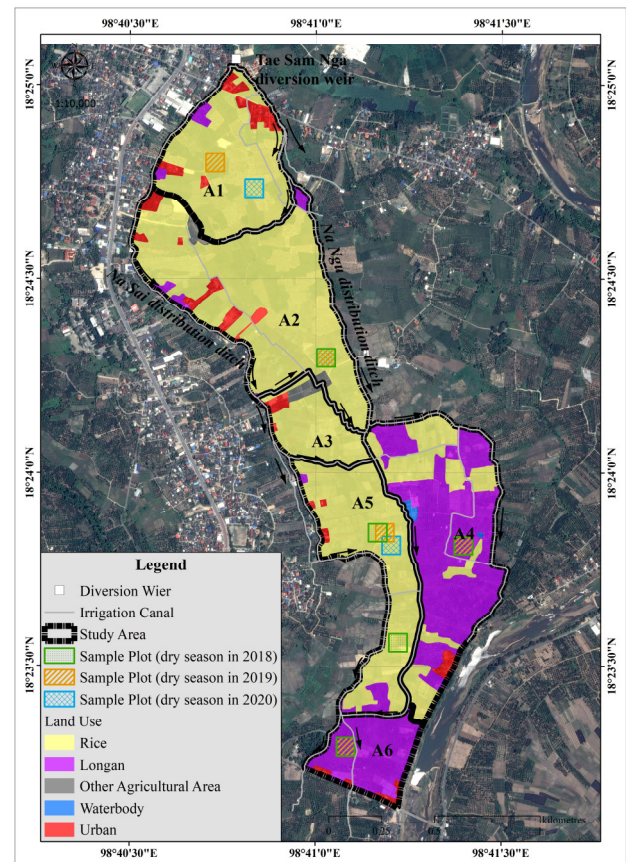


Fig. 2. Study area

#### 3) Ground Truth Data

Ground truth data has been collected to verify the accuracy of land use data for the year 2018 from the Land Development Department.

### C. Reference Evapotranspiration ( $ET_0$ ) Calculation

The FAO Penman-Monteith equation is the equation used to calculate the  $ET_0$  based on the FAO guidelines as described by publication No. 56 of the Irrigation and Drainage Series of FAO [10] as follows:

$$ET_o = \frac{0.408 (R_n - G) + \gamma \frac{900}{(T + 273)} u_2 (e_s - e_a)}{\gamma(1 + 0.34u_2)} \quad (1)$$

where  $ET_o$  is the grass reference ET ( $\text{mm} \cdot \text{day}^{-1}$ ),  $R_n$  is the net radiation ( $\text{MJ m}^{-2} \text{d}^{-1}$ ),  $G$  is the soil heat flux transferred to the ground ( $\text{MJ m}^{-2} \text{d}^{-1}$ ),  $T$  is the mean daily air temperature ( $^{\circ}\text{C}$ ),  $u_2$  is the mean daily wind speed at a height of 2 m ( $\text{m} \cdot \text{s}^{-1}$ ),  $e_s$  is the saturation vapour pressure (kPa),  $e_a$  is the actual vapour pressure (kPa),  $\gamma$  is the slope vapour pressure curve ( $\text{kPa } ^{\circ}\text{C}^{-1}$ ), and  $\gamma$  is the psychrometric constant ( $\text{kPa } ^{\circ}\text{C}^{-1}$ ),

#### D. NDVI Calculations

The NDVI can be obtained from the ratio of two bands between near-infrared and red waveband reflectances. The near-infrared band is subtracted from the red band and divided by the sum of the near-infrared and red bands [11]. For Landsat 8, NDVI was calculated as follows:

$$\text{NDVI} = (\text{Band 5} - \text{Band 4}) / (\text{Band 5} + \text{Band 4}) \quad (2)$$

where Band 5 and Band 4 refer to the surface reflectance values in the near-infrared and red bands of Landsat 8, respectively.

#### E. Crop Evapotranspiration

The single-crop coefficient approach is based on the FAO-56 method for estimating the  $ET_c$ . The crop transpiration and soil evaporation factors are combined into a single crop coefficient.  $ET_c$  is calculated by multiplying the  $ET_o$  with  $K_c$ . In this study, the  $ET_c$  under standard conditions can be determined as follows [10], [12] and [13]:

$$ET_c = K_c * ET_o \quad (3)$$

where  $ET_c$  is crop evapotranspiration ( $\text{mm} \cdot \text{day}^{-1}$ ) and  $K_c$  is the crop coefficient (dimensionless). The  $K_c$  of rice can be separated into three stages, including the initial growth stage ( $K_{c \text{ ini}}$ ), mid-season stage ( $K_{c \text{ mid}}$ ), and end of the growing period ( $K_{c \text{ end}}$ ). The  $K_c$  of rice varies between 0.90–1.20. The  $K_c$  of fruit trees varies between 0.80–1.20,  $K_c$  of both types as suggested by Allen et al. [10] and Pereira et al. [13].

#### F. Evapotranspiration Using Vegetation Index method

##### 1) Filling Image Gaps and Interpolation of the Daily Image

Cloud masking is the first process for satellite images in each scene before NDVI calculation. Thus, NDVI were used to fill data gaps due to the cloud mask to provide missing values. The next step is to generate the daily NDVI image between two dates of satellite image captures using the cubic spline interpolation method via Decomposition and Analysis of Time Series software (DATimeS) which is developed by Belda et al. [14].

##### 2) Determination of Crop Growing Period

The daily NDVI image time series was applied to extract the crop phenology and identify crop development stages (initial, developing, middle, and end). The amplitude of the

NDVI values during the growing season was analyzed to identify the crop growing period and interpretation the image for the rice cultivated area. The maximum NDVI usually occurs during the growth stage, which is the peak of NDVI.

##### 3) Relation between NDVI and $K_c$ for Rice

To determine the relation between NDVI derived from Landsat-8 imagery in each scene and the  $K_c$  derived from FAO-56 single crop coefficient method for rice using linear regression. While the  $K_c$  of longan is not available for the FAO-56 single crop coefficient method. Therefore, to estimate the  $ET_c$  of longan, the equation between NDVI and  $K_c$  relation was obtained from the study of Belmonte et al. [15] and was used as a representative estimate  $ET_c$  for longan and other agriculture as follows:

$$K_c = 1.25 \times \text{NDVI} + 0.2 \quad (4)$$

The date of each growing stage was obtained from the crop phenology identified by the NDVI.

##### 4) Estimate the $ET_c$ Using Vegetation Index Method

To estimate the  $ET_c$  during crop growth period of all sample plots in dry season year 2018-2020 by using  $K_c$  from the NDVI- $K_c$  relationship multiplied by  $ET_o$ . Also, spatiotemporal distributions of average daily  $ET_c$  for agriculture areas, including paddy fields and longan, was generated by multiplying the daily image of  $K_c$  derived from NDVI- $K_c$  relation with  $ET_o$  for each day. Then was calculated in average daily  $ET_c$ , which was over the period from October to May, covering the dry seasons in 2018, 2019, and 2020.

#### G. Evaluation of the Crop Evapotranspiration

This study evaluates  $ET_c$  by comparing the  $ET_c$  obtained from the relation between NDVI and  $K_c$  with that calculated with the FAO-56 single crop coefficient method of all sample plots (as shown in Fig. 2) in the dry season year 2018-2020. The accuracy of the  $ET_c$  values was assessed using statistical analysis methods, including coefficient of determination ( $R^2$ ) and percentage difference of  $ET_c$  between the cumulative  $ET_c$  values of each plot for paddy field and longan.

### III. RESULTS AND DISCUSSION

#### A. Analysis of the Crop Growth Period and Identification of Rice Cultivated Area

The analysis of the cultivation area from Landsat-8 satellite imagery between October 1 to May 31 in the dry seasons year 2018, 2019, and 2020 shows that the rice cultivation area in the study area was 0.35, 0.53, and 0.62  $\text{km}^2$ , respectively. The rice cultivation areas differ yearly because the study area is the joint water allocation area managed by the water management committee and farmers. The farmer's decision to cultivate rice depends on the amount of water budget each year and water allocated for cultivation in the plot area.

In the study area, the period of rice cultivation in the dry season from planting to harvest was approximately 120 days.



Considering the crop phenology of rice from NDVI, it was found that the highest NDVI occurred in the middle of the rice season. Farmers started planting rice in the southern part of the study area from A5 and then A2 and A1, respectively. For longan plantations, most of area are located in areas A4 and A6, with NDVI values between 0.4-0.65. It was found that the period between March and April had the lowest NDVI. The crop phenology for the sample plots based on the NDVI in the dry season, as shown in the NDVI graph of each area in Fig. 3.

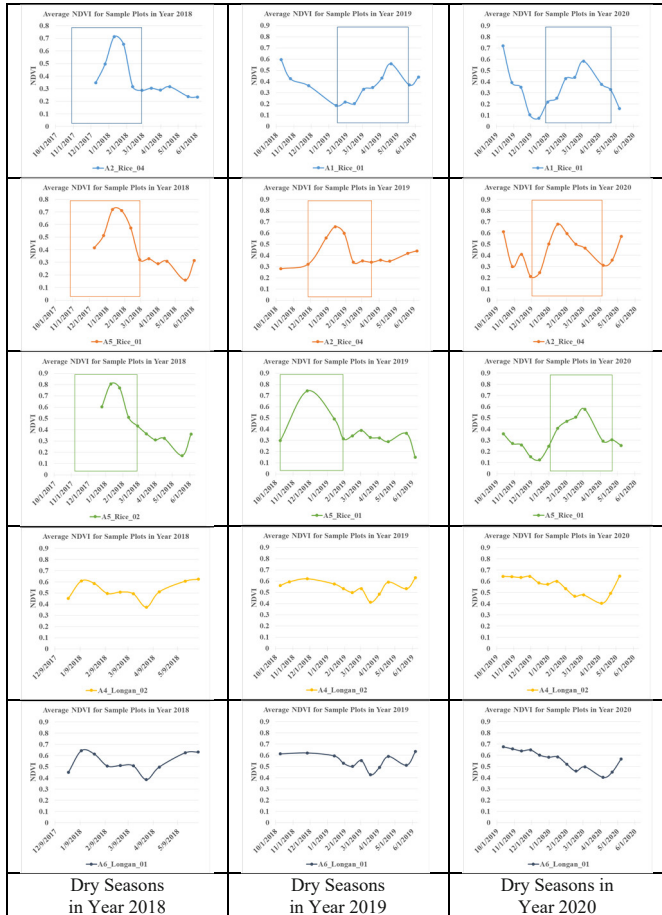


Fig. 3. Crop phenology for the sample plots based on the NDVI in the dry season

### B. Relation between NDVI and $K_c$ for Rice

All paddy fields sample plots in the dry season year 2018-2020, as shown in Fig. 2, are used as a proxy to determine the relation between NDVI and  $K_c$  for rice. The  $K_c$  value of each growing stage was obtained from FAO-56 single crop coefficient based on as suggested by Allen et al. [10] and Pereira et al. [13] and compared with the NDVI of each growing stage, which was an extract from the crop phenology identified by the NDVI curve as shown in Fig. 3.

The results showed that the correlation between the  $K_c$  values obtained with NDVI and FAO-56 single crop coefficient method for rice at the satellite acquisition date was in good agreement with the coefficient of determination

( $R^2$ ) of 0.74 as shown in Fig. 4. The relation between NDVI and  $K_c$  for rice is expressed as the following equation:

$$K_{c(FAO-56)} = 0.6242 * NDVI + 0.7802 \quad (5)$$

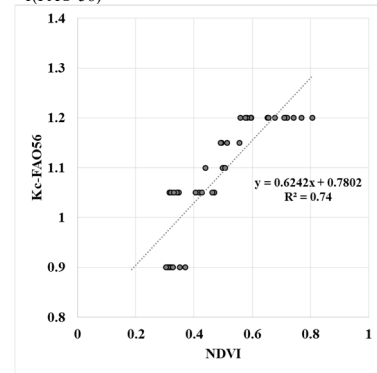


Fig. 4. Correlation between the NDVI and  $K_c$  from FAO-56 method for rice at the satellite acquisition date for all sample plots

### C. Estimate the $ET_c$ Using Vegetation Index Method

The results of  $ET_c$  using the VI method from all sample plots during 2018-2020 found that the average daily  $ET_c$  of rice sample plots in the study area was calculated using  $K_c$  obtained from NDVI (Eq. (5)) of 2018, 2019, and 2020 with an average of 3.34, 3.93, and 4.48 mm/day, respectively. The average daily  $ET_c$  of longans sample plots were calculated using  $K_c$  obtained from NDVI (Eq. (4)) of 2018, 2019, and 2020 with an average of 3.26, 3.60, and 3.59 mm/day, respectively. The average daily  $ET_c$  in agricultural areas showed that the  $ET_c$  values for paddy fields were higher than longan.

The spatiotemporal distribution of the seasonal  $ET_c$  during the dry season is shown in Fig. 5. Overall, the spatial distributions and temporal changes were consistent with climate variations (affect to  $ET_c$ ), crop phenology (e.g., crop growth period, crop health, and characteristics of each plant type), and human activities (e.g., the date of cultivation begins, amount of water budget and also water allocated for cultivation in the plot area).

### D. Evaluation of the Crop Evapotranspiration

For accuracy assessment, the  $ET_c$  obtained from NDVI- $K_c$  method was compared with that calculated with the FAO-56 single crop coefficient method of all sample plots in the dry season year 2018-2020 as shown in Table 1. The difference between the cumulative  $ET_c$  values of each plot from the FAO-56 single crop coefficient method and NDVI- $K_c$  method ranged from 0.91%–7.53% for rice and 8.03%–12.02% for longan.

The results of the study on the relation between the NDVI based on satellite remote sensing and the  $K_c$  were consistent with the various study such as those by González et al. [16] and Kamble et al. [17], which found a good correlation.

For further study,  $ET_c$  derived from VI method should be calibrated for accuracy with other measurement methods such as eddy covariance, lysimeters and even satellite-based energy balance [1].

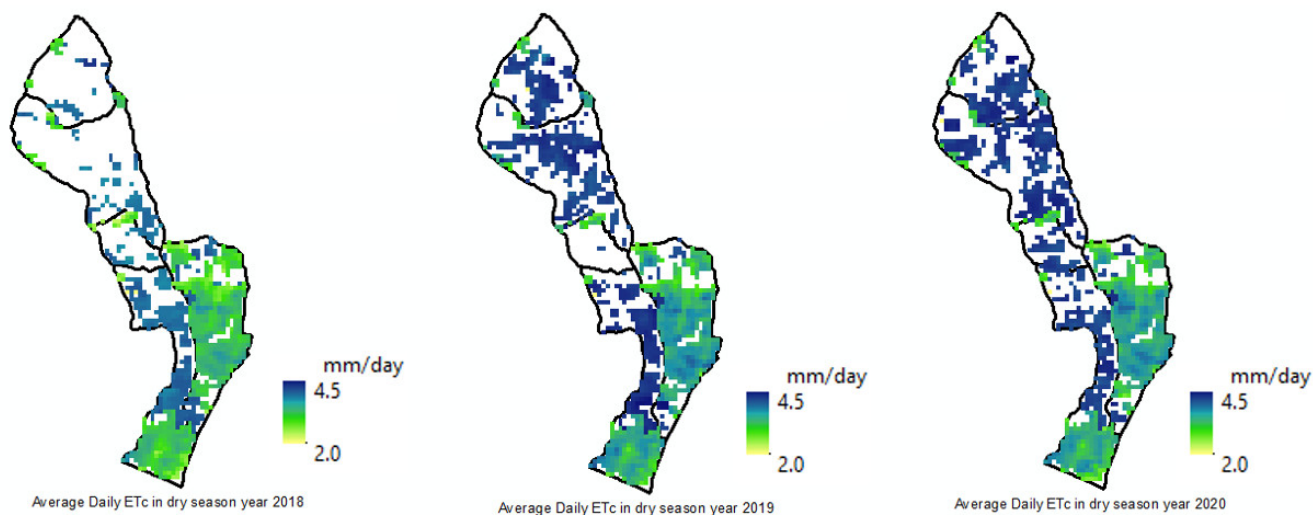


Fig. 5. Spatial distribution of average daily  $ET_c$  for agriculture area in the dry season

Table 1. Cumulative  $ET_c$  from FAO-56 single crop coefficient method and NDVI-FAO56 method for each sample plot covering the dry season in 2018-2020

Dry Season	Plot Name	Seasonal Duration	Cumulative $ET_c$ (FAO-56)	Cumulative $ET_c$ (NDVI-FAO56)	Percentage Difference (%)
Year 2018	A2_Rice_04	2017/10/28 to 2018/02/25	392.51	381.73	2.78
	A5_Rice_01	2017/10/28 to 2018/02/25	392.51	399.38	1.74
	A5_Rice_02	2017/10/28 to 2018/02/25	392.51	420.09	6.79
	A4_Longan_02	2017/10/01 to 2018/05/31	707.10	784.46	10.37
	A6_Longan_01	2017/10/01 to 2018/05/31	707.10	797.55	12.02
Year 2019	A1_Rice_01	2019/01/19 to 2019/05/19	653.32	605.90	7.53
	A2_Rice_04	2018/10/31 to 2019/02/28	411.29	400.27	2.72
	A5_Rice_01	2018/10/01 to 2019/01/29	403.85	407.37	0.87
	A4_Longan_02	2018/10/01 to 2019/05/31	788.96	869.77	9.74
	A6_Longan_01	2018/10/01 to 2019/05/31	788.96	877.59	10.64
Year 2020	A1_Rice_01	2019/12/25 to 2020/04/23	584.94	551.31	5.92
	A2_Rice_04	2019/12/07 to 2020/04/05	513.56	508.89	0.91
	A5_Rice_01	2019/12/25 to 2020/04/23	584.94	552.02	5.79
	A4_Longan_02	2019/10/01 to 2020/05/31	799.98	883.73	9.95
	A6_Longan_01	2019/10/01 to 2020/05/31	799.98	866.87	8.03

#### IV. CONCLUSION

This study applied the satellite-based VI method to estimate  $ET_c$  during the crop growth period for the agricultural area, especially paddy fields sample plots in the dry season year 2018-2020, and longan, in the study area as a part of the Northern Region of Thailand. Also, determine the relation between the NDVI derived from Landsat-8 imagery and the Kc derived from FAO-56 single crop coefficient method for rice using linear regression.

The daily NDVI image time series applied to extract the crop phenology and identify crop development stages showed that the rice cultivation areas differed yearly. The farmer's decision to cultivate rice depends on the amount of water budget each year and the water allocated for cultivation in the plot area. Farmers start planting rice in the southern part of the study area from area A5, followed by the northern part with A2 and A1, respectively. For longan plantations, it was found that the period between March and April had the lowest NDVI. The relation between NDVI derived from Landsat-8 imagery and Kc for rice obtained from FAO-56 single crop coefficient method for rice in the dry season year 2018-2020 showed that the correlation was in good agreement with  $R^2$  of 0.74. The difference between the cumulative  $ET_c$  values of each plot from the FAO-56 single crop coefficient method and NDVI-Kc method ranged from 0.91%–7.53% for rice and 8.03%–12.02% for longan. The  $ET_c$  based on VI method showed that the average daily  $ET_c$  in agricultural areas for paddy fields was higher than longan. Overall, the spatial distributions and temporal changes were consistent with climate variations, crop phenology, and human activities.

#### ACKNOWLEDGMENT

The authors would like to thank the Thai Meteorological Department for providing the climate and rainfall data. The authors also thank the Land Development Department for providing the land-use data used in this study.

#### REFERENCES

[1] R.G. Allen, L.S. Pereira, T.A. Howell, M.E. Jensen, "Evapotranspiration information reporting: I. Factors governing measurement accuracy". *Agric. Water Manag* 2011(98):899–920, 2011.

[2] S. Altendorf, "Minor Tropical Fruits (Mainstreaming a Niche Market)". *Food Outlook*. 8:67–75, 2018. Available online: [http://www.fao.org/fileadmin/templates/est/COMM\\_MARKETS\\_MONITORING/Tropical\\_Fruits/Documents/Minor\\_Tropical\\_Fruits\\_FoodOutlook\\_1\\_2018.pdf](http://www.fao.org/fileadmin/templates/est/COMM_MARKETS_MONITORING/Tropical_Fruits/Documents/Minor_Tropical_Fruits_FoodOutlook_1_2018.pdf) (accessed on 28 April 2023).

[3] W. Spreer, K. Schulze, S. Ongprasert, W. Wiriya-Alongkorn, J. Müller, "Mango and longan production in northern Thailand: The role of water saving irrigation and water stress monitoring". In *Sustainable Land Use and Rural Development in Southeast Asia: Innovations and Policies for Mountainous Areas*; H.L. Fröhlich, P. Schreinemachers, K.

Stahr, G. Clemens, Eds.; Springer Environmental Science and Engineering; Springer: Berlin, Germany. 215–228, 2013.

[4] N. Nam-in, K. Sittichok, C. Chompuchan, "Estimating Crop Coefficient (Kc) of Lowland Irrigated Rice using Multi-temporal Satellite-Derived Vegetation Index". *Journal of Remote Sensing and GIS Association of Thailand*. 20:331-344, 2019.

[5] N. Nam-in, C. Chompuchan, K. Sittichok, "Application of NDVI-based Kc for Irrigation Performance Evaluation of Chao Chet - Bang Yihon Operation and Maintenance Project". The Proceedings of the 17th National Kasetsart University Kamphaeng Saen Conference, Nakhon Pathom, Thailand, 2–3 December 2020.

[6] N. Yensakunsuk, T. Chayakula, "Estimation of wet direct-seeding rice Evapotranspiration in Irrigated Areas of Chao Phraya Basin by using remote sensing technology". The 25th National Convention on Civil Engineering, Chonburi, Thailand, 15-17 July 2020.

[7] O.M. Adisa, J.O. Botai, A. Hassen, D. Darkey, A.M. Adeola, E. Tesfamariam, C.M. Botai, A.T. Adisa, "Variability of Satellite Derived Phenological Parameters across Maize Producing Areas of South Africa". *Sustainability*. 10:3033, 2018.

[8] X. Li, W. Zhu, Z. Xie, P. Zhan, X. Huang, L. Sun, Z. Duan, "Assessing the Effects of Time Interpolation of NDVI Composites on Phenology Trend Estimation". *Remote Sens*. 13:5018, 2021.

[9] T. Supriyasilp, K. Pongput, S. Boonyanupong, T. Suwanlertcharoen, "Enhanced water management for muang Fai irrigation systems through remote sensing and SWOT analysis". *Water Resour Manage* 35(1):263–277, 2021.

[10] R.G. Allen, L.S. Pereira, D. Raes, M. Smith, "Crop evapotranspiration-Guidelines for computing crop water requirements-FAO Irrigation and drainage paper 56". FAO: Rome, Italy, 1998.

[11] R. Crippen, "Calculating the vegetation index faster". *Remote Sens Environ*. 34:71–73, 1990.

[12] M.E. Jensen, R.G. Allen, "Evaporation, Evapotranspiration, and Irrigation Water Requirements". 2nd ed; American Society of Civil Engineers: Reston, VA, USA, 2016.

[13] L.S. Pereira, P. Paredes, D.J. Hunsaker, R. López-Urrea, Z. M. Shad, "Standard single and basal crop coefficients for field crops. Updates and advances to the FAO56 crop water requirements method". *Agric. Water Manag*. 243:106466, 2021.

[14] S. Belda, L. Pípiá, P.M. Pallarés, J.P.R. Caicedo, E. Amin, C.D. Grave, J. Verrelst, "DATimeS: A machine learning time series GUI toolbox for gap-filling and vegetation phenology trends detection". *Environmental Modelling & Software*. 127:104666, 2020.

[15] A.C. Belmonte, A.M. Jochum, A.C. García, A.M. Rodríguez, P.L. Fuster, "Irrigation management from space: Towards user-friendly products". *Irrig Drainage Syst*. 19:337–353, 2005.

[16] A.R. González, J. Kjaersgaard, T. Trooien, C. Hay, L. Ahiablame, "Estimation of Crop Evapotranspiration Using Satellite Remote Sensing-Based Vegetation Index". *Advances in Meteorology*. 2018:1-12, 2018.

[17] B. Kamble, A. Irmak, K. Hubbard, “Estimating Crop Coefficients Using Remote Sensing-Based Vegetation Index”. Remote Sens. 5:1588-1602, 2013.

# Physically-distributed hydrological model for the poorly gauged basin of Nong Han Lake

Thodsapol Chaturabul<sup>1\*</sup>, Kobkiat Pongput<sup>2</sup>, Thanaporn Supriyasilp<sup>3</sup>, Jongkon Chongwilaikasem<sup>4</sup>

<sup>1\*</sup> Department of Water Resources Engineering, Faculty of Engineering,  
Kasetsart University, Bangkok, Thailand, thodsapol.ch@ku.th

<sup>2</sup> Department of Water Resources Engineering, Faculty of Engineering,  
Kasetsart University, Bangkok, Thailand, kobkiat.p@ku.th

<sup>3</sup> Department of Civil Engineering, Faculty of Engineering,  
Chiang Mai University, Chiangmai, Thailand, thanaporn @eng.cmu.ac.th

<sup>4</sup> TEAM Consulting Engineering and Management Public Company Limited,  
Bangkok, Thailand, jongkon\_c@team.co.th

**Abstract:** Nong Han Lake (NHL) is situated in the Nong Han River Basin (NHB), a sub-basin of the Nam Kam River Basin and the Mekong River Basin. It is the largest natural freshwater lake in Northeastern Thailand and the second-largest lake in Thailand. Despite receiving water from 16 rivers, the area surrounding the NHL still experiences floods and droughts annually. This study aimed to estimate the inflow of NHL in poorly gauged NHB using the SWAT model. At two runoff gauging stations, coefficient of determination ( $R^2$ ), root mean square error (RMSE), and volume error from model calibration and validation ranged between 0.52 and 0.69, 18.98 m<sup>3</sup>/s and 33.74 m<sup>3</sup>/s, and (-21.00) % and (-41.00) %, respectively. The five rainfall scenarios were simulated to determine the inflow of 16 rivers around NHL, including (1) average rainfall; (2) heavy rainfall; (3) low rainfall; (4) highest rainfall; and (5) lowest rainfall. More than 60 percent of the total runoff into NHL is produced by the Huai Nam Phung, making it the most influential river. Simultaneously, the Huai Diek is the second influential rivers that contribute approximately 10 percent of the total runoff, respectively. Following the SWAT simulation, it was recommended that 16 climate stations and 16 water level measuring stations were developed and installed at 16 centers of gravity of the sub-basin and the outlet of the main sub-basin to enhance the SWAT model and develop the river models.

**Index Terms**— Nong Han Lake, physically-distributed hydrological model, poorly gauged basin, runoff assessment, SWAT model.

## I. INTRODUCTION

The Nong Han River Basin (NHB) is a sub-basin of the Nam Kam River Basin and the Mekong River Basin. Its primary water resource is Nong Han Lake (NHL), the largest natural freshwater lake in Northeastern Thailand and the second-largest lake in Thailand. In 1932, NHL had announced as a place to nourish the aquatic life of the northeastern region by the Department of Fishery and named Thailand's internationally important wetland by the Office of Natural Resources and Environmental Policy and Planning in 2009.

For decades, the development around NHL and urban expansion have caused difficulties for NHL, such as lake shallowness, depletion of aquatic species, floods, drought, and deterioration of water quality [1]. Ruekaewma [2] and CSS [3] recognized three current concerns of NHL: (1) imbalance between water supply and water demand; (2) water quality problems; and (3) lack of integration and cooperation in management.

Although NHL has a vast storage capacity and obtains

water from surrounding 16 rivers, people around NHL still experience floods and drought alternately yearly. The NHL needs to be administered in an integrated and systematic manner.

Hydrological and hydraulics models are widely used tools for evaluating the watershed capacity and planning for watershed management. These models must possess accurate climate, rainfall, runoff, physical characteristics data, variables, and parameters to assess the potential flow and behavior change due to climate variation, land use alteration, and water development projects.

The main objective of this research was to develop a hydrological model for estimating the flow capacity of NHL which is located in the poorly gauged NHB. Due to the unique physical characteristics of the NHB, the western and southern borders of the basin are hilly and steep, whereas the basin's center is lowland. The SWAT model, a physically distributed hydrological model, was utilized to simulate the diverse physical characteristics of the basin. The findings of the simulation of the water flowing into NHL may be used for integrated and systematic water planning, development, and management.

## II. MATERIAL AND METHODS

Although the purpose of this study was to determine the volume of water flowing into Nong Han Lake (NHL), which is located in the Nong Han River Basin (NHB). As NHB is a poorly gauged basin with no streamflow measuring station, the study area for model development has been expanded to encompass the Nam Phong Basin in the upstream and the Kam Nam Basin in the downstream.

The detail of the study area, data used, and framework of this research are as follow:

### A. Study Area

The study area of this research is the Nong Han Lake (NHL), located in Nong Han River Basin (NHB). Nong Han River Basin (NHB) is a part of the Namkam River Basin, which covers three sub-basins from upstream to downstream: the Nam Phong, Nong Han, and Namkam River basins. These three basins are tributaries of the Mekong River Basin in northeastern Thailand.

The general geography of NHB is generally low and flat. The southern and western regions of the basin watershed are the Phu Phan Mountain range which slopes with undulating hills down to the lowland around NHL, which is in the heart of the basin. This area is a dipterocarp and dry evergreen forest interspersed with agricultural areas. In contrast, the northern and eastern regions are plains interspersed with low-slope areas. NHL receives water from 16 streams in Sakon Nakhon Province. All the water flows through the Surasawadi drainage gate into the Nam Kam River and finally to the Mekong River at Nakhon Phanom Province [4], as shown in Fig 1.

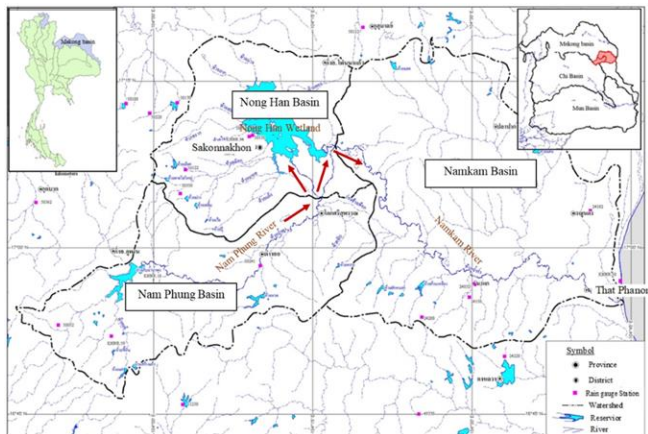


Fig. 1. The overview of the study area. (modified from [4])

### B. Data collection

The water cycle data for the SWAT model includes

- Atmospheric data: rain and climatic data.
- Surface data: topography, land use, and surface runoff.
- Subsurface data: shallow soil layer data such as soil type, soil moisture, and seepage; deep soil layers, such as infiltration depth; and groundwater layers, such as geological features.

All data used in this research is secondary data collected

from the various government agencies, as shown in Table 1. The collected data consists of topographical data, climate, daily rainfall and runoff, land use, and soil type.

TABLE I  
TYPE, DETAIL, AND SOURCE OF COLLECTED DATA

No.	Data types	Details	Source
1	Digital Elevation Model (DEM)	Resolution of 30 x 30 m	Royal Thai Survey Department
2	Soil type	5-year map between 2005-2010	Land Development Department
3	Land use	5-year map between 2012-2016	Land Development Department
4	Climate	The 30-year climate of Sakonnakhon station between 2529-2558	Thai Meteorology Department
5	Daily rainfall	30-year data statistics of 18 stations from 1986 to 2015	Royal Irrigation Department and Department of Water Resources
6	Daily runoff	30-year data statistics of 2 stations from 1986 to 2015	Royal Irrigation Department and Department of Water Resources

### C. Methodology

The framework for this research is divided into five steps: (1) Data collection and prepare the model database; (2) model development: (3) model calibration and verification; and (4) scenarios simulation, as shown in Fig.2

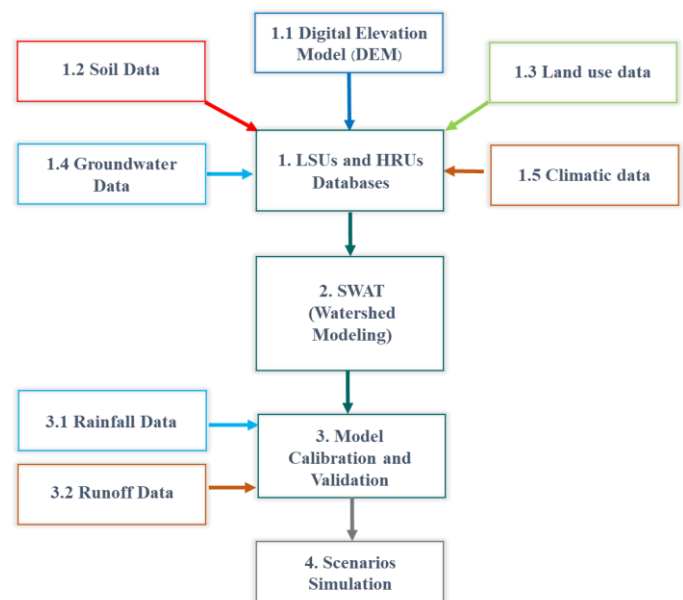


Fig. 2. The framework of research

The inflow of NHL is analyzed using the rainfall-runoff relationship model SWAT, which is a model that considers the physical characteristics of the surface and sub-surface in the basin. The detail of each step in Fig.2 is as follow:

1. Prepare the database for SWAT according to framework dialog 1 in Fig 2. The database consisted of secondary data collected in table 1.
2. Develop the SWAT model according to framework dialog 2 in Fig 2. As illustrated in Fig. 3, this study identified 18 main and 87 secondary sub-basins according to the topography, reservoir and weir location, runoff monitoring stations, river confluences, and road. After that, 763 HRUs were divided according to 5% distribution of each land uses soil type and slope, as shown in Fig. 4.

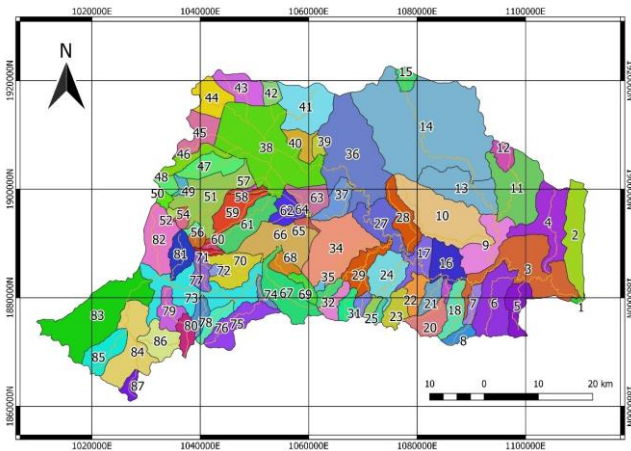


Fig. 3. Division of sub-basins in NPB, KHB, and NKB.

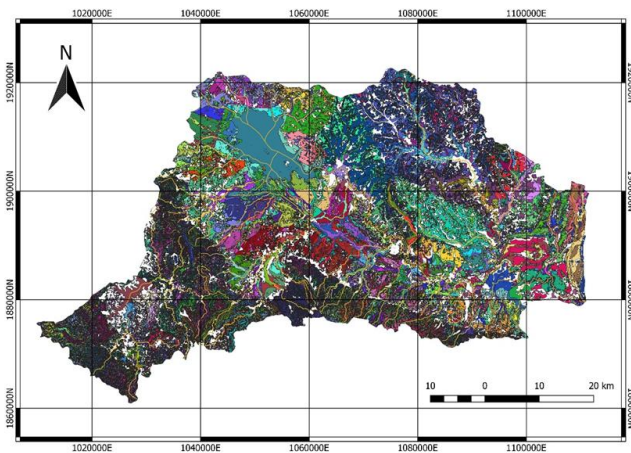


Fig. 4. Hydrological Response Units or HRUs of NPB, KHB, and NKB.

3. Calibrate and validate the developed SWAT models with rainfall and runoff time series according to framework dialog 3 in Fig 2. Because NHB is a poorly gauged basin with no runoff station, the runoff time series used for calibration and validation was from two stations: KH.90 in Namphung river, one of 16 rivers that flow to NHL; and KH.63 located downstream from the NHL outlet in Namkam river.

4. Simulate the existing state and other four scenarios of NHL according to framework dialog 4 in Fig 2. The five rainfall scenarios used in this research were selected from annual rainfall as shown in Fig. 5., including (1) average rainfall in 2015; (2) heavy rainfall in 2009; (3) low rainfall in 2013; (4) highest rainfall in 2006; and (5) lowest rainfall in 1999.

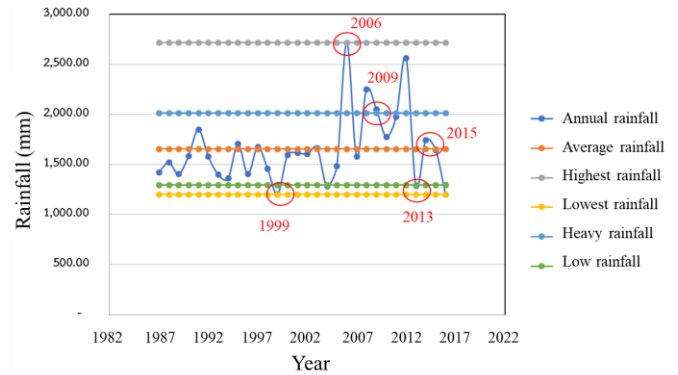


Fig. 5. Selection of rainfall scenarios

### III. RESULTS AND DISCUSSION

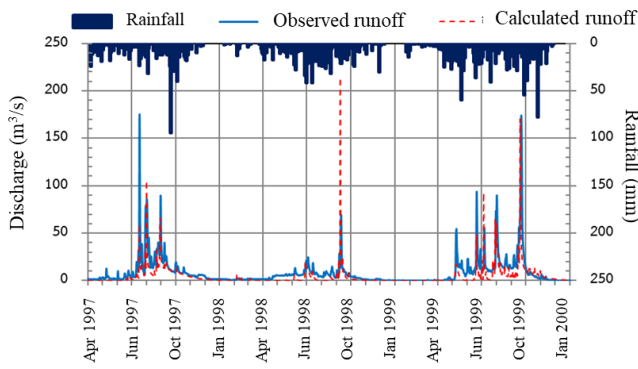
#### A. Model calibration and validation

The model was calibrated and validated with observed runoff data during 1997-1999 and 2000-2002, respectively, at KH.90 station in Namphung river and KH.63 station located downstream from the NHL outlet in Namkam river. The results of model calibration and validation are shown in table 2 and Fig. 6.

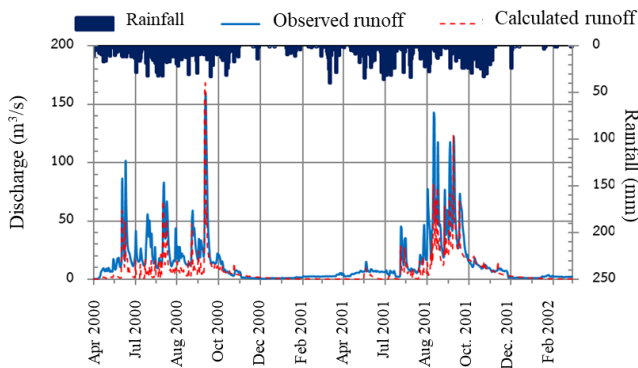
The statistical analysis in table 2 reveals that  $R^2$  is more significant than 0.6, while RMSE and the volume error of accumulated runoff are less than  $\pm 30$  percent, which is an acceptable hydrological criterion [5]. When examining the calibration and validation results of runoff estimated using the model, the observed runoff and rainfall data in Fig. 6 demonstrate that consistency exists. Consequently, it may be stated that the model's parameters are representative enough to predict runoff behavior from rainfall in the basin.

TABLE 2  
RESULT OF MODEL CALIBRATION AND VALIDATION

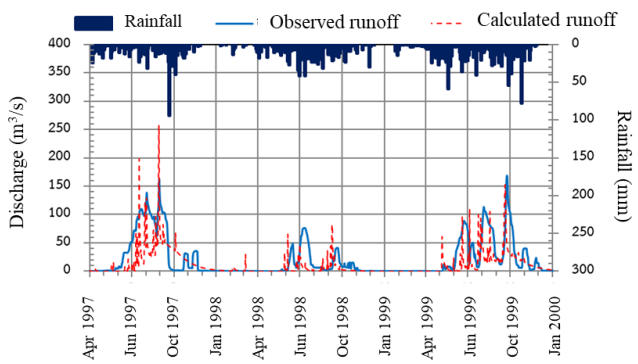
Station	Calibration			Validation		
	$R^2$	RMSE (m <sup>3</sup> /s)	Volume Error (%)	$R^2$	RMSE (m <sup>3</sup> /s)	Volume Error (%)
KH.90	0.69	33.74	-31.00	0.61	32.78	-21.00
KH.63	0.56	18.98	-33.30	0.59	24.49	-41.80



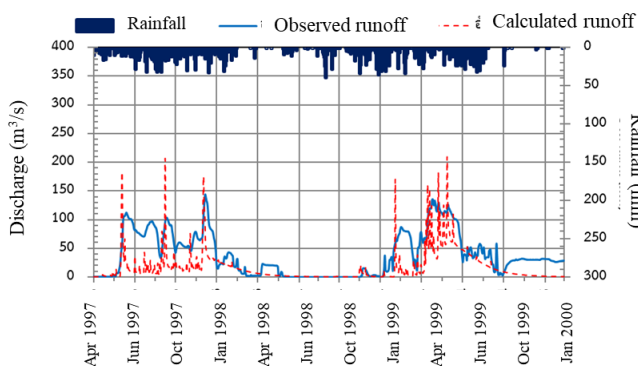
(a) Model calibration at KH.90KH.90 station



(b) Model validation at KH.90KH.90 Station



(c) Model calibration at KH.63 station



(d) Model validation at KH.63 station

Fig. 6. Model calibration and validation at KH.90 and KH.63 stations.

### B. Inflow assessment of Nong Han Lake

According to the average rainfall scenario, 704.82 MCM of water is flowing into NHL. Huai Nam Phung accounts for 60.59 percent of the annual inflow to NHL, with 427.04 MCM/year. Following is Huai Diek, whose 70.64 MCM production represents 10.02 percent of the NHL's annual inflow. In contrast, each remaining river provides less than 5% of the total annual inflow to NHL, as shown in table 3 and Fig. 7. Additionally, table 3 demonstrates that 98% of each river's annual runoff occurs during the rainy season and annual runoff yield is not much difference. Annual runoff yield is between 1.48-1.98 m<sup>3</sup>/s/km<sup>2</sup>.

The remaining scenarios tend to follow the same pattern. The only difference is the quantity of water.

TABLE 3  
THE INFLOW OF NONG HAN LAKE WITH AN AVERAGE RAINFALL

No	River Name	Catchment Area (km <sup>2</sup> )	Runoff Volume (MCM)			Runoff Volume (%)	Annual Yield (m <sup>3</sup> /s/km <sup>2</sup> )
			Rainy	Dry	Annual		
1	Huai Hue	4.31	2.18	0.01	2.19	0.31	1.61
2	Huai Pa da	10.12	5.12	0.02	5.14	0.73	1.61
3	Huai Long	71.30	33.15	0.05	33.20	4.71	1.48
4	Huai Nong Hae	11.00	5.56	0.04	5.60	0.79	1.61
5	Huai Muang	12.14	6.14	0.04	6.18	0.88	1.61
6	Huai Lak	51.63	26.54	0.35	26.89	3.82	1.65
7	Huai Samor	23.17	12.76	0.21	12.97	1.84	1.78
8	Huai Sai	32.03	17.76	2.26	20.02	2.84	1.98
9	Huai Mong	29.88	16.47	0.27	16.74	2.38	1.78
10	Huai Dieak	122.38	69.75	0.89	70.64	10.02	1.83
11	Huai He	23.76	13.37	0.28	13.65	1.94	1.82
12	Huai Wang Chang	4.87	2.74	0.06	2.80	0.40	1.82
13	Huai Na kae	38.37	21.14	0.37	21.51	3.05	1.78
14	Huai Kang	52.61	27.46	0.43	27.89	3.96	1.68
15	Huai Song Khon	28.06	12.20	0.16	12.36	1.75	1.40
16	Nam Phung	901.91	423.19	3.85	427.04	60.59	1.50
		1417.54	695.53	9.29	704.82	100.00	

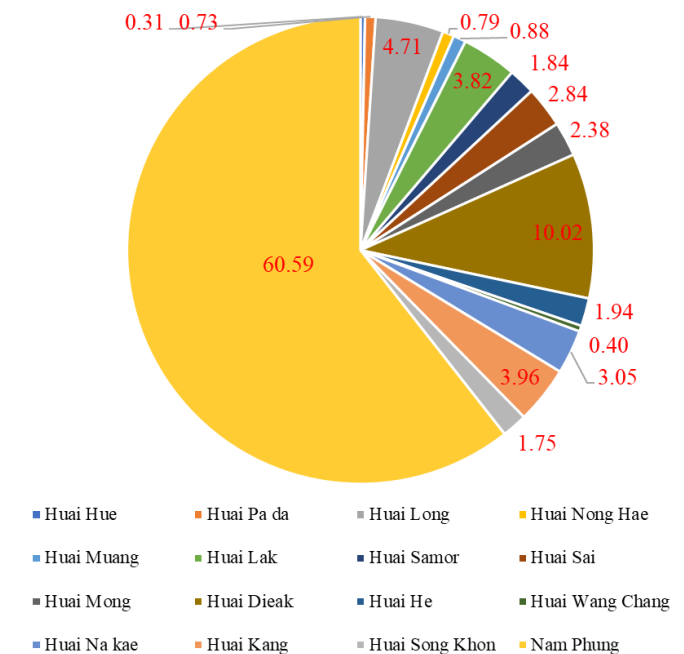


Fig. 7. Percentage of inflow to Nong Han Lake from average rainfall



scenario.

The simulation findings allow for the classification of river development potential into three groups:

- 1) Group of high potential, namely Nam Phung and Huai Dieak
- 2) Group of medium potential, namely Huai Long, Huai Kang, Huai Lak, Huai Sai Huai Mong, Huai Na Kae, Huai He, Huai Samor, and Huai Song Khon, and
- 3) Group of low potential, namely Huai Muang, Huai Nong Hae, Huai Pada, and Huai Hue.

The document reviewed [6] revealed that nine rivers were already included in the plan of the government's water agencies for the wholes river, leaving just seven rivers with only the downstream development plan near NHL, namely: Huai Mong, Huai Sai, Huai Samor, Huai Nong Hae, Huai Long, Huai Nakae, Huai Diek.

Since these seven rivers are in the medium and low river development potential groups and the quantity of water, more than 98 percent occur in the rainy season. The development of the river should consider expanding the river's capacity, developing hydraulic structures i.e. weir, and watergate in the river to store water during the wet season, and diverting water into public ponds for the dry season.

NHL was announced as a conservation area for aquatic wildlife and national and international wetland. The water management in NHL is natural marsh management and has no water allocation for agricultural areas. Since the entire volume of water flowing into NHL during the rainy season is 695.53 MCM per year, while its capacity is 260 MCM. Thus, the river development should also incorporate water pumping back systems before the dry season flows into the NHL to assure the water security of riverside residents.

### C. Discussion

Even though the model calibration and validation results were within acceptable criteria, this value is still low because NHB is a radial basin with independent tributaries. The runoff measuring stations is, therefore, insufficient for the area. It does not cover all rivers flowing into the NHL. In addition, there was only one climate station in NHB. It was situated in a lowland area near NHL, which may not accurately reflect the climate of the mountainous region in the west and south of the basin, which is the headwaters of most NHL tributaries.

Based on the model simulation, 16 climatological stations were proposed to be installed in the center of gravity of the main sub-basin to provide representative basin data. These stations should be installed in schools, temples, or government areas because it has enough unobstructed space and an attendant. The recommended climatological station locations are shown in Fig. 7.

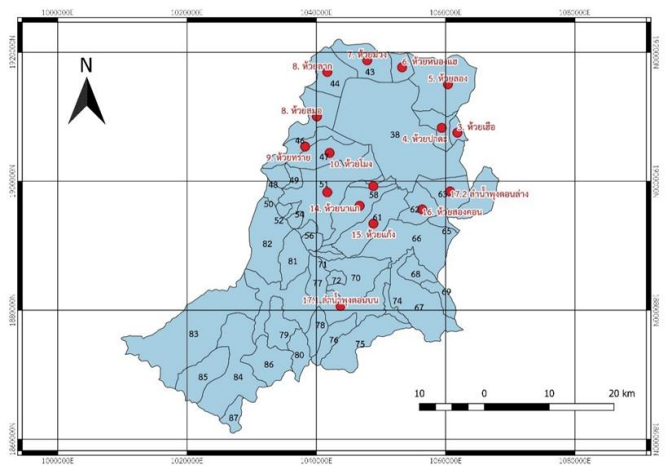


Fig. 7. Location of the recommended climatological station at the center of gravity of the sub-basin.

In addition, 16 runoff measurement stations are also recommended to install at the outlet of the main sub-basin to calibrate and validate models and serve as a monitoring point for stakeholders. The stations should be installed on the bridge rails of highways and roads because it is an open space, convenient to install and maintain. The recommended runoff station locations are shown in Fig. 8.

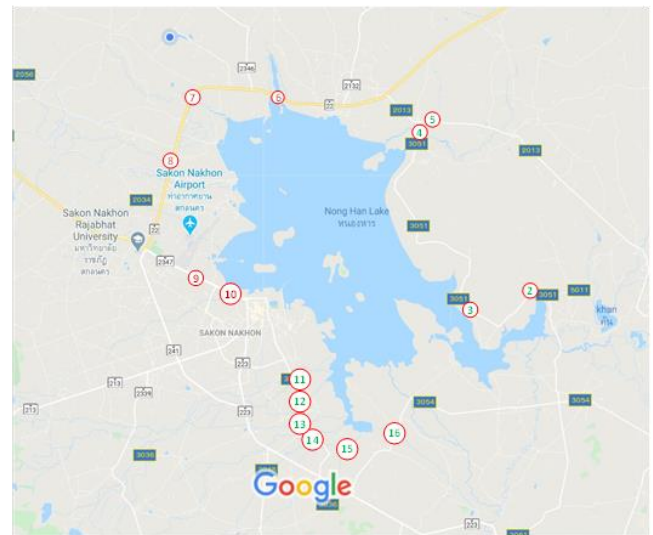


Fig. 8. Location of the recommended runoff measurement station at the outlet of gravity of the sub-basin.

The data from these suggestion stations are anticipated to be used to improve the SWAT model's ability to account for the physical characteristics of the basin, as well as to calibrate and validate the model for greater precision and be utilized for future river model development.

## IV. CONCLUSION

This study developed the SWAT model, a distributed hydrological model, for NHB. The model calibration and validation obtained the  $R^2$ , RMSE, and volume between 0.56 - 0.69, 18.98  $m^3/s$  - 33.74  $m^3/s$ , and (-21.00%) - (-

41.80%), respectively, which is an acceptable hydrological criterion.

Five rainfall scenarios were simulated to evaluate the inflow trend of each river to NHL. According to all scenarios, the Phung river has the highest annual runoff among the 16 rivers, and hence the Huai Hue river. These two rivers provide almost 70% of the total annual NHL runoff. In contrast, the Huai Hae river experiences the least runoff in every scenario.

Based on model calibration and validation, this research suggests the installation of an additional 16 climatological stations at the center of gravity of the sub-basin and also suggest 16 runoff measurement station at the outlet of the sub-basin to increase the efficiency of the model and to serve as an observation point for the local people.

This research and the developed model may be utilized to create planning and construct an agreed and effective water management plan and strategy for NHL. The appropriate water management will enhance the quality of life and livelihood of the people, create water security in terms of production for the dry season comprehensively and transparently, creating safety for life and property from flooding. People in the area can increase productivity and income, affecting the economy of Sakon Nakhon Province.

#### ACKNOWLEDGMENT

The authors would like to acknowledge the Thai Meteorological depart for providing climate data, the Royal Irrigation Department and the Department of Water Resources for rainfall and runoff data, and the Land Development Department for land use and soil maps. Moreover, this research is financially supported by the Agricultural Research Development Agency (Public Organization) (grant number: PRP610502269).

#### REFERENCES

- [1] Mekong River Commission. "Trans-boundary cooperation for river basin management between Lao PDR and Thailand in Xe Bang Hieng Basin-Lao PDR and Nam Kam Basin-Thailand. Joint Report on Wetland Management between Xe Champhone-Lao PDR and Nong Han-Thailand project", 106 pages, 2017.
- [2] Ruekaewma, Pramook. "Freshwater fishery management". PowerPoint Presentation, 2015. (in Thai)
- [3] Chor-Sor-Sor Sakon Nakhon Association "Nong Han: problems and solution Guidelines", 2016. (in Thai)
- [4] Chaturabul, T., and Pongput, K. "Nong Han: A physical view". In "Lesson learnt from Nong Han" S. Petcham, (Ed.). Pornsiri Publishing, pp 32-52. (in Thai)
- [5] Moriasi, D. N., Arnold, J. G., Van Liew, M. W., Bingner, R. L., Harmel, R. D., and Veith, T. L. "Model evaluation guidelines for systematic quantification of accuracy in watershed simulations",
- [6] Sakon Nakhon Provincial Office. "Master plan study for Nong Han development: Final report" 396 pages, 2019. (in Thai)

# Crash-Simulation-based Validation of a Safety-Frame Concept with Crash-Boxes for Maximized Protection of Motorcycle Taxi Passengers

Phairat Yuenyong<sup>1\*</sup>, Alexander N. Brezing<sup>2</sup>

<sup>1\*</sup> Department of Mechanical and Automotive Engineering, The Sirindhorn International TGS, KMUTNB, Bangkok, Thailand, s6009092860033@email.kmutnb.ac.th

<sup>2</sup> Department of Mechanical and Automotive Engineering, The Sirindhorn International TGS, KMUTNB, Bangkok, Thailand, alex.b@tgs.kmutnb.ac.th

**Abstract:** Motorcycle Taxis (MT) are an important part of the available mobility modes in Bangkok, covering short to medium distances, especially on narrow and congested roads and bridging public transportation grids and “the last mile” of individual transport. The disadvantage of motorcycle taxis is that the passenger is not protected in case of collisions or similar accidents in spite of a legal obligation to wear helmets, which is generally ignored by MT-passengers for reasons of practicality with this mobility mode. This study aims at validating a concept of specifically protecting the passengers of MTs by means of a light sub-frame that allows for the use of safety belts and that absorbs sufficient amounts of crash energy by using crumpling elements (“crash boxes”) to significantly reduce the risk of fatal injuries in case of head-on collisions. Crash simulations with Hybrid III human dummy models and simple passenger frames, with and without crash-boxes, are compared. The results of these simulations, performed with LS-DYNA, clearly demonstrate that the passenger frame concept with safety belts significantly reduces the risk of lethal head injuries for MT-passengers without helmets. Furthermore, it is demonstrated that crash-boxes can be integrated into such frames to minimize the risk of chest and neck injuries by absorbing kinetic energy during the initial phase of the crash. It is concluded that further studies need to focus on the compliance of the frame as a whole to realize the full potential of this safety concept.

**Index Terms—** Small Motorcycle Crash Safety, Motorcycle crash simulation, Passive Safety, Dummy Kinematics, Axial Crushing of Thin-Walled Structure, Finite Elements.

## I. INTRODUCTION

Small motorcycles or scooters are the most popular vehicles in Southeast Asian countries. With regards to sales figures, the market in Thailand is in the leading group of the world, with over 80% of Thai households owing at least one small motorcycle [1]. The reasons for the popularity of this vehicle class are manifold: low maintenance cost, low fuel consumption, and it can be moved dexterously through traffic jam in rush hours. In Thailand, small motorcycles are not only used privately, but also for commercial transportation of people: The “Motorcycle Taxi” is especially popular in Bangkok and perimeter provinces, where more than 84,000 registered drivers [2] provide cheap rides on routes that cannot be covered by public transport systems.

Legally, drivers and passengers on motorcycles are

obliged to wear helmets [3], but the regulation is mostly ignored and seldom enforced with passengers [4], while the drivers can generally be observed wearing helmets. The risks are accepted by most because of the practicalities of the transportation mode: passengers generally refuse the helmet offered by the driver for reasons of convenience (size, hygiene, etc.) and bringing one’s own helmet simply seems too much effort to be justified by need for safety on a relatively short trip.

According to a global status report on road safety of the world health organization (WHO) of 2018, 21,745 people died from road accidents in Thailand in 2016, and over 74% of these fatalities were caused by motorcycle accidents [5],[6]. A more recent analysis by the Thai Accident Information Center for Strengthening Road Safety Culture (ThaiRSC) in 2019 states a total of 23,530 fatalities from motorcycle accidents for the three years of 2017 - 2019 [7]. Furthermore, the study reveals that over 50% of fatalities are the result of head injuries, with most of fatal accidents

being collisions with moving or still objects, specifically 48% head-on collisions resulting from a failure or inability of the driver to perform a maneuver to avoid a collision with a velocity of typically 30-60 km/h [7]. Available statistics include so-called pillion passengers, meaning additional riders who are not the driver, but do not differentiate statistics between drivers and passengers. The ISO 13232 standard describes impact constellations and crash tests with motorcycles, and it has been applied to research the effectiveness of airbags for mid-sized and larger motorbikes impacting a car and the effects of different designs of roadside guard rails and barriers [ISO13232, 8]. However, neither this standard or any other standard for motorcycle crash testing is applied in Thailand. Carmai et al. researched driver and child pillion passenger kinematics and injury mechanisms by means of crash-simulations [9]. Berg conducted full size tests in 7 of the standard's configurations, all with the motorcycle impacting a stationary car head-on with 48 km/h, with a dummy Hybrid III, 50th percentile male, representing the rider, [8].

While improving the safety of motorcycle riders in general remains an important task for research, this study specifically focuses on improving the safety of the passengers of motorcycle taxis. The authors consider this a matter of public responsibility, as MT-transportation as a whole is a part of the public transportation system in Bangkok, even if the public does not operate MTs. The considerable responsibility for the wellbeing of the passenger is currently born by the individual driver as a result of a private contract for mobility services with the passenger, but it is obvious that this private service provider is not able to stand up to this responsibility. This research therefore serves the interest of the general public and the group of entrepreneurs that offers this mobility service.

#### A. Background: A reviewed concept for a Motorcycle Taxi

The "Motorcycle Taxi" is popular in Bangkok because it is an efficient solution to the congested traffic on main roads and the narrow alleys in the "villages" between the main roads. When the mobility mode was reviewed in multiple design-centric courses at TGGS, this type of agility was recognized as most important characteristic for the effectiveness and acceptance of this mobility mode. Conventional moped and scooter types of motorcycles are used in most cases, and the short wheelbase and low weight allows the driver to maneuver all the narrow spaces left between the cars using the regular lanes on the main streets and use the narrow paths and sharp turns that are typical for living areas off the main streets.

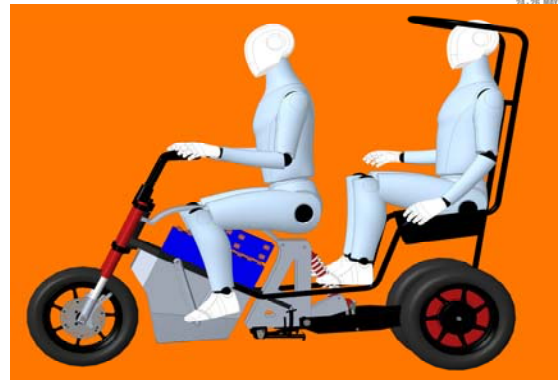


Fig. 1. The reviewed concept for a Motorcycle taxi to be validated in this study.

The revised vehicle concept therefore keeps the main vehicle dimensions and driver's posture but improves on the passenger's convenience and passive safety by adding a "passenger frame", which is mounted to the rear of the compact main frame of the electric vehicle, a tilting tricycle in delta-configuration, Fig. 1. The passenger frame offers the benefits of comfortable mounting and seating as well the protection of the complete passenger's body including the head against low-velocity impacts from all sides. The main feature of this concept however is the use of safety belts in combination with crash-energy absorbing elements in the passenger-frame to substantially increase passive safety in case of head-on collisions. It is argued that this concept would be successful in application because it does not sacrifice any of the existing MT's advantages of agility and convenience (including not having to wear a helmet) for improved safety. The focus of the study discussed in this paper has been on the validation of this safety concept for head on collisions. Other crash configurations, like lateral or rear impacts from other vehicles, are not addressed by the crumpling frame concept, as the vehicle concept does not allow for substantial amounts of crumpling structure on the sides and rear of the vehicle, although the frame offers some additional protection.

#### B. Crumpling Frame, Crash Box

In cases of collisions of vehicles, any absorption of kinetic energy by plastic deformation of parts of the vehicle will reduce the amount of energy that will act on the bodies and therefore the risk or severity of injuries of passengers. In order to minimize deceleration and maximize energy absorption in relation to the weight of the vehicle body structure, the sheet-metal parts of the forward-section of road vehicles have "bead"-features stamped into them to result in a controlled collapsing in longitudinal direction while the large size and complex shape of the parts allow them to fulfil their primary structural functions as parts of a rigid car body. The design of "Crash-Boxes" used to mount bumpers however is optimized exclusively for the function of absorbing the energy of low-velocity impacts by axial collapse, Fig 2. Here, bead-features are also used to support a controlled collapsing of the thin-walled tube.



Fig. 2. Crash-boxes used on automotive bumpers. Image: [10]

The idea behind this research is to integrate similar elements into the tubular elements of a frame that can collapse in the direction of their length (“axial”) if loads resulting from a frontal vehicle-crash act on them. However, as frame elements (beams) typically are under lateral and bending loads, such “frame-crash-boxes” must be designed in a way that they can sustain and support such operating loads without premature buckling of the thin-walled tube, which should only act as energy absorber by a controlled axial collapse.

### C. Objective, Scope and Strategy

The objectives of this study are to evaluate potential benefits of a safety concept for passengers of MTs with a passenger frame, safety belts and crash boxes, to demonstrate how crash-boxes improve passenger safety and to derive design recommendations for future implementation.

The scenario chosen to evaluate “safety” is a head-on collision of the vehicle with an initial speed of 48 km/h in accordance with FMVSS 208 [11]. In order to obtain data for this evaluation, different configurations of the scenario are simulated by means of FEM, with the models including a human-body dummy model (or “anthropomorphic test device”, ATD) as well as appropriately detailed models of the structural components, especially the thin-walled tubes which represent the crash-boxes. In order to evaluate the effect of crash-boxes by themselves, configurations with and without crash-boxes are simulated individually and compared. All simulations are performed with the LS-DYNA software package.

## II. BARRIER COLLISION AND INJURY ASSESSMENT

The conditions of the crash simulations in this study are defined in accordance with the full-frontal crash scenario according to the Federal Motor Vehicle Safety Standard No. 208 (FMVSS 208) [11] by The National Highway Traffic Safety Administration (NHTSA). It represents a real-world crash scenario with significant frontal engagement in perpendicular impact direction at an impact velocity of 48 km/h.

### A. Injury criteria

A model of a Hybrid III 50th percentile male dummy is used to evaluate the injury criteria, which are summarized below.

- Head injury criteria (HIC)

HIC-values represent the severity of injury of the human head which results from its acceleration, caused for example by an impact of the head with the road surface. Head acceleration values  $a$ , taken from sensor readings in a crash-test with a dummy or from simulation results, are used to calculate the HIC value as expressed in equation 1, with  $(t_2, - t_1) = 15\text{ms}$  being the time interval with the maximum acceleration values :

$$HIC = \left[ \frac{1}{t_2 - t_1} \int_{t_1}^{t_2} a dt \right]^{2.5} (t_2 - t_1) \quad (1)$$

For 50th percentile male Hybrid III dummy, an HIC-value of 700 is an injury criterion.

- Chest injury criteria

NHTSA mandates two chest injury criteria for the 50th percentile male Hybrid III dummy: A chest acceleration value (“CLIP”) of 60g, and chest deflection of 76.2 mm.

- Neck injury criteria

Neck injury values  $N_{ij}$  express combinations of load factors “ij”, with “i” indicating axial loads (tension or compression) and “j” indicating sagittal plane moments (Flexion or Extension), equation 2

$$N_{ij} = \frac{F_z}{F_{crit}} + \frac{M_y}{M_{crit}} \quad (2)$$

The forces  $F_z$  and moments  $M_y$  are divided by their relative “critical intercept values”, and a sum of both factors of 1 or more is an injury criterion in any of the 4 quadrants visualized in Fig 3, which gives the critical intercept values for the 50th percentile male Hybrid III dummy.

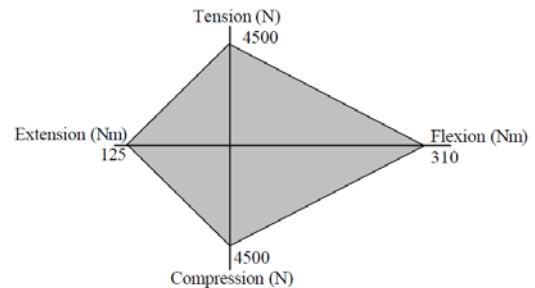


Fig. 3. Critical intercept values for the 50th percentile male Hybrid III dummy.

### B. Abbreviated Injury Scale, Injury Risk Functions

The Abbreviated Injury Scale (AIS) is an anatomical-base coding system to classify and represent the severity levels of injuries [9], Table 1.

TABLE I  
ABBREVIATED INJURY SCALE

AIS Code	Injury Level	Fatality Range
0	No injury	0%
1	Minor	0%
2	Moderate	1-2%
3	Serious (not life threatening)	8-10%
4	Severe (life threatening)	5-50%
5	Critical (Survival uncertain)	5-50%
6	Maximum	100%

The relation of the values of the various Injury Criteria and corresponding Injury Risks are represented by Injury Risk Functions.

- Head Injury Risk Function

The Head Injury Risk Function was developed by combining human surrogate test data and skull fracture data from drop tests fitted to the best curve using the maximum likelihood method [12]-[16]. Fig 4 shows the Head Injury Risk Function, the probability of injury at AIS level 2 or higher against the HIC value.

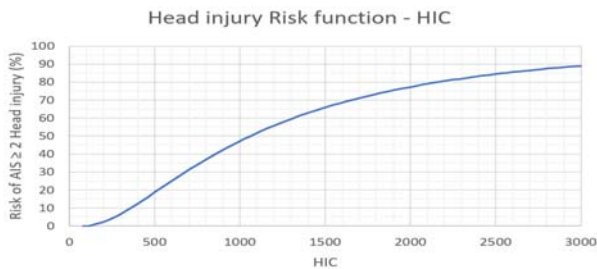


Fig. 4. Critical intercept values for the 50th percentile male Hybrid III dummy.

- Neck Injury Risk Function

The Neck Injury Risk Function was developed by Mertz in 1997 from porcine test data [17], adjusted with data from human dummy tests and real-world injury rates to establish a risk curve for a live human [18]-[20]. Fig 5 shows this function for a probability of injury at AIS level 3 or higher.

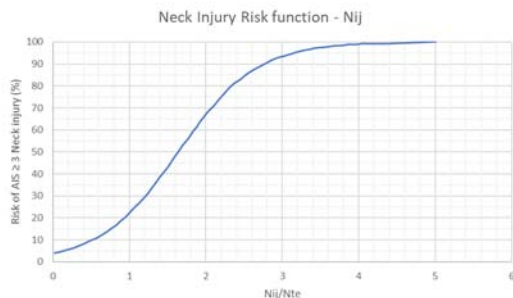


Fig. 5. Neck Injury Risk Function

- Chest Injury Risk Function

The Chest Injury Risk Function has been developed from sled test data with human surrogates available from an NHTSA database [11]. Figure 6 shows this function, the probability of injury from chest deflection at AIS level 3 or higher.

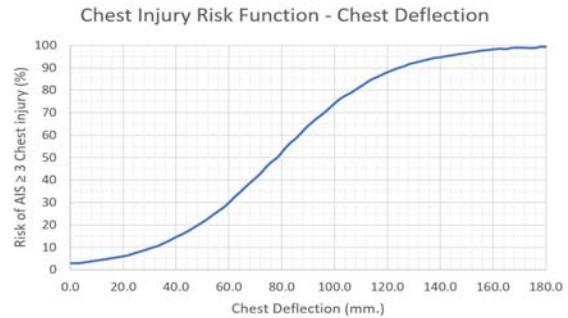


Fig. 6. Chest Injury Risk Function

### III. PASSENGER-FRAME FEASIBILITY STUDY

A series of simulations of a full-frontal crash scenario with an initial velocity of 48 km/h has been executed in accordance with FMVSS208 to demonstrate and evaluate the feasibility of the safety-concept of using safety-belts and crash-elements on a passenger-frame on a light motorcycle. Other motivations of this study are (I) to visualize a reference collision without a restraining system, (II) to understand how the deformation of crash-elements works together with the deformation of the rest of a frame to reduce the injury-risk, and (III) to obtain an initial assessment of the improvement of injury risks that can be expected from the measures. Three variants of a simplified configuration were simulated on the nonlinear explicit LS-DYNA software. The simulations differ with regards to the configuration of the passenger frame and the restraint system, Fig. 8-10:

- no passenger restraint, no crash elements
- safety-belts, no crash elements
- safety belts and crash elements on the interface between forward structure and passenger-frame

In this study, the vehicle itself, which would impact the target wall first and therefore absorb a substantial amount of kinetic energy, lessening the impact on the passenger-frame mounted to the back of it, is not modelled, but replaced with a pyramid-shaped forward-structure which impacts the rigid wall in the simulations. While the passenger frame is modelled to deform realistically, the forward-structure is modelled to behave as a rigid body to ensure identical force introduction into the passenger-frame for all configurations and a purely axial deformation of the crash-elements. The frames are constructed from circular tubes of SS400 steel with an outer diameter of 37.5 mm and a wall-thickness of 3.2 mm, while the crash-elements are modelled as round aluminum 6063-T5 tubes with an

external diameter of 50 mm, a wall thickness of 2mm and an initial length of 150 mm using a material model with a “true effective plastic stress-strain curve” with an initial yield stress  $\sigma_y = 180$  MPa [21] as shown in table 2 for the tube. The shell element formulation used for the tube is Belytschko-Tsay with five integration points through the thickness. In order to ensure the validity of the modelling strategy for these axially crushed tubes, the study of Acar [21]-[23] has been replicated, which includes the modelling technique and a comparison of the simulation results with physical experiments, Fig.7.

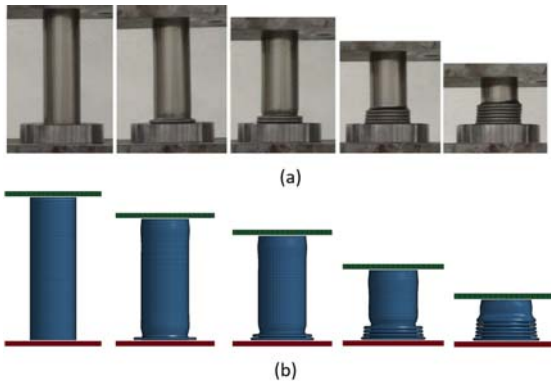


Fig. 7. Comparison of the simulation results (b) with the experiment (a) by Acar et al. [21]

TABLE II  
TRUE EFFECTIVE PLASTIC STRAIN CURVE  
OF ALUMINUM 6063-T5

$\sigma_t$ [MPa]	$\epsilon_p$	$\sigma_t$ [MPa]	$\epsilon_p$
180	0	<i>(continued)</i>	
183	0.006	218	0.038
189	0.011	222	0.044
196	0.016	231	0.057
204	0.023	239	0.071
212	0.031	245	0.084

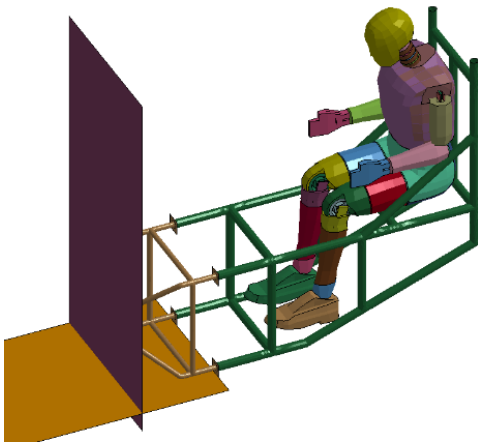


Fig. 8. Configuration a): no passenger restraint, no crash elements

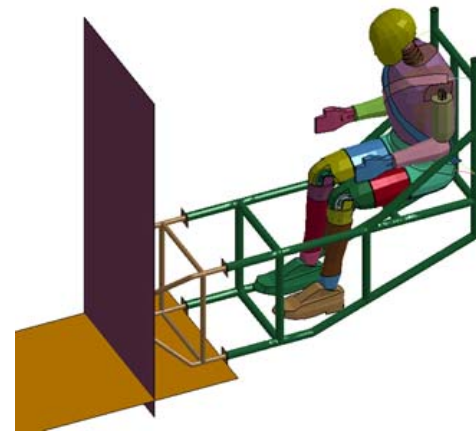


Fig. 9. Configuration b): safety-belts, no crash elements

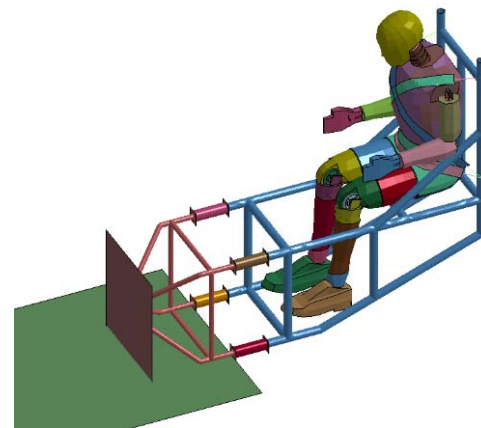


Fig. 10. Configuration c): safety belts and crash elements

#### IV. DISCUSSION OF RESULTS

Fig 11 gives an overview of the kinematic results of the three simulations while Fig 12 compares the velocities of the passenger frame and the dummy, measured at a point on the seat and the dummy’s buttocks respectively. These points are chosen to represent relevant information on the decelerations, represented by the slopes of the curves, of the bodies as a whole. For example, the initial deceleration of the frame in configurations a) and b) can be easily estimated to be about 170g as the first section of the graphs is straight

Configuration a), the human body dummy is not restraint to the passenger frame and continues on its trajectory after the frame has made contact with the impact wall ( $t=0$ ms) until its legs impact the frame at around 54 ms. The passenger frame deforms under the deceleration force resulting from its own mass, buckling immediately at the angle on the lower tubes.

Configuration b), the movement of the dummy is slowed down by the engaging safety belts after about 5ms, with the combined compliance of belts and dummy resulting in a “cushioning” effect, until at around  $t=27$ ms, the “joint”

between dummy and frame stiffens and the dummy's deceleration parallels that of the frame.

Configuration c) behaves similarly to configuration b), albeit with a substantially reduced deceleration (roughly 64g), which is a result of the crash-elements collapsing immediately after the initial impact. The initial deceleration of the dummy profits little from this effect, but the second deceleration phase beginning at about  $t=28\text{ms}$  again parallels that of the frame, so that the dummy's deceleration of configuration c) is indeed somewhat lower than that of configuration b) most of the time. However, a comparison of the maximum values does not reveal a substantial difference. This is also demonstrated by the only marginal difference of the chest deflection values of configurations b) and c), which are listed in Table 3 together with the values for head and neck injury. The crash-elements however result in a substantial improvement for the acceleration of the dummy's head.

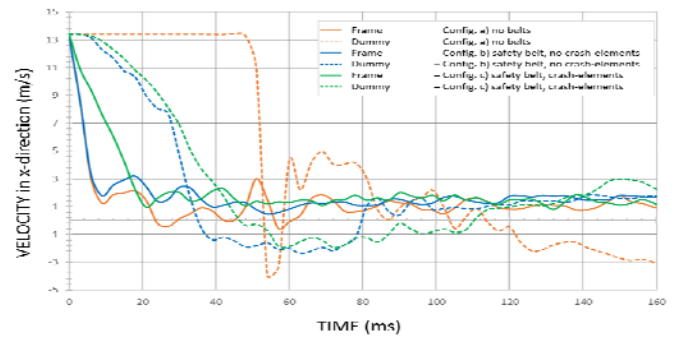


Fig. 12. Velocities of frame and dummy for the three configurations, measured at the seat and the buttocks of the dummy respectively

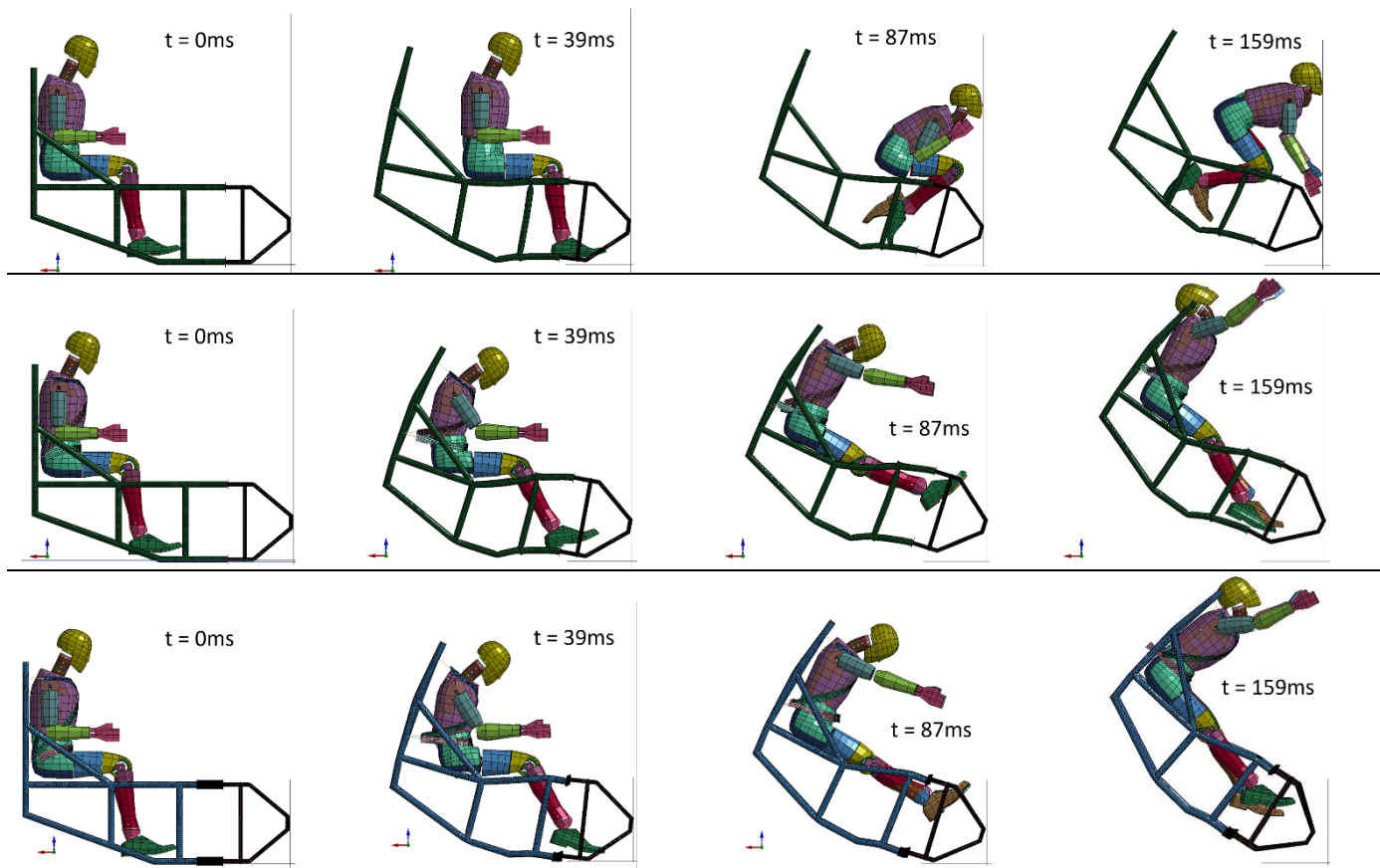


Fig. 11. Kinematic results of the initial study. Top row: config. a), no belts; middle row: config. b), safety belts; bottom row: config. c), safety belts + crash-elements



TABLE III  
INJURY ASSESSMENT OF THE CONFIGURATIONS SIMULATED IN THE FEASIBILITY STUDY. CONFIGURATION A) IS NOT LISTED HERE AS THE VALUES DO NOT RESULT FROM THE FRAME CONFIGURATION BUT WALL IMPACT, WHICH FOR EXAMPLE RESULTS IN HIC15 = 28,630.

Injury-values, AIS risks	Config. b)	Config. c)
Head Injury, HIC15 <700 Prob. of AIS ≥ 2	503.2 19.1%	412.3 13.1%
Chest Deflection <76.2mm Prob. of AIS ≥ 3	52.0 22.7%	50.9 21.8%
Neck Injury N <sub>TE</sub> Prob. of AIS ≥ 3	1.20 29.4%	1.03 23.4%
Neck Injury N <sub>TF</sub> Prob. of AIS ≥ 3	0.80 16.0%	0.84 17.0%

## V. CONCLUSION

The study demonstrates that safety belts and a “passenger frame” on a light motorcycle result in a substantially improved safety for the passenger in case of head-on collisions: while a passenger without a helmet has practically no chance of surviving a head-on collision with 48 km/h, the frame and belt concept reduces this risk to only being a likelihood of less than 20% for injuries. Furthermore, it is demonstrated that it is feasible to equip such frame made from circular tubes with crash-elements, which collapse first in case of a head-on collision and thereby reduce the deceleration acting on the passenger, who is constraint to the frame with safety belts. The comparison of the results of crash-simulations of frames with and without crash-boxes show that the initial deceleration of the frame is reduced by more than 60% through the collapsing of the elements. However, the study also shows that the crash-elements do not result in substantial reductions of chest and neck-injury parameter values if the frame itself is not compliant enough to absorb kinetic energy after the crash-boxes have completely collapsed. Further design studies will therefore demonstrate the full potential of this approach with a frame design which is compliant enough to allow for a continuous deceleration after the crash-elements have fully collapsed.

## REFERENCES

[1] W. Youngpisanphob. (2019, May). Motorcycle Industry [Online]. Available: <https://www.krungsri.com/th/research/industry/industry-outlook/Hi-tech-Industries/Motorcycles/IO/io-motorcycles-20>

[2] Department of Land Transport (2020, June) Statistic on the number of public motorcycle riders in Bangkok [Online]. Available: <https://data.go.th/dataset/pubmotorcycle>

[3] General Office of the Attorney (1995, Mar). Helmet enforcement law [Online]. Available: <http://www.ogad.ago.go.th/dagsu/images/stories/v38/v40.pdf>

[4] Thai Roads Foundation (2019, Sep). Helmet wearing rate of motorcycle user in Thailand [Online]. Available: <http://trso.thairoads.org/-resources/8403>

[5] World Health Organization, “Global status report on road safety,” World Health Organization, Geneva, Switzerland, 2018.

[6] Office of Transport and Traffic Policy and Planning, “Road accident analysis report of ministry of transport,” Ministry of Transport, Bangkok, Thailand, 2018.

[7] Thai Accident Information Center for Strengthening Road Safety Collaboration (ThaiRSC) (2019, July). In-depth Accident Investigation in Thailand [Online]. Available: [http://www.accident.or.th/index.php/2017-11-03-04-01-18/245-2020-07-22-09-18-53?fbclid=IwAR2-RK4EtcTONGd65pD\\_w0KiGBnvUrKWiLayY4mIoDy1QQqkHnJzXE7Z\\_A](http://www.accident.or.th/index.php/2017-11-03-04-01-18/245-2020-07-22-09-18-53?fbclid=IwAR2-RK4EtcTONGd65pD_w0KiGBnvUrKWiLayY4mIoDy1QQqkHnJzXE7Z_A)

[8] F. A. Berg, P. Rücker, J. König, “Motorcycle crash tests — an overview,” DEKRA Automobil GmbH, July 2010.

[9] J. Carmai, S. Koetniyom, W. Hossain, “Analysis of rider and child pillion passenger kinematics along with injury mechanisms during motorcycle crash” Traffic Injury Prevention, vol. 20, pp. S1, S13–S20, 2019.

[10] WAGON Automotive GmbH, Advertising brochure, Waldaschaff, 2001

[11] NHTSA (1999, Nov), Development of improved injury criteria for the assessment of advanced automotive restraint systems - II [Online] Available: <https://www.nhtsa.gov/document/development-improved-injury-criteria-assessment-advanced-automotive-restraint-systems>.

[12] P. D. Bois, et al., “Vehicle Crashworthiness and Occupant Protection” American Iron and Steel Institute, 2004.

[13] P. Prasad, H. J. Mertz, “The position of the United States Delegation to the ISO Working Group 6 on the Use of HIC in the Automotive Environment,” SAE Government/Industry Meeting and Exposition, SAE paper no. 851246, June 1985.

[14] VR. Hodgson, LM. Thomas, “Breaking Strength of the Human Skull Versus Impact Surface Curvature,” Wayne State University, DOT report no. DOT-HS-146-2-230, 1973.

[15] VR Hodgson, LR. Thomas, J. Brinn, “Concussion Levels Determined by HPR Windshield Impacts,” Proceedings of the Seventeenth Stapp Car Crash Conference, SAE Paper No. 730970, 1973.

[16] C. Got, A. Patel, “Results of Experimental Head Impacts on Cadavers: The Various Data Obtained and Their Relations to Some Measured Physical Parameters,” Proceedings of the twenty-second Stapp Car Crash Conference, SAE Paper No. 780887, 1978.

[17] E. Hertz, “A Note on the Head Injury Criteria (HIC) as a Predictor of the Risk of Skull Fracture,” 37th Annual Proceedings of the Association for the Advancement of Automotive Medicine, Paper No. SH-041 720, pp. 303-312, 1993.

[18] HJ. Mertz, P. Prasad, A.L. Irwin, “Injury Risk Curves for Children and Adults in Frontal and Rear Collisions,” Proceedings of the Forty-First Stapp Car Crash Conference, SAE Paper No. 973318, 1997.

[19] HJ. Mertz, G. D. Driscoll, J. B. Lenox, G. W. Nyquist, D. A. Weber., “Responses of Animals Exposed to Development of Various Passenger Inflatable Restraint System Concepts for a Variety of Collision Severity and Animal Positions,” Proceedings of the Ninth International Technical Conference on Experiment Safety Vehicles, pp. 352-368, 1982.

[20] P. Prasad, RP. Daniel, “A Biomechanical Analysis of Head, Neck, and Torso Injuries to Child Surrogates Due to Sudden Torso Acceleration,” Twenty-Eighth Stapp Car Crash Conference, SAE Paper No. 841656, 1984.

[21] E. Acar, M. Altin, M.A. Güler, “Evaluation of Multi-Cell Design Concepts for Crashworthiness Design of Thin-Walled Aluminum Tubes,” Thin-walled Structures, vol. 142, pp. 227-235, 2019.

[22] Z. Ahmad, D.P. Thambiratnam, “Crushing Responses of Foam-Filled Conical Tubes Under Quasi-Static Axial Loading,” Materials and Design, vol. 30, pp. 2393-2403, 2009.

[23] S. P. Santosa, T. Wierzbicki, A. G. Hanssen, M. Langseth, “Experimental and Numerical Studies of Foam-Filled Sections,” International Journal of Impact Engineering, vol. 24, pp. 509-534, 2000.

# Nanoporous carbon materials synthesized by carbonization of hemp waste as bio-based adsorbents

**Korn Sukphunphoncharoen<sup>1</sup>, Napat Kaewtrakulchai<sup>2</sup>, Sutee Chutipaijit<sup>1</sup>,  
Tawat Suriwong<sup>3</sup>, Pramote Puengjinda<sup>4</sup>, Gasidit Panomsuwan<sup>5</sup>,  
Masayoshi Fuji<sup>6</sup> and Apiluck Eiad-ua<sup>1\*</sup>**

<sup>1</sup>College of Materials Innovation and Technology, King Mongkut's Institute of Technology Ladkrabang, Thailand

<sup>2</sup>Kasetsart Agricultural and Agro-Industrial Product Improvement Institute, Kasetsart University, Thailand

<sup>3</sup>School of Renewable Energy and Smart Grid Technology, Naresuan University, Thailand

<sup>4</sup>PTT Innovation Institute (InI) New Energy Research Technology, Thailand

<sup>5</sup>Department of Materials Engineering, Faculty of Engineering, Kasetsart University, Thailand

<sup>6</sup>Advanced Ceramic Center, Nagoya Institute of Technology, Japan

\* corresponding author, E-mail: apiluck.ei@kmitl.ac.th

**Abstract:** Nanoporous carbon materials (NPCs) have been widely utilized for various applications owing to their attractive physicochemical properties. In this work, nanoporous carbon materials were synthesized as bio-based adsorbents using hemp waste via hydrothermal treatment followed by carbonization. The sequential porous adsorbent was prepared by chemical activation (KOH) using carbon materials as a carbonaceous framework. The adsorbent was characterized by XRD, FTIR, Raman, SEM, and BET. From the results, compared to the traditional method of HTC and pyrolysis, HTC was found to be better option to develop the specific surface area, porosity, and yield of the NPCs, which presented porous structure and carbon content higher than. NPCs have highest surface area of 1,557 m<sup>2</sup>/g and Total pore volume of 0.747 cc/g. The adsorption performance of the adsorbent was tested using the batch adsorption method. The effect of parameters such as type of sorbent and residence time.

**Keywords:** *Hemp waste; Nanoporous Carbon; Hydrothermal treatment; Carbonization; Pollutants*

## I. INTRODUCTION

Nowadays, hemp is a plant that is gaining a lot of attention. Hemp can be used every parts. From flowers, leaves, seeds, stalks, fibers, including roots, all can be used and moreover hemp can be used as raw materials in a variety of industries, including medicine, food supplements, cosmetics and market demand is high. Development of carbon materials from biomass resources. In general, the major process for conversion of biomass is thermochemical conversion such as chemical vapor deposition, hydrothermal treatment, pyrolysis or carbonization to synthesis carbon nanotube, carbon fiber, charcoal and porous carbon. Then, what different between carbonization and hydrothermal carbonization. Carbonization is process of heating lignocellulose substance into elemental carbon and chemical compounds and some carbon in chemical structure via inert atmosphere from 500-900°C with low yield, low carbon content, low surface area and low porous structure. While, hydrothermal carbonization (HTC) is process of thermochemical treatment of biomass in pressurized water at low temperatures between 180 - 250°C at saturated pressure called hydrolysis reaction followed by carbonization in nitrogen atmospheres from 500-900°C leading to high yield,

high carbon content, high surface area and high porous structure. Porous carbon have some significant properties such as eco-friendly, adsorptive, mechanical, thermal and electrical characteristics for novel application such as electronic device, catalyst support and adsorbent. The main reason which is the causes of water pollution first one is from dump raw sewage into community river and second is industrial waste. Oil refineries, chemical factories, textile and sugar mills are responsible for water pollution. These industries discharge harmful chemicals into rivers and streams and pollute water. We can solve these issues by synthesizing activated carbons (ACs) for use in adsorption of contaminants in water to reduce the amount of contaminants in the water. This technique is widely used. Because the adsorbent absorbs well, it can be reused many times, it is simple to do, and the investment is low. And also extremely effective adsorbent. In the experiment, we will absorb Tetracycline, Methylene blue, Methyl orange, Methyl red and Phenol red. Which is a simulation absorption of pollutants.

## II. EXPERIMENTAL

Preparation of nanoporous carbon divide into 4 steps

### Material preparation

- Cut & Grind hemp waste to a small size.
- Wash by DI water at 55 °C for 1 h.
- Dried at 105 °C for 24 h.

### Hydrothermal process

- Prepared hemp waste powder 30 g mix with 120 ml of DI water.
- Pack into the stainless-steel autoclave and perform hydrothermal treatment at 200 °C for 12 h to get hydrochar.
- Dried at 105 °C for 24 h.

### Chemical activation process

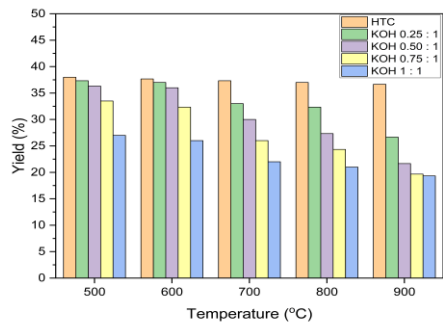
- Prepared hydrochar 3 g. mixed with KOH at several concentration (25, 50, 75 and 100 %wt) for 30 min.

### Carbonization process

- Bring activated hydrochar put into rotary tube furnace to carbonization at 500 – 900 °C for 1 h.
- Then wash several times with HCl and DI water for clean up impurities.
- Dried at 105 °C for 24 h to obtain nanoporous carbon for adsorption applications.

## III. RESULTS AND DISCUSSION

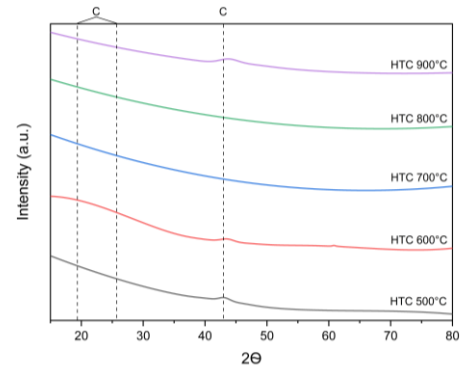
### 3.1 Yield



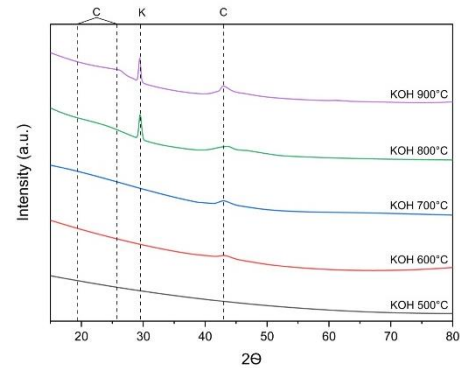
**Fig. 1.** Carbon yield of hydrothermal and Carbonization result

Fig. 1 show higher temperature and higher ratio KOH resulted in lower yield percentage.

### 3.2 XRD



(a) Hydrothermal treatment followed by carbonization at 500 – 900°C

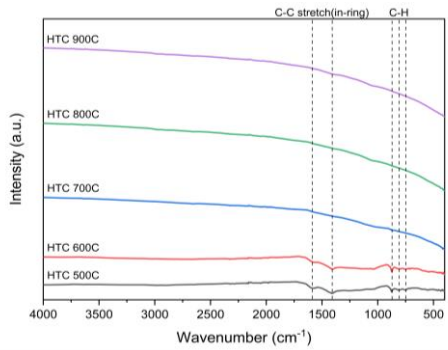


(b) KOH 0.5:1 (500-900°C)

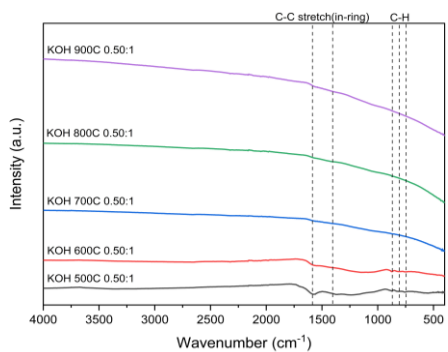
**Fig. 2.** XRD patterns (a) varying carbonization temperature and (b) KOH activation at different carbonization temperature

Fig. 2 show broad peak at 2-theta of 19° to 26° and 43° which can be identified to the (004), (101) and (100) planes of amorphous carbon. Peaks at 2-theta of 29° which can be identified to the (105) planes of potassium phase. Amorphous carbon increased with increasing of carbonization temperature.

### 3.3 FTIR analysis



(a) Hydrothermal treatment followed by carbonization at 500 – 900°C

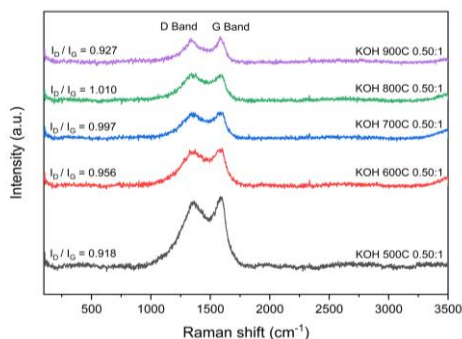


(b) KOH 0.5:1 (500-900°C)

**Fig. 3.** FTIR spectra (ATR mode) of (a) varying carbonization temperature and (b) KOH activation at different carbonization temperature

Fig. 3 show band located at 1,580 and 1,408  $\text{cm}^{-1}$  indicate C-C stretch vibrations in aromatics groups. Band located at 874, 812 and 751  $\text{cm}^{-1}$  indicate C-H vibrations in aromatics groups. Increase of temperature representing the functional structures are gradually decreased compared with hemp waste and pure carbon is generated more than 700°C.

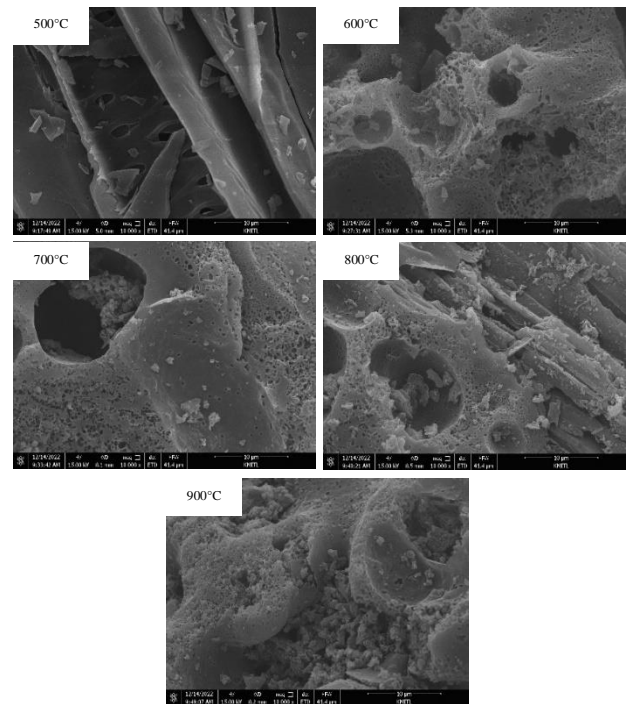
### 3.4 Raman analysis



**Fig. 4.** Raman spectra of hydrothermal-carbonization and KOH activation (ratio 0.5:1) to carbonization (500-900°C).

Fig. 4 show intensity of the D band is higher than intensity of the G band. The closer it is to one, the more amorphous is presented. It is relationship to entropy in Thermodynamic.

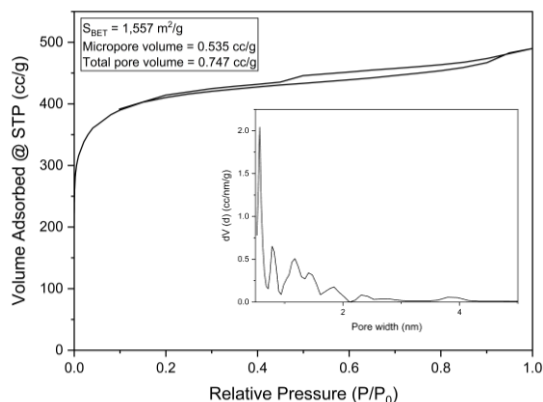
### 3.5 SEM



**Fig. 5.** SEM micrographs of hydrothermal – carbonization and KOH activation

Fig. 5 show hydrothermal and carbonization temperature significantly affects porosity. The surface morphology and porosity tends to increased with increasing of carbonization temperature compared with hemp waste because potassium was served as activating agent therefore causing pores of different shapes.

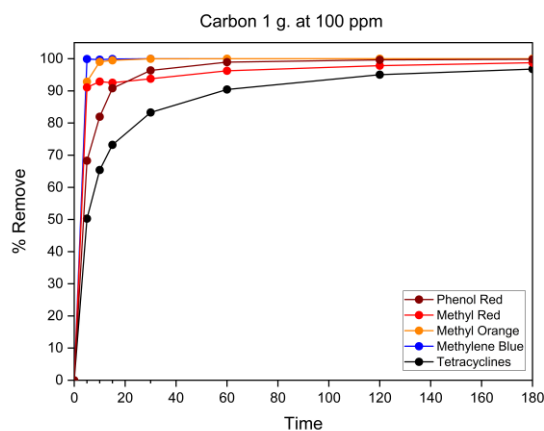
### 3.6 Sorption analysis



**Fig. 6.** Sorption isotherms, Pore volume and Pore size distributions of Carbonization 900 °C & KOH activation ratio 0.5:1

Fig. 6 show optimum condition presented type 1 & type 4 isotherm according to IUPAC classification that indicating the microporous structure and mesoporous structure. The optimum condition to obtained Highest surface area of 1,557 m<sup>2</sup>/g and Total pore volume of 0.747 cc/g were hydrothermal process at 200 °C for 12 h followed by carbonization at 900 °C for 1 h with KOH activation.

### 3.7 Adsorption test using nanoporous carbon



**Fig. 7.** Adsorption curves for nanoporous carbon (KOH 0.5:1 at 900 °C) at 100 ppm

Fig. 7 show adsorption tast at 100 ppm. With nano-porous carbon (KOH 0.5:1 at 900 °C) from this results, Adsorption of pollutants increased with increasing time.

## IV. CONCLUSION

Surface, Porosity, and Morphology increased with increasing carbonization temperature. Nanoporous carbon (NPC) have been successfully synthesized from hemp waste via hydrothermal carbonization (200 °C for 12 h) and KOH activation (ratio 0.5:1) at 900 °C for 1 h. Highest surface area of 1,557 m<sup>2</sup>/g and Total pore volume of 0.747 cc/g. Therefore, the production of nanoporous carbon was applied the usage of a sorbent for efficiency adsorption of pollutants. Adsorption of pollutants increased with increasing time.

## ACKNOWLEDGMENT

Author thank to the College of Materials Innovation and Technology, King Mongkut's Institute of Technology Ladkrabang, Thailand for their supporting.

## REFERENCES

- [1] Ping Feng, Jie Li, Huan Wang, and Zhiqiang Xu, "Biomass-Based Activated Carbon and Activators: Preparation of Activated Carbon from Corn cob by Chemical Activation with Biomass Pyrolysis Liquids". ACS Omega. 5, 24064–24072, 2020.
- [2] Catalina Rodríguez Correa, Moritz Stollovsky, Tobias Hehr, Yannik Rauscher, Birgit Rolli, and Andrea Kruse, "Influence of the Carbonization Process on Activated Carbon Properties from Lignin and Lignin-Rich Biomasses". ACS Sustainable Chem. Eng. 5, 8222–8233, 2017.
- [3] Emine Yagmura, Yavuz Gokcea, Suheyla Tekina, N. Isik Semercib, Zeki Aktasa, "Characteristics and comparison of activated carbons prepared from oleaster (*Elaeagnus angustifolia* L.) fruit using KOH and ZnCl<sub>2</sub>". Fuel, 267, 117232, 2020.
- [4] Osman U'ner, U'nal Gec'gel, Yu'ksel Bayrak, "Preparation and characterization of mesoporous activated carbons from waste watermelon rind by using the chemical activation method with zinc chloride". Arabian Journal of Chemistry, 12, 3621–3627, 2019.
- [5] Md. Azharul Islam, I.A.W. Tan, A. Benhouria, M. Asif, B.H. Hameed, "Mesoporous and adsorptive properties of palm date seed activated carbon prepared via sequential hydrothermal carbonization and sodium hydroxide activation". Chemical Engineering Journal, 270, 187-195, 2015.
- [6] Hui Wang, Liang Shan, Qiuyan Lv, Sixiang Cai, Guixiang Quan, Jinlong Yan, "Production of hierarchically porous carbon from natural biomass waste for efficient organic contaminants adsorption". Journal of Cleaner Production, 263, 121352, 2020.
- [7] Małgorzata Wilka, Aneta Magdziarz, Kandasamy Jayaraman, Monika Szymańska-Chargot, Iskender Gökalp, "Hydrothermal carbonization characteristics of sewage sludge and lignocellulosic biomass. A comparative study". Biomass and Bioenergy, 120, 166-175, 2019.

# An innovative solar reactor for thermochemical conversion process: concept design, fabrication, and temperature test

Attawit Saengpradab<sup>1</sup>, Jirayut Tathong<sup>1</sup>, Hattakit Kongsrichay<sup>1</sup>, Srirat Chuayboon<sup>1,\*</sup>

<sup>1</sup> Department of Mechanical Engineering, King Mongkut's Institute of Technology Ladkrabang, Prince of Chumphon Campus, Chumphon 86160, Thailand

\* E-mail address: srirat.ch@kmitl.ac.th

## Abstract

The need to mitigate climate change using renewable energy sources has become increasingly important. Among these sources, solar energy has become attractive for solar thermochemistry. In the solar thermochemistry process, a solar chemical reactor is one of the highly essential components. In this study, an indirectly irradiated solar reactor is designed, fabricated, and temperature tested. The experimental setup utilizes a manual heliostat to track and concentrate sunlight onto a Fresnel lens, directing the concentrated sunlight to the solar chemical reactor. The reactor temperatures were experimentally tested under on-sun, off-sun, and hybrid conditions. As a result, the solar chemical reactor achieved high absorption temperatures, which exceeded 500 °C. However, the reactor encountered high heat losses, which can improve by adding more thermal insulation. The reactor demonstrated a day-and-night operation concept using an electrical heat source to maintain the temperature.

**Keywords:** Solar reactor, Concentrated solar power, solar day-and-night operation

## I. INTRODUCTION

Solar energy has emerged as a promising renewable energy source worldwide, owing to its abundant availability and eco-friendliness [1]. Solar resource is estimated to exceed other energy sources by a factor of thousands when assuming perfect conversion efficiency [2]. Thailand, recognizing the significance of renewable energy, has been actively pursuing methods to harness this sustainable energy source. Thailand's average high solar radiation is estimated at 1875 kW/m<sup>2</sup> annually [3].

In Thailand, solar power is mostly used for generating electricity, primarily using non-concentrating solar power systems. Alternatively, it is worth noting that concentrating solar power (CSP) is a promising method of harnessing solar energy, which is more efficient than non-concentrating solar power systems [4]. CSP technologies are the parabolic trough, linear Fresnel, dish/engine, and central receiver.[4] They can provide very high-temperature heat, which can be utilized for the solar thermochemical conversion process. [5]

Solar thermochemical processes represent a form of renewable energy technology that can convert solar energy into chemical fuels. This process involves using a solar reactor to facilitate a chemical reaction between reactants and concentrated solar power that absorb solar radiation and facilitate chemical reactions. In a packed bed solar reactor, the reactant is passed through the bed of solid particles, which are heated by solar radiation. The reactant undergoes chemical reactions in the bed, releasing energy in the form of heat, which can be used for various applications [9].

The reactor's design plays a significant role in a solar reactor performance. It is necessary to be optimized to maximize the absorption of solar radiation, minimize heat loss, and ensure efficient mass transfer between the reactant and catalyst. An indirect solar reactor separates light from the reaction zone. This results in no soot or particles sticking to the windows. This stabilizes the operation of the reactor over a long period [10]. To operate solar processes around the clock, the hybrid solar reactor is of particular interest.

In this study, we aim to design, fabricate, and test a hybrid solar chemical reactor. The present solar reactor prototype is designed based on the indirect concept of heat radiation, consisting of a tube containing the reactant, which is placed vertically inside. The reactor design and performance are addressed. Temperature evaluation during on-sun, off-sun, and hybrid conditions are highlighted.

## II. SOLAR HYBRID REACTOR DESIGN

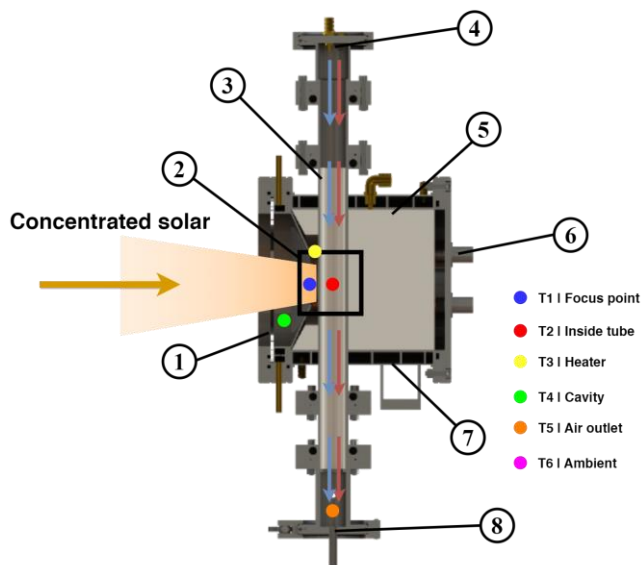
The solar chemical reactor design and fabrication involves using high-quality materials to ensure the reactor's robustness and efficiency. Fig. 1 shows the cross-section of the solar tubular reactor made of stainless steel 304, which can withstand high temperatures up to 1400 °C.

The design of this solar reactor was inspired by an indirect irradiated solar chemical reactor, which comprises a tube inside the reactor where the chemical reaction takes place. The tube inside the reactor is made of alumina thanks to its excellent thermal and chemical stability, high mechanical strength, and good corrosion resistance. This solar chemical reactor comprises three primary sections. According to Fig. 1, the upper section of the reactor is where the reactants are

fed. The reactor's top has a tube inserted into a stainless-steel tube, allowing the reactants in the form of gas to enter the tube from the side. At the top of the tube, there is a hole for the reactants in liquid form to enter the tube, where the chemical reaction takes place. K-type thermocouples are installed around the reactor to measure the temperature at each point. Additionally, one thermocouple is in the middle of the tube to measure the reactor cavity temperature. The upper section also features two tube cooling systems to cool the tube down when it operates for long durations.

The middle section of the reactor has an aperture with a 30 mm diameter at the front that allows concentrated solar power to enter the reactor. The focal point is set in the middle of an alumina tube to achieve high temperatures for the chemical reaction. The reactor cavity is filled with insulation, including fire brick, widely used in furnaces, to maintain high temperatures during the solar thermochemical process. Furthermore, the reactor features electrical heat sources on both sides of the tube to increase the temperature, particularly during unfavorable weather conditions or overnight operations. The reactor shell has a cooling system to maintain the reactor's temperature and prevent melting.

The lower section of the reactor is similar to the upper section, featuring a tube cooling system, a middle hole for the liquid product to flow out of the tube, and another tube on the side of the bottom section for the gas phase product to exit and enter a gas analyzer to analyze the yield being produced. The set-up is located on the rooftop of a building to ensure clear access to sunlight.

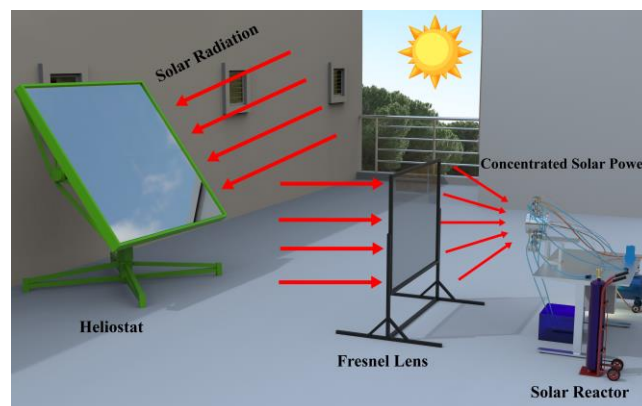


**Fig.1** Schematic diagram of the cross-section of a solar reactor: (1) glass window, (2) reaction zone, (3) alumina tube, (4) reactants inlet, (5) insulation, (6) heater, (7) reactor's shell, (8) products outlet.

### III. SETUP AND METHODS

Fig. 2 illustrates the setup of the solar reactor system used in this experiment. The system consisted of a tracking heliostat measuring 2x2 meters and about 3 meters tall,

which reflected sunlight to a Fresnel lens (1.05x1.4 meters) with a focal length of 1.2 meters. The concentrated solar power was directed to a tubular cavity receiver in the reactor with very high solar intensity, rapidly increasing the temperature. In addition, two 500W electrical heaters were supplied to heat the reactor during unstable conditions of solar DNI, demonstrating the hybrid system. Once the reactor reached the targeted temperature, a heat transfer fluid of air was fed into the reactor, and the temperature was evaluated. The reactor's performance was tested with on-sun, off-sun, and hybrid heating methods. During on-sun heating, a shutter was used to control the solar intensity passing through the Fresnel lens. This enabled the reactor to be heated throughout the entire reactor's body. Liquid cooling water was employed to protect the reactor's components and maintain the material's properties. After warming up the reactor, the shutter was opened more to receive the concentrated sunlight. In the hybrid heating method, the heater was turned on during bad weather or low DNI conditions to keep the reactor running. Operating parameters were recorded with an automatic data logger system to present the time, temperature, and DNI data. Off-sun heating was similar to the on-sun methods, except that the heliostat was not utilized.



**Fig.2** On-sun solar reactor set-up

### IV. RESULTS AND DISCUSSION

Fig. 3 shows the temperature profiles of the solar chemical reactor along with DNI during on-sun heating for 120 min. Overall, it was found that the reactor can achieve very high temperatures from concentrated sunlight only above 560 °C according to the focus point area (T<sub>1</sub>). A fluctuation in the T<sub>1</sub> was encountered due to a change of the focal point resulting from a delay in the manual solar tracking. Moreover, the heating process was slow while having high heat losses. This led to the temperature inside the tube (T<sub>2</sub>) decreasing to 254 °C. During on-sun testing, the DNI was relatively high, approaching 1000 W/m<sup>2</sup> thanks to the clear sky in the summer season, and then it decreased slightly with operating time. Similar to T<sub>2</sub>, the temperature at cavity (T<sub>4</sub>) was up to 286 °C. The temperature at the outlet (T<sub>5</sub>) was still high

(above 200 °C after 80 min) even if being far from the reaction zone, thus pointing out high convective heat transfer in the reactor. The ambient temperature ( $T_6$ ) was found to be 38 °C.

alumina tube's temperature ( $T_2$ ) increased by 40 °C more than using on-sun heating.

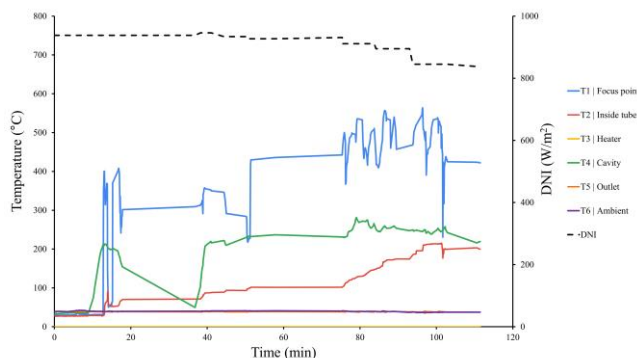


Fig. 3 Solar reactor temperature profile during on-sun heating

Temperature distribution during off-sun heating is shown in Fig.4 (electrical heat only). Two heaters with 1000 W were employed to heat the solar reactor. In this case, we aim to use electrical heat when solar irradiation is unstable due to cloud passage. Two significant temperatures with respect to heater temperature ( $T_1$ ) and inside tube ( $T_2$ ) were reported as representative reactor temperatures. As a result,  $T_1$  and  $T_2$  increased gradually with time.  $T_1$  of 300 °C and  $T_2$  above 200 °C were achieved after 120 min. The gap between them was pretty high, indicating a significant heat loss. Therefore, it is crucial to improve the reactor temperature by reducing heat losses, such as by adding more insulation in the reactor or reducing natural convection in the experimental area.

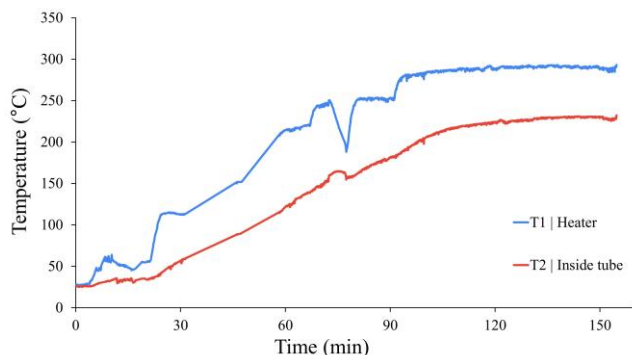


Fig. 4 Solar reactor temperature profile during off-sun heating

Fig. 5 shows the temperature outlines of the hybrid heating test (solar heat +electrical heat) of the solar reactor along with DNI for 80 minutes. The result showed that the temperatures increased more rapidly than the only solar heat system (Fig.3). In addition, hybrid heating resulted in a fast increase in the reactor temperatures, as evidenced by slopes in  $T_1$ - $T_5$  even if the DNI is decreased. The maximum temperature was found to be 560 °C ( $T_1$ ), followed by 360 °C ( $T_3$ ), and 200 °C ( $T_4$ ,  $T_5$ ). Thus, the additional heat source from the electrical heater was found to play a major role in the solar reactor system, which can support the solar reactor, especially when the DNI declined. In comparison, the

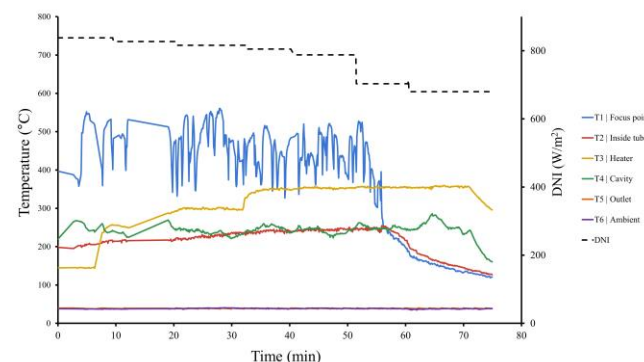


Fig. 5. Solar reactor temperature profile during hybrid heating

## V. CONCLUSION

The indirect irradiated solar hybrid chemical reactor has been successfully designed, fabricated, and tested. Experimental investigation on reactor temperature phenomena during on-sun, off-sun, and hybrid heating was carried out. As a result, the reactor temperature can reach temperatures above 500°C at the focal point area and above 200°C at the cavity zone for both on-sun and hybrid testing. During on-sun testing, a fluctuation in the temperature associated with  $T_1$  was high, which led to low heat transfer to the inside tube, leading to low  $T_2$  (200 °C). During hybrid testing, the reactor temperatures increased significantly and rapidly, pointing out important assistance from electrical heating, which is very helpful for the solar reactor operation as DNI is unstable due to cloud. Reducing heat losses is recommended to increase the reactor temperature. Real-time automatic solar tracking is necessary to keep a stable solar input. Future work will focus on the analysis of solar reactor efficiency and a combination of the solar reactor with the thermochemical process.

## ACKNOWLEDGMENT

This work was supported by King Mongkut's Institute of Technology Ladkrabang (Grant number: 2564-02-08-002)

## REFERENCES

- [1] O. Koskinen, "Evaluation of the main energy scenarios for the global energy transition. Energy Strategy Reviews". 12, 167-173, 2016.
- [2] M. Perez and R. Perez, "A Fundamental Look at Supply Side Energy Reserves for the Planet," Update 2015, IEA-SHCP-Newsletter Vol. 62 No, 2015.
- [3] RatedPower. "Solar Energy in Thailand: Market Outlook and Future Prospects". <https://ratedpower.com/blog/solar-energy-thailand/>, 2021.
- [4] Asif, "Fundamentals and Application of Solar Thermal Technologies". Elsevier, 27-36, doi:10.1016/B978-0-12-409548-9.10093-4, 2017.
- [5] M. Romero and A. Steinfeld, "Concentrating solar thermal power and thermochemical fuels Energy and Environmental Science". doi: 10.1039/c2ee21275g, 2012.



- [6] R. Bader and W. Lipiński, “Solar Thermochemical Processes”. 2016.
- [7] A. Steinfeld, “Solar thermochemical production of hydrogen - A review”. *Solar Energy*, 78(5), 603-615. doi:10.1016/j.solener.2003.12.012, 2005.
- [8] Bellouard et al., “Solar thermochemical gasification of wood biomass for syngas production in a high-temperature continuously-fed tubular reactor”. doi:10.1016/j.ijhydene.2016.08.196, 2017.
- [9] T. Kodama et al., “Particle reactors for solar thermochemical processes”. *Solar Energy*, 156 113-132, doi:10.1016/j.solener.2017.05.084, 2017.

# The Improvement of Loss Time Recording System for Grout Packing Process

Phummarin Thavitchasri<sup>1</sup> and Jakrapan Nanthaphunkul<sup>2</sup>

<sup>1</sup> Industrial Electrical Technology, Valaya Alongkorn Rajabhat University under the Royal Patronage,  
Pathum Thani, Thailand, Email : [phummarin@vru.ac.th](mailto:phummarin@vru.ac.th)

<sup>2</sup> Mechatronics and Robotics Engineering, Rajamangala University of Technology Thanyaburi,  
Pathum Thani, Thailand, Email : [jakrapan\\_n@rmutt.ac.th](mailto:jakrapan_n@rmutt.ac.th)

**Abstract:** This research is a comparative study and experimental of loss time recording system for grout packing process. The key objective of this research focuses on the semi-automatic loss time data tracking system controlled by microcontroller model Arduino Mega 2560 and received data from infrared sensor model E-18-D80NK be used to detect the grout bag that has been filled from the production line and flows to the conveyer grout packing machine. It is a system to record lost time and compared with the existing system that uses people for manual record, which has inaccurate and inaccurate loss time data recorded that impact to overall efficiency in packing line process. The results of using the loss time data recording system can record more loss data than the manual recording system up to 17 percent loss reduction, representing a time that can be improved up to 8.30 hours or equivalent to a production opportunity able to produce 23,870 bags of grout per month.

**Index Terms**—time record, microcontroller, Packing process, Production loss.

## I. INTRODUCTION

Planning and estimating for manufacturing processes or indicators in the industrial sector. It is necessary and very important to determine the direction of production and plan to deliver product to customer, this is necessary and appropriate cost management in the production business in order to have a profitable, competitive and turnover in the economy in the factory. Currently, there is high competition, due to the current economic was slowdown in the past 3 years during COVID-19 crisis; overall industrial factories need to be manage production costs as efficiently as possible, such as reducing losses in the production process and also must be reduce products that produced without a good quality, unnecessary stopping the machine in term of un plan downtime. Overall all problems that makes the total results in the production line not being produced and loses of time. The improvement system will increase the value of overall system, including expenses in other area, for example, reducing the use of main energy and turning to invest in renewable energy in the long term. Reduce overtime or other activities in all sectors of the business to increase profits. From the above problems, the current industry focuses on the opportunity to reduce cost lose in terms of producing products out of the production process, which without proper control of these costs. It may affect the loss of the overall business. Therefore, in the industry

must be necessary to have an action plan to reduce the costs incurred. The loss of time in the production process (Loss time) is a part that causes unnecessary expenses and records of lost time will be attributed to the analysis all of the problems that arise, to lead to problem solving or fine the root cause analysis, This is an important part that must be accurate and complete, otherwise it may fix a mistake all process. This is to improve the causes time and expenses to improve.

As mentioned above, the grout filling department of Saint-Gobain Weber Co., Ltd. has been organized to increase production efficiency and reduce operating costs by focusing on reducing wasted time in the production process, therefore the current system to record the lost time in the production process by using employees to record time loss for each problems that occur during operation. That causes no output from the production line caused by various parts such as, machine stopping due to machine failure for more than 10 minutes this problem will called break down, short stop of the machine for no longer than 10 minutes will called change over, various waiting processes such as waiting for raw materials, waiting for moving vehicles, waiting for energy and waiting for employees, etc., which information of lost time obtained from the employee's record. There is a discrepancy that does not match with actual problem which, when analyzed. It was found that the recorded information was incomplete can be observed from unspecified lost time (No-identify) up to 10 percent of the total lost time and information from records taken by

employees were conflicts with the information of related to departments, such as maintenance departments and store departments, etc., where the analysis of data leads to lack of credibility and unreliable troubleshooting to system.

This research use microcontroller for control the loss time recording in grout packing process, The microcontroller that use in this research were model Arduino Mega2560. The project team decision to use this controller in small laboratory and applied to install at the packing line because the resulted from laboratory very low and not complicated during installation and commissioning and this controller for the initial test for loss tracking and loss reduction project startup. The resulted were make decision to company will use other more efficiency controller if the result were improved than the existing process. The technical characteristic of this model will show in Table I [3-4].

TABLE I

TECHNICAL CHARECTERISTIC OF ARDUINO MEGA 2560

No.	Characteristic of Arduino Mega 2560.		
	Specific	Number	Unit
1	IC microtroller Arduino Mega 2560	-	-
2	Rate voltage	5.0	volt
3	Digital port I/O	54.0	Port
4	Analog input	16.0	Port
5	Rate current	40.0	Milliampare
6	Inside program	256	KB
7	RAM	8	KB
8	EEPROM	4	KB
9	FREQUENCY	16	MHz

II. OVERALL GROUT PACKING PROCESS.

A. Overall effectiveness of equipment

In term of overall effectiveness of equipment will annualize the analysis during machine operation, there are various devices with different functions, but their behavior is the same at the level of functionality, i.e. they consist of the normal working state up and the status is failing is state down based on the principle of operation of those devices will follow the time cycle [1-2-3]. The long-term operation of machine or equipment is estimated to be the average time that the device is in a normal working state and has continuity, and the average amount of time that the device is in a failed state, there is a repair process in order to bring the system back to normal operation again. The working behavior can be shown in Fig.1.

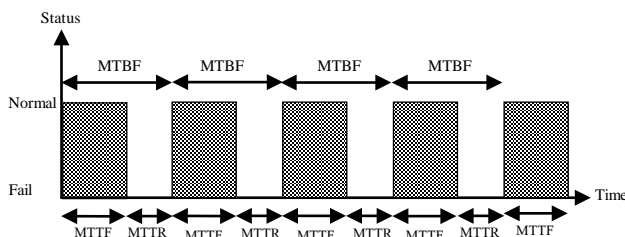


Fig.1. Estimated device operating time is the average

Where MTTF (Mean Time to Failure) is the average amount of time the device stays in a normal operating state, with the MTTF value being the inverse of the failure rate. This can be obtained as in (1)

$$MTTF = \frac{1}{\lambda} \tag{1}$$

Then

*MTTF* is Mean Time to Failure  
 $\lambda$  is Failure rate

MTTR (Mean Time to Repair) is the average time a device is in a failed state or the mean time it takes to repair the system. The MTTR value is inverses to the repair rate. This can be obtained as in (2)

$$MTTR = \frac{1}{\mu} \tag{2}$$

Then

*MTTR* is Mean Time to Failure  
 $\mu$  is Repair rate

MTBF (Mean Time Between Failures) is the time period in which a device operates, or can be described as the total time value. Therefore, the MTBF value is the sum of the average time the device was in normal operation (MTTF) and the duration. The average device failure state (MTTR) can be obtained from as in (3)

$$MTBF = MTTF + MTTR \tag{3}$$

B. Theory

Microcontroller; A microcontroller is a compact integrated circuit designed to govern a specific operation in an embedded system and a typical of microcontroller includes a processor, memory and input/output (I/O) peripherals on a single chip, the microcontrollers is a compressed microcomputer manufactured to control the functions of embedded systems in office machines, robots, home appliances, motor vehicles, and a number of other gadgets. Microcontroller bought a revolution in modern electronics. Normally, C and assembly languages are used to program microcontroller. For the example a microcontroller advantages is suppose if user want to increase the ON period of Green LED in traffic signal lights, if user are working on DLD circuit then will have to change hardware components, such as changing resistances values, but if user are working on microcontroller just need to make changes in the software and upload the code in the microcontroller, Therefore with the invention of microcontroller, the system no need to design logics using electronics hardware components anymore, instead user can design logics in programming or code. A microcontroller is comprises components such as; memory, peripherals and most importantly a processor. The structure of microcontroller is an integrated circuit (IC) device used for controlling other portions of an electronic system, usually via a microprocessor unit (MPU), memory, and some peripherals. The data RAM (Random Access Memory) is

the data space that is used for temporarily storing constant and variable values that are used by the microcontroller during normal program execution. The amount of physical RAM space on a given microcontroller varies from one microcontroller device. From the most important of microcontrollers have some amount of internal RAM, commonly 256 bytes; although some microcontrollers have more and some have lower than the specification, for example, the PIC18F452 microcontroller has 1536 bytes of RAM, which should be enough for most microcontroller-based applications. The general structure of microcontroller can be shown in Fig.2

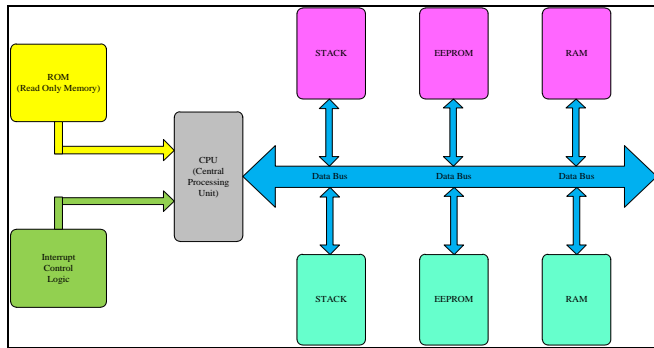


Fig.2. Structure of microcontroller

C. Working model of the device

The simulation model of the device will look like a 2-state model, which the state model. The operation of the 2 state of the device consists of the normal operating state (Up) and the failed states (Down) [2-3] are shown in Fig. 3.

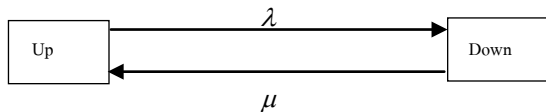


Fig.3. Operation model 2 device status

Where  $\lambda$  is failure rate  
 $\mu$  is repair rate

D. Working model of the device

The calculation of the overall equipment effectiveness or OEE (Overall Equipment Effectiveness) can be found in Equation (4)

$$OEE = Availability \times P.E. \times QualityRate \quad (4)$$

Where

- OEE is the working efficiency of Machinery and equipment
- Availability is the running rate
- P.E. is the operating efficiency
- Quality Rate is the quality rate

which when the factors that affect the production system, including employees, machines and work pieces produced come to analyze The OEE is an index that indicates the overall condition of the production system. The OEE benchmark measures the overall effectiveness of standardized equipment run the engine (Availability) equal to 90 percent Performance Efficiency equal to 95 percent and the quality rate (Quality Rate) equal to 99 percent. Therefore, the overall effectiveness of the equipment is  $0.90 \times 0.95 \times 0.99 \times 100 = 85$  percent. Such values are not applicable target values or can set target values in the factory, normally; all industrial plants have overall equipment efficiency (OEE) higher than 85 percent.

III. METHODOLOGY

In this part that will include the simulated block diagram model of loss time recording system, the simulate program and parameter setting will follows the basic routine functional human recorder, the functional human recorder will follow as Fig. 4.

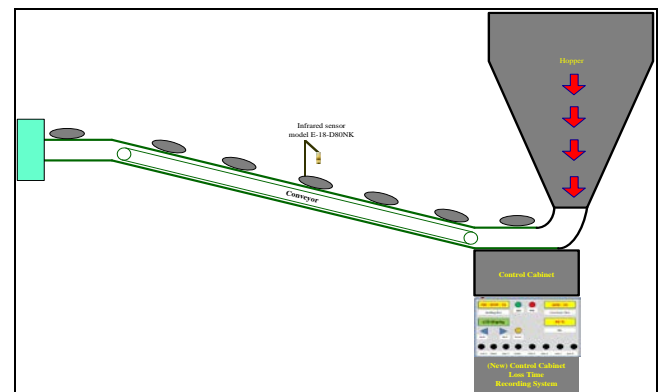


Fig.4. Data recording system design cycle

The figure as Fig.4 is the block diagram and initial parameter set point was set up and followed existing operating process for example, the grout bags were drop from hopper tank and moved to packing area via conveyor. This process were additional the sensor to check status of process and counting the total number of grout bag. The overall results of total number were displayed at new control cabinet.

E. Working model of the device

The design of the semi-automatic loss time data recording system for the grouting filling line is shown in Fig.5. This research were use microcontroller model Arduino Mega2560 for control all of the system. [3-4]

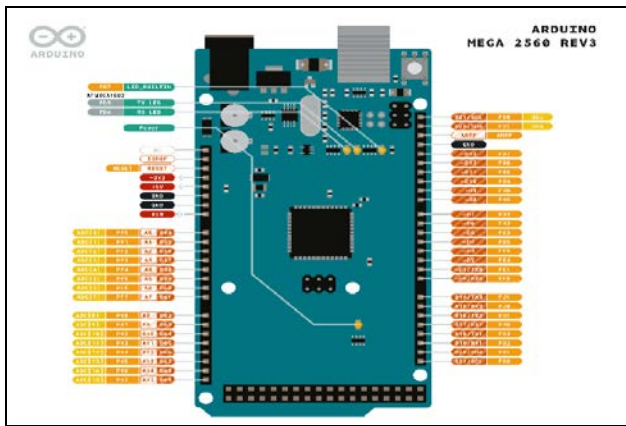


Fig.5. Drawing of microcontroller Arduino Mega2560

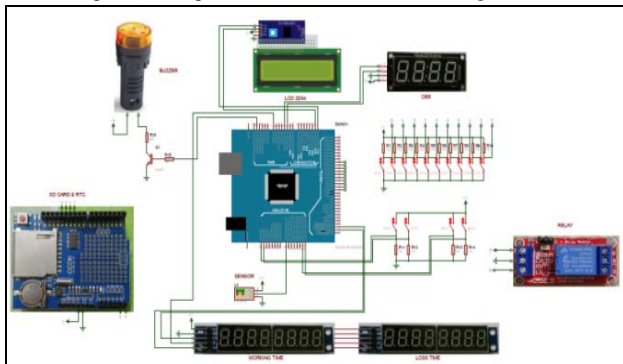


Fig.6. Circuit diagram in the research

As circuit diagram from Fig.6, the semi-automatic loss time data recording system for the grouting packing line is a microcontroller-controlled design with a working process in the production process when data recording is started. of lost time in the production process by using employees to record time loss of all problems that occur during production, that cause no output from the production line (No product). Caused by various parts, such as a stop due to a machine broken for more than 10 minutes (Break down), a temporary stop of no more than 10 minutes (Short stop), the process of changing the model of the product (Change over), various waiting processes, such as waiting Raw materials waiting for a forklift waiting for energy and waiting for employees, etc., which information of lost time obtained from the employee's record There are discrepancies that do not match the actual problem. Which, when analyzed It was found that the recorded information was incomplete.

#### F. Time, Semi-Automatic Pharmaceutical Packaging Line

The design of the control panel for semi-automatic loss time data recording system for the grouting filling line is shown in Fig. 7

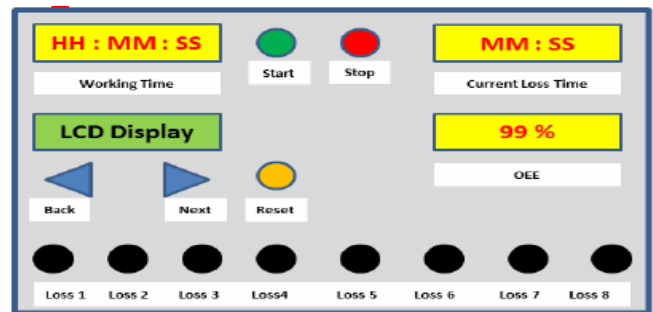


Fig.7 Control cabinet for the data recording system

The figure as Fig.7 is the new control panel of loss time recording system were created by general loss in production process and classifier via manufacturing requirement that block diagram and initial parameter set point was set up and followed existing operating process for example, the grout bags were drop from hopper tank and moved to packing area via conveyor. This process were additional the sensor to check status of process and counting the total number of grout bag. The overall results of total number were displayed at new control cabinet.

#### G. Installation of control unit, data recording system, loss of time, semi-automatic sealant filling line

The installation of a semi-automatic loss time data recording system on the grouting filling line is shown in Fig.8



Fig.8. location of the installation of the control cabinet

#### H. Semi-automatic loss time data recording control system test of sealant filling line.

The test of the semi-automatic loss time data recorder on the grouting filling line is shown in Fig. 9



Fig.9. Testing of the data logging control cabinet.

#### IV. RESULTS AND DISCUSSION

In this part that will show the result of loss time recording system for grout packing process.

##### I. PACKAGING TEST RESULT

In this section were shows the testing of 4 products containing sealant four types of products has been selected in this production line by the nature of the product that contains grout is shown in Fig. 10



Fig.10. Product contains all 4 types of grout adhesive.

##### J. Sensor Deviation Test Result

System tests of tolerances the packaging products during the production line. The result as Table II

TABLE II

SUMMARIZE THE PRODUCT DETECTION OF THE SENSOR.

Product name	The gloss of file at 45 degree (GU)	Target Number of production (Bag)	Number of bags the sensor can detect (Bag)	Number of bags error the sensor can detect (Bag)	Percentage of error the sensor can detect (%)
Product 1 (Power)	67.04	2,400	2,465	65	2.7%
Product 2 (Classic)	50.46	2,400	2,496	96	4.0%
Product 3 (HR)	74.30	2,400	2,526	126	5.3%
Product 4 (Slim)	69.12	2,400	2,470	70	2.9%

From table II were testing the tolerances for 4 products containing sealant four types of packaging products during the production line. The result were show that sensor model

E-18-D80NK, The result were product 3 (HR) to most error 5.3 percent that compare with other 3 product, because the problem with the accuracy of sensor when detect to black color and the resulted were same in the laboratory.

##### H. Sensor Deviation Test Result.

Comparison results of data collection of employees compared to time recorders It can be summarized as Table III.

TABLE III  
SUMMARIZE THE RESULTS OF DATA RECORDING BETWEEN HEMAN RECORD AND SYSTEM RECORDER.

Month (2022-2023)	Production time (min)	Number of production (Bag)	Efficiency (%OEE)	Loss the system cannot detect (min)	Loss the system cannot detect (percentage)
July-2022	11,340	257,510	56%	2,832	25%
Aug-2022	12,120	239,945	49%	773	6%
Sep-2022	11,020	233,240	40%	852	7%
Oct-2022r	12,460	240,205	35%	742	6%
Nov-2022	12,210	238,741	51%	730	6%
Dec-2022	13,110	300,345	55%	726	5%
Jan-2023	13,230	290,295	38%	760	7%
Feb-2023	12,980	300,560	49%	741	6%
May-2023	13,350	305,720	52%	749	6%
average	12,424	267,396	47%	989	8%

From Table III, the results were that the loss of time data from the recording system was more efficient. The recording data from employees during July 2022 to Mar 2023 showed a recording error of 25 percent error, and after the system use recorded system the error were average 6 percent discrepancy with efficiency and 17 percent reduction in wasted time.

#### V. CONCLUSION

This research is a comparative study and experimental of loss time recording system for grout packing process. The key objective of this research focuses on the semi-automatic loss time data tracking system controlled by microcontroller be used to detect the grout bag that has been filled from the production line and flows to the conveyer grout packing machine. It is a system to record lost time and compared with the existing system that uses people for manual record, which has inaccurate and inaccurate loss time data recorded that impact to overall efficiency in packing line process. The results of using the loss time data recording system can record more loss data than the manual recording system up to 17 percent loss reduction, representing a time that can be improved up to 8.30 hours or equivalent to a production opportunity able to produce 23,870 bags of grout per month.

#### REFERENCES

- [1] T. Rugthum. (2018). *An Adaptive Control Scheme for Robotic Systems with Uncertainties Using a Finite State Machine Based Adaptation Technique*. The 15th International Conference on Electrical Engineering/Electronics, Computer, Telecommunications and Information System. (ECTI-CON2018). (pp130-133). Thailand.
- [2] R. Wongtanawijit. (2018). *Rubber Tapped Path Detection using K-Means Color Segmentation and Distance to Boundary Feature*. The 15th International Conference on Electrical Engineering/Electronics, Computer, Telecommunications and Information System. (ECTI-CON2018). (pp. 761-764). Thailand.
- [3] K. Ansari and K. D. Park. (2018). *Multi constellation GNSS precise point positioning and prediction of propagation errors using singular spectrum analysis*". *Astrophys Space Sci.* 363(12):1-7.
- [4] F. Meng, S. Wang, and B. Zhu, (2015). *GNSS reliability and positioning accuracy enhancement based on fast satellite selection algorithm and RAIM in Multiconstellation*. *IEEE Aerospace and Electronic Systems Magazine*, vol. 30, no. 10, pp. 14-27, 2015.
- [6] C. Deerada, K. Phromsuthirak, V. Areekul, (2018). *Reference Point Detection for Latent Fingerprint Image Based on Spectrum Anlysis*. The 15th International Conference on Electrical Engineering/Electronics, Computer, Telecommunications and Information System. (ECTI-CON2018). (pp777-780). Thailand.
- [7] Arduino Mega2560 Database.  
<https://store.arduino.cc/products/arduino-mega-2560-rev3>
- [8] E18-D80NK Infrared Distance Ranging Sensor Database.  
<https://www.arduino4.com/product/217/e18-d80nk-infrared-distance-ranging-sensor>

# An investigation of micro-scale flow boiling in serpentine tube

Suphattharachai Khauntakob<sup>1\*</sup>, Sira Saisorn<sup>1</sup>, Adirek Suriyawong<sup>1</sup>, Sakkarin Chingulpitak<sup>1</sup>

<sup>1</sup> Department of Mechanical Engineering, King Mongkut's Institute of Technology Ladkrabang Prince of Chumphon campus, Chumphon 86160, Thailand

\*Corresponding Author : E-mail: Suphattharachai.kha@gmail.com

**Abstract:** This paper is a two-phase flow study which pertains to flow pattern and heat transfer behaviors in serpentine tube with confinement number greater than 0.5. The serpentine configuration was deployed as a test section corresponding to horizontal flow in a 1 mm the diameter tube the diameter tube, and R134a was used as working fluid. Flow boiling was conducted under saturated flow, i.e. mass flux of 381 kg/m<sup>2</sup>s heat flux of 0.1-10 kW/m<sup>2</sup>, and pressure of 0.6-0.7 MPa. The research, based on a constant surface heat flux, showed the dependence of heat transfer coefficient (HTC) on flow pattern and heat flux, The result revealed nucleate boiling as well as convective heat transfer mechanisms.

**Keywords:** Flow pattern, Heat transfer coefficient, Serpentine tube.

## 1. Introduction

Due to the rapid development of modern thermal equipment, one of the challenges is to design and develop efficient micro-channel heat exchangers which are vital components in electronic cooling applications found in EV cars and supercomputers. As pointed by [1], the two-phase flow in ultra-small passages was reported in numerous publications. The corresponding results were different from the behaviors observed in conventional channels. The micro-scale flow was identified by confinement number [8] expressed by

$$Co = \frac{\sqrt{\sigma/g(\rho_L - \rho_G)}}{D_h}$$

Kirpalani [2] reported advantages of micro-scale heat transfer mechanisms over the case of macro-scale phenomena. They also indicated significant influence affecting the micro-channel flow.

Wang [3] showed important parameters for curved tube, which induced secondary flow or Dean flow affecting heat transfer performance and pressure drop penalty. The additional flow was mainly governed by centrifugal force.

Donaldson [4] discussed the curvature effect causing the difference in the two-phase morphology. The single-phase and two-phase flows were analyzed to detect bubble dynamics in curved channel.

The evaporation process in U-bend tubes was carried out by Jaten et al. [9] The flow boiling of R134a was investigated under mass flux of 200-600 kg/m<sup>2</sup>s, vapor quality of 0.01-0.9. They reported the heat transfer characteristics with variations in mass flux and vapor quality. Flow visualization in adiabatic section showed high HTC during annular flow.

Jatau and Ochende [18] proposed the optimal design for boiling flow in a U-bend channel to improve the thermal performance.

Jatau and Ochende. [19] investigated phase-change during R-134a boiling flow in U-bend channel. The development of flow patterns and relevant thermal performance were reported.

As shown in the above discussion the micro-scale flow boiling in the serpentine channel is still scarce. The new data for this configuration is presented in this paper.

## 2. Materials and experimental methodology

The experimental apparatus deployed in this work is shown in fig 1 The main component are similar to that presented in Saisorn et al.[17] except the test section. In this work, R134a boiling flow took place in a horizontally Serpentine tube having a diameter of 1 mm. The phase-change system comprised pre-heater section, test section. (constant surface heat flux condition), condensing units, and data acquisition system. The circulation of the flow was driven by micro-gear pump and the flow rate was monitored by using mass flow meter. Heat load to the test section was Provided by power supply. The flow patterns were observed through a transparent section having the same diameter as the test section's diameter. A stainless steel tube was arranged in serpentine configuration associated with four curved sections (radius of curvature of 3 mm for each), five straight sections (length of 1069 mm for each). Surface temperature were measured by 18 thermocouples covering both straight and curved sections. Although the test section was insulated, heat loss estimation was performed before the HTC was determined.



A. Schematic diagrams

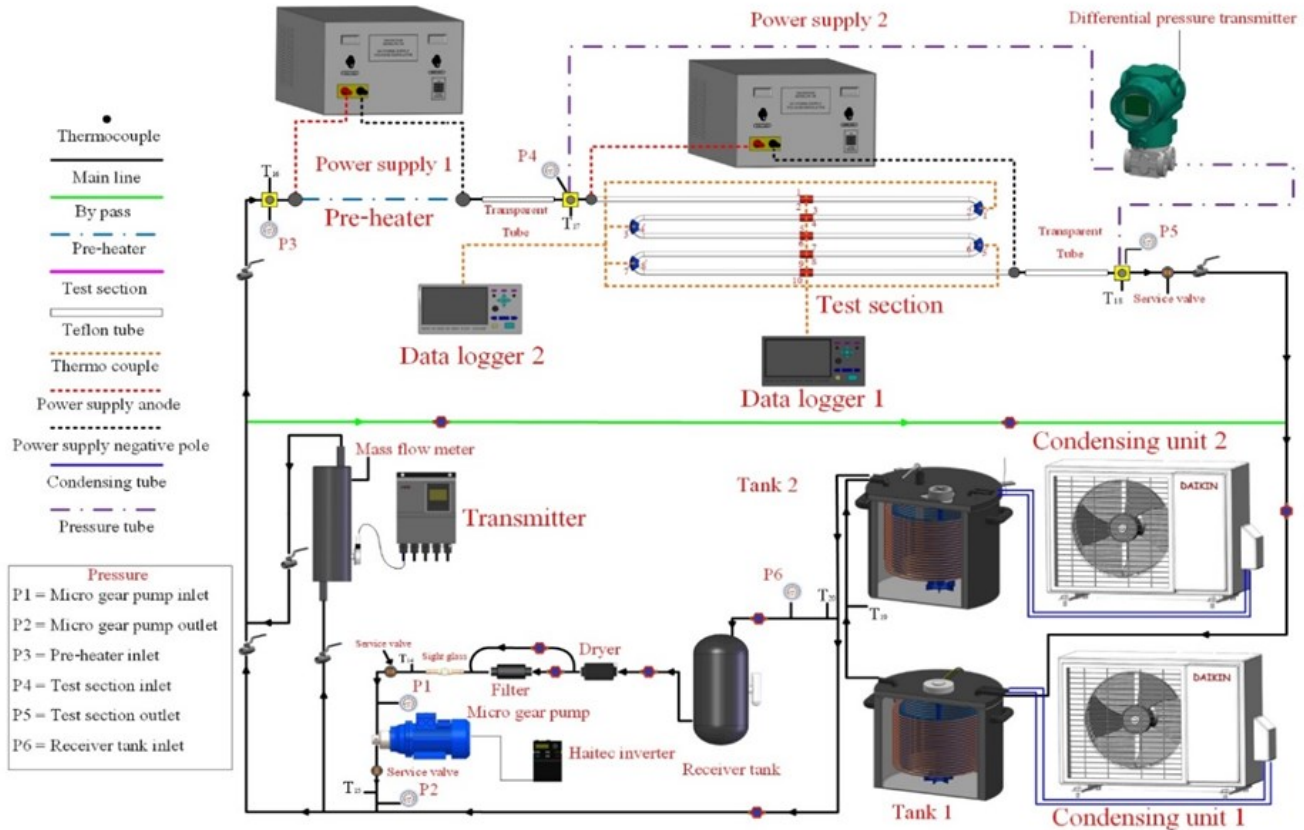


Fig. 1. Schematic diagram of the test facility.

Table 1 Experimental Conditions.

Parameter	Range
Diameter (mm)	1
Length(mm)	1069
Mass flux (kg/m <sup>2</sup> s)	381
Heat flux (kW/m <sup>2</sup> )	1-10
Saturation pressure (MPa)	0.6-0.7
Vapor quality	0.1-1
Test-Section material	Stainless steel

3. Data reduction

3.1 The local HTC,  $h_{loc}$  calculated from :

$$h_{loc} = \frac{q''}{T_{s,in,local,n} - T_{f,local,n}} \quad (1)$$

The local inner wall temperature  $T_{(s,in,local,n)}$  of the tube can be determined using the equation for steady-state one-dimensional heat conduction. The local fluid temperature.

$T_{(f,local,n)}$  of two-phase region can be obtained based on the assumption corresponding to a linear variation of the fluid temperature along the test section.

3.2 The average HTC was also presented, which can be determined by

$$h_{avg} = \frac{q''}{(T_{s,in,avg} - T_{f,avg})} \quad (2)$$

Where  $T_{(s,in,avg)}$  is the average temperature of the inner wall surface in the Test section.  $T_{(f,avg)}$  is the mean temperature of the fluid and

3.3 Heat flux  $q''$ , transferred to the test section can be calculated from

$$q'' = \frac{q - q_{loss}}{2\pi r_{in} L} \quad (3)$$

Where  $q$  is electrical power transferred to the serpentine test section.  $q_{loss}$  is estimated before determining HTC by determined using the energy balance.

The relevant vapor quality of the refrigerant R134a at the test section inlet was determined from :

$$X_z = \frac{i - i_L}{i_{LV}} \quad (4)$$

Where  $i_L$  is the specific enthalpy of the saturated liquid,  $i_{LV}$  is the enthalpy of vaporization and  $i$  is the local fluid enthalpy.

## 4. Result and Discussion

### 4.1 Flow patterns

The followings are the flow pattern classification which is used to identify the observed flow morphology.

**Slug flow:** the entrainment of elongated bubble and liquid slug flowing intermittently along the tube axis.

**Throat-annular flow:** occurred a combination of the elongated vapor bubbles engender vapor core.

**Churn flow:** the breaking up of elongated bubble due to high wake in liquid slug.

**Annular flow:** stable of gas-core flow surrounded by thin liquid film .

### 4.2. Flow boiling heat transfer

#### 4.2.1 HTC data

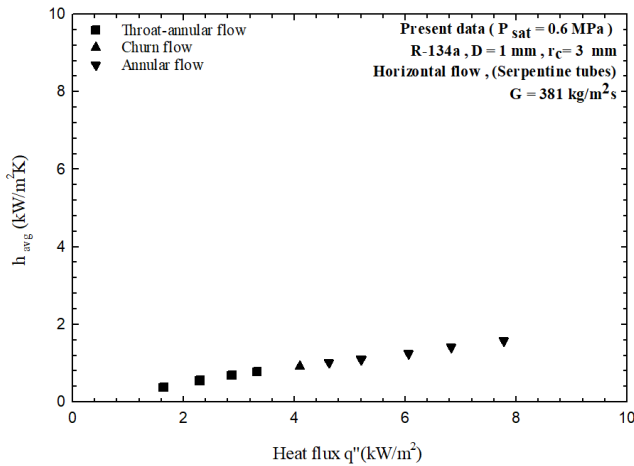


Figure 3 The average HTC versus the heat flux at mass flux of 381 kg/m<sup>2</sup>s and pressure of 0.6 MPa

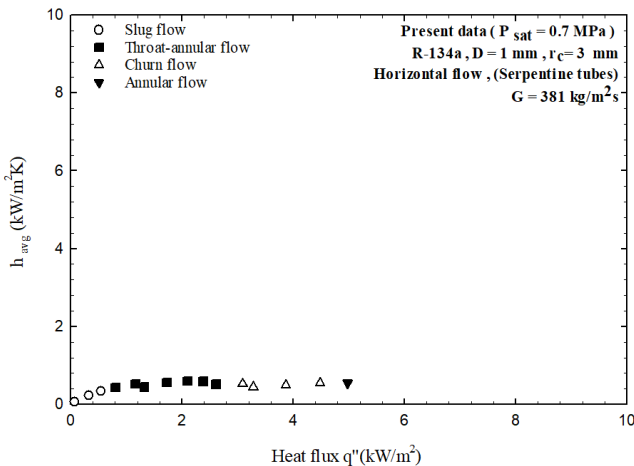


Figure 4 The HTC versus heat flux at mass flux of 381 kg/m<sup>2</sup>s and pressure of 0.7 MPa

Figure 3 shows data of the average HTC at different heat flux values 0.07-7.78 kw/m<sup>2</sup> Result show that the increase of heat flux gives higher HTC Flow patterns observed in this boiling process under a pressure of 0.6 MPa and heat flux of 381 kg/m<sup>2</sup>s include throat-annular flow, churn flow , and annular flow. Annular flow results in high heat transfer performance in comparison to the other flow regimes.

Figure 4 illustrates HTC characteristics with a variation of heat flux under constant mass flux and pressure of 381 kg/m<sup>2</sup>s and 0.7 MPa, respectively. The figure indicates that heat flux has slight influence on the heat transfer behaviors. Also, HTC is less affected by the change in flow pattern. Convective boiling seems dominant at higher pressure (0.7 MPa).

## 5. Conclusion

This paper presents new data based on two-phase flow patterns and HTC of R134a for flow boiling in serpentine tube micro-channel with a diameter of 1 mm and total length of 1069 mm . From observing the flow, it was found that the flow pattern consisted of Slug flow , Throat-annular flow ,Churn flow,and Annular flow.

The heat transfer results showed that at pressure of 0.6 MPa, the dependence of HTC on heat flux was able to be explained based on nucleate boiling. However, the increase in pressure (0.7 MPa) led to the suppression of nucleate mechanism, showing the insignificant effect of heat flux on HTC.

### Nomenclature

Dh	hydraulic diameter (mm)
G	mass flux (kg/m <sup>2</sup> s)
HTC	heat transfer coefficient (kW/m <sup>2</sup> K)
q''	heat flux (W/m <sup>2</sup> )
q	heat applied to test section, IV q <sub>in</sub> , (KW)
q <sub>loss</sub>	heat loss (KW)
r	radius of the tube (m)

### Greek symbols

$\sigma$	surface tension (N/m)
$\rho$	density (kg/m <sup>3</sup> )

### Subscripts

g	gravitation
L	liquid phase
G	Vapour phase
h	hydraulic diameter
in	inner wall surface

### Acknowledgment

The authors would like to express their appreciation to the KMITL Research Fund for providing financial support for this study.

### References

- [1] Prakash, R., Verma, R. K., & Ghosh, S. (2019). Liquid-liquid mass transfer in a serpentine miniature geometry-effect on pressure drop. *Chemical Engineering Journal*, 369, 489-497.
- [2] Kirpalani, D. M., Patel, T., Mehrani, P., & Macchi, A. (2008). Experimental analysis of the unit cell approach for two-phase flow dynamics in curved flow channels. *International journal of heat and mass transfer*, 51(5-6), 1095-1103.
- [2] Thangam, S., & Hur, N. (1990). Laminar secondary flows in curved rectangular ducts. *Journal of Fluid Mechanics*, 217, 421-440.
- [3] Wang, C. C., Chen, I. Y., & Yang, Y. W. (2002). Influence of horizontal return bend on the two-phase flow pattern in a 6.9 mm diameter tube. *The Canadian Journal of Chemical Engineering*, 80(3), 478-484.
- [4] Donaldson, A. A., Kirpalani, D. M., & Macchi, A. (2011). Single and two-phase pressure drop in serpentine mini-channels. *Chemical Engineering and Processing: Process Intensification*, 50(8), 877-884.
- [5] Martin, J., Oshkai, P., Djalili, N., 2005. Flow structures in a U-shaped fuel cell flow channel: quantitative visualization using particle image velocimetry. *J. Fuel Cell Sci. Technol.* 2, 70-80.
- [6] Xiong, R., Chung, J.N., 2007. Flow characteristics of water in straight and serpentine micro-channels with miter bends. *Exp. Therm. Fluid Sci.* 31, 805-812.
- [7] Huh, C., Kim, J., Kim, M.H., 2007. Flow pattern transition instability during flow boiling in a single microchannel. *Int. J. Heat Mass Transfer* 50, 1049-1060.
- [8] Kew, P. A., & Cornwell, K. (1997). Correlations for the prediction of boiling heat transfer in small-diameter channels. *Applied thermal engineering*, 17(8-10), 705-715.
- [9] Jatau, T., & Bello-Ochende, T. (2021). Heat transfer and flow pattern map development of R134A in a U-bend tube for flow boiling evaporation. *International Communications in Heat and Mass Transfer*, 128, 105629.
- [10] Keeapai boon, C., & Wongwises, S. (2015). Two-phase flow patterns and heat transfer characteristics of R134a refrigerant during flow boiling in a single rectangular micro-channel. *Experimental Thermal and Fluid Science*, 66, 36-45.
- [11] Saisorn, S., Kaew-On, J., & Wongwises, S. (2010). Flow pattern and heat transfer characteristics of R-134a refrigerant during flow boiling in a horizontal circular mini-channel. *International Journal of Heat and Mass Transfer*, 53(19-20), 4023-4038.
- [12] Saisorn, S., Wongpromma, P., & Wongwises, S. (2018). The difference in flow pattern, heat transfer and pressure drop characteristics of mini-channel flow boiling in horizontal and vertical orientations. *International Journal of Multiphase Flow*, 101, 97-112.
- [13] Wang, C. C., Chen, Y., Yang, Y. W., & Chang, Y. J. (2003). Two-phase flow pattern in small diameter tubes with the presence of horizontal return bend. *International Journal of Heat and Mass Transfer*, 46(16), 2975-2981.
- [14] Wang, C. C., Chen, Y., Yang, Y. W., & Hu, R. (2004). Influence of horizontal return bend on the two-phase flow pattern in small diameter tubes. *Experimental Thermal and Fluid Science*, 28(2-3), 145-152.
- [15] Ong, C. L. (2010). Macro-to-microchannel transition in two-phase flow and evaporation (No. THESIS). EPFL.
- [16] Donaldson, A. A., Kirpalani, D. M., & Macchi, A. (2011). Single and two-phase pressure drop in serpentine mini-channels. *Chemical Engineering and Processing: Process Intensification*, 50(8), 877-884.
- [17] Saisorn, S., Suriyawong, A., Srithumkhant, P., Wongpromma, P., & Wongwises, S. (2021). An investigation of horizontal and vertical flow boiling in a single channel with a confinement number beyond the threshold of micro-scale flow. *Physics of Fluids*, 33(11), 113302.
- [18] Jatau, T., & Bello-Ochende, T. (2023). Minimization of entropy generation in U-bend tube heat exchanger during flow boiling of R134a. *International Journal of Thermal Sciences*, 185, 108032.

# Effect of Irradiation and *Wolbachia* Endosymbiont on Flight Ability of *Aedes aegypti* Mosquito Vector

Jiraporn Yongyai<sup>1</sup>, Parinda Thayanikul<sup>1,2</sup>, Pattamaporn Kittayapong<sup>2\*</sup>

<sup>1</sup>Department of Biology, Faculty of Science, Mahidol University,  
jiraporn.yon@gmail.com and parinda.tha@mahidol.ac.th

<sup>2</sup>Center of Excellence for Vectors and Vector-Borne Diseases, Faculty of Science,  
Mahidol University at Salaya, Nakhon Pathom, Thailand, \*pkittayapong@gmail.com

**Abstract:** *Aedes aegypti* mosquito vector transmits four infectious viruses, i.e., Zika, Dengue, Chikungunya, and Yellow fever. Sterilization of *Ae. aegypti*, which is the recent development in biological control, has been implemented worldwide to suppress vector populations. Male mosquitoes can be sterilized by ionizing radiation (Sterile Insect Technique: SIT), *Wolbachia* endosymbionts (Incompatible Insect Technique: IIT), or a combined approach (SIT/IIT). *Wolbachia*-infected males can induce cytoplasmic incompatibility when mating with uninfected females, resulting in sterility and no fertile eggs. Male mosquitoes were irradiated by X-ray radiation. After irradiation, flight ability, which was one of the fitness parameters of mosquitoes, was evaluated. Releasing high-quality sterile males enhances the efficiency of mosquito control programs. Therefore, sterile mosquitoes should have good performance of flight ability before being implemented in SIT, IIT, or a combined approach (SIT/IIT) in mosquito controls. This study aims to investigate the effect of different radiation doses (30 Gy, 50 Gy and 70 Gy) on the flight ability of wild-type and *wAlbB*-infected *Ae. aegypti* mosquitoes. Results showed that the flight ability of non-irradiated, 30 Gy, and 50 Gy irradiated wild-type and *wAlbB*-infected *Ae. aegypti* males were in the range of 47.3 to 55.3% and 49.00 to 51.7%, respectively. The percentages of flight ability in both wild-type and *wAlbB*-infected *Ae. aegypti* males were reduced to 22.7 and 22.0% at 70 Gy radiation dosage. Both wild-type and *wAlbB*-infected *Ae. aegypti* males were radio-sensitive at high X-ray radiation dosage. Meanwhile, the flight ability of wild-type and *wAlbB*-infected *Ae. aegypti* females were in the range of 11.4 to 20.7% and 12.7 to 27.7%, respectively. Both wild-type and *wAlbB*-infected *Ae. aegypti* males were stronger than females in terms of flight ability at high X-ray doses. The results of this study suggested that the efficiency of SIT, IIT, or a combined approach (SIT/IIT), depending on both radiation dosage and *Wolbachia* infection, could be evaluated by flight ability.

**Index Terms**— *Aedes aegypti* mosquito, flight ability, Incompatible Insect Technique, Sterile Insect Technique, *Wolbachia* bacteria

## I. INTRODUCTION

*Aedes aegypti* mosquitoes transmit many infectious viruses including Zika, Dengue, Chikungunya and Yellow fever. Their habitats are distributed largely in tropical and subtropical regions in various continents. Numerous efforts have been implemented worldwide in order to reduce this mosquito vector.

The populations of *Ae. aegypti* mosquitoes can be controlled by environmental, chemical, and biological methods [2]. The environmental control was mostly applied in households such as removing water-filled containers to eliminate the oviposition of mosquitoes [1]. Insecticide is often used in chemical control; however, this approach is harmful to the non-targeted organisms. In biological control, biological agents, which are non-toxic to the environment, are introduced to limit vector populations [3]. Sterilizing vector mosquitoes is one of the biological

control methods that suppress vector populations in a wide area. There are three main male sterilization techniques; these are Incompatible Insect Technique (IIT), Sterile Insect Technique (SIT), and a combined approach (SIT/IIT).

The SIT method depends on the release of irradiated sterile male mosquitoes into uninfected *Ae. aegypti* populations. Ionizing irradiation breaks the molecular bond and forms the free radical, which subsequently attacks germ cells causing sterility [8]. Gamma-ray produced from cobalt-60 and X-ray were commonly applied for insect sterilization [2], [6].

*Wolbachia* infected mosquitoes have been applied in an Incompatible Insect Technique (IIT). *Wolbachia* induces cytoplasmic incompatibility (CI) phenotype and reduces viral transmission [4]. CI is the effect of mating between *Wolbachia*-infected males and uninfected females (or females infected with different *Wolbachia* strains) which causes the incompatibility of fertilized eggs, triggering embryo death [5]. Although *Wolbachia* bacteria have been

found in several mosquito species, for example, *Culex pipiens*, *Aedes albopictus*, and *Armigeres subalbatus*, they have not likely been found in natural *Ae. aegypti* populations. Therefore, *Wolbachia* bacteria have been microinjected into *Ae. aegypti* mosquitoes and recently those trans-infected mosquitoes have been used for suppressing natural *Ae. aegypti* populations [7].

Moreover, both IIT and SIT can be combined, in which *Wolbachia* trans-infected *Ae. aegypti* mosquitoes are irradiated to ensure sterility of the released males. In addition, *Wolbachia* can also block viral transmission, increasing the benefit of mosquito mass release programs.

Flight ability is one of important mosquito life history traits, which is the primary mechanism for dispersal in order to search for food resources, seek hosts, and access mating [9]. Flight ability of mosquitoes is a critical parameter to the success of SIT, IIT and combined SIT/IIT that are applied in an area-wide integrated pest management programs [12]. The efficiency of mosquito control programs depended on the quality of sterile males. Thus, sterile mosquitoes should have a good performance of flight ability before being implemented in the SIT, IIT or combined SIT/IIT. This study aims to investigate the effect of different X-ray radiation dosages (30 Gy, 50 Gy and 70 Gy) on the flight ability of wild-type and *wAlbB*-infected *Ae. aegypti* mosquitoes.

## II. METHODOLOGY

### A. Mosquito colony maintenance

The wild-type and *wAlbB*-infected *Ae. aegypti* colonies were used in this study. The *wAlbB*-infected *Ae. aegypti* has been prepared previously using the adult microinjection technique following Ruang-Areerate and Kittayapong (2006) [7]. Both mosquito colonies were maintained in the insectary of the Center of Excellence for Vectors and Vector-Borne Diseases, Faculty of Science, Mahidol University, Thailand at the relative humidity of 70 ± 5%, temperature control of 25 ± 2°C, and light-dark cycle of 12: 12 period. Eggs were hatched by submerging them under cool boiled-dechlorinated carbon filtered water in a bottle with a tight cap. The diet of larvae was a mixture of fish meal (Chanpongcharoen Kankaset Supplier, Thailand), crushed chicken liver, and yeast powder (*Saccharomyces cerevisiae*; Cheese Powder Supplier, Thailand) at a ratio of 3.3: 0.1: 0.56 by weight. Larvae were reared in a tray containing 2 liters of water. The larval densities were below 0.5 larvae/mL [13].

### B. Pupal irradiation

Irradiation of wild-type and *wAlbB*-infected *Ae. aegypti* in both male and female mosquitoes was processed at the pupal stage. The size of pupae was a sex-determination characteristic. Female pupae were larger than male ones.

Male and female pupae were separated by using larval-pupal separators (Model 5412, John W. Hock Company, Gainesville, FL, USA) [2] and kept in transparent plastic containers with 300 mL of dechlorinated water for X-ray irradiation. Three X-ray radiation dosages were performed, i.e., 30 Gy, 50 Gy, and 70 Gy, using the RS 2400•Q Irradiator (Rad Source Technologies Inc, USA) at the Thailand Institute of Nuclear Technology (TINT). Non-irradiated (0 Gy) mosquitoes were used as a control set.

### C. Flight ability test

Flight ability was measured by aspirating 100 males and 100 females of each mosquito colony and each radiation dosage into the flight test devices (FTD) for three replications [14]. The FTD contains many flight tubes in a flight cage. Mosquitoes were introduced to the FTD via a small hole (diameter 1 cm) at the bottom of the device using a mouth aspirator. After filling mosquitoes into the FTD, the cotton soaked with 10% sucrose was placed on top of the test device. Mosquitoes are allowed to fly in FTD for 2 hours. Mosquitoes that escape from the flight tube would be counted to calculate the percent of flight ability.

### D. Analysis

All statistical analyses were performed using SPSS 18.0 (Chicago, SPSS Inc.). One-way ANOVA and Tukey's post-hoc tests were used to analyze the percent of flight ability between non-irradiated and irradiated groups of *Ae. aegypti* male, *Ae. aegypti* female, *wAlbB*-infected *Ae. aegypti* male, and *wAlbB*-infected *Ae. aegypti* female. T-tests were used to compare the flight ability percentage between male and female in each radiated dosage and non-irradiated treatment of wild-type and *wAlbB*-infected *Ae. aegypti*. Two-way ANOVA was used to investigate the interaction effects of two parameters including sex, radiation dosage, and mosquito colony.

## III. RESULTS

The flight ability percentages of non-irradiated and irradiated (30 Gy, 50 Gy, and 70 Gy) *Ae. aegypti* males were 55.3±4.9%, 47.3±2.2%, 47.3±3.4%, and 22.7±5.5% respectively (Fig. 1). While the percentages of male mosquitoes escaped from the flight tube in non-irradiated and irradiated (30 Gy, 50 Gy, and 70 Gy) *wAlbB*-infected *Ae. aegypti* male treatments were 51.7±1.8%, 49.0±3.0%, 50.0±3.2%, and 22.0±4.6%, respectively (Fig. 2). Both wild-type and *wAlbB*-infected *Ae. aegypti* males had no difference in the percentages of flight ability among non-irradiated control, 30 Gy, and 50 Gy irradiated treatments, although, the percentages at 70 Gy irradiated treatment were significantly different (wild-type male:  $F_{3,8} = 11.333$ ,  $P = 0.003$ ; *wAlbB*-infected male:  $F_{3,8} = 18.305$ ,  $P = 0.001$ ).

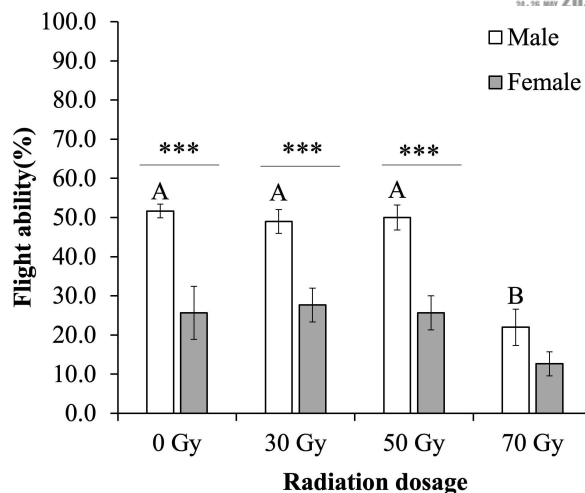
The flight ability percentages of non-irradiated, and irradiated (30 Gy, 50 Gy, and 70 Gy) wild-type *Ae. aegypti*

females were in the ranges of 11.4 to 20.7% (0 Gy = 20.7±4.3%, 30 Gy = 13.7±2.2%, 50 Gy = 22.3±1.5%, and 70 Gy = 11.4±2.0%) (Fig. 1). The range of flight ability percentage in non-irradiated and irradiated at 0 Gy, 50 Gy, and 70 Gy *wAlbB*-infected *Ae. aegypti* females were 25.7±6.8%, 27.7±4.3%, 25.7±4.3%, and 12.7±3.1%, respectively (Fig 2). The flight ability of wild-type *Ae. aegypti* females and *wAlbB*-infected *Ae. aegypti* females were not significantly different between control and irradiated treatments (wild-type female:  $F_{3,8} = 3.881$ ,  $P = 0.056$ ; *wAlbB*-infected female  $F_{3,8} = 18.305$ ,  $P = 0.200$ ). The flight ability of 70 Gy-irradiated treatments in both wild-type and *wAlbB*-infected *Ae. aegypti* females were lower than the non-irradiated, 30 Gy or 50 Gy treatments.

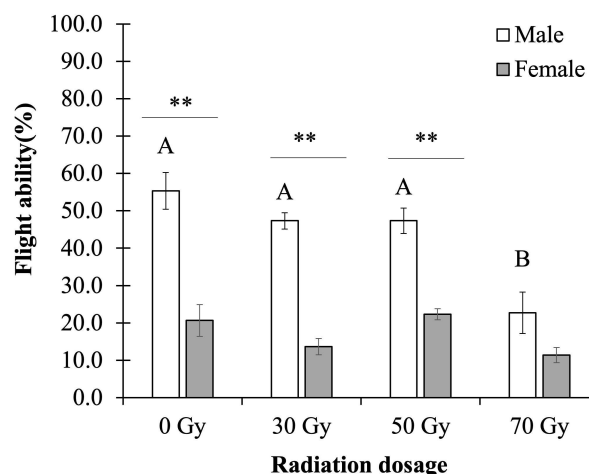
The flight ability percentages between males and females were significantly different in non-irradiated, 30 Gy-irradiated and 50 Gy-irradiated for both wild-type and *wAlbB*-infected *Ae. aegypti* tests (wild-type *Ae. aegypti*: 0 Gy,  $P = 0.006$ ; 30 Gy,  $P = 0.000$ ; and 30 Gy  $P = 0.002$ , *wAlbB*-infected *Ae. aegypti*: 0 Gy,  $P = 0.021$ , 30 Gy,  $P = 0.016$  and 50 Gy,  $P = 0.011$ ). For 70 Gy-irradiated treatments in both wild-type and *wAlbB*-infected *Ae. aegypti*, the flight ability of males was higher than female although it was not statistically different.

When comparing between male and female mosquitoes, the flight ability percentages of male mosquitoes were higher than female mosquitoes in all tested conditions.

The interaction effect of sex and radiation dosage on the percentage of flight ability of wild-type *Ae. aegypti* was observed ( $F_{3,16} = 4.670$ ,  $P = 0.016$ ), while it had no significant impact on *wAlbB*-infected *Ae. aegypti* ( $F_{3,16} = 1.606$ ,  $P = 0.227$ ). The interaction of radiation dosage and *Ae. aegypti* colonies on the flight ability percentage were not observed either on both male and female ( $F_{3,16} = 0.278$ ,  $P = 0.841$  and  $F_{3,16} = 0.993$ ,  $P = 0.421$ , respectively). The flight ability of wild-type and *wAlbB*-infected *Ae. aegypti* was not significantly different in both male and females ( $F_{1,16} = 0.000$ ,  $P = 0.997$  and  $F_{1,16} = 4.412$ ,  $P = 0.052$ , respectively).



**Fig. 1.** The percentage of flight ability of wild-type *Ae. aegypti* males (white bar) and wild-type *Ae. aegypti* females (grey bar) were treated at different radiation doses (30 Gy, 50 Gy, and 70 Gy) in comparison to non-irradiated ones (0 Gy). Bars indicated with different letters were significantly different for comparisons among treatments applied to male in white bar (One-way ANOVA Tukey,  $P < 0.05$ ). Bars indicated without letters were not significantly different for comparisons among treatments applied to female in grey bar (One-way ANOVA Tukey,  $P > 0.05$ ). Bars labeled with star marks indicate the *t*-test statistical analysis with significant difference as follows; \*\*\* for  $P < 0.01$ . Bars without stars were not significantly different (*t*-test,  $P > 0.05$ ). Vertical error bars indicate standard error (SE).



**Fig. 2.** The percentage of flight ability of *wAlbB*-infected *Aedes aegypti* males (white bar) and *wAlbB*-infected *Ae. aegypti* females (grey bar) treated at different radiation doses (30 Gy, 50 Gy, and 70 Gy) in comparison to non-irradiated ones (0 Gy). Bars indicated with different letters were significantly different for comparisons among treatments applied to male in white bar (One-way ANOVA Tukey,  $P < 0.05$ ). Bars indicated without letters were not significantly different for comparisons among treatments applied to female in grey bar (One-way ANOVA Tukey,  $P > 0.05$ ). Bars labeled with star marks indicate the *t*-test statistical analysis with significant difference as follows; \*\* for  $P < 0.05$ . Bars without stars were not significantly different (*t*-test,  $P > 0.05$ ). Vertical error bars indicate standard error (SE).

#### IV. DISCUSSION

In this study, the flight ability of wild-type and *wAlbB*-infected *Ae. aegypti* males were obviously decreased in 70 Gy X-ray irradiation treatment. Still, the flight ability percentages of all tested were higher in male when compared to those of females. Both wild-type and *wAlbB*-infected *Ae. aegypti*, males were less sensitive to radiation at high X-ray doses than female mosquitoes [15], [16]. The radiation dosage and sex had strong effects on flight ability.

The application of high radiation dosage resulted in complete sterility but lower flight ability. Previous studies found that the radiation dosages to obtain the 100% sterility were up to 90 Gy in *Ae. aegypti*, up to 70 Gy in *Ae. albopictus*, and up to 120 Gy in *Anopheles arabiensis* [10]. Lower flight ability reduces the survival chance and mating competitiveness in male mosquitoes when releasing into the wild. Male sterility should be investigated further in order to define the suitable radiation dosage for mosquito control in Thai mosquitoes.

Besides, the previous FTD work using Biogents pellets (BG-lure) on top of the device demonstrated that the mosquito escape rate of non-irradiated *Ae. aegypti* male was more than 75% [11]. However, the flight ability of male mosquitoes in this study was less than 60%. The 10% sucrose solution in a tiny cotton might be less attractive than BG-lure in order to encourage mosquitoes to escape from the flight tube. Thus, an attractant on top of the FTD device could affect the number of mosquitoes that escape from the flight tube.

#### V. CONCLUSION

Flight ability is one of the critical fitness parameters of mosquitoes. Therefore, the efficiency of SIT, IIT, or combined SIT/IIT might be able to be predicted using the flight ability test. In this study, the wild-type and *wAlbB*-infected *Ae. aegypti* sterile males irradiated at the 70 Gy radiation dosage had reduced flight ability significantly. *Aedes aegypti* males were stronger than females in terms of flight ability, not only in non-irradiated control, but also at 30 Gy and 50 Gy treatments.

#### ACKNOWLEDGMENT

This study was supported by IAEA/CRP/D44004/23918 on The Effect of Irradiation and *Wolbachia* endosymbiosis on Sterilization and Vector Competence of *Aedes aegypti* Vector and IAEA/TC/5095 on Enhancing the Capacity and the Utilization of the Sterile Insect Technique for *Aedes* Mosquito Control. Moreover, partial support was from the Development and Promotion of Science and Technology Talents Project (DPST) scholarship, and the Department of Biology, Mahidol University. The authors would like to acknowledge the support of the Thailand Institute of

Nuclear Technology (TINT) on irradiation methods and applications.

#### REFERENCES

- [1] L. Cheng, K. Wang, M.F. Ren, X.Y. Xu, "Comprehensive analysis of F. E. Champion de Crespigny and N. Wedell, "Wolbachia infection reduces sperm competitive ability in an insect", *Proceedings of the Royal Society B: Biological Sciences*, vol. 273, no. 1593, pp. 1455–1458, Mar. 2006, doi: <https://doi.org/10.1098/rspb.2006.3478>.
- [2] P. Kittayapong, N. Kaeothaisong, S. Nimphanomchai, and W. Limohpasmanee, "Combined sterile insect technique and incompatible insect technique: Sex separation and quality of sterile *Aedes aegypti* male mosquitoes released in a pilot population suppression trial in Thailand," *Parasites & Vectors*, vol. 11, no. S2, Dec. 2018, doi: <https://doi.org/10.1186/s13071-018-3214-9>.
- [3] M.D. Proverbs, "Induced sterilization and control of insects," *Annual Review of Entomology*, vol. 14, no. 1, pp. 81–102, Jan. 1969, doi: <https://doi.org/10.1146/annurev.en.14.010169.000501>.
- [4] S.P. Sinkins, "Wolbachia and cytoplasmic incompatibility in mosquitoes," *Insect Biochemistry and Molecular Biology*, vol. 34, no. 7, pp. 723–729, Jul. 2004, doi: <https://doi.org/10.1016/j.ibmb.2004.03.025>.
- [5] U. Tram, K. Fredrick, J.H. Werren, and W. Sullivan, "Paternal chromosome segregation during the first mitotic division determines *Wolbachia*-induced cytoplasmic incompatibility phenotype," *Journal of Cell Science*, vol. 119, no. 17, pp. 3655–3663, Sep. 2006, doi: <https://doi.org/10.1242/jcs.03095>.
- [6] J.G. Bond *et al.*, "Optimization of irradiation dose to *Aedes aegypti* and *Ae. albopictus* in a sterile insect technique program," *PLOS ONE*, vol. 14, no. 2, p. e0212520, Feb. 2019, doi: <https://doi.org/10.1371/journal.pone.0212520>.
- [7] T. Ruang-areerate and P. Kittayapong, "Wolbachia transfection in *Aedes aegypti*: A potential gene driver of dengue vectors," *Proceedings of the National Academy of Sciences*, vol. 103, no. 33, pp. 12534–12539, Aug. 2006, doi: <https://doi.org/10.1073/pnas.0508879103>.
- [8] M.E.H. Helinski and L.C. Harrington, "Male mating history and body size influence female fecundity and longevity of the dengue vector *Aedes aegypti*," *Journal of Medical Entomology*, vol. 48, no. 2, pp. 202–211, Mar. 2011, doi: <https://doi.org/10.1603/me10071>.
- [9] C. Lebon, K. Soupapoule, D.A. Wilkinson, G. Le Goff, D. Damiens, and L.C. Gouagna, "Laboratory evaluation of the effects of sterilizing doses of  $\gamma$ -rays from Caesium-137 source on the daily flight activity and flight performance of *Aedes albopictus* males," *PLOS ONE*, vol. 13, no. 8, p. e0202236, Aug. 2018, doi: <https://doi.org/10.1371/journal.pone.0202236>.
- [10] H. Yamada *et al.*, "The role of oxygen depletion and subsequent radioprotective effects during irradiation of mosquito pupae in water," *Parasites & Vectors*, vol. 13, no. 1, Apr. 2020, doi: <https://doi.org/10.1186/s13071-020-04069-3>.
- [11] H. Maïga *et al.*, "Standardization of the FAO/IAEA flight test for quality control of sterile mosquitoes," *Frontiers in Bioengineering and Biotechnology*, vol. 10, Jul. 2022, doi: <https://doi.org/10.3389/fbioe.2022.876675>.
- [12] V.A. Dyck, J. Hendrichs, and A.S. Robinson, *Sterile Insect Technique: Principles and Practice in Area-Wide Integrated Pest Management*. Dordrecht, Netherlands: Springer, 2005.
- [13] P.A. Ross, J.K. Axford, K.M. Richardson, N.M. Endersby-Harshman, and A.A. Hoffmann, "Maintaining *Aedes aegypti* mosquitoes infected with *Wolbachia*," *Journal of Visualized Experiments*, no. 126, Aug. 2017, doi: <https://doi.org/10.3791/56124>.
- [14] N.J. Culbert *et al.*, "A rapid quality control test to foster the development of genetic control in mosquitoes," *Scientific Reports*,

vol. 8, no. 1, Nov. 2018, doi: <https://doi.org/10.1038/s41598-018-34469-6>.

- [15] D.L. Williamson, S. Mitchell, and S.T. Seo, "Gamma Irradiation of the Mediterranean Fruit Fly (Diptera: Tephritidae): Effects of Pupal Age under Induced Hypoxia on Female Sterility," *Annals of the Entomological Society of America*, vol. 78, no. 1, pp. 101–106, Jan. 1985, doi: <https://doi.org/10.1093/aesa/78.1.101>.
- [16] R.R. Cogburn, E.W. Tilton, and J.H. Brower, "Almond Moth: Gamma Radiation Effects on the Life Stages<sup>13</sup>," *Journal of Economic Entomology*, vol. 66, no. 3, pp. 745–751, Jun. 1973, doi: <https://doi.org/10.1093/jee/66.3.745>.



# Production of activated carbon from *Typha angustifolia* Linn. using $ZnCl_2$ and KOH as activating reagent

Lapprasertmesuk, S.<sup>1</sup>, Pornpakakul, S.<sup>2\*</sup>

<sup>1</sup> Petrochemical and polymer science program, Faculty of Science, Chulalongkorn University

<sup>2\*</sup> Research Center for Bioorganic Chemistry, Department of Chemistry, Chulalongkorn University, Phayathai road, Wangmai, Pathumwan, Bangkok, 10330, Thailand corresponding author: surachai.p@chula.ac.th

**Abstract:** Activated carbon (AC) is an efficient universal adsorbent used in many applications. Since the price of commercial activated carbon are costly, many researches have been focusing to reduce the AC production cost. In this study, we used a low cost biomass *Typha angustifolia* Linn. (TA) in the production of AC through carbonization and activation with  $ZnCl_2$  and KOH at various temperatures and ratios. By SEM, FT-IR and BET surface area analysis, the prepared ACs were characterized as mesoporous materials with C=C as main functional group. The highest specific surface area ( $166.32\text{ m}^2\text{g}^{-1}$ ) and total pore volume ( $0.1689\text{ cm}^3\text{g}^{-1}$ ) were obtained by activation with  $ZnCl_2$ .

**Index Terms—** activated carbon, activating reagent, characterization, *Typha angustifolia* Linn.

## I. INTRODUCTION

Activated carbon (AC) is the universal adsorbent with high surface area and high porosity with unique chemical properties. There are many uses of AC for heavy metal adsorption, organic compounds adsorption, dyes adsorption,  $CO_2$  capture, catalyst,  $CH_4$  storage and  $NH_3$  adsorption [1]. Because commercial grade available ACs are high price [2], many researchers have developed process to reduce the cost and energy consumption to synthesis AC, for example using inexpensive lignocellulosic biomass (agriculture waste, parts of plants, and industrials biomass) as raw materials and chemical reagents in activation step [1, 2].

*Typha angustifolia* Linn. is a wetland plant which rich in lignocellulose biomass [1]. Because this plant is high porous biomass and widely distributed, it will be an inexpensive biomass for production of ACs [2]. In the literatures, ACs with the specific surface area of  $130.42$  and  $789.32\text{ m}^2\text{g}^{-1}$  were produced by *T. angustifolia* under temperature at  $450^\circ\text{C}$  with  $H_3PO_4$  (40% v/v) [2] and under temperature at  $469.02^\circ\text{C}$  with  $H_3PO_4$  (80% w/w) [3], to give ACs and they showed high capacity on the adsorption of heavy metal [2, 3].

There are two main steps in the ACs production, which are carbonization and activation [1]. In activation step, chemical activation process not only consumed lower energy, but also gave higher quality material than physical activation [2]. Many factors such as type of biomass, temperature, ratio of biomass with activating reagent, and type of activating reagent influence the quality of ACs [1, 4]. The commonly used activating reagents are acids ( $H_3PO_4$ ,  $H_2SO_4$ , and  $HNO_3$ ), bases (KOH and NaOH) and salt ( $ZnCl_2$ ) [1]. Among

the activating reagent, ACs prepared by KOH and  $ZnCl_2$  showed high specific surface area [5, 6, 7].

Although ACs have been produced through  $H_3PO_4$  carbonization of *T. angustifolia*, the use of  $ZnCl_2$  and KOH as activating reagent in the production of AC has not been reported. Herein, we report the production of ACs from *T. angustifolia* through carbonization and activation with  $ZnCl_2$  and KOH under various heating temperature and ratios of activating reagent.

## II. METHODOLOGY

### 2.1 Materials

The aerial parts of *T. angustifolia* (TA) collected from Banglen, Nakorn Pathom, Thailand, was cleaned, cut into small pieces, oven dried at  $60^\circ\text{C}$  for a week and crushed by blender. The zinc chloride ( $ZnCl_2$ ) (AR grade) was purchased from QR&C. Potassium hydroxide (KOH) (AR grade) was purchased from Fluka AG. Commercial grade (ACC) and laboratory grade (ACL) of activated carbons were purchased from M&B laboratory chemical. Hydrochloric acid (HCl) (AR grade) was purchased from Supelco.

### 2.2 Production of activated carbon

#### 1. Carbonization process

The dried crushed plant materials were heated in muffle furnace at room temperature with ramping rate of  $10^\circ\text{C}/\text{min}$  to  $300$ ,  $400$  and  $500^\circ\text{C}$ , and carbonized at the required temperature for 2 hours.

#### 2. Activation process

After drying the raw materials in the oven at  $60^\circ\text{C}$  for a week,

the crushed TA materials were impregnated separately with KOH (4:1 of reagent/precursor weight ratio) and ZnCl<sub>2</sub> (2:1 and 4:1 of reagents/precursor weight ratios) and then dried in the hot air oven at 70°C for 24 hours. Each dried materials was heated in the muffle furnace at room temperature with ramping rate of 10°C/min to 300°C for 2 hours, cooled down to room temperature and rinsed with 1M HCl and DI water until pH at 7. Finally, the AC was dried in the oven at 100°C.

### 2.3 Analysis of physicochemical properties

BET analysis was used to determine the surface area, total volume porosity and mesoporosity of each prepared ACs were determined by N<sub>2</sub> adsorption/desorption analysis (BEL, Japan). Adsorption data were obtained at P/P<sub>0</sub> range 0.02-0.98. The samples were vacuum at 300°C for 2 hours. Specific surface area were calculated by BET equation. The pore volume analyzed by N<sub>2</sub> adsorption on adsorbent at relative pressure 0.99 (cross-sectional area of N<sub>2</sub> of 0.162 nm<sup>2</sup>). Mesoporous size distributions were obtained by Barrett-Joyner-Halenda (BJH) method.

Surface functional groups on ACs were used to define the interactions between adsorbent and adsorbate. The chemical characterization analyzed by ATR/FT-IR spectroscopy. The infrared transmission spectra recorded with Nicolet 6700 spectrometer in the range 3700-700 cm<sup>-1</sup> with a resolution at 16 cm<sup>-1</sup>.

Morphology and surface texture of ACs determined by SEM/EDX microscopy (JSM-IT 100).

## III. RESULTS AND DISCUSSION

ACs are adsorbent materials that have pore structure. The physicochemical properties of ACs depended on the production condition. The yields of ACs from carbonization at 300, 400, and 500°C were 45.91, 34.99 and 30.69% (Table 1), respectively. The absent of vibration around 1050 cm<sup>-1</sup> [8] in FT-IR spectra of AC carbonized at 300 (A), 400 (B), and 500°C (C) (Figure 1) indicated that hemicellulose was completely decomposed (180-270°C) [1]. Furthermore, the FT-IR spectra of AC carbonized B and C at 1450 cm<sup>-1</sup> [8] were disappeared due to the decomposed cellulose (270-400°C) [1]. The vibration of A, B and C at 1440 cm<sup>-1</sup> indicated that a small amounts of lignin [8] still presented because lignin hardly and slowly decomposed at 200-900°C [1]. The yield of ACs activated by using ZnCl<sub>2</sub>/precursor weight ratios of 4:1 and 2:1 were 20.12 and 38.72%, respectively. The higher amount of ZnCl<sub>2</sub> resulted in lower yield of AC because the more activating reagent may be increased the effectiveness of activation process [9]. The dehydration caused by ZnCl<sub>2</sub> on lignocellulosic materials was revealed by no vibration at 3300 cm<sup>-1</sup>, around 2800-2900 cm<sup>-1</sup> (H-C sp<sup>3</sup>) and 1700-1800 cm<sup>-1</sup> (C=O) in FT-IR analysis [1, 10] while very weak adsorptions at around 1580 and 1440 cm<sup>-1</sup> in the ZnCl<sub>2</sub> ACs indicated the presence of small amounts of cellulose and lignin [8]. The yield of ACs activated by using KOH/precursor weight ratios of 4:1 were 10.15%. During neutralization and rinse of acid residue by

DI water, the decomposition of raw materials were caused by high concentration of KOH. We found that the DI water residue was dark in color. FT-IR spectrum of AC prepared by activation with KOH showed weak vibration at 3300 cm<sup>-1</sup> (-OH) which might be arisen by free hydroxyl group on AC surface [11] or adsorption of water on AC [9].

TABLE I  
YIELD OF AC PRODUCED BY *T. ANGUSTIFOLIA* UNDER DIFFERENT CARBONIZATION TEMPERATURE AND ACTIVATING REAGENT: PRECURSOR RATIOS

AC	CT* (°C)	Precursor/activating reagent ratio	AT** (°C)	t (h)	Yield (%)
A	300	-	-	2	45.91
B	400	-	-	2	34.99
C	500	-	-	2	30.69
D	-	1:2 precursor/ZnCl <sub>2</sub>	300	2	38.72
E	-	1:4 precursor /ZnCl <sub>2</sub>	300	2	20.12
F	-	1:4 precursor /KOH	300	2	10.15

\*CT: Carbonization temperature, \*\*AT: Activation temperature

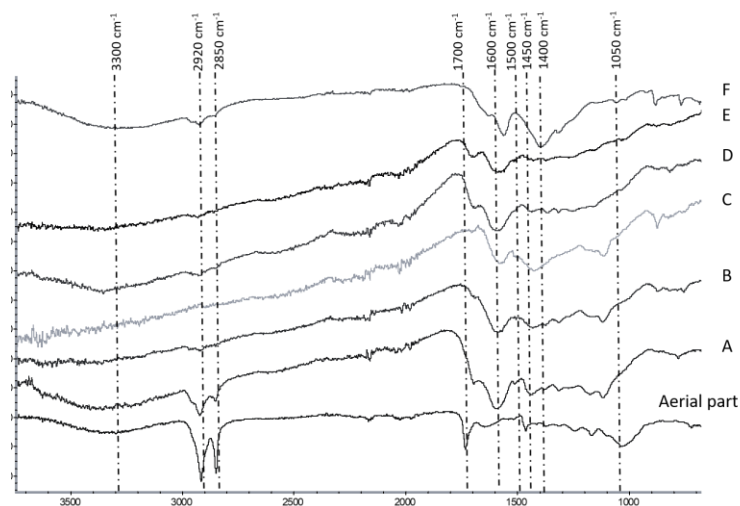
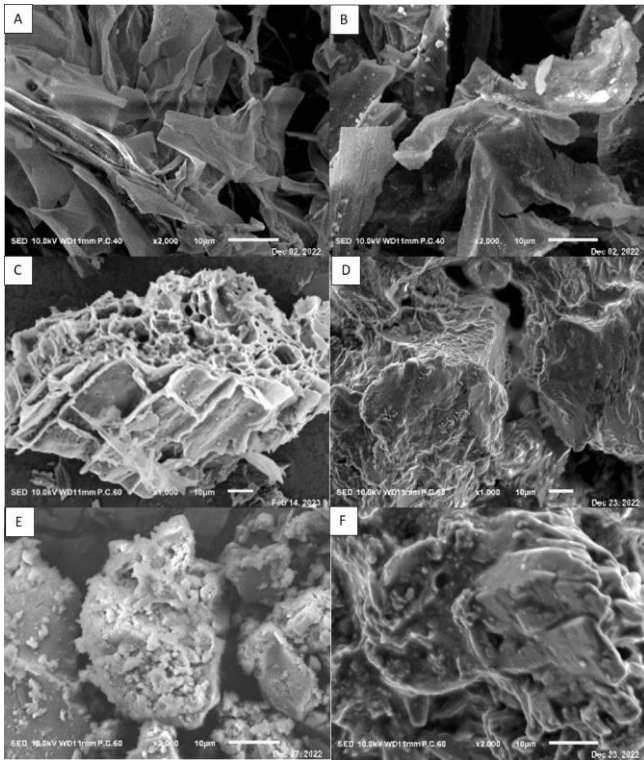


Fig 1 FT-IR spectra of activated carbons prepared by carbonization at (A) 300°C, (B) 400°C, (C) 500°C and activation at 300°C using precursor/chemical reagent weight ratios of (D) 1:2 ZnCl<sub>2</sub>, (E) 1:4 ZnCl<sub>2</sub> and (F) 1:4 KOH

SEM micrographs (Fig 2) showed that the ACs carbonized at 500°C (C) and activated with activating reagent (ZnCl<sub>2</sub> (D and E) and KOH (F)) had the cracked, rough surface and irregular pores compared with ACs carbonized at 300°C (A) and 400°C (B). It seemed that the activating reagents changed the structure and denatured the lignocellulosic of raw material to build the porous structure [1, 9]. In comparison of the surface texture between D and E, D had more cracked and rough surface than E because D was produced by using higher activating reagents which caused higher dehydration rate of lignocellulose [10].



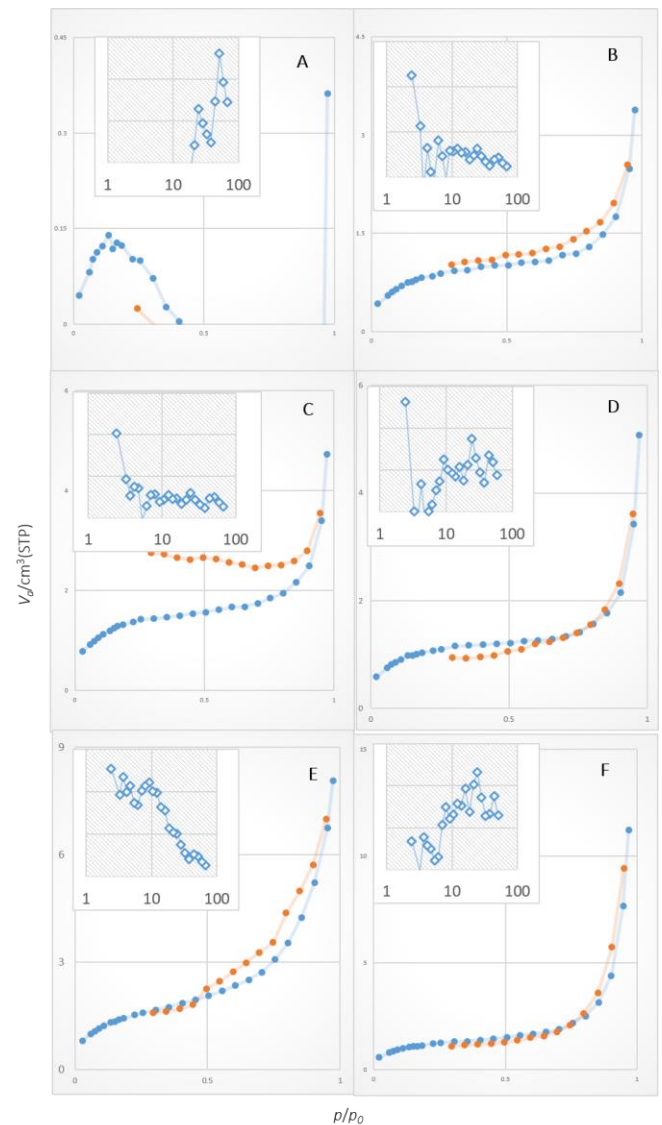
**Fig 2** SEM micrographs of activated carbons prepared by carbonization at (A) 300°C, (B) 400°C, (C) 500°C and activation at 300°C using precursor/chemical reagent weight ratios of (D) 1:2 ZnCl<sub>2</sub>, (E) 1:4 ZnCl<sub>2</sub> and (F) 1:4 KOH

The N<sub>2</sub> adsorption/desorption analysis (Fig 3) showed the isotherms at 77K for the ACs powders produced at 300, 400 and 500°C for 2 hours. There are six types of isotherm [12] depending on the nature between adsorbent and adsorbate to characterize the type of porosity [13]. In this study, isotherm of B-F ACs defined to type IV isotherm. This results showed two stages [initial part of adsorption isotherm (P/P<sub>0</sub> < 0.4) and second part of adsorption isotherm (P/P<sub>0</sub> > 0.4)] for adsorption which was defined mesoporous [13].

Mesoporous distributions were calculated by BJH method. Mean pore diameter (d<sub>p, BJH</sub>) of 2.43 nm was found in ACs carbonized at 400 (B) and 500°C (C) and ACs prepared by activation with 4:1 ZnCl<sub>2</sub>/precursor weight ratio (E) (see Table 2). Mean pore diameter (d<sub>p, BJH</sub>) of 3.28 nm was found in ACs prepared by activation with 4:1 of KOH/precursor weight ratio (F). Mean pore diameter (d<sub>p, BJH</sub>) of 24.49 nm was found in ACs prepared by activation with 2:1 of ZnCl<sub>2</sub>/precursor weight ratio (D). Most of the prepared ACs had pore size ranged in 2-50 nm which defined as mesoporous materials [12, 13].

The specific surface area (a<sub>s, BET</sub>) of ACs carbonized at 300, 400, 500°C were 0.3220, 3.0863, 4.9415 m<sup>2</sup>g<sup>-1</sup> and the total volume (V<sub>p</sub>) were 0.5589, 5.2372 and 7.3008 mm<sup>3</sup>g<sup>-1</sup>, respectively (Table 2). It was obvious that the higher temperature caused the higher decomposition of lignocellulosic contents and resulted in more moisture and volatile matter [1]. The ACs prepared by activation with 2:1 and 4:1 ZnCl<sub>2</sub>/precursor weight ratios displayed specific

surface area (a<sub>s, BET</sub>) of 4.3484 and 166.32 m<sup>2</sup>g<sup>-1</sup> and total volume (V<sub>p</sub>) of 17.318 and 168.9 mm<sup>3</sup>g<sup>-1</sup>, respectively. It revealed that the increased amount of ZnCl<sub>2</sub> in gave more dehydration, aromatization, charring, and created more pore structure of AC [10]. The specific surface area (a<sub>s, BET</sub>) and total pore volume (V<sub>p</sub>) of ACs activated by ZnCl<sub>2</sub> and KOH at the same weight ratio of 4:1 were 166.32 m<sup>2</sup>g<sup>-1</sup> and 168.9 mm<sup>3</sup>g<sup>-1</sup> (for ZnCl<sub>2</sub>) and 19.729 m<sup>2</sup>g<sup>-1</sup> and 26.122 mm<sup>3</sup>g<sup>-1</sup> (for KOH). It seems that decomposition and dehydration of lignocellulosic materials due to ZnCl<sub>2</sub> occurred at temperature lower than 500 °C. Meanwhile, the reaction of KOH with lignocellulosic materials occurred at higher temperature and lower concentration to avoid excessive denaturation of lignocellulosic materials [1].



**Fig 3** Nitrogen adsorption/desorption isotherm and pore size distribution of activated carbons prepared by carbonization at (A) 300°C, (B) 400°C, (C) 500°C and activation at 300°C using precursor/chemical reagent weight ratios of (D) 1:2 ZnCl<sub>2</sub>, (E) 1:4 ZnCl<sub>2</sub> and (F) 1:4 KOH

TABLE II  
PHYSICO-CHEMICAL PROPERTIES OF THE PREPARED AC

AC <sup>*</sup>	a <sub>s,BET</sub> (m <sup>2</sup> g <sup>-1</sup> )	V <sub>p</sub> (mm <sup>3</sup> g <sup>-1</sup> )	d <sub>p,BET</sub> (nm)	d <sub>p,BJH</sub> (nm)
A	0.3220	0.5589	6.9426	51.1
B	3.0863	5.2372	6.9426	2.43
C	4.9415	7.3008	5.9098	2.43
D	4.3484	17.318	15.93	24.49
E	166.32	168.9	4.0623	2.43
F	19.729	26.122	5.2963	3.28

<sup>\*</sup> Activated carbons prepared by carbonization at (A) 300°C, (B) 400°C, (C) 500°C and activation at 300°C using precursor/chemical reagent weight ratios of (D) 1:2 ZnCl<sub>2</sub>, (E) 1:4 ZnCl<sub>2</sub> and (F) 1:4 KOH  
<sup>\*\*</sup> a<sub>s, BET</sub>: Specific surface area, <sup>\*\*\*</sup> V<sub>p</sub>: total volume, d<sub>p,BET</sub>: Mean pore diameter (BET), d<sub>p,BJH</sub>: Mean pore diameter (BJH).

#### IV. CONCLUSION

In this work ACs could be produced by *Typha angustifolia* Linn. under carbonization at 300-500°C and activation at 300°C with ZnCl<sub>2</sub> at 2:1 and 4:1 ZnCl<sub>2</sub>/precursor weight ratio. The highest specific surface area and total pore volume were obtained by activation with 4:1 ZnCl<sub>2</sub>/precursor weight ratio at 300°C for 2 hours.

#### V. ACKNOWLEDGEMENT

We thank the Ratchadaphiseksomphot Endowment Fund of Chulalongkorn University for Research Center for Bioorganic Chemistry and the Department of Chemistry, Faculty of Science, Chulalongkorn University for financial support and instrumental facilities.

#### REFERENCES

- [1] González-García, P. Activated carbon from lignocellulosic precursors: A review of the synthesis methods, characterization techniques and applications. *Renewable and Sustainable Energy Reviews*, 82, 1393-1414, 2018
- [2] Tang, C., Shu, Y., Zhang, R., Li, X., Song, J., Li, B., Zhang, Y. and Ou, D. Comparison of the removal and adsorption mechanisms of cadmium and lead from aqueous solution by activated carbons prepared from *Typha angustifolia* and *Salix matsudana*. *Royal Society of Chemistry Advances*, 7, 16092–16103, 2017
- [3] Shu, Y., Tang, C., Hu, X., Jiang, L., Hu, X., and Zhao, Y., H<sub>3</sub>PO<sub>4</sub>-Activated cattail carbon production and application in chromium removal from aqueous solution: process optimization and removal mechanism. *Water*, 10, 2-17, 2018.
- [4] Soonmin, H. and Kabbashi, N. A. Review on activated carbon: Synthesis, properties and applications. *Journal of Engineering Trends and Technology*, 69, 124-139, 2021.
- [5] Yorgun, S., Vural, N., and Demiral, H. Preparation of high-surface area activated carbons from Paulownia wood by ZnCl<sub>2</sub> activation. *Microporous and Mesoporous Materials*, 122, 189–194, 2009.
- [6] Jin, H., Wang, X., Gu, Z., Anderson, G., and Muthukumarappan, K. Distillers dried grains with soluble (DDGS) bio-char based activated carbon for supercapacitors with organic electrolyte tetraethylammonium tetrafluoroborate. *Journal of Environmental Chemical Engineering*, 2, 1404–1409, 2014.
- [7] Caturla F., Molina-Sabio M., and Rodriguez-Reinoso F., Preparation of activated carbon by chemical activation with ZnCl<sub>2</sub>. *Carbon*, 29, 999-1007, 1991.
- [8] Galletti, R. M. A., Alessio, D. A., Licursi, D., Antonetti, C., Valentini, G., Galia, A. and Nasso, D. N. N. Midinfrared FT-IR as a tool for

- monitoring herbaceous biomass composition and its conversion to furfural. *Journal of Spectroscopy*, 1, 1-12, 2015.
- [9] Özsın, G., Kılıç, M., Apaydın-Varol, E. and Pütün, E. A. Chemically activated carbon production from agricultural waste of chickpea and its application for heavy metal adsorption: equilibrium, kinetic, and thermodynamic studies. *Applied Water Science*, 9, 1-14, 2019
  - [10] Yorgun, S., Vural, N. and Demiral, H. Preparation of high-surface area activated carbons from Paulownia wood by ZnCl<sub>2</sub> activation. *Microporous Mesoporous Materials*, 122, 189–194, 2009.
  - [11] Joshi, S. and Pokharel, B. P. Preparation and characterization of activated carbon from Lapsi (*Choerospondias axillaris*) seed stone by chemical activation with potassium hydroxide. *Journal of the Institute of Engineering*, 9, 79-88, 2013
  - [12] Kecili, R. and Hussain, M. C. Mechanism of adsorption on nanomaterials. *Nanomaterials in Chromatography*, 4, 89-115, 2018.
  - [13] Dias, A. and Ciminelli S. T. V. Analysis of nitrogen adsorption-desorption isotherms for the estimation of pore-network dimensions and structure of ferroelectric powders. *Fermelectrics*, 241, 9-16, 2000.

# The Optimal Portfolio in Semi-Static Investment with Multiple Maturity Assets by Conditional Value-at-Risk

Sirinya Nawamawat<sup>1</sup>, Walailuck Chavanasporn<sup>1</sup>, Phiraphat Sutthimat<sup>2</sup>,  
Udomsak Rakwongwan<sup>2\*</sup>

<sup>1</sup> Department of Mathematics, Faculty of Applied Science, King Mongkut's University of Technology North Bangkok, Bangkok 10800, Thailand; s6304021810028@email.kmutnb.ac.th (S.N.); walailuck.c@sci.kmutnb.ac.th (W.C.)

<sup>2</sup> Department of Mathematics, Faculty of Science, Kasetsart University, Bangkok 10900, Thailand; 6172835323@student.chula.ac.th (P.S.)

\* Correspondence: udomsak.ra@ku.th (U.R.)

**Abstract:** Finding the portfolio with the minimal risk given a required return has always been a hot topic in Financial Mathematics. In this work, we develop the semi-static model combining the buy-and-hold and dynamic strategies in standard put and call options and their underlying index, respectively. We obtain the optimal portfolio where the risk is measured by the Conditional Value-at-Risk (CVaR) in the options market. We assume that the tradable assets are a bank account, standard put and call options, and the index. The quotes come with bid-ask spreads as well as limited buy and sell quantities. To illustrate the technique, we apply the model to the S&P 500 options market. The histogram of the net payoff of the optimal portfolio obtained with out-of-sample simulations shows that the optimal portfolio has minimal probability of having the big loss in the tail, especially below the Value-at-Risk (VaR). In addition, we found that together with a buy-and-hold position in the options, allowing the dynamic trading in the index enhances the portfolio efficiency greatly.

**Index Terms**—CVaR, semi-static investment, portfolio optimization, market illiquidity

## I. INTRODUCTION

“Don’t put all your eggs in one basket” is the proverb taught from one generation to another. This old saying, in investment, encourages portfolio diversification, a risk management strategy investing in a wide variety of assets, to have a healthy growth in wealth and to minimize unexpected risk. However, as there are so many assets in financial markets, choosing the right combination is not an easy task. Moreover, there is no portfolio which works for all individuals as their risk preferences, initial financial positions, and probabilistic views of the future values of the assets are subjective [1,2]. They may also have their own investment requirements and conditions such as minimum average returns, investing constraints, or investment horizons. In Financial Mathematics, asset allocation can essentially be seen as a stochastic optimization problem where an agent chooses the portfolio which minimizes his or her risk given a required return. The problem is stochastic thanks to the fact that the future values of investing assets are random. The investment requirements and conditions can be seen as optimization constraints. Moreover, the asset allocation problem, are highly subjective in practice. Different agents give different financial positions, view risk differently, and have different

views on the future values of the underlying assets, see [3-7] for more details.

There have been numerous works on asset allocation which formulated the problem as portfolio optimizations in the past decades. However, their objective functions are different as they perceive the risk differently. Markowitz, who received the John von Neumann Theory Prize in 1989 and the Nobel Memorial Prize in Economic Sciences in 1990, measured the risk of a portfolio by the variance of its return [8]. The higher the variance, the higher the risk. Although his work was groundbreaking and has laid a solid background for portfolio optimization, the problem is quadratic and large making it non-practical. The improvement of the work in this regard was proposed by [9-12]. However, there is also another critical drawback to Markowitz’s work. Minimizing the risk measured by the variance of the return penalizes both downside and upside deviations [13].

A great deal of literature has perceived risk as the loss in the tail such as Value-at-Risk (VaR) [14-17] and Conditional Value-at-Risk (CVaR) [18-20]. However, VaR has several disadvantages compared with CVaR as it lacks smoothness, usually required for most optimization techniques, and is not a convex risk measure as opposed to CVaR [21,22]. However, most works mentioned above are based on static setting. Semi-static which combines dynamic

trading with static trading has been actively studied recently. However, most works assume that the markets are perfectly liquid; see, e.g. [23,24]. The practical semi-static hedging of exotic options under the exponential utility function was carried out [25]. To the best of our knowledge, the portfolio optimization under semi-static setting in illiquid options markets under CVaR has not yet to be studied.

In this work, we extended the model presented by Rockafeller and Uryasev [20], which is in static setting, to incorporate dynamic trading. The strategy involves buy-and-hold positions in standard put and call options while allows their underlying index and a bank account to be traded dynamically. In addition to the integration quadrature used to estimate the expectation similar to [20], we use the Galerkin method to make the problem finite-dimensional. The technique is illustrated in S&P 500 options market. The numerical results show that the optimized portfolios under CVaR have significantly small magnitude of loss in the tail. In other words, the loss at the tail of the optimized portfolios has decreased sharply especially above the VaR. In addition, it is shown that incorporating the dynamic trading of the underlying index improves the efficiency of the allocation greatly. The optimized portfolio under semi-static setting attains the lower CVaR for a given required return compared with that under static setting.

## II. RESEARCH METHODOLOGY

### A. The Market and Probabilistic View

The traded instruments are a bank account, standard put and call options and their underlying index. For simplicity, we consider the options with only two different maturities  $T_1$  and  $T_2$ . The model setup for more maturities can be done in the same manner. Assume that the options expiring at both maturities can be traded at the beginning,  $T_0$ , while the underlying index can be traded at  $T_1$  and  $T_2$ . However, at  $T_2$ , the position in the index will be dependent on that of  $T_1$  as all positions must be liquidated at the end of the investment. The bank account can be traded dynamically at any times  $T_0$ ,  $T_1$  and  $T_2$ . The interest rate is assumed to be zero. In other words, the cost of buying  $x$  units of cash is simply  $x$ . The payoff of cash in bank account is  $e^{rT}x$ . The payoffs of units of the European put and call options are  $\max\{K - S_T, 0\}x$  and  $\max\{S_T - K, 0\}x$  respectively, where  $x$  is the unit held in each asset,  $S_T$  is the value of the underlying at the maturity, and  $K$  is a strike price of an option.

The underlying index is modeled by the variance gamma process with the parameters  $\mu$ ,  $\sigma$ ,  $\nu$  and  $\theta$ , see [26, 27]. The variance gamma process is the geometric Brownian motion (GBM) process with the gamma distributed time increment. The model can describe fat tails and is more general than GBM. Moreover, the analytical form of the

distribution is readily available. Unless otherwise stated, the modeling parameter values are as in Table I. The parameters are calibrated using 10-year historical data.

TABLE I  
THE BASE PARAMETERS FOR VARIANCE GAMMA PROCESS

$\mu$	$\sigma$	$\nu$	$\theta$
0.00000001	0.1206	0.0005	0

### B. Rockafeller and Uryasev Setup for Two-Period Model

In this section, we extend the CVaR optimization model developed by Rockafeller and Uryasev [20] to incorporate the dynamic trading of the underlying of the options expiring on two different maturities.

Let  $f(x, (S_{T_1}, S_{T_2}))$  be the loss associated with the decision vector  $x$ , to be chosen from a certain subset  $X$  of  $\mathbb{R}^n$  where the price process  $S = (S_t)_{t=T_1}^{T_2}$  is modeled as an adapted stochastic process in a filtered probability space  $(\Omega, \mathcal{F}, (\mathcal{F}_t)_{t=T_1}^{T_2}, P)$ . Since  $S_{T_1}$  and  $S_{T_2}$  are random, the loss function  $f(x, (S_{T_1}, S_{T_2}))$  is also random. Let  $p(S_{T_1}, S_{T_2})$  be the probability distribution of  $S_{T_1}$  and  $S_{T_2}$ . Thus, the probability of  $f(x, (S_{T_1}, S_{T_2}))$  does not exceed  $\alpha$ , the cumulative distribution function for the loss associated with  $x$ , is given by

$$\psi(x, \alpha) = \iint_{f(x, (S_{T_1}, S_{T_2})) \leq \alpha} p(S_{T_1}, S_{T_2}) dS_{T_1} dS_{T_2} \quad (1)$$

The  $\beta$ -VaR and  $\beta$ -CVaR values for the loss random variable associated with  $x$  and a specified probability level  $\beta$  denoted by  $\alpha_\beta(x)$  and  $\phi_\beta(x)$ , respectively, can be written as

$$\alpha_\beta(x) = \min\{\alpha \in \mathbb{R} : \psi(x, \alpha) \geq \beta\} \quad (2)$$

and

$$\phi_\beta(x) = (1 - \beta)^{-1} \iint_{f(x, (S_{T_1}, S_{T_2})) \geq \alpha} f(x, (S_{T_1}, S_{T_2})) p(S_{T_1}, S_{T_2}) dS_{T_1} dS_{T_2} \quad (3)$$

Since the function as defined in (3), which is an objective function of the problem, is not convex continuous differentiable, it is difficult to apply optimization techniques to find the solution. To tackle this, we define the new function,  $F_\beta$  on  $x \times \mathbb{R}$ , which will be a key point in solving the optimization problem as

$$F_\beta(x, \alpha) = \alpha + (1 - \beta)^{-1} \iint_{S_{T_1}, S_{T_2} \in \mathbb{R}} [f(x, (S_{T_1}, S_{T_2})) - \alpha]^+ p(S_{T_1}, S_{T_2}) dS_{T_1} dS_{T_2} \quad (4)$$

where

$$[t]^+ = \begin{cases} t & \text{when } t > 0, \\ 0 & \text{when } t \leq 0. \end{cases}$$

**Theorem 1:** As a function of  $\alpha$ ,  $F_\beta(x, \alpha)$  is convex and continuously differentiable. The  $\beta$ -CvaR of the loss associated with any  $x \in X$  can be determined from the formula

$$\phi_\beta(x) = \min_{\alpha \in \mathbb{R}} F_\beta(x, \alpha) \quad (5)$$

and moreover

$$\alpha_\beta(x) \in \arg \min_{\alpha \in \mathbb{R}} F_\beta(x, \alpha_\beta(x)) \text{ and } \phi_\beta(x) = F_\beta(x, \alpha_\beta(x)). \quad (6)$$

**Theorem 2:** Minimizing the  $\beta$ -CvaR of the losses associated with  $x$  overall  $x \in X$  is equivalent to minimizing  $F_\beta(x, \alpha)$  over all  $(x, \alpha)$ , that is

$$\min_{x \in X} \phi_\beta(x) = \min_{(x, \alpha) \in X \times \mathbb{R}} F_\beta(x, \alpha). \quad (7)$$

Theorem 2 is the main technique proposed by [20] for CVaR optimization. The minimization of the original objective function which is not a convex and continuously differentiable function can be done through the minimization of the newly defined  $F_\beta(x, \alpha)$ : see, [28].

By using Monte Carlo technique to approximate the integral term in (4),  $F_\beta(x, \alpha)$  can be approximated by

$$\tilde{F}_\beta(x, \alpha) = \alpha + \frac{1}{q(1-\beta)} \sum_{b=1}^q [f(x, (S_{T_1}^b, S_{T_2}^b)) - \alpha]^+. \quad (8)$$

Let  $u_k = [f(x, (S_{T_1}^b, S_{T_2}^b)) - \alpha]^+$ . We can write down the CVaR optimization problem as a linear optimization problem

$$\tilde{F}_\beta(x, \alpha) = \alpha + \frac{1}{q(1-\beta)} \sum_{k=1}^q u_k, \quad (9)$$

where setting  $u_k$  for  $k = 1, \dots, q$  is the term of auxiliary real variables.

### C. The Loss Function

Assume that there are  $N$  and  $M$  options expiring at  $T_1$  and  $T_2$  respectively. The portfolio  $X$  can be expressed as

$$X = [X_0 \ X_1^1 \ X_1^2 \ \dots \ X_1^N \ X_2^1 \ X_2^2 \ \dots \ X_2^M \ X_1(S_{T_1})],$$

where  $X_0$  is weight of initial wealth invested in cash,  $X_1^i$  for  $i = 1, 2, \dots, N$  and  $X_2^j$  for  $j = 1, 2, \dots, M$  are the weights of the initial wealth invested in the options with maturity  $T_1$  and  $T_2$  respectively, and  $X_1(S_{T_1})$  is the unit invested in the underlying at  $T_1$  which is the function of the underlying value at  $T_1$ .

The loss associated  $X$ , which is a negative of the return, can then be expressed as

$$f(x, (S_{T_1}, S_{T_2})) = - \left[ P_0 X_0 + \sum_{i=1}^N P_1^i(S_{T_1}) X_1^i + \sum_{j=1}^M P_2^j(S_{T_2}) X_2^j + \frac{S_{T_2} - S_{T_1}}{W} X_1(S_{T_1}) \right],$$

where  $P_0$  is return of a bank account,  $P_1^i$  for  $i = 1, \dots, N$  and  $P_2^j$  for  $j = 1, \dots, M$  are the returns of the options with maturities  $T_1$  and  $T_2$  respectively, and  $W$  is the initial wealth.

It can be seen that the optimization problem is infinite-dimensional as  $X_1(S_{T_1})$  is an infinite-dimensional function. We employ the Galerkin method to reduce the problem to the finite dimensional convex optimization problem [25] by estimating the function  $X_1(S_{T_1})$  using a step function as

$$X_1(S_{T_1}) = \sum_{h=0}^{N_s} a_j \mathbf{1}_{(k_h, k_{h+1})}(S_{T_1}),$$

where  $N_s$  is the number of strikes of the options at time  $s$ ,  $k_h$  are the strikes of the options available at time  $s$  while  $k_0 = 0$  and  $k_{N_s+1} = +\infty$ .

Hence, the loss associated with the portfolio becomes

$$f(x, (S_{T_1}, S_{T_2})) = - \left[ P_0 X_0 + \sum_{i=1}^N P_1^i(S_{T_1}) X_1^i + \sum_{j=1}^M P_2^j(S_{T_2}) X_2^j + \frac{S_{T_2} - S_{T_1}}{W} \sum_{h=0}^{N_s} a_j \mathbf{1}_{(k_h, k_{h+1})}(S_{T_1}) \right].$$

Hence, instead if minimizing the function  $F_\beta(x, \alpha)$  over  $x \times \mathbb{R}$  as (8), one can work with the following linear optimization problem,

$$\min \alpha + \frac{1}{q(1-\beta)} \sum_{k=1}^q u_k$$

subject to

$$X_0 + \sum_{i=1}^N X_1^i + \sum_{j=1}^M X_2^j = 1,$$

$$u_k \geq 0,$$

$$\begin{aligned} & \left[ P_0 X_0 + \sum_{i=1}^N P_1^i(S_{T_1}) X_1^i + \sum_{j=1}^M P_2^j(S_{T_2}) X_2^j + \frac{S_{T_2} - S_{T_1}}{W} \sum_{h=0}^{N_s} a_j \mathbf{1}_{(k_h, k_{h+1})}(S_{T_1}) \right] \geq r, \\ & \left[ P_0 X_0 + \sum_{i=1}^N P_1^i(S_{T_1}) X_1^i + \sum_{j=1}^M P_2^j(S_{T_2}) X_2^j + \frac{S_{T_2} - S_{T_1}}{W} \left[ \sum_{j=0}^{N_s} a_j \mathbf{1}_{(k_h, k_{h+1})}(S_{T_1}) \right] + \alpha + u_k \right] \geq 0. \end{aligned}$$

### III. RESULTS AND DISCUSSION

To illustrate the technique, we consider 100 put and call options written on S&P 500 index. Table 2 gives an example of the quotes of the options available on 10 January 2021 with maturities 19 February 2021 and 19 March 2021 extracted from Interactive Broker. The spot was \$3,768.25 at the time. It can be seen that the prices come with bid and ask spreads and there are limited quantities one can take in each option. The prices shown in Table II are per option, while the quantities are in terms of contracts. One contract is equivalent to 100 options. For example, the first row of Table II means there is a put option with strike price \$3,770 expiring on 19 February 2021 whose cost of selling and buying are \$92.8 and \$93.8 per option respectively. There are 32 contracts (3,200 options) available for selling, and only 11 contracts (1,100 options) are available for buying. Unless otherwise stated, we assume that the initial wealth is \$10,000 and the required average return is 10%.

TABLE II  
MARKET QUOTES FOR CALL AND PUT OPTIONS

Ticker	Bid	Ask	Bid size	Ask size
SPX US 021921 P3770	92.8	93.8	32	11
SPX US 021921 C3770	71.4	74.9	38	23
SPX US 031921 P3795	112.7	113.6	25	40
SPX US 031921 C3795	122.6	123.6	24	64

#### A. Optimized Portfolio

Fig. 1-3 show the quantities of the options expiring at  $T_1$ , the options expiring at  $T_2$ , and the underlying as a function of its value at  $T_1$  of the optimized portfolio under CVaR with 99.5% confidence level for the required return of 10%. The positions of the options shown in Fig. 1-2 are taken at  $T_0$  and hold until  $T_2$ . For the put options, the model suggests shorting at the strike \$3,625 and taking the long positions at higher strikes for both maturities. However, the positions on the call options are long only for maturity  $T_1$  and short only for maturity  $T_2$ .

At  $T_1$ , to obtain the minimal risk, the user needs to adjust the portfolio by taking position in the underlying as in Fig. 3. The quantity the user takes in the underlying depends on its value at  $T_1$ . If the index value at  $T_1$  is less than \$3,600, it is more optimal not to invest in the index. However, if the index value at  $T_1$  is higher than about \$3,800, then it will be better to buy around 6.5 unites of the index.

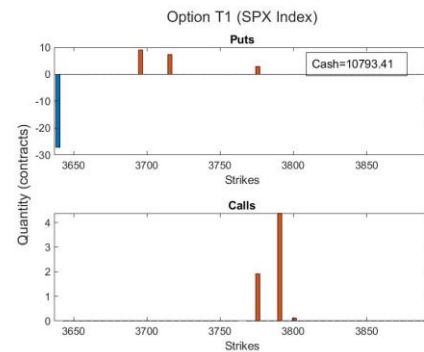


Fig. 1. The semi-static optimal quantities of the options maturing at  $T_1$

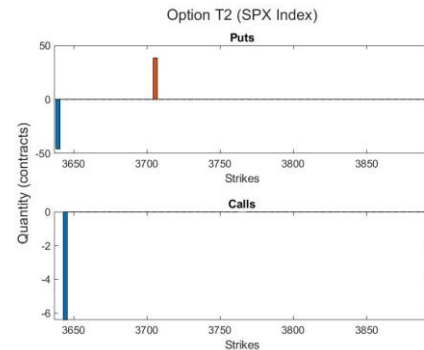


Fig. 2. The semi-static optimal quantities of the options maturing at  $T_2$

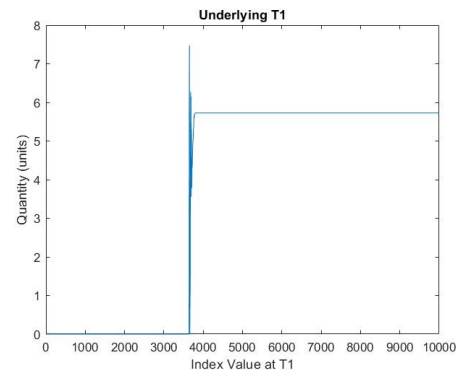


Fig. 3. The optimal quantity of underlying

The mean, standard deviation, VaR, and CVaR of the optimized portfolio is given in Table III. It is worth noting that the mean of the portfolio is \$998.00 which is equivalent to approximately 10% of return as the initial wealth is \$10,000.

TABLE III  
THE DETAILS OF THE PORTFOLIO FOR SEMI-STATIC INVESTMENT

Mean	SD	VaR	CVaR
998.00	1734.30	209.8857	390.0509

Fig. 4 shows the histogram of the net payoff of the optimized portfolio obtained with 10,000 out-of-sample simulations. We can see that the optimal portfolio has significantly small magnitude of loss in the tail. In other



words, the probability of losing money falls sharply at the left tail. This is not surprising as the model is supposed to give the portfolio with the minimum CVaR, the average loss at the tail.

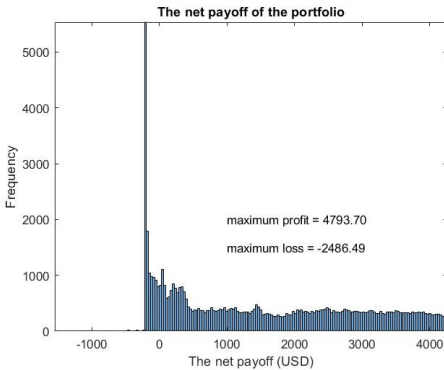


Fig. 4. The net payoff of the semi-static portfolio obtained with required return 10% and 99.5% confidence level

Taking a closer look at Fig. 4 (as shown in Fig. 5), we noticed that value where the probability of losing money falls sharply is roughly the same as the portfolio VaR, which is \$209.89. This is due to the fact that we are minimizing the portfolio CVaR, which is the average loss below VaR. Hence, the sharp fall in probability of losing money more than VaR is expected.

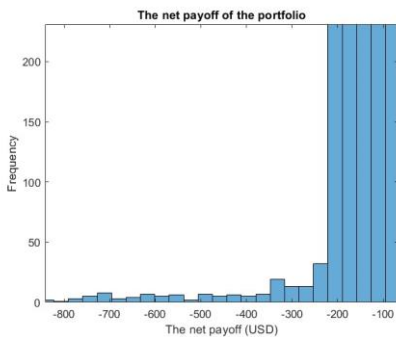


Fig. 5. The closer look of Fig. 4.

To investigate this further, we compare the histogram of the zoom-in of the net payoff of the portfolio obtained with required return 10% for the confidence level 99.5% with other lower confidence levels. It is shown that, similarly to Fig. 5, the net probability of loss of lower confidence level portfolio also falls sharply. However, it falls at the lower value compared with the 99.5% confidence level portfolio.

Moreover, the results in Fig. 6 confirm that the higher the confidence level value, the higher optimal CVaR. This is expected because having a higher  $\beta$  level means an agent is less sensitive to the risk. The agent is happy with the portfolio which has a small risk at the very end of the left tail. In contrast, an agent who is more risk averse, he or she will use a smaller  $\beta$  level as the average of the loss above  $\beta$  level will all be perceived as a risk.

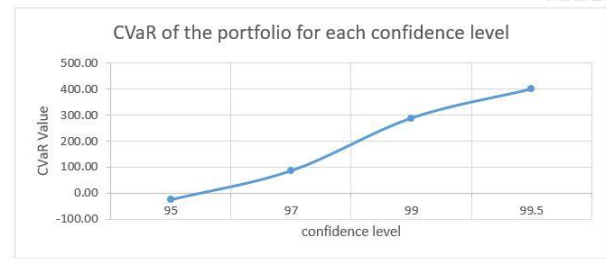


Fig. 6. CVaR value of the optimized portfolio with required return 10% as a function of a confidence level

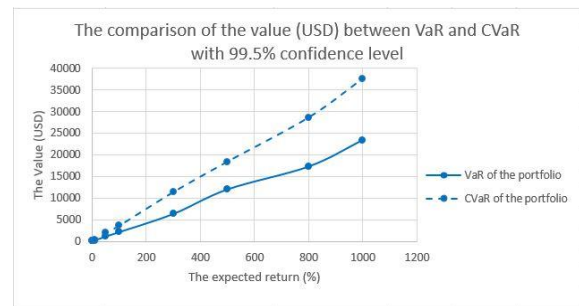


Fig. 7. VaR (line) and CVaR (dash) of the optimized portfolios with 99.5% confidence level as functions of required expected return

Fig. 7 plots the VaR and CVaR of the optimized portfolio as a function of the required expected return. The fact that value of CVaR is always higher than VaR is clear from the definitions as CVaR is the average loss below VaR. However, we can observe that the difference between the two is higher as the required expected return is higher.

We can see that the higher the expected return, the higher the VaR and CVaR. As VaR and CVaR are perceived as risk, this result supports the saying “high risk, high return” which is a very well-known investment mantra.

### B. The Comparison with Static Optimization

To investigate the effect of the dynamic trading in semi-static optimization, we find the optimized portfolio where the only tradable assets are the bank account and the options, and the trading strategy is buy-and-hold. Fig. 8-9 show the structure of the optimized portfolio consisting of the options expiring at  $T_1$  and  $T_2$ , respectively.

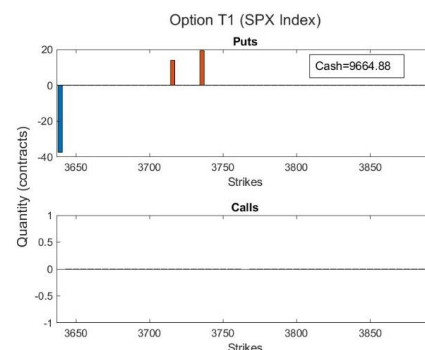


Fig. 8. The static optimal quantities of the options maturing at  $T_1$

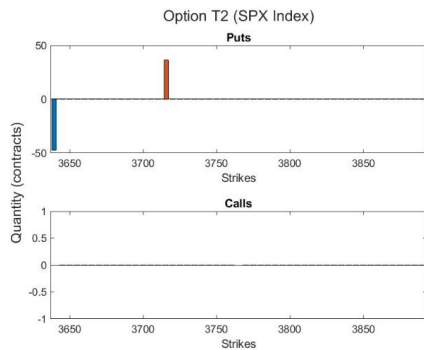


Fig. 9. The static optimal quantities of the options maturing at  $T_2$

It is noticeable that the optimal portfolios of semi-static investment (Fig. 1-2) and of static investment (Fig. 8-9) are different. Under static setting, optimal portfolio does not consist of call options in the trading strategy.

The mean, the standard deviation, the 99.5% VaR, and the 99.5% CVaR of the optimal portfolio of static investment obtained with required return 10% are shown in the Table IV.

TABLE IV

THE DETAILS OF THE PORTFOLIO FOR STATIC INVESTMENT

Mean	SD	VaR	CVaR
1000.00	1741.20	349.9170	485.2057

Compared with those obtained under the semi-static setting, as shown in Table V, the VaR and CVaR for the static setting are much higher. This shows the benefit of incorporating the dynamic part in the static setting. With the same investment conditions, e.g., the required return 10% and 99.5% confidence level, optimized portfolio under semi-static setting has smaller risk.

TABLE V

THE COMPARISON OF THE OPTIMAL PORTFOLIO BETWEEN SEMI-STATIC AND STATIC SETTINGS

Investment	Mean	SD	VaR	CVaR
semi-static	998.00	1734.30	209.8857	390.0509
static	1000.00	1741.20	349.9170	485.2057

Fig. 10 shows the comparison of the optimal CVaRs for different required expected returns obtained under semi-static and static settings. The optimal CVaR obtained under the semi-static setting is lower than that under the static setting. Moreover, the semi-static performs increasing better as the required return increases.

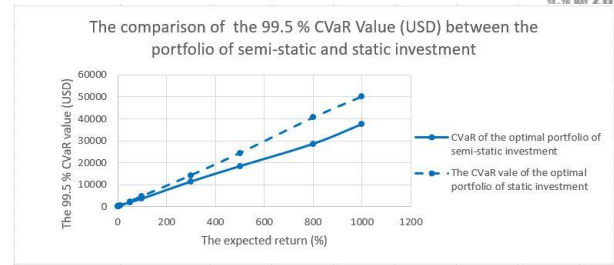


Fig. 10. The comparison of the CVaR value of the portfolio for each required return with 99.5% confidence level between static investment (dash) and semi-static (line) investment

#### IV. CONCLUSION

In this paper, we study semi-static optimal investment with multiple maturity assets under CVaR. The problem is formulated to a mathematical model and numerically solved by utilizing Monte Carlo method, linear programming, and Galerkin method.

We apply the technique to the S&P 500 options market in which the tradable assets are a bank account, standard call and put options, and the index. We found that the portfolio obtained under CVaR risk measure has low probability of losing money at the tail, especially at VaR where we notice the sharp decreasing in the probability. Moreover, the optimal CVaR increases as the required expected return increases.

We also show that by incorporating the dynamic trading of the index in the strategy, the efficiency of the optimized portfolio is enhanced significantly especially for a higher required return.

The application of the model in the S&P 500 options here is just an example. The scheme can also be easily applied in any derivative market. An agent just needs to change the data and the probabilistic model corresponding to his or her belief in that market. The rest would stay the same. The possible extension of the work is to consider derivatives in multiple markets such as options in the S&P 500 market and VIX market. The challenge is to come up with a joint realistic probabilistic process to model the two random factors. Further work will be aimed to consider the portfolio with  $n$  period time and setup the model for more maturities which is more realistic. In addition, we can setup the model for trading at any time.

#### ACKNOWLEDGMENT

The authors are grateful to the editors and anonymous reviewers for all of their valuable comments and suggestions, which have substantially improved the quality of this work. The authors are also grateful to the Development and Promotion of Science and Technology Talents Project (DPST) for the financial support. And I would like to thank Graduate College of King Mongkut's University of Technology North Bangkok for providing a grant support my study.

## REFERENCES

- [1] T. Pennanen, "Introduction to convex optimization in financial markets", *Mathematical programming*, 134(1):157-186, 2012
- [2] T. Pennanen, "Optimal investment and contingent claim valuation in illiquid markets", *Finance and Stochastics*, 18(4):733-754, 2014
- [3] R. Boonklurb, A. Duangpan, U. Rakwongwan, P. Sutthimat, "A novel analytical formula for the discounted moments of the ECIR process and interest rate swaps pricing", *Fractal and Fractional*, 6(2), 58, 2002
- [4] K. Chumpong, K. Mekchay, N. Thamrongrat, "A simple closed-form formula for the conditional moments of the Ornstein-Uhlenbeck process", *Songklanakarinn Journal of Science and Technology*, 43(2):1-6, 2002
- [5] P. Nonsoong, K. Mekchay, S. Rujivan, "An analytical option pricing formula for mean-reverting asset with time-dependent parameter", *The ANZIAM Journal*, 63(2):178-202, 2021
- [6] F. Nualsri and K. Mekchay, "Analytically pricing formula for contingent claim with polynomial payoff under ECIR process", *Symmetry*, 14(5), 933, 2022
- [7] P. Sutthimat and K Mekchay, "Closed-form formulas for conditional moments of inhomogeneous Pearson diffusion processes", *Communications in Nonlinear Science and Numerical Simulation*, 106(106095), 2022
- [8] H. Markowitz, "Portfolio selection", *Journal of Finance*, 7(1):77-91, 1952
- [9] H. Konno and H. Yamazaki, "Mean-absolute deviation portfolio optimization model and its applications to Tokyo stock market", *Management Science*, 37(5):519-531, 1991
- [10] W.F. Sharpe, "A linear programming algorithm for mutual fund portfolio selection", *Management Science*, 13(7):499-510, 1967
- [11] W.F. Sharpe, "A linear programming approximation for the general portfolio analysis problem", *Journal of Financial and Quantitative Analysis*, 6(5):1263-1275, 1971
- [12] B.K. Stone, "A linear programming formulation of the general portfolio selection problem", *Journal of Financial and Quantitative Analysis*, 8(4):621-636, 1973
- [13] A.A. Karacabey, "Risk and investment opportunities in portfolio optimization", *European Journal of Finance and Banking Research*, 1(1):1-15, 2007
- [14] A.A. Gaivoronski and G. Pflug, "Value-at-risk in portfolio optimization: properties and computational approach", *Journal of Risk*, 7(2):1-31, 2005
- [15] R.S. Hiller, J. Eckstein, "Stochastic dedication: Designing fixed income portfolios using massively parallel Benders decomposition", *Management Science*, 39(11):1422-1438, 1993
- [16] A.V. Puelz, "Value-at-risk based portfolio optimization. In *Stochastic optimization: Algorithms and applications*", Springer, Boston, MA. pp.279-302, 2001
- [17] M.R. Young, "A minimax portfolio selection rule with linear programming solution", *Management science*, 44(5):673-683, 1998
- [18] P. Krokmal, J. Palmquist, S. Uryasev, "Portfolio optimization with conditional value-at-risk objective and constraints", *Journal of Risk*. 4:43-68, 2002
- [19] R.T. Rockafellar and S. Uryasev, "Optimization of conditional value-at-risk", *Journal of Risk*, 2(3):21-42, 2000
- [20] R.T. Rockafellar and S. Uryasev, "Conditional value-at-risk for general loss distributions", *Journal of Banking & Finance*, 26(7):1443-1471, 2002
- [21] S. Basak and A. Shapiro, "Value-at-risk-based risk management: optimal policies and asset prices", *The Review of Financial Studies*. 14(2):371-405, 2001
- [22] G.C. Pflug, "Some remarks on the value-at-risk and the conditional value-at-risk in Probabilistic constrained optimization", Boston: Springer Science, 2000
- [23] A. Ilhan, M. Jonsson, R. Sircar, "Optimal static-dynamic hedges for exotic options under convex risk measures. *Stochastic Processes and their Applications*", 119(10):3608-3632, 2009
- [24] A. Ilhan and R. Sircar, "Optimal static-dynamic hedges for barrier options", *Mathematical Finance: An International Journal of Mathematics, Statistics and Financial Economics*. 16(2): 359-385, 2006
- [25] T. Pennanen and U. Rakwongwan, "Optimal semi-static hedging in illiquid markets", arXiv preprint arXiv: 2008.01463. 2020.
- [26] D.B. Madan, P.P. Carr, E.C. Chang, "The variance gamma process and option pricing", *Review of Finance*, 2(1):79-105, 1998
- [27] D.B. Madan and E. Seneta, "The variance gamma (vg) model for share market returns", *Journal of Business*, 63(4):511-524, 1990
- [28] A. Shapiro and Y. Wardi, "Nondifferentiability of the steady-state function in discrete event dynamic systems", *IEEE Transactions on Automatic Control*, 39(8):1707-1711, 1994

# Isolation of gamma oryzanol through chromatographic and precipitation techniques

Muhammad Waqar Nasir<sup>1</sup>, Surachai Pornpakakul<sup>2\*</sup>

<sup>1</sup> Research Center for Bio-Organic Chemistry, Department of Chemistry, Faculty of Science, Chulalongkorn University, Bangkok, Thailand.

<sup>2</sup> Research Center for Bio-Organic Chemistry, Department of Chemistry, Faculty of Science, Chulalongkorn University, Bangkok, Thailand.  
Surachai.p@chula.ac.th

**Abstract:** Rice Bran Acid Fraction (RBAF) is a by-product of the rice bran oil refining process, and it contains  $\gamma$ -oryzanol. The primary goal of this research was to isolate and purify  $\gamma$ -oryzanol using chromatographic and precipitation methods. Using chromatographic techniques eluting with hexane to ethyl acetate mixture as the appropriate eluent about 80% of  $\gamma$ -oryzanol was obtained for further purification. The repeated precipitation process afforded  $\gamma$ -oryzanol product with 95% purity in 0.2% weight by weight of RBAF. By using chromatographic and precipitation method at least twice, a high purity  $\gamma$ -oryzanol product could be obtained from RBAF.

Keywords: Rice Bran Acid Fraction,  $\gamma$ -oryzanol, Chromatographic and precipitation method, Purification.

## I. INTRODUCTION

Rice bran oil (RBO) is a rich source of dietary minor elements, such as  $\gamma$ -oryzanol, tocopherols, tocotrienols, phytosterols, and polyphenols.<sup>1</sup> It is one of the three high-valued edible vegetable oils that the World Health Organization recommends.<sup>2</sup> These inconsequential ingredients made edible oil have a greater physiological activity.<sup>3</sup> Among these tocopherols and tocotrienols (0.15-0.2%),  $\gamma$ -oryzanols (1.2-1.8%), and phytosterols (1.5-2%) in RBO endowed the edible oil with excellent strong antioxidant and anticancer properties as well as the ability to lower serum cholesterol levels.<sup>4</sup> It also slows the pathogenesis of neurological disorders, cancer, inflammation, and cardiovascular illnesses by preventing lipid peroxidation.<sup>5</sup> Vitamin E (tocotrienols and tocopherols) exhibit antioxidant activity when combined mutually among with  $\gamma$ -oryzanol, the mixture should have the same biological activity.<sup>6,7</sup>  $\gamma$ -oryzanol is made up of caffeic acid and ferulic acid esters of phytosterols (campesterol, sitosterol, and stigmasterol) and of triterpene alcohols (cycloartenol and 24-methylenecycloartenol).<sup>8</sup> Since one of the most potent antioxidants in nature is  $\gamma$ -oryzanol, many researcher have developed the process for isolation and purification using semi-preparative chromatography<sup>9</sup> method, SPE sorbents coupled with UHPLC-MS/MS analysis<sup>10</sup>, high speed countercurrent chromatography method<sup>11</sup>, and some other various method affecting the isolation recoveries<sup>12</sup>. The objective of this study was to isolate the  $\gamma$ -oryzanol with a more efficient and cost-effective method through chromatographic and precipitation techniques. Our method could improve the

scalability of its production, making it more accessible for commercial use.

## II. METHODOLOGY

### 2.1 Materials

Rice bran acid fraction (RBAF) was obtained from the Thai Edible Oil Co. Ltd., Samutprakarn, Thailand. Commercial hexane, and ethyl acetate were purchased from LABSOLV Co. Ltd, Bangkok, Thailand and distilled prior to used. Thin Layer Chromatography silica gel 60 F<sub>254</sub> Aluminium sheets and Silica Gel 60 (0.040-0.063 mm) for column chromatography were purchased from Merck KGaA, 64271 Darmstadt Germany.

### 2.2 Isolation of $\gamma$ -oryzanol

RBAF (53 g) was subjected to silica gel column chromatography (310 g of silica gel in column with 13 cm diameter and 16 cm length), eluting with hexane, hexane-ethyl acetate (20:1, 15:1, 10:1, and 5:1) and ethyl acetate in stepwise fashion. The  $\gamma$ -oryzanol in each collected fraction was monitored by TLC analysis and similar fractions were combined. After evaporation of the solvent, the residue was dissolved with ethyl acetate and  $\gamma$ -oryzanol was precipitated by adding hexane dropwise. The precipitated solids were filtered through filter paper and purity of  $\gamma$ -oryzanol of the precipitation product was analyzed by TLC and <sup>1</sup>H NMR. Repeated precipitation was used to ensure that the pure  $\gamma$ -oryzanol was obtained.

### 2.3 <sup>1</sup>H NMR analysis

NMR spectroscopic data was recorded on 500 MHz Bruker AVANCE spectrometer at 298 K. All the spectra were referenced to the solvent residue at  $\delta_H$  7.26 ppm (for CDCl<sub>3</sub>). The MestreNova 14.2 software was used to process the spectra. In NMR analysis the sample solutions were

prepared by dissolving 12 mg of sample in 0.6 mL of deuterated chloroform- $\text{CDCl}_3$  (99.8%).

### 2.4 Calculation of % purity of $\gamma$ -oryzanol

The NMR analysis was used to confirm the existence of  $\gamma$ -oryzanol in the product. The % yield of  $\gamma$ -oryzanol product and % purity of  $\gamma$ -oryzanol were calculated according to Eq.1 and Eq.2 as follows:

% yield of  $\gamma$ -oryzanol product =

$$\frac{\text{Amount of } \gamma\text{-oryzanol product from precipitate (mg)}}{\text{Amount of RBAF (mg)}} \times 100$$

Eq. (1)

$$\% \text{ purity of } \gamma\text{-oryzanol} = \frac{I_\gamma/3}{\frac{I_\gamma}{3} + I_\alpha} \times 100 \quad \text{Eq. (2)}$$

Whereas  $I_\gamma$  is integral of the methoxy protons of  $\gamma$ -oryzanol ( $\delta_{\text{H}}$  3.94, 3.91 and 3.97 ppm) and  $I_\alpha$  is integral of triplet signal for  $\alpha$ -proton of the fatty acid moiety ( $\delta_{\text{H}}$  2.33 ppm). To calculate the purity of  $\gamma$ -oryzanol through NMR analysis.

### III. RESULTS AND DISCUSSION

$^1\text{H}$  NMR spectrum of the crude rice bran acid fraction (Fig 1), showed weak aromatic proton signals at  $\delta_{\text{H}}$  7.58, 7.04, 7.02 and 6.9 ppm and two methoxy signals ( $\delta_{\text{H}}$  3.92 and 3.91 ppm) of the ferulate moiety in structure of  $\gamma$ -oryzanol, and  $\alpha$ -proton signals ( $\delta_{\text{H}}$  2.33 ppm) of free fatty acid (FFA) as major component. In comparison of integral of the methoxy signals and  $\alpha$ -proton of fatty acyl moiety, purity of  $\gamma$ -oryzanol was calculated according to Eq.2.

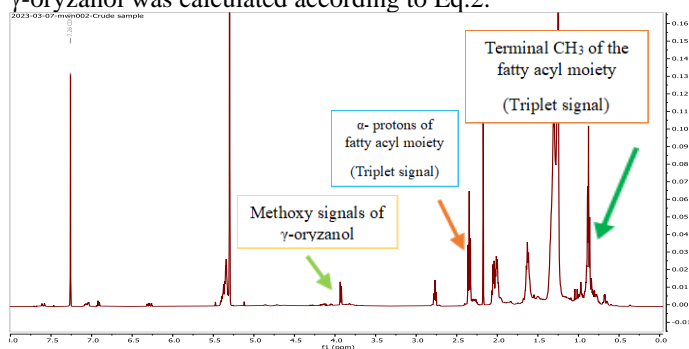


Fig 1:  $^1\text{H}$  NMR of Crude Oil.

During the column chromatographic isolation, 10 fractions were collected from elution with 15:1 ratio of hexane and ethyl acetate. The fractions containing  $\gamma$ -oryzanol were combined by TLC monitoring. According to TLC and  $^1\text{H}$  NMR analysis, the combined fractions 7 and 8 contained about (29%) of  $\gamma$ -oryzanol and free fatty acids as a main component (see Fig 2). Further purification of the combined fractions 7 and 8 through precipitation as above described gave  $\gamma$ -oryzanol product as a solid after precipitation twice (see Fig 3).  $^1\text{H}$  NMR of solid phase after twice precipitation in (Fig 3) showed three methoxy proton signals at  $\delta_{\text{H}}$  3.97

(s), 3.94 (s) and 3.91 (s), cycloartenol signals at  $\delta_{\text{H}}$  0.60 (1H, d,  $J = 4.2$  Hz, H-19), 0.36 (1H, d,  $J = 4.1$  Hz, H-19) and ferulate signals at  $\delta_{\text{H}}$  6.30 (1H, dd,  $J = 16, 2.4$  Hz, H-3'), 6.91 (1H, d,  $J = 8.2$  Hz, H-8'), 7.04 (1H, d,  $J = 1.8$  Hz, H-5'), 7.09 (1H, dd,  $J = 8$  and 1.8 Hz, H-9'), and 7.60 (1H, d,  $J = 16$  Hz, H-2'), while  $\gamma$ -oryzanol (about 28%), free fatty acid (FFA), monoacylglycerol, squalene, and phytosterols were left in the mother liquor (see Fig 4).  $^1\text{H}$  NMR of mother liquor after precipitation twice (Fig 4) showed the  $\alpha$ -proton of fatty acyl signal at  $\delta_{\text{H}}$  2.34 (2H, t,  $J = 7.5$  Hz,  $\alpha$ -H<sub>2</sub>), and terminal  $\text{CH}_3$  of the fatty acyl moiety at 0.90-0.86 (3H, m) and allylic protons  $\delta_{\text{H}}$  (2.77 t,  $J = 7.0$  Hz). The precipitated product (solid and the mother liquor) was precipitated repeatedly to afford the final  $\gamma$ -oryzanol product (95% purity) in 0.2% weight by weight of RBAF.

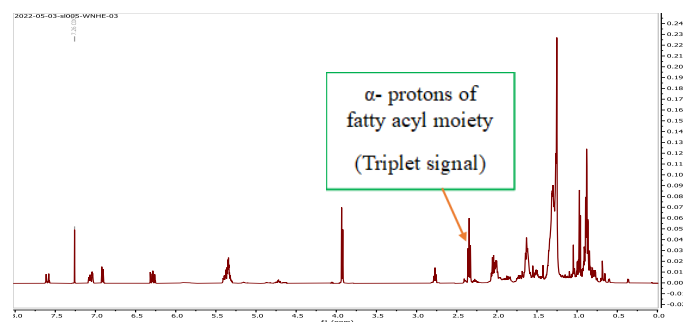


Fig 2:  $^1\text{H}$  NMR of combined fraction before precipitation method.

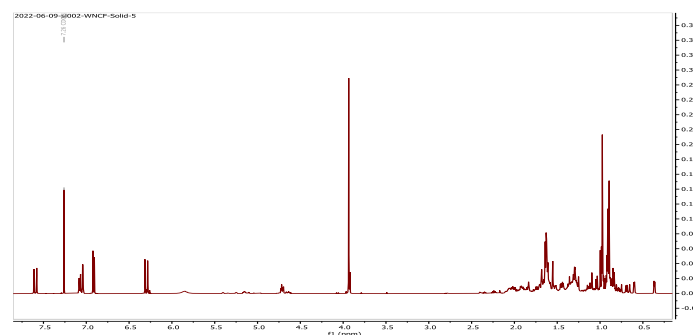


Fig 3:  $^1\text{H}$  NMR of solid phase after two precipitation steps

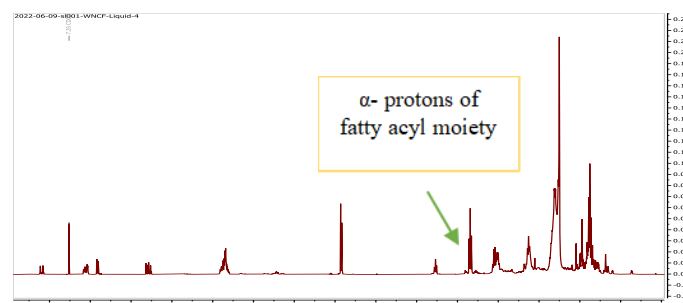


Fig 4:  $^1\text{H}$  NMR of the mother liquor after two precipitation steps

500 MHz  $^1\text{H}$  NMR of the final  $\gamma$ -oryzanol in  $\text{CDCl}_3$  (Fig 5):  $\delta_{\text{H}}$  7.60 (1H, d,  $J = 16$  Hz, H-2'), 7.09 (1H, dd,  $J = 2$  Hz, H-9'), 7.04 (1H, d,  $J = 2$  Hz, H-5'), 6.91 (1H, d,  $J = 8$  Hz, H-8'), 6.30 (1H, d,  $J = 16$  Hz, H-2'), 4.72 (s), 4.70 (1H, d,  $J = 4.6$  Hz, H-3), 3.97 (3H, s, OMe), 3.94 (3H, s, OMe), 3.92 (3H, s, OMe), 0.60 (1H, d,  $J = 4.2$  Hz, H-19) and 0.36 (1H, d,  $J = 4.1$  Hz, H-19). For the three methoxy protons at  $\delta_{\text{H}}$

3.97, 3.94 and 3.91 ppm, the signal at  $\delta_H$  3.94 ppm was the strongest signal as compared to another methoxy protons at  $\delta_H$  3.97 and 3.91 ppm as shown in Fig 5. It seemed that one of the 19 structures of  $\gamma$ -oryzanol was predominant after this precipitation method.

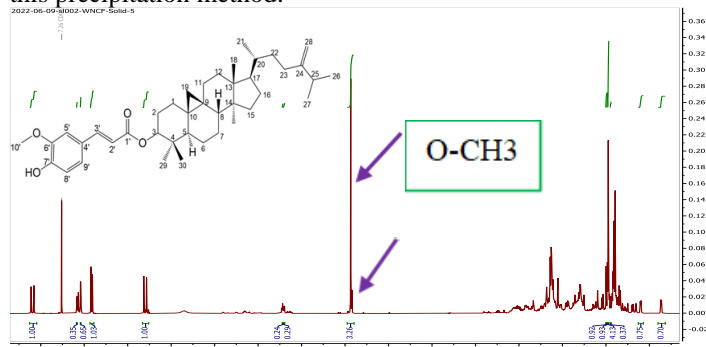


Fig 5: <sup>1</sup>H NMR spectrum of the final gamma-oryzanol product

#### IV. CONCLUSION

This study demonstrated that high purity  $\gamma$ -oryzanol (> 95%) could be isolated from RBAF through chromatographic and precipitation techniques at least two times of precipitation, providing up to 0.2%  $\gamma$ -oryzanol yield. This primary findings in this work will be used to further develop large-scale isolation and purification of  $\gamma$ -oryzanol from RBAF.

#### ACKNOWLEDGMENT

We thank the Ratchadaphiseksomphot Endowment Fund of Chulalongkorn University for Research Center for Bioorganic Chemistry and the Department of Chemistry, Faculty of Science, Chulalongkorn University for financial support and instrumental facilities.

#### REFERENCES

- [1] Chen, B., Qiao, Y., Wang, X., Zhang, Y., & Fu, L. (2023). Extraction, Structural Characterization, Biological Functions, and Application of Rice Bran Polysaccharides: A Review. *Foods*, 12(3), 639.
- [2] Liu, R., Liu, R., Shi, L., Zhang, Z., Zhang, T., Lu, M., & Wang, X. (2019). Effect of refining process on physicochemical parameters, chemical compositions, and in vitro antioxidant activities of rice bran oil. *LWT*, 109, 26-32.
- [3] Ballus, C. A., Meinhart, A. D., de Souza Campos, F. A., Jr, & Godoy, H. T. (2015). Total phenolics of virgin olive oils highly correlate with the hydrogen atom transfer mechanism of antioxidant capacity. *Journal of the American Oil Chemists' Society*, 92(6), 843-851.
- [4] Liu, R., Xu, Y., Chang, M., Tang, L., Lu, M., Liu, R., & Wang, X. (2021). Antioxidant interaction of  $\alpha$ -tocopherol,  $\gamma$ -oryzanol and phytosterol in rice bran oil. *Food Chemistry*, 343, 128431.
- [5] Saikia, S., & Dutta, H. (2022). Gamma oryzanol. In *Nutraceuticals and Health Care* (pp. 245-257). Academic Press.

[6] Kushwaha, R. (2018). Pharmacognosy of rice bran oil-A review. *International Journal of Green Pharmacy (IJGP)*, 12(04).

[7] Perez-Ternero, C., de Sotomayor, M. A., & Herrera, M. D. (2017). Contribution of ferulic acid,  $\gamma$ -oryzanol and tocotrienols to the cardiometabolic protective effects of rice bran. *Journal of Functional Foods*, 32, 58-71.

[8] Saikia, S., & Dutta, H. (2022). Gamma oryzanol. In *Nutraceuticals and Health Care* (pp. 245-257). Academic Press.

[9] Anjinta, A., Usaku, C., Boonnoun, P., Daisuk, P., & Shotipruk, A. (2023). Method Development for Purification of  $\gamma$ -oryzanol from Hydrolyzed Rice Bran Acid Oil by Semi-preparative Chromatography. *Journal of Oleo Science*, 72(1), 39-47.

[10] Lv, L., Zhang, L., Gao, M., & Ma, F. (2023). Simultaneous Determination of  $\gamma$ -Oryzanol in Agriproducts by Solid-Phase Extraction Coupled with UHPLC-MS/MS. *Agriculture*, 13(3), 531.

[11] Liu, C., Xi, X., Liu, Y., Lu, Y., Che, F., Gu, Y., & Wei, Y. (2021). Isolation of four major compounds of  $\gamma$ -oryzanol from rice bran oil by ionic liquids modified high-speed countercurrent chromatography and antimicrobial activity and neuroprotective effect of cycloartenyl ferulate in vitro. *Chromatographia*, 84(7), 635-644.

[12] Lv, L., Zhang, L., Gao, M., & Ma, F. (2023). Simultaneous Determination of  $\gamma$ -Oryzanol in Agriproducts by Solid-Phase Extraction Coupled with UHPLC-MS/MS. *Agriculture*, 13(3), 531.

# qNMR Application for the Quantification of eugenol and methyl eugenol in essential oil

Sirinat Chalkual<sup>1</sup> and Surachai Pornpakakul<sup>2\*</sup>

<sup>1</sup>Program of biotechnology of Science. Chulalongkorn University, Phayathai Road, Wangmai, Pathumwan, Bangkok 10330 Thailand.

<sup>2</sup>Research Centre for Bioorganic Chemistry Department of Chemistry, Faculty of Science. Chulalongkorn University, Phayathai Road, Wangmai, Pathumwan, Bangkok 10330 Thailand.  
Email: Surachai.p@chula.ac.th

**Abstract:** Nuclear magnetic resonance (NMR) spectroscopy is a well-known analytical technique for characterizing and identifying compounds. Since eugenol and methyl eugenol are the main components in the essential oils and spices and exhibit biological activities, we have developed an alternative method for the determination of both compounds with the assistance of 4-chlorobenzaldehyde as internal standard through an advantage of quantitative nuclear magnetic resonance spectroscopy (qNMR). In this study, the quantification of two major compounds, eugenol and methyl eugenol, in clove basil oil and holy basil oil was performed by qNMR. The results showed that the percentage of methyl eugenol and eugenol in essential oil could be analyzed by the qNMR analysis and 4-chlorobenzaldehyde as the internal standard due to no overlap between signal and sample signal <sup>1</sup>H NMR spectra.

Keywords: Nuclear magnetic resonance, 4-chlorobenzaldehyde, eugenol, methyl eugenol

## I. INTRODUCTION

Nuclear magnetic resonance (NMR) spectroscopy is an advanced characterization technique. It has been used to determine the molecular structure at the atomic level of a sample. Apart from the molecular structure, NMR spectroscopy can determine phase changes, conformational and configurational alterations, solubility, and diffusion potential.(1) Quantitative NMR (qNMR) refers to the use of NMR to determine the concentration of one or more chemicals. One of the major advantages of qNMR is its primary analytical characteristic because it can be applied in the quantitative estimation of the purity of compounds without using any specific reference standard.(2)

Methyl eugenol and eugenol are natural compounds found in many aromatic plants and have been used extensively by humans as flavoring agents in daily life.(3) Eugenol possesses significant antioxidant, anti-inflammatory and cardiovascular properties, in addition to analgesic and local anesthetic activity. The metabolism and pharmacokinetics of the compounds in humans have been studied. Eugenol has also been

used as a penetration enhancer. The compound is a very promising candidate for versatile applications, and the design of new drugs based on the pharmacological effects of eugenol could be beneficial.(4) Methyl eugenol exhibited anticancer, anti-inflammatory, antibacterial, antinociceptive, anxiolytic(5) and antioxidant activities.(6)

In this study, we developed an alternative method for quantification of eugenol and methyl eugenol with the assistance of 4-chlorobenzaldehyde as an internal standard through an advantage of qNMR.

## II. METHODOLOGY

### Plants

Clove basil and holy basil were collected from Bang Len, Nakhon Pathom in March 2021.

### Extraction of essential oils

Essential oils were extracted from holy basil (5.0214 Kg) and clove basil (990 g) through a hydrodistillation technique to give holy basil oil 0.033% and clove basil oil 0.306% (w/w) respectively.

### Quantitative NMR analysis

NMR spectroscopic data were recorded on Jeol 500 MHz NMR spectrometer. The chemical shifts ( $\delta$ ) were reported in part per million (ppm) and a residual solvent (at  $\delta_H$  7.26 ppm and  $\delta_C$  77.17 ppm for  $CDCl_3$ ) was used as a reference. Nuclear magnetic resonance spectral data were reprocessed by MestReNova NMR software version 14.1.1-24571, Mestrelab Research

2.5 mg of 4-chlorobenzaldehyde (Merck, Schuchardt, Germany) and 5 mg of essential oils were dissolved in 700  $\mu$ l of  $CDCl_3$ . Eugenol and methyl eugenol (myskinrecipes, Thailand) content in each sample were calculated by the formula(7):

$$\%P_t = \frac{I_t}{I_{is}} \times \frac{N_{is}}{N_t} \times \frac{MW_t}{MW_{is}} \times \frac{m_{is}}{m_{oil}} \times 100$$

In the formula,  $\%P_t$  represents the percentage of the target compound, in essential oil;  $I_t$  represents the integral of methoxy protons of the methyl eugenol ( $\delta_H$  3.86 ppm) or eugenol ( $\delta_H$  3.87 ppm);  $I_{is}$  represents the integral of an aldehyde proton of the internal standard.  $N_t$  and  $N_{is}$  represent the number of hydrogen atoms corresponding to the quantitative signal in the structure of the target compound and the internal standard;  $m_{oil}$  and  $m_{is}$  represent the weight of the essential oils and the internal standard, and  $MW_t$  and  $MW_{is}$  represent the molecular weight of the target compound and the internal standard, respectively.

### III. RESULTS AND DISCUSSION

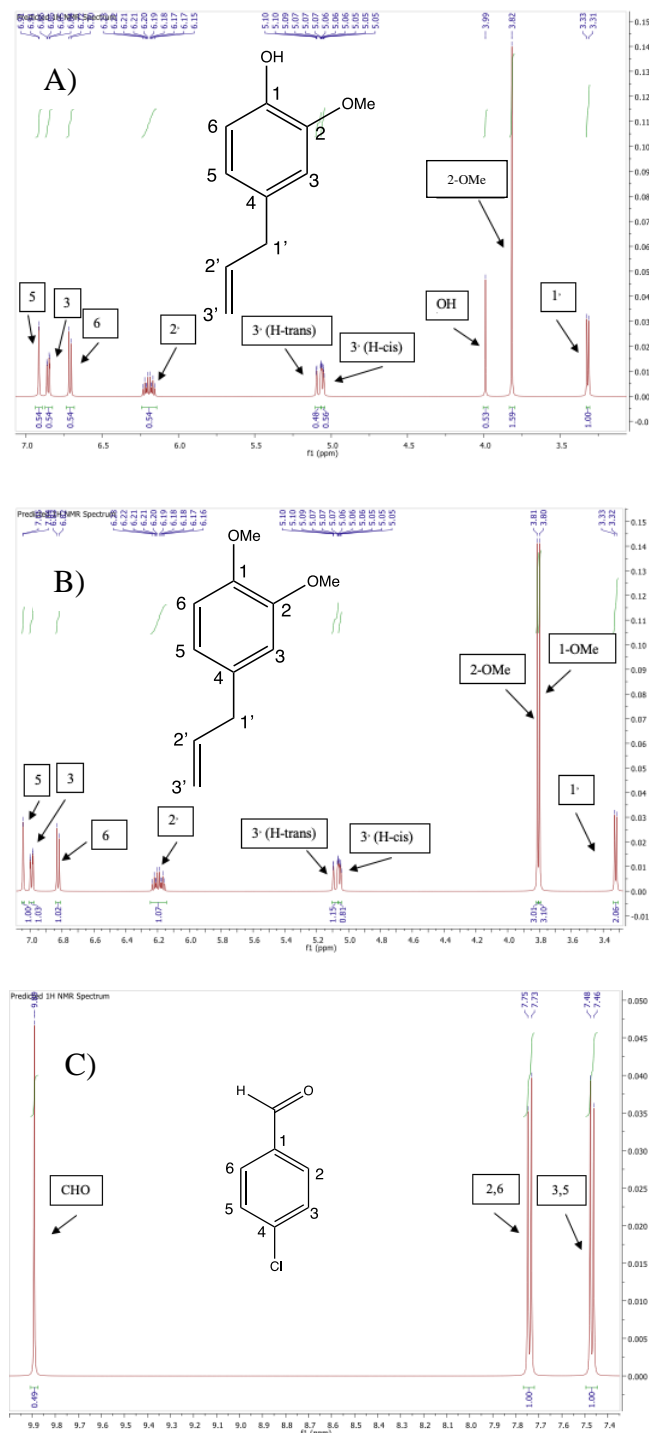
<sup>1</sup>H NMR chemical shifts of eugenol, methyl eugenol, and 4-chlorobenzaldehyde are as follows:

eugenol (Fig 1A):  $\delta_H$  6.91 (1H, d,  $J = 1.4$  Hz, 3-H), 6.87 (1H, dd,  $J = 7.5, 1.4$  Hz, 5-H), 6.71 (1H, d,  $J = 7.5$  Hz, 6-H), 6.19 (1H, ddt,  $J = 16.4, 10.1, 6.2$  Hz, 2'-H), 5.08 (1H, m, 3'-H (*trans*)), 5.06 (1H, m, 3'-H (*cis*)), 3.99 (1H, s, OH), 3.82 (3H, s, 2-OMe), 3.30 (2H, d,  $J = 6.2$  Hz, 1'-H).

methyl eugenol (Fig 1B):  $\delta_H$  7.04 (1H, d,  $J = 1.4$  Hz, 3-H), 6.99 (1H, dd,  $J = 7.5, 1.4$  Hz, 5-H), 6.83 (1H, d,  $J = 7.5$  Hz, 6-H), 6.19 (1H, ddt,  $J = 16.2, 9.9, 6.2$  Hz, 2'-H), 5.08 (1H, m, 3'-H (*trans*)), 5.06 (1H, m, 3'-H

(*cis*)), 3.81 (3H, s, 1-OMe), 3.80 (3H, s, 2-OMe), 3.32 (2H, d,  $J = 6.2$  Hz, 1'-H).

4-chlorobenzaldehyde (Fig 1C):  $\delta_H$  9.89 (1H, s, CHO), 7.74 (2H, d,  $J = 7.5$  Hz, 2, 6-H), 7.47 (2H, d,  $J = 7.5$  Hz, 3, 5-H)



**Figure 1:** <sup>1</sup>H NMR spectra of A) eugenol (2-methoxy-4-(prop-2-en-1-yl)phenol), B) methyl eugenol (4-allyl-1,2-dimethoxybenzene) and C) 4-chlorobenzaldehyde



Considering <sup>1</sup>H NMR chemical shift of eugenol, methyl eugenol, and 4-chlorobenzaldehyde, it was obvious that there is no overlap of their signals for OMe and aldehyde. Thus, we studied the suitable amount of 4-chlorobenzaldehyde in the sample, clove basil oil and basil oil, by <sup>1</sup>H NMR analysis of the mixture. We found that a mixture of 2.5 mg of 4-chlorobenzaldehyde and 5 mg of essential oils (see Fig 2A and 2B) was one of the suitable mixtures for quantitative analysis.

4-Chlorobenzaldehyde is an appropriate internal standard a quantitative analysis of eugenol and methyl eugenol in essential oils due to the aldehyde peak being a singlet, having one proton with a chemical shift of about 9.89 ppm and no overlap of signals in <sup>1</sup>H NMR spectrum of the essential oils.

In literatures, the internal standards (IS) having been used for <sup>1</sup>H NMR analysis are maleic acid, 1,2,4,5-tetra chlorobenzene, 1,4-dinitrobenzene, or benzyl benzoate(8) and IS must be a high purity, possess adequate solubility and inert to the analyte. In methyl eugenol and eugenol, we chose the signal of the methoxy proton at δ<sub>H</sub> 3.18 (or 3.80) and 3.82 ppm, respectively, for the quantitative analysis.

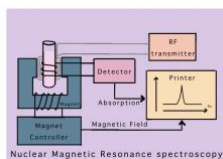
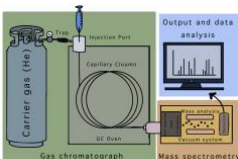
According to the calculation of the relation between integrals of a corresponding proton (internal standard, eugenol, and methyl eugenol) and the weight of a sample (as shown in the above mentioned formula), clove basil oil comprised of eugenol 38.54% w/w and methyl eugenol 4.48% w/w while holy basil oil comprised of eugenol 9.34% w/w and methyl eugenol 29.40% w/w.

We also analyzed the amount of eugenol and methyl eugenol through GC/MS due to both GC/MS and qNMR can quantifiability compounds in a mixture of compounds which by each technique so different (shown table 1). GC/MS analysis calculated by the formula.(9)

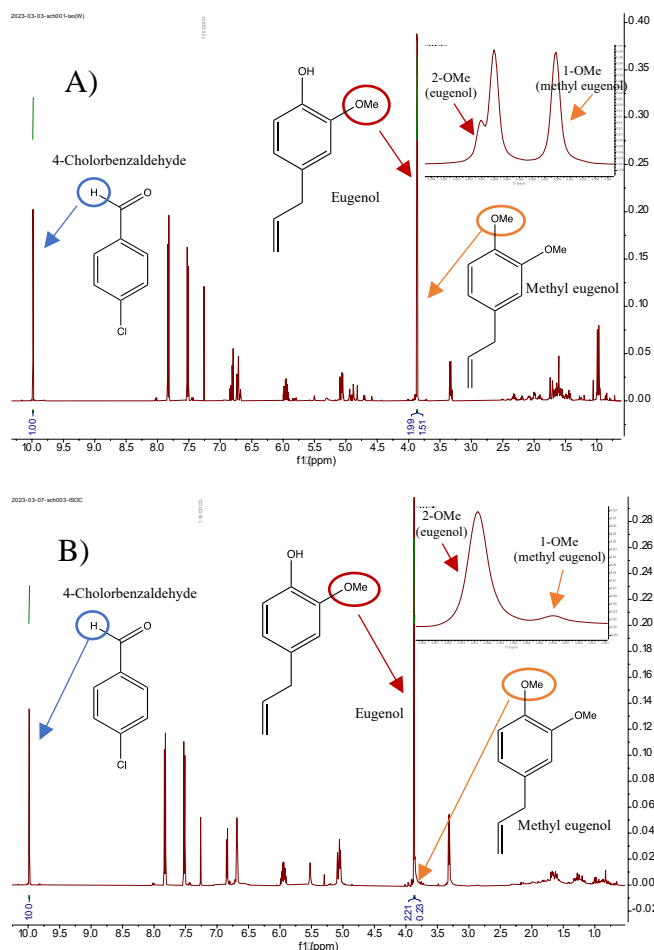
$$\%P_t = \frac{\text{peak area of target (eugenol or methyl eugenol)}}{\text{total peak area of essential oil}} \times 100$$

The results were similar to our analysis through <sup>1</sup>H NMR with the assistance of 4-chlorobenzaldehyde as the internal standard.

**Table 1:** Comparison of chromatography and NMR

Technique	NMR		GC/MS	
Principle	 <p>A diagram NMR qNMR is a quantitative technique using the ratio of the signal area observed and a molar ratio of the target compound and IS thus the integral is proportional to the number of nuclei from the corresponding signal and the substrate concentration.</p>		 <p>A simplified diagram of a gas chromatograph–mass spectrometer GC/MS instrument separates chemical mixtures (GC) and identifies the components (MS).</p>	
advantages	<ul style="list-style-type: none"> <li>- lower analysis time</li> <li>- easy to prepare a sample</li> <li>- require very small sample volumes</li> <li>- high reproducibility</li> <li>- %w/w is calculated through molar concentration of the target compound</li> <li>- IS is cheap</li> </ul>		<ul style="list-style-type: none"> <li>- enhanced sample identification</li> <li>- higher sensitivity</li> <li>- increased range of analyzable samples</li> <li>- limit of detection higher than qNMR = 300 pg</li> </ul>	
disadvantages	<ul style="list-style-type: none"> <li>- expensive instrument</li> <li>- limit of detection ≥ 0.5%</li> </ul>		<ul style="list-style-type: none"> <li>- limited to thermally stable</li> <li>- volatile compounds</li> <li>-peak area depended on ionization ability of organic molecules</li> <li>- expensive IS are required for accuracy and precision of the target compounds</li> </ul>	
calculated	qNMR can quantify by integral of methoxy protons compared with proton of internal standard (w/w).		GC/ms can quantify by peak area	
% eugenol	holy basil 9.34%	clove basil 38.54%	holy basil 10.92%	clove basil 50.54%
% methyl eugenol	holy basil 29.40%	clove basil 4.48%	holy basil 40.17%	clove basil 6.33%

Center for Bioorganic Chemistry and the Department of Chemistry, Faculty of Science, Chulalongkorn



**Figure 2:** <sup>1</sup>H NMR spectra of A) 4-chlorobenzaldehyde and holy basil essential oil and B) 4-chlorobenzaldehyde and clove basil essential oil.

#### IV. CONCLUSION

4-Chlorobenzaldehyde can be used determination of the percentage of eugenol and methyl eugenol in an essential oil with accuracy and precision compared to previous research in another technique (gas chromatography-mass spectrometry).(10) The literature study showed that eugenol and methyl eugenol were the main active chemical of holy basil and clove basil, respectively.(11)

#### ACKNOWLEDGMENTS

We thank the Ratchadaphiseksomphot Endowment Fund of Chulalongkorn University for Research

University for financial support and instrumental facilities. We also thank Assistant Professor Dr. Chadin Kulsing and his research group for GCMS analysis.

#### REFERENCES

- [1] Krishnan V.V., “Molecular thermodynamics using nuclear magnetic resonance (NMR) spectroscopy”. Inventions (Basel). **2019**, vol. 4, no. 1, pp. 13.
- [2] Zhang Y.Y., Zhang J., Zhang W.X., Wang Y., Wang Y.H., Yang Q.Y., Wu S., “Quantitative <sup>1</sup>H Nuclear Magnetic Resonance Method for Assessing the Purity of Dipotassium Glycyrrhizinate”. *Molecules*. **2021**, vol. 26, pp. 3549.
- [3] Vincenzi M.D., Silano M., Stacchini P., S.B. cchio, “Constituents of aromatic plants: I. Methyl eugenol”. *Fitoterapia*. **2000**, vol. 71, no. 2, pp. 216-21.
- [4] Pramod K., Ansari S.H., Ali J., “Eugenol: A Natural Compound with Versatile Pharmacological Actions”. *Natural Product Communications*. **2010**, vol. 5, no. 12, pp. 1999-2006.
- [5] Singh D., Chaudhuri P. K., “A review on phytochemical and pharmacological properties of Holy basil (*Ocimum sanctum* L)”. *Industrial Crops and Products*. **2018**, vol. 118, pp. 367-382.
- [6] Ma L., Liu J., Lin Q., Gu Y., Yu W., “Eugenol protects cells against oxidative stress via Nrf2”. *experimental and therapeutic medicine*. **2021**, vol. 21, pp. 107.
- [7] Miura T. *et al.*, “Collaborative Study to Validate Purity Determination by <sup>1</sup>H Quantitative NMR Spectroscopy by Using Internal Calibration Methodology”. *The Pharmaceutical Society of Japan*. **2020**, vol. 68, no. 9, pp. 868.
- [8] Evillia R.F., “Quantitative NMR Spectroscopy”. *Original Articles*. **2022**, vol. 34, no. 13, pp. 2227-2236.
- [9] Macherone A., “A Brief review of derivatization chemistries for the analysis of cannabinoids using GC-MS” *Cannabis Science and Technology*. **2020**, vol. 3, no. 7, pp. 42-48.
- [10] Tangpao T., Chung H.H., Sommano S.R., “Aromatic Profiles of Essential Oil from 5 Commonly Used Thai Basils”. *Creative Commons*. **2018**, vol. 7, pp. 175.

The 4<sup>th</sup> International Conference on Informatics, Agriculture,

Management, Business administration, Engineering, Science and Technology

[11] Benitez N.P., Leon E.M.M., Stashenko E.E.,  
“Eugenol and Methyl Eugenol Chemotypes of  
Essential Oil of Species *Ocimum gratissimum* L. and  
*Ocimum campechianum* Mill. from Colombia”.

Journal of Chromatographic Science. **2009**, vol. 47,  
no. 9, pp. 800



# Forecasting PTT and BCP Stock Prices in the Stock Exchange of Thailand: An Application of ARIMA and ARIMAX Models

**Patchanok Srisuradetchai**

Thammasat University, Department of Mathematics and Statistics,  
Pathum Thani, Thailand 12120, and patchanok@mathstat.sci.tu.ac.th

**Abstract:** Bangchak Corporation PCL (BCP) and Petroleum Authority of Thailand (PTT) are leading companies in Thailand's energy sector and rank among the top 100 firms listed on the Stock Exchange of Thailand (SET). Accurate stock price forecasting is critical for devising investment strategies, managing risks, and fostering the sustained growth and development of the energy sector. This study employs ARIMA and ARIMAX models to predict BCP and PTT stock prices. The optimal models for BCP and PTT achieve mean absolute percentage errors of 5.336% and 13.277% in the validation datasets, respectively. Although it may be tempting to assume that PTT and BCP stock prices would exhibit similar patterns, the models reveal distinct behaviors for each company. PTT's stock price is better captured by a simpler model, while BCP demands a more complex approach to minimize errors.

**Index Terms**—Time series model, ARIMA, ARIMAX, stock price, forecasting.

## I. INTRODUCTION

The stock market plays a crucial role in the global economy by facilitating the exchange of capital between investors and businesses. Forecasting stock prices accurately is vital for investment decisions and strategic planning. In this research, we focus on predicting the stock prices of Bangchak Corporation PCL (BCP) and the Petroleum Authority of Thailand (PTT), two major players in Thailand's energy sector. Both companies are involved in the entire supply chain of the oil industry, from exploration to end customer. Accurate predictions of their stock prices can provide valuable insights for investors and stakeholders, enabling them to make informed decisions and potentially gain substantial returns.

The Autoregressive Integrated Moving Average Model (ARIMA) has been widely used for time series forecasting due to its ability to capture linear relationships and predict future values based on past observations. Extending the capabilities of ARIMA, the ARIMAX model incorporates exogenous variables to improve prediction accuracy further. This study aims to explore the predictive power of ARIMA and ARIMAX models for forecasting the stock prices of BCP and PTT in the Stock Exchange of Thailand (SET), using the gold spot and West Texas Intermediate (WTI) as explanatory variables.

The importance of BCP and PTT in Thailand's energy sector cannot be overstated. These companies contribute

significantly to the country's economy and energy security. Accurate forecasting of their stock prices can assist in shaping investment strategies, mitigating risks, and ensuring the continued growth and development of the energy sector. Furthermore, understanding the relationships between key economic variables, such as gold spot and WTI, can provide valuable insights into market dynamics and help identify potential investment opportunities.

Gold has long been considered a safe-haven asset in times of economic uncertainty and financial market turbulence [1]. As a result, its price tends to have an inverse relationship with stock market performance, particularly during periods of economic stress [2]. Gold's role in the global economy makes it an essential variable to consider when predicting stock prices. The Gold Spot price refers to the current market price of gold per troy ounce for immediate delivery or settlement. It is a globally recognized benchmark that reflects the real-time fluctuations in the value of gold, as traded in international commodity markets. The gold spot price is influenced by various factors, including global economic conditions, geopolitical events, and central bank policies.

WTI, a benchmark for crude oil prices, is a significant determinant of global energy markets, with direct implications for the profitability of energy companies [3]. Changes in WTI prices can significantly impact the financial performance of oil-related companies, such as BCP and PTT, as fluctuations in crude oil prices directly affect their revenues and costs [4]. Thus, incorporating WTI as an explanatory variable in the ARIMAX model can

potentially enhance the prediction accuracy for the stock prices of BCP and PTT.

The existing literature has highlighted the importance of both gold spot and WTI as crucial variables in understanding financial market dynamics [5]. For instance, Basher and Sadorsky [4] found that oil prices and gold prices are cointegrated, indicating a long-term relationship between them.

Box and Jenkins [6] were pioneers in introducing the ARIMA model as a powerful forecasting tool for time series data. Since then, many researchers have adopted ARIMA models for stock price prediction, contributing to the growing body of literature on this subject. For example, Adebisi et al. [7] used ARIMA to forecast stock prices in the Nigerian Stock Exchange and found the model to be effective in capturing the historical trends and predicting future values.

In the context of the energy sector, several studies have applied ARIMA and ARIMAX models to predict stock prices of energy-related companies. Yu and Zhang [8] used ARIMA models to forecast the stock prices of four Chinese oil companies and concluded that the models provided reliable predictions, making them valuable tools for investment decision-making. Similarly, Al-Shiab [9] employed ARIMA models to predict the stock prices of three energy companies in the Amman Stock Exchange and found that the models yielded satisfactory results in terms of forecasting accuracy.

ARIMAX models, which extend the capabilities of ARIMA by incorporating exogenous variables, have also been applied in various studies for stock price prediction. For instance, Predictions regarding Nigeria's gross domestic product were made by Abdulazeez and S. Adeyinka [10] with the assistance of the ARIMAX model for gross domestic product. The data that was used for this study is one that is compiled on an annual basis and obtained from the Central Bank of Nigeria for the years 1981–2020.

Additionally, Mohammadi and Su [11] used ARIMAX models to predict the stock prices of European energy companies, incorporating oil price and exchange rate variables. They found that the models exhibited superior forecasting performance compared to traditional ARIMA models, highlighting the benefits of incorporating exogenous variables in the forecasting process.

In conclusion, this study aims to utilize ARIMA and ARIMAX models to predict the stock prices of BCP and PTT in the SET, taking into account the gold spot and WTI as explanatory variables. By exploring the relationships between these variables and their impact on BCP and PTT stock prices, this research seeks to provide valuable insights for investors and stakeholders in Thailand's energy sector.

## II. DATA USED

Data on the daily closing stock prices for BCP (Bangchak Corporation Public Company) and PTT (Petroleum Authority of Thailand) from the Stock

Exchange of Thailand (SET) were used to calculate monthly averages, serving as dependent variables. The predictor variables include the gold price (Gold Spot) and the price of WTI (West Texas Intermediate) crude oil, which are averaged from daily to monthly values. The data, spanning from January 2017 to December 2022, a total of 72 months, can be retrieved from the website <https://www.investing.com>.

### A. Monthly BCP and PTT Prices

Upon examining the BCP price, we discovered that the average stands at 29.64, with a minimum of 15 and a maximum of 42.1. As illustrated in Fig. 1., the BCP price exhibits a downward trend from October 2017 to October 2020, followed by an upward trajectory. Regarding the PTT price, the average stands at 41.79, with a minimum of 30.85 and a maximum of 55.87. As depicted in Fig. 2., the trend shows an increase from the beginning of 2017 until April 2018, when the PTT price peaks. Subsequently, the PTT price experiences a noticeable decline up to the present. The lowest price occurs in March 2020.

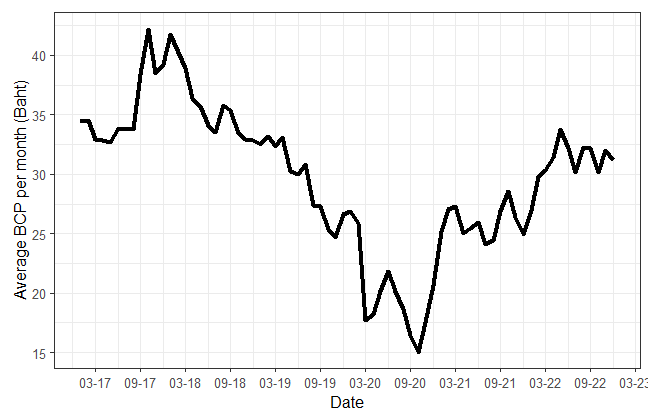


Fig. 1. Average prices of BCP stock per month from January 2017 to December 2022.

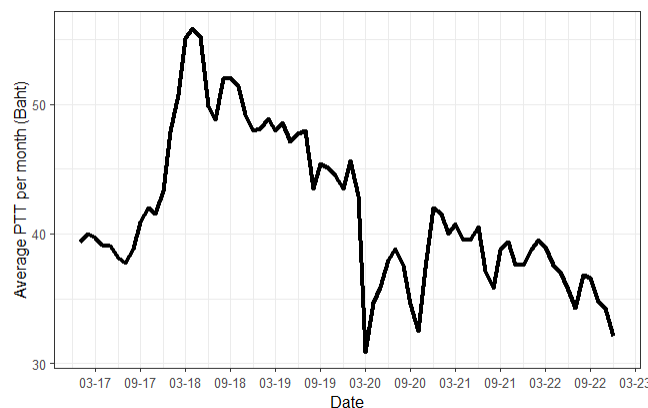


Fig. 2. Average prices of PTT stock per month from January 2017 to December 2022.

### B. Gold Spot and West Texas Intermediate

The unit of the Gold Spot price is typically measured in US dollars per troy ounce (USD/ozt). By quoting the Gold

Spot price in USD per troy ounce, market participants can easily compare and trade gold on a standardized basis in international commodity markets. And, the unit of WTI crude oil is typically measured in US dollars per barrel (USD/bbl).

As illustrated in Fig. 3., WTI values do not exhibit a clear trend, as they fluctuate between 45 and 75 from the beginning of 2017 until February 2020. The price then experiences a sharp drop to 16.7 in April 2020. Following that, the price begins to rise, reaching its peak at 113.87 in June 2022, and subsequently displays a downward trend up to the present. In contrast, as depicted in Fig. 4., gold spot demonstrates an upward trend from the beginning until August 2020. After that, the price mostly oscillates between 1700 and 1900.

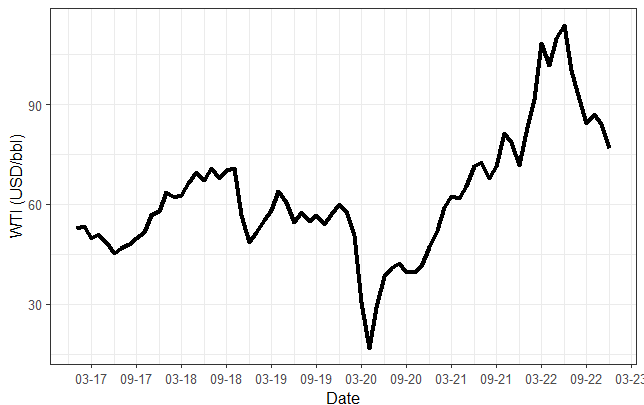


Fig. 3. Average prices of WTI per month from January 2017 to December 2022.

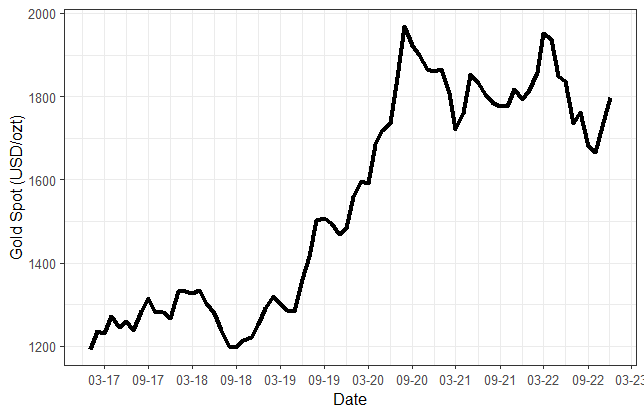


Fig. 4. Average prices of gold spot per month from January 2017 to December 2022.

### C. Relationship Between Predictors and Stock Prices

The BCP price exhibits a significant linear relationship with both WTI and gold spot, as indicated by the p-values in Table I, which are below 0.05. But, the PTT price is only correlated to spot. As the gold spot increases, both BCP and PTT significantly decrease. Fig. 5. shows both scatter plots among variables and distributions. The prices of BCP, PTT, and WTI do not show obvious left- or right-skewed patterns. The distribution of gold spots tends to be bimodal.

TABLE I

CORRELATION ANALYSIS FOR PREDICTORS AND RESPONSES

Stock Price	Predictor	Correlation Coefficient	P-value
BCP	WTI	0.3348	0.004
BCP	Gold Spot	-0.6916	< 0.0001
PTT	WTI	-0.0438	0.715
PTT	Gold Spot	-0.6542	< 0.0001

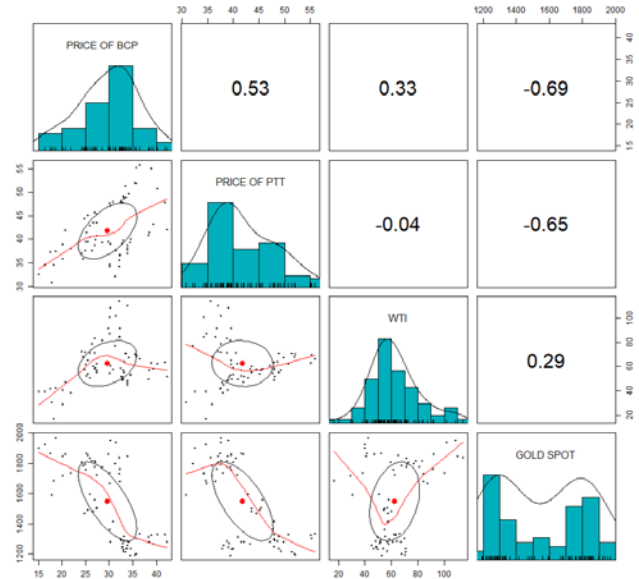


Fig. 5. Scatter plots among variables.

### III. METHODOLOGY

This section presents the methodology employed in this study, focusing on the theoretical background of the Autoregressive Integrated Moving Average (ARIMA) and Autoregressive Integrated Moving Average with Exogenous Variables (ARIMAX) models.

#### A. ARIMA Model

The ARIMA model is a popular time series forecasting method that combines autoregressive (AR), differencing (I), and moving average (MA) components. The ARIMA model can be represented as  $ARIMA(p, d, q)$ , where  $p$  is the order of the autoregressive component (AR),  $d$  is the order of differencing,  $q$  is the order of the moving average component (MA). The AR captures the linear dependency of the current value on its previous values, while MA models the dependency of the current value on past errors. The differencing component is used to transform the time series into a stationary series. The ARIMA model can be written in (1), as follows:

$$\Delta^d y_t = \phi_0 + \phi_1 \Delta^d y_{t-1} + \phi_2 \Delta^d y_{t-2} + \dots + \phi_p \Delta^d y_{t-p} + \varepsilon_t + \theta_1 \varepsilon_{t-1} + \theta_2 \varepsilon_{t-2} + \dots + \theta_q \varepsilon_{t-q}, \quad (1)$$

where

- $y_t$  is the value of the time series at time  $t$ ,
- $\Delta^d y_t$  represents the  $d$ -th differenced series,
- $\phi_i$  ( $i = 1, 2, \dots, p$ ) are the autoregressive parameters,
- $p$  is the order of the autoregressive component (AR),
- $d$  is the order of differencing (I),
- $\theta_j$  ( $j = 1, 2, \dots, q$ ) are the moving average parameters,
- $q$  is the order of the moving average component (MA),
- $\varepsilon_t$  is the error term at time  $t$ .

### B. ARIMAX Model

The mathematical notation for the ARIMAX ( $p, d, q; k = 2$ ) model with  $k = 2$  exogenous variables can be written as follows:

$$\Delta^d y_t = \phi_0 + \phi_1 \Delta^d y_{t-1} + \phi_2 \Delta^d y_{t-2} + \dots + \phi_p \Delta^d y_{t-p} + \beta_1 \text{WTI}_t + \beta_2 \text{GOLD}_t + \varepsilon_t + \theta_1 \varepsilon_{t-1} + \theta_2 \varepsilon_{t-2} + \dots + \theta_q \varepsilon_{t-q}. \quad (2)$$

### C. Steps for Analysis

To implement ARIMA and ARIMAX models, the following steps are typically performed:

- i. Transform the time series into a stationary series using differencing,
- ii. Model selection: determine the optimal values of  $p$ ,  $d$ , and  $q$  using criteria such as the Akaike Information Criterion (AIC),
- iii. Model estimation: estimate the ARIMAX model parameters ( $\phi_i$ ,  $\theta_j$ , and  $\beta_k$ ) using techniques such as Maximum Likelihood Estimation (MLE),
- iv. Model diagnostics: check the adequacy of the estimated model by analyzing the residuals, ensuring that they are uncorrelated and normally distributed. Perform tests such as the Ljung-Box test for residual autocorrelation,
- v. Model validation: validate the model using out-of-sample forecasts and compare the model's performance with benchmark models or other competing models. Common performance metrics include Root Mean Squared Error (RMSE) and Mean Absolute Percentage Error (MAPE) which are:

$$\text{RMSE} = \sqrt{\frac{\sum_{t=1}^n (y_t - \hat{y}_t)^2}{n}}$$

and  $\text{MAPE} = \frac{1}{n} \left( \sum_{t=1}^n \left| \frac{y_t - \hat{y}_t}{y_t} \right| \right) 100\%$ , respectively.

In this paper, we use R Studio version 2023.03.0 [12] and package forecast [13] to perform ARIMA and ARIMAX analysis. The first 60 months of observations are used as the training dataset, and the rest of the 12 months are the validation dataset.

## IV. RESULTS

In this section, we present the results and discuss the findings of our study that utilizes ARIMA and ARIMAX models to predict the stock prices of BCP and PTT listed on the SET. The performance of the models is analyzed, and the influence of exogenous variables, specifically gold spot and WTI, is assessed. Through the discussion, we aim to provide insights into the efficacy of these models and their implications for investors and financial analysts.

### A. Models for PTT

The resulting ARIMA model is  $\Delta^1 y_t = -0.0253 - 0.7736 \Delta^1 y_{t-1} + \varepsilon_t + 0.9997 \varepsilon_{t-1}$ , and the p-values of AR(1) and MA(1) are less than 0.0001 and 0.004, respectively. Using ARIMAX, the resulting model is

$$\Delta^2 y_t = -1.148 \Delta^2 y_{t-1} + 0.169 \Delta^2 y_{t-2} + 0.424 \Delta^2 y_{t-3} + \varepsilon_t + 0.168 \varepsilon_{t-1} - 1.608 \varepsilon_{t-2} - 0.161 \varepsilon_{t-3} + 0.723 \varepsilon_{t-4} + 0.261 \text{WTI}_t + 0.009 \text{GOLD}_t.$$

The p-values of AR(3) and MA(4) are less than 0.10, so the model with  $p = 3$  and  $q = 4$  is suitable for PTT prices. The p-value of gold spot is not statistically significant, but keeping it helped the prediction ability. In evaluating the predictive accuracy, the RMSE and MAPE values derived from both the ARIMA and ARIMAX models are presented in Table II. While the ARIMAX model provides a better fit for the training dataset compared to the ARIMA model, the ARIMA model outperforms the ARIMAX model for the validation dataset. This suggests that the ARIMAX model is more likely to be an over-fitted model. Checking residuals is not presented here, but they are uncorrelated and normally distributed.

TABLE II  
BEST ARIMA AND ARIMAX MODELS FOR PTT

Model ( $p, d, q, k$ )	Training Dataset		Validation Dataset	
	MAPE	RMSE	MAPE	RMSE
ARIMA (1, 1, 1)	4.002%	2.4437	5.336%	2.6988
ARIMAX (3, 2, 4, 2)	3.814%	2.1157	8.638%	4.6116

### B. Models for BCP

The ARIMA obtained is  $\Delta^1 y_t = -0.154 - 0.6189 \Delta^1 y_{t-1} + \varepsilon_t + 0.8324 \varepsilon_{t-1}$ , and the p-values of AR(1) and MA(1) are less than 0.05, respectively; therefore, the autoregressive, differencing, and moving average components are needed for this model. The values of RMSEs and MAPEs, as presented in Table III, indicate that the ARIMA model may suffer from overfitting. In comparison, the ARIMAX model

demonstrates significantly better performance, as evidenced by its considerably lower RMSE and MAPE values for the validation dataset. Thus, the ARIMAX model proves to be a superior choice over the ARIMA model. Here, the ARIMAX model is  $\Delta^1 y_t = -0.2168 - 0.6950\Delta^1 y_{t-1} + \varepsilon_t + 0.7955\varepsilon_{t-1} + 0.1813WTI_t$ . The gold spot variable is not statistically significant and does not help reduce the RMSE and MAPE of the prediction, so it was excluded from the model.

TABLE III  
BEST ARIMA AND ARIMAX MODELS FOR BCP

Model (p, d, q, k)	Training Dataset		Validation Dataset	
	MAPE	RMSE	MAPE	RMSE
ARIMA (1, 1, 1)	5.605%	2.0194	29.263%	7.2714
ARIMAX (1, 1, 1, 1)	5.134%	1.7954	13.277%	4.3619

### C. Predicting the Stock Price

The models fitted using the training datasets were employed to predict stock prices in the validation datasets. Tables IV and V present the forecasted PTT and BCP stock prices, respectively.

Upon closer examination of Table IV, the forecasted values from the ARIMA model tend to hover around 37. However, after August 2022, the actual price visibly declines until it reaches 32.07 in December 2022. In contrast, the forecasted values from the ARIMAX model are higher than the corresponding actual values between February and June 2022. Following this period, the ARIMAX model successfully captures the downward trend in the actual values.

TABLE IV  
FORECASTED STOCK PRICES OF PTT

2022 Month	Actual Value	Forecasted PTT	
		ARIMA	ARIMAX
Jan	38.7375	38.2940	39.3937
Feb	39.5394	37.6833	41.5002
Mar	39.0217	38.1109	45.9330
Apr	37.6029	37.7352	43.3876
May	37.0657	37.9810	44.2712
Jun	35.6309	37.7460	44.4108
Jul	34.2500	37.8829	39.6041
Aug	36.8181	37.7321	36.7299
Sep	36.5568	37.8039	33.7440
Oct	34.7361	37.7035	33.5575
Nov	34.2727	37.7363	32.9907
Dec	32.0750	37.6661	31.0349

Regarding the BCP prices, the ARIMA model is evidently less effective than the ARIMAX model. The

forecasted values from the ARIMA model are consistently lower than the corresponding actual values. In contrast, the ARIMAX model yields forecasted values that are much closer to the actual values.

TABLE IV  
FORECASTED STOCK PRICES OF BCP

2022 Month	Actual Value	Forecasted BCP	
		ARIMA	ARIMAX
Jan	26.9500	25.0667	26.8819
Feb	29.8026	24.9872	28.1588
Mar	30.2826	25.0361	30.9982
Apr	31.3823	25.0060	29.5465
May	33.7763	25.0245	30.8507
Jun	32.1428	25.0131	31.3366
Jul	30.1388	25.0201	28.6689
Aug	32.2386	25.0158	26.8479
Sep	32.2045	25.0185	25.3196
Oct	30.1388	25.0169	25.6086
Nov	32.0454	25.0179	24.8618
Dec	31.2000	25.0172	23.3406

## V. CONCLUSION AND DISCUSSION

The ARIMA and ARIMAX models can be useful for forecasting the stock prices of PTT and BCP. For PTT, although the ARIMAX model is preferred for the training dataset, it does not outperform the ARIMA model for the validation dataset. This might suggest the need to explore other potential explanatory variables. For BCP, including only WTI significantly improves the model.

In conclusion, although both companies are involved in the entire supply chain of the oil industry, from exploration to end customers, and one might assume the stock prices of PTT and BCP should be similar, the resulting different models reveal that the movements of PTT and BCP are not the same. The PTT stock price is better explained by a simpler model, while BCP still requires a more complex model to reduce errors. One reason for the relative ease of forecasting PTT is its stock price has exhibited an obvious downward trend since the beginning of 2021, which is easily captured by time series models.

## REFERENCES

- [1] D. G. Baur and B. M. Lucey, "Is gold a hedge or a safe haven? An analysis of stocks, bonds, and gold and commodities," *The Financial Review*, Eastern Finance Association, vol. 45, no. 2, pp. 217-229, 2010.
- [2] D. G. Baur and T. K. McDermott, "Is gold a safe haven? International evidence," *Journal of Banking & Finance*, vol. 34, no. 8, pp. 1886-1898, 2010.
- [3] J. D. Hamilton, "Understanding crude oil prices," *The Energy Journal*, vol. 30, no. 2, pp. 179-206, 2009.
- [4] S. A. Basher and P. Sadorsky, "Oil price risk and emerging stock markets," *Global Finance Journal*, vol. 17, no. 2, pp. 224-251, 2006.
- [5] P. Sadorsky, "Risk factors in stock returns of Canadian oil and gas companies," *Energy Economics*, vol. 23, no. 1, pp. 17-28, 2001.



- [6] G. E. Box and G. M. Jenkins, Time series analysis: forecasting and control. San Francisco: Holden-Day, 1976.
- [7] A. A. Adebisi, A. O. Adewumi, and C. K. Ayo, "Comparison of ARIMA and Artificial Neural Networks Models for Stock Price Prediction," Journal of Applied Mathematics, vol. 2014, pp. 1-7, 2014.
- [8] W. Fenghua, G. Xu, and C. Shenghua, "Forecasting the volatility of crude oil futures using HAR-type models with structural breaks," Energy Economics, vol. 59, pp. 400-413, 2016.
- [9] M. S. Al-Shiab, "The Predictability of the Amman Stock Exchange using the Univariate Autoregressive Integrated Moving Average (ARIMA) Model," Journal of Economic and Administrative Sciences, no. 2, pp. 17-35, 2006.
- [10] Abdulazeez and S. Adeyinka, "A comparative study between ARIMA and ARIMAX in Forecasting Gross Domestic Product (GDP) in Nigeria," Kasu Journal of Mathematical Sciences, vol. 2, no. 2, 2021.
- [11] H. Mohammadi and L. Su, "International evidence on crude oil price dynamics: Applications of ARIMA-GARCH models," Energy Economics, vol. 32, no. 5, pp. 1001-1008, 2010.
- [12] Posit team, "RStudio: Integrated Development Environment for R," Posit Software, PBC, Boston, MA, 2023.
- [13] R. J. Hyndman and Y. Khandakar, "Automatic time series forecasting: The forecast package for R," J. Stat. Softw., vol. 26, no. 3, pp. 1-22, 2008.

# Thermal characteristic and morphology of biodegradable blends containing grafted nanocomposites

Phanitchanun Thanawattana<sup>1</sup>, Siriwan Phattanasuddee<sup>1,2\*</sup>

<sup>1</sup> Program of Petrochemistry and Polymer Science, Faculty of Science, Chulalongkorn University, Bangkok 10330, Thailand, thanawattana@gmail.com

<sup>2\*</sup> Department of Imaging and Printing Technology, Faculty of Science, Chulalongkorn University, Bangkok 10330, Thailand, Siriwan.Ph@chula.ac.th

**Abstract:** Surface modifications of nanofillers have been widely studied to promote interfacial interaction between the filler such as hydroxyapatite (HA) and polymer matrix phases, and consequently enhance mechanical property. Thus, the current research focused on preparation of poly(lactic acid) grafted hydroxyapatite (PLA-g-HA) by using melt grafting method and subsequently added into poly(lactic acid) (PLA) and polycaprolactone (PCL) blends at various concentrations. %Grafting and functionality of the grafted HA were characterized by thermogravimetric analysis and Fourier-transform infrared spectroscopy. Morphology and thermal property of the obtained blend nanocomposites were then analyzed by scanning electron microscopy, differential scanning calorimeter, and thermogravimetric method. The results showed that increasing in the PLA-g-HA concentration, %crystallinity of PLA phase, and onset temperature of the blend nanocomposites were simultaneously escalated, whereas smaller sizes of dispersed PCL phase were observed.

**Index Terms**— Grafting, Hydroxyapatite, Poly(lactic acid), Polycaprolactone

## I. INTRODUCTION

Biodegradable blend nanocomposites can be utilized in various fields of applications, such as biomedical, tissue engineering, packaging, structural, conductive, etc. [1-5]. PLA/PCL blends are among the most studied biodegradable blends because of the biodegradability, biocompatibility, and flexibility. Nano-hydroxyapatite is mostly used in the biomedical field involved hard tissue regeneration since it contains similar inorganic component of bones and teeth. By incorporating hydroxyapatite into biopolymer matrix, it is able to enhance not only osteoinductivity, osteoconductivity, bone tissue formation but also mechanical and thermal properties of the nanocomposite materials. Recently, Hassanajili et al. prepared and characterized PLA/PCL/HA composites using indirect 3D printing for bone tissue engineering [6]. The results revealed that the scaffold composed of PLA/PCL at 70/30 weight ratio and 35% HA was more favorable. The scaffold contained a porosity of 77%, an average pore size of 160  $\mu\text{m}$ , and Young's modulus of 1.35 MPa. Peponi et al. studied the effect of nano-hydroxyapatite on the shape memory behavior of PLA/PCL blends. It was found that excellent thermally-activated shape memory response could be obtained for all nanocomposites at 55 °C [7].

To improve interfacial bonding between the polymer phases, surface modifications of nanofillers are frequently integrated. By surface modifying nano-hydroxyapatite with ethylene glycol and PCL, affinity was improved between the polymer and ceramic interphases [8]. Due to better affinity, the compressive strength of grafted HA/polymer was significantly enhanced. Moreover, interfacial adhesion, biological activity and affinity between the osteoblast cells

and polymer composite cement were also increased. Park et al. prepared high strength poly(lactic-co-glycolic acid) (PLGA)/hydroxyapatite composites, in which PLGA could be directly grafted to HA surface in polymer state using melt grafting. The use of PLGA-g-HA increased the strength to more than twice that of the existing blended system [9].

The objective of this research is to prepare PLA-g-HA with different grafting amounts, and later added into PLA/PCL blends at various concentrations (20-60 phr). Morphology and thermal property of the resultant blend nanocomposites are characterized.

## II. METHODOLOGY

### Materials

PLA 2003D with D-Lactide content of 4.3%, a weight average molecular weight ( $M_w$ ) of 230 kDa was supplied by Nature Works. PCL with a number average molecular weight ( $M_n$ ) of 80,000 g/mol and HA (average particle size <200 nm) were obtained from Sigma Aldrich. Dichloromethane used as a solvent was purchased from Ajax Finechem.

### Preparation of PLA-g-HA

PLA-g-HA was prepared by grafting reaction via a melt process. Firstly, PLA was dissolved in dichloromethane under magnetic stirring for 2 h. While, HA suspension (at 30%wt) was homogenized at 20000 rpm for 20 min to obtain a fine dispersion of the composite, and subsequently added to the PLA solution. The mixture was continuously stirred for 2 h to obtain a homogeneous mixing. After that, the mixed solution was dried at 50°C in an oven for 1 h to remove the solvent then heated to 200°C for 30 min. Later, the finished product

was washed with the solvent to separate supernatant and sediment by centrifugation at 5000 rpm. The extracted sediment was dried at 50°C for 1 h.

#### Preparation of blend nanocomposites films

PLA was dissolved in dichloromethane under magnetic stirring for 2 h. PCL was added to the PLA solution and mixed for 1 h. PLA/PCL ratio was studied at 80/20. The prepared PLA-g-HA was subsequently added to the blend system at different concentrations (20-60 phr). After homogeneous mixing, the solution was poured into a petri dish to obtain a film by solution casting method. Film samples were dried in an oven for 1 h to remove the remaining solvent.

#### Characterizations and films testing

Fourier transform infrared (FT-IR) spectroscopy was employed to characterize the functional groups of grafted HA. Infrared spectra were obtained using an FT-IR spectrometer (PERKIN ELMER Spectrum One model). The spectra were collected from 4000 cm<sup>-1</sup> to 500 cm<sup>-1</sup>.

Thermogravimetric analysis (TGA) NETZSCH TG 209 F3 Tarsus model was used to determine thermal stability of the blend nanocomposites. The temperature was scanned from 35°C to 700°C at a heating rate of 20°C/min under a nitrogen atmosphere. The results were reported from the selected region from 100-700°C.

Differential scanning calorimetry (DSC) NETZSCH DSC 204 F1 Phoenix model was utilized to evaluate the thermal quantities, such as glass transition (T<sub>g</sub>), melting (T<sub>m</sub>), and crystallization (T<sub>c</sub>) temperatures, and degree of crystallinity. The sample was heated from -100°C to 250°C with a heating rate of 10°C/min, then cooled to -100°C, and secondly heated to 250°C with the same heating rate under a nitrogen atmosphere.

Scanning electron microscopy (SEM) JEOL JSM-IT500HR model was applied to capture morphology images of the blend nanocomposites. The experiment was performed at an accelerating voltage of 10 kV and 5000x magnification.

### III. RESULTS AND DISCUSSION

To investigate the grafting reaction through the melt process, the chemical structures of pristine HA, PLA, and PLA-g-HA were determined by FT-IR (Fig. 1). For PLA spectrum, the peak appears at 1757 cm<sup>-1</sup>, suggesting the carbonyl band in the ester structure, which has a strong stretching intensity in the range of 1735-1750 cm<sup>-1</sup>. While, the peaks at 1184 and 1026 cm<sup>-1</sup> correspond to C-H bending and C-O stretching, respectively. Moreover, the peaks near 2918 and 2849 cm<sup>-1</sup> are due to the C-H stretching [10]. In case of pristine HA, the strong signals are observed at 1416 cm<sup>-1</sup>, conforming to CO<sub>3</sub><sup>2-</sup>, whereas 1026 and 561 cm<sup>-1</sup> represent PO<sub>4</sub><sup>3-</sup> [6]. It is found that the spectrum of PLA-g-HA contains both significant peak positions belong to PLA and HA, verifying the chemical bonding structure between HA and PLA. Since the unreacted PLA was completely removed by centrifugation after the grafting reaction and subsequent dissolution of the product, the detected carbonyl peak arose from PLA surface grafting on the reacted HA [9].

The content of polymer grafted on the surface of HA was examined by TGA. HA is an inorganic substance and has a high heat resistance, whereas the PLA polymer structure grafted on the HA surface has a lower heat resistance. It is assuming that the polymer chains become decomposed through heating to a high temperature, and all the PLA chains that participated in the reaction are subsequently removed, and only HA is remained. Therefore, the mass difference between samples at high temperature is correlated with the grafting weight fraction, and the equation is shown below in (1) [9]. The difference between the residual weight of pristine HA and that of the PLA-g-HA product is related to the ratio of PLA that was substituted on the HA surface. The experiment was performed at a temperature of 650°C or more, at which point the organic matter was completely decomposed.

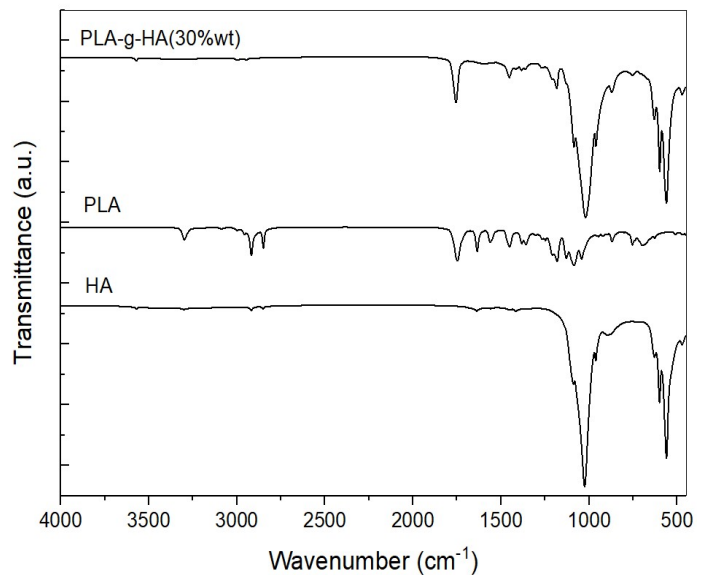


Fig. 1. FTIR spectra of HA, PLA and PLA-g-HA(30%wt).

$$\%Grafting = \frac{R_{HA} - R_{PLA-g-HA}}{R_{PLA-g-HA}} \cdot 100 \quad (1)$$

In the equation (1), R<sub>HA</sub> represents the residual weight of HA, and R<sub>PLA-g-HA</sub> represents the residual weight of PLA-g-HA. The TGA thermograms are illustrated in Fig. 2a. By adding HA at 30%wt, the residual weight of PLA-g-HA was found at 83.8%, and that of pristine HA was obtained at 95.7%, yielding the grafting weight fraction at 14.2%.

Thermal stability of the blend nanocomposites was also characterized by TGA. The TGA thermograms of the samples are shown in Fig. 2b. The onset of weight loss due to degradation of the sample (at 20 phr) took place around 300°C, and the weight was continued to decrease till around 440°C. It can be seen in TABLE I that the temperature at 50% weight loss as an indication of the destabilization is reported at 376°C, and the residual weight at 600°C remains at 13.3%. By increasing the grafted-HA (40 and 60 phr), the thermal stability of the samples is proceeded, in which the T<sub>onset</sub> is apparently shifted to higher temperature by 10-20°C.

TABLE I  
THERMAL STABILITIES OF THE BLENDS  
CONTAINING PLA-g-HA AT VARIOUS  
CONCENTRATIONS

Samples	T <sub>onset</sub> (°C)	T <sub>50%</sub> (°C)	T <sub>max</sub> (°C)	%Residue
20 phr	300	376.2	440	13.3
40 phr	310	375.3	443	13.7
60 phr	320	372.9	445	23.1

The results of %residue remaining at high temperature might show a little scatter at low concentrations of PLA-g-HA, in which it might be due to a random dispersion of the PLA-g-HA in the blends. However, at the highest concentration (60 phr), the highest amount of residue (about 23.1%) is attained. It is known that the addition of nano-filler into a matrix can enhance thermal stability of the nanocomposites. The existence of nano-HA exhibited the thermal improvement since it performs heat transfer blocking and prevents evaporation of small-molecule gases during the decomposition process [11]. Moreover, one of the major factors influenced thermal stability in nanocomposites involves the nature and strength of interfacial bonding between the matrix and the filler.

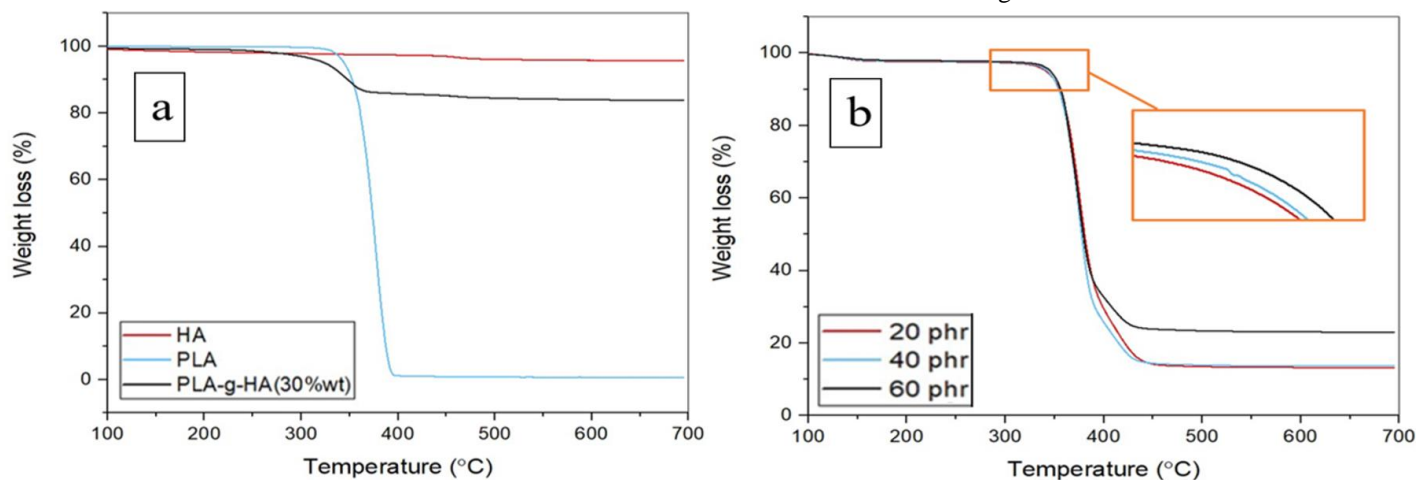


Fig. 2. TGA thermograms of (a) HA, PLA, PLA-g-HA(30%wt) and (b) the blends containing PLA-g-HA at different concentrations.

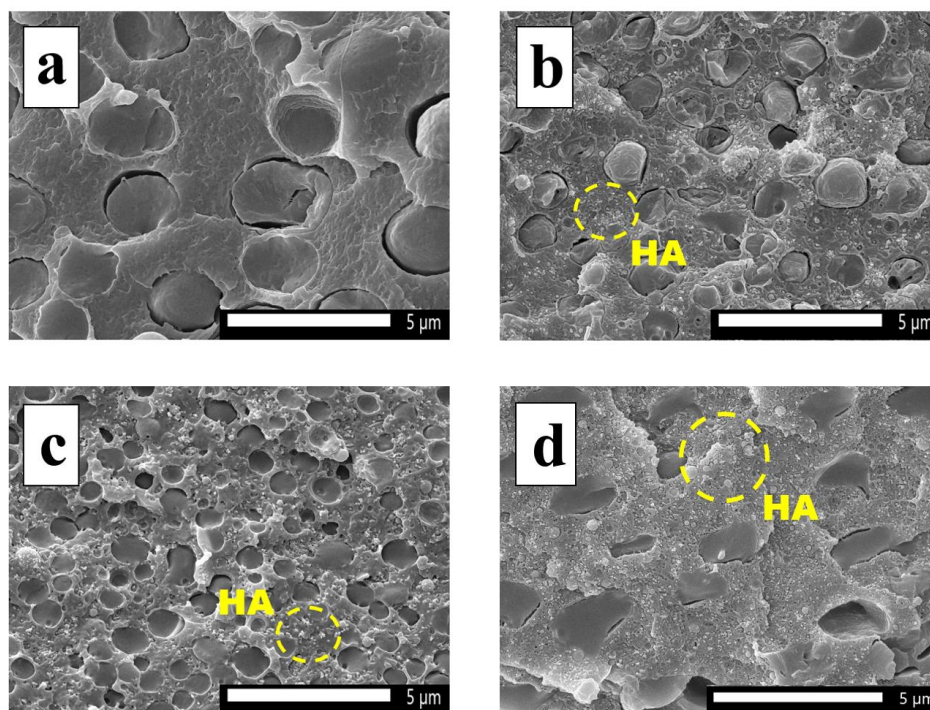


Fig. 3. SEM images of the blends with different PLA-g-HA contents: (a) 0 phr, (b) 20 phr, (c) 40 phr and (d) 60 phr.

Other researches have shown that by surface modification of HA would possibly enhance hydrogen bonding with the interested polymer matrix. Consequently, formation of intermolecular bonding between modified HA and PLA results in thermal stability enhancement. The obtainable results are in accordance with other studies [12, 13].

The morphology of PLA/PCL nanocomposites was examined by SEM analysis. The SEM images of the fractured film samples are illustrated in Fig. 3. The blends exhibit typical “island” morphologies, where small PCL spheres are randomly dispersed in the PLA matrix, indicating low interfacial adhesion between phases, which validates their immiscibility. The size of PCL spheres appears less than 5 μm. By adding PLA-g-HA at 40 phr, it is noticeable that the dispersed PCL phase tends to breakup into smaller micro-domains (about 1-2 μm) compared with the result at 20 and 60 phr, suggesting better compatibility between PLA and PCL phases. At 60 phr, the grafted-HA is densely dispersed in some area of the PLA matrix, and partially aggregates around the phase boundary of PCL. The previous study showed that the compatibility between PLA and PCL phases was increased by the addition of polyester-grafted-cellulose nanofillers, mainly located at the interface, and acting as a compatibilizer [12]. Since loading the nanofiller into the blends results in the migration of nanoparticles into the polymeric phases, providing stronger affinity and lower interfacial tension, enhancing compatibility in the blends.

$$\chi_c^a = \frac{1}{1 - x^a} \left[ \frac{\Delta H_m}{\Delta H_{m0}} \right] \cdot 100 \quad (2)$$

$\chi_c^a$  represents the degree of crystallinity of the component a,  $\Delta H_m$  is the melting enthalpy,  $\Delta H_{m0}$  is the melting enthalpy for a 100% crystalline material and  $x^a$  is the percentage of the crystalline component a in the sample. The value taken for  $\Delta H_{m0}$  of PCL was 148 KJ/mol, while for PLA was 93 KJ/mol [13].

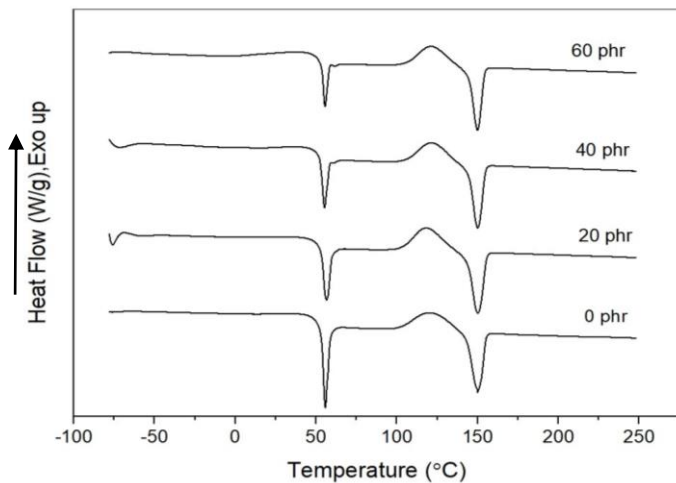


Fig. 4. DSC thermograms of the blends containing PLA-g-HA at different concentrations.

DSC measurements were performed to study the thermal properties of the blend nanocomposites. The DSC thermograms taken from the second heating scans of the blend nanocomposites are exhibited in Fig. 4. It is observed that there are three dominate stages of transition. Firstly, an endothermic transition (melting temperature,  $T_m$  of PCL, which partially overlapped with the glass transition temperature,  $T_g$ , of PLA. Next, an exothermic transition (crystallization temperature,  $T_c$ ), and endothermic transition ( $T_m$ ) of PLA phase are accompanied. To further investigate the crystallization behavior of the samples, the %crystallinity was calculated using equation (2) [13]. The measured parameters ( $T_m$  and %crystallinity) of the nanocomposites are reported in TABLE II. For PLA phase, the results show a remarkable increase in %crystallinity (24.2%) when PLA-g-HA is added. At 60 phr, the highest crystallinity is reached at 26.7%. The higher crystallinity suggests the presence of more crystallites within the blend nanocomposites. The surface modified HA not only acts as heterogeneous nucleation, creating the formation of new crystallites, it also enhances the growth of existing spherulites [12]. Moreover, improved interfacial adhesion between modified HA and PLA might additionally enhance transcrystallinity in the nanocomposites. While, a slight decrease in %crystallinity is observed in PCL phase.  $T_c$  of the blend is found at 120°C in comparable with those of the blend nanocomposites.  $T_m$  of PLA and PCL nanocomposites is slightly decreased compared to that of the blend, suggesting a better compatibilization between phases or plasticization effect. Typically, around the  $T_g$  of polymer matrices, the molecular chains become more flexible and chain mobility is enhanced. Additionally, the elastic modulus decreases when the PCL content is increased, due to the plasticizer effect of the PCL, as reported also by Simoes et al. [14].

TABLE II  
THERMAL STABILITIES OF THE BLENDS WITH  
PLA-g-HA AT VARIOUS CONCENTRATIONS

Samples	PCL		PLA		
	$T_m$ PCL (°C)	$\chi_c^a$ PCL	$T_c$ PLA (°C)	$T_m$ PLA (°C)	$\chi_c^a$ PLA
0 phr	56.4	7.6	120.2	152.6	18.4
20 phr	56	7.5	118.1	150.1	24.2
40 phr	55.5	6.3	121.3	150.1	24.9
60 phr	55.2	5.8	121.3	149.9	26.7

#### IV. CONCLUSION

The PLA-g-HA was successfully prepared by a melt process and incorporated in the PLA/PCL blends. Increasing in the grafted HA concentration, thermal stability of the blend nanocomposites was improved, whereas the %crystallinity was also elevated. The addition of PLA-g-HA rendered better compatibility of the blends, in which smaller sizes of dispersed phase was obtained.

#### ACKNOWLEDGMENT

The authors would like to thank the Program of Petrochemistry and Polymer Science, Faculty of Science, Chulalongkorn University for partially financial support.

#### REFERENCES

- [1] K. E. Uhrich, D. Abdelhamid, "Biodegradable and bioerodible polymers for medical applications". Biosynthetic Polymers for Medical Applications. Woodhead Publishing Series in Biomaterials, pp. 63-83, 2016.
- [2] L. Grøndahl, K.S. Jack, C.S. Goonasekera, "Composite materials for bone repair". Biomedical Composites (2<sup>nd</sup> Edition). Woodhead Publishing Series in Biomaterials, pp. 83-110, 2017.
- [3] N.J. Kim, S.J. Lee, A. Atala, "Biomedical nanomaterials in tissue engineering". Nanomaterials in Tissue Engineering ( Fabrication and Applications) . Woodhead Publishing Series in Biomaterials, pp.1-25, 2013.
- [4] X. Zhao et al. "Enhanced interfacial adhesion by reactive carbon nanotubes: new route to high-performance immiscible polymer blend nanocomposites with simultaneously enhanced toughness, tensile strength, and electrical conductivity". ACS Appl. Mater. Interfaces. 10:8411-8416, 2018.
- [5] J. Sarfraz et al. "Nanocomposites for Food Packaging Applications: An Overview". Nanomaterials. 11(1):10, 2021. <https://doi.org/10.3390/nano11010010>
- [6] S. Hassanajili et al. "Preparation and characterization of PLA/PCL/HA composite scaffolds using indirect 3D printing for bone tissue engineering". Mater. Sci. Eng. C. 104:109960, 2019.
- [7] L. Peponia et al. "Thermally-activated shape memory effect on biodegradable nanocomposites based on PLA/PCL blend reinforced with hydroxyapatite". Polym. Degrad. Stab. 151:36-51, 2018.
- [8] K-L Ku et al. "Incorporation of surface-modified hydroxyapatite into poly( methyl methacrylate) to improve biological activity and bone ingrowth". R. Soc. Open Sci. 6(5):182060, 2019.
- [9] J-W Park et al. "High strength PLGA/Hydroxyapatite composites with tunable surface structure using PLGA direct grafting method for orthopedic implants". Compos. B. Eng. 178:107449, 2019.
- [10] W.H. Hoidy et al. "Preparation and characterization of polylactic acid/polycaprolactone clay nanocomposites". J. Applied Sci. 10(2):97-106, 2010.
- [11] W. Lai et al. "Hydroxyapatite/polyetheretherketone nanocomposites for selective laser sintering: Thermal and mechanical performances". e-Polymers. 20: 542-549, 2020.
- [12] J.O. Akindoyo et al. "Impact modified PLA-hydroxyapatite composites – Thermo-mechanical properties". Compos. Part A Appl. 107:326-333, 2018.
- [13] V. Sessini et al. "Effect of the addition of polyester-grafted-cellulose nanocrystals on the shape memory properties of biodegradable PLA/PCL nanocomposites". Polym. Degrad. Stab. 152:126-138, 2018.
- [14] C. Simoes, J. Viana, A. Cunha, "Mechanical properties of poly( $\epsilon$ -caprolactone) and poly(lactic acid) blends". J. Appl. Polym. Sci. 112:345-352, 2009.

# Decomposing cortical alpha suppression during dexterity performance in healthy aging participants

Rodiya Manor<sup>1,2</sup>, Dania Cheaha<sup>2,3</sup>, Nifareeda Samerphob<sup>1,2</sup>, Ekkasit Kumarnsit<sup>1,2\*</sup>

<sup>1</sup>Division of Health and Applied Sciences, Faculty of Science, Prince of Songkla University, Hat Yai, Songkhla, 90110, Thailand

<sup>2</sup>Biosignal Research Center for Health, Faculty of Science, Prince of Songkla University, Hatyai, Songkla 90112, Thailand

<sup>3</sup>Division of Biological Science, Faculty of Science, Prince of Songkla University, Hat Yai, Songkhla, 90110, Thailand

\*Corresponding author: Ekkasit Kumarnsit, E-mail address: rodiya.m@psu.ac.th

**Abstract:** There is a strong relationship between cognitive function and fine motor performance. A deteriorating motor performance might be caused by the aging brain. Electroencephalography (EEG) can be used to detect brain activity. Alpha suppression is a dominant activity during cognitive tests, especially dexterity tests. Therefore, it is interesting to investigate brain activity during motor performance. Age-related fine motor performance using dexterity test and brain activity were demonstrated in this study. Thirteen healthy young participants (20-35 yrs) and thirteen aging participants (60 yrs and over) were included in this study. All participants were assessed cognitive function using The Mini-Mental State Examination-Thai version (MMSE-Thai). The study included participants with MMSE-Thai scores of 24 or higher. Experimental procedures were performed with open-eyes, close-eyes, and dexterity test, respectively. In addition, the Fz, Cz, Pz, Oz, P3, P4, T5, and T6 EEGs were recorded simultaneously with all activities. Moreover, the dexterity time was also recorded. The results of this study indicated that older participants took longer to complete the dexterity test than younger participants (aging  $94.64 \pm 9.03$  s, younger  $60.38 \pm 5.16$  s). In addition, the percentage of alpha suppression in young participants revealed a significantly higher during dexterity test than resting state in all brain regions. However, aging participants showed significant differences in Fz, T5, and T6 regions. This finding indicated that increasing age affected motor task. In addition, the healthy young brain produced a distinct percentage of alpha suppression during performing. While in aging participant was not dominant. This finding can suggest that aging leads to the deterioration of the brain, resulting in impaired cognitive function. Moreover, alpha suppression can be one of the markers of brain deterioration or dysfunction, particularly in the context of aging, neurodegenerative disease, and cognitive impairment.

**Keywords:** Aging, Alpha suppression, Dexterity test, Electroencephalography (EEG), MMSE

## I. INTRODUCTION

Nowadays, the number of older people is growing, and the aging society is a global issue. Thailand is one of the countries that facing to this phenomenon. It is possible for aging people to experience some deterioration of their physical as well as cognitive functions. One of the common changes of aging is associated with slowing down the processing speed of the brain [1]. Moreover, the decline in cognitive performance was related to increasing age [2]. Electroencephalography (EEG) is a method that measures the electrical activity of the brain [3]. Therefore, it can be used to evaluate brain activity during cognitive tests. Alpha-band (8-13 Hz) EEG is associated with cognitive processes; however, it is suppressed during cognitive

performance [4]–[6]. Previous study reported that aging people showed slowing down of alpha EEG power during resting state [7], [8]. However, alpha suppression during resting state and cognitive performance, particularly fine motor performance, remains interesting in aging people. Therefore, the purpose of this study is to investigate the effect of aging on the suppression of alpha during resting state and modified dexterity test in people who are young and old.

## II. MATERIAL AND METHODS

### *Participants*

The study included twenty-six volunteers in two groups: thirteen young, healthy volunteers aged 20-35 and thirteen aging volunteers aged 60 and over. The sample size of

participants was calculated using n4Studies. Healthy young participants were recruited from Prince of Songkla University, Hatyai, Songkhla, Thailand while aging participants were members of the Center of Health Promotion and Rehabilitation of the elderly, Faculty of Nursing, Prince of Songkla University, Hatyai, Thailand. All participants were right-handed and had no history of stroke, epilepsy, neurological or psychiatric condition. This study, carried out in accordance with the principles laid down in the Declaration of Helsinki and approved by the Health Science Human Research Ethics Committee at Prince of Songkla University. Prior to the experimental study, all participants provided written informed consent.

### Task and Procedures

Participant sat in comfortable chair and all participants were screening cognitive function and cognitive impairment

using The Mini-Mental State Examination-Thai (MMSE-Thai) prior to the EEG recording. Participants with a score of 24 or higher were included in the study. The MMSE test is widely used to evaluate cognitive function. The maximum score on the test is 30 and below 24 is considered abnormal and indicates cognitive impairment. Therefore, participants with scores below 24 were excluded. The experimental protocol started after the EEG setup had been completed. While the experiment was being conducted, the EEG was continuously recorded. The experimental procedures started with 3 minutes of open eyes and 3 minutes with closed eyes, followed by a dexterity test with 25 small pegs and 25 holes and the dexterity test time was recorded. The timeline of experimental procedures was shown in Fig.1.

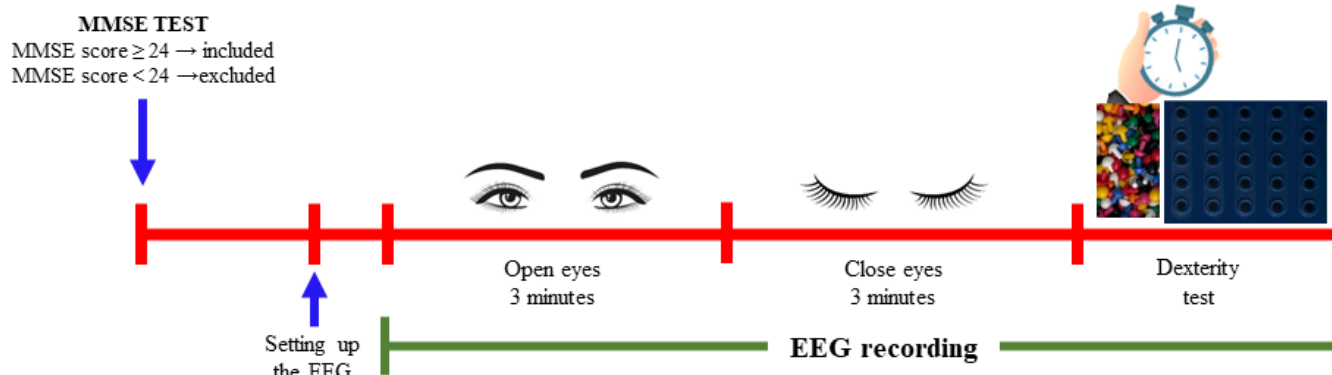


Fig. 1. Timeline of experimental procedures

### EEG recordings and Data processing

The EEG was recorded using the eego™ mini-series (ANT Neuro Company, Enschede, the Netherlands) and ASA Lab 4.10.2 acquisition system. EEG electrode cap was used to assist with electrode placement. The electrode site was located around Fz, Cz, Pz, Oz, P3, P4, T5, and T6 according to the international 10/20 system (Fig. 2). The impedance of electrodes was kept lower than 5 k $\Omega$ , the sampling rate was digitized at 2 kHz, and a band-pass filter of 4.5-45 Hz was used. The power line artifacts were eliminated using a notch filter at 50 Hz.

### Data analysis

The EEG data were analyzed in terms of power density of alpha oscillation (8-13 Hz). Then the percentage of alpha suppression in each activity (open-eyes and dexterity test) was calculated using the brain activity during closed eyes as a baseline interval. The percentage of alpha suppression was calculated using the formula (1).

$$\text{Alpha suppression (\%)} = \frac{\text{baseline interval band power} - \text{test interval band power}}{\text{baseline interval band power}} \times 100 \quad (1)$$

### Statistical analysis

All data were expressed as mean  $\pm$  Standard Error of Mean (S.E.M). The difference in dexterity time in young and aging was analyzed using an unpaired t-test. Moreover, percentage of alpha suppression during resting state with open-eyes and dexterity test in both groups was tested using one-way repeated measures ANOVA followed by Tukey's post hoc method for multiple comparisons. Statistical significance was accepted at  $P < 0.05$ .

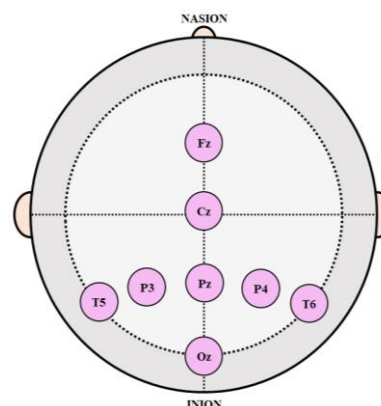


Fig. 2. Electrode site according to the international 10/20 system



### III. RESULTS

#### Dexterity time

The unpaired t-test analysis revealed that the dexterity time was significantly different between healthy young and aging participants ( $t = 3.427$ ,  $df = 24$ , and  $p < 0.01$ ). The older participants spend more time than healthy young with  $94.64 \pm 9.03$  s and  $60.38 \pm 5.16$  s, respectively (Fig. 3).

#### Percentages of alpha suppression

As shown in Fig. 4, one-way repeated measures ANOVA revealed that the percentage of alpha suppression significantly differed between resting state with open-eyes and cognitive performance using dexterity test among all brain regions [Fz: ( $F(3,48)=9.059$ ,  $p < 0.0001$ ); Cz: ( $F(3,48)=5.548$ ,  $p = 0.0024$ ); Pz: ( $F(3,48)=16.120$ ,  $p < 0.0001$ ); Oz: ( $F(3,48)=3.778$ ,  $p = 0.0136$ ); P3: ( $F(3,48)=12.16$ ,  $p < 0.0001$ ); (F(3,48)= 10.15,  $p < 0.0001$ ); T5: ( $F(3,48) = 9.303$ ,  $p < 0.0001$ ); T6: ( $F(3,48) = 8.399$ ,  $p = 0.0001$ ]. Turkey's post hoc test was used for multiple comparison analysis. The percentage of alpha suppression in healthy young participants was significantly higher in the dexterity test than the open-eyes session Fz: ( $p = 0.0004$ ), Cz: ( $p = 0.0042$ ), Pz: ( $p < 0.0001$ ), Oz: ( $p = 0.0294$ ), P3: ( $p < 0.0001$ ), P4: ( $p < 0.0001$ ), T5: ( $p = 0.0003$ ), and T6: ( $p = 0.0008$ ). Moreover,

the aging group showed higher significance in the Fz: ( $p = 0.0318$ ), T5: ( $p = 0.0354$ ), and T6: ( $p = 0.0036$ ) regions.

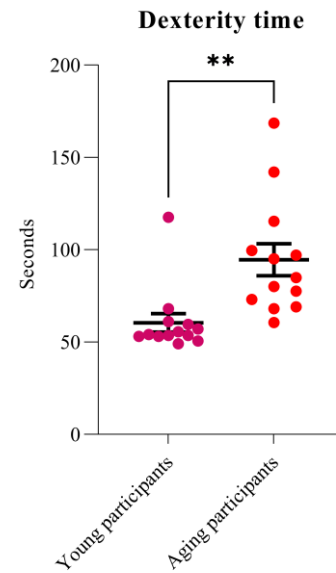


Fig. 3. Scatter plot of the dexterity time between young and aging participants. (\*\* $p < 0.01$ )

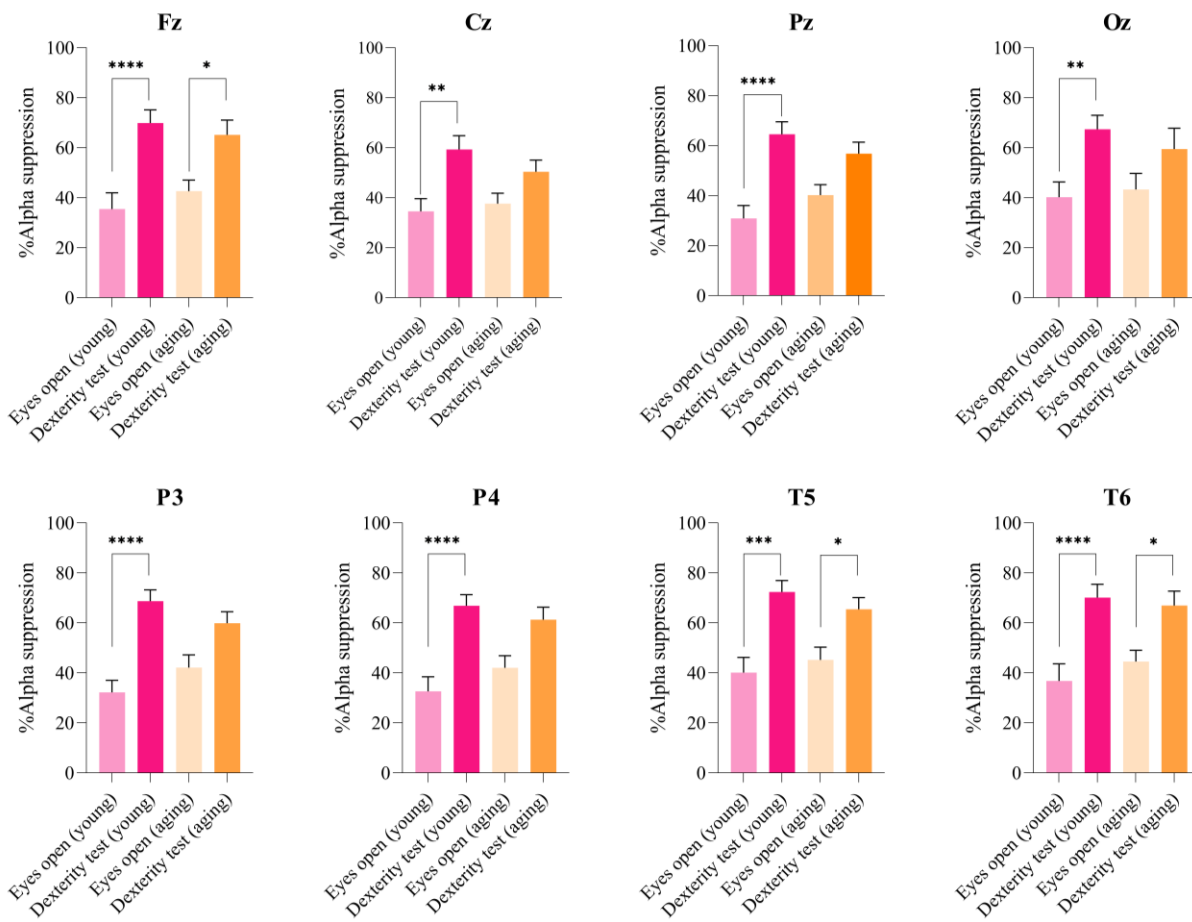


Fig. 4. Percentage of alpha suppression during open-eyes and dexterity test in healthy young and aging participants from Fz, Cz, Pz, Oz, P3, P4, T5, and T6 brain regions. (\* $p < 0.05$ , \* $p < 0.01$ , \*\*\* $p < 0.001$ , and \*\*\*\*  $p < 0.0001$ )

#### IV. DISCUSSION

This study was focused on cognitive functions respecting fine motor movement and agility. The results of the study suggested that the deterioration of motor performance, especially fine motor movement, declines due to the deterioration of brain function, particularly in the context of age. The dexterity test is widely used to assess fine motor skills including hand-eye coordination, agility, motor performance [9]. It has been reported in a previous study that age-related decreased dexterity performance (an increase in time taken to complete the test) [2], [10]. Alpha wave is a type of neural oscillation that occur in the frequency range of 8-13 Hz and are typically generated in the cortical regions and alpha modulations are predominately regulated by cortico-cortical networks with possible secondary influences from thalamo-cortical networks [11]. Moreover, the previous study reported that in wakefulness, alpha oscillations are the most salient EEG events and may contribute to top-down cognitive processes. These processes contributed with alpha rhythms propagate toward the posterior of the brain and that waves in cortex lead alpha oscillations in the thalamus [12]. Alpha activities are more prominent when the brain is at rest or performing a task that requires minimal cognitive effort [13], [14]. Therefore, during cognitive performance alpha oscillation was suppressed. This study showed that during a dexterity test in healthy young participants, alpha suppression was predominant. The finding is related to previous reports that explained alpha suppression associated with cognitive performance. Suppression of alpha was modulated by sensory stimulation, movement, attention, working memory, and mental tasks. Furthermore, higher motor control function suppressed alpha activity [11]. As a result, the suppression of alpha activity in all brain regions of healthy young participants may contribute to dexterity performance since all regions of cortical activation suppressed alpha rhythm. Despite this, only the Fz, T5, and T6 regions were significantly higher in aging participants during the dexterity test than during resting state. This is related to a previous study reported that the frontal region strongly modulated cognitive function such as attention, working memory, motor performance [15]. Therefore, alpha suppression continues to be prominent among healthy aging participants, since this region is one of the regions responsible for processing motor activity. Moreover, there was a significant difference in regions T5 and T6. This result is similar to a previous report about oscillatory alpha power suppression in the temporal region associated with awareness [16]. In addition, when participants are engaged in motor activities, they are forced to focus on the test, which causes alpha suppression in the temporal region. This research found that Alpha suppression is an effective indicator of cognitive processing and its relationship with aging.

#### V. CONCLUSION

The finding of this study confirmed that the increasing of age lead to a gradual decline in motor function, resulting in slower movement and reduced agility. Moreover, alpha suppression was dramatically higher during motor performance in all regions when compared to the resting state among young healthy adults. On the other hand, activity levels of dexterity performance were significantly higher than the resting state among aging participants in only the Fz, T5, and T6 regions. This finding indicated that alpha suppression can be one of the markers of brain deterioration or dysfunction, particularly in the context of aging, neurodegenerative disease, and cognitive impairment.

#### ACKNOWLEDGMENT

This research was supported by the graduate school and Division of Health and Applied Sciences, faculty of Science, Prince of Songkla University, Songkhla, Thailand and Education Hub for ASEAN Countries Scholarship supported by the Graduate School, Prince of Songkla University, Songkhla, Thailand.

#### REFERENCES

- [1] A. B. Roggeveen, D. J. Prime, and L. M. Ward, "Lateralized Readiness Potentials Reveal Motor Slowing in the Aging Brain," 2007. [Online]. Available: <https://academic.oup.com/psychogerontology/article/62/2/P78/548957>
- [2] L. Carment et al., "Manual dexterity and aging: A pilot study disentangling sensorimotor from cognitive decline," *Front Neurol*, vol. 9, no. OCT, Oct. 2018, doi: 10.3389/fneur.2018.00910.
- [3] M. Teplan, "FUNDAMENTALS OF EEG MEASUREMENT," 2002.
- [4] P. Sauseng et al., "A shift of visual spatial attention is selectively associated with human EEG alpha activity," *European Journal of Neuroscience*, vol. 22, no. 11, pp. 2917–2926, Dec. 2005, doi: 10.1111/j.1460-9568.2005.04482.x.
- [5] T. Ergenoglu, T. Demiralp, Z. Bayraktaroglu, M. Ergen, H. Beydagi, and Y. Uresin, "Alpha rhythm of the EEG modulates visual detection performance in humans," *Cognitive Brain Research*, vol. 20, no. 3, pp. 376–383, 2004, doi: <https://doi.org/10.1016/j.cogbrainres.2004.03.009>.
- [6] W. Klimesch, P. Sauseng, and S. Hanslmayr, "EEG alpha oscillations: The inhibition–timing hypothesis," *Brain Res Rev*, vol. 53, no. 1, pp. 63–88, 2007, doi: <https://doi.org/10.1016/j.brainresrev.2006.06.003>.
- [7] B. Scally, M. R. Burke, D. Bunce, and J.-F. Delvenne, "Resting-state EEG power and connectivity are associated with alpha peak frequency slowing in healthy aging," *Neurobiol Aging*, vol. 71, pp. 149–155, 2018, doi: <https://doi.org/10.1016/j.neurobiolaging.2018.07.004>.
- [8] R. Manor, D. Cheaha, E. Kumarnsit, and N. Samerphob, "Age-related Deterioration of Alpha Power in Cortical Areas Slowing Motor Command Formation in Healthy Elderly Subjects," *In Vivo*, vol. 37, no. 2, pp. 679–684, Mar. 2023, doi: 10.21873/invivo.13128.
- [9] K. E. Yancosek and D. Howell, "A Narrative Review of Dexterity Assessments," *Journal of Hand Therapy*, vol. 22, no. 3, pp. 258–270, Jul. 2009, doi: 10.1016/j.jht.2008.11.004.
- [10] L. Tesio, A. Simone, G. Zebellin, V. Rota, C. Malfitano, and L. Perucca, "Bimanual dexterity assessment: Validation of a revised form of the turning subtest from the Minnesota dexterity test," *International Journal of Rehabilitation Research*, vol. 39, no. 1, pp. 57–62, 2016, doi: 10.1097/MRR.000000000000145.
- [11] J. Foxe and A. Snyder, "The Role of Alpha-Band Brain Oscillations as a Sensory Suppression Mechanism during Selective Attention," *Front Psychol*, vol. 2, 2011, [Online]. Available: <https://www.frontiersin.org/articles/10.3389/fpsyg.2011.00154>
- [12] M. Halgren et al., "The generation and propagation of the human alpha rhythm," *Proceedings of the National Academy of Sciences*, vol. 116, no. 47, pp. 23772–23782, Nov. 2019, doi: 10.1073/pnas.1913092116.

- [13] O. M. Bazanova and D. Vernon, "Interpreting EEG alpha activity," *Neuroscience and Biobehavioral Reviews*, vol. 44. Elsevier Ltd, pp. 94–110, 2014. doi: 10.1016/j.neubiorev.2013.05.007.
- [14] W. Klimesch, M. Doppelmayr, H. Russegger, T. Pachinger, and J. Schwaiger, "Induced alpha band power changes in the human EEG and attention," 1998.
- [15] H. A. ElShafei, L. Fornoni, R. Masson, O. Bertrand, and A. Bidet-Caulet, "Age-related modulations of alpha and gamma brain activities underlying anticipation and distraction," *PLoS One*, vol. 15, no. 3, pp. e0229334-, Mar. 2020, [Online]. Available: <https://doi.org/10.1371/journal.pone.0229334>
- [16] L. Magazzini, P. Ruhnau, and N. Weisz, "Alpha suppression and connectivity modulations in left temporal and parietal cortices index partial awareness of words," *Neuroimage*, vol. 133, pp. 279–287, 2016, doi: <https://doi.org/10.1016/j.neuroimage.2016.03.025>.

# Antiproliferative activity of Kratinphiman mushroom (*Phellinus* sp.) extract against lung cancer and neuroblastoma cell lines

Kulrut Pichayaphinyo<sup>1</sup>, Surachai Pornpakakul<sup>2\*</sup>

<sup>1</sup> Program in Biotechnology, Faculty of Science, Chulalongkorn University, Bangkok 10330, Thailand

<sup>2\*</sup> Research Centre of Bioorganic Chemistry, Department of Chemistry, Faculty of Science, Chulalongkorn University, Bangkok 10330, Thailand, Surachai.p@chula.ac.th

**Abstract:** The Kratinphiman mushroom, a well-known medicinal mushroom of genus *Phellinus*, has been found in East Asia countries. In Thailand this mushroom has been found in the northeastern part of the country and it also is rich in biologically active compounds with therapeutic potential for anticancer, antioxidant, antidiabetic, anti-inflammation properties, hepatoprotective, and antimicrobial. In this study, the antiproliferative activity of the mushroom extracts against human lung cancer (A549) and neuroblastoma (SH-SY5Y) cell lines was evaluated via MTT cytotoxicity assay. The results showed that dichloromethane extract (CDE) exhibited antiproliferative activity with IC<sub>50</sub> values of 132.4 and 106.87 µg/mL against human lung cancer and neuroblastoma cell lines, respectively. Furthermore, ethyl acetate extract (CEE) exhibited antiproliferative activity against human neuroblastoma and lung cancer cell lines with IC<sub>50</sub> values of 138.64 µg/mL and >250 µg/mL, respectively.

**Keywords:** Antiproliferative, biological activity, *Phellinus* genus, Kratinphiman mushroom.

## I. INTRODUCTION

Kratinphiman mushroom, also known as Sanghuang, Meshimakobu and Sanghwang [1], belonging to genus *Phellinus* in the family of Hymenochaetaceae, is one of well-known medicinal mushroom in China and Thailand [1-2]. There are around 220 species in the genus *Phellinus* and mainly distributed in East Asia countries such as China, Korea, and Japan [1]. The characteristics of mushroom are perennial pileated fruiting bodies as woody-hard, hoof or disc-shaped or horseshoe-shaped, imbricate hymenophores show a difference color, including yellowish to rusty brown to grey to black. Hymenium is brown color with round to angular pores. Characterization under microscopy, branched of hyphal system with simple septate. The subhyaline that generate hyphae and aseptate had pale yellow color and thick wall. Basidia had four spores which were many forms such as broadly ellipsoid, subglobose to globose with smooth and thin to thick wall [3]. In Thailand, Kratinphiman mushroom is found on trees in Dipterocarpaceae, Fabaceae and Moraceae family [4] and more than 100 species of *Phellinus* mushroom have been found in the northeastern part of the country (from the database of the museum of medicinal mushrooms Mahasarakham University). The species of Kratinphiman mushroom in Thailand has been reported as *P. rimosus*, *P. linteus*, *P. igniarius*, *P. tuberculosis* and *P. pomaeos*

[4]. *Phellinus* mushroom contained polysaccharides, terpenoids, and phenolic compounds, which were associated to some therapeutical potencies such as anticancer, antioxidant, antidiabetic, anti-inflammatory properties, hepatoprotective, antiviral, and antimicrobial activity [5]. In Thai traditional medicinal uses, Kratinphiman mushroom was used in treatment of cancer, diabetes, hypertension, infected wound, abscess, melasma, and fever [4]. Decoction of this mushroom has been used for cancer and diabetes therapy [4]. In addition, the powder of the mushroom mixed with water or honey is useful for skin therapy [4]. In the previous report, ethanol extract from fruiting bodies of *Phellinus* genus showed anticancer activity at a dose of 1,100 µg/mL against colorectal, gastric, prostate, and cervical cancer with percent inhibition of 41.8, 40.3, 44.8, and 11.9%, respectively [6]. Another report mentioned that the ethanol extract exhibited anticancer activity against gastric, cervical, liver, and lung cancer, lymphoma, and ascites carcinoma with IC<sub>50</sub> values of 110.7, 314.2, 361.6, 531.7, and 184.0, and 92.0 µg/mL, respectively [7-8]. Moreover, the percent inhibition of the mushroom extract against mouse hepatocellular carcinoma cell and mouse melanoma cell showed potential activity at a dose of 200 and 1000 g/day with percent inhibition of 76.18 and 29.71%, respectively [8]. Isolation of the ethanol extracts of *Phellinus* fruiting bodies through chromatographic method afforded hispolon, meshimakobnol A, meshimakobnol B, atraclyenolone I, phellifuropyranone A, hispidin, igniarine, phelligridin G,

phelligrudin J, ergosterol, ergosterol peroxide, phellinignin A, phellinignin B, phellinignin D, conocenol A, conocenol B, phelliigniarin B, phellibaumin A, phellibaumin D, 3,4-dihydroxybenzalacetone, phelligrudin F and 4-(3,4-dihydroxyphenyl)but-3-en-2-one [9-18]. However, there is no report on antiproliferative activity of the extract of *Phellinus* mushrooms against human neuroblastoma cancer cell lines (SH-SY5Y). In this study, we reported the antiproliferative activity of the mushroom extracts against two human cancer cell lines, lung cancer (A549) and human neuroblastoma (SH-SY5Y).

## II. METHODOLOGY

### General experimental procedures

All organic solvents such as dichloromethane, ethyl acetate and methanol were purchased from Sigma-Aldich, Burdick & Jackson, and Merck® (Germany). Dulbecco's Modified Eagle Medium (DMEM) medium, fetal bovine serum (FBS), penicillin, sodium pyruvate solution and MTT (3-[4,5-dimethylthiazol-2-yl]-2,5-diphenyltetrazolium bromide) were purchased from Thermo Fisher Scientific (U.S.A). Human cancer cell lines, lung cancer (A549) and human neuroblastoma (SH-SY5Y cell lines), were provided from Chanat Aonbangkhen Lab (Chulalongkorn University). In vitro assay was conducted in 96-well microplate purchased from SPL Life Sciences Co., Ltd. (Korea).

### Mushroom materials

Kratinphiman mushroom, fruiting bodies of the mushroom, was collected in Ubon Ratchathani, Thailand in 2020. The mushroom was dried, powdered and stored at -20 °C until use.

### Identification of the mushroom

The characterization of Kratinphiman mushroom was identified on basis of morphology observation such as the shape and color of pileus, the color of hymenophores, and the texture of fruiting body [19].

### Extraction of the mushroom

The dried mushroom powders were extracted by maceration, reflux, and decoction as shown in Fig 1. The dried mushroom powders (600 g) were extracted by maceration in methanol with methanol/material ratio of 2.5:1 (v/w) (x5 times) at room temperature for 24 h followed by filtration and evaporation of the solvent. The methanol extract (26.7 g) was partitioned with four organic solvents as hexane, dichloromethane, ethyl acetate and methanol to give hexane extract (CHE) (2.39 g), dichloromethane extract (CDE) (2.32 g), ethyl acetate extract (CEE) (1.10 g) and methanol extract (CME) (3.16 g) respectively. The mushroom powder was extracted with water under reflux and decoction. The 5 g of mushroom powder in water at a ratio of 1:15 (w/v) was refluxed for 8 h and the mixture was then filtered under vacuum, followed by lyophilization to give RE extract (0.65 g).

The 10 g of mushroom powder was decocted with 400 ml water for 8 h and the mixture was then filtered under vacuum, followed by lyophilization to give DE extract (0.40 g).

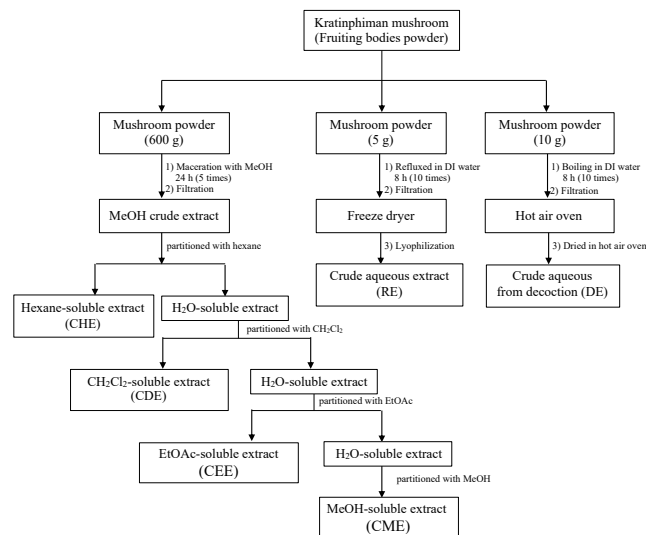


Fig. 1 The extraction procedure of Kratinphiman mushroom

### Nuclear magnetic resonance spectrometer (NMR)

The <sup>1</sup>H NMR spectra was recorded on Jeol 500 MHz NMR spectrometer. Chloroform (CDCl<sub>3</sub>) was used as NMR solvent. Chemical shifts were given in ppm (δ) and referenced to the residual solvent signal at 7.26 ppm. MestReNova NMR software version 14.1.1 was used to preprocess the spectral data.

### Cell culture

Human lung cancer (A549) cell line in Dulbecco's Modified Eagle Medium (DMEM) medium and human neuroblastoma (SH-SY5Y) cell line in Dulbecco's Modified Eagle Medium F12 (DMEM/F12) (containing 10% FBS, 100 µg/mL streptomycin and 100 U/mL penicillin) were cultured in an incubator at 37 °C in a humidified atmosphere containing 5% CO<sub>2</sub> [16].

### Sample preparation

For a stock solution, the dichloromethane (CDE), ethyl acetate (CEE) and methanol (CME) extract (10 mg each) were dissolved in 100 µL DMSO while reflux (RE) and decoction (DE) extract (10 mg each) were dissolved in 100 µL sterilized water. The stock solution (CDE, CEE and CME extracts) was diluted in DMSO to give concentration of 10, 15, 20 and 25 mg/mL and then the solution (10 µL) of each extract was further diluted with 990 µL of the culture medium to result in the final concentration of each extract and DMSO per well of 100, 150, 200 and 250 µg/mL and of 1% v/v, respectively.

A 5 mg/mL of MTT solution was prepared by dissolving 0.005 g of MTT powder in sterilized water (1 mL) and a clear yellow solution of the MTT was then

stored in -20 °C until use. The stock MTT solution (10 µL) was diluted in 990 µL of culture medium to give the final concentration of MTT solution is 0.05 mg/mL.

#### Cytotoxicity assay (MTT assay)

Two human cancer cell lines (A549 and SH-SY5Y) were seeded in each 96-well plates at 1x10<sup>5</sup> cell/well (100 µL/well) and incubated at 37 °C under 5% CO<sub>2</sub> incubator for 24 hours. 100 µL of the extract with different concentrations were added into each test and incubated at 37 °C under 5% CO<sub>2</sub> for 24 hours. The culture medium was removed and 100 µL of the MTT solution (0.05 mg/mL) was added. After incubation for 3 hours, the MTT was removed and the formazan remained in each well was dissolved by 100 µL DMSO. Then absorbance (Abs) of formazan was measured by a microplate reader at 570 nm. The cytotoxicity was expressed as IC<sub>50</sub> values (50% inhibitory concentration) [20].

$$\% \text{Inhibition} = 100 - \left( \frac{\text{Abs of sample} [-\text{blank}]}{\text{Mean Abs of negative control} [-\text{blank}]} \right) 100$$

A<sub>sample</sub> is absorbance of sample

A<sub>blank</sub> is absorbance of blank

A<sub>control</sub> is absorbance of control

### III. RESULTS AND DISCUSSION

In Kratinphiman mushroom is a Thai common name of mushrooms in the genus *Phellinus* [4]. The mushroom was identified on basis of morphology observation including the shape and color of pileus, the color of hymenophores, the texture of fruiting body [19]. For Kratinphiman mushroom in this study the shape of pileus was dark brown horseshoe-shaped. The hymenophores were cinnamon-brown fine pore surface and the texture of fruiting body was deeply cracked and woody-hard (Fig 2). Thus, morphological characterization of this mushroom was similar to *Phellinus igniarius* [21].



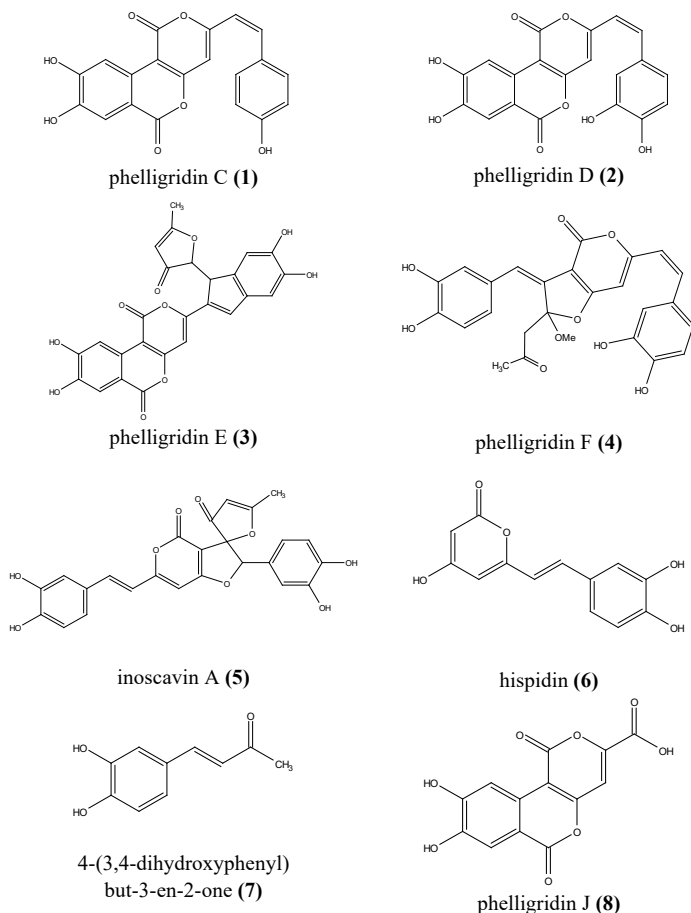
Fig. 2 Fruiting body of Kratinphiman mushroom

TABLE I

*In vitro* antiproliferative activity human cancer by MTT assay against two cell lines.

Treatment	IC <sub>50</sub> (µg/mL)	
	Lung cancer (A549)	Neuroblastoma (SH-SY5Y)
CDE	132.4	106.87
CEE	>250	138.64
CME	>250	>250
RE	>250	>250
DE	>250	>250

The results (TABLE I) showed that dichloromethane extract (CDE) exhibited cytotoxic activity against A549 and SH-SY5Y cell lines with IC<sub>50</sub> values of 132.4 and 106.87 µg/mL, respectively. It was obvious that the activity against A549 cell line was higher than the previous study (IC<sub>50</sub> values of 531.7 µg/mL) [7]. The previous result tested on the ethanolic crude extract was not very active due to its polar and nonpolar mixture content, while the dichloromethane partition from the methanolic crude extract provided polar bioactive compounds known for its anticancer substances [22]. Furthermore, the ethyl acetate extract (CEE) showed IC<sub>50</sub> values of 138.64 and >250 µg/mL against SH-SY5Y and A549, respectively. The methanol extract (CME), reflux extract (RE), and decoction extract (DE) showed the activity with IC<sub>50</sub> >250 µg/mL against both cell lines. In literature searching, the extract from *Phellinus* has never been tested on neuroblastoma SH-SY5Y cell line. Even though the phytochemicals of the *Phellinus* genus including alkaloids, flavonoids, and polysaccharides have been reported and phytochemicals of *Phellinus igniarius* exhibited antiproliferative activity against A549 (TABLE II) [13,15]. The bioactive compounds with anticancer activity were not specifically identified in this study. However, we analyzed the dichloromethane extract exhibited IC<sub>50</sub> values of 132.4 µg/mL against A549 and the <sup>1</sup>H NMR spectrum (Supplement data, Fig. 4) showed the similar chemical shift of compound 1-8 (Supplement data, Fig. 4) reported in the literature (6-8 ppm) as the anticancer agents of *Phellinus igniarius* as shown in TABLE II (Supplement data) [13, 15]. The chemical shifts of the CDE revealed that it contained mainly aromatic protons at δ<sub>H</sub> 8.33 (s), 8.30 (s), 7.86 (s), 7.51 (s), 7.24 (s), 7.16 (d, *J*=15.8 Hz), 7.07 (d, *J*=1.8 Hz), 7.05 (s), 7.01 (s), 6.98 (s), 6.88 (d, *J*=7.8 Hz), 6.76 (d, *J*=7.8 Hz), 6.71 (s), 6.55 (d, *J*=16.3 Hz), 6.51 (s) and 6.86 (d, *J*=8.1 Hz) (Supplement data, Fig. 4). Furthermore, some chemical shifts were different from 1-8. The compounds in the extract were probably active against both lung cancer and neuroblastoma cell lines we will isolate to pure compounds for further study on antiproliferative activity against A549 and SH-SY5Y cell lines.



**Fig. 3** Chemical structure of chemical constituents of anticancer agents of *Phellinus*

#### IV. CONCLUSION

In conclusion, the dichloromethane extract of Kratinphiman mushroom, collected from Ubon Rachathani, Thailand showed the highest antiproliferative activity against cancer cell lines of lung cancer (A549) and neuroblastoma (SH-SY5Y) cell lines compared to ethyl acetate extract (CEE), methanol extract (CME), reflux extract (RE), and decoction extract (DE) and it was a new finding that the extract of this mushroom exhibited antiproliferative activity against neuroblastoma (SH-SY5Y).

#### ACKNOWLEDGMENT

We would like to thank the Ratchadaphiseksomphot Endowment Fund of Chulalongkorn University for Research Center for Bioorganic Chemistry and the Department of Chemistry, Faculty of Science, Chulalongkorn University for financial support and instrumental facilities. Moreover, we also thank Dr. Chant Aonbangkhen laboratory for cytotoxicity assay.

#### References

- [1]Chen, H., Tian, T., Miao, H. and Zhao, Y. Y. Traditional uses, fermentation, phytochemistry and pharmacology of *Phellinus linteus*: a review. *Fitoerapi*. 113: 1-78, 2016.
- [2]Chen, W., Tan, H., Lui, Q., Zheng, X., Zhang, H., Lui, Y. and Xu, L. A Review: The bioactivities and phamacological applications of *Phellinus linteus*. *Molecules*. 24:1-24, 2019.
- [3]Azeem, U., Dhinra, G. S. and Shri, R. Pharmacological potential of wood inhabiting fungi of genus *Phellinus* Qué!.: An Overview. *Journal of Pharmacognosy and Phytochemistry*. 7(2): 1161-1171, 2018.
- [4]Chanboonyasit, F., Noophung, S., Thongprakob, K., Suthiklom, N., Klinhom, W. and Klinhom, U. Traditional uses of phiman or sang hwang mushroom in health care. *Journal of Thai Traditional & Alternative Medicine*. 18(2): 245-258, 2020.
- [5]He, P., Li, N. and Zhang, Y. The Phytochemistry and pharmacology of medicinal fungi of the genus *Phellinus*: A Review. *Food and Function*. 12: 1856-1881, 2012.
- [6]Ajith, T. A. and Janardhanan, K. K. Cytotoxic and antitumor activities of a polypore macrofungus *Phellinus rimosus* (Berk) Pilat. *Journal of Ethnopharmacology*. 84: 157-162, 2003.
- [7]Wang, F. F., Shi, C., Yang, Y., Fang, Y., Sheng, L. and Li, N. Medical mushroom *Phellinus igniarius* Induced cell apoptosis in gastric cancer SGC-7901 though a mitochondria-dependent pathway. *Biomedicine & Pharmacotherapy*. 102: 18-25, 2018.
- [8]Zhou, C., Jiang, S. S., Wang, C. Y., Li, R. and Che, H. L. Different immunology mechanisms of *Phellinus igniarius* in inhibiting growth of liver cancer and melanoma cells. *Asian Pacific Journal of Cancer Prevention*. 15(8): 3659-3665, 2014.
- [9]Chen, W., He, F. Y. and Li, Y. Q. The Apoptosis effect of hispolon from *Phellinus linteus* (Berkeley & Curtis) teng on human epidermoid KB cells. *Journal of Ethnopharmacology*. 105: 280-285, 2006.
- [10] Huang, G. J., Deng, J. S., Huang, S. S. and Hu, M. L. Hispolon induces apoptosis and cell cycle arrest of human hepatocellular carcinoma Hep3B cells by modulating ERK phosphorylation. *Journal of Agricultural and Food Chemistry*. 59: 7104-7113 (2011).
- [11] Kojima, K., Ohno, T., Inoue, M., Mizukami, H. and Nagatsu, A. Phellifuropyranone A: a new furopyranone compound isolated from fruit bodies of wild *Phellinus linteus*. *Chemical Pharmaceutical Bulletin*. 56(2): 173-175, 2008.
- [12] Jeon, T. I., Jung, C. H., Cho, J. Y., Park, D. K. and Moon, J. H. Identification of an anticancer compound against HT-29 cells from *Phellinus linteus* grown on germinated brown rice. *Asian Pacific Journal of Tropical Biomedicine*. 3(10): 785-789, 2013.
- [13] Mo, S., Wangm S., Zhou, G., Yang, Y., Li, Y., Chen, X. and Shi, J. Phelligrudins C-F: cytotoxic pyrano-[4,3-c][2] benzopyran-1,6-dione and furo[3,2-c] pyran-4-one derivatives from the fungus *Phellinus igniarius*. *Journal Natural Product*. 67: 823-828, 2004.
- [14] Wang, Y., Mo, S. Y., Wang, S. J., Li, S., Yang, Y. C. and Shi, J. G. A unique highly oxygenated pyrano [4,3-c][2] benzopyran-1,6-dione derivative with antioxidant and cytotoxic activities from the Fungus *Phellinus igniarius*. *Organic Letters*. 7(9): 1675-1678, 2005.
- [15] Wang, Y., Shang, X. Y., Wang, S. J., Mo, S. Y., Li, S., Yang, Y. C., Shim J. G. and He, L. Structures, biogenesis, and biological activities of Pyrano[4,3-c] isochromen-4-one derivatives from the fungus *Phellinus igniarius*. *Journal Natural Product*. 70(2): 296-299, 2007.
- [16] Thanh, N. T., Tuan, N. N., Kuo, P. C., Dung, D. M., Phuong, D. L., Giang, D. T. T., Wu, T. S. and Thang, T. D. Chemical constituents from the fruiting bodies of *Phellinus igniarius*. *Natural Product Research*. 32(20): 2392-2397, 2017.
- [17] Wu, P. F., Ding, R., Tan, R., Liu, J., Hu, E. M., Li, C. Y., Liang, G. Y. and Yi, P. Sesquiterpenes from Cultures of the Fungus *Phellinus igniarius* and Their Cytotoxicities. *Fitoterapia*. 140: 1-5, 2019.
- [18] Cao, Y., Liu, Y., Wang, G., Wang, W., Li, Y. and Xuan, L. Styryl pyranones with apoptosis activities from the sporocarps of *Phellinus igniarius*. *Phytochemistry Letters*. 44(1): 154-159, 2021.
- [19] Indrek, S. Systematics and ecology of selected taxa of wood-decaying basidiomycetes. Doctoral dissertation, Department of Philosophy in Mycology, Faculty of Science, Estonian University of Life Sciences, 2012.
- [20] Walker, J. M. Cancer cell culture. *Methods in Molecular Biology*. 731: 237-245, 2011.

- [21] Bakier, S., Wolkowycki, M., Zapora, E. and Zjawiony. *Phellinus igniarius*: A pharmacologically active polypore mushroom. *Natural Product Communications*. 11(7): 1043-1046, 2016.
- [22] Pandey, A. and Tripathi, S. Concept of standardization, extraction and pre phytochemical screening strategies for herbal drug. *Journal of Pharmacognosy and Phytochemistry*. 2(5): 115-119, 2014.



# Investigation of the GloA-homologous Gene Function under Stressful Conditions in *Pseudomonas aeruginosa*

Chalita Homjan<sup>1</sup>, Jintana Duang-nkern<sup>2</sup> and Adisak Romsang<sup>1,3\*</sup>

<sup>1</sup> Department of Biotechnology, Faculty of Science, Mahidol University, Bangkok 10400, Thailand,

<sup>2</sup> Laboratory of Biotechnology, Chulabhorn Research Institute, Bangkok 10210, Thailand

<sup>3</sup> Center for Emerging Bacterial Infections, Faculty of Science, Mahidol University, Bangkok 10400, Thailand, adisak.rom@mahidol.ac.th

**Abstract:** *Pseudomonas aeruginosa*, a pathogenic bacterium, was considered an important cause of infection in compromised host defense. Drug resistance in *P. aeruginosa* has emerged and it has become a serious issue in hospital settings. Since its multidrug resistance by nature, *P. aeruginosa* still poorly documented. The glyoxalase I, a gene product of *gloA*, widely revealed that exerted role in detoxify electrophile toxicity and this gene has not been well studied in *P. aeruginosa*. In this study, we investigated one of the *gloA*-homologous genes as *gloA3* in *P. aeruginosa*. First, the physiological role of *gloA3*<sup>-</sup> mutant against different oxidants studied through the gene mutation by using pKNOCK system. The mutant's ability to survive under stress environments analyzed by plate sensitivity assay to compare the bacterial growth with *P. aeruginosa* wild type. The results showed an increased susceptibility level against electrophile and hydrogen peroxide in the *gloA3*<sup>-</sup> mutant compared to that in the wild type. Mutant's phenotype confirmation conducted using expression vector harboring a full-length *gloA3* in the complementation assay. Last, the gene expression analysis during stress conditions was done by using reverse transcription PCR, and found an inducible pattern of the *gloA3* expression under an oxidant's exposure. Altogether, these data could provide role of *P. aeruginosa gloA3* in response to oxidative stress and would be one of the potential targets for drug development against *P. aeruginosa* infections.

**Index Terms**— *Pseudomonas aeruginosa*, *gloA*-homologous gene, *gloA3*, glyoxalase I, stress condition.

## I. INTRODUCTION

*Pseudomonas aeruginosa* is one the human pathogen that causes opportunistic infection leads to life-threatening acute and chronic infection, especially in patients with compromised immune system [1]. *P. aeruginosa* also has several mechanisms against host defensive immune system during infection and exhibits high resistance to disinfectants and wide range of antibiotics by nature, so *P. aeruginosa* infection it is difficult to treat [2]. Furthermore, in 2017, The World Health Organization (WHO) published *P. aeruginosa* as a priority list to guide development of new antibiotics from its carbapenem resistance [3]. For this reason, its antibacterial resistance cause *P. aeruginosa* recognized as an acute problem in hospital.

Glyoxalase I, which is typically encoded by the *gloA* gene, is an essential enzyme for bacteria to detoxify electrophile to its non-toxic compound [4]. The *gloA* encoding glyoxalase I widely revealed that exert a role in detoxifying pathway of electrophile such as methylglyoxal in *Escherichia coli* (*E. coli*) [5]. Methylglyoxal is natural toxic electrophile that cell generated during sugars utilization [6]. They contain highly reactive group that can interact with diverse molecule and push cell encounter with cellular redox stress [7,8]. When

cells are exposed to electrophile either produced by cells and exogenously supplied, the mutant strain rapidly lose viability [9]. This suggest that glyoxalase I is the major electrophile including methylglyoxal detoxification in *E. coli*.

Although *E. coli* has revealed quite a lot of relative information of this detoxification, but there is a lack of similar information in *P. aeruginosa* on the relative importance of different group of bacteria. In this study, we clarified one of the *gloA*-homologous genes as *gloA3* in *P. aeruginosa*. We focused on the physiological analysis for the *gloA3* under oxidative stress. The role of this gene could be a potential target for antibacterial therapy by possibly inhibiting methylglyoxal-related toxicity in *P. aeruginosa*.

## II. MATERIALS AND METHODS

### A. Bacterial strains and growth conditions

*P. aeruginosa* and *E. coli* strains were grown aerobically in Luria-Bertani (LB) medium which contains 1% Tryptone, 0.5% Yeast extract and 1% NaCl at pH 7.0. Bacterial strains grown at 37°C with continuous shaking at 180 rpm. The medium for *E. coli* growth, the medium was supplemented with 100 µg/ml ampicillin (Ap) whereas for *P. aeruginosa* growth, the medium was supplemented with 200 µg/ml carbenicillin (Cb) and 30 µg/ml gentamicin (Gm) as

required. All bacterial strains in this study were cultured, maintained and experiments were conducted following procedures approved by the Committee of Biosafety, Faculty of Science, Mahidol University (MUSC2022-029). Bacterial strains, plasmids and primers are listed in Table 1, 2, and 3 respectively.

TABLE I  
BACTERIAL STRAINS USED IN THIS STUDY

Bacterial strain	Purpose	Source
<i>E. coli</i> DH5 $\alpha$	Recombinant DNA construction	Laboratory stock
<i>E. coli</i> BW20767	Gene transfer into PAO1 via conjugation	Laboratory stock
<i>P. aeruginosa</i> PAO1	Wildtype strain	Laboratory stock
<i>P. aeruginosa</i> ( <i>gloA3</i> <sup>-</sup> )	<i>gloA3</i> mutant, knockout on <i>gloA3</i> coding region	This study

TABLE II  
PLASMIDS USED IN THIS STUDY

Plasmid	Genotype or characteristic	Source
pBBR1MCS-4	Medium-copy-number expression vector, Ap <sup>r</sup>	Laboratory stock
pBBR <sub>Ap</sub> <i>gloA3</i>	pBBR1MCS-4 containing full length, Ap <sup>r</sup>	This study
pKNOCK <sub>Gm</sub>	Suicide vector, Gm <sup>r</sup>	Laboratory stock
pKNOCK <sub>Gm</sub> <i>gloA3</i>	pKNOCK containing <i>gloA3</i> coding region, Ap <sup>r</sup>	This study

TABLE III  
PRIMERS USED IN THIS STUDY

Primer	Sequence (5'→3')	Purpose
FLFW	TTCGTTTCGAGGGAATCGC	Full length forward primer
FLRV	GATCGACGGTCGTCAGCC	Full length reverse primer
KOFW	CTGGATTTTCGAGGAAGGC	Knockout forward primer
KORV	TGCCGTTGTGGTACTGGC	Knockout reverse primer

BT87	CACTTAACGGCTGACATGG	Reverse primer in pKNOCK
BT543	TGACGCGTCCTCGGTAC	Forward primer in pKNOCK
M13F	GTAAAACGACGGCCAGT	Universal forward primer
M13R	AAACAGCTATGACCATG	Universal reverse primer

#### B. Construction of *P. aeruginosa gloA3*<sup>-</sup> mutant

The *gloA3*<sup>-</sup> was constructed by using pKNOCK system, as a vector for knockout the gene with insertion inactivation concept. The knockout fragment of *gloA3* coding region was amplified by using an extracted *P. aeruginosa* PAO1 chromosome as template and with primers, primers KOFW and KORV. Amplification product was isolated and ligated into cloning vector pKNOCK<sub>Gm</sub> at *Sma*I site, then transformed into *E. coli* BW20767. The transformants was screened by PCR to confirm plasmid insertion and direction using primers BT543 and KOFW, and then sequenced to verify the correction of inserted plasmid, before integrate into *P. aeruginosa* PAO1 chromosome by using conjugation technique. The mutant strain named as *gloA3*<sup>-</sup> selected from the phenotype and confirmed by PCR amplification.

#### C. Construction of *P. aeruginosa* full-length *gloA3*

The full-length *gloA3* from the *P. aeruginosa* genome was amplified by using the extracted *P. aeruginosa* genomic DNA as a template with primers FLFW and FLRV, designed primer that cover full-length coding region of *gloA3* gene. A 484-bp PCR product was ligated with expression vector pBBR1MCS-4 into *Sma*I site. The plasmid that contains *gloA3* gene was transformed into the *E. coli* (DH5 $\alpha$ ). Transformants screened from blue white screening technique and PCR to confirm plasmid insertion using primers M13F and FLFW, and then sequenced to verify the correction of the constructed plasmid. This recombinant plasmid was used to study the complementation assay and over-expression of *gloA3* genes.

#### D. Growth curve assay

The parental strains PAO1 and *gloA3* mutants were grown in LB broth at 37°C. The growth was measured optical density (OD) at 600 nm at intervals of 0 h up to 30 h.

#### E. Plate sensitivity assay

The plate sensitivity assay was performed to determine the susceptibility level of mutants referred to PAO1 wild-type as previously described [10]. Briefly, each dilution of 10-fold serially diluted of exponential phase cell was spotted on plate were contained appropriate concentration of various oxidants including 250  $\mu$ M *N*-ethylmaleimide (NEM), 1200  $\mu$ M 2,2'-dipyridyl (DIPY), 450  $\mu$ M hydrogen peroxide (H<sub>2</sub>O<sub>2</sub>). The plates were incubated at 37°C overnight and observed the difference growth between these strains.

**F. Gene expression analysis by endpoint RT-PCR and real-time PCR**

To determine the *gloA3* expression level under with and without treatment, including 0.1 mM NEM and 1 mM H<sub>2</sub>O<sub>2</sub>, end-pointed RT-PCR and real-time PCR was performed as previously described [11]. Briefly, total RNA extraction was extracted from both with and without oxidant treatment and treated with DNase I. First strand of cDNA synthesis was performed to synthesize complementary DNA (cDNA) from mRNA template using Reverse Transcriptase. The cDNA was used as a template for PCR amplification using specific primers. Amplification of *16S rRNA* was required to standardize the expression.

**III. RESULT AND DISCUSSION**

**Identify *gloA3* in PAO1 genome database**

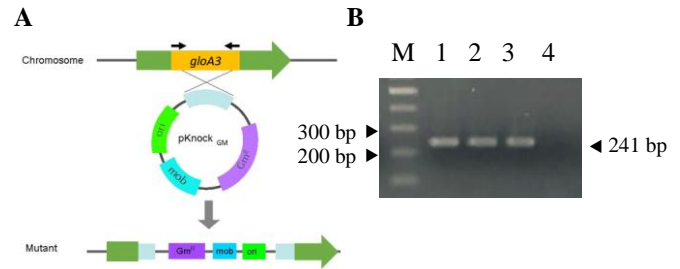
From Pseudomonas genome database, *P. aeruginosa gloA3* contains 531 nucleotides with 176 amino acids. Applying *in siligo* analysis in Pseudomonas genome database [12], a ribosome-binding site was found in front of the translational start site and a Rho-independent transcription terminator was predicted behind the stop codon. A glyoxalase I, gene product of *gloA3* shares 44.62%, 38.64%, 34.92% and 31.71% similarity to glyoxalase I in *Acinetobacter nosocomialis* [13], *E. coli* [14], *Listeria monocytogenes* [15] and *Streptococcus pyogenes* [16], respectively (Fig. 1). The sequences were obtained from the online genome database website, Kyoto Encyclopedia of Genes and Genomes (KEGG). Moreover, glyoxalase I in *E. coli*, require a metal ion for catalytic activity were previous described [17, 18]. The metal binding site was coordinated by 4 amino acid residues including His5, Glu56, His74 and Glu122. These residues were conserved among bacterial GloA-homologous proteins including GloA3 in *P. aeruginosa*. Using bioinformatics analyses that mentioned above, *P. aeruginosa gloA3* could be a putative *E. coli* GloA-homologous gene that is responsible for electrophile detoxification.

Pae	MSFNTEVQPGICMEPDAITQEVVFNHTMLRVKDKPKRSLDFYSRVVLGMR	
Ano	-----MRMLHTMLRVGNLEQSLKFYTEVLGMR	
Eco	-----MRLLLHTMLRVGDLQRSIDFYTKVVLGMR	
Lmo	-----MTAKMLHTCIRVKNLTESINIFYEKALGLK	
Spy	-----MKALHTCIRVKDLDSVAIFYTSAFFPK	
		*
Pae	LLRRLDFEGRFSTLYFLAMTRGEEVDPDAVDERQRYTFGRQSVLELTHN	
Ano	LLRKRDRYEGRFTLAFVGYGDEE-----NNTVLELTHN	
Eco	LLRTSENPEYKYSIAFVGYGPET-----EAVIELTYN	
Lmo	EVRRRKDFDFEFTLVYMAFEEG-----FELELTYN	
Spy	ENYRKDFPDSQFTLVYLALEGES-----YELELTYN	
		*
Pae	WGS-ESDDSQYHNGNDPRGFHICFVSPDLVAACERFETLVNFEV--	
Ano	WDT-SSYDL-----GNAYGHIAIGVDDAYKACEEIKARCGKVVRE	
Eco	WGV-DKYEL-----GTAYGHIALSVDNAEACEKIRQNGNVTRE	
Lmo	YDQKEAYDL-----GNGYGHILAVGVPDVRALLKEHQAAQYTVT-D	
Spy	YGH-GDYDL-----GNGYGHIALGSEHFEADHKHRQAGFPVT-D	
		*
Pae	-KPLDRGMKNVAIISDPDGYVVEIVQASLNGEMGRG	100%
Ano	AGPMKGGVTVIAFVDEPDGYKIELIQDANARN--	44.62%
Eco	AGPVKGGTIVIAFVDEPDGYKIELIEKDAQRGLGN	38.64%
Lmo	LKGLPGEPPFYFYLTPDGYKTEI IQDGAL----	34.92%
Spy	IKELADKSARYYI IQDDGYKIEVIDLNN-----	31.71%
		*

**Fig. 1.** Multiple sequence alignment of *gloA3* analyzed by an online Clustal Omega program. The amino acid sequence of *gloA3* in *P. aeruginosa*, *Acinetobacter nosocomialis*, *E. coli*, *Listeria monocytogenes* and *Streptococcus pyogenes* was compared. The conserved residues are marked with grey box. The asterisks (\*) indicate conserved metal binding residues for catalytic activity.

**P. aeruginosa *gloA3* mutant construction**

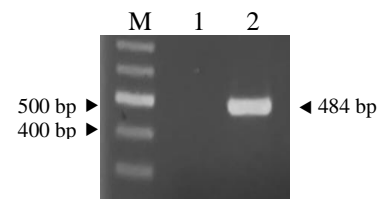
The *gloA3* mutant was constructed by pKNOCK system using an insertion inactivation technique as mentioned in the methods. The constructed mutants were confirmed by PCR amplification with primers, KOFW and BT87, as showed in Fig. 2B.



**Fig. 2.** Schematic diagram of *P. aeruginosa gloA3* knock-out technique (A) and construction confirmation by PCR amplification (B). The *gloA3* was confirmed by PCR amplification with primers, KOFW and BT87, to amplify an expected size of 241 bp; lane 1-3 represented a 241 bp fragment of *gloA3* coding region in the mutant; lane 4 represented negative control as the PAO1, and M showed bands from a commercial 100-bp DNA marker.

**Construction gene expression vector, pBBRIMCS-4**

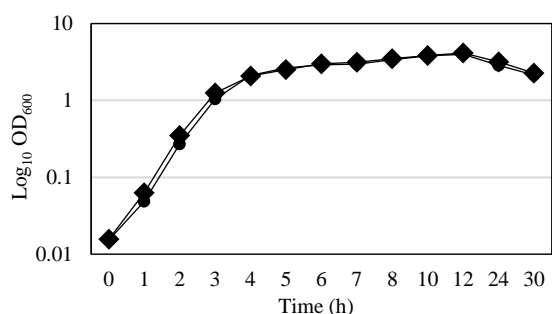
The 484-bp full-length *gloA3* was amplified, cloned into *E. coli*, and selected from blue white screening technique as previously mentioned in the methods. The recombinant plasmid was named pBBR*gloA3*. We picked colonies to confirm by PCR amplification with primers, M13F and FFW. The correct size of PCR product could be shown at 484 bp as shown in Fig. 3. Colony no.2 and 4 was exhibited the correct PCR size and chosen to confirm by DNA sequencing analysis. The result showed that it had 100% DNA sequence similarity to PAO1 *gloA3* in Pseudomonas genome database. The pBBR*gloA3* was transformed into *P. aeruginosa* PAO1 wild type and *gloA3*-knockout mutant by electroporation and named as PAO1/pBBR*gloA3* and *gloA3*<sup>-</sup>/pBBR*gloA3*, respectively.



**Fig. 3.** PCR amplification to confirm a full-length *gloA3* using primers, M13F and FFW, with an expected size of 484 bp; lane M determined the bands from a commercial 100 bp DNA marker; lane 1 was the PCR product amplified from the template of a blue colony; lane 2 represented a white colony with the expected size.

**Growth of *gloA3*-knockout strain**

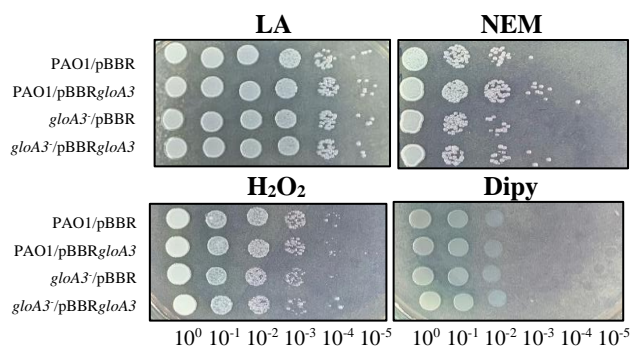
To determine the growth change of the constructed *gloA3* mutant compared to that in the parental strain PAO1 in Luria–Bertani (LB) broth at 37°C. The growth was measured optical density (OD) at 600 nm at intervals of 0 h up to 30 h. The growth pattern of the *gloA3* mutant was similar to that in the parental strain PAO1 as shown in Fig. 4.



**Fig. 4.** Growth curve of *P. aeruginosa* PAO1 (◆) and *gloA3*<sup>-</sup> (●) in Luria-Bertani (LB) broth at 37°C. The growth was measured at OD<sub>600</sub> until the 30-h incubation.

### The *gloA3*<sup>-</sup> mutant exhibits an increased susceptibility against *N*-ethylmaleimide and hydrogen peroxide

To determine a susceptibility level against oxidants in the *gloA3*<sup>-</sup> mutant compared to that in the wild type, the plate sensitivity assay was performed as previously mentioned in the methods. The results in Fig. 5 showed that the *gloA3*<sup>-</sup> mutant exhibited an increased susceptibility (10-fold) against an electrophilic agent, *N*-ethylmaleimide (NEM) compared with that in the wild type. NEM is an electrophilic agent that can modify the thiol groups in residues of protein, lead to enzyme inactivation and affect the balance of redox reactions in cells. Accordingly, NEM is a toxic substance for cell growth [19, 20]. Since the function of glyoxalase I, the gene product of *gloA3* is responsible to detoxify electrophilic species, particularly a methylglyoxal. The increased susceptibility to NEM observed in the *gloA3*<sup>-</sup> mutant may result from the cells having to cope with an increased electrophilic load. The results suggest that the *gloA3* may be one of the key processes for detoxifying an intracellular electrophile toxicity.



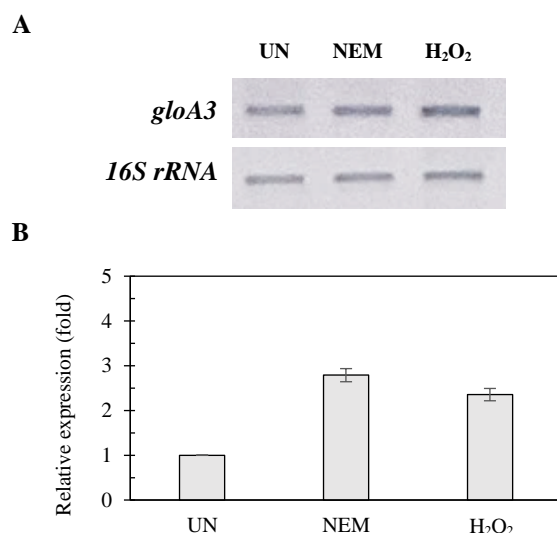
**Fig. 5.** Determination of the susceptibility level of *P. aeruginosa* strains PAO1 and *gloA3*<sup>-</sup> mutant under oxidants exposure. The exponential-phase cells grown in LB medium were 10-fold serially diluted, and spotted on plate containing oxidants as indicated. After incubation at 37°C for 18 h, growth between these strains was observed. The data presented were a representative of three similar results.

The results in Fig. 5 showed a slightly decreased susceptibility level in the *gloA3*<sup>-</sup> mutant towards hydrogen peroxide (H<sub>2</sub>O<sub>2</sub>). H<sub>2</sub>O<sub>2</sub> is one of reactive oxygen species (ROS) generated when bacteria grow aerobically and causes an oxidative damage [21]. Bacteria have to protect

themselves against H<sub>2</sub>O<sub>2</sub> toxicity. Fenton reaction is one of mechanism for H<sub>2</sub>O<sub>2</sub> decomposition using iron ions [22]. However, in iron chelating agent, DIPY, the *gloA3*<sup>-</sup> mutant exhibit no significant difference observed between tested strains, suggesting that H<sub>2</sub>O<sub>2</sub> might not decompose through the Fenton reaction. There are possibilities for the detoxification of H<sub>2</sub>O<sub>2</sub> through other pathways such as antioxidant enzymes including catalases [23].

### An increased *gloA3* expression under oxidant exposures

End-pointed RT-PCR and real-time PCR was performed to determine the expression level of *gloA3* under stress conditions. Total RNA was extracted from *P. aeruginosa* PAO1 under with and without oxidants treatment. After cDNA synthesis was done, PCR and gel electrophoresis were used to analyze the gene expression level as described in the methods. The results in Fig. 6 showed that the *gloA3* expression was increased under conditions treated with electrophilic agent (NEM) and hydrogen peroxide (H<sub>2</sub>O<sub>2</sub>). These results suggested that an increased *gloA3* expression was required under these stress conditions and correlated to the physiological analysis of the *gloA3*<sup>-</sup> mutant.



**Fig. 6.** Gene expression analysis. The expression of *gloA3* during oxidant exposure determined by end-pointed RT-PCR (A) and real-time PCR (B). *P. aeruginosa* PAO1 was induced with and without (UN) oxidants including NEM and H<sub>2</sub>O<sub>2</sub>. Relative expression was normalized to the *16S rRNA* and results are expressed as the fold-expression relative to the level of uninduced condition. The data shown are means and standard deviations of three independent experiments.

An increased expression of the *P. aeruginosa gloA3* under NEM treatment as shown in the Fig. 6. This is similar to the physiological function of the *gloA* in *E. coli*. In *E. coli*, the *gloA* is a member of the *nemRA-gloA* operon that plays a role in both regulation and reducing electrophiles including NEM and methylglyoxal [24]. This suggests that the *gloA3* in *P. aeruginosa* may have a similar function as the *gloA* in *E. coli* and might contribute to the NemRA system in *P. aeruginosa*. However, the *nemRA-gloA* operon was not found in the *P. aeruginosa* genome, only putative *nemRA* operon was predicted and needs to be further studied.

NemR was reported as a bleach-sensing transcription factor that involves in response to several oxidizing agents including H<sub>2</sub>O<sub>2</sub> and hypochlorous acid, HOCl [25]. Herein, *P. aeruginosa gloA3* could play a role in the oxidative stress response and may help the bacteria to protect against H<sub>2</sub>O<sub>2</sub> toxicity as shown in the other antioxidant proteins including GshAB [26], Tpx [27] and MsrAB [28]. However, this mechanism may not relate to the intracellular iron homeostasis in the cell but might be a part of other mechanisms such as catalases. Most bacteria possess catalase to neutralize H<sub>2</sub>O<sub>2</sub> and reduce ROS accumulation. *kata* encodes catalase and regulate by transcriptional regulator OxyR, which required the cys residues in its regulatory mechanism [29, 30].

#### IV. CONCLUSION

*P. aeruginosa gloA3* exhibited an important role under stress conditions. An inducible pattern of the *gloA3* expression under NEM and H<sub>2</sub>O<sub>2</sub> treatment was found and could provide an insight of the gene regulation involved in these stress condition. The promoter analysis of the *gloA3* gene and its transcriptional regulation is being investigated. Overall data could provide an important role of *P. aeruginosa gloA3* under oxidative stress. This could be a one of the potential targets for drug development against *P. aeruginosa* infections.

#### ACKNOWLEDGEMENT

This research was supported by Mahidol University (Fundamental Fund: fiscal year 2023 by National Science Research and Innovation Fund (NSRF)) under A.R.'s project (Grant number FF-053/2566). Parts of this work are from C.H. thesis submitted for a Master degree in Biotechnology from Mahidol University.

#### REFERENCES

[1] M. F. Moradali, S. Ghods, & B. H. Rehm. "Pseudomonas aeruginosa Lifestyle: A Paradigm for Adaptation, Survival, and Persistence," *Frontiers in cellular and infection microbiology*, vol. 7, no. 39, 2017.

[2] R. F. Langendonk, D. R. Neill, and, J. L. Fothergill. "The Building Blocks of Antimicrobial Resistance in *Pseudomonas aeruginosa*: Implications for Current Resistance-Breaking Therapies," *Front Cell Infect Microbiol*, vol. 11, no. 665759, 2021.

[3] G. V. Asokan, T. Ramadhan, E. Ahmed, and H. Sanad. "WHO Global Priority Pathogens List: A Bibliometric Analysis of Medline-PubMed for Knowledge Mobilization to Infection Prevention and Control Practices in Bahrain," *Oman Medical Journal*, vol. 34, no. 3, pp.184-193, 2019.

[4] U. Suttisansanee, and J. F. Honek. "Bacterial glyoxalase enzymes," *Seminars in cell & developmental biology*, vol. 22, no. 3, pp.285-292, 2011.

[5] S. L. Clugston, J. F. Barnard, R. Kinach, D. Miedema, R. Ruman, E. Daub, and J. F. Honek. "Overproduction and Characterization of a Dimeric Non-Zinc Glyoxalase I from *Escherichia coli*: Evidence for Optimal Activation by Nickel Ions," *Biochemistry*, vol. 37, no. 24, pp.8754-8763, 1998.

[6] I. Allaman, M. Bélanger, and P. J. Magistretti. "Methylglyoxal, the dark side of glycolysis," *Frontiers in neuroscience*, vol. 9, no. 23, 2015.

[7] Y. Kumagai, and Y. Abiko. "Environmental Electrophiles: Protein Adducts, Modulation of Redox Signaling, and Interaction with Persulfides/Polysulfides," *Chemical research in toxicology*, vol. 30, no. 1, pp.203-219, 2017.

[8] L. Changhan, & P. Chankyu. "Bacterial Responses to Glyoxal and Methylglyoxal: Reactive Electrophilic Species," *International journal of molecular sciences*, vol. 18, no. 1, pp.169, 2017.

[9] M. J. MacLean, L. S. Ness, G. P. Ferguson, and I. R. Booth. "The role of glyoxalase I in the detoxification of methylglyoxal and in the activation of the KefB K<sup>+</sup> efflux system in *Escherichia coli*," *Molecular microbiology*, vol. 27, no. 3, pp. 563-571, 1998.

[10] A. Romsang, J. Duang-Nkern, K. Saninjuk, P. Vattanaviboon, and S. Mongkolsuk. "*Pseudomonas aeruginosa nfuA*: Gene regulation and its physiological roles in sustaining growth under stress and anaerobic conditions and maintaining bacterial virulence," *PloS one*, vol 13, no.8, pp. e0202151, 2018.

[11] A. Romsang, J. Duang-Nkern, W. Wirathorn, P. Vattanaviboon, and S. Mongkolsuk. "*Pseudomonas aeruginosa* IscR-Regulated Ferredoxin NADP(+) Reductase Gene (*fprB*) Functions in Iron-Sulfur Cluster Biogenesis and Multiple Stress Response," *PloS one*, vol. 10, no. 7, pp. e0134374, 2015.

[12] G. L. Winsor, E. J. Griffiths, R. Lo, B. K. Dhillon, J. A. Shay, and F. S. Brinkman. "Enhanced annotations and features for comparing thousands of *Pseudomonas* genomes in the *Pseudomonas* genome database," *Nucleic Acids Research*, vol. 44, no. D1, pp.D646-653, 2016.

[13] B. Subhadra, S. Surendran, D. H. Kim, K. Woo, MH. Oh, and CH. Choi. "The transcription factor NemR is an electrophile-sensing regulator important for the detoxification of reactive electrophiles in *Acinetobacter nosocomialis*," *Research in Microbiology*, vol. 170, no. 3, pp.123-130, 2019.

[14] C. Lee, J. Shin, and C. Park. "Novel regulatory system *nemRA-gloA* for electrophile reduction in *Escherichia coli* K-12," *Molecular Microbiology*, vol. 88, no. 2, pp.395-412, 2013.

[15] A. Anaya-Sanchez, Y. Feng, J. C. Berude, and D. A. Portnoy. "Detoxification of methylglyoxal by the glyoxalase system is required for glutathione availability and virulence activation in *Listeria monocytogenes*," *PLoS pathogens*, vol. 17, no. 8, pp.e1009819, 2021.

[16] M. Zhang, C. L. Ong, M. J. Walker, and A. G. McEwan. "Defence against methylglyoxal in Group A *Streptococcus*: a role for Glyoxylase I in bacterial virulence and survival in neutrophils?," *Pathogens and disease*, vol. 74, no. 2, pp.ftv122, 2016.

[17] M. M. He, S. L. Clugston, J. F. Honek, and B. W. Matthews. "Determination of the structure of *Escherichia coli* glyoxalase I suggests a structural basis for differential metal activation," *Biochemistry*, vol. 39, no. 30, pp.8719-8727, 2000.

[18] G. Davidson, S. L. Clugston, J. F. Honek, and M. J. Maroney. "XAS investigation of the nickel active site structure in *Escherichia coli* glyoxalase I," *Inorganic chemistry*, vol. 39, no. 14, pp.2962-2963, 2000.

[19] G. Ferguson, and I. Booth. "Importance of Glutathione for Growth and Survival of *Escherichia coli* Cells: Detoxification of Methylglyoxal and Maintenance of Intracellular K<sup>+</sup>," *Journal Of Bacteriology*, vol. 180, no. 16, pp.4314-4318, 1998.

[20] Y. Umezawa, T. Shimada, A. Kori, K. Yamada, and A. Ishihama. "The uncharacterized transcription factor YdhM is the regulator of the *nemA* gene, encoding *N*-ethylmaleimide reductase," *Journal of bacteriology*, vol. 190, no. 17, pp.5890-5897, 2008.

[21] L. H. Li, Y. L. Shih, and J. Y. Huang. "Protection from hydrogen peroxide stress relies mainly on AhpCF and KatA2 in *Stenotrophomonas maltophilia*," *Journal of Biomedical Science*, vol. 27, no. 37, 2020.

[22] X. Liu, Y. Sang, H. Yin, A. Lin, Z. Guo, & Z. Liu. "Progress in the Mechanism and Kinetics of Fenton Reaction," *Ecology & Environmental Sciences*, vol. 3, no. 1, pp. 2573-2919. 2018.

[23] S. S. Wijeratne, S. L. Cuppett, and V. Schlegel, "Hydrogen peroxide induced oxidative stress damage and antioxidant enzyme response in Caco-2 human colon cells," *Journal of agricultural and food chemistry*, vol. 53, no. 22, pp.8768-8774, 2005.

[24] E. Ozyamak, C. de Almeida, A. P. de Moura, S. Miller, and I. R. Booth. "Integrated stress response of *Escherichia coli* to methylglyoxal: transcriptional readthrough from the *nemRA* operon enhances protection through increased expression of glyoxalase I," *Molecular microbiology*, vol. 88, no. 5, pp.936-950, 2013.

[25] M. J. Gray, W. Y. Wholey, B. W. Parker, M. Kim, and U. Jakob. "NemR is a bleach-sensing transcription factor," *The Journal of biological chemistry*, vol. 288, no. 19, pp.13789-13798, 2013.

[26] L. Wongsaroj, K. Saninjuk, A. Romsang, J. Duang-Nkern, W. Trinachartvanit, P. Vattanaviboon, and S. Mongkolsuk. "*Pseudomonas aeruginosa* glutathione biosynthesis genes play multiple roles in stress protection, bacterial virulence and biofilm formation," *PloS one*, vol. 13, no. 10, pp.e0205815, 2018.

[27] N. Somprasong, T. Jittawuttipoka, J. Duang-Nkern, A. Romsang, P. Chaiyen, H. P. Schweizer, P. Vattanaviboon, and S. Mongkolsuk. "*Pseudomonas aeruginosa* thiol peroxidase protects against hydrogen

peroxide toxicity and displays atypical patterns of gene regulation,” *Journal of bacteriology*, vol. 194, no. 15, pp. 3904-3912, 2012.

[28] A. Romsang, S. Atichartpongkul, W. Trinachartvanit, P. Vattanaviboon, and S. Mongkolsuk. “Gene expression and physiological role of *Pseudomonas aeruginosa* methionine sulfoxide reductases during oxidative stress,” *Journal of bacteriology*, vol. 195, no. 15, pp.3299–3308, 2013.

[29] Y. J. Heo, I. Y. Chung, W. J. Cho, B. Y. Lee, J. H. Kim, K. H. Choi, J. W. Lee, D. J. Hassett, & Y. H. Cho. “The major catalase gene (*katA*) of *Pseudomonas aeruginosa* PA14 is under both positive and negative control of the global transactivator OxyR in response to hydrogen peroxide,” *Journal of bacteriology*, vol. 192, no. 2, pp. 381–390, 2010.

[30] B. Pedre, D. Young, D. Charlier, A. Mourenza, L. A. Rosado, L. Marcos-Pascual, K. Wahni, E. Martens, A. G de la Rubia, V. V. Belousov, L. M. Mateos, and J. Messens. “Structural snapshots of OxyR reveal the peroxidatic mechanism of H<sub>2</sub>O<sub>2</sub> sensing,” *Proceedings of the National Academy of Sciences of the United States of America*, vol. 115, no. 50, E11623–E11632, 2018.

# Functional Characterization of *Pseudomonas aeruginosa* *ppk* encoding Polyphosphates Biosynthesis Enzyme in an Oxidative Protection from Host Immunity

Kritaun Thammakitkosol<sup>1</sup>, Chanikarn Jantharakarnkun<sup>1</sup>,  
Chularat Luangjindarat<sup>2</sup>, Pongsak Utaisincharoen<sup>2</sup>, Adisak Romsang<sup>1,3\*</sup>

<sup>1</sup> Department of Biotechnology, Faculty of Science, Mahidol University, Bangkok, Thailand

<sup>2</sup> Department of Microbiology, Faculty of Science, Mahidol University, Bangkok, Thailand

<sup>3</sup> Center for Emerging Bacterial Infections, Faculty of Science, Mahidol University, Bangkok, Thailand

\*Corresponding author. E-mail: adisak.rom@mahidol.ac.th

**Abstract:** In bacteria, polyphosphate (polyP) is a key molecule serving several biological functions including energetic metabolism, motility, and gene regulation. The *ppk* encoded a polyphosphate kinase (PPK) that is responsible for polymerization which regulates the polyphosphate homeostasis pathway. To investigate the role of polyP, the *ppk*-knockout mutant was constructed by an insertion-inactivation technique using pKNOCK system in *P. aeruginosa* PAO1. Here in this study, we found that the number of living *ppk*-knockout mutants inside the RAW264.7 murine-like macrophages was significantly decreased compared to that in the wildtype PAO1 treatment raised by an impairing of bacterial motility. Moreover, the oxidant susceptibility profiles among the PAO1 and the *ppk*-knockout mutant suggest that *P. aeruginosa* PPK could play a role in oxidative stress response including superoxide anion and hydrogen peroxide. To determine whether the alteration of oxidant-sensitive phenotype in the *ppk*-knockout mutant raised from the mutation of *ppk* gene in the genome or not, the complementation assay was performed by using an ectopic *ppk* expression in the expression vector, pBBR system. The resistance level towards oxidants was observed in the *ppk*-knockout mutant harboring the *ppk* expression plasmids compared to PAO1's level. The results suggested the complete restoration of the mutant's phenotype and clearly stated that the expression of *ppk* could be a part of the oxidative stress response in *P. aeruginosa*. Last, the nitric oxide production in the macrophages treated with the *ppk*-knockout mutant was less than that treated with the wildtype PAO1. These results imply the contribution of PPK in the phagocytosis inside the macrophage mechanism. Overall data presented that the maintenance of intracellular polyP levels via PPK mechanism could play a key role in bacterial survival under oxidative stress and macrophage response during infection.

**Index Terms**—*ppk*, polyP, *Pseudomonas aeruginosa*, macrophage, RAW264.7

## I. INTRODUCTION

*PSEUDOMONAS AERUGINOSA* is classified as an opportunistic pathogen and represented as the major cause of nosocomial infections in immunocompromised patients, cystic fibrosis, cancer-treated, HIV infections, and severe burn wounds. In some cases, the primary cause of death comes from virtually untreatable with currently known antibiotics [1]. Polyphosphate (polyP) are linearly conserved polymers in pathogenic bacteria, yeasts, and mammalian cells. In bacteria, polyP homeostasis is required for their biological functions, including growth, stress response mechanisms, and pathogenesis [2]. These polymers contain 10-10000 orthophosphate residues (Pi) linked by phosphor-anhydride bonds[3]. The intracellular polyP can be polymerized by polyphosphate kinase encoded by *ppk* [4] that is polymerized at the terminal phosphate of ATP into the intracellular polyP chain. On the other hand, the polyP

chain can be cleaved by exopolyphosphatase, encoded by *ppx*, to release free orthophosphate residues, which could play with various signaling molecules in terms of (p)ppGpp that regulate the survival ability under oxidative stress and bacterial virulence production [5].

Polyphosphate kinase (PPK) is highly conserved in several pathogenic bacteria such as *P. aeruginosa* and is essential for infection of *P. aeruginosa* in animal models [6]. During *P. aeruginosa* infection, the first immune system in mammals reacting to this infection is an innate immunity including neutrophils and macrophages [7] by phagocytosis. After being absorbed into the phagosome through one of several methods of receptor stimulation, microbes, and apoptotic cells are immediately exposed to reactive oxygen species (ROS) that perform a sterilization effect against bacteria [8] and nitric oxide synthesized by inducible nitric oxide synthase (iNOS) to play as a mediator and regulator of inflammatory responses and nitric oxide [9]. These reactive biomolecules directly damage bacterial enzymes thereby compromising pathogen fitness and curtailing microbial growth during immune responses [10].

## II. HYPOTHESIS STATEMENT

This study aims to *in vitro* and *in vivo* investigate the role of *P. aeruginosa ppk* in response to various bio-mimic oxidative stresses (ROS) such as superoxide anion and hydrogen peroxide. Moreover, the macrophage-*P. aeruginosa* interaction was analyzed. RAW264.7 murine-like macrophage was used in this study to determine both living intracellular bacteria and the nitric oxide production in the *P. aeruginosa*-treated macrophage cells.

## III. METHODOLOGY

### A. Bacterial growth and maintenance

*Pseudomonas aeruginosa* and *Escherichia coli* strains were grown in Luria-Bertani (LB) broth (Lennox, USA) at 37°C with continuous shaking at 180 rpm under aerobic conditions. For *E. coli* growth, the medium was supplemented with 100 µg/ml ampicillin (Ap) whereas for *P. aeruginosa* growth, the medium was supplemented with 200 µg/ml carbenicillin (Cb) and 30 µg/ml gentamicin (Gm) as required.

### B. Construction of *P. aeruginosa ppk* knockout mutant

In this study, mutants including *P. aeruginosa ppk* mutant was constructed using the pKNOCK<sub>GM</sub> system as described in [11]. Polymerase chain reaction (PCR) was used to amplify DNA fragment in the *ppk*-coding region with gene-knockout primers including GCCTCAACTTCATCGTCG (KOFW) and GTATCCACCACCTCCAGG (KORV) using genomic DNA isolated from *P. aeruginosa* PAO1 as the template. The pKNOCK<sub>GM</sub> digested with *Sma*I was ligated with a 350-bp PCR product to generate pKNOCK*ppk* and introduce it into *E. coli* BW20767. The correct transformants were screened by PCR amplification with specific primers to confirm the direction of *ppk* knockout fragment insertion. DNA sequencing was used to verify the correction of all inserted DNA sequences. pKNOCK*ppk* was transformed into *P. aeruginosa* PAO1 by conjugation with *E. coli* BW20767. Then, the conjugants were isolated by the gentamicin resistance (Gm<sup>r</sup>) phenotype. The *ppk* region on pKNOCK*ppk* was recombined onto the *ppk* knockout region on PAO1 chromosome resulting in a single homologous recombination and inactivates *ppk* then, the *P. aeruginosa ppk* mutant was confirmed by PCR analyses.

### C. Construction of *P. aeruginosa ppk* expression mutants

The functional *ppk*-coding region was amplified from PAO1 genomic DNA using the full-length gene primers including CCGGAAGATGAATGAATACG (FLFW) and GCTACAGCC TCAACGTGC (FLRV). The PCR products were cloned into the medium-copy-number expression vector pBBR1MCS-4 [12] at the *Sma*I site to generate pBBR*ppk*. pBBR1MCS-4 was commonly used as an expression plasmid in bacteria to express protein [13, 14]. These recombinant plasmids were then confirmed by PCR and DNA sequence analyses after introducing pBBR*ppk* into *E. coli* DH5α for plasmid maintenance.

### D. Bacteria treated with RAW264.7

To determine the survival ability of each mutant after macrophage treatment, the exponential phase bacteria were washed with sterile PBS buffer and adjusted the concentration to be equal. The bacteria were treated in the RAW264.7 culture with the specific ratio at MOI 1:1 and the viable count was done for calculating the number of bacteria treated (CFU). After incubation periods, the intracellular bacteria after macrophage phagocytosis was harvested. Finally, the number of viable invaded bacteria was calculated as bacterial CFU and used to compare among different strains.

### E. RAW264.7 growth and maintenance

RAW264.7 growth and maintenance were described in American standard from American Type Culture Collection (ATCC® TIB-71™). RAW264.7 was grown in DMEM supplemented with 0.5% L-glutamine and 5% fetal bovine serum and sub-cultured in every 3 days. The RAW264.7 was recommended for use within passage no. 18. After passage no. 18 performed the increasing induction efficacy and consequently phenotype changing [15].

### F. *ppk* susceptibility profiles against oxidative stresses

The plate sensitivity assay was performed to compare the bacterial growth on the plate referred to the oxidant susceptibility level between PAO1 wild type and *ppk* mutant strains. Plate sensitivity assay was done as previously described [14]. The exponential-phase cultures were adjusted to OD<sub>600</sub>, and 10-fold serially diluted in LB medium. Spotting 10 µl of each dilution on LA plates containing testing reagents including 225 µM of paraquat and 140 µM of hydrogen peroxide. The plates were incubated at 37 °C for 18 hours before colony-forming units (CFU) were scored. Percent survival was defined as the percentage of the CFU on plates containing an oxidant divided by the CFU on plates without oxidants. The experiments were repeated three times.

### G. RAW264.7 infected with bacterial heat killed lysates

The equal concentration of bacteria in the exponential phase was washed in sterile PBS buffer and boiled at 100°C for 30 min. The bacterial heat-killed lysates were ready to treat with macrophages or aliquots in microtubes for storage at -80°C. Then, the macrophage was treated with bacterial heat-killed lysates with MOI1:1.

### H. Nitric oxide detection

Griess assay [16] was used to determine the level of nitric oxide production. After a certain period of macrophage treatment via bacterial heat-killed lysates, the cell culture medium suspension was aliquoted and transferred to 96-well plates, then mixed well with the equal volume of Griess reagents including sulfanilamide and *N*-1-naphthylethylenediamine respectively. The OD540 was analyzed by a microplate reader using various determined concentrations of NaNO<sub>2</sub>, the concentration of NaNO<sub>2</sub> was



diluted to generate the standard nitric oxide at 0, 20, 40, 60, 80, and 100  $\mu$ M and used to generate the standard curve which then also was used to calculate the level of produced nitric oxide.

### I. Statistical and ethical statements

All groups of data sets were performed in MEAN  $\pm$  Standard Deviation. The Student's *t*-test and ANOVA analyses were used to determine a difference between data sets with *p*-value < 0.05 which were considered significant. *P. aeruginosa* and macrophage cell line in this study were cultured, maintained, and conducted the experiments following procedures approved by the Committee of Biosafety, Faculty of Science, Mahidol University (MUSC2022-029).

## IV. RESULTS AND DISCUSSION

### A. Identification of *P. aeruginosa ppk* gene cassette

According to Pseudomonas genome database, *P. aeruginosa ppk* is a small gene that composes 2211 nucleotides with 737 amino acids, encoded polyphosphate kinase enzyme (PPK). PPK catalyzes a polymerization reaction between intracellular inorganic polyphosphate and phosphate in ATP. The gene *ppk* is located behind *hemB* gene in the possibly shared operon and is probably regulated by AmrZ. The gene *ppk* is also located tail-to-tail with *ppx* gene that encodes exopolyphosphate enzyme, which catalyzes a hydrolytic reaction of inorganic polyphosphate to orthophosphate. Their regulations of intracellular polyphosphate polymerization particularly perform the importance for virulence factor production in several pathogenic bacteria including *P. aeruginosa* [6, 17].

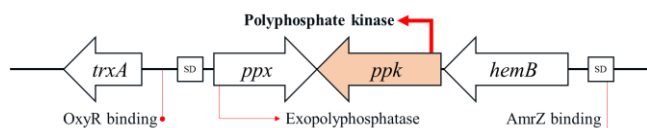


Fig. 1. Gene organization around the *ppk* gene in *P. aeruginosa* PAO1 genome. The gene *ppk* is located behind the gene *hemB* and tail-to-tail organized with the gene *ppx*. SD is referred to as a putative Shine-Dalgarno sequence.

### B. Construction of *P. aeruginosa ppk*-knockout mutant

The 350-bp *ppk*-coding PCR product was cloned into pKNOCK<sub>GM</sub> that was digested with *Sma*I, creating pKNOCK<sub>ppk</sub>. Correct ligation and transformation were analyzed by observing a shifted band (409-bp) from the non-inserted clone (as a control) in the phenol-extracted lysates using genomic PCR with specific primers, KORV and CACTTAACGGCTGACATGG (BT87). This recombinant plasmid was conjugated into *P. aeruginosa* PAO1 (Fig. 2A). The transformants were screened by genomic PCR amplification by specific gene-knockout primers similar to *E. coli* (Fig. 2B).

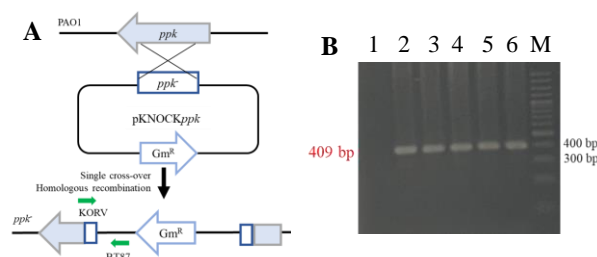


Fig. 2. Schematic diagram of *P. aeruginosa ppk* mutation (A) and confirmation of mutation by PCR amplification (B). Gel electrophoresis showed a size of PCR product amplified from *ppk*-knockout mutants by using primers BT87 and KORV, giving the expected 409-bp of PCR products. Lane 1, PAO1 wild type (no expected band); lane 2, *E. coli* containing pKNOCK<sub>ppk</sub>; lane 3, an extracted pKNOCK<sub>ppk</sub>; lane 4-6, *P. aeruginosa ppk* mutant; lane M, molecular weight marker (GeneRuler 100-bp DNA ladder; Thermo Scientific).

### C. Construction of *P. aeruginosa ppk*-expression mutants

The 2231 bp full-length *ppk* was cloned into *E. coli* DH5 $\alpha$  and selected from blue-white screening technique as mentioned generating pBBR<sub>ppk</sub>. The transformants were picked and confirmed using PCR amplification with AACAGCTATGACCATG and KORV. The correct PCR product could be obtained and confirmed by DNA sequencing analysis and resulted in 100% DNA sequence similarity to PAO1 *ppk* proposed in Pseudomonas genome database. Then, the pBBR<sub>ppk</sub> and its empty vector were transformed into *P. aeruginosa* PAO1 and *P. aeruginosa ppk* mutant using electroporation to generate PAO1/pBBR named wild type, *ppk*/pBBR named *ppk* and *ppk*/pBBR<sub>ppk</sub> (a complementation strain) as shown in Fig. 3A. All ectopic *ppk* expression strains were confirmed by PCR amplification using mutant cell lysate with specific primers as previously mentioned (as shown at the 1713-bp PCR product in Fig. 3B).

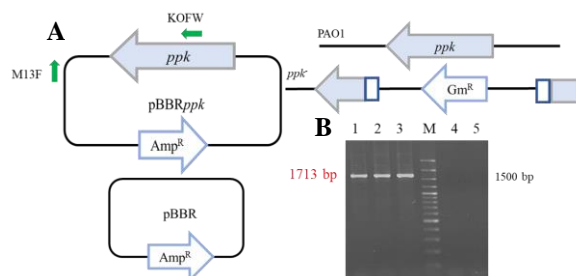


Fig. 3. Schematic diagram of full-length *ppk* expression vector (A) and the confirmation by PCR amplification (B). Gel electrophoresis showed a size of PCR product amplified from indicated *ppk* transformants by using described primers, giving the expected 1713-bp of PCR products. Lane 1, positive control (pBBR<sub>ppk</sub>); lane 2-3 *ppk*/pBBR<sub>ppk</sub>; lane 4, PAO1/pBBR, lane 5, *ppk*/pBBR; lane M, molecular weight marker (GeneRuler 100-bp DNA ladder; Thermo Scientific).

### D. Number of intracellular bacteria infecting RAW264.7

RAW264.7 cells were incubated together with either *P. aeruginosa* PAO1 or  $\Delta$ *ppk* mutants at MOI 1:1. The number of treating bacteria was in the range of  $10^5$  cells and the number of treated macrophages ( $10^5$  cells) was equal in each tested sample. After 1 hour of post-infection, gentamicin was used to kill the extracellular bacteria then the number of intracellular bacterial populations was

counted. The results in Fig. 4 showed the amount of intracellular *ppk* mutant was greater than the PAO1 treatment. These results suggested that the PPK directly or indirectly affected bacterial virulence [6], which may be through a defect in the swimming and swarming motility of *P. aeruginosa* [17]. As a similar observation in this research, the lower ability of the *ppk* mutant to escape the macrophage phagocytosis was found as shown in the higher number of the *ppk* mutant than the number of the PAO1 engulfed in the RAW264.7 cells (Fig. 4).

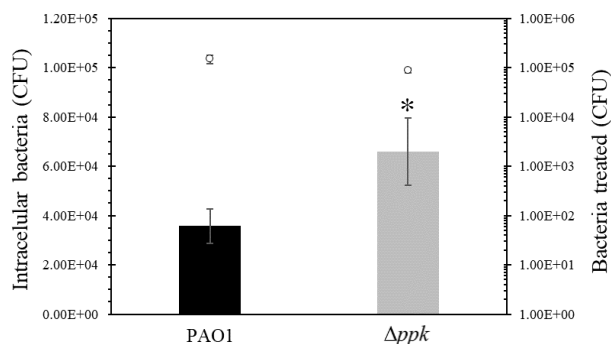


Fig. 4 CFU of bacterial viable count infecting RAW264.7 before incubation and the number of bacterial viable count infecting RAW264.7 (CFU) after incubation for 1 hour. Data shown were MEANS  $\pm$  SD from three biological replications and the asterisk (\*) indicates a significant difference with *p*-value < 0.05 compared to the PAO1's level.

#### E. *ppk* response profile to oxidative stress in *P. aeruginosa*

To determine a susceptibility level against oxidants and biocides in the *ppk*-knockout mutant (*ppk*/pBBR) compared to that in the wild type, the plate sensitivity assay was performed as previously described in the methods. The results in Fig. 5 showed that the *ppk* mutant exhibited a significantly increased susceptibility against conditions under exposure to inorganic hydroperoxide (hydrogen peroxide) and superoxide anion generator (paraquat) [18]. All Phenotypic differences towards paraquat and hydrogen peroxide in the *ppk* mutant were completely restored by an ectopic *ppk* expression via a pBBR*ppk* vector as shown in the complementation strain, *ppk*/pBBR*ppk* (Fig. 5). These results suggest that when *P. aeruginosa* infected to mammals, macrophage was going to be one of the primary immune response used to kill the bacterial invaders [19]. After the invaders were engulfed by macrophage, it would release several forms of ROS such as superoxide anion and hydrogen peroxide to eliminate the invading bacteria [20]. The results of the oxidant susceptibility profiles showed that *P. aeruginosa ppk* mutant exhibited an increased susceptibility against paraquat and hydrogen peroxide representing oxidative damage released by the macrophages [21]. Since the Ppk functions in polyphosphate polymerization and polyphosphate were also classified as a protein-like chaperone in bacteria. They could restore and re-fold protein that was damaged by oxidative damage depending on polyP length [22]. Therefore, the shorter chain of polyP could affect the efficacy of restoring and re-folding protein [23]. Together with the previous results, *P. aeruginosa* PPK plays an important role in contributing to bacterial virulence in both early phagocytoses through an

ability to motile and oxidative damages in the phagolysosome inside the macrophages.

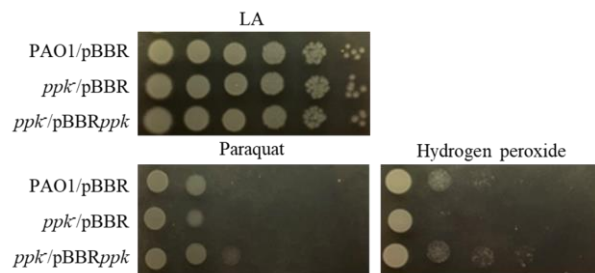


Fig. 5. Sensitivities of wild-type *P. aeruginosa* and *ppk* mutants to oxidants. Exponential-phase cells grown in LB medium were serially diluted (10-fold dilutions), and 10  $\mu$ l of each dilution was spotted onto LA containing either paraquat and hydrogen peroxide After incubation at 37°C for approximately 18 h, growth of the bacteria was observed. The data shown were representative of three similar independent results.

#### F. Nitric oxide determination detected by Griess's assay

Nitric oxide (NO) performs as a signaling molecule to recruit the immunity cells to the site of infection. The released NO from the bacteria-treated macrophage represents the ability of phagocytosis in the immune cells. If the macrophages can kill the invaders, no need to activate the NO production. To exhibit the measurement of released NO using the colorimetric method, the concentration of NaNO<sub>2</sub> was diluted to generate the standard nitric oxide as mentioned in method H and then detected at wavelength 540 nm which showed R<sup>2</sup> of 0.9974 and  $y = 0.0069x + 0.0462$  as a linear equation. To determine the NaNO<sub>2</sub>, each sample was prepared as bacterial heat-killed lysates as described. Each bacterial lysate from the wildtype PAO1 and the  $\Delta ppk$  mutant was then used to treat RAW264.7 cells at MOI 1:1.

After 24 hours of incubation, the samples were collected and transferred into a 96-well plate and supplied the Griess reagents. Then the measured optical densities were used to calculate the nitric oxide level through the equation,  $y = 0.0069x + 0.0462$ . The level of nitric oxide and relative nitric oxide production were shown in Table 1, the experiments were performed in three replications. The results in Table 1 showed that the NaNO<sub>2</sub> level treated with *P. aeruginosa* PAO1 lysate was increased (3.3 folds) compared to the control as an untreated RAW264.7 cell. Furthermore, the NaNO<sub>2</sub> of RAW264.7-treated with the  $\Delta ppk$  mutant lysate showed a significant decrease (62%) compared to that in the PAO1 treatment (Table 1). NO was released from the invaded macrophage to play a role in the signaling pathway resulting in macrophage physiological responses and pathogen-killing abilities [24], which could be suggested that the mutation on the *ppk* causes less virulence than that in the wildtype PAO1 leading to a decreased NO production in the *ppk* mutant. These results also correlated with the previous results showing an increased susceptibility level against several macrophage-mediated oxidants. The more killed bacteria, the less requirement of NO production and released to recruit other immune cells to the site of infection. A similar observation was found in RAW264.7 treated with *Porphyromonas gingivalis* LPS [25].

Table 1. *The level of nitric oxide produced by macrophages*

Samples	Level of NaNO <sub>2</sub> (μM) after 24 hours	Relative nitric oxide production (fold)
Untreated	8.472 ± 0.002	1.000
PAO1	28.038 ± 0.008	3.309
Δ <i>ppk</i>	17.406 ± 0.006	2.055

\*PAO1 and Δ*ppk* treated with RAW264.7 compared to untreated for 24 hours of treating time. Data shown were MEANS ± SD from three biological replications.

## V. CONCLUSION

Polyphosphate kinase (PPK) is responsible for the accumulation of intracellular polyP in *P. aeruginosa* [4]. In the previous report, the imbalance of polyP affects swimming and swarming motility [17]. Herein, the mutation on *P. aeruginosa ppk* exhibited impaired virulence as shown that the number of intracellular *ppk* mutants was greater than PAO1 after treatment with RAW264.7. Then mutation of *P. aeruginosa ppk* also caused an increased susceptibility against several oxidants including paraquat (a superoxide anion generator) and hydrogen peroxide. We suggest that *ppk* plays a role in the protection of bacteria against oxidative stress. Moreover, the enhanced nitric oxide level in a signaling pathway was found in the macrophage during *P. aeruginosa* PAO1; however, a less level was shown when treated with the *ppk* mutant. Overall data emphasize the role of *ppk* in oxidative stress and virulence during infection in macrophage cells.

## ACKNOWLEDGMENT

This research was supported by Mahidol University (Fundamental Fund: fiscal year 2023 by National Science Research and Innovation Fund (NSRF)) under A.R.'s project (Grant number FF-053/2566). Parts of this work are from K.T. thesis submitted for a Master's degree in Biotechnology from Mahidol University.

## REFERENCES

- Hirsch, E.B. and V.H. Tam, *Impact of multidrug-resistant Pseudomonas aeruginosa infection on patient outcomes*. Expert Rev Pharmacoecon Outcomes Res, 2010. **10**(4): p. 441-51.
- Rao, N.N. and A. Kornberg, *Inorganic polyphosphate regulates responses of Escherichia coli to nutritional stringencies, environmental stresses and survival in the stationary phase*. Prog Mol Subcell Biol, 1999. **23**: p. 183-95.
- Rao, N.N., M.R. Gómez-García, and A. Kornberg, *Inorganic polyphosphate: essential for growth and survival*. Annual review of biochemistry, 2009. **78**: p. 605-647.
- Kornberg, A., N.N. Rao, and D. Ault-Riché, *Inorganic polyphosphate: a molecule of many functions*. Annu Rev Biochem, 1999. **68**: p. 89-125.
- Malde, A., et al., *Functional characterization of exopolyphosphatase/guanosine pentaphosphate phosphohydrolase (PPX/GPPA) of Campylobacter jejuni*. Virulence, 2014. **5**(4): p. 521-33.
- Parks, Q.M. and J.A. Hobden, *Polyphosphate Kinase I and the Ocular Virulence of Pseudomonas aeruginosa*. Investigative Ophthalmology & Visual Science, 2005. **46**(1): p. 248-251.

- Hirayama, D., T. Iida, and H. Nakase, *The Phagocytic Function of Macrophage-Enforcing Innate Immunity and Tissue Homeostasis*. Int J Mol Sci, 2017. **19**(1).
- Moncada, S., R.M. Palmer, and E.A. Higgs, *Nitric oxide: physiology, pathophysiology, and pharmacology*. Pharmacol Rev, 1991. **43**(2): p. 109-42.
- Korhonen, R., et al., *Nitric oxide production and signaling in inflammation*. Curr Drug Targets Inflamm Allergy, 2005. **4**(4): p. 471-9.
- Flannagan, R.S., B. Heit, and D.E. Heinrichs, *Antimicrobial Mechanisms of Macrophages and the Immune Evasion Strategies of Staphylococcus aureus*. Pathogens, 2015. **4**(4): p. 826-68.
- Romsang, A., et al., *Gene expression and physiological role of Pseudomonas aeruginosa methionine sulfoxide reductases during oxidative stress*. J Bacteriol, 2013. **195**(15): p. 3299-308.
- Kovach, M.E., et al., *Four new derivatives of the broad-host-range cloning vector pBBR1MCS, carrying different antibiotic-resistance cassettes*. Gene, 1995. **166**(1): p. 175-176.
- Romsang, A., et al., *Mutation of the gene encoding monothiol glutaredoxin (GrxD) in Pseudomonas aeruginosa increases its susceptibility to polymyxins*. Int J Antimicrob Agents, 2015. **45**(3): p. 314-8.
- Romsang, A., et al., *Pseudomonas aeruginosa IscR-Regulated Ferredoxin NADP(+) Reductase Gene (fprB) Functions in Iron-Sulfur Cluster Biogenesis and Multiple Stress Response*. PLOS ONE, 2015. **10**(7): p. e0134374.
- Taciak, B., et al., *Evaluation of phenotypic and functional stability of RAW 264.7 cell line through serial passages*. PLoS One, 2018. **13**(6): p. e0198943.
- Sun, J., et al. *Measurement of Nitric Oxide Production in Biological Systems by Using Griess Reaction Assay*. Sensors, 2003. **3**: 276-284.
- Rashid, M.H. and A. Kornberg, *Inorganic polyphosphate is needed for swimming, swarming, and twitching motilities of Pseudomonas aeruginosa*. Proceedings of the National Academy of Sciences of the United States of America, 2000. **97** 9: p. 4885-90.
- Cochemé, H.M. and M.P. Murphy, *Complex I is the major site of mitochondrial superoxide production by paraquat*. J Biol Chem, 2008. **283**(4): p. 1786-98.
- Elhelu, M.A., *The role of macrophages in immunology*. J Natl Med Assoc, 1983. **75**(3): p. 314-7.
- Canton, M., et al., *Reactive Oxygen Species in Macrophages: Sources and Targets*. Frontiers in Immunology, 2021. **12**.
- Forman, H.J. and M. Torres, *Redox signaling in macrophages*. Mol Aspects Med, 2001. **22**(4-5): p. 189-216.
- Gray, M.J. and U. Jakob, *Oxidative stress protection by polyphosphate—new roles for an old player*. Current Opinion in Microbiology, 2015. **24**: p. 1-6.
- Gray, M.J., et al., *Polyphosphate is a primordial chaperone*. Mol Cell, 2014. **53**(5): p. 689-99.
- Palmieri, E.M., et al., *Nitric Oxide in Macrophage Immunometabolism: Hiding in Plain Sight*. Metabolites, 2020. **10**(11).
- Pudla, M., R. Srisatjaluk, and P. Utaisinchareon, *Induction of inducible nitric oxide synthase (iNOS) in Porphyromonas gingivalis LPS-treated mouse macrophage cell line (RAW264.7) requires Toll-like receptor 9*. Inflamm Res, 2018. **67**(9): p. 723-726.

# Digital data analytics platform for Community Innovation 4.0 model community on the banks of the Mekong River, Nakhon Phanom Province.

Decha Wongpatsa<sup>1</sup>, Montri Sangsuriyun<sup>2</sup>, Saravut Rachamane<sup>2\*</sup>

<sup>1</sup>Faculty of Agriculture and Technology, Nakhon Phanom University  
103 Tambon Kham Thao, Amphoe Mueang Nakhon Phanom, Nakhon Phanom. decha@npu.ac.th

<sup>1</sup>Faculty of Engineering, Nakhon Phanom University  
214 Nong Yat Subdistrict, Amphoe Mueang Nakhon Phanom, Nakhon Phanom. montri.sang@npu.ac.th

<sup>2\*</sup>Faculty of Management Sciences and Information Technology, Nakhonphanom University  
Amphoe Mueang Nakhon Phanom, Nakhon Phanom. saravut\_r@npu.ac.th

**Abstract:** The Mekong 4.0 digital model community platform has revolutionized farmers, entrepreneurs, and communities in Nakhon Phanom Province by providing efficient and cost-effective solutions. Farmers now have access to high quality agricultural products and services, entrepreneurs can benefit from the platform to buy, sell, and do business quickly, and the communities have access to new communication channels through chatbots installed in the platform. The platform also helps reduce production costs, improve productivity, promote food safety, and increase the income of farmers and entrepreneurs. As a result, more people are finding it profitable to engage in businesses in the Mekong region. Moreover, the platform has facilitated trade in the region, enabling a win-win situation for farmers, entrepreneurs, and communities.

**Index Terms— Digital Platform; Data Analytics; Community Innovation; 4.0.**

## I. INTRODUCTION

FARMERS, entrepreneurs, and community enterprises may have trouble incorporating digital platforms into their operations for advancing their business models. The integration of digital technology and connectivity can enhance the operations of farmers, entrepreneurs, and community enterprises, leading to sustainable business growth and development. This approach is often referred to as a "smart business" or a "digital business" and involves a connected ecosystem where all business functions are streamlined and optimized. The implementation of this approach in the context of Thailand 4.0 can potentially unlock significant business value and support sustainable development in the country. [1] [2] Digital platforms can create new market opportunities and facilitate interactions between customers and companies. For example, digital platforms can make it easier for SMEs to find customers, increase their visibility and showcase their services in a larger marketplace. Additionally, digital platforms can facilitate the efficient delivery of services, improved customer experience and greater access to financial services. Moreover, digital platforms can help SMEs to access innovative technologies and opportunities in domains such as artificial intelligence, machine learning and the internet of things. Lastly, digital platforms can make it easier for SMEs to collaborate with other companies and organizations, enabling them to scale and grow. [3]

Big data analytics can be used to identify potential areas for

improvement, identify inefficiencies, or identify opportunities for cost savings. Big data analytics can also be used to track performance metrics to identify trends and adjust strategies as needed for improved performance. By using predictive analytics, organizations can identify potential disruptions in the supply chain before they occur and take appropriate action. Finally, big data analytics can be used to analyze customer feedback and identify opportunities for increased customer satisfaction. [4] big data and artificial intelligence in the current digital era and how they have become fundamental elements in various industries, including marketing and agriculture. Big data helps marketers make accurate predictions based on their knowledge of marketing behavior. In agriculture, new technologies and innovations such as wireless sensor networks and the Internet of Things (IoT) are being implemented to facilitate automation and decision-making. Overall, big data and AI are beneficial for production success and aid in making the best business decisions. [5]

Nakhon Phanom Province, in northeast Thailand, has an area of 5,690.834 square kilometers and is divided into 12 districts and 99 sub-districts. Many communities that live in or close to the river are facing concerns with farming, such as high production costs and lack of access to new technologies and practices, which are impacting communities living near the river. To help resolve these issues, state agencies have realized the need for an education-based transition to a more industrialized agricultural model. This change has measurable ramifications for the local farming industry and could help alleviate poverty in the area. In addition, establishing a supportive digital innovation platform

model 4.0 community could help better the living environment of these communities. [6] [7]

An agricultural innovation platform can help farmers prepare for problems that may arise due to changes in weather, temperature, humidity, and pest control. This platform also utilizes farmers' strengths and expertise to reduce societal inequalities resulting from poverty. The platform employs various digital technologies, such as IoT (through sensors and satellite image processing), AI (using precision farming), and big data. Utilizing mobile technology and IoT sensors, farmers can observe, track, and receive timely alerts regarding any changes in their crops, such as weather, temperature, light, pest infestations, and soil conditions. [8] [9]

Industry 4.0 technology is being introduced to the agricultural communities in the Mekong River region to address the challenges faced by farmers, such as climate change, water scarcity, and food security. To create a flexible agricultural system that can adapt to change, it is important to involve the community in the design and execution of the plan. This will ensure that it is catered to their unique needs and resources. The use of durable and locally relevant technology and practices is also crucial. It is also essential to provide training and resources to farmers and other stakeholders to enable them to use the new technologies effectively.

Furthermore, it is necessary to establish a baseline of data related to factors like weather, soil composition, and water usage to identify trends and changes in the environment and croplands of the Mekong River region. With the growing capabilities of artificial intelligence and machine learning in agriculture, there is potential for more intelligent and efficient solutions to farming challenges. However, it is equally important to prioritize sustainable practices and utilize locally relevant technology for long-term success. To achieve this, it is crucial to gain the support of the local community and government agencies in promoting sustainable agricultural practices and utilizing the latest technology. [10][11]

Researchers' interest in a digital platform for data analysis in the Mekong River Basin, Nakhon Phanom Province, for a better understanding of the regional agricultural context. Farmers can make decisions that result in better yields and community security. The platform can also be useful for scientists. It can be used to study climate change and its impact on local agricultural systems. A digital platform for data analytics will enable decision-makers in the Mekong region to make more informed and informed decisions. This could ultimately lead to positive improvements in agricultural productivity and economic stability in the region.

## II. DATA AND METHODOLOGY

Operational guidelines state that the research project will be conducted in three phases. In phase 1, sub-activity 1, the focus will be on studying the community innovation development 4.0 model along the Mekong River in Nakhon Phanom Province. Feasibility of developing the basic system in agriculture for plants and animals will also be studied. In phase 2, sub-activity 2, product information for safety products of prototype communities will be developed by collecting Big Data and analyzing and predicting productivity in Nakhon Phanom Province. Finally, in phase

3, sub-activity 3, a route platform and digital market will be developed to enhance the development of entrepreneurs and online business applications for the Mekong River Community in Nakhon Phanom Province. Additionally, online business applications will be created and supported by a mobile chatting program. [12]

The researcher has selected a sample group for the research, which includes 100 members of enterprises, entrepreneurs, and farmers aged not over 60 years old, along with 30 healthy elderly individuals aged between 60-75 years old. The selection criteria for volunteers included being a member of a community enterprise or an enterprise, entrepreneur, or farmer aged not over 60 years old. The target area comprises 5 sub-districts, which have a total of 121 locations. In addition, the researcher has included Ah Samat Subdistrict and Mueang District in Nakhon Phanom Province in the target area. The community enterprise group is comprised of entrepreneur groups and farmers who are in the same 5 sub-districts.

In the target area of five sub-districts, namely Chaiburi sub-district, Tha Uthen sub-district, Tha Champa sub-district, Ween Phrabad sub-district, and Ah Samat sub-district located in the Mueang district of Nakhon Phanom Province, there are a total of 121 locations where community enterprise groups, entrepreneur groups and groups of farmers have been selected. These groups were identified as model community enterprises along the Mekong River using a specific method in Nakhon Phanom Province that involved considering three criteria and dividing the population into three groups - Platinum, Gold, and Silver. All three groups are equally important, and the target is to work with five community enterprises from these groups. [13]

In summary, the research shed light on the entrepreneurial and farming activities of the communities surveyed. The analysis indicated that the entrepreneurial and farming activities of these communities are crucial to their economic well-being and way of life. Furthermore, the study revealed that many farmers and entrepreneurs faced challenges due to limited access to agricultural inputs, putting them at a disadvantage and creating difficulties for their livelihoods. Based on the findings, it is recommended that initiatives be taken to improve the access of these communities to agricultural inputs and technologies, which would support and enhance their entrepreneurial and farming activities.

### A. Data collection

Given that this research is in an emerging area with little existing knowledge, we chose an exploratory approach with qualitative research design for data collection and analysis. The researcher collected data through semi-structured interviews. Finally, the respondents with roles in Product Development, Operations, Marketing, Media Communication, Finance and General Management came from Media, Internet, and Finance organizations, as they were expected to have knowledge ability.

Questionnaire Design and Data Collection, the researcher constructed the research instrument based on a

thorough review of the literature. The questionnaire consisted of five Parts.

- Part 1 General Information
- Part 2 Application Usage Digital Platform 4.0
- Part 3 Application Usage Activities Digital Platform 4.0
- Part 4 Trust and Digital Security
- Part 5 Opinions on the implementation of government digital policies and measures

The management principle of exploratory surveys involves utilizing a combination of online and offline methods. This approach incorporates semi-structured interviews that encourage respondents to provide free-form data. By leveraging these methods, engagement is improved, trust is established, and the risk of bias in writing is minimized. Additionally, semi-structured interviews and free-form data entry afford greater flexibility and customization during the data collection process. As a result, researchers can tailor their approach to meet the unique needs of their study. [13]

### B. Design of a demonstration platform

Step for Design of Digital Platform Data Analytics for Community Innovation Pilot City 4.0 along the Mekong River in Nakhon Phanom. [14]

#### Phase 1 - Planning:

1. Understand the business context and define the project scope.
2. Identify stakeholders and their requirements.
3. Create a project management plan.
4. Define the target architecture and develop an analysis of technology platforms and tools.

#### Phase 2 - Design:

1. Design the data architecture.
2. Design the data model.
3. Develop the user interface and workflow.
4. Develop the security and integration architecture.

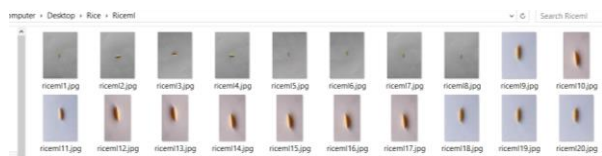


Fig. 1 Displays the page for putting the rice images in the folder.

#### Phase 3 - Implementation:

1. Develop the platform.
2. Test and deploy the platform.
3. Monitor and optimize the platform performance.

#### Phase 4 - Maintenance and Support:

1. Monitor and troubleshoot system issues.
2. Maintain and update the platform.
3. Provide user training and support.

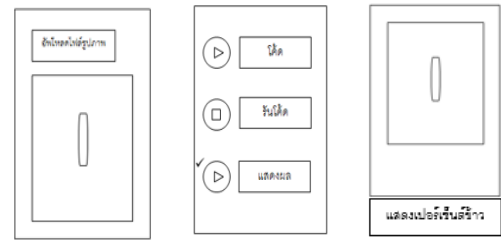


Fig. 2 Screen design.

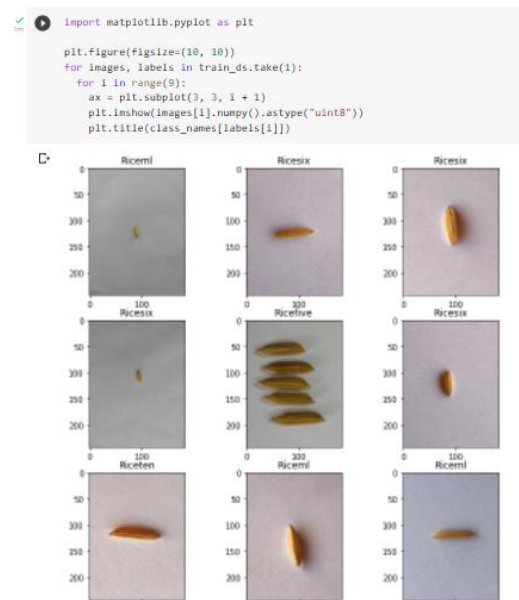


Fig. 3 Check images to see if the images are sorted correctly by class or not, displaying the first 9 images from the train data set.

### C. Data Analysis

The statistical tools used to analyze the data consisted of descriptive statistics (frequency, percentage, mean, and standard deviation). The evaluation criteria consist of a Rating Scale, which utilizes Likert's method and has five levels. The scores on the evaluation criteria are as follows: an average score of 4.51-5.00 is considered the most appropriate rating, while a score of 3.51-4.50 is deemed very appropriate. The scores on the evaluation criteria, based on the Rating Scale, range from a moderately suitable score of 2.51-3.50 to a slightly suitable score of 1.00-1.50. The evaluation criteria utilize a Rating Scale with five levels, each with its own interpretation. For instance, a score of 1.51-2.50 is considered slightly suitable. [14]

## III. RESULTS

The participants in the research project were volunteers, and it was discovered that 52 of them were rice farmers, representing 34.70 percent of the total number of respondents. Additionally, there were 35 fish processing farmers, making up 23.30 percent of the participants, and 28 fish farmers, representing 18.70 percent. Out of the total

number of respondents, 85 were females, or 56.7 percent, while 65 were males, representing 43.3 percent. Regarding age, the research project found that 48 people, representing 32.0 percent, were in the 51-60 age group, followed by 27 people, representing 18.0 percent, in the 41-50 age group and 26 people, accounting for 17.3 percent, in the 61 years and older age group. In terms of interest, skills, and demand for 4.0 technology platforms related to IoT systems and Bigdata AI image processing for community agricultural products, 71 people, representing 47.3 percent, showed interest. *as shown in the table I and II.*

*A. The Results of Requirements for Develop an Innovative Platform 4.0, a Model Community Along the Mekong River. Nakhon Phanom Province*

TABLE I

VOLUNTEERS TO PARTICIPATE IN RESEARCH

ID	Participate		
	Schedule	Number (people)	Percentage
1	Rice farmers group	52	34.7
2	Farmers Group Processing Som Pla	35	23.3
3	pineapple farmers	21	14.0
4	fish farmers group	28	18.7
5	Farmers group processing fermented fish	14	9.3

The results shown in Table 1 indicate that out of the 150 volunteers included in the research project, 52 (34.70%) specialize in rice farming, 35 (23.30%) have experience in fish processing, 28 (18.70%) tend to fish-related activities, and 14 (9.30%) are involved in pineapple production

TABLE II

INTERESTS, SKILLS, AND REQUIREMENTS

ID	REQUIREMENTS TECHNOLOGY		
	Schedule	Number (people)	Percentage
1	IoT system and Bigdata AI image processing for community agriculture products	71	47.3
2	Applications in social media for trade and business and Chatbot	61	40.7
3	Business Intelligence (BI) Analytics for Community Enterprises	17	11.3
4	travel route application system Along the Mekong River	1	7
5	IoT system and Bigdata AI image processing for community agriculture products	71	47.3

The interests, abilities, and platform conditions of all volunteers participating in the research project were outlined, as demonstrated by Table II.

According to the data highlighted in the table, 71 volunteers, which equates to 47.3 percent, expressed interest

in using IoT systems and Big Data AI image processing for agricultural production.

Additionally, 61 volunteers, making up 40.7 percent, expressed interest in applications in social media for business trading and Chatbots.

These findings indicate that many of the volunteers are interested in applying 4.0 technology platforms to improve agricultural production and trading.

Therefore, this can be a beneficial contribution to forming the 4.0 model community, specifically in Nakhon Phanom Province along the Mekong River.

*B. The Results of Develop an Innovative Platform 4.0, a Model Community Along the Mekong River. Nakhon Phanom Province*

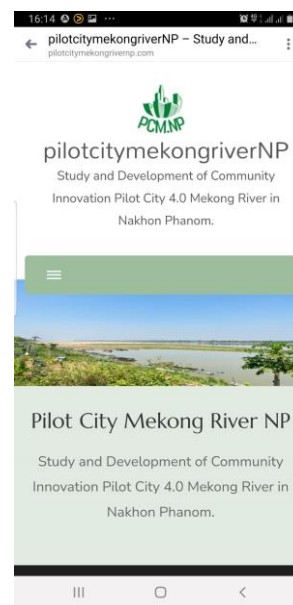


Fig. 1. Example of An innovation platform 4.0, a model community along the Mekong River Nakhon Phanom Province

Through <http://pilotcitymekongrivernp.com/wp>, Learning Innovation and Platform 4.0 can be accessed by community members, entrepreneurs, and community enterprise groups from around the world. To raise awareness of these agencies, the main website domain should be promoted on social networks like Facebook. In addition, offline and online marketing strategies can be implemented while creating engaging digital media content to capture the attention of consumers and encourage their participation in activities related to online stores, plans, and marketing strategies.

The development of a local rice quality classification system with rice grain image recognition technique in Waen Phra Bat Subdistrict, Tha Uthen District, Nakhon Phanom Province utilized the System Development Life Cycle (SDLC) as a methodology for the system development process. Information technology systems can be used to assist in solving business problems or fulfilling the needs of the organization. The system to be developed may be a new system or an improvement of an existing one.



Fig. 2 Displays the results of the train.



Fig. 3 Example of An innovation platform 4.0, a model community along the Mekong River Nakhon Phanom Province

From Figure 2 and 3, the result of Train Dataset to see the error. How accurate is it? Is a graph format or Visualize training results and retrieve the address of the image, use the array command to cycle through the image and give the score to predict how many percent and show it as a picture?

### C. The Results of Performance Evaluation Results Overview of The Expert System

TABLE III  
EXAMINATION OF OUTPUTS FROM THE EXPERT SYSTEM

ID	EXAMINATION				
	ITEM	n	mean	sd.	level
1	Display performance evaluations in terms of functionality according to system functions.	3	4.19	.64	great
2	Performance evaluation in terms of ease of use of the system	3	4.21	.62	great
3	Evaluation of the efficiency of data security in the system	3	4.24	.61	great

According to Table 3, the expert evaluation of the system's ease of use showed the highest level of appreciation, reaching a peak mean of 4.79 with a standard deviation of 0.29. The data security efficiency was also evaluated and received a high rating of 0.58.

Furthermore, the functionality-based presentation performance evaluation was deemed to be at a high rate with a mean of 4.24 and a standard deviation of 0.76.

When assessing Table III, Nakhon Phanom Province's rice grain image recognition technique achieved the highest evaluation score of 4.51 with a standard deviation of 0.54.

### D. The Results of The Overall Evaluation of The System in Terms of Meeting the Needs of System Users

TABLE IV  
The results of the overall evaluation of the system in terms of meeting the needs of system users.

ID	EXAMINATION				
	Schedule	n	mean	Sd.	level
1	Assess performance in terms of meeting requirements.	30	4.19	0.64	great
2	Evaluate performance in the field of testing.	30	4.21	0.62	great
3	Efficiency evaluation in terms of usability	30	4.24	0.61	great
4	Evaluate safety performance	30	4.20	0.68	great

According to Table 4, the test results from Table III indicated that the system's usability garnered the most positive response from users, with a mean score of 4.24 and a standard deviation of 0.61. The system's performance closely followed with a mean score of 4.21 and a standard deviation of 0.62. Meanwhile, both system security and overall usability were rated at 4.20 and 4.19, respectively, with standard deviations of 0.68 and 0.64. Overall, the system received a favorable rating of 4.22.

## IV. DISCUSSION

Digital data analytics platforms have had a significant impact on farmers, entrepreneurs, and community enterprises by creating international marketplaces that can be utilized by both local micro-entrepreneurs and established businesses. Digital platforms can assist SMEs in gaining access to innovative technologies and opportunities in domains such as artificial intelligence, machine learning, and the Internet of Things. The requirements for developing an Innovative Platform 4.0 and a model community along the Mekong River in Nakhon Phanom Province include interest, skills, and demand for 4.0 technology platforms related to IoT systems and big data AI image processing for community agricultural products. As per the research [3] [4], digital platforms make it easier for SMEs to collaborate with other companies and organizations, allowing them to scale and grow, and leverage the benefits offered by big data and AI to achieve production success and make better business decisions. Among the survey



respondents, 71 individuals or 47.3% expressed interest in developing an Innovative Platform 4.0 in Nakhon Phanom Province. The platform would focus on IoT systems, Bigdata AI, and image processing for community agricultural products, aligning with the research that suggests digital platforms can help SMEs collaborate with other businesses and scale their operations for growth. The platform's implementation would benefit the farmers, entrepreneurs, and community enterprises by creating international marketplaces, which both local micro-entrepreneurs and established businesses can utilize to explore innovative technologies and opportunities in fields like artificial intelligence and machine learning. [5]

The local rice quality classification system was developed with the assistance of rice grain image recognition techniques in Waen Phra Bat Subdistrict. During the learning process, the system achieved a 100% accuracy, leading to the successful creation of a reliable identification system for different types of native rice varieties found in Nakhon Phanom Province with the help of rice grain image recognition techniques.[15] The application of the PCA segregation method revealed that the results obtained for classification and quality analysis were 92.3% and 89.5% respectively

Suggestions and Limitations for Further Research: Due to limited diversity in information as well as the costs of collecting, processing, and storing data, it is recommended that an open-source system be developed. This system could reduce costs across various platforms including social media, chatbots, and image processing. The system should be easy to use and streamlined as an application.

#### ACKNOWLEDGMENT

The research team extends its sincere appreciation to the Fundamental Research and Innovation budget for Fiscal Year 2022, and to the Institute of Research and Development at Nakhon Phanom University, Faculty of Management Science and Information Technology, for their generous support in enabling the successful completion of this research project. We would also like to thank the farmers and relevant agencies for their assistance and dedication.

#### REFERENCES

- [1] Anupong Avirutha. The Impact of Digital Transformation to Business Performance in Thailand 4.0 Era. " Veridian E-Journal, Silpakorn University (Humanities, Social Sciences and Arts) 11.5 (2018): 295-307.
- [2] Khalid, Bilal, and Elena Naumova. "Digital transformation SCM in view of Covid-19 from Thailand SMEs perspective." *Global Challenges of Digital Transformation of Markets* (2021): 49-66.
- [3] Xie, X.; Han, Y.; Anderson, A.; Ribeiro-Navarrete, S. Digital platforms and SMEs' business model innovation: Exploring the mediating mechanisms of capability reconfiguration. *Int. J. Inform. Manag.* 2022, 65, 102513.
- [4] Zhang, X., Yu, Y., & Zhang, N. "Sustainable supply chain management under big data: A bibliometric analysis." *Journal of Enterprise Information Management* 34.1 (2021): 427-445.
- [5] Jaipong, Parichat, et al. "A review of intentions to use artificial intelligence in Big Data Analytics for Thailand agriculture." *Review of Advanced Multidisciplinary Science, Engineering & Innovation* 1.2 (2022): 1-8.

- [6] Nakhon Phanom Provincial Agriculture Office. 2021. Annual Report Nakhon Phanom Provincial Agriculture Office. Source: [http://www.nakhonphanom.doae.go.th/?page\\_id=1295](http://www.nakhonphanom.doae.go.th/?page_id=1295) , 4 July 2022
- [7] Community Organization Development Institute (Public Organization). (2020). Mekong Riverside Agriculture: Unforgettable Subdistrict Development Plan. Source: <https://web.codi.or.th/20190331-1726/>, 4 July 2022
- [8] Srivetbodee, Sorawadee, and Barbara Igel. "Digital technology adoption in agriculture: Success factors, obstacles and impact on corporate social responsibility performance in Thailand's smart farming projects." *Thammasat Review* 24.2 (2021): 149-170.
- [9] Matthews, J., Love, P. E., Porter, S. R., & Fang, W. "Smart data and business analytics: A theoretical framework for managing rework risks in mega-projects." *International Journal of Information Management* 65 (2022): 102495.
- [10] Zhang, L., Chen, F., Xia, S., Cao, D., Ye, Z., Shen, C., ... Li, Y "Value co-creation and appropriation of platform-based alliances in cooperative advertising." *Industrial Marketing Management* 96 (2021): 213-225.
- [11] K. Perakis, F. Lampathaki, K. Nikas, Y. Georgiou, O. Marko, J. Maselyne "CYBELE–Fostering precision agriculture & livestock farming through secure access to large-scale HPC enabled virtual industrial experimentation environments fostering scalable big data analytics." *Computer Networks* 168 (2020): 107035.
- [12] Bundit Innawong. Personnel Potential Development in Network Universities and establishing an area-based research system: a case study of propelling the grassroots economy with indigenous products to commercialization: a complete report. [M.P.A.]: Office of the Science Promotion Commission research and innovation; 2018.
- [13] Debrah, Caleb, Albert PC Chan, and Amos Darko. "Artificial intelligence in green building." *Automation in Construction* 137 (2022): 104192.
- [14] Boonchom Srisa-ard. (2002). Preliminary research. 7th Edition. Bangkok: Suviriyasan.
- [15] Asif, Muhammad Junaid, et al. "Rice grain identification and quality analysis using image processing based on principal component analysis." 2018 International symposium on recent advances in electrical engineering (RAEE). IEEE, 2018.

# Poster presentation

# Study on the efficiency of Nickel Manganese Cobalt Oxides cylindrical Li-ion battery under ambient temperature adjustment condition

Wiwat Keyoonwong<sup>1\*</sup>, Nataphol Boonsai<sup>2</sup>, Natthaphol Wongwiriyankit<sup>3</sup>  
Nutthaphon Siripitakchai<sup>4</sup>, Thanomphon Fungpaisanpong<sup>5</sup>

Department of Electrical Engineering, Faculty of Engineering,  
King Mongkut's Institute of Technology Ladkrabang, Bangkok, Thailand  
wiwat.ke@kmitl.ac.th

**Abstract:** Several batteries are used in the electric vehicle market, and the primary factors that impact battery efficiency are heat and temperature. This paper outlines a battery experiment that can be used to determine the various ambient temperatures that affect the efficiency of Li-ion batteries for an application in electric vehicles. In this experiment, we utilized the constant-current-constant-voltage (CC-CV) method to charge and discharge nickel manganese cobalt aluminum oxides (NCA) cylindrical Li-ion batteries with ambient temperature adjustment. When the ambient temperature rises, battery efficiency will increase. As the C-rate increases, it can lead to decreased charging efficiency due to factors such as increased internal resistance and heat generation. Additionally, this information can be used to develop strategies for mitigating the effects of temperature on battery efficiency. Ultimately, this study will be beneficial for the development of safer and more reliable batteries for any applications.

**Index Terms**— Li-ion battery, ambient temperature, electric vehicles, energy efficiency, charge-discharge testing

## I. INTRODUCTION

Due to the current global situation, more clean energy is being promoted. Many countries have been attempting to reduce fossil energy consumption, which is the main reason why, in recent years, cars that use electricity instead of fuel energy [1]. According to the International Energy Agency (IEA), it is expected that by 2030, the number of electric cars, electric buses, electric vans, and electric trucks on the road will increase to 145 million worldwide due to government policies aimed at reducing energy consumption and carbon emissions [2]. Electric cars have many major components that are necessary to drive. One of the key components of electric vehicles is the battery, which serves as the primary source of energy storage.

Nowadays, battery technology in electric vehicles has continuously developed. The most popular battery used in electric cars is the lithium-ion battery because it is a type that provides high energy capacity and higher power than other types such as lead-acid batteries or nickel batteries, etc. Lithium-ion batteries can still be classified into many types. The classification based on the battery's chemistry gives it varied features that allow it to be used for several purposes. The major considerations for selecting a lithium-ion battery for electric vehicles are safety, high energy capacity, and a large number of cycles.

The temperature of the environment also plays a significant role in the efficiency of electric vehicle batteries because temperature effects are related to several other factors, including (1) electrolyte conductivity: The

conductivity of the electrolyte, which acts as a medium for the flow of ions between the electrodes, is affected by temperature. At low temperatures, the electrolyte becomes more viscous and its conductivity decreases, resulting in reduced battery capacity and power output. (2) Internal resistance: Temperature also affects the resistance of the battery's internal components, including the electrodes and electrolytes. As the temperature increases, the resistance decreases, leading to an increase in battery power output. However, at high temperatures, the resistance can become too low, resulting in safety issues and a reduced battery lifespan. (3) Chemical reactions in the batteries: As chemical reactions can be explained by Arrhenius' chemical equation, there is a relationship between the rate of chemical reactions and reaction temperature, and temperature variation can lead to a change in the electrochemical reaction rate in batteries. Besides chemical reactions, the ionic conductivities of electrodes and electrolytes are also affected by temperature [3]. Temperatures can have a significant impact on a vehicle's driving range when temperatures are outside of the maximum cycle life range of 15°C to 48°C. The driving range of a vehicle is reduced by nearly 33% in hot temperatures ranging between 48°C and 90°C and by nearly 60% in cold temperatures ranging between 15°C and -40°C [4]. In another report, it was shown that the power and energy densities of the Panasonic 18650 Li-ion battery were ~800 W/L and ~100 Wh/L at 25 °C, and these values were reduced by 98.75% and 95% to < 10 W/L and ~5 Wh/L at -40 °C [3,5]. And final report, operating at various ambient temperatures affects the efficiency of NCA batteries. From the test from -20 degrees Celsius to 60 degrees Celsius, it

was found that the higher the ambient temperature, the shorter the charging time, the longer the battery's usage time, and the longer the life cycle of the battery [6].

Therefore, the research team has studied and conducted experiments with the objectives of studying the effects of ambient temperature adjustments with an ambient temperature range of 20°C to 40°C, which is the average temperature range in Thailand, on the behavior of NCA cylindrical Li-ion batteries under ambient temperature adjustment conditions as well as analyzing and comparing the relationship between temperature and efficiency of NCA cylindrical Li-ion batteries by charging and discharging with the CC-CV method. In this experiment, the potential impact of internal resistance within the battery during testing is not being taken into consideration.

## II. STANDARD IEC 62660-1

The standard of the IEC 62660-1 for automobile traction Li-ion cell is presented. In particular, the efficiency test is described to understand the existing condition [7].

### A. General charge conditions

Prior to charging, the Li-ion cell shall be discharged down to an end-of-discharge voltage specified by the cell manufacturer while operating at room temperature with a constant current as shown in Table I. The cell must then be charged at room temperature using the method specified by the cell manufacturer.

### B. General discharge conditions

The cell shall be discharged at a specific temperature using a constant current  $I_t$  (A) as provided by the cell manufacturer to reach the end-of-discharge voltage. It is mandatory to use the discharge current and cell temperatures as mentioned in Table I

TABLE I  
DISCHARGE CONDITIONS [7]

Cell temperature [ °C]	Discharge current [A]	
	BEV	HEV
0	1/3 $I_t$	1 $I_t$
25		
45		

### C. Calculation of Energy Efficiency

Determine the energy efficiency of Li-ion batteries by using equation.

$$\eta_{e1} = \frac{W_{d1}}{W_{c1}} \times 100 \quad (1)$$

Where

$\eta_{e1}$  is the energy efficiency (%)

$W_{d1}$  is the discharge electric energy (Wh)

$W_{c1}$  is the charge electric energy (Wh)

## III. EXPERIMENTAL SETUP

In this experiment, we utilized the CC-CV to charge and discharge NCA cylindrical Li-ion batteries. However, the experiment did not include discharging because the battery usage during driving an electric vehicle varies depending on the situation, resulting in the discharging being inconsistent. Therefore, this experiment emphasizes the importance of charging as the main factor. To achieve this, we set the C-rate of charging to three different conditions, which are C/3, C/2 and C. The battery was charged until the voltage reached 4.2 V, after which the charging current was reduced to 0.065 A to fully charge the battery. The battery was discharged at a rate of 2C until the voltage reached 2.5 V. In accordance with the IEC 62660-1 standard, detailed and easily computable efficiency graphs were obtained from the experiment.

The experiment team used MATLAB and Ultrasigma software to control Rigol DC Power Supply model DP811 and Rigol DC Electronic Load model DL3021. By using a total of six command code files in the form of m files, which were divided into three files for the charging process (ocvprofileC.m, recorderC.m, and runC.m) and three files for the discharging process (ocvprofileD.m, recorderD.m, and runD.m). In all three code files, the ocvprofile.m is used to call files, the recorder.m file is used to record values, and the run.m file is used to run MATLAB. These command codes were configured with various parameters, including VISA, which is the address that must be copied from the Ultrasigma software, charge-discharge current and operating mode of the DC power supply and DC electronic load to run in combined CC-CV mode. The purpose that must be set this way is to require a real-time value from MATLAB, which can export as Excel files.

The equipments for testing are the following. The battery cell under study is a NCA cylindrical Li-ion batteries cell NCR18650B manufactured by Panasonic Industry Co., Ltd. The main parameters of the cell are summarized in Table II.

TABLE II  
BATTERY CELLS SPECIFICATION

Parameter	Value	Units
Rated Capacity	3200	mAh
Capacity	Min. 3250 Typ. 3350	mAh
Nominal Voltage	3.60	V
Standard Charging Current	1625	mA
Charge Cut-off Voltage	4.20	V
Discharge Cut-off Voltage	2.50	V
Weight	48.5	g



Fig. 1. Panasonic NCR18650B (NCA cylindrical Li-ion batteries).

To conduct battery testing, Regarding the environmental temperature, a Temperature Test Chamber will be used to adjust the temperature range from 20°C to 40°C, with increments of 5°C. As for the C-rate, tests will be carried out starting from C/3, C/2, and C, respectively. A total of 15 battery samples will be utilized for the testing, and the test conditions and sample distribution will be summarized in Table III

TABLE III  
TEST CONDITIONS AND SAMPLE DISTRIBUTIONS

C-RATE/ TEMP	20°C	25°C	30°C	35°C	40°C
C/3	1	2	3	4	5
C/2	6	7	8	9	10
C	11	12	13	14	15

DC Power Supply Rigol DP811 and DC Electronic Load Rigol DL3021 are used for charging and discharging batteries. The DC power supply can be charged in two modes: CC and CV, while the DC Electronic Load can be discharged in a total of four: CC, CV, CP and CR.

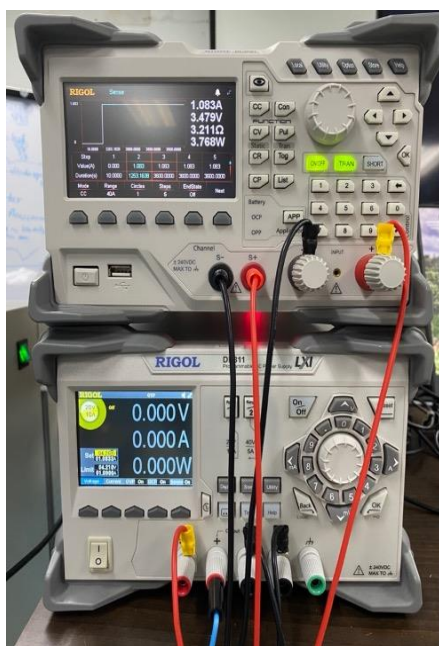


Fig. 2. DC Electronic Load (Top) and DC Power Supply (Bottom).

Temperature Test Chamber used to control the ambient temperature for battery charge-discharge testing. The temperature can be adjusted from 0-60 °C.



Fig. 3. Temperature Test Chamber.

#### IV. RESULTS AND DISCUSSION

Figures 4 to 6 show the voltage and current profile while charging at three different C-rate conditions. The graph shows that the X axis is time (s), and the Y axes are voltage (V) and current (A), both axes related to each other. As the time increases (X-axis), it will result in the value of voltage (V) (Y-axis) increasing until it reaches 4.2 V, and the value of current (A) (Y-axis) will remain constant at C-rate: (C/3 = 1.0833A, C/2 = 1.625A, C = 3.25A) for a period of time until the battery is fully charged to 4.2 V, then the value of current will gradually decrease until it finishes at 0.065A because of the CC-CV method for charging the Li-ion battery. In addition, the graph shows the tendency of the Li-ion battery voltage and current at different temperatures of 20°C, 25°C, 30°C, 35°C, and 40°C.

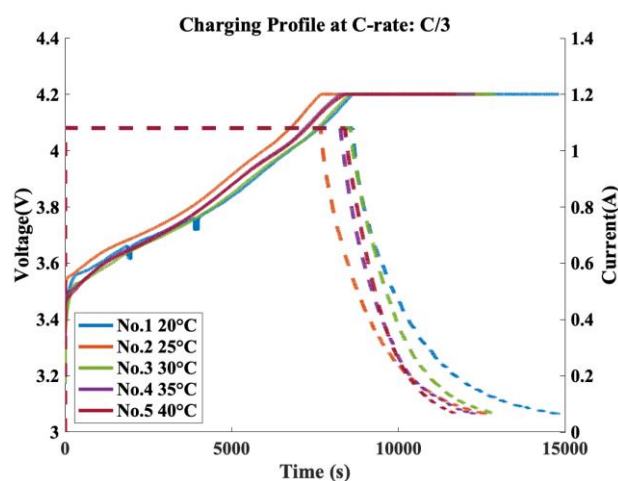


Fig. 4. Charging profile while testing at C-rate: C/3.

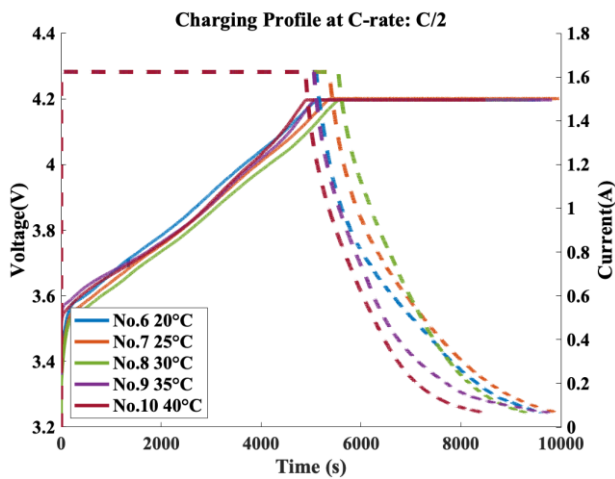


Fig. 5. Charging profile while testing at C-rate: C/2.

As a result, the charging profile obtained from the C-rate tendency experiment (C/3, C/2, and C) has the same pattern when batteries are charged at all ambient temperatures. It is noticeable that the charging time of Li-ion batteries at high ambient temperatures is less than at low ambient temperatures. As the ambient temperature rises, the electrochemical kinetics become faster [8].

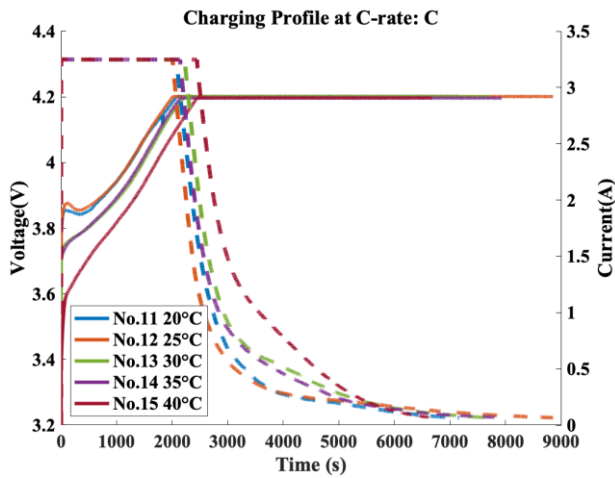


Fig. 6. Charging profile while testing at C-rate: C.

Figures 8 to 10 illustrate the energy efficiency of 15 NCA cylindrical Li-ion batteries tested at ambient temperatures of 20°C, 25°C, 30°C, 35°C, and 40°C. Energy efficiency was determined by analyzing voltage and current data using an energy efficiency equation. The batteries were divided into three groups of five, with batteries 1–5 charged at a C-rate of C/3 (1.0833A), batteries 6–10 charged at a C-rate of C/2 (1.625A), and batteries 11–15 charged at a C-rate of C (3.25A). From the experimental graph, it can be seen that the battery has the lowest energy efficiency when the ambient temperature is 20°C, 25°C, 30°C, 35°C, and 40 °C, respectively.

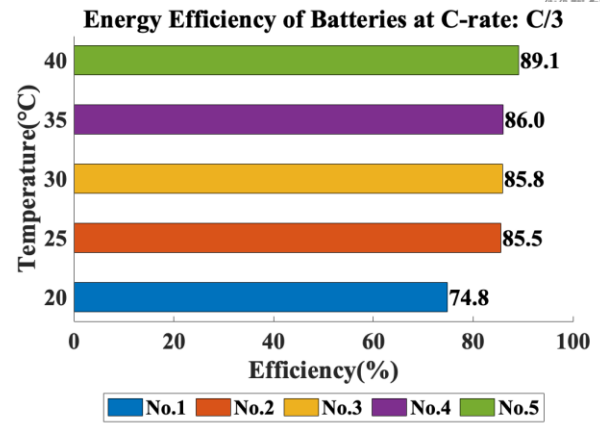


Fig. 8. Energy efficiency of NCA cylindrical li-ion batteries while testing at C-rate: C/3.

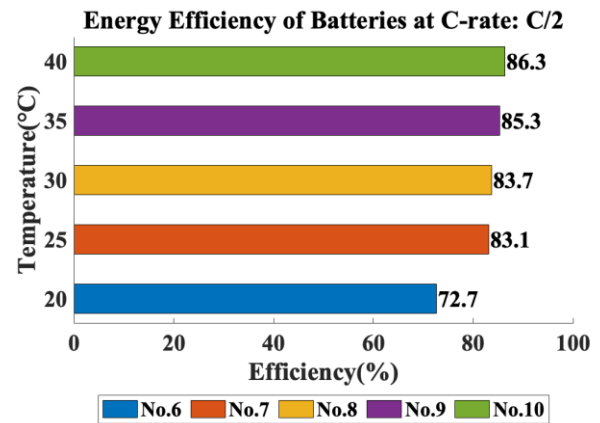


Fig. 9. Energy efficiency of NCA cylindrical li-ion batteries while testing at C-rate: C/2

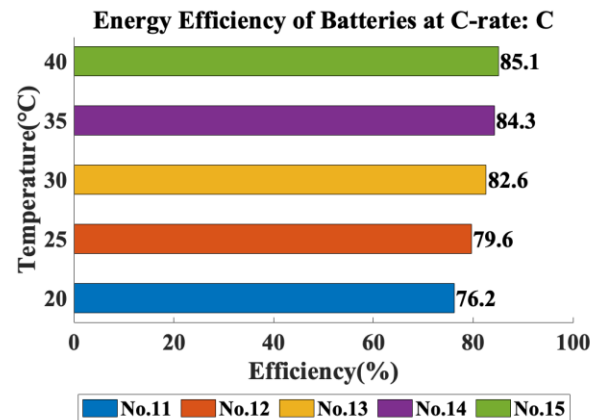


Fig. 10. Energy efficiency of NCA cylindrical li-ion batteries while testing at C-rate: C.

Therefore, the battery's energy efficiency will tend to increase with increasing ambient temperatures because, due to increased ambient temperatures, the electrical energy in the battery can move faster. Including a greater rate of chemical reactions. The efficiency obtained from the C-rate tendency experiments (C/3, C/2, and C) has the same pattern. It can be concluded that the energy efficiency of the battery also depends on the ambient temperature.

Moreover, from all three C-rates it is still evident that at the same temperature, charging with a lower C-rate results in higher charging efficiency.

## V. CONCLUSION

From the charge-discharge testing of the Li-ion batteries under ambient temperature adjustment conditions by adjusting the temperature test chamber to obtain different temperatures. We used 15 NCA cylindrical Li-ion battery cells, each with a capacity of 3.25 Ah, divided into three groups with different C-rates for testing at each temperature. The temperature test was started at 20°C and increased in 5°C increments until reaching a final temperature of 40°C with the CC-CV method.

The results can be summarized as follows:

The efficiency of charging a battery can vary depending on the C-rate used. Lower C-rates generally result in higher charging efficiency due to less heat generation and less stress on the battery. In contrast, higher C-rates can lead to decreased charging efficiency due to factors such as increased internal resistance, heat generation, and the risk of damage.

When the ambient temperature is increased, it can lead to faster battery charging and improved battery efficiency compared to when the battery is operated in low-temperature conditions. However, raising the temperature increases the battery's energy efficiency, but it also affects the safety of using it at high temperatures.

## REFERENCES

- [1] IEA (2022), Global EV Outlook 2021, IEA, Paris <https://www.iea.org/reports/global-ev-outlook-2021>, License: CC BY 4.0 (references)
- [2] IEA, Global electric car stock, 2010-2021, IEA, Paris <https://www.iea.org/data-and-statistics/charts/global-electric-car-stock-2010-2021>, IEA. Licence: CC BY 4.0
- [3] Shuai Ma, Modi Jiang, Peng Tao, Chengyi Song, Jianbo Wu, Jun Wang, Tao Deng, Wen Shang, Temperature effect and thermal impact in lithium-ion batteries: A review, Progress in Natural Science: Materials International, Volume 28, Issue 6, 2018, Pages 653-666, ISSN 1002-0071, <https://doi.org/10.1016/j.pnsc.2018.11.002>.
- [4] Seyed Mohammad Rezvanizani, Zongchang Liu, Yan Chen, Jay Lee, Review and recent advances in battery health monitoring and prognostics technologies for electric vehicle (EV) safety and mobility, Journal of Power Sources, Volume 256, 2014, Pages 110-124, ISSN 0378-7753
- [5] Nagasubramanian, G. Electrical characteristics of 18650 Li-ion cells at low temperatures. Journal of Applied Electrochemistry 31, 99–104 (2001). <https://doi.org/10.1023/A:1004113825283>
- [6] Xiao-Guang Yang, Teng Liu, Chao-Yang Wang, “Thermally modulated lithium iron phosphate batteries for mass-market electric vehicles”. Nature Energy 6, Pages 176-185, 2021, <https://doi.org/10.1038/s41560-020-00757-7>
- [7] IEC 62660-1:2018 | IEC Webstore | battery, energy efficiency, energy storage, smart city, transportation, mobility.” [Online]. Available: <https://webstore.iec.ch/publication/28965>. [Accessed: 12-Jan-2018]

- [8] Wang, X.; Zhang, Y.; Deng, Y.; Yuan, Y.; Zhang, F.; Lv, S.; Zhu, Y.; Ni, H. Effect of Different Charging Currents and Temperatures on the Behavior of Li-Ion Battery Voltage Plateau. Batteries 2023, 9, 42. <https://doi.org/10.3390/batteries9010042>

# Estimating efficiency and life cycle of different types of Li batteries for EVs

Wiwat Keyoonwong<sup>1</sup>, Korn Ratsamipenyathip<sup>2</sup>, Kamolpach Inkleang<sup>3</sup>,  
Kulthida Klomkleang<sup>4</sup>, Kunakorn Kakandee<sup>5</sup>

<sup>1</sup> Department of Electrical Engineering, Faculty of Engineering,  
King Mongkut's Institute of Technology Ladkrabang, Bangkok, Thailand  
wiwat.ke@kmitl.ac.th

**Abstract:** This study aims to compare the performance and capacity of INR and NCR EV batteries in sizes 18650 and 21700, which are crucial factors in determining the efficiency and lifespan of these batteries. Battery capacity refers to the amount of energy stored, while the study will collect data on capacity and charging performance, analyzing correlations and patterns to determine the best battery type. The results will benefit EV manufacturers and researchers in developing more efficient and durable EV batteries, promoting sustainable transportation to reduce emissions. Understanding capacity and swelling will help to determine suitable materials and designs to improve performance and lifespan, supporting long-term EV use and reducing emissions.

**Keywords - INR, NCR, EV batteries, 18650, 21700, performance, capacity, efficiency, lifespan, charging performance, correlations, patterns, suitable materials, designs, sustainable transportation, emissions reduction.**

## I. INTRODUCTION

Electric vehicle technology is rapidly growing in popularity worldwide, with sales of electric vehicles reaching 6.6 million units in 2021, which is double that of 2020, according to the International Energy Agency (IEA). China leads the world in electric vehicle sales, accounting for 53% of global sales, followed by Europe (33%) and the United States (11%) in 2021. Electric vehicles represented 8.6% of global car sales in 2021, a significant increase from 0.9% in 2016.

One of the most important components of electric vehicles is the battery, with most electric vehicles using lithium-ion batteries. Tesla is the company with the largest market share in electric vehicle sales, and it uses lithium-ion batteries produced by various battery manufacturers. Panasonic is the primary battery manufacturer for Tesla, producing cylindrical 18650 and 21700 NCR type batteries, while LG Energy Solution produces cylindrical 21700 NCR type batteries and CATL produces prismatic LFP type batteries. Tesla has also started producing 46800 batteries but has not disclosed the chemistry of the battery.

The popularity of electric vehicles has made battery health an important factor to consider, as replacing the battery in an electric vehicle can be more expensive than replacing the battery in a conventional car, as high-energy density batteries are required to provide sufficient range and performance for

electric vehicles. In addition, battery production and disposal also need to be considered for their environmental impact.

## II. EXPERIMENTAL SETUP

This experiment involves testing batteries using NCR18650, 21700, INR18650, and 21700 cells within the temperature range of the indoor environmental conditions of a building. The battery's charge and discharge capabilities were measured using a DC Power Supply and a DC Electronic Load, respectively. Both the DC Power Supply and Electronic Load were programmed using Matlab2022a to perform the charging and discharging of the batteries, as well as record the results, including current, voltage, battery capacity, and time.

TABLE I  
BATTERY SPECIFICATION TABLE

Set up	Table column subhead	Nominal capacity (mAh)	Charging voltage(V)	Discharge cut-off voltage (V)	End Current (mA)
1	INR18650	3000	4.20	2.5	50
2	INR21700	4800	4.20	2.5	200
3	NCR18650B	3350	4.20	2.5	65
4	NCR21700B	5000	4.20	2.5	100





Fig. 1. Batteries used in the test Batteries.

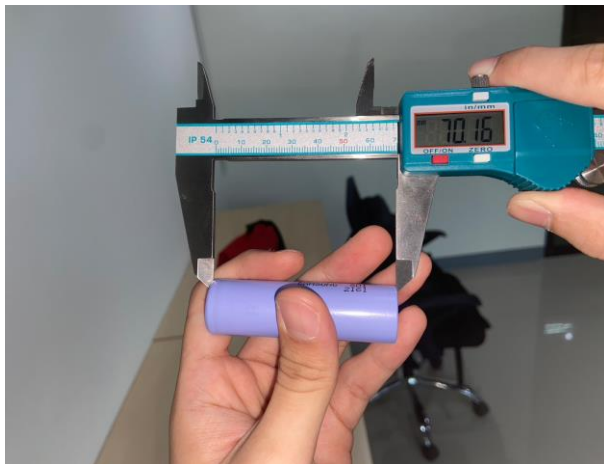


Fig.2. Measure Battery Size

To install the equipment, the positive terminal of the DC Power Supply was connected to the positive terminal of the battery, and the negative terminal of the DC Power Supply was connected to the negative terminal of the battery. The Sense function was used to ensure that the measurement parameters were accurate, and the DC Electronic Load was installed in the same manner as the DC Power Supply. Both devices were connected to a computer and commanded using a code in Matlab2022a to charge and discharge the batteries as specified.

In this experiment, all batteries were tested using the CC-CV method, and their charge capacity and discharge were measured using a DC Power Supply and a DC Electronic Load, respectively. The settings related to the connection of the positive and negative terminals of the battery to the equipment were configured, and the Sense function was used to ensure accurate parameter measurement. Matlab2022a was used to command the charging and discharging of the batteries and record the results. The battery's external dimensions were measured using a digital caliper.

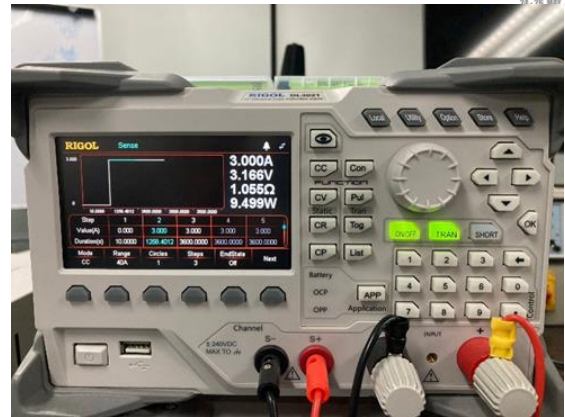


Fig. 3. DC power supply (DP811)

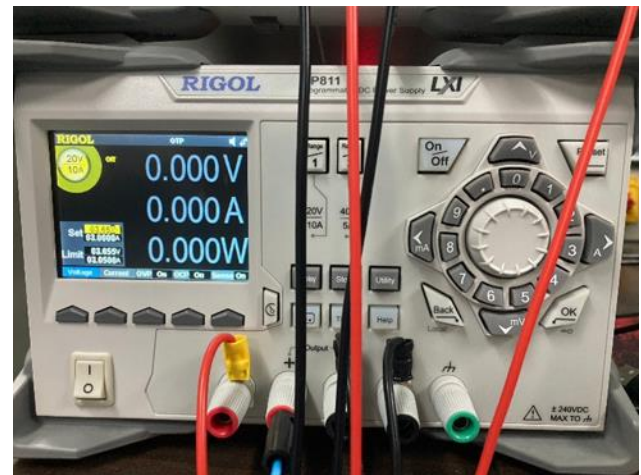


Fig. 4. DC electronic load(Rigal DL3021)

### III. RESULTS

The graph displays the results of a battery charge and discharge test conducted over 15 cycles at a current rate of C/1. The x-axis represents the time in seconds, while the y-axis represents the voltage in volts and the current in amperes. The blue line represents the voltage used to charge the battery, the gray line represents the voltage used to discharge the battery, and the orange line represents the current used to charge the battery. The capacity measurement is the average of three samples tested.

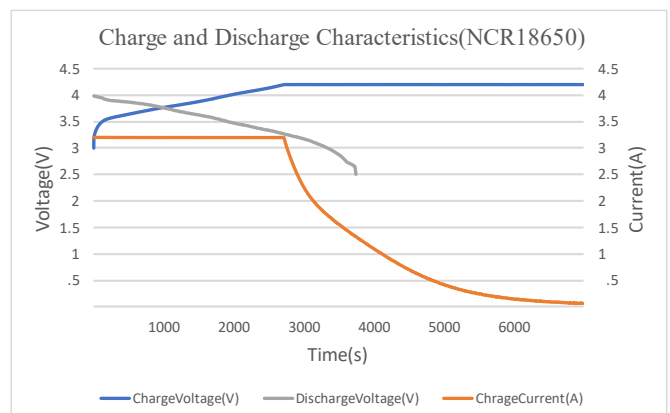
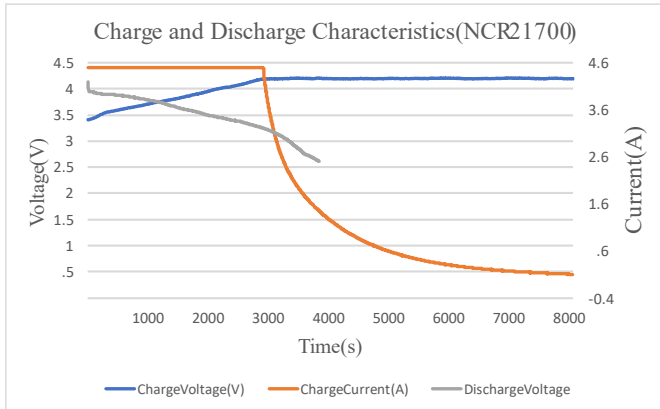


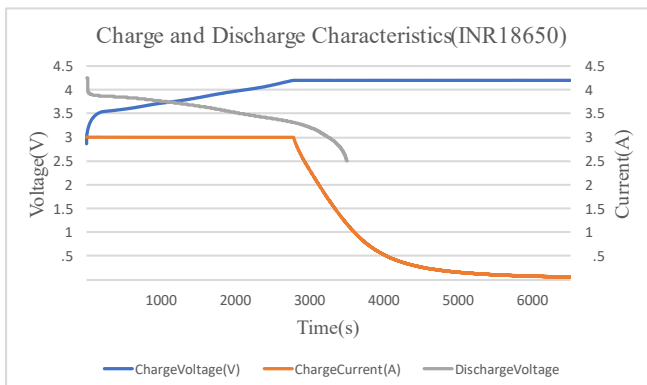
Fig. 5. Charge and Discharge Characteristics(NCR18650)

The testing conditions for the NCR18650 battery are as follows: a charging current of  $C_{rate} = C/1$  with a battery capacity of 3350 mAh, a charging voltage of 4.20 V, and a charging end current of 65 mA. The discharging current is also set at  $C_{rate} = C/1$  with a battery capacity of 3350 mAh, and the cutoff voltage is set at 2.5 V.



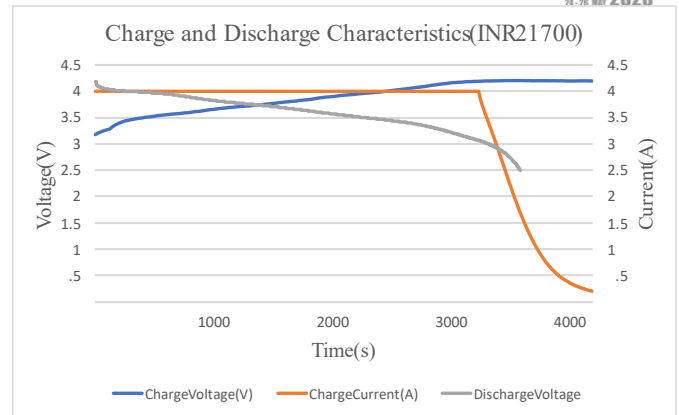
**Fig. 6.** Charge and Discharge Characteristics (NCR21700)

The testing conditions for the NCR21700 battery are as follows: a charging current of  $C_{rate} = C/1$  with a battery capacity of 4800 mAh, a charging voltage of 4.20 V, and a charging end current of 100 mA. The discharging current is also set at  $C_{rate} = C/1$  with a battery capacity of 4800 mAh, and the cutoff voltage is set at 2.5 V.



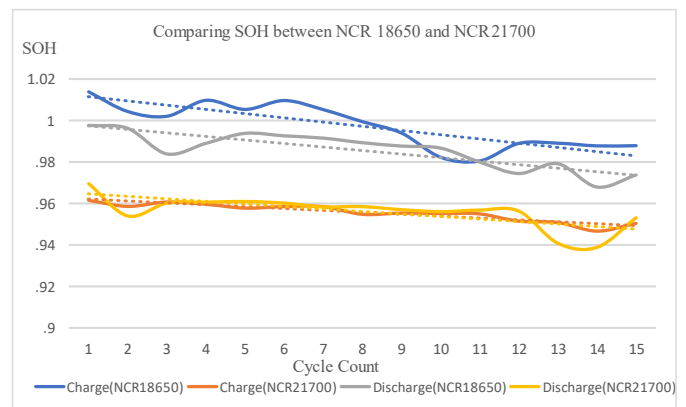
**Fig. 7.** Charge and Discharge Characteristics (INR18650)

The testing conditions for the INR18650 battery are as follows: a charging current of  $C_{rate} = C/1$  with a battery capacity of 3000 mAh, a charging voltage of 4.20 V, and a charging end current of 50 mA. The discharging current is also set at  $C_{rate} = C/1$  with a battery capacity of 3000 mAh, and the cutoff voltage is set at 2.5 V.



**Fig. 8.** Charge and Discharge Characteristics (INR21700)

The testing conditions for the INR21700 battery are as follows: a charging current of  $C_{rate} = C/1$  with a battery capacity of 4000 mAh, a charging voltage of 4.20 V, and a charging end current of 200 mA. The discharging current is also set at  $C_{rate} = C/1$  with a battery capacity of 4000 mAh, and the cutoff voltage is set at 2.5 V.



**Fig. 9.** Comparing SOH between NCR18650 and NCR21700

From the graph, it can be observed that both NCR18650 and NCR21700 batteries experience a reduction in State of Health (SOH) over the course of their usage cycles, with the NCR18650 battery having a higher average SOH value than the NCR21700 battery throughout the first 15 cycles. When comparing the trend lines of the blue and orange lines, it can be observed that the trend of SOH degradation for the blue line (NCR18650) is greater than that of the orange line (NCR21700). Next, when comparing the gray and yellow lines, it can be observed that the trend of SOH degradation for the gray line (NCR21700) is greater than that of the yellow line (NCR18650).

The reason why NCR18650 has a higher rate of degradation than NCR21700 may be related to the surface area of the battery. NCR18650 has a smaller size than NCR21700, which means it has a smaller surface area. This results in NCR18650 having a smaller surface area for heat dissipation, making it more difficult for it to dissipate heat compared to NCR21700. As a result, the temperature inside the battery increases and energy is lost in the form of heat,

which leads to a higher rate of degradation of SOH for NCR18650 compared to NCR21700.

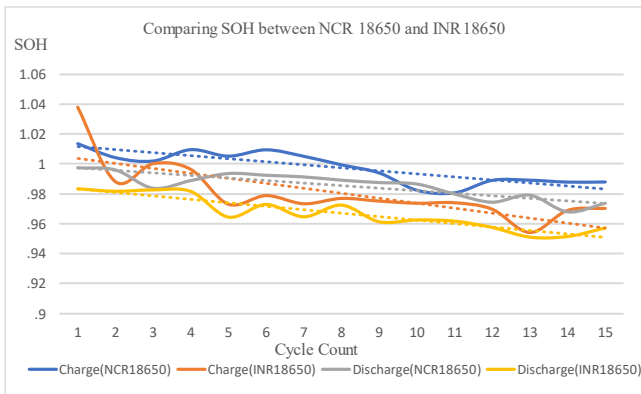


Fig. 10. Comparing SOH between NCR18650 and INR18650

From the graph, it can be observed that both INR18650 and NCR18650 batteries experience a reduction in State of Health (SOH) over the course of their usage cycles. However, the NCR18650 battery has a higher average SOH value than the INR18650 battery throughout the first 15 cycles. When comparing the trend lines of the blue and orange lines, it can be observed that the trend of SOH degradation for the orange line (NCR18650) is like that of the blue line (INR18650). Next, when comparing the gray and yellow lines, it can be observed that the trend of SOH degradation for the yellow line (INR21700) is like that of the gray line (NCR21700).

Therefore, it can be concluded that both INR18650 and NCR18650 batteries experience degradation from usage, and the rate of degradation for both types is almost similar during the first 15 cycles of usage.

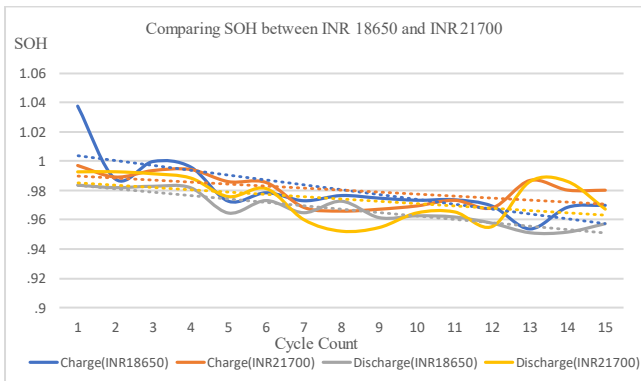


Fig. 11. Comparing SOH between INR18650 and INR21700

From the graph, when comparing the trend lines of the blue and orange lines, it can be observed that the trend of SOH degradation for the blue line (INR18650) is greater than that of the orange line (INR21700). Next, when comparing the gray and yellow lines, it can be observed that the trend of SOH degradation for the yellow line (INR21700) is smaller than that of the gray line (INR18650).

The reason for the higher State of Health (SOH) value in the INR21700 battery compared to the INR18650 battery could be due to the difference in battery size. The INR21700 battery is larger than the INR18650 battery, which increases

the surface area for electrolyte contact. This results in a more efficient flow of electricity, which makes the INR21700 battery more efficient than the smaller INR18650 battery.

This difference in efficiency could be due to the design of the INR21700 battery, which has a larger size and more space for active material. This allows for better long-term storage and less energy loss during charging, resulting in a higher SOH value than the INR18650 battery.

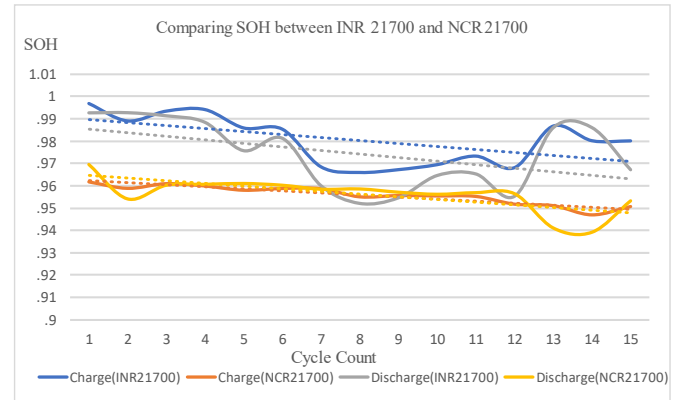


Fig. 12. Comparing SOH between INR21700 and NCR21700

Based on the graph, it can be observed that the average SOH value of the INR21700 battery is higher than that of the NCR21700 battery during the first 15 cycles of usage. When comparing the trend lines of the blue and orange lines, it can be observed that the trend of SOH degradation for the blue line (INR21700) is greater than that of the orange line (NCR21700). Next, when comparing the gray and yellow lines, it can be observed that the trend of SOH degradation for the yellow line (NCR21700) is like that of the gray line (INR21700).

Therefore, it can be concluded that both INR21700 and NCR21700 batteries experience degradation from usage, and the rate of degradation for both types is almost similar during the first 15 cycles of usage. However, the INR21700 battery has a slightly higher rate of SOH degradation when compared to the NCR21700 battery, which has a lower starting SOH value.

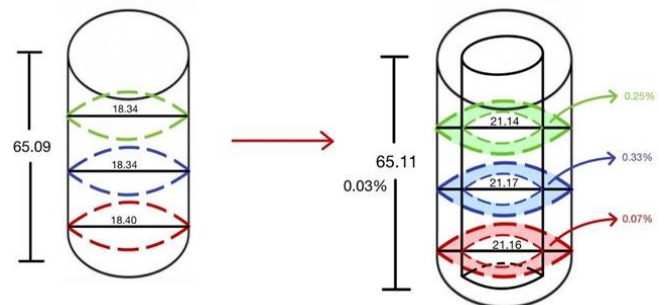
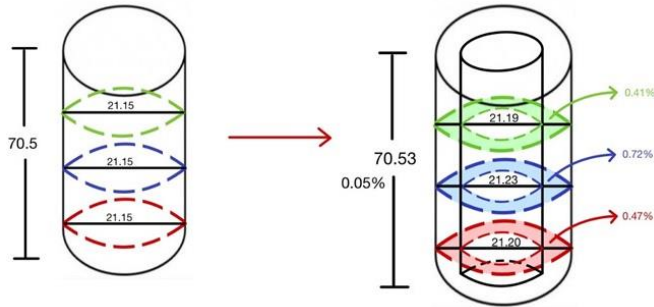


Fig. 13. Battery swelling of NCR18650 after 15 cycles.

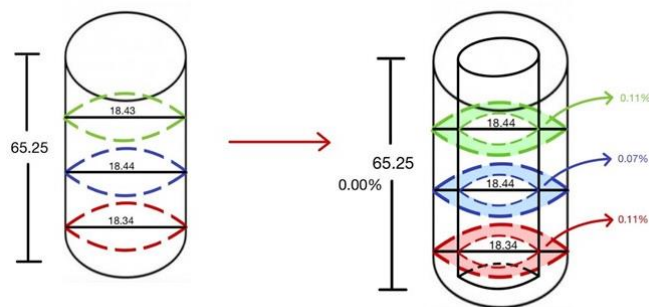
From the experimental results, there was swelling observed in the battery. The swelling percentages in the green cross-sectional area, blue cross-sectional area, and red cross-sectional area were 0.25%, 0.33%, and 0.07%, respectively. The length also increased by 0.03%. These

measurements were taken after 15 charge and discharge cycles.



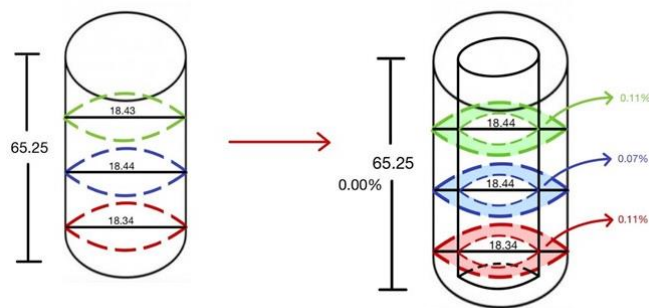
**Fig. 14.** Battery swelling of NCR21700 after 15 cycles.

From the experimental results, there was swelling observed in the battery. The swelling percentages in the green cross-sectional area, blue cross-sectional area, and red cross-sectional area were 0.41%, 0.72%, and 0.47%, respectively. The length also increased by 0.05%. These measurements were taken after 15 charge and discharge cycles.



**Fig. 15.** Battery swelling of INR18650 after 15 cycles.

From the experimental results, there was some swelling observed in the battery. The swelling percentages in the green cross-sectional area, blue cross-sectional area, and red cross-sectional area were 0.11%, 0.07%, and 0.11%, respectively. The length did not increase, with a swelling percentage of 0.00%. These measurements were taken after 15 charge and discharge cycles.



**Fig. 16.** Battery swelling of INR21700 after 15 cycles.

From the experimental results, there was some swelling observed in the battery. The swelling percentages in the green cross-sectional area, blue cross-sectional area, and red

cross-sectional area were 0.00%, 0.03%, and 0.00%, respectively. The length did not increase, with a swelling percentage of 0.00%. These measurements were taken after 15 charge and discharge cycles.

#### IV. CONCLUSION

In this study, the performance of cylindrical NCR18650, NCR21700, INR18650, and INR21700 batteries for electric vehicles were investigated in terms of their capacity and swelling. All batteries were cylindrical in shape and tested using a current rate of C/1 for charging and discharging at room temperature. The battery capacity was measured for each of the 15 test cycles, and the charging behavior was compared between all battery types.

The research results showed that the 18650-sized NCR and INR batteries had higher rates of charge loss than the 21700-sized NCR and INR batteries in terms of capacity. The 21700-sized batteries were better than the 18650-sized batteries because the larger battery size increased the space for heat dissipation, which increased the battery's lifespan. However, it was not possible to conclude which chemical compounds were used in each battery type due to the limited number of test cycles. Additional experiments are necessary to determine the trend of decreasing capacity and compare the performance of each battery type in terms of capacity.

Regarding the comparison of battery swelling, it was found that NCR batteries had more swelling than INR batteries due to the higher concentration of cobalt oxide in NCR batteries. Therefore, NCR batteries were generally less stable than INR batteries in terms of swelling in lithium-ion batteries.

From the experimental results, it can be concluded that the 21700-sized NCR and INR batteries have better capacity performance than the 18650-sized batteries, while INR batteries have less swelling than NCR batteries. However, the data obtained is not sufficient to determine which battery type is the best. Further studies are necessary by conducting additional experiments with a greater number of test cycles to obtain clearer trends.

#### REFERENCES

- [1] BloombergNEF, "Electric Vehicle Outlook 2021," International Energy Agency, April 2021. (*references*)
- [2] M report, "Electric car sales 2021 Toprush 109% Tesla occupies number 1," February 2021
- [3] Mr. Mark Kane, "What Batteries Are Tesla Using In Its Electric Cars?," insideevs, May 2022.
- [4] Daozhong Hu, Gang Chen, Jun Tian, Ning Li, Lai Chen, Yuefeng Su, Tinglu Song, Yun Lu, Duanyun Cao, Shi Chen, Feng Wu, "Unrevealing the effects of low temperature on cycling life of 21700-type cylindrical Li-ion batteries," *Journal of Energy Chemistry*, Volume 60, 2021, Pages 104-110
- [5] M. Waseem Marzook, Alastair Hales, Yatish Patel, Gregory Offer, Monica Marinescu, Thermal evaluation of lithium-ion batteries: Defining the cylindrical cell cooling coefficient, *Journal of Energy Storage*, Volume 54, 2022, 105217.
- [6] Thomas Waldmann, Rares-George Scurtu, Karsten Richter, Margret Wohlfahrt-Mehrens, 18650 vs. 21700 Li-ion cells – A direct comparison of electrochemical, thermal, and geometrical properties, *Journal of Power Sources*, Volume 472, 2020, 228614.
- [7] IEC 62660-1 Edition 2.0 (2018-12) Secondary lithium-ion cells for the propulsion of electric road vehicles – Part1: Performance testing

- [8] Technical Information of LG 18650HG2 (3.0Ah), High Power Cell Development Team, Dec. 05. 2014
- [9] Panasonic Lithium Ion NCR18650B Description, NCR18650B Datasheet, NCR18650B view \_\_\_ ALLDATASHEET \_\_\_
- [10] SPACIFICATION OF PRODUCT Tentative version (TBD) for Lithium-ion rechargeable cell Model : INR21700-48G, Samsung SDI Co., Ltd Battery Business Division, Oct., 2015
- [11] Panasonic NCR21700T 3.7v lithium battery 4800mAh, Batemo Cell Library, Panasonic TESLA Model 3, <https://www.batemo.de/products/batemo-cell-library/panasonic-tesla-model-3/>
- [12] Product Specification Rechargeable Lithium-Ion Battery Model : ICR18650 D1 3000mAh
- [13] Cheng Lin, Aihua Tang, Wenwei Wang, A Review of SOH Estimation Methods in Lithium-ion Batteries for Electric Vehicle Applications, *Energy Procedia*, Volume 75, 2015, Pages 1920-1925.
- [14] Anthony Barré, Benjamin Deguilhem, Sébastien Grolleau, Mathias Gérard, Frédéric Suard, Delphine Riu. "A review on lithium-ion battery ageing mechanisms and estimations for automotive applications", *Journal of Power Sources*, 241, 2013.
- [15] Ellen Ivers-Tiffée "Electrochemical characterization and post-mortem analysis of aged LiMn2O4-NMC/graphite lithium ion batteries part II: Calendar aging", *Journal of Power Sources*, 258, 2014, pp. 61-75.
- [16] Madeleine Ecker\*, B. Jochen, Gerschler, Jan Vogel, Stefan Käbitz, Friedrich Hust, Philipp Dechent, et al. "Development of a lifetime prediction model for lithium-ion batteries based on extended accelerated aging test data", *Journal of Power Sources*, 215, 2012.
- [17] Bor Yann Liaw, Rudolph G. Jungst, Ganesan Nagasubramanian, Herbert L. Case, Daniel H. Doughty, "Modeling capacity fade in lithium-ion cells", *Journal of Power Sources*, Volume 140, Issue 1, 2005, Pages 157-161.
- [18] Xiongwen Zhang, Thermal analysis of a cylindrical lithium-ion battery, *Electrochimica Acta*, Volume 56, Issue 3, 2011, Pages 1246-1255.
- [19] Doron Aurbach, Boris Markovsky, Alexander Rodkin, Miriam Cojocaru, Elena Levi, Hyeong-Jin Kim, An analysis of rechargeable lithium-ion batteries after prolonged cycling, *Electrochimica Acta*, Volume 47, Issue 12, 2002, Pages 1899-1911.
- [20] Huang, S., Sun, F., Chen, C., Liu, Y., Xu, L., & Wang, C. (2019). Comparative Study of Heat Dissipation Characteristics of Lithium-Ion Battery Packs with Different Structures. *Energies*, 12(10), 1982. <https://doi.org/10.3390/en12101982>
- [21] "Comparison of the Performance of Li-ion Batteries with Different Shapes and Sizes" From *Journal of The Electrochemical Society* The group of researchers consisted of Heng Zhang, Xingxing Chen, Zongping Shao, Jun Chen, Xinyong Tao, Ruying Li and Yuping Wu. <https://iopscience.iop.org/article/10.1149/2.0661910jes>
- [22] Sandeep Kumar, Anil Kumar, Ashish Kumar, and Anurag Kumar, "State of Health Estimation of Lithium-Ion Batteries Using Different Adaptive Filters," *International Journal of Emerging Electric Power Systems*, vol. 20, no. 3, pp. 1-10, 2019.

# A Novel Diazotizing Agent for Determination of Nitrite in Sausage

Aekgphonnada Yenuthok<sup>1,2</sup>, Tharinee Saleepochn<sup>1</sup>, Saijai Charnsethikul<sup>1</sup>,  
Pongsak Lowmunkhong<sup>1\*</sup>

<sup>1</sup> Department of Chemistry, Faculty of Science, Kasetsart University, Bangkok, Thailand

<sup>2</sup> Bureau of Quality and Safety of Food, Department of Medical Sciences, Ministry of Public Health, Nonthaburi, Thailand,  
e-mail address: aekgphonnada.y@ku.th

\*Corresponding author: Pongsak Lowmunkhong, e-mail address: fscipl@ku.ac.th

**Abstract:** Nitrite can generate a strong and stable curing color in cured meat products. Over recent years, various techniques for nitrite determination in food have been investigated due to inappropriate nitrite use. The colorimetric method is one of the spectrophotometry that was used frequently. This study aimed to evaluate a novel diazotizing agent for determining nitrite in sausage. In this study, the pioneer use of m-anisidine with coupling agent, N-(Naphthyl) ethylenediamine dihydrochloride (NED) for nitrite determination was demonstrated. The absorbance of yellow water-soluble azo compound was measured at 460 nm, which is the maximum absorption wavelength ( $\lambda_{\max}$ ) for this proposed method. The developed method has been validated with the linear range of nitrite concentration at 0.05 and 5.0  $\mu\text{g/mL}$  ( $r^2 > 0.995$ ). The limit of detection (LOD) and limit of quantification (LOQ) were 0.02  $\mu\text{g/mL}$ , 0.06  $\mu\text{g/mL}$  respectively. The validation results showed excellent accuracy with high recovery ( $98.8 \pm 3.90\%$ ). This method was achieved the satisfactory precision with the Association of Official Agricultural Chemists (AOAC) (HORRAT < 2). The comparison between the proposed and AOAC standard method indicated that there was no difference significantly at the 95% confidence interval ( $p > 0.05$ ). These results can be assumed that this developed method was suitable for the determination of nitrite in sausage using m-anisidine as the novel diazotizing agent.

**Index Terms—** Diazotization, m-Anisidine, Spectrophotometry, Nitrite, Sausage.

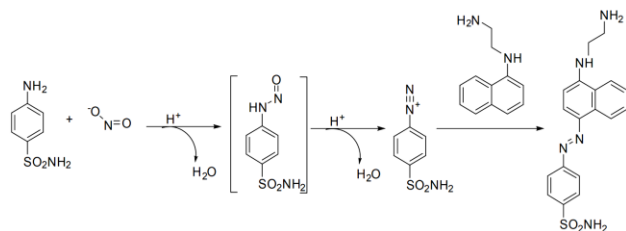
## I. INTRODUCTION

Nitrite ( $\text{NO}_2^-$ ) is an inorganic compound widely used as a food additive in cured meat products to enhance flavor, it obtains a stable red curing color and it also prevents bacterial spoilage. Nitrite is a white to slightly yellowish odorless crystalline powder that was high water solubility and is hygroscopic. It can cause pinking in noncured meat products at levels as low as 3–5 mg/kg of meat product. Inappropriate nitrite use has been found around 30–50 mg/kg in cured meat products [1] such as low-quality sausage, bacon and “white” products such as chicken loaf. Nitrite also presents different concentrations in the natural environment. The primary route of nitrite exposure in humans is through daily food consumption. Vegetables and cured meat products are the largest sources of nitrites in food, but small amounts may also be present in fish and dairy products. Meat products may contain < 0.2–6.4 mg/kg while dairy product contain < 0.2–1.7 mg/kg [2]. Sodium nitrite is a powerful oxidizing agent that can cause hypotension and limits oxygen transport. The delivery of nitrite into the body occurs through the formation of methemoglobin. This condition is called methemoglobinemia which is more commonly known as brown blood disease. The International Agency for Research on Cancer (IARC) classifies nitrites as “probably

carcinogenic to humans” (Group 2A) under certain conditions [3] (i.e., ingested nitrite under conditions that result in endogenous nitrosation). which could lead to the formation of known carcinogens, such as N-nitroso compounds. The current acceptable daily intakes (ADIs) for nitrite, set by the European Commission’s former Scientific Committee for Food (SCF) in 1997 and the Joint FAO/WHO Expert Committee on Food additives (JECFA) in 2002 were 0.06 and 0.07 mg/kg body weight/day, respectively [4].

In recent years, the number of developments in nitrite determination methods have increased to improve the analysis potential. There are several analytical methods for measuring nitrite levels such as chemiluminescence, capillary electrophoresis (CE), chromatography, colorimetry and electrochemistry [5]. Among those amended methods, colorimetry is one of the spectrophotometry methods that was frequently used since it was simple and sensitive. Additionally, nitrite can be investigated based on the diazotization coupling reaction and formed an azo compound called the Griess reaction, as shown in Fig. 1. The mechanism of this reaction occurred via the formation of diazonium salt between nitrite ions and sulfanilamide under acidic conditions. This diazonium salt intermediate was subsequently coupled with N-(1-Naphtyl)-ethylenediamine dihydrochloride (NED) to produce a red-violet color and

a water-soluble azo compound under an alkaline condition. These two reagents were typically and widely used. Griess reaction is still the most used methodology for the determination of nitrite until now [6]. Thus, the present work aimed to evaluate a novel diazotizing agent for determining nitrite in sausages. To the best of our knowledge, this study represents the first report on the application of m-anisidine in combination with the coupling agent, N-(Naphthyl) ethylenediamine dihydrochloride (NED), for the determination of nitrite.



**Fig. 1.** Detection mechanisms of the Griess reaction in the AOAC method (973.31).

## II. MATERIALS

### i. Chemicals and reagents

All chemicals and reagents used in the present work were of analytical grade, consisting of sodium nitrite, hydrochloric acid (37%), ethylene diamine tetraacetic acid (EDTA), m-anisidine, N-(1-Naphthyl) ethylenediamine dihydrochloride (NED), glacial acetic acid and potassium phosphate monobasic. Deionized water (with specific conductance of 18.2 mΩ) was produced in-house and was used for the preparation of all solutions.

### ii. Instruments

Spectrophotometer (UV/Visible) (Thermo Fisher Scientific, Model GENESYS™ 40 Vis/UV-Vis Spectrophotometers) equipped with a 1-cm glass cuvette was used for all absorbance measurements. Electronic balance, ultrasonic bath and pH meter were also used.

## III. METHODOLOGY

### i. Preparation of nitrite standards and reagents solutions

A stock solution of 500 µg/mL nitrite was prepared by dissolving an appropriate weight of sodium nitrite (NaNO<sub>2</sub>) in deionized water. A working solution was prepared daily by dilution of the stock solution in various concentrations. The 0.03 M diazotizing agent was prepared by dissolving m-anisidine in ethanol. The coupling NED reagent was prepared by dissolving N-(1-Naphthyl) ethylenediamine dihydrochloride in 20% acetic acid to obtain 1.0 mM NED solution. An acid solution of 1.0 M hydrochloric acid was prepared by dissolving 37% HCl in deionized water. In addition, 1.5 M phosphate buffer solution (PBS) was prepared by dissolving in deionized water. The pH was then adjusted by NaOH.

### ii. Development and validation procedure

#### a. Optimization of reaction conditions

First, the absorption spectra of the azo compound were obtained from wavelength scanning at 350–700 nm. The wavelength that offered the highest absorbance was chosen as the suitable wavelength for nitrite detection. Then, various parameters including 0.03 M m-anisidine volume, 1.0 mM NED volume and pH of 1.5 M PBS were all investigated. Furthermore, the type and concentration of acid, the reaction time and other relevant factors were evaluated to optimize the complex formation.

#### b. Investigation of ion interference

The optimal condition from the previous section was subsequently used to explore the effects of various cations and anions using 2.5 µg/mL nitrite ion solution and 2% EDTA solution as a masking agent. Absolute percentage of relative error that was less than 5% was used to evaluate the effect of each interference ion.

#### c. Method validation of nitrite determination in sausage

To evaluate the performance of the developed method for nitrite determination in sausage, the validation was carried out according to the Eurachem Guide [7]. The study investigated the linear range, limit of detection (LOD), limit of quantification (LOQ), accuracy and precision of the method. Subsequently, local market sausage samples were analyzed using the developed method and the resulting data were compared with those obtained from the validation study using statistical tests such as F-test and t-test to determine any significant differences.

### iii. The determination of nitrite in sausage samples

The homogenized sausage sample 5 g (±0.005 g) was transferred into a glass vial. After that, 25 mL of deionized water was added to the mixture and swirled gently for 2 minutes. The mixture was then boiled for 20 minutes. Then, the sample was filtered into a 50 mL falcon tube and allowed to cool to room temperature before being centrifuged for 5 minutes at 6000 rpm. The supernatant was transferred to a 50 mL volumetric flask and adjusted with deionized water. Next, 2.0 mL of the extracted solution was transferred to a 10.0 mL volumetric flask which 0.4 mL of 2% EDTA, 1 mL of m-anisidine and 0.05 mL of 1.0 M HCl were added, respectively. After shaking to homogeneous, the solution was allowed to stand at room temperature for 15 minutes. Then, 2.5 mL of NED reagent and 0.5 mL of pH 6 PBS was added into the same flask and adjusted to the mark with deionized water. Subsequently, the solution was shaken again and allowed to stand for another 10 minutes at room temperature. After 10 minutes, the clear solution was transferred into a 1-cm glass cuvette and measured the absorbance at 460 nm against a blank solution.

### iv. The determination of nitrite in sausage by the AOAC standard method (973.31)

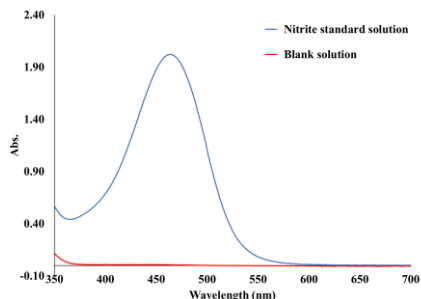
A 5.0 mL of extracted solution from above section was transferred to 25 mL volumetric flask, followed by adding 2.5 mL of sulfanilamide in 20% acetic acid. The mixture was homogenized and allowed to stand for 15 minutes at room temperature. Then, 2.5 mL of NED reagent was added to the same flask. The volume was adjusted to the

mark with deionized water and waited for 15 minutes to complete color development. The absorbance was measured at 540 nm in a 1-cm glass cuvette against a blank solution.

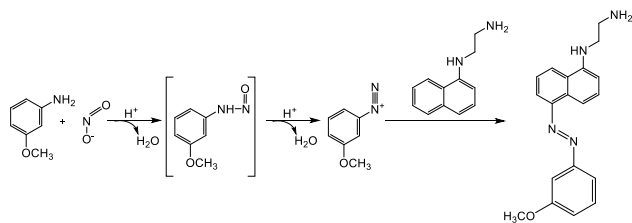
#### IV. RESULTS AND DISCUSSION

##### i. Reaction between nitrite, m-anisidine and NED

The azo dye compound was measured between 350 and 700 nm, using UV-Visible spectrophotometer in wavelength scanning mode. The absorption spectrum of azo compound from nitrite standard solution was showed in blue line (Fig. 2) which maximal absorption wavelength ( $\lambda_{max}$ ) was observed at 460 nm. The reaction between the amino group of the m-anisidine and nitrous acid, generated from the nitrite ion and a strong acid, results in the formation of diazonium salt, a key intermediate in the synthesis of azo compounds as seen in Fig. 3. Then, diazonium salt was coupled with the NED reagent to produce a yellow water-soluble azo compound. On the contrary, the absence of signal was observed in the blank solution (red line).



**Fig. 2.** The azo compound's absorption spectra contained 5  $\mu\text{g/mL}$  nitrite (blue line) and blank solution (red line).



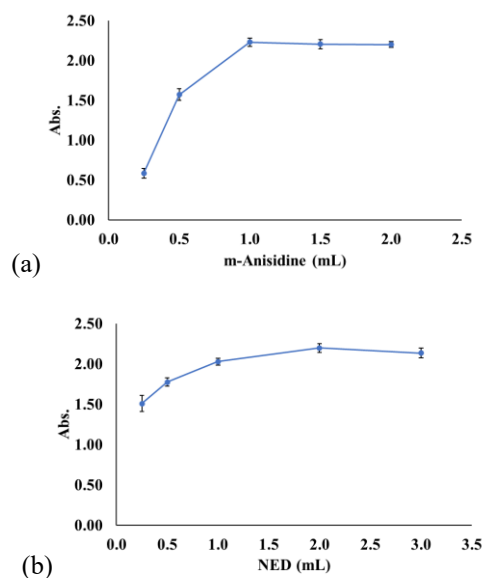
**Fig. 3.** The reaction mechanism between nitrite, m-anisidine and NED reagent.

##### ii. Optimization of reaction conditions

The absorbance of azo compound generated from 5  $\mu\text{g/mL}$  nitrite was investigated by varying different volumes of 0.03 M m-anisidine and 1.0 mM NED reagent. The results in Fig. 4 showed that the reaction between 1 mL of m-anisidine and 2 mL of NED reagent promoted the greatest absorbance. Therefore, this condition was used in the subsequent experiments. The effect of different acids at 1.0 M concentration on absorbance was summarized in Table 1. The result showed that hydrochloric acid provided superior results compared to sulfuric acid. However, 0.05 mL of this acid was used for subsequently trial due to the highest absorbance, as seen in Fig. 5. Furthermore, the effect of pH of the 1.5 M phosphate buffer solution on the coupling

step was then examined ranging from pH 2-12. According to the results in Fig. 6, the most suitable pH for this proposed method was established at pH 6 where this pH presented weak acid behavior. However, the condition at pH 2-4 and pH 7-11 provided extremely acidic and basic respectively, which inhibited generation of stable azo compound. On the other hand, the sausage samples contained a variety of ingredients that could cause the change of pH in sample solution. As a result, using a buffer solution with a suitable pH would be desirable.

In addition, the reaction time was determined to achieve a stable color and intensity. Fig. 7 demonstrated the change in absorbance of an azo compound from 2.5  $\mu\text{g/mL}$  nitrite as a function of time with 1-minute intervals. The absorbance was slightly increased and became stable after 8 - 25 minutes. As a result, in all subsequent experiments, the absorbance was measured after 10 minutes of incubation at room temperature using a UV-Visible spectrophotometer at 460 nm.



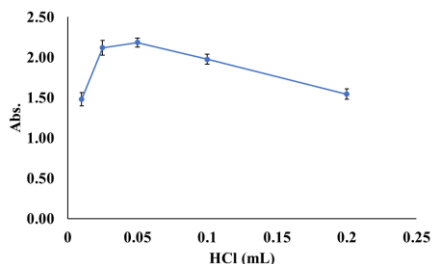
**Fig. 4.** The effect of 0.03 M m-Anisidine (a) and 1.0 mM NED reagent (b) volume on azo compound absorbance at 5  $\mu\text{g/mL}$  nitrite (n=3).

TABLE 1

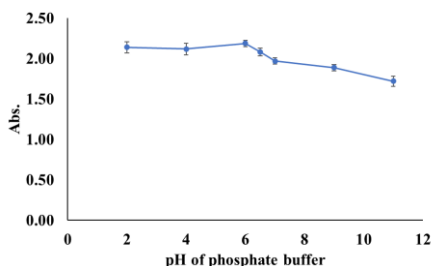
Effect of acid type on absorbance

Acid type	Absorbance
1.0 M Sulfuric acid	1.471
1.0 M Hydrochloric acid	2.185

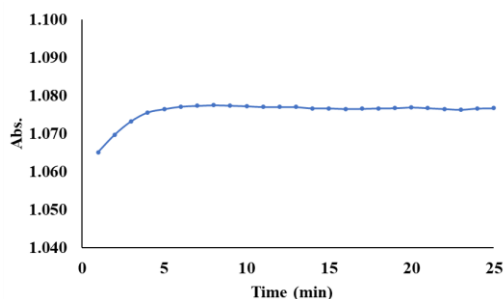




**Fig. 5** The influence of 1 M HCl volume on azo compound absorbance at 5 µg/mL nitrite (n=3).



**Fig. 6.** The optimum pH of 1.5 M Phosphate buffer solution for the coupling reaction between diazonium salt and NED (n=3).



**Fig. 7** Change in absorbance as a function of time on the reaction equilibrium at nitrite concentration of 2.5 µg/mL.

TABLE 2

Tolerance limits of ion interference species in the spectrophotometric determination

Ion interference specie	Form added	Tolerance limit (mg/kg)
Na <sup>+</sup>	NaCl	> 10000
Ca <sup>2+</sup>	CaCl <sub>2</sub>	2500
Mg <sup>2+</sup>	MgCl <sub>2</sub>	2000
Mn <sup>2+</sup>	MnCl <sub>2</sub>	1000
Fe <sup>2+</sup>	FeCl <sub>2</sub>	750
Cl <sup>-</sup>	NaCl	> 10000
CO <sub>3</sub> <sup>2-</sup>	Na <sub>2</sub> CO <sub>3</sub>	1250
F <sup>-</sup>	NaF	1000
I <sup>-</sup>	NaI	1000

iv. Method validation of nitrite determination in sausage

One of the sausage samples was chosen as a representative matrix for method validation. The calibration plot between nitrite ion concentration (µg/mL) and absorbance of yellow water-soluble azo compound at 460 nm was used to quantify nitrite concentrations; the linear range of this calibration curve was demonstrated at 0.05-5.0 µg/mL with an excellent correlation coefficient ( $r^2 = 0.9996$ ). Limit of detection (LOD) and limit of quantification (LOQ) were 0.02 and 0.06 µg/mL, respectively. After that, accuracy was investigated using ten replicated spiking samples at three different concentrations. The obtained absorbances were calculated to concentration in µg/mL units and expressed in terms of recovery. The mean of recoveries demonstrated excellent accuracy at all concentration levels. Precision was examined using the Horwitz equation and HORRAT. The results indicated that this proposed method is satisfactory as summarized in Table 3.

F-test and t-test were used to compare the proposed method to AOAC [9] standard method for nitrite determination. The nitrite concentration in four sausage samples was determined and expressed as a mean ± standard deviation. The results in Table 4 revealed that two samples among four samples, sausage A and C, contained higher nitrite concentrations than LOQ. Hence, F-test and t-test were calculated using a mean of three replicates. At 95% confidence interval, there were no significant differences between these two analytical methods, which means that all values were greater than the p-value ( $p > 0.05$ ). As a result, it can be concluded that the proposed analysis method is appropriate to determine nitrite concentrations in sausage.

iii. Ion interferences

The ion interferences of possible ions in the food matrix that affected the absorbance change were evaluated. In this proposed method, 2.5 µg/mL nitrite was investigated against various concentrations of each interference ion and 0.4 mL of 2% EDTA was used as a masking agent before adding further reagents. The solution in presence of EDTA, indicated interferences had been minimized. Table 2 summarizes the tolerance limits with a relative error percentage less than 5%. Colman P. and Schimel P. [8] collected the data and they also used EDTA to reduce iron interferences in the colorimetric detection of nitrite and nitrate.

TABLE 3

Analytical performance of the proposed method for nitrite determination in sausage

Parameter	Value
Linear range / (µg/mL)	0.05 – 5.0
Correlation coefficient (r <sup>2</sup> )	0.9996
Regression equation	Abs = 0.485 [NO <sub>2</sub> <sup>-</sup> ] + 0.0012
Limit of detection (LOD) / (µg/mL)	0.02
Limit of quantification (LOQ) / (µg/mL)	0.06
Accuracy (%Recovery)	
- at LOQ / (%)	95.6 ± 4.47
- at maximum limit* (1.6 µg/mL) / (%)	102.5 ± 1.34
- at high level (5 µg/mL) / (%)	98.4 ± 0.94
Precision (HORRAT)	
- at LOQ / (%)	0.27
- at maximum limit (1.6 µg/mL) / (%)	0.23
- at high level (5 µg/mL) / (%)	0.21

\* Maximum limit is 80 mg/kg for all food sample based on Notification of the Ministry of Public Health (No. 418) B.E. 2563 Issued by virtue of the Food Act B.E. 2522

TABLE 4

Comparison of the proposed and AOAC method for the determination of nitrite in sausage

Sample	This study (mg/kg)	AOAC (mg/kg)	F-test (P value)	t-test (P value)
Sausage A	100.2 ± 3.12	94.5 ± 1.96	0.283	0.056
Sausage B	< LOD	< LOD	-	-
Sausage C	243.1 ± 1.69	247.3 ± 3.31	0.207	0.124
Sausage D	< LOD	< LOD	-	-
Sausage E	< LOD	< LOD	-	-

## V. CONCLUSION

This spectrophotometric technique for determining nitrite in sausage used a novel diazotizing agent (m-anisidine) to quantify the intensity of absorbance at 460 nm, which is the maximal absorption wavelength ( $\lambda_{\max}$ ) for this proposed method. The conditions of the experiment were also optimized and validated. While the results revealed an excellent performance with a good linear relationship between azo compound absorbance and nitrite concentration up to 5 µg/mL ( $r^2 = 0.9996$ ). The limit of detection and limit of quantification were 0.02 and 0.06 µg/mL, respectively. In terms of recovery, the accuracy was excellent. The approach method acquired satisfactory precision with the Association of Official Agricultural Chemists (AOAC) (HORRAT < 2). At 95% confidence interval, there was no significant difference between the developed method and the AOAC standard method ( $p > 0.05$ ). The advantages of this study were that m-anisidine could be used as an alternative reagent for diazotization reactions and the total reaction time and chemical waste generated were less than the standard method.

## ACKNOWLEDGMENT

The authors thank Kasetsart University Research and Development Institute (KURDI) for financial support.

## REFERENCES

- Feiner, G., Color in Cured Meat Products and Fresh Meat, in Salami. 2016. p. 89-101.
- Marija Nujić, M.H.-S., Nitrates and Nitrites, Metabolism and Toxicity. Food in Health and Disease, scientific-professional journal of nutrition and dietetics, 2017. **6**(2): p. 63-72.
- IARC, Ingested Nitrate and Nitrite and Cyanobacterial Peptide Toxins IARC Monographs on the Evaluation of Carcinogenic Risks to Humans. 2010.
- Additives, E.P.o.F., et al., Re-evaluation of sodium nitrate (E 251) and potassium nitrate (E 252) as food additives. EFSA J, 2017. **15**(6): p. e04787.
- Lucas, S.B., et al., Nitrite Determination in Environmental Water Samples Using Microchip Electrophoresis Coupled with Amperometric Detection. Micromachines (Basel), 2022. **13**(10).
- Wang, H., et al., A novel and simple spectrophotometric method for detection of nitrite in water. Analyst, 2018. **143**(19): p. 4555-4558.
- Örnek, B.M.a.U., Eurachem Guide: The Fitness for Purpose of Analytical Methods – A Laboratory Guide to Method Validation and Related Topics. 2 ed. 2014.
- Colman, B.P. and J.P. Schimmel, Understanding and eliminating iron interference in colorimetric nitrate and nitrite analysis. Environ Monit Assess, 2010. **165**(1-4): p. 633-41.
- Mohamed, A.A., et al., Modification of AOAC Method 973.31 for Determination of Nitrite in Cured Meats. Journal of AOAC INTERNATIONAL, 2008. **91**(4): p. 820-827.

# Fabrication and Characterization of Eco-friendly Ethyl Cellulose Nanofibers for Use as Air Filtration

**Sarat Nudchamong, Jate Panichpakdee, Busarin Noikaew, and Siriporn Larpkittaworn**

Thailand Institute of Scientific and Technological Research, Khlong Luang, Pathum Thani, 12120, Thailand  
E-mail: sarat@tistr.or.th

**Abstract:** Ethyl cellulose nanofibers are widely used in many applications such as protective clothing, biomedical applications, and filtration due to its nontoxicity and stable during storage. However, ethyl cellulose nanofibers, based on electrospinning process, still used toxic solvent in the preparation process. In this research, absolute ethanol, eco-friendly solvent, was used as a solvent for preparation of homogeneous ethyl cellulose solutions. Various parameters for electrospinning of ethyl cellulose nanofibers via direct electrospinning of homogeneous ethyl cellulose solutions, including viscosity, needle-to-collector distance, and electric potential were investigated. At the optimum conditions (solution viscosity of 2,221.7 cP, voltage of 40 kV, and needle-to-collector distance at 150 mm), the electrospun nanofibers observed by Scanning Electron Microscope (SEM) have a smooth surface with a relatively uniform diameter with an average diameter in the range of 226.05 nm. In addition, the efficiency of filtering particles according to TIS. 2480-2562 was also evaluated. The result showed that the particle filtration efficiency (0.3  $\mu$ m MMAD) was measured at 95.93%, which met the TIS requirements ( $\geq 95$  %) and can be used to form N95 air filters.

**Index Terms**—Air Filtration, Ethyl Cellulose, Nanofiber, Electrospinning

## I. INTRODUCTION

Air pollution is a common problem in many countries around the world. Especially, Thailand is now facing air pollution from both heavy traffic and dust particle from construction sites. This particulate matter is smaller than 2.5 microns (PM<sub>2.5</sub>) that cannot be seen with the naked eye. Moreover, some dust particles can reach deep into the respiratory tract, lungs, and possibly into the bloodstream, causing serious harm and health problems. The World Health Organization or World Health Organization (WHO) classified PM<sub>2.5</sub> dust as group 1 of carcinogens. The World Bank report (World Bank) has reported that Thailand has lost up to 50,000 deaths from air pollution, which affects the people's life quality and economy, including the cost that the government state has to lose in medical expenses for patients from air pollution [1]. Therefore, there is a demand for personal protective equipment (PPE) such as medical gloves, and protective clothing, as well as highly efficient N95 respirators for air filtration and dust protection that is suitable for use in hospitals and operating rooms.

The N95 mask is a high-quality air filter mask that helps protect against not only harmful germs but also particulate dust. N95 masks are made from microfiber polypropylene which makes them effective in trapping small harmful particles of PM<sub>2.5</sub> and PM<sub>10</sub> at least 95%.

Although the resulting N95 mask on the market has high filtration efficiency nevertheless it has a large fiber size in the micrometer scale, resulting in air exchange being less possible which causes breathing difficulties as well as carbon dioxide accumulation when worn for a long time. In addition, the polymer used as a raw material in N95 filters cannot be degraded naturally, causing waste and pollution problems to the environment.

Ethyl cellulose polymers are naturally occurring cellulose derivatives and are found in large quantities, especially in agricultural crops. Ethyl cellulose is a hydrophobic polymer whose properties are nontoxicity and stable during storage which makes it useful in areas such as protective clothing, and biomedical and filtration applications [1,2]. Electrospinning or electrostatic spinning is a process that is widely used to produce polymer fibers ranging in diameter from nanometers to micrometers from polymer solutions [1]. The advantages of electrospinning are the ability to produce high-quality fine fibers, non-complicated equipment, low production cost, and the use of less substrate polymer solutions [3,4]. Currently, there are studies on fiber production from ethyl cellulose by the electrospinning method. The ethyl cellulose was mixed with the multicomponent solvent system such as tetrahydrofuran/dimethylacetamide (THF/DMAc) [5,6] and N, N-dimethylformamide (DMF)/Acetone [7], Methylene blue/anhydrous ethanol [8], and N-methyl-morpholine / N-oxide/lithium chloride /dimethyl acetamide (NMMO/LiCl/DMAc) [9]. In addition, electrospun nanofibers have been used as a pharmaceutical encapsulate in medical applications by using cellulose acetate and ethyl cellulose polymer as a precursor mixed with N, N dimethyl

acetamide. (DMAc)/acetone/anhydrous ethanol [10]. However, these solutions are highly toxic and non-biodegradable. It is therefore not suitable for use in biomedical and filtration applications.

The purpose of this research is to produce ethyl cellulose nanofibers for use as N95 air filters, we also study the characteristic of electrospun nanofibers from ethyl cellulose /ethanol solution as bio-based material via the electrospinning method. The resulting electrospun nanofibers have not only high filtration efficiency (>95%), and no toxic residue but the production process is also environmentally friendly as well.

## II. METHODOLOGY

### Materials

Ethyl cellulose (C<sub>20</sub>H<sub>38</sub>O<sub>11</sub>, AR grade) was purchased from Sigma Aldrich. Ethyl cellulose (C<sub>20</sub>H<sub>38</sub>O<sub>11</sub>, commercial grade) with different viscosities (label denoted as 7, 20, 50, and 100 cP) was purchased from Chanjao longevity Co., Ltd. Absolute ethanol (C<sub>2</sub>H<sub>5</sub>OH, 99%) was obtained from Merck.

### Preparation of ethyl cellulose electrospun nanofibers

The commercial-grade ethyl cellulose powder with different viscosities was dissolved in absolute ethanol at a concentration of 12 % w/v as the optimum concentration to produce electrospun ethyl cellulose nanofibers for this experiment. If concentration is too high, ethyl cellulose was not dissolved completely. While analytical grade ethyl cellulose was also performed using the same procedure as commercial grade. The homogeneous ethyl cellulose solutions obtained were used as a precursor solution for producing the electrospun fiber. The viscosity and electrical conductivity of the precursor solution were measured by a viscometer (DV-3P R, Anton Paar GmbH) and conductivity meter (HI 9835, HANNA instrument). The resulting unit measure of dynamic viscosity were denoted as cP.

Typically, electrospun nanofibers were prepared from ethyl cellulose solution using an electrospinning process. The ethyl cellulose solution with different viscosities was carefully loaded in a 10-mL syringe to which a stainless-steel capillary metal-hub needle was attached. The inside diameter of the metal needle was 0.4 mm. The positive electrode of the high-voltage power supply was connected to the needle tip and the grounded electrode was linked to a metal collector wrapped with aluminum foil. According to the electrospinning parameters, the flow rate of the precursor solution was supplied at 1.0 mL/h using a single syringe pump. The electrical potential was controlled at 14 and 40 kV. The resulting electrospun nanofibers were collected on an aluminum foil which was distanced from the needle to the collector at 150 and 200 mm. The electrospinning process was carried out under ambient conditions.

### Characterization

The morphology of electrospun nanofiber was examined by using field emission scanning electron microscopy (FE-SEM). The average diameter of the resulting electrospun nanofiber was determined by using ImageJ software.

### Filtration efficiency testing

Prepare the air filter specimen to test the particle filtration efficiency (0.3 μm MMAD, mass median aerodynamic diameter) according to TIS. 2480-2562 that described single-use N95 masks to reduce the risk of airborne infection. TIS (Thai Industrial Standard) is a technical requirement that the Thai Industrial Standards Institute (TISI) has established as a manufacturing guideline in order to undertake standardization and aim for products with optimal quality.

The composition is as follows:

1. Coarse filter outer layer (1st Layer) spunbond fabric, size 50 grams (50 g/sq m.)
2. Fine filter layer (2nd layer), ethyl cellulose nanofiber sheet.
3. Inner layer (3rd layer) spunbond fabric, size 50 grams (50 g./sq m.)

## III. RESULTS AND DISCUSSION

### Chemical Properties of Ethyl Cellulose Solutions

The viscosity and conductivity of the polymer precursor solution influence both fiber forming in the electrospun process and resulting electrospun nanofiber morphology. Since viscosity is one of the important factors of the polymer solution in electrospinning, there is a critical viscosity for each polymer solution; when the polymer solution has appropriate viscosity allowing the polymer chains to intertwine and cause forming a strong polymer fiber structure. The viscosity of 12%w/v ethyl cellulose solution that was synthesized from ethyl cellulose AR grade and commercial grade (viscosity at 7, 20,50, and 100 cP) are compared in Figure 1. The commercial-grade ethyl cellulose solution at 50 cP had an estimated viscosity of 2,221.7 cP, which is the highest value while ethyl cellulose solution prepared from commercial grade at 7, 20, and 100 cP have the measured viscosities of 182.2, 147.3, 1201.2, and 24.1 cP, respectively.

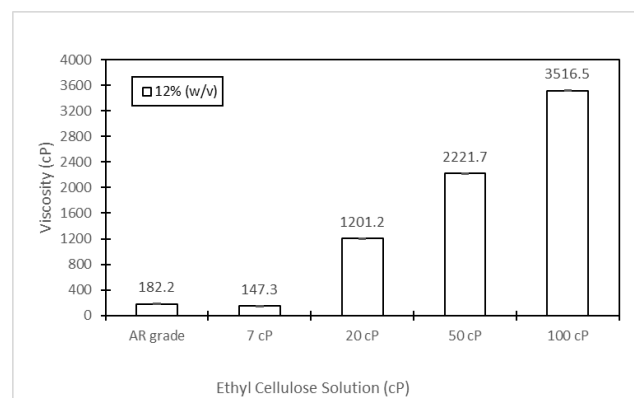
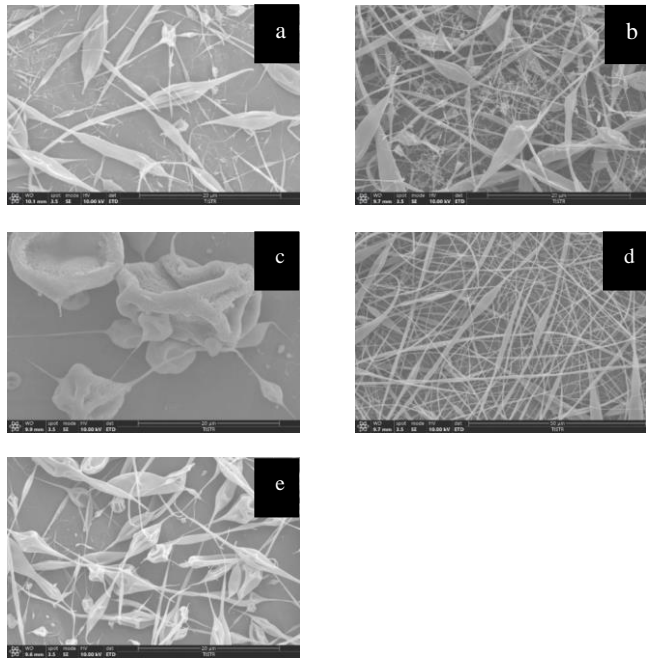


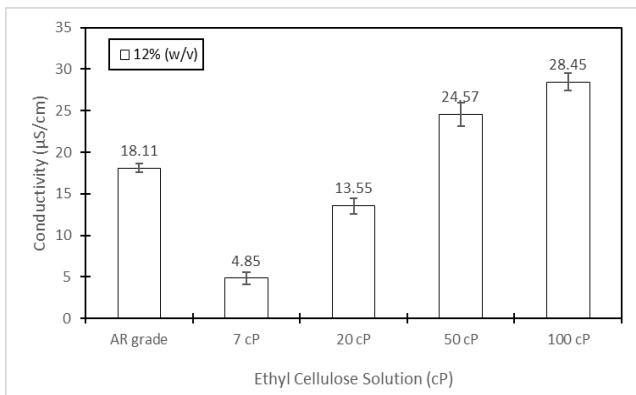
Fig 1. Viscosity of ethyl cellulose solution.

The effect of precursor viscosity on the structural properties of electrospun nanofiber attained is revealed in Figure 2. The case of commercial-grade ethyl cellulose solution at 50 cP (Figure 2 (d)) shows electrospun nanofibers have a smooth surface with a relatively uniform diameter with an average diameter in the range of 568.43 nm. On the other hand, two shapes are found in the commercial grades at 7, 20, and 100 cP, mostly bulbous or

granular and large diameter fibers which are revealed in Figures 2 (a), (b), (c), and (e). This phenomenon can be explained that the polymer solution being less viscous, resulting in an insufficient amount of polymer to form binding fibers. The solution ejected from the tailer cone break up into small droplets.



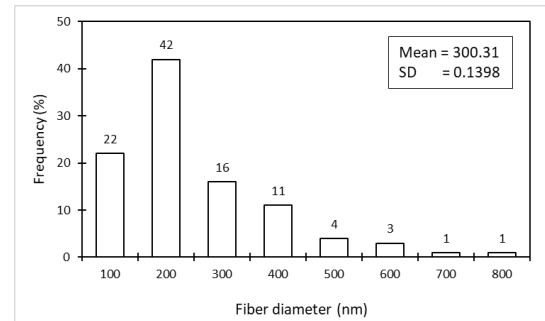
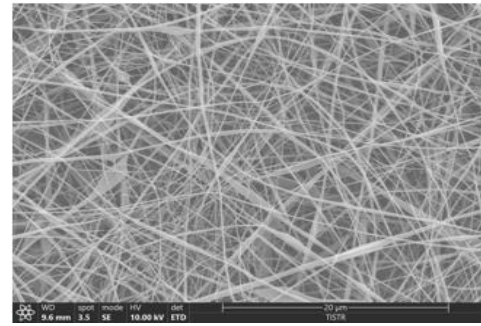
**Fig 2.** FE-SEM image of electrospun ethyl cellulose prepared from ethyl cellulose 12 % (w/v), (a) AR grade and commercial grade with viscosity at (b) 7 cP, (c) 20 cP, (d) 50 cP, and (e) 100 cP under applied voltage; 14 kV, flow rate; 1 mL/h, distanced from the needle to the collector; 200 mm.



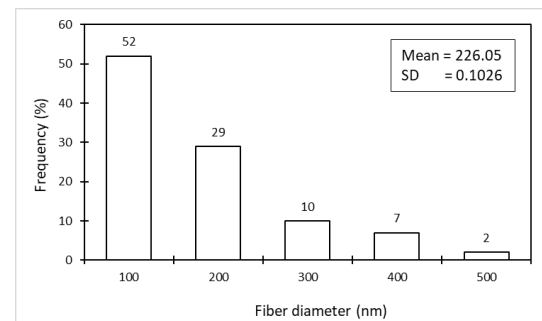
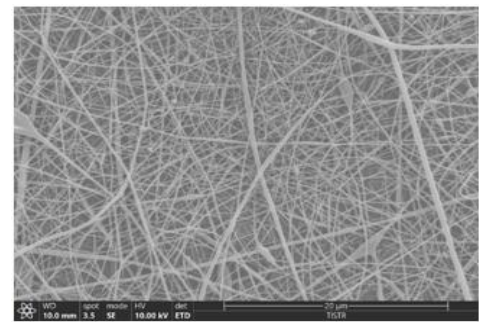
**Fig 3.** Conductivity of ethyl cellulose solution.

The electrical conductivity of ethyl cellulose solution at a concentration of 12 % w/v of analytical grade, and commercial grade at 7, 20, 50, and 100 cP are exhibited in Figure 3. The results revealed the electrical conductivity of commercial grade at 7, 20, 50, and 100 cP was 18.11, 4.85, 13.55, 24.57, and 28.45 μS/cm. Increasing the electrical conductivity cause increased mobility of the molecule in polymer solution in the high voltage of the electric field. As a result, the diameter and average shape of the electrospun nanofibers tend to decrease with increasing electrical conductivity. Besides, if the conductivity of the polymer

solution is too high, conductivity has no significant effect on the average fiber diameter and shape.



(a)



(b)

**Fig 4.** FE-SEM image of electrospun ethyl cellulose prepared from ethyl cellulose 12 % (w/v), commercial grade with viscosity at 50 cP under applied (a) voltage; 14 kV and (b) voltage; 40 kV, flow rate; 1 mL/h, distanced from the needle to the collector; 150 mm.

### Effect of Factors on Electrospinning Process

Focusing on the morphology of commercial-grade ethyl cellulose at 50 cP attained from the electrospinning process, the flow rate and electric conductivity constant were applied with a flow rate of 1 mL/h and a voltage of 14 kV. The distance from the needle to the fiber collector is an

important parameter to characterize the nanofiber shape. It indicated that when the distance from the needle to the fiber collector was reduced from 200 mm to 150 mm, the average diameter of the electrospun nanofiber tended to decrease from 568.43 nm (Figure 2 (d)) to 300.31 nm (Figure 4 (a)). The rapid evaporation rate of absolute ethanol used as the solvent for the ethyl cellulose solution, resulted in the stretching of the fibers as they pass through the air for a short period of time to allow the fibers to dry completely before reaching the fiber collector.

Figure 4 shows the effect of electric potential on the resulting nanofiber morphology obtained from ethyl cellulose solution commercial grade at 50 cP. The electrospinning parameter was applied with a flow rate of 1 mL/h, distanced from the needle to the collector at 150 mm. The electric potential (kV) applied in the electrospinning process is an important factor and affects the diameter of the electrospun nanofibers. Besides, the average diameter of the resulting electrospun nanofiber tended to decrease from 300.31 nm (Figure 4 (a)) to 226.05 nm (Figure 4 (b)) when the electric potential increased from 14 kV to 40 kV. A decrease in average diameter with increasing electric potential leads to an increase in the density of electric charges. Therefore, when the electric conductivity is high enough to overcome the surface tension of the polymer solution, it will make the droplets of solution change into the cone of the pourer quickly and evenly, resulting in the average diameter of the electrospun nanofibers looking significantly smaller.

The results described above suggest the appropriate condition for producing the prototype N95 air filters was the ethyl cellulose/ethanol ratio at a concentration of 12% w/v, synthesized from commercial grade ethyl cellulose at 50 cP due to the maximum viscosity at 2,221.7 cP and the electrical conductivity was 24.57  $\mu$ S/cm. In addition, the selected electrospinning parameters were applied with a flow rate of 1 mL/h, an electric potential of 40 kV, and distanced from the needle to the collector at 150 mm since the resulting electrospun nanofibers have a smooth surface with a relatively uniform diameter in the range of 226.05 nm. Compared to the diameter of electrospun nanofibers (800-1200 nm) prepared from the toxic solvents [6, 7], the diameter obtained in this study was smaller (226.05 nm). For testing the efficiency of filtering particles according to TIS. 2480-2562 that described the Single-use N95 mask to reduce the risk of airborne infection. The results observed that the particle filtration efficiency (0.3  $\mu$ m MMAD) was measured at 95.93%, which met the TIS requirements ( $\geq$ 95 %). This was consistent with the commercial one.

#### IV. CONCLUSION

Bio-based material ethyl cellulose nanofibers mixed with absolute ethanol used as a green solvent were successfully performed via the electrospinning process. The optimum conditions are as follows the 12 % w/v ethyl cellulose/ethanol ratio obtained from commercial grade ethyl cellulose at 50 cP under the electrospinning parameter; applied voltage of 40 kV, a flow rate of 1 mL/h, and distance from the needle to the fiber collector 150 mm.

The resulting electrospun nanofiber also exhibited an average diameter in the range of 226.05 nm and a particle filter efficiency of 95.93%, which can be used to form N95 air filters. Furthermore, this electrospinning process is not only environmentally friendly but the resulting electrospun nanofibers are also biodegradable green materials.

While N95 filters in the market have high filtration efficiency but there are large fiber sizes on the micrometer scale and also made from synthetic plastic fibers that cannot be degraded naturally, causing waste and pollution problems to the environment.

#### ACKNOWLEDGMENT

This work was supported by the Thailand Institute of Scientific and Technological Research (TISTR).

#### REFERENCES

- [1] D. Lv, M. Zhu, Z. Jiang, S. Jiang, Q. Zhang, R. Xiong, C. Huang, "Green Electrospun Nanofibers and Their Application in Air Filtration," *Macromolecular Materials and Engineering*, vol. 303, no. 12, pp. 1800336. 2018.
- [2] A. Gonçalves, F. Rocha, B. N. Estevinho, "Application of Ethyl Cellulose and Ethyl Cellulose + Polyethylene Glycol for the Development of Polymer-Based Formulations Using Spray-Drying Technology for Retinoic Acid Encapsulation" *Foods*, vol. 11, no. 16, pp. 1-11, 2022.
- [3] W.F.W. Fathilah, R. Othaman, "Electrospun Cellulose Fibres and Applications," *Sains Malaysiana*, vol. 48, no. 7, pp. 1459-1472, 2019.
- [4] R. Fatahian, M. Mirjalili, R. Khajavi, M.K. Rahimi, N. Nasirzadeh, "Effect of Electrospinning Parameters on Production of Polyvinyl Alcohol/Polylactic Acid Nanofiber Using a Mutual Solvent" *Polymers and Polymer Composites*, vol. 29, no. 9, pp. S844-S856, 2021.
- [5] X. Wu, L. Wang, H. Yu, Y. Huang, "Effect of Solvent on Morphology of Electrospinning Ethyl Cellulose Fibers," *Journal of Applied Polymer Science*, vol. 97, no. 3, pp. 1292-1297, 2005.
- [6] J.Y. Park, S.W. Han, I.H. Lee, "Preparation of Electrospun Porous Ethyl Cellulose Fiber by THF/DMAc Binary Solvent System," *Journal of Industrial and Engineering Chemistry*, vol. 13, no. 6, pp. 1002-1008, 2007.
- [7] X. Wang; G. He; H. Liu, G. Zheng, D. Sun, "Fabrication and Morphological Control of Electrospun Ethyl Cellulose Nanofibers," *The 8th Annual IEEE International Conference on Nano/Micro Engineered and Molecular Systems*, Suzhou, pp. 324-327, 2013.
- [8] D.G. Yu, X.X. Li, J.W. Ge, P.P. Ye, X. Wang, "The Influence of Sheath Solvent's Flow Rate on the Quality of Electrospun Ethyl Cellulose Nanofibers," *Modeling and Numerical Simulation of Material Science*, vol. 3, no. 4, pp. 1-5, 2013.
- [9] Y.L. Hsieh, "Cellulose Nanofibers: Electrospinning and Nanocellulose Self-Assemblies," *Advanced Green Composites*, pp. 67-95, 2018.
- [10] S. Um-i-Zahra, X.X. Shen, H. Li, L. Zhu, "Study of Sustained Release Drug-Loaded Nanofibers of Cellulose Acetate and Ethyl Cellulose Polymer Blends Prepared by Electrospinning and Their In-Vitro Drug Release Profiles," *Journal of Polymer Research*, vol. 21, no. 602, pp. 1-12, 2014.

# A Case Study on Ex Situ Conservation of Keaw Savoey and Nam Dok Mai Mango (*Mangifera indica* L.) Trees from Ban Noin Thong, Ban Kho, Mueang District, Khon Kaen Province through Local Plantation

Preeya Puangsomlee Wangsomnuk\*

Department of Biology, Faculty of Science, Khon Kaen University, Khon Kaen 40002, Thailand

Email: preeyakku04@gmail.com

**Abstract:** Keaw Savoey and Nam Dok Mai mangoes are popular mango varieties for consumption in Thailand. This has led to farmers preferring to grow these varieties as well as Ban Noin Thong, Ban Kho, Mueang District, Khon Kaen Province where 36 and 14 trees of "Keaw Savoey" and "Nam Dok Mai" mango varieties were randomly collected from 17 locations in this study to determine their level of genetic differentiation and microsatellite alleles. Microsatellite DNA, which consists of repeating DNA markers with high repeatability and polymorphism, was used to differentiate between these mango varieties. Mango DNA was extracted using a modified version of the Noveas et al. (2009) method, which yielded between 8.21 and 41.51 µg of high-quality amplifiable DNA from as little as 0.1 g of dry weight mature leaf tissue. Eight pairs of primers were used for SSR-PCR to amplify the DNA, resulting in the synthesis of 1,524 DNA fragments with sizes ranging from 100 to 500 base pairs. Jaccard's coefficient was used to analyze the genetic similarity of Keaw Savoey and Nam Dok Mai mangoes, and they were grouped using the unweighted pair group method arithmetic average (UPGMA). The results showed that even though both varieties had different genetic diversity, they could be divided into two major groups. Fourteen Nam Dok Mai mango trees showed higher genetic dissimilarity than 36 Keaw Savoey mango trees. These small sets of mango trees belong to the leading varieties can be preserved as ex situ conservation.

**Keywords**—Mango, Keaw Savoey, Nam Dok Mai, Ex situ conservation, Microsatellite

## INTRODUCTION

In the year 2021, the total area of mango cultivation in Thailand was 913,901 rai, and there were 200,932 households engaged in mango farming, with a total national production of 903,311.82 tons. Popular mango varieties include Nam Dok Mai, Keaw Savoy, Fa Lan, Ok Rong, Mankunsri, Chok Anan, and Mahachanok [1]. Keaw Savoey and Nam Dok Mai mangoes are cultivated in 62 and 60 provinces, covering an area of 129,459 and 276,270 rai, respectively. The most common variety in Thailand is Nam Dok Mai mango, which is predominantly grown in Phitsanulok Province with an area of 82,928 rai. Keaw Savoey mango, on the other hand, is primarily grown in Suphanburi Province with an area of 10,566 rai. In Khon Kaen Province, Keaw Savoey and Nam Dok Mai mangoes are grown on 6,770 and 2,048 rai, respectively [2].

Mango trees can be propagated through both sexual and asexual means, but the presence of polyembryonic and monoembryonic mango plants determines the method of propagation. Currently, nearly all commercial mango plantations are established using mangoes propagated

through grafting or budding techniques with polyembryonic mangoes serving as rootstocks [3] to produce planting material of a uniform and true type in a relatively short time. The propagation of seed is the easiest way, however in the modern cultivation of mango this process needs to be avoided since the crosspollinated crop does not produce true progenies.

Local plantation can be used as an ex situ conservation strategy to conserve plant species that can also serve as a source of plant material for research, education, and reintroduction programs. Ex situ conservation refers to the conservation of species outside their natural habitat, typically in gardens or other managed areas.

According to Umar et al. [4] and Hidayat et al. [5], microsatellite polymorphism is a reliable marker for analyzing genetic profiles, providing a high degree of reproducibility, and have been demonstrated to differentiate between mango cultivars with very similar phenotypes.

This study aimed to discover genetic diversity and identify microsatellite alleles that can differentiate Keaw Savoey and Nam Dok Mai mangoes collected from 17 local plantations at Nerthong Village, Ban Kho Subdistrict, Mueang District, Khon Kaen Province.

## METHODOLOGY

### Plant Sample Preparation

Random samples of mango (*Mangifera indica*) trees, Keaw Savoey and Nam Dok Mai, were collected from Nernthong Village, Ban Kho Subdistrict, Mueang District, Khon Kaen Province. These samples were gathered from 36 Keaw Savoey and 14 Nam Dok Mai mango trees, situated in 12 (consisting of 1, 1, 1, 1, 2, 2, 2, 3, 4, 4, 5 and 10 trees) and 5 (consisting of 1, 1, 2, 3 and 7 trees) different locations, respectively. Mature leaves were collected from each tree and preserved in silica gel.

### Efficient DNA Extraction from Mango Leaves

Dry mango leaves were extracted using various methods to determine the most efficient method. Two extraction methods were tested, the modified Tai and Tanksley method [6] and the modified Novaes et al. method [7]. The results showed that the modified Novaes et al. method [7] was the most efficient for DNA extraction from mango leaves. Therefore, the modified method of Novaes et al. [7] was chosen to extract DNA from at least two leaves of each mango sample. Dry leaf samples weighing 0.1 grams were finely ground in liquid nitrogen and then added to CTAB - Extraction buffer (composed of 2% CTAB, 1.4 M NaCl, 100 mM Tris-HCl pH 8.0, 20 mM EDTA pH 8.0, and 2% PVP) at a volume of 1000 microliters and 3 microliters of  $\beta$ -mercaptoethanol. The sample was then ground until it was finely powdered and transferred to a microtube with a volume of 1.5 milliliters. Then, 35 microliters of 20% SDS was added and the mixture was incubated at 65 degrees Celsius for 60 minutes, with the tube being inverted every 10 minutes. The debris was pelleted by adding chloroform: isoamyl alcohol (24:1) 500 microliters and centrifuged at 12,000 rpm for 3 minutes. The upper aqueous phase was transferred to a new tube and 120 microliters of 10% CTAB and 280 microliters of 5 M NaCl were added, mixed, and incubated for 10 minutes. The debris was again pelleted by adding chloroform: isoamyl alcohol (24:1) 500 microliters and centrifuged at 12,000 rpm for 3 minutes. The upper aqueous phase was transferred to a new tube and 400 microliters of isopropanol were added to precipitate the DNA. The mixture was then centrifuged at 12,000 rpm for 3

minutes, and the supernatant was discarded. The DNA pellet was washed with 70% ethanol, air-dried. Then dissolve the genomic DNA pellet in TE buffer (consisting of 10 mM Tris-HCl pH 8 and 1 mM EDTA pH 8), and digest the DNA with RNase A enzyme (at a concentration of 2 micrograms per milliliter, US biological) by incubating the mixture at 37 degrees Celsius for 30 minutes with a volume of 0.5 microliters. After obtaining the DNA, its quality and quantity were analyzed by using agarose gel electrophoresis and a NanoDrop<sup>TM</sup> spectrophotometer. The DNA was combined with loading buffer that contained 1.0% bromophenol blue and then placed onto the agarose gel. RedSafe<sup>TM</sup> nucleic acid staining solution was used to stain the gel, and the DNA band size was compared to a standard DNA ladder (100 bp DNA ladder plus, Vivantis) by visualizing it under UV transilluminator. The image was recorded by a Vilber Lourmat camera (France). The DNA sample was preserved at -20°C as a template for the subsequent use in the PCR reaction.

### Microsatellite amplification and size

PCR amplification using microsatellite primers was employed to clone specific SSR loci. A total of eight pairs of microsatellite primers were chosen from the research papers of Yu-Chung Chiang et al. [8] and Ravishankar et al. [9] for synthesis, and subsequently utilized in experiments to amplify DNA (Table 1). A 10  $\mu$ L PCR reaction was conducted to amplify the diluted mango DNA using microsatellite-specific primers. The reaction mixture contained about 30 ng of DNA, 8 pairs of microsatellite primers (synthesized based on Yu-Chung Chiang et al. [8] and Ravishankar et al. [9] listed in Table 1, 1.6  $\mu$ L of 10X buffer S (composed of 160 mM (NH<sub>4</sub>)<sub>2</sub>SO<sub>4</sub>, 500 mM Tris-HCl (pH 9.2 at 20°C), 17.5 mM MgCl<sub>2</sub>, and 0.1% Triton<sup>TM</sup> X-100), 1  $\mu$ L of 2 mM dNTP (Fermentas, USA), 2.4  $\mu$ L of sterile distilled water, 2  $\mu$ L of 5 mM primer, and 0.08  $\mu$ L of Taq DNA polymerase (Vivantis) at a concentration of 5 units/ $\mu$ L. The PCR reaction involved the following program: Step 1: 1 cycle of 1 minute at 94°C; Step 2: 35 cycles of 30 seconds at 94°C, 30 seconds at 55°C, and 1 minute at 72°C; and Step 3: 5 minutes at 72°C and 5 minutes at 25°C.

TABLE 1

MICROSATELLITE LOCI AND THEIR CORRESPONDING PRIMER SEQUENCES

Locus	Repeat Sequences	Primer Name	Sequences (5' - 3')	References
Min154	(CT) <sub>16</sub>	Min154_F Min154_R	AGTAAACCAGTTTGACGTCC TGTTTAGCAGCTCAGTCCTC	[8]
Min253	(AT) <sub>5</sub> (AC) <sub>17</sub> (AT) <sub>8</sub>	Min253_F Min253_R	ACCTTTTCCTGAATCCCTGG ACTCTCTCAAGCTTCCCTG	[8]
MiIIHR02	(CA) <sub>2</sub> A(CA) <sub>7</sub> AG(CA) <sub>5</sub>	MiIIHR02_F MiIIHR02_R	CCCCAACATTTTCATAAACACA CCTCCTTACATGCCTCCTTG	[9]
MiIIHR04	(CA) <sub>11</sub>	MiIIHR04_F MiIIHR04_R	CGTTTTTGACCCTCTTGAGC CCGCATACTTCCCTTACAT	[9]
MiIIHR05	(CT) <sub>8</sub> C(CT) <sub>2</sub> TTTT(CT) <sub>4</sub>	MiIIHR05_F MiIIHR05_R	CTCTCCCTCACTTGCTCCAC AGACCACCGACAACGAAAAC	[9]
MiIIHR06	(CA) <sub>7</sub> CG(CA) <sub>5</sub>	MiIIHR06_F	CGCCGAGCCTATAACCTCTA	[9]



		MiIHR06_R	ATCATGCCCTAAACGACGAC	
MiIHR17	(GT) <sub>13</sub> GAGT(GA) <sub>10</sub>	MiIHR17_F MiIHR17_R	GCTTGCTTCCAACCTGAGACC GCAAAAATGCTCGGAGAAGAC	[9]
MiIHR19	(AC) <sub>11</sub>	MiIHR19_F MiIHR19_R	TGATATTTTCAGGGCCCAAG AAATGGCACAAAGTGGGAAAG	[9]

### Analysis of microsatellite alleles

The PCR products were analyzed through polyacrylamide gel electrophoresis (PAGE) and silver staining, and compared against the 100 bp DNA ladder plus (Vivantis) as a reference.

### Genetic differentiation

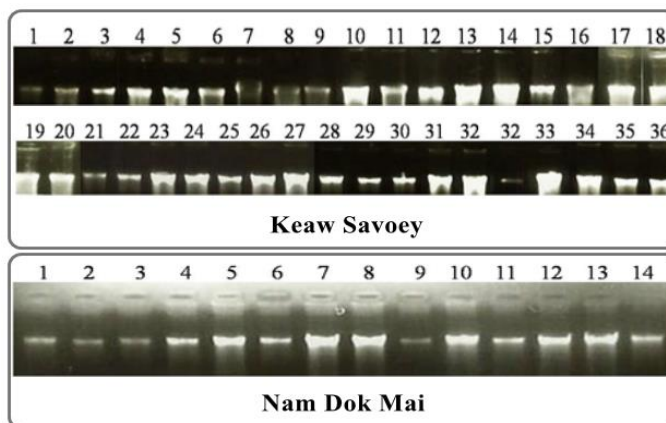
The collected Keaw Savoey and Nam Dok Mai mango samples were examined using microsatellite molecular markers. Gel electrophoresis was used to analyze the

number of alleles (banding pattern) of all samples obtained from the synthesis of microsatellite markers. The resulting banding patterns were recorded as 1 if present and 0 if absent and entered into an Excel spreadsheet for analysis using NTSYSpc version 2.1. Jaccard's coefficient [10] was used to calculate the similarity index (SI) within each variety. Finally, a dendrogram was constructed using the UPGMA method based on the SI values to evaluate the genetic relationships between the two mango varieties.

## RESULTS AND DISCUSSION

High-quality DNA obtained from individual specimens was essential to detect genetic differentiation among ex situ collections of Keaw Savoey and Nam Dok Mai mango in Nernthong Village, Ban Kho Subdistrict, Mueang District, Khon Kaen Province. In this study, DNA was extracted from dried leaves of 36 and 14 Keaw Savoey and Nam Dok Mai mango accessions using a modified version of Novaes

et al. [7] method. The integrity of isolated genomic DNA showed good quality based on agarose gel electrophoresis (Fig. 1) and acceptable quality and quantity based on NanoDrop<sup>TM</sup> spectrophotometer. The 260/280 ratio was obtained for purity of each DNA sample [11], with ranged from 1.86-1.94 which was good quality according to [12].



**Fig 1.** Gel electrophoresis of 36 Keaw Savoy and 14 Nam Dok Mai mango genomic DNA samples.

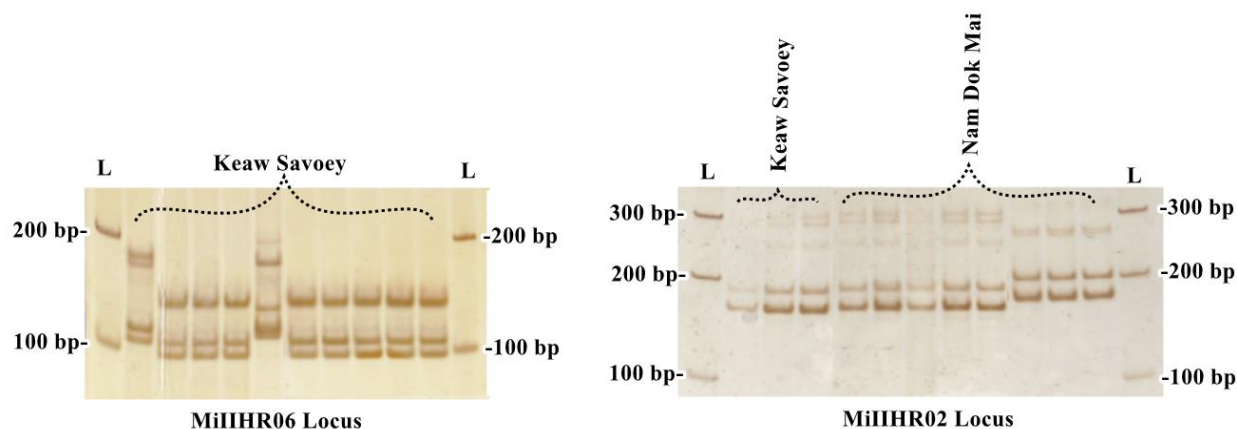
The analysis of the genetic differentiation among 36 Keaw Savoey and 14 Nam Dok Mai mango varieties collected from 17 locations in Ban Noin Thong area, Ban Kho district, Mueang district, Khon Kaen province using 8 microsatellite loci (Table 1) discovered a total of 1,524 bands amplified across all loci, ranging in size from 100-500 base pairs with varying numbers of 8 to 15 alleles for each locus. The results show that the eight microsatellite loci showed different level of informativeness on these two mango culti-

vars. MiIHR04, MiIHR05, MiIrh06, and Min253 were found to be the most effective polymerase chain reaction (PCR) amplification markers for Keaw Savoey mango, capable of amplifying a total of eight alleles. On the other hand, in Nam Dok Mai mango, the most efficient microsatellite markers for PCR amplification were Min154, which could amplify a total of fifteen alleles. MiIHR02 alleles can differentiate mango trees both at cultivars and sub-cultivar levels (Fig. 2). The alleles of these loci can differentiate mango varieties are mainly supported by

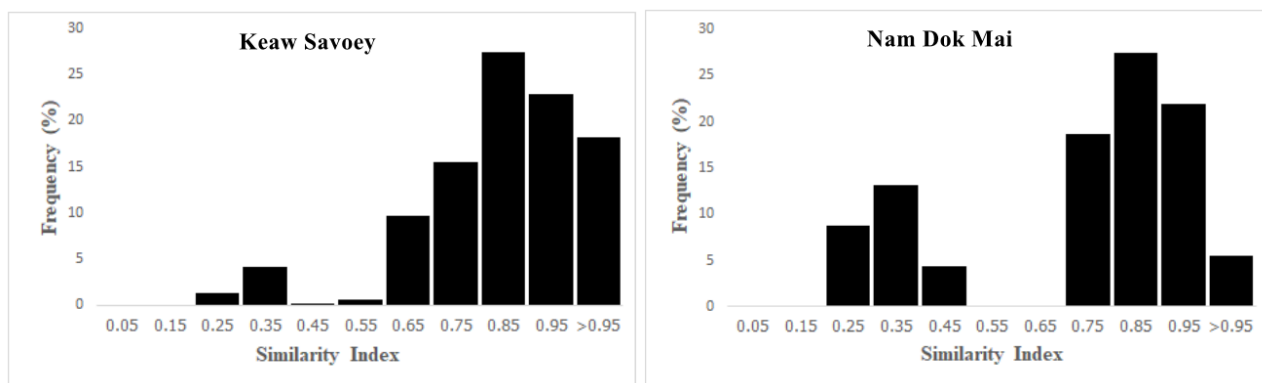
similarity index calculated from the allele-based produced by PCR reactions.

The frequency of the similarity index, as indicated by microsatellite molecular markers, demonstrated that 36 Keaw Savoey trees have higher similarity compared to 14 Nam Dok Mai trees (Fig. 3). 68.57% of genetic similarity values between two accessions of Keaw Savoey variety having more than 0.85 which is higher than that of Nam

Dok Mai variety (54.95%). The results confirmed that the genetic basis of 14 Nam Dok Mai trees are more diverse than Keaw Savoey variety. The mango trees that show less genetic similarity also means they are highly dissimilarity which are very useful for germplasm collection and can be used as gene banks for future selection and breeding. It is strongly believed that the diverse mechanisms of mango pollination played a significant role in contributing to the high genetic diversity of *M. mangifera* [13-14].



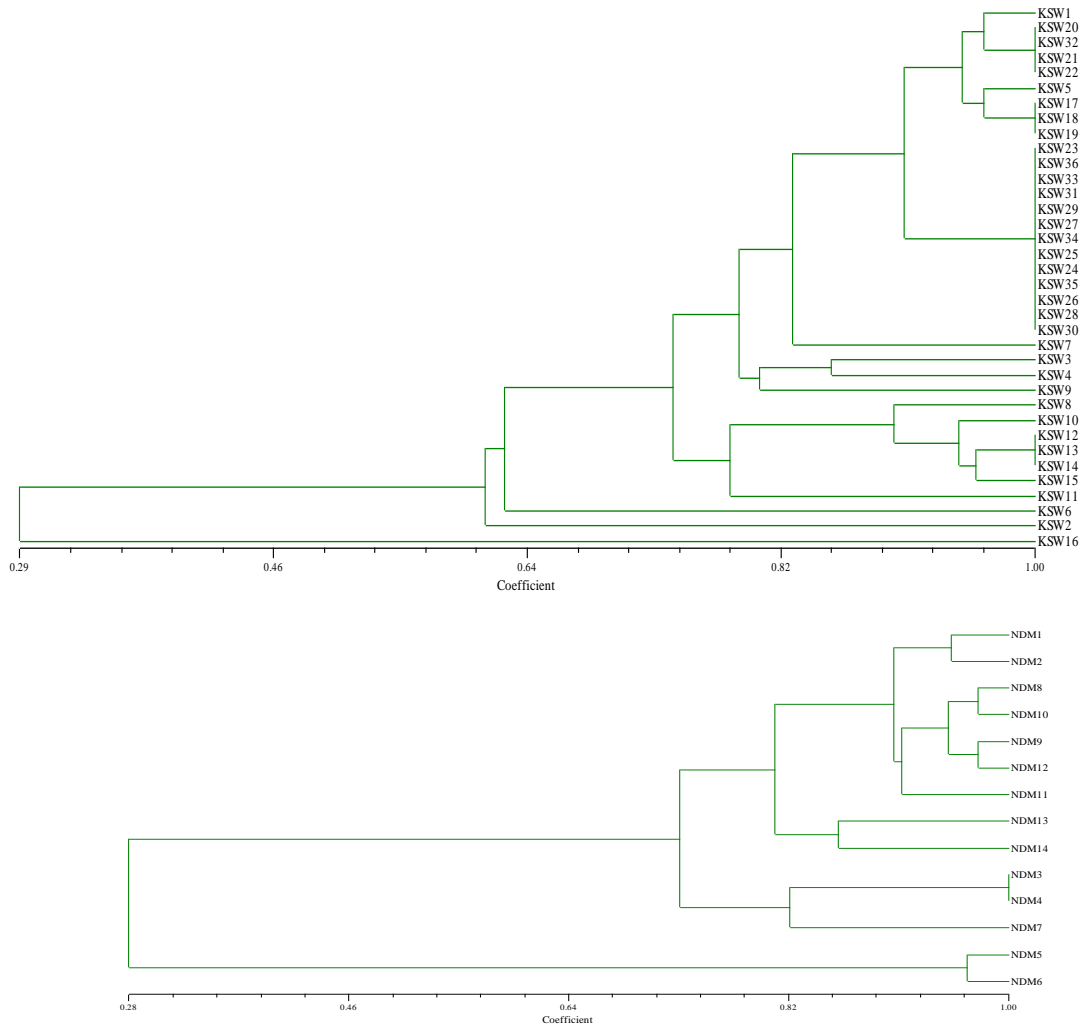
**Fig 2.** Examples of DNA fingerprints of Keaw Savoey and Nam Dok Mai mango trees were amplified using the primer pairs specific to MiIHR06 and MiIHR02, and then were analyzed using the polyacrylamide gel electrophoresis (PAGE) technique. The results were compared with a 100 bp DNA ladder plus, Vivantis (L).



**Fig 3.** Frequency of Jaccard's similarity index that quantifies the similarity between two sample sets of Keaw Savoey and Nam Dok Mai mango trees

Based on similarity coefficients and UPGMA clustering to generate a dendrogram, it was found that 36 Keaw Savoey mango trees belongs to two clusters. Group I consisted only one genotyp while the second group contained the other 35 trees. On the other hand, the Nam Dok Mai mango can be grouped into two groups (Fig. 4) consisted of 2 and 12 trees in each group. It is possible that collected mango trees arise from seeds that have been cross-pollinated with other mango varieties in the nearby area. According to [15], mango pollen can undergo hybridization and fertilization both within and between varieties. Microsatellite markers show variation in alleles due to the fusion of genetically distinct individuals. It was found that there were mango

trees with variations in microsatellite loci available in the collection of Keaw Savoey and Nam Dok Mai mango varieties from 12 and 5 locations, respectively, from Nernthong Village, Ban Kho Subdistrict, Mueang District, Khon Kaen Province. These mango trees grew well in the gardens which are beneficial for conservation. Recognizing the significance and essentiality of possessing a range of genetic resources for research, testing, selection, and enhancement of species, it is crucial to have adequate genetic diversity to enable the selection, development, and improvement of breeds from available genetic resources to progress, expand, or enhance them.



**Fig 4.** The dendrogram was created through cluster analysis using the Jaccard coefficient, using a combined similarity matrix obtained from microsatellite markers of 36 Keaw Savoey (above) and 14 Nam Dok Mai (below) mango trees.

### CONCLUSION

According to the findings of this study, the microsatellite markers utilized can differentiate between the Keaw Savoey and Nam Dok Mai mango varieties and confirm the genetic diversity that exists within individual trees of the same mango variety. These can be good genebank for conservation and breeding program for the future.

### ACKNOWLEDGMENT

The author would like to acknowledge the people who give their mango materials and information to this research and Khon Kaen University for the research fund.

#### REFERENCES

- [1] Analysis of Thailand's Regional Economy. [http://www.tpso.moc.go.th/sites/default/files/wiekhraaahesrsthkicchphuumiphaakhpracchameduene\\_msaay.pdf](http://www.tpso.moc.go.th/sites/default/files/wiekhraaahesrsthkicchphuumiphaakhpracchameduene_msaay.pdf) accessed 23 March, 2023.
- [2] Online Agricultural Production Information System, Department of Agricultural Promotion. <https://production.doae.go.th/> accessed 29 April, 2023.
- [3] C. Kole. (Ed.). The mango genome (Compendium of plant genomes). Springer. 2021.
- [4] M. Umar, M. Ponnuswami, P. Nagarajan, P. Eyakumar, S. Enthil. Molecular characterization of ten mango cultivars using simple sequences repeat (SSR) markers. African Journal of Biotechnology, 12(47):6568-6573. 2013.
- [5] A. Hidayat, E.S. Rahayu, M. Abdullah, A. Retnoningsih. Microsatellites to reveal genetic diversity and to distinguish four mangoes of Tegal District, Central Java, Indonesia. Biodiversitas Journal of Biological Diversity, 22(8): 3467-3473, 2021.
- [6] T.H. Tai, S.D. Tanksley. A rapid and inexpensive method for isolation of total DNA from dehydrated plant tissue. Plant Molecular Biology Report 8:297-303, 1990.
- [7] R.M.L. Novaes, J.G. Rodrigues, M.B. Lovato. An efficient protocol for tissue sampling and DNA isolation from the stem bark of Leguminosae trees. Genetics and Molecular Research, 8(1):86-96, 2009.
- [8] Y.C. Chiang, C.Y. Hung, C.-Y. Hsu, S.S. Huang, Chiang, T.Y. Development and characterization of 20 new polymorphic microsatellite markers from *Mangifera indica* (Anacardiaceae). American Journal of Botany, e117–e119, 2012.
- [9] K.V. Ravishankar, M. Anandakumar, M. Raja, M. Baskaran, M. Ignacimuthu, Development of New Microsatellite Markers from Mango (*Mangifera indica*) and Cross-Species Amplification. American Journal of Botany: e96–e99, 2011.
- [10] P. Jaccard. Étude comparative de la distribution florale dans une portion des Alpes et des Jura. Bulletin de la Société Vaudoise des Sciences Naturelles, 37:547–579, 1901.
- [11] J.A. Glasel. Validity of nucleic acid purities monitored by 260 nm/280 nm absorbance ratios. Biotechniques, 18:62–63, 1995.
- [12] J. Sambrook, E.F. Fritsh, T. Maniats. Molecular Cloning; a Laboratory Manual. Cold Spring Harbor Laboratory Press, New York, 1989.
- [13] M. Sandip. A.N. Makwana, A.V. Barad, B.D. Nawade. Physiology of flowering-the case of mango. International Journal of Applied research, 1(11):1008-1012, 2015.
- [14] I.S. Bally, N.L. Dillon. Mango (*Mangifera indica* L.) Breeding. In Advances in Plant Breeding Strategies: Fruits. Springer, Cham. 2018.
- [15] E.J. Warschefsky, E.J. von Wettberg. Population genomic analysis of mango (*Mangifera indica*) suggests a complex history of domestication. New Phytologist, 222(4):2023-2037, 2019.

# Isolation of rhizospheric and endophytic actinomycetes from five medicinal plants and their antimicrobial activities

Khanungkan Klanbut<sup>1\*</sup>, Praewpilai Jaidee<sup>1</sup>, Supanida Saykaew<sup>1</sup> and Supawich Natanod<sup>1</sup>

<sup>1</sup>Department of Biology, School of Science, King Mongkut's Institute of Technology Ladkrabang, Bangkok, Thailand 10520

<sup>1</sup>Corresponding author E-mail: [khanungkan.kl@kmitl.ac.th](mailto:khanungkan.kl@kmitl.ac.th)

**Abstract:** In this study, actinomycetes isolated from leaves and roots endophytic and rhizospheric soils of five medicinal plants in Thailand, including gombo (*Abelmoschus esculentus* (L.) Moench), bergamot (*Citrus hystrix* DC.), carunda (*Carissa carandas* L), papaya (*Carica papaya* L.) and marigold (*Tagetes erecta* L.). A total of fifty-five strains of actinomycetes were isolated by using Starch Casein Nitrate Agar (SCNA), Yeast Extract Mannitol Agar (YMA), Bennet's Agar medium and Zhang'Starch Soil Extract (ZSSE) agar supplemented with 100 µg/ml nystatin. Cultural characteristics were performed using 14-day cultures grown at 30°C on International Streptomyces Project 2 (ISP2) media. Preliminary screening for their antimicrobial activities of fifty-five isolates were tested against *Kocuria rhizophila* ATCC 9341, *Staphylococcus aureus* ATCC 25923, *Bacillus subtilis* ATCC 6633, *Pseudomonas aeruginosa* ATCC 27853, *Escherichia coli* ATCC 25922 and *Candida albicans* ATCC 10231 using T'streak method, found six isolates could inhibit test microorganisms including strains AM231, CA131, CA331, RO232, RO321 and RO331. Antimicrobial activities of crude ethyl-acetate extracts were examined against test microorganisms using disc diffusion method with the concentration of 50 mg/ml, only strains AM231 and CA131 were able to inhibit *Kocuria rhizophila* ATCC 9341. The inhibition zones were 34.5 and 4 mm., respectively.

**Index Terms— Rhizospheric actinomycetes, Endophytic actinomycetes, Antimicrobial activity, Thai medicinal plants**

## I. INTRODUCTION

Nowadays almost all groups of important antibiotics are in danger of losing their efficacy by drug resistance [1]. The discovery of new antibiotics from microbial and plant products are playing an important role in the antimicrobial compounds discovered until now [2]. Soil produces many useful biologically active natural products; thousands of antibiotics have been isolated from gram positive bacteria [3]. Actinomycetes are increasingly receiving attention as a main producer of secondary metabolites and antibiotics [4]. Therefore, isolation of new actinomycetes species is a valuable endeavor, the species belonging to the genus *Streptomyces* constitutes 50% of the total population of soil actinomycetes [5]. Actinomycetes, the gram-positive soil dwelling bacteria, aerobic microorganisms with high DNA G+C contents which has the particularly geosmin odour [6]. Actinomycetes are the most widely distributed group of microorganisms in nature. They are also well known as saprophytic soil inhabitants [7]. Actinomycetes occur in the plant rhizosphere soil and produce active compounds [8]. However, the rate of discovery of new secondary metabolites has been decreasing, so the discovery of

actinomycetes in several sources increases the chance for the discovery of new secondary metabolites [9]. Active actinomycetes may be found in medicinal plant root rhizosphere soils and may have the ability to produce new inhibitory compounds. Since plant habitats were rarely investigated for actinomycetes, therefore, the focus of attention for isolation purpose has switched from soil to plants to find out novel actinomycetes for screening of bioactive compounds [10].

The aims of this work were to search for a new strain of actinomycetes that can produce antimicrobial substances from medicinal plants in Thailand which are the good resource to study the diversity. endophytic actinomycetes associated with medicinal plants are an unexplored resource for the discovery of biologically active compounds. Microorganisms associated with medicinal plants are increasingly receiving attention as the producers of important bioactive compounds. To date, the diversity of culturable endophytic actinomycetes associated with medicinal plants is in its initial phase of exploration.

## II. METHODOLOGY

### A. Isolation of Actinomycetes

Samples were collected from 5 medicinal plant rhizospheres, epiphytic and endophytic in Thailand, including gombo (*Abelmoschus esculentus* (L.) Moench), bergamot (*Citrus hystrix* DC.), carunda (*Carissa carandas* L.), papaya (*Carica papaya* L.) and marigold (*Tagetes erecta* L.). Plant samples (leaves, roots) were washed thoroughly with tap water for 10 min followed by sterile double distilled water and drained. Each plant part was cut aseptically into 1cm long segments using a sterile blade under the laminar flow hood. Immersion in 0.1% Tween 20 for 30s followed by sodium hypochlorite solution (1%) for 5 min and then rinsed with sterile double distilled water for 5 min. The plant parts were then immersed in 70% ethyl alcohol for 5 min followed by Sodium bicarbonate solution (10%) for 10 min [11] and then rinsed with sterile double distilled water and allowed to dry under the laminar flow hood. The cut surfaces of the segments were placed on Petri-plates containing three different media viz., Starch Casein Nitrate Agar (SCNA), Yeast Extract Mannitol Agar (YMA) and Bennet's Agar medium.

Soil samples were air dried at room temperature for 5 days. Soil pH was analyzed according to the method of [12] Suzuki et al. (2000). Ten grams of each air-dried soil sample was crushed by the mortar. The actinomycetes were isolated by plating serially diluted samples on to Zhang'Starch Soil Extract (ZSSE) agar, pH 7.0 supplemented with 100 µg/ml nystatin [13] and incubated at 30°C for 7-14 days. The physiological and biochemical results indicate actinomycete strains, formed abundant, extensively branched substrate and aerial hyphae were observed directly on the agar. The color designation of substrate mycelium and aerial mycelium was determined using the ISCC-NBS Color Charts standard sample [14].

### B. Characterization of Actinomycetes

All the isolates were morphological and biochemically characterized and classified by using colors of aerial mycelium on ISP2 medium by the ISCC-NBS color system [14]. Biochemical characterizations were obtained from peptonization on skim milk agar, gelatinization on Bouillon Gelatin broth, nitrate reduction on Peptone KNO<sub>3</sub> broth and starch hydrolysis on Inorganic salt-starch agar (ISP4) as described by [15-16].

### C. Antimicrobial Activity

#### Tested organisms.

*Kocuria rhizophila* ATCC 9341, *Staphylococcus aureus* ATCC 25923, *Bacillus subtilis* ATCC 6633, *Pseudomonas aeruginosa* ATCC 27853, *Escherichia coli* ATCC 25922 and *Candida albicans* ATCC 10231.

#### Determination of the antibacterial activity

The screening method of isolates consists of two steps: primary screening and secondary screening. In primary screening, the antibacterial activity of pure isolates was

determined by cross-streak method on Glucose Yeast extract agar (GYE). Secondary screening of isolate was done by agar disc diffusion method with crude extract of ethyl acetate after secondary metabolite extraction. Production of bioactive compounds was done by submerged fermentation.

#### Agar disc diffusion

Actinomycetes isolates were grown in 200 ml of Yeast extract Malt extract (YEME) broth with 0.1% CaCO<sub>3</sub> in a 500-ml-capacity conical flask under sterile conditions and incubated at 30°C for 16 days at 200 rpm rotation. After fermentation, cells were harvested through Whatman filter paper No.1 and supernatants were harvested for fermented broth. Resultant fermented broths were added to equal volume of ethyl acetate and evaporated. Harvested cells were fermented in equal volume of methanol for another 3 days and then also evaporated. The solvent phase was collected and evaporated in a desiccator. The completely dried residues were re-dissolved in ethyl acetate and methanol respectively, to be used for further studies. Antibacterial activity of partially purified extracellular and intracellular crude extracts; were determined by agar disc diffusion method. Cell Concentration of all test microorganisms were adjusted at 0.5 McFarland turbidity standards and inoculated on Mueller Hinton Agar (MHA) for bacterial cells and Sabouraud Dextrose Agar (SDA) plates for yeast cell by using sterilized cotton swabs. Sterile disc containing 20 µl of each crude extract (1 and 50 mg/ml) were placed on the agar plates. with Positive control; Kanamycin 1.5 and 5 µg/ml and Negative control; Methanol. Plates were incubated at 37°C for 24 h [17].

## III. RESULTS AND DISCUSSION

### A. Isolation of Actinomycetes

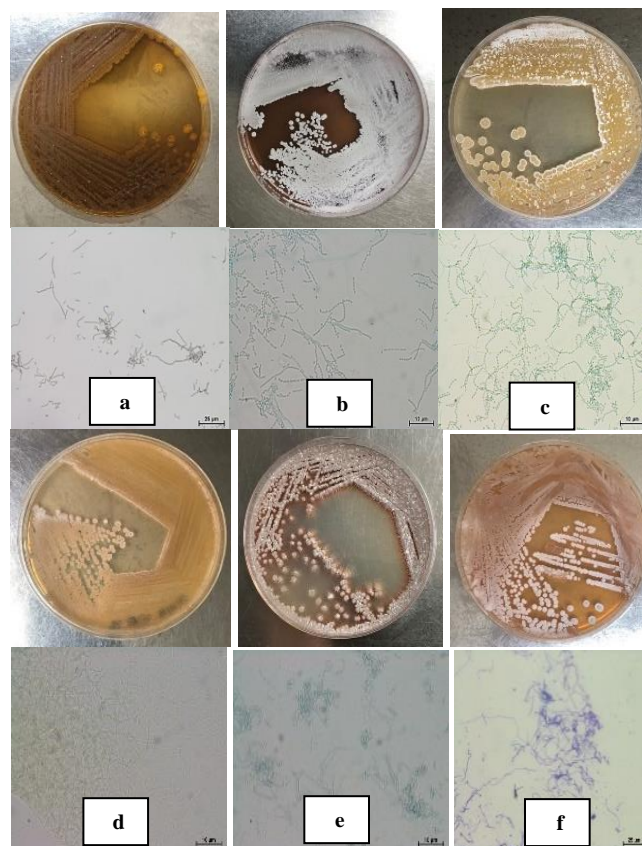
A total of fifty-five actinomycete isolates had been isolated from endophytic and epiphytic actinomycetes from leaves and roots of five medicinal plants in Thailand, including gombo (*Abelmoschus esculentus* (L.) Moench), bergamot (*Citrus hystrix* DC.), carunda (*Carissa carandas* L.), papaya (*Carica papaya* L.) and marigold (*Tagetes erecta* L.), which pH measurement are made at a field site; 7-8. All strains were collected by using Starch Casein Nitrate Agar (SCNA), Yeast Extract Mannitol Agar (YMA), Bennet's Agar medium and Zhang'Starch Soil Extract (ZSSE) agar, pH 7.0 supplemented with 100 µg/ml nystatin. Cultural characteristics were performed using 14-day cultures grown at 30°C on International Streptomyces Project 2 (ISP2) media. The isolates were identified according to the morphological criteria including characteristic colony on plates, morphology of spores on pigment production, results are indicated of actinomycete strains, formed abundant, extensively branched substrate and aerial hyphae (Fig. 1) were observed directly on the agar.

The results on morphological, physiological and biochemical activity revealed that all isolated strains obtained from five medicinal plants were characterized

based on the biochemical tests- Peptonization test, Coagulation test, Nitrate reduction, Gelatin liquefaction and Starch hydrolysis; thirty isolates of peptonization test were positive and twenty-five isolates were negative, fifty one strains of coagulation test were positive and four strains were negative, twenty seven isolates of nitrate reduction were positive and twenty eight isolates were negative, forty three isolates of gelatin liquefaction were positive and twelve isolates were negative and thirty seven isolates of starch hydrolysis were positive and eighteen isolates were negative (Table 1).

The color designation of substrate and aerial mycelium (Fig. 1) was determined using the ISCC–NBS Color Charts standard sample [14] of Aerial mycelium into not produced (AM231), light grayish brown (CA131), light yellow (CA331), pale orange (RO232), dark reddish orange (RO321) and light brown (RO331) on ISP 2 agar medium.

One of the major constituents of the rhizospheric microbial community are actinomycetes, they were subjected for their potential as antagonists of soil born phytopathogens [18, 19, 20]. Endophytic actinomycetes are now considered as a new source for achieving bioactive compounds [21]. Plant-associated bacteria include endophytic and rhizospheric, are valued of constructive effects on the host plant [22]. Medicinal plants are the vital resource to isolate endophytic actinomycetes as a significant source of secondary metabolite. There are many literatures showed that in many countries exploit traditional medicinal plants in treatment of various types of illness, several types of plants are disguised with actinomycetes, it is known that not all plants contain endophytic



**Fig. 1.** Morphological appearance colonies on ISP2 agar medium and spore arrangements of actinomycete strains AM231 (a), CA131 (b), CA331 (c), RO232 (d), RO321 (e) and RO331 (f).

TABLE I

MORPHOLOGICAL BIOCHEMICAL AND PHYSIOLOGICAL CHARACTERIZATION OF THE SELECTED ACTINOMYCETES STRAINS.

Strains.; 1. AM231, 2. CA131, 3. CA331, 4. RO232, 5. RO321 and 6. RO331.

The symbol, + means the positive reaction or appearance of growth while symbol – means the negative or absence of growth and W means weak or weak of growth.

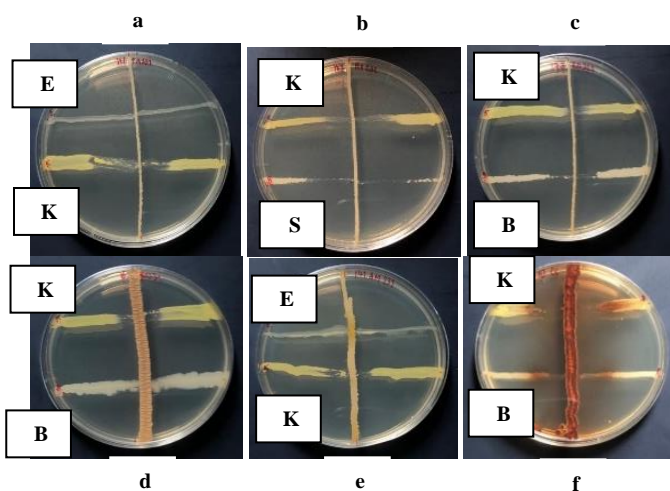
Characteristics	Actinomycete strains					
	1	2	3	4	5	6
<b>Color of</b>						
<b>Aerial mycelium</b>	-	Light grayish brown	Light yellow	Pale orange	Dark reddish orange	Light brown
<b>Substrate mycelium</b>	Deep orange	Dark brown	Light yellow	Light orange yellow	Strong reddish brown	Dark orange yellow
<b>Spore</b>	Dark grayish yellowish brown	Light grayish olive	Vivid orange yellow	Yellowish white	Yellowish gray	Pale yellowish
<b>Soluble pigment</b>	Strong yellowish brown	Dark yellowish brown	-	-	-	Light orange yellow
<b>Spore arrangement</b>	Rectiflexbiles	Retinaculiaperti	Retinaculiaperti	Rectiflexbiles	Spiral	Retinaculiaperti
<b>Peptonization</b>	-	-	-	+	+	-
<b>Coagulaion</b>	+	+	+	+	+	+
<b>Gelatinization</b>	-	+	-	+	+	-
<b>Nitrate reduction</b>	+	-	-	-	+	-
<b>Starch hydrolysis</b>	+	-	+	+	+	-

actinomycetes [23]. The mutually beneficial of

endophytic actinomycetes in medicinal plants and their role in determining the medicinal value of plants by reason of the production of various bioactive compounds is worth probing [24].

### B. Antimicrobial activity tested by Agar disc diffusion.

Preliminary screening for antimicrobial activity of fifty-five isolates were tested against *Kocuria rhizophila* ATCC 9341, *Staphylococcus aureus* ATCC 25923, *Bacillus subtilis* ATCC 6633, *Pseudomonas aeruginosa* ATCC 27853, *Escherichia coli* ATCC 25922 and *Candida albicans* ATCC 10231 using T'streak method, found 6 isolates which have inhibition zone. The isolates that gave positive result (Fig. 2.) in preliminary screening for antimicrobial activity were used for secondary metabolite screen using agar disc diffusion method eventually.

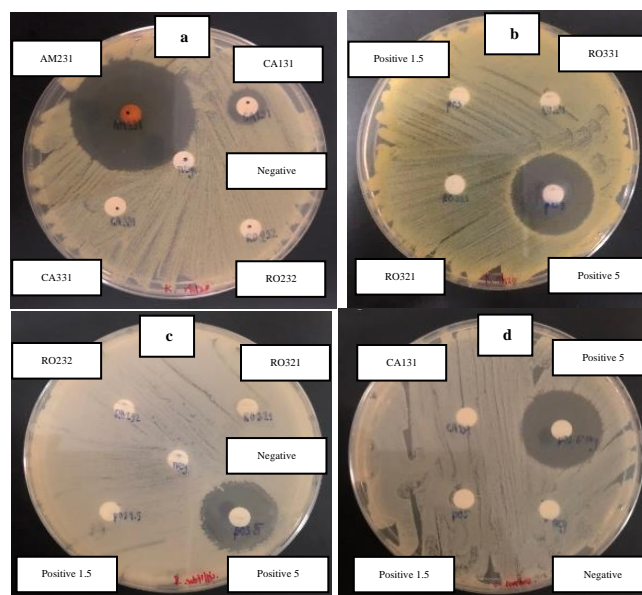


**Fig. 2.** Preliminary screening of some actinomycetes against *Kocuria rhizophila* ATCC 9341, *Staphylococcus aureus* ATCC 25923, *Bacillus subtilis* ATCC 6633, *Pseudomonas aeruginosa* ATCC 27853, *Escherichia coli* ATCC 25922 and *Candida albicans* ATCC 10231 using T'streak method of actinomycete strains AM231 (a), CA131 (b), CA331 (c), RO232 (d), RO321 (e) and RO331 (f) where E: *Escherichia coli* ATCC 25922; K: *Kocuria rhizophila* ATCC 9341; S: *Staphylococcus aureus* ATCC 25923 and B: *Bacillus subtilis* ATCC 6633.

In Fig. 3. show some results of secondary metabolite screening by using agar disc diffusion was performed with the concentration of 50 mg/ml, only strains AM231 and CA131 were able to inhibit *Kocuria rhizophila* ATCC 9341. The inhibition zones were 34.5 and 4 mm., respectively with the concentration of crude extract at 50 mg/ml. and almost of the active compounds had the ability to inhibit gram positive rather than gram negative.

## IV. CONCLUSION

Upon the discovery of new antibiotics from actinomycetes, Thai medicinal plants had been proven as an important resource to study because of abundance numbers of actinomycetes with various distinct morphological and biochemical appearances. The test of antimicrobial activity showed that partially purified extracellular crude extracts of two isolates were able to inhibit the test organisms.



**Fig. 3.** Secondary metabolite screen using agar disc diffusion method of actinomycetes strains AM231, CA131, CA331, RO232, RO321 and RO331 against *Kocuria rhizophila* ATCC 9341 (a) and (b), against *Bacillus subtilis* ATCC 6633 (c) and against *Staphylococcus aureus* ATCC 25923 (d) with Positive control; Kanamycin 1.5 and 5 µg/ml and Negative control; Methanol.

Although partially purified extracellular crude extracts of the isolated strains AM231 and CA131 were able to inhibit *Kocuria rhizophila* ATCC 9341. The inhibition zones were 34.5 and 4 mm. respectively with the concentration of crude extract at 50 mg/ml.

## ACKNOWLEDGMENT

This research was supported by Faculty of Science, King Mongkut's Institute of Technology Ladkrabang, Bangkok, Thailand.

## REFERENCES

- [1] M. Balouiri, M. Sadiki, SK. Ibsouda, "Methods for in vitro evaluating antimicrobial activity". *Journal of Pharmaceutical Analysis* 6:71-79, 2016.
- [2] J. Berdy, "Bioactive microbial metabolites: A personal view". *The Journal of Antibiotics* 58(1):1-26, 2005.
- [3] PS. Kumar, V. Duraipandiyar, S. Ignacimuthu, "Isolation, screening and partial purification of antimicrobial antibiotics from soil *Streptomyces* sp. SCA 7". *The Kaohsiung Journal of Medical Sciences* 30:435-446, 2014.
- [4] M. Mohseni, H. Norouzi, J. Hamed, A. Roohi, "Screening of antibacterial producing actinomycetes from sediments of the Caspian sea". *International Journal of Molecular and Cellular Medicine* 2(2):64-71, 2013.
- [5] L. Mellouli, RB. Ameer-Mehdi, S. Sioud, M. Salem, S. Bejar, "Isolation, purification and partial characterization of antibacterial activities produced by a newly isolated *Streptomyces* sp. US24 strain". *Research in Microbiology* 154:345-352, 2003.
- [6] S. Miyadoh, "Research on antibiotic screening in Japan over the last decade: A producing microorganisms approach". *Actinomycetologica*, 9: 100-106, 1993.
- [7] M. Takisawa, RR. Colwell, RT. Hill, "Isolation and diversity of actinomycetes in the Chesapeake Bay". *Applied and Environmental Microbiology* 59:997-1002, 1993.



- [8] S. Suzuki, K. Yamamoto, T. Okuda, M. Nishio, NK. Nakanishi, S. Matsubara, "Selective isolation and distribution of *Actinomadura rugatobispora* strains in soil". *Actinomycetology* 14:27–33, 2000.
- [9] M. Hayakawa, Y. Yoshida, Y. Iimura, "Selection of bioactive soil actinomycetes belonging to the *Streptomyces violaceusniger* phenotypic cluster". *Journal of General Applied Microbiology* 96:973–981, 2004.
- [10] D. Sharma, T. Kaur, BS. Chadha, RK. Manhas, "Antimicrobial activity of actinomycetes against multidrug resistant *Staphylococcus aureus*, *E. coli* and various other pathogens". *Tropical Journal of Pharmaceutical Research* 10:801–808, 2011.
- [11] R. Barzanti, F. Ozino, M. Bazzicalupo, R. Gabbrielli, F. Galardi, C. Gonnelli, A. Mengoni, "Isolation and characterization of endophytic bacteria from the nickel hyper accumulator plant *Alyssum bertolonii*". *Microbial Ecology* 53:306–316, 2007.
- [12] S. Suzuki, K. Yamamoto, T. Okuda, M. Nishio, N. Nakanishi, S. Komatsubara, "Selective isolation and distribution of *Actinomadura rugatobispora* strains in soil". *Actinomycetology* 14:27–33, 2000.
- [13] T. Teachowisan, JF. Peberdy, S. Lumyong, "Isolation of endophytic actinomycetes from selected plants and their anti-fungal activity". *World Journal of Microbiology and Biotechnology* 19:381–385, 2003.
- [14] KL. Kelly, "Inter-Society Color Council–National Bureau of Standard Color Name Charts Illustrated with Centroid Colors". Washington, DC: US Government Printing Office, 1964.
- [15] T. Arai, "Culture Media for Actinomycetes". Tokyo, Japan: The Society for Actinomycetes, 1975.
- [16] ST. Williams and T. Cross, "Actinomycetes. Methods in Microbiology". London: Academic Press. 295–334, 1971.
- [17] L. Selvameenal, M. Radhakrishnan, R. Balagurunathan, "Antibiotic pigment from desert soil Actinomycetes; biological activity, purification and chemical screening". *Indian Journal of Pharmaceutical Sciences* 71:499–504, 2009.
- [18] DL. Crawford, JM. Lynch, JM. Whipps, MA. Ousley, "Isolation and characterization of actinomycete antagonists of a root pathogen". *Appl Env Microbiol* 59:3889–3905, 1993.
- [19] D. Valois, K. Fayad, T. Barasubiye, M. Garon, C. Dery, R. Brzezinski, C. Beaulieu, "Glucanolytic actinomycetes antagonistic to *Phytophthora fragariae* var. *rubi*, the causal agent of raspberry root rot". *Appl Env Microbiol* 62:1630–1635, 1996.
- [20] WM. Yuan and DL. Crawford, "Characterization of *Streptomyces lydicus* WYEC108 as a potential agent against fungal root and seed rot". *Appl Env Microbiol* 61:3119–3128, 1995.
- [21] VC. Verma, SK. Gond, A. Kumar, A. Mishra, RN. Kharwar, AC. Gange, "Endophytic Actinomycetes from *Azadirachta indica* A. Juss.: Isolation, Diversity, and Anti-microbial Activity". *Microb Ecol* 57:749–756, 2009.
- [22] C. Taule, C. Mareque, C. Barlocco, F. Hackembruch, VM. Reis, "The contribution of nitrogen fixation to sugarcane (*Saccharum officinarum* L.), and the identification and characterization of part of the associated diazotrophic bacterial community". *Plant Soil* 356:35–49, 2012.
- [23] K. Waheeda and KV. Shyam, "Formulation of Novel Surface Sterilization Method and Culture Media for the Isolation of Endophytic Actinomycetes from Medicinal Plants and its Antibacterial Activity". *J Plant Pathol Microbiol* 8(2):1–9, 2017.
- [24] J. Zhang, JD. Wang, CX. Liu, JH. Yuan, XJ. Wang, "A new prenylated indole derivative from endophytic actinobacteria *Streptomyces* sp. neau-D50". *Nat Prod Res* 28:431–437, 2014.

# Isolation of acidophilic fungi for probable using in copper bioleaching process

Nilnate Assavasirijinda<sup>1\*</sup>

<sup>1\*</sup> School of Science, King Mongkut's Institute of Technology Ladkrabang, Bangkok 10520,  
Thailand

E-mail: nilnate.as@kmitl.ac.th

**Abstract:** The rapidly increases improvement of technology, an electrical, and electronic devices become feasibility and essential to life. However, it makes an enormous toxic waste which widely spread to environment due to it is difficult to decompose. Scientists try to overcome this problem. Waste electrical and electronic equipment (WEEE) contains 3-5 wt% of waste printed circuit boards (WPCBs) which comprising of precious metal such as Au, Ag, Ni, Cu etc. Bioleaching method can use to recover metal ion from WPCBs which are low-cost, low energy consume and eco-friendly method. Filamentous fungi can be used in bioleaching of metals belong to it contain acid secretion ability and metal solubilizing ability. In this study, the researcher focuses on filamentous fungi that can be applied to copper bioleaching from WPCBs. The soil samples were collected from heavy metal contaminated areas at Ladkrabang Bangkok, Thailand. The fungi were isolated on 9K medium and tested the resistant ability against various copper sulphate concentrations. Besides, the growth on complex PDA medium were compared with defined 9K medium with and without copper sulphate. The result shown that the isolated fungi can be tolerated to the highest copper sulfate concentration of 1,000 mM in 9K medium. Moreover, all isolated fungi were shown higher copper-tolerant ability in 9K medium than PDA. This study suggested that 9K medium is suitable for isolating metal ion tolerant fungi for further study.

**Index Terms—** Acidophilic fungi, Bioleaching, Copper tolerant, 9K medium

## I. INTRODUCTION

Due to technology accelerating, an electrical, and electronic devices have escalated the amount of electronic waste (E-waste) generation. Waste printed circuit boards (WPCBs) are the integral component of E-waste by 3-5 wt% which comprising of precious metal such as Au, Ag, Ni, Cu etc [1,2]. WPCBs usually discards to land fill or improper incinerates by the user and spread a toxic contaminant to environment [3,4]. Many methods can be used for value metal extraction and followed by recycle such as pyrometallurgical, hydrometallurgical, and electrochemical process. However, those are not considered environmentally friendly as it

generates hazardous gases, discard a large volume of effluents and high-energy consumption rates [5]. Bioleaching is an eco-friendly method for recovery metal ion from WPCBs which are low-operating cost and low energy consume [6]. Several microorganisms have ability to use in bioleaching process for recoveries of Cu, Sn, Al, Ni, Pb and Zn from WPCBs such as bacteria (*Acidithiobacillus ferrooxidans*, *Acidithiobacillus thiooxidans*) and fungi (*Aspergillus niger* and *Penicillium simplicissimum*) [7-9].

Dissolution of metals is mainly caused by the ability of fungi to secrete acid. The bioleaching reaction such acidolysis (acid-base reaction), redoxolysis, bioaccumulation, chelate, and complex formation mechanisms will associate metal solubilization [10-12]. Many fungi were

Management, Business administration, Engineering, Science and Technology investigated biological recovery of WPCBs such as *Aspergillus niger*, *Aspergillus tubingensis*, and *Penicillium simplicissimum* and shown high copper leaching capacity of 65-95% [13].

In this study, the researcher interest and focuses on filamentous fungi belonging to their organics secretion ability. Besides, filamentous fungi usually can be tolerant to high metal ion concentrations [14,15]. 9K medium is a defined medium which normally use to culture lithotroph microorganism at pH 2.0 [16]. The iron-oxidizing bacteria which one of the lithotroph organism is well known to be use in bioleaching process of low-grade ores, urban waste, mine tailings, spent catalyst, and electronic waste [17-19]. The aim of this study is to use 9K medium for isolating acidophilic filamentous fungi with copper tolerant ability which is potentially used in copper bioleaching from WPCBs.

## II. METHODOLOGY

### 1. Sample collection



The soil samples were collected from PCBs contaminating area at Lardkrabang Bangkok, Thailand. The sample collecting sites were named as YGS and YGD with GPS coordinates of 13.699956595521988°N, 100.78521106392145°E. The samples were determining soil pH and temperature and shown in table I.

### 2. Fungal isolation

Microorganism was enriched by adding 10g of soil sample in 100 ml modified 9K medium with altered pH about of 2.0 [16] comprising of 10 mM of copper sulphate. Cultures were incubated at 37 °C, 180 rpm for 14 days. After incubation, cultures were serial diluted and spreaded on 9K agar medium following by 37 °C incubation until colony were appeared. Isolated fungi were sub-cultured and kept in the same medium for further use. Each isolate was stained by lactophenol cotton blue and observed under microscope.

TABLE I

SAMPLE COLLECTING SITE AND DESCRIPTIONS

Sample name	Picture at site of sample taken	pH	Temp (°C)
YGS		6	32
YGD		8	28







### 3. Copper tolerant and effect of growth media

Copper tolerant ability were tested on 9K agar medium with various concentrations of 20, 50, 100, 500, 1,000 and 1,500 mM. The test cultures were incubated at 37 °C for 21 days. Then effect of culture medium was observed and compared between complex PDA and defined 9K agar medium, colony diameter was observed under the same previous condition.

## III. RESULTS AND DISCUSSION

The soil samples were collected from PCBs contaminated area. Acidophilic fungi were isolated on 9K agar with 10 mM of copper sulfate and was sub-cultured as a pure culture. Three strains were primarily observed mycelia under microscope as shown in table II and the strains were named as YGS1, YGD1 and YGD2. The YGS1 was obtained from YGS sampling site which collecting at 10cm in depth under the soil surface. The YGD1 and YGD2 were obtained from YGD sampling site which collecting at the soil surface. The characteristic conidia of three fungi shown vesicle, sterigma and conidiospore which belonging to *Aspergillus* species.

TABLE II  
ISOLATED FUNGI ON 9K AGAR AND CONIDIA  
CHARACTERISTICS

Strain	Colony on 9K agar	Conidia
YGS1		
YGD1		
YGD2		

The three strains were tested on 9K medium with various copper sulfate concentrations and colony were observed. The result showed that all three strains can tolerance to copper sulfate up to 1000 mM in 9K medium with 21 days of incubation and cannot grow at above concentration (data not shown). However, colony diameter in 1000 mM of copper sulfate is significant smaller than in 500 mM as showed in Table III. Therefore, effect of medium culture experiment will use 500 mM of copper sulfate in 9K agar to compare with PDA medium.

When cultured the three strains in PDA, its show rapidly growth and full plate of colony size were observed within 14 days. However, the strain can tolerance to copper sulfate up to 50 mM in PDA and cannot grow at above concentration (data not

shown). In PDA medium, conidia and spore formation were observed from 14 days of incubation (full plate with spore formation; FWS) while 9K medium can promote full plate of growth but lack of spore formation (full plate without spore formation; FWOS) (Table IV). However, it can produce spore after 28 days of incubation. The results can be noted that when the three strain were cultured in defined 9K medium, the spore formation of fungi will be retarded. However, three acidophilic fungi were showing higher copper tolerant ability in defined 9K medium than complex PDA medium. Colony diameter in PDA with 50 mM copper sulphate were smaller than in 9K agar with 500 mM copper sulfate. (Table IV) Therefore, high copper tolerant stain will be obtained by using defined 9K medium for isolation.

Reyes Sierra-Alvarez [20] had been reported Cu tolerant threshold of white-rot and brown-rot fungi. The brown-rot fungi including many *Aspergillus* species generally showed higher tolerance towards copper inhibition than white-rot fungi which the highest Cu concentration threshold of 32 mM.

Cánovas et.al. [21] had been isolated *Aspergillus* sp. P37 from the River Tinto in Spain. The fungi can be tolerant to many metal ions such as arsenic, chromium and copper. *Aspergillus* sp. P37 can tolerate up to 50 mM of copper sulphate. However, this study has achieved *Aspergillus* sp. YGS1, YGD1 and YGD2 strains which can tolerate 20-fold higher than those *Aspergillus* sp. P37.

Thenmozhi et.al. [22] had been isolated *Aspergillus* species from an abandoned copper mine soil by using PDA medium and reported MIC value against copper (II) concentration. The *Aspergillus hiratsukae* LF1 and *Aspergillus terreus* LF2 grew well till the Cu (II) concentration of 500 mg/L which equal to 3.133 mM. This previous research revealing that the use of PDA medium for isolation will obtain lower copper tolerant than using 9K medium.

TABLE III  
COPPER SULFATE TOLERANT OF THREE ACIDOPHILIC FUNGI




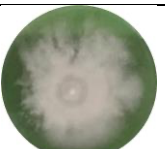

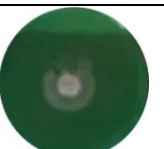



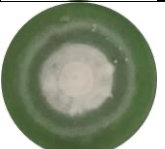

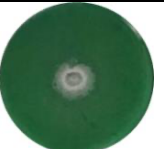




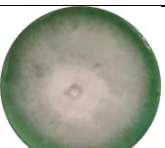
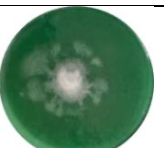
Strain	Copper sulfate concentration in 9K agar medium (mM)					
	0	20	50	100	500	1000
YGS1						
YGD1						
YGD2						

TABLE IV  
EFFECT ON COPPER TOLERANT BY COMPLEX PDA AND DEFINED 9K MEDIUM

Time (days)	Colonies diameter (cm)											
	9K			9K with 500 mM CuSO <sub>4</sub>			PDA			PDA with 50 mM CuSO <sub>4</sub>		
	YGS1	YGD1	YGD2	YGS1	YGD1	YGD2	YGS1	YGD1	YGD2	YGS1	YGD1	YGD2
7	4.72±0.48	4.77±0.38	5.66±0.33	0.69±0.15	0.82±0.27	1.17±0.07	4.45±0.07	3.88±0.11	4.38±0.16	-	-	-
14	FWOS	FWOS	FWOS	2.60±0.07	2.38±0.43	2.91±0.14	FWS	FWS	FWS	2.33±1.27	0.49±0.26	2.62±0.12
21	FWOS	FWOS	FWOS	4.75±0.10	5.05±0.16	4.00±0.49	FWS	FWS	FWS	2.18±1.48	1.10±0.00	4.10±0.71

FWOS - Full plate without spore formation

FWS – Full plate with spore formation

suitable for isolating acidophilic fungi with metal

### I. CONCLUSION

This study successfully isolates acidophilic fungi with copper tolerant ability by using defined 9K medium. The three fungi, *Aspergillus* sp. YGS1, YGD1 and YGD2 are shown highest copper sulphate tolerance up to 1000 mM which is 20-fold higher than previous report. Besides, the comparison between complex PDA and defined 9K medium with and without copper sulfate showing that defined 9K medium is

tolerant ability and high metal tolerant stain will be achieved. Since, The YGS1, YGD1 and YGD2 grew in the 9K containing 1000 mM of copper sulphate with pH2.0, this might be suitable and favorable for using in copper bioleaching process of PCBs. However, copper bioleaching ability should be performed for future research.

ACKNOWLEDGMENT

The authors would like to acknowledge the Yingcharoen recycling shop, soi Lardkrabang 54 for providing the soil samples.

REFERENCES

- [1] Kaya, M., (2017) Recovery of metals and nonmetals from waste printed circuit boards (PCBs) by physical recycling techniques. In: Energy Technology, Springer, pp. 433e451. <https://doi.org/10.1007/978-3-319-52192-3>.
- [2] Priya, A., Hait, S., (2017) Comparative assessment of metallurgical recovery of metals from electronic waste with special emphasis on bioleaching. Environ. Sci. Pollut. Res. 24, 6989e7008. <https://doi.org/10.1007/s11356-016-8313-6>.
- [3] Cao, J., Lu, B., Chen, Y., Zhang, X., Zhai, G., Zhou, G., Jiang, B., Schnoor, J.L., (2016) Extended producer responsibility system in China improves e-waste recycling: government policies, enterprise, and public awareness. Renew. Sustain. Energy Rev. 62, 882e894. <https://doi.org/10.1016/j.rser.2016.04.078>.
- [4] Jagannath, A., Vidya Shetty, K., Saidutta, M.B., (2017) Bioleaching of copper from electronic waste using *Acinetobacter* sp. Cr B2 in a pulsed plate column operated in batch and sequential batch mode. J. Environ. Chem. Eng. 5, 1599e1607. <https://doi.org/10.1016/j.jece.2017.02.023>.
- [5] Ilyas, S., Anwar, MA., Niazi, SB., Afzal Ghauri, M., (2007) Bioleaching of metals from electronic scrap by moderately thermophilic acidophilic bacteria. Hydrometallurgy 88:180–188. <https://doi.org/10.1016/j.hydromet.2007.04.007>.
- [6] Brierley, CL., (2016) Innovative process development in metallurgical industry: Concept to commission. Innov Process Dev Metall Ind Concept to Comm 1–140. <https://doi.org/10.1007/978-3-319-21599-0>
- [7] Arshadi, M., Mousavi, S.M., (2014) Simultaneous recovery of Ni and Cu from computer-printed circuit boards using bioleaching: statistical evaluation and optimization. Bioresour. Technol. 174, 233e242. <https://doi.org/10.1016/j.biortech.2014.09.140>.
- [8] Brandl, H., Bosshard, R., Wegmann, M., (1999) Computer-munching microbes: metal leaching from electronic scrap by bacteria and fungi. Process Metall. 9, 569e576. [https://doi.org/10.1016/S1572-4409\(99\)80146-1](https://doi.org/10.1016/S1572-4409(99)80146-1).
- [9] Jadhav, U., Su, C., Hocheng, H., (2016) Leaching of metals from printed circuit board powder by an *Aspergillus Niger* culture supernatant and hydrogen peroxide. RSC Adv. 6, 43442e43452. <https://doi.org/10.1039/C6RA04169H>.
- [10] Asghari, I., Mousavi, S.M., Amiri, F., Tavassoli, S., (2013) Bioleaching of spent refinery catalysts: a review. J. Ind. Eng. Chem. 19, 1069–1081. <https://doi.org/10.1016/j.jiec.2012.12.005>.
- [11] Borja, D., Nguyen, K.A., Silva, R.A., Park, J.H., Gupta, V., Han, Y., Lee, Y., Kim, H., (2016) Experiences and future challenges of bioleaching research in South Korea. Minerals 6, 1–21. <https://doi.org/10.3390/min6040128>.
- [12] Le, L., Tang, J., Ryan, D., Valix, M., (2006) Bioleaching nickel laterite ores using multi-metal tolerant *Aspergillus foetidus* organism. Miner. Eng. 19, 1259–1265. <https://doi.org/10.1016/j.mineng.2006.02.006>.
- [13] Dusengemungu, L., Kasali, G., Gwanama, C., Mubemba, B., (2021) Overview of fungal bioleaching of metals. Environ. Adv. 5, 100083.
- [14] Burgstaller, W., Schinner, F., (1993) Leaching of metals with fungi. J. Biotechnol. 27, 91–116. [https://doi.org/10.1016/0168-1656\(93\)90101-R](https://doi.org/10.1016/0168-1656(93)90101-R).
- [15] Gadd, G.M., Bahri-Esfahani, J., Li, Q., Rhee, Y.J., Wei, Z., Fomina, M., Liang, X., (2014) Oxalate production by fungi: Significance in geomycology, biodeterioration and bioremediation. Fungal Biol. Rev. 28, 36–55. <https://doi.org/10.1016/j.fbr.2014.05.001>.
- [16] Silverman, MP., Lundgren, DG. (1959) Studies on the chemoautotrophic iron bacterium *Ferrobacillus ferrooxidans*. J Bacteriol, 78:326
- [17] Ilyas, S., Chi, R., Lee, J.-C., (2013) Fungal bioleaching of metals from mine tailing. Miner. Process. Extr. Metall. Rev. An Int. J. 37–41. <https://doi.org/10.1080/08827508.2011.623751>.
- [18] Kumar, A., Prabhu, S.V., (2015) Fungal and Bacterial Bioleaching Studies On Bauxite Fungal and Bacterial Bioleaching Studies On Bauxite. <https://doi.org/10.13140/RG.2.1.4730.7367>.
- [19] Mulligan, C.N., Kamali, M., Gibbs, B.F., (2004) Bioleaching of heavy metals from a low- grade mining ore using *Aspergillus niger*. J. Hazard. Mater. 110, 77–84. <https://doi.org/10.1016/j.jhazmat.2004.02.040>.
- [20] Reyes Sierra-Alvarez. (2007) Fungal bioleaching of metals in preservative-treated wood Process Biochemistry, 42(5): 798-804.
- [21] Cánovas, D., Durán, C., Rodríguez, N., Amils, R. and De Lorenzo, V. (2003), Testing the limits of biological tolerance to arsenic in a fungus isolated from the River Tinto. Environmental Microbiology, 5: 133-138. <https://doi.org/10.1046/j.1462-2920.2003.00386.x>
- [22] Thenmozhi M. Palanivel, Bernhard Pracejus, Luís A. B. Novo. (2023), Bioremediation of copper using indigenous fungi *Aspergillus* species isolated from an abandoned copper mine soil. Chemosphere, 314: 137688



**Organized by** King Mongkut's Institute of Technology Ladkrabang  
Prince of Chumphon Campus, Chumphon  
(KMITL Prince of Chumphon)